Université de Lille
École Doctorale Sciences de l'ingénierie et des systèmes (ENGSYS)
———————
Institut d'Electronique,
de Microélectronique et de Nanotechnologie (IEMN)
&
THÈSE DE DOCTORAT :

A multiscale mechanical study of flax stems and fibres for the development of an in-the-field tool capable of predicting optimum retting

———————

Une étude mécanique multi-échelle des tiges et des fibres de lin pour le développement d'un outil de terrain capable de prédire le rouissage optimal

Thèse préparée et soutenue à huis-clos par **Ali REDA**
le 07 décembre 2023, pour l'obtention du grade de Docteur de L'Université de Lille en

MICRO-NANOSYSTÈMES ET CAPTEURS

Membres du jury

Ingrid Proriol-Serre, Directeur de Recherche, Université de Lille	**(Présidente)**
Christian Bergaud, Directeur de Recherche, Laboratoire d'Analyse et d'Architecture des Systèmes	**(Rapporteur)**
Pierre Ouagne, Professeur, Ecole Nationale d'Ingénieurs de Tarbes	**(Rapporteur)**
Karine Charlet, Professeur, Université Clermont Auvergne	**(Examinatrice)**
Vincent Placet, Ingénieur de Recherche, Université de Franche-Comté	**(Examinateur)**
Sébastien Grec, Maître de Conférences, Université de Lille	**(Examinateur)**
Simon Hawkins, Professeur, Université de Lille	**(Examinateur)**
Lionel Buchaillot, Directeur de Recherche, Université de Lille	**(Invité)**
Steve Arscott, Directeur de Recherche, Université de Lille	**(Directeur)**

Abstract

Agriculture 4.0, also known under several aliases such as ‘digital agriculture’, ‘smart farming’, and ‘e-farming’ is currently developing rapidly in terms of research, development, and commercial applications. As with Agriculture 1.0, 2.0, and 3.0, the objective of Agriculture 4.0 is the use of technology to improve all areas of agriculture. In Agriculture 4.0 it is the application of microelectronics and microtechnologies. Unlike before, these technologies bring things such as the internet-of-things, big data, telecommunications, novel sensing, rapid feedback, data analysis, connectivity, artificial intelligence etc. In principle, all these areas should result in a massive modernization of farming in terms of organisation, yield, efficiency, and quality of produce. However, Agriculture 4.0 is so vast that if one is to contribute to it, even in a minor way, one has to choose a specific area to contribute. The area chosen for the study in this PhD was flax fibre production. Flax fibres are naturally strong fibres which can be extracted from flax stems. The flax stems have evolved to have robust micrometre-diameter fibres running the length of the outside of the stem, and held in place in the external tissue of the stem. Once extracted and isolated, flax fibres have numerous applications ranging from textiles to composite materials. In order to facilitate the mechanical extraction of flax fibres from their parent stems, the stems undergo a process known as ‘retting’. Retting leads to the breakdown of the external tissue (known as the middle lamella) between the fibres. A common form of retting is known as ‘dew retting’. In dew retting, natural processes such as bacteria and fungi result in enzymes which break down the middle lamella and gradually separate fibre bunches and fibres from bunches. The length of dew retting depends heavily on the weather. Too little retting results in difficult fibre extraction in the factory, too much retting can result in a compromise in fibre quality. It has long been known that there is an optimum retting point–even the ancients knew this. Certain skilled artisan farmers are able to judge this point via a combination of manual manipulation of the stems, observation of damage caused to the external tissue via this manoeuvre, and also observing the colour and the smell of the stems during this very skilled, but artisanal, testing. It is clear that the artisan is performing rudimentary laboratory tests quite literally ‘in-the-field’. It would seem logical therefore to try to quantify such tests and see if a reliable tool can be made to help the artisan. And indeed, this is exactly what others have attempted. The introduction of the PhD gives examples of attempts to make optimal-retting tools in the 1980s and after. Inspired by this early work, the work of this PhD attempts a full multiscale mechanical characterization of flax stems and fibres during a retting cycle (summer 2022) and, somewhat ambitiously, performed in real time–to our knowledge for the first time. The mechanical characterization involved macroscopic mechanical tests (stem bending, crushing, and twisting), as well as novel microscopic mechanical testing of single flax fibres using novel methods inspired by microelectromechanical systems (MEMS) methods. In addition, the nanoscopic mechanical properties of the primary cell wall of retting flax fibres was characterised using nanoindentation atomic force microscopy (AFM). As the experimental work, analysis via analytical modelling, and interpretation descends in scale from macro, through micro, to nano, we learn a little more of how the retting affects the stems, their properties, and their fibres. In addition to simply learning, a very positive outcome of the PhD is that one is able to suggest a mechanically-induced damage mechanism in stems which could be the basis for a tool. One can note however, that the uncontrollable multiparameter nature of the subject, e.g. the weather, means that several studies would be needed to confirm beyond doubt observations from a single retting cycle.

Résumé

L'agriculture 4.0, également connue sous plusieurs pseudonymes tels que "agriculture numérique", "agriculture intelligente" et "agriculture électronique", se développe actuellement rapidement en termes de recherche, de développement et d'applications commerciales. Comme pour l'agriculture 1.0, 2.0 et 3.0, l'objectif de l'agriculture 4.0 est d'utiliser la technologie pour améliorer tous les domaines de l'agriculture. Dans l'agriculture 4.0, il s'agit de l'application de la microélectronique et des microtechnologies. Contrairement à ce qui se passait auparavant, ces technologies apportent des éléments tels que l'internet des objets, les données massives, les télécommunications, les nouveaux capteurs, le retour d'information rapide, l'analyse des données, la connectivité, l'intelligence artificielle, etc. En principe, tous ces domaines devraient entraîner une modernisation massive de l'agriculture en termes d'organisation, de rendement, d'efficacité et de qualité des produits. Cependant, l'agriculture 4.0 est tellement vaste que si l'on veut y contribuer, même de façon mineure, il faut choisir un domaine spécifique. Le domaine choisi pour l'étude de ce doctorat est la production de fibres de lin. Les fibres de lin sont des fibres naturellement solides qui peuvent être extraites des tiges de lin. Les tiges de lin ont évolué pour avoir des fibres robustes d'un diamètre de l'ordre du micromètre qui courent le long de l'extérieur de la tige et sont maintenues en place dans le tissu externe de la tige. Une fois extraites et isolées, les fibres de lin ont de nombreuses applications, allant des textiles aux matériaux composites. Afin de faciliter l'extraction mécanique des fibres de lin de leurs tiges mères, les tiges subissent un processus connu sous le nom de « rouissage ». Le rouissage entraîne la décomposition du tissu externe (appelé lamelle moyenne) entre les fibres. Une forme courante de rouissage est connue sous le nom de « rouissage de rosée ». Dans le rouissage de la rosée, des processus naturels tels que les bactéries et les champignons produisent des enzymes qui décomposent la lamelle centrale et séparent progressivement les grappes de fibres et les fibres des grappes. La durée du rouissage dépend fortement des conditions météorologiques. Un rouissage insuffisant entraîne une extraction difficile des fibres dans l'usine, tandis qu'un rouissage excessif peut compromettre la qualité des fibres. On sait depuis longtemps qu'il existe un point de rouissage optimal - même les anciens le savaient. Certains agriculteurs artisans qualifiés sont capables de juger ce point par une combinaison de manipulation manuelle des tiges, d'observation des dommages causés aux tissus externes par cette manœuvre, et aussi d'observation de la couleur et de l'odeur des tiges au cours de ce test très habile, mais artisanal. Il est clair que l'artisan effectue des tests de laboratoire rudimentaires littéralement « sur le terrain ». Il semblerait donc logique d'essayer de quantifier ces tests et de voir si un outil fiable peut être mis au point pour aider l'artisan. Et c'est exactement ce que d'autres ont tenté de faire. L'introduction de la thèse donne des exemples de tentatives de fabrication d'outils de rouissage optimal dans les années 1980 et suivantes. Inspirés par ces premiers travaux, les travaux de cette thèse tentent une caractérisation mécanique multi-échelle complète des tiges et des fibres de lin pendant un cycle de rouissage (été 2022) et, de manière quelque peu ambitieuse, réalisée en temps réel - à notre connaissance pour la première fois. La caractérisation mécanique comprend des essais mécaniques macroscopiques (flexion, écrasement et torsion de la tige), ainsi que des essais mécaniques microscopiques inédits sur des fibres de lin individuelles à l'aide de nouvelles méthodes inspirées des systèmes microélectromécaniques (MEMS). En outre, les propriétés mécaniques nanoscopiques de la paroi cellulaire primaire des fibres de lin en cours de rouissage ont été caractérisées à l'aide de la microscopie à force atomique (AFM) par nanoindentation. Au fur et à mesure que le travail expérimental, l'analyse via la

modélisation analytique et l'interprétation descendent en échelle, de la macro au nano en passant par le micro, nous en apprenons un peu plus sur la manière dont le rouissage affecte les tiges, leurs propriétés et leurs fibres. En plus de l'apprentissage, un résultat très positif du doctorat est que l'on est capable de suggérer un mécanisme de dommage induit mécaniquement dans les tiges, qui pourrait être la base d'un outil. On peut cependant noter que la nature multiparamétrique incontrôlable du sujet, par exemple le temps, signifie que plusieurs études seraient nécessaires pour confirmer sans aucun doute les observations d'un seul cycle de rouissage.

Acknowledgements

Overcoming self-doubt and having faith in your ability to contribute significantly to your field through your PhD research is crucial. I want to express my gratitude to those who played an indispensable role in the completion of this Ph.D. work and its journey.

Firstly, I extend my thanks to the members of the Ph.D. jury for accepting the task of reviewing and evaluating my work. Their supportive feedback on the manuscript and the enriching discussion, comments, and advice during the defence were invaluable.

I want to express my appreciation to Lionel Bouchaillot and Steve Arscott, my supervisors, for their guidance throughout my Ph.D.. Lionel supervised me for the first year and a half, demonstrating kindness and support that motivated me to explore and develop my ideas. His thoughtful messages during Christmas and New Year were a testament to his encouraging nature. Lionel always believed in my ability to overcome challenges, assuring me that the Ph.D. journey would be successful. Steve's support extended beyond academic matters, teaching me the importance of working smart rather than simply working hard. His emphasis on simplicity and the continuous flow of insightful ideas significantly contributed to the success of the Ph.D. Steve's commitment was evident in his active participation in the project. I must highlight Steve's involvement in the flax sample gathering, an activity I considered my absolute duty. Our journeys from Lille to Killem, the memorable stops at the gas station for coffee, and the humorous debates over who would pay the bill for the coffee! The experiences we shared during mechanical testing, including bending stalks and crushing samples in the clean room using water-filled beakers on a microscope worth a lot of money, were truly memorable. No amount of thanks can adequately convey my appreciation for Steve's mentorship and support.

I extend my sincere thanks to the VRF Company for granting us permission to gather flax samples from their fields. Additionally, I want to express my gratitude to the Glycoprotein team at the UGSF lab, particularly Simon Hawkins and Sebastien Grec, for their efforts during the first year of the Ph.D. and in facilitating the collaboration between the IEMN and VRF. Special appreciation also goes to Anne-Sophie Blervacq and Anne Creach for their guidance during the biochemical experiments. Their support was invaluable, particularly in the initial phase before the re-orientation of the project.

I want to extend my appreciation to Louis Thomas for his significant contributions to the nanoindentation experiments during my PhD. His assistance and expertise were invaluable in designing and executing these experiments. I also want to express my gratitude to Thomas Dargent for his support in conducting experiments and designing the setup for dynamic micromechanical tests. A special thank you goes to Jean-Michel Mallet for the designing and fabrication of all the mechanical apparatuses used in the thesis experimentations. Their contributions played a crucial role in the success and advancement of this PhD.

I want to express my great gratitude to the administrative staff at IEMN, with special appreciation for Nathalie and Nora. They have consistently shown patience and

understanding, never tiring of my inquiries and requests. Their support has been crucial throughout, and I'm truly thankful for their dedication. A special mention goes to Fanny, whose assistance has significantly contributed to the improvement of my French. Fanny deserves the utmost thanks for her invaluable help and support.

A big thank you goes to Mohammad Jaber and my friends, the three Alis, for attending the defence. Your presence on that significant day means a lot to me. Our friendship spans nine years, and from the beginning of our journey in France until now, holds cherished memories. Your unwavering support played a crucial role in making my educational journey and graduation possible.

I extend my sincere gratitude to Pinar Eriboll for being a constant presence during my thesis journey. Your support, especially during health challenges, has been invaluable, and I appreciate your unwavering companionship.

Finally, to all my Lebanese friends, with whom I shared the best moments during lunch breaks in SH1, I want to express my deepest thanks. The camaraderie and memories created during my thesis journey are treasured, and I am truly grateful to have you as friends. Your presence during the "Defense pot" celebration meant a lot to me. The support you brought into that moment, coupled with the thoughtful gift you shared, touched me in ways words fail to capture. Thank you, from the depths of my heart, for being an integral part of this beautiful chapter in my life. Special thanks to Eyad Alsouki for sharing the best Sobheyye ever with shisha during my thesis journey. Our friendship added a special touch to this memorable period.

أَحْبَائِي الْغَالِيِينَ أَبِي وَأُمِي، أَخِي الْعَزِيزِ،

" تَتَعْثَرُ كَلِمَاتِي فِي مُحَاوَلَةِ الْتَّعْبِيرِ عَنِ الشُّكْرِ الْعَمِيقِ وَالِامْتِنَانِ الَّذِي يَمْلَأُ قَلْبِي نَحْوَكُم. كُنتُمْ رُكَيْزَةَ حَيَاتِي وَمَصْدَرَ قُوَّتِي، تَشْرَقُونَ بِالْحُبِّ وَالْعِنَايَةِ، وَتُضِيءُونَ لِي الطَّرِيقَ بِكُلِّ اخْتِصَارَاتِهِ وَتَفَاصِيلِهِ. لَقَدْ كُنتُمْ الرُّوحَ الدَّاعِمَةَ، وَالْيَوْمَ وَصَلْتُ إِلَى قُمَّةِ رَحِيلَتِي الْعِلْمِيَّةِ بِفَضْلِ صَبْرِكُمُ اللَّا مَحْدُودِ وَتَضْحِياتِكُمُ الْكَبِيرَةِ. فِي هَذِهِ اللَّحْظَةِ الْفَارِقَةِ، أَدْرَكُ بِوَضْوحِ أَنَّ النَّجَاحَ الَّذِي حَقَّقْتُهُ لَيْسَ إِلَّا ثَمَرَةً حُبِّكُمْ وَتَحْفِيزِكُمُ الدَّائِمِ.

شُكْرًا لَكُمْ عَلَى كُلِّ دَمْعَةٍ وَابْتِسَامَةٍ، عَلَى كُلِّ لَحْظَةٍ قَضَيْتُمُوهَا فِي الدَّعْمِ وَالتَّشْجِيعِ. لَقَدْ جَعَلْتُمُونِي أُدْرِكُ أَنَّ الْحُبَّ الْعَائِلِيَّ هُوَ الْقُوَّةُ الْحَقِيقِيَّةِ وَرَاءَ أَيِّ إِنْجَازٍ. شُكْرًا لَكُمْ عَلَى كُلِّ شَيْءٍ، أَنْتُمْ أَغْلَى مَا أَمْلِكُ وَأَنَا مُمْتَنٌ بِلَا حُدُودٍ لَكُمْ فِي كُلِّ لَحْظَةٍ مِنْ حَيَاتِي."

Contents

Chapter 1

Introduction

The emergence of Agriculture 4.0

Agriculture is a fundamental sector that provides people with essential food and raw materials. As the world's primary source of food, agriculture has played a central role in the progress of civilisations throughout human history. According to the United Nations (UN), the world's population is expected to grow by around 2 billion people by 2050, reaching a total of around 11 billion by the end of the century. As a result, there is an urgent need to increase global food production to meet the demands of this growing population. However, according to the Food and Agriculture Organization of the United Nations (FAO), the imperative of alleviating hunger and ensuring food security may not necessarily require a significant increase in agricultural production, even up to 50%, provided that agricultural production systems adopt greater sustainability measures.

In today's world of significant technological advances in a wide range of fields, the integration of technology and research efforts will be key to the achievement of sustainable agriculture. In this context, precision agriculture is of paramount importance to ensure food security for a growing world population (Chanal & Kakkasageri, 2020). Precision agriculture also known as “Smart Agriculture”, “Smart Farming”, “Digital Agriculture” or Agriculture 4.0 aims to optimise productivity, efficiency and sustainability in the agricultural sector. This involves the use of technologies such as microelectronics, micro- and nanotechnologies, communications, Internet of Things (IoT), cloud computing, robotics, and artificial intelligence (AI) to improve various aspects of farming practices. As a result, digital data plays an important role in agriculture, including electronic communication between suppliers and end customers (Fortino et al., 2018) (X. Yang et al., 2021).

Smart agriculture is emerging as a product of an agricultural revolution that is intertwined with the trajectory of the industrial revolution. This symbiotic relationship stems from the central role of industry, machinery and technology in shaping the landscape of smart agriculture. The industrial revolution, with its transformative impact, serves as the cornerstone upon which the agricultural revolution builds and evolves. This transformation has also had a profound impact on various aspects of society (Patil & S. P. Shekhawat, n.d.). The confluence of these revolutions has ushered in an era where technological advances harmonise with agricultural practices, leading to the emergence of smart agriculture as a powerful and federative force. Today, as a result of these revolutions, smart agriculture and the integration of digital technology are emerging as dominant trends in the agricultural sector in European countries. The number of farmers using digital technologies in their operations is steadily increasing. This paradigm shift promises to increase productivity, reduce crop damage and optimise the use of resources such as water, fuel and fertiliser through the potential offered by precision farming practices (Patil & S. P. Shekhawat, n.d.).

Why Agriculture 4.0?

Throughout history, several industrial revolutions have shaped industry and introduced mechanisms to improve production efficiency-see Figure 1.

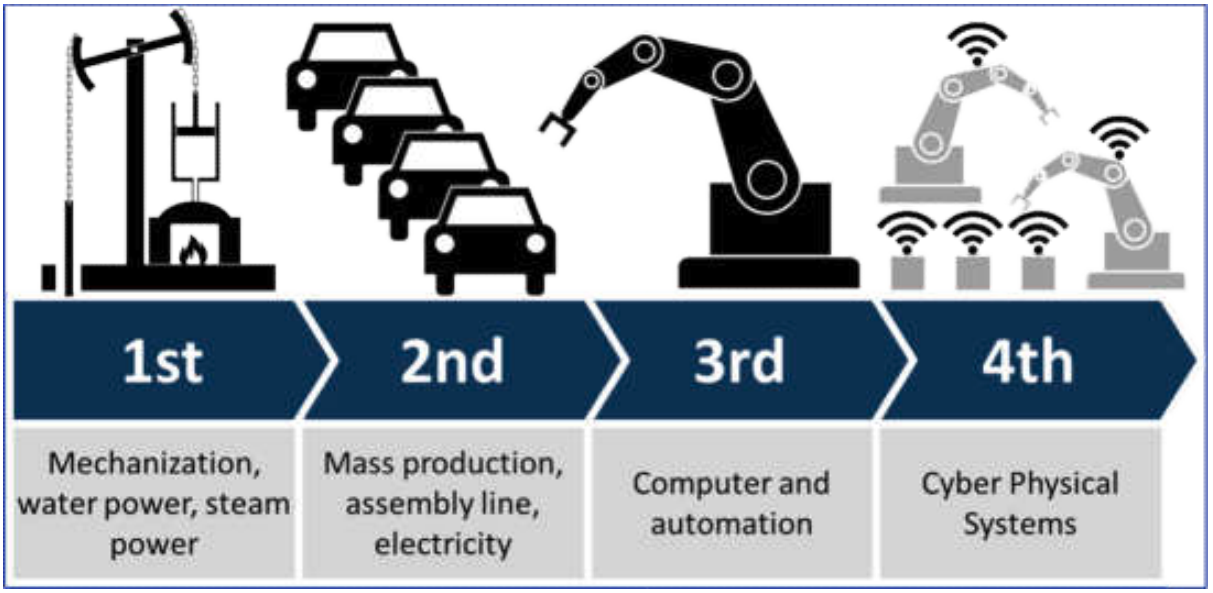

Figure 1: The 4th Industrial Revolution - Industry 4.0. Image taken from (Patil & S. P. Shekhawat, n.d.)

The first revolution, known as Industry 1.0, began in the mid-17th century with the advent of the steam engine, which paved the way for the integration of machines into production processes. The second revolution, Industry 2.0, took place in the late 19th century and was characterised by the widespread use of electricity for both domestic and industrial purposes. The third revolution, Industry 3.0, unfolded throughout the 20th century and was characterised by the introduction of robots and automation into factory processes. We are currently at the Fourth Industrial Revolution, commonly referred to as Industry 4.0. This era is characterised by the concept of the intelligent enterprise, in which interconnected machines and systems aim to achieve the efficiency and adaptability of production systems. In this context, the collection of information plays a central role in production processes. Sensors and other deployed technologies collect data throughout the production area, requiring significant capacity for data storage, processing and analysis to turn it into actionable insights that improve performance (Patil & S. P. Shekhawat, n.d.).

As industry and technological innovation proliferated, a parallel wave of change was set in motion in agriculture. This confluence marked the beginning of an agricultural revolution, a period characterised by the assimilation of industrial principles and technologies into agricultural processes. Agriculture is a large-scale manufacturing industry, and all the industrial revolutions mentioned above have had an impact on the way it is produced today (Patil & S. P. Shekhawat, n.d.).

The progress of agricultural development can be traced through four distinct revolutions discussed by (Liu et al., 2021), as shown in Figure 2. These revolutions include: Agriculture 1.0 the era of traditional agriculture, which relied on human and animal labour. The era of Agriculture 2.0, in parallel with Industry 2.0, significant advances were made with the introduction of the steam engine and electricity to agriculture. The steam tractor played a crucial role in increasing production capacity, particularly in post-harvest processes. The 20th century saw the emergence of Agriculture 3.0, which marked a significant shift towards

the automation of agricultural processes. This era saw the integration of complex machines capable of performing various tasks throughout the agricultural cycle, including planting, harvesting, fertilising, and basic sorting.

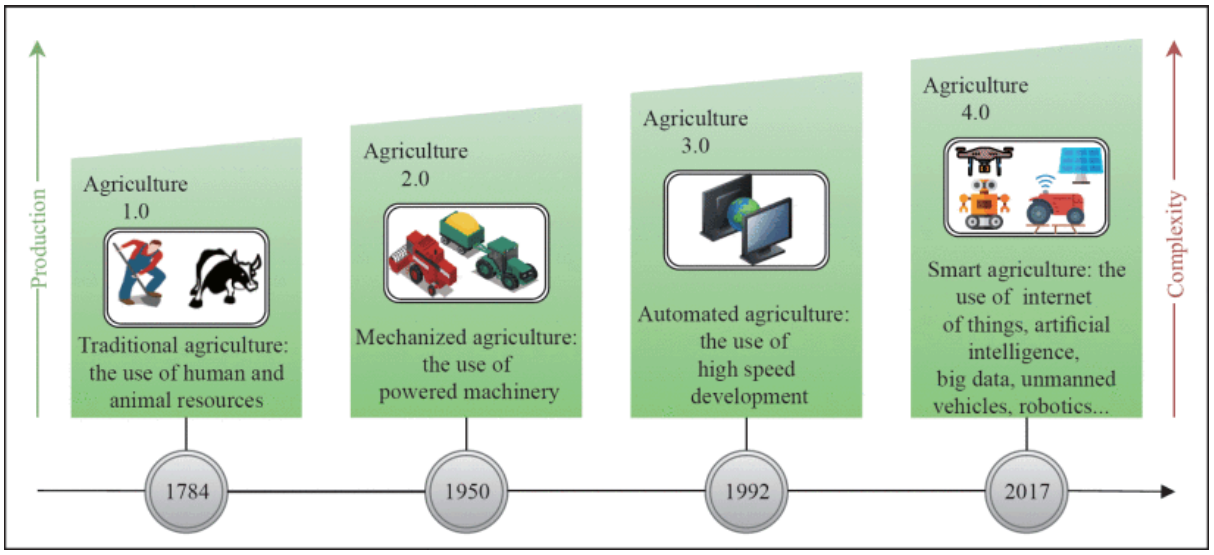

Figure 2: The four agricultural revolutions. In 2023, we are at the start of Agriculture 4.0., taken from (Liu et al., 2021).

At the time of writing this thesis (2023), we are at the beginning of the 4th agricultural revolution. The current era of agriculture, known as Digital Farming or Agriculture 4.0 but also colloquially as Smart Farming, is characterised by the integration of advanced technologies and data-driven approaches into farming operations. This revolution will benefit from two technologies: artificial intelligence, which will assist in decision making, and Big Data, which helps to analyse vast statistical data collected by various techniques(Patil & S. P. Shekhawat, n.d.) (Friha et al., 2021).

These technologies have been developed by various advanced organisations within the Smart Agriculture sector. These sectors play a pivotal role in various agricultural operations, encompassing critical tasks such as soil moisture analysis, crop health assessment, accurate prediction of optimal harvesting times and strategic planning of pest management activities. Using the Internet of Things (IoT) framework technology, agricultural systems can now be remotely controlled via mobile devices, facilitating real-time monitoring of vital parameters such as temperature, humidity and sunlight exposure in production farms. Furthermore, the integration of ‘blockchain technology’ in the agricultural sector, particularly through the implementation of automatic actions or ‘smart contracts’, facilitates the secure storage and traceability of data throughout the supply chain, ensuring the authenticity and provenance of each transaction. This has the potential to reduce instances of dishonesty and fraudulent practices among the various partners involved in the supply chain. The use of drone analytics technology contributes to this technological advancement by capturing high-resolution images of crops. These images are then subjected to extensive analysis using artificial intelligence (AI) techniques, providing valuable insights into crop yield patterns and performance (Chow et al., 1975). The term ‘big data' refers to the storage and analysis of very large volumes of data collected by information and communication technologies

(ICT). This accumulation and rapid analysis of data enables timely decision making, ultimately leading to increased productivity in agriculture. This integration of such advanced technologies not only increases agricultural productivity, but also adds value to the agricultural process (Sung, 2018).

In addition, the notion of smart agriculture encompasses the evolution towards smart farming practices, which involves the modernisation and enhancement of traditional agricultural tools. The ageing of these tools has created the need for their integration into the digital realm (Patil & S. P. Shekhawat, n.d.). The current landscape requires tools that are both robust and universally interoperable, without the need for specialised training to operate them. Agricultural robotics has found applications in various areas, including production, processing, distribution and consumption. Within the agricultural sector, robots have been integrated into a range of equipment for purposes such as product selection and precise distribution of pesticides. This technological approach extends to aerial vehicles used to systematically monitor the health status of fruit, vegetables and livestock in the agricultural environment. Specifically tailored to the Agriculture 4.0 revolution, robotic systems can be divided into three distinct classes. The first category includes open-field robots, strategically deployed for tasks such as crop irrigation and cultivation. In the second, facility robots play a key role in yield assessment and the regulation of farming activities. The third classification relates to livestock robots, which are designed to look after the welfare of animals that are an integral part of the agricultural domain. This diverse integration of robots into agricultural practices underlines their potential to revolutionise and increase the efficiency of modern farming processes (Sung, 2018). In addition, addressing the challenge posed by the limited telecommunications infrastructure in rural areas, the development of Agriculture 4.0 tools has introduced solutions capable of operating seamlessly even in areas without mobile phone coverage, and spanning different sectors of the growing regions (Patil & S. P. Shekhawat, n.d.).

In recent years, significant progress has been made in the automation of mechanical equipment used in agricultural practices, resulting in increased agricultural production. The ability to collect real-time data on various environmental factors, plant growth parameters and crop health has enabled farmers and researchers to make informed decisions, optimise resource allocation and mitigate potential risks. As a result, significant advances have been made in crop management, resulting in improved yields, reduced environmental impact and enhanced product quality (Patil & S. P. Shekhawat, n.d.). This section looks at the latest advances in the use of IoT technology to improve the efficiency of mechanical equipment and systems in the agricultural sector.

Given this context, it is therefore very clear that a key issue in smart agriculture is that of sensor technologies. Let us now have a look at this evolving area.

The development of sensors for Agriculture 4.0

Classification of sensors according to the domain

It is evident, even to the amateur, that there are a myriad of parameters involved in every aspect of agriculture. Until the advent of Agriculture 4.0 most of these parameters were

measured in a very rudimentary way or just ‘judged’ by the artisan farmer. Technological sensing enables one to envisage the quantification of farming parameters like never before.

Sensors used in smart agriculture have a taxonomy based on the specific agricultural areas they monitor (Rajak et al., 2023). For example, optical sensors mounted on vehicles, satellites, drones or robots can use light to assess soil properties and capture plant colour data, while also measuring attributes such as clay content and moisture. Electrochemical sensors, mounted on specialised sledges, contribute to the collection of chemical data, including nutrient levels and pH, with error-free measurements facilitated by ion-selective electrodes. Mechanical soil sensors measure soil compaction by evaluating the forces exerted during soil penetration. Dielectric soil moisture sensors measure moisture content based on the dielectric constant, which is particularly valuable where vegetation is sparse. Location sensors, similar to agricultural weather stations, use GPS satellites to determine positional data across fields. Electronic sensors attached to field equipment monitor operations and transmit data via communication systems. Airflow sensors, which produce unique signatures influenced by different soil properties, measure air infiltration into the soil. With the advent of the IoT, agricultural sensors now provide real-time data covering various parameters such as air and soil temperature, rainfall, wind speed, chlorophyll content and atmospheric pressure. These sensor classifications contribute significantly to the development and realisation of intelligent agricultural systems, increasing productivity and sustainability (Rajak et al., 2023).

Therefore, the integration of precision agriculture sensors gives farmers access to vital information about various aspects of their crops, including harvest timing, water use, soil health and the need for additional inputs. This data is systematically measured and recorded at regular intervals, enabling informed decision-making and optimised farming practices. The wide range of sensors used in agriculture, collectively referred to as Internet of Things (IoT) sensors or smart farming solutions, holds great promise for the agricultural industry. Through the use of precision agriculture sensors, crop production can be significantly improved, the introduction of pest-resistant and high-yielding crop varieties can be facilitated, and the ever-increasing global demand for food can be more effectively met.

Examples of sensor integration in agriculture.

Nitrogen and phosphorus as essential nutrients for plant growth and their variable availability in soils due to factors such as soil type, location and environmental conditions (H. Singh et al., 2023). Traditional farming practices have relied on outdated methods that lack accurate soil assessments. These methods, based on chemical reactions, have been widely used for their simplicity and cost-effectiveness, but suffer from limitations such as low sensitivity and time-consuming procedures (Saha et al., 2021) (Aragón-Briceño et al., 2021). Recent advances in sensor technology, particularly for monitoring nitrogen and phosphorus (NP), have shown significant progress. Singh and Halder (H. Singh et al., 2023) have used the Internet of Things (IoT) principle to develop an IoT-based (Nitrogen, phosphorus, and potassium) NPK monitoring device–see Figure 3. This real-time wireless sensor system detects soil conditions and accurately determines the optimal timing for fertiliser application. The system integrates a chemical kit and a wireless sensor network, with a compact device containing a Light Dependent Resistor (LDR) and a Light Emitting Diode (LED). The device

is seamlessly connected to an Android-based application via an Arduino Uno and a Wi-Fi module. Initial results from this study show promising results, validated by several field measurements, and demonstrate the potential for further research to improve the functionality of the device and expand its applications. Furthermore, the future prospects of this sensing technology are very promising.

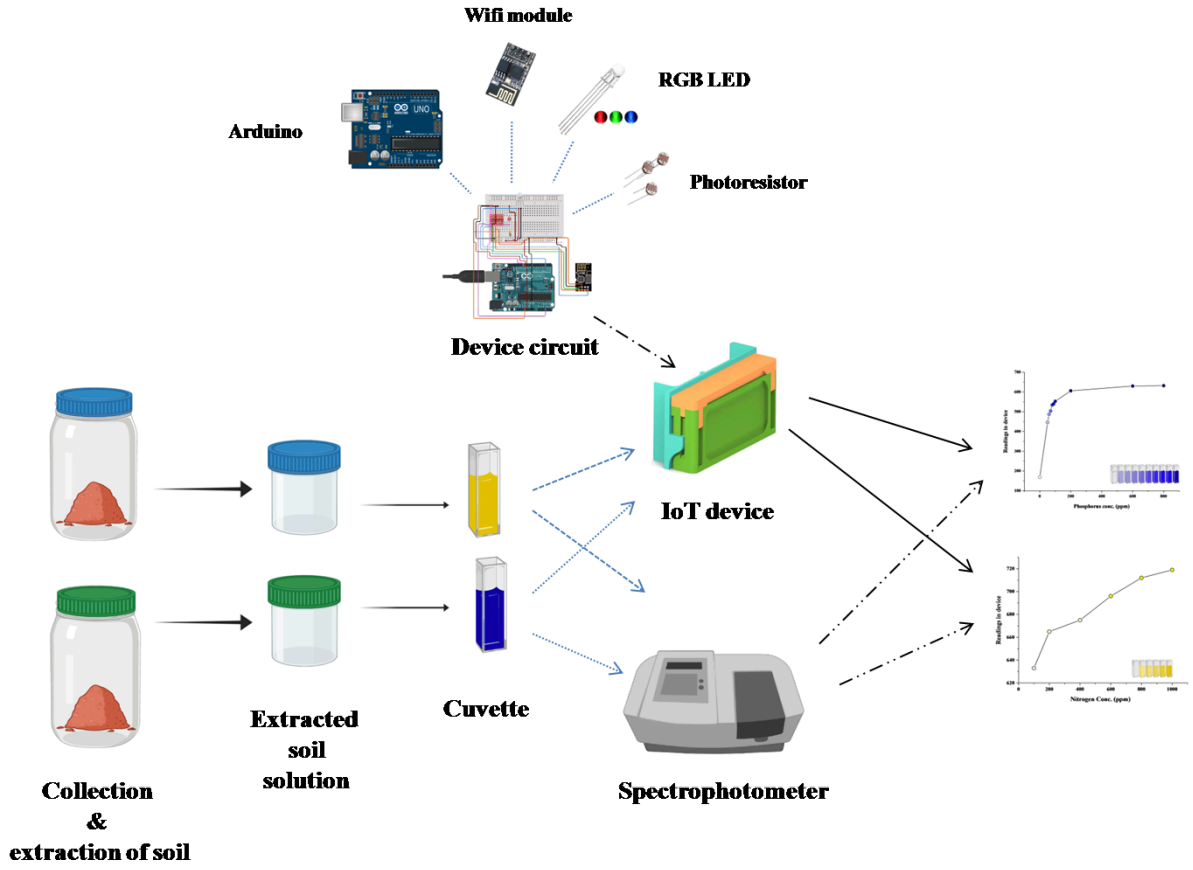

Figure 3. Internet of Things (IoT) principle to develop an IoT-based nitrogen, phosphorous, and potassium (NPK) monitoring device, taken from (H. Singh et al., 2023).

Water flux density (WFD) is a critical parameter for the implementation of smart agriculture, helping to evaluate soil transport properties under extreme conditions (N. Singh & Singh, 2020) (Z. Yang et al., 2015). The Heat Pulse Probe (HPP) technique provides transient measurements of soil thermal and various other properties both in the laboratory and in the field (Z. Yang et al., 2015). By measuring the thermal response of the soil to a heat pulse introduced by the heat probe, the HPP, in particular the Dual Probe Heat Pulse (DPHP), provides enhanced precision and accuracy. The application of the open hardware philosophy allows for improved hardware design and access to code, complementing the open source software (Savanto S, n.d.). Using this philosophy, a sustainable soil irrigation and monitoring system has been developed Figure 4. The system includes steps such as data download, storage and transmission to a web server via GSM communication. The benefits of the open hardware approach include dual data storage for security, full accessibility to authorised

individuals, and convenient data delivery through mobile devices. This platform also creates opportunities for small businesses and reduces costs for end users, as external companies can efficiently design anti-theft systems (Dhall & Agrawal, 2018).

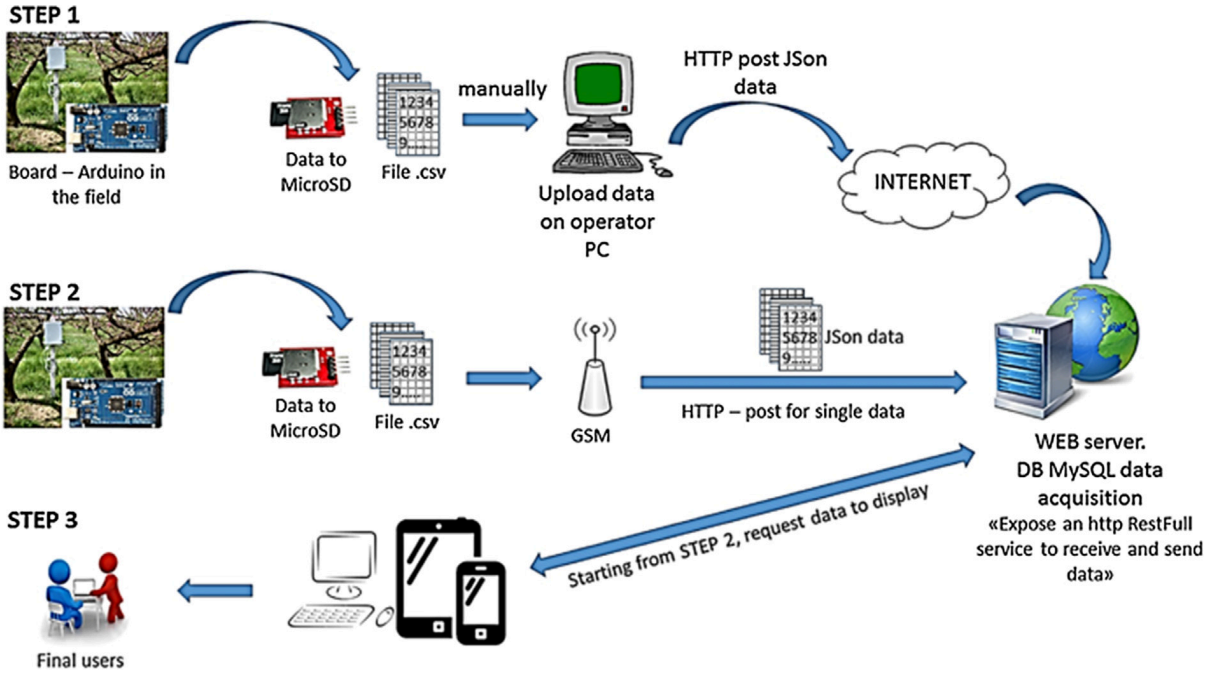

Figure 4. A sustainable soil irrigation and monitoring system developed by Sevanto. Schematic diagram showing how information flows from the field to the end user using different available telecommunications (Perämäki et al., 2001).

Electrical conductivity (EC), along with water content flux density, is a critical factor in understanding soil behaviour and its impact on overall soil productivity. A multi-function probe has been developed to allow simultaneous measurement of EC (Rong et al., 2017)--see Figure 5. The probe incorporates a Wenner array ring with four parallel ring electrodes that measure electrical resistivity and indirectly estimate soil EC. The design of the probe takes into account the dual nature of the soil as a dielectric and a conductor. To accurately measure soil EC, a sinusoidal current source or a scaled current mirror can be used to account for the conductive and capacitive behaviour of the soil. Peak detectors measure the voltage drop across the internal electrodes and the resulting voltage is converted to digital format using an analogue-to-digital converter (ADC) (Z. Yang et al., 2015).

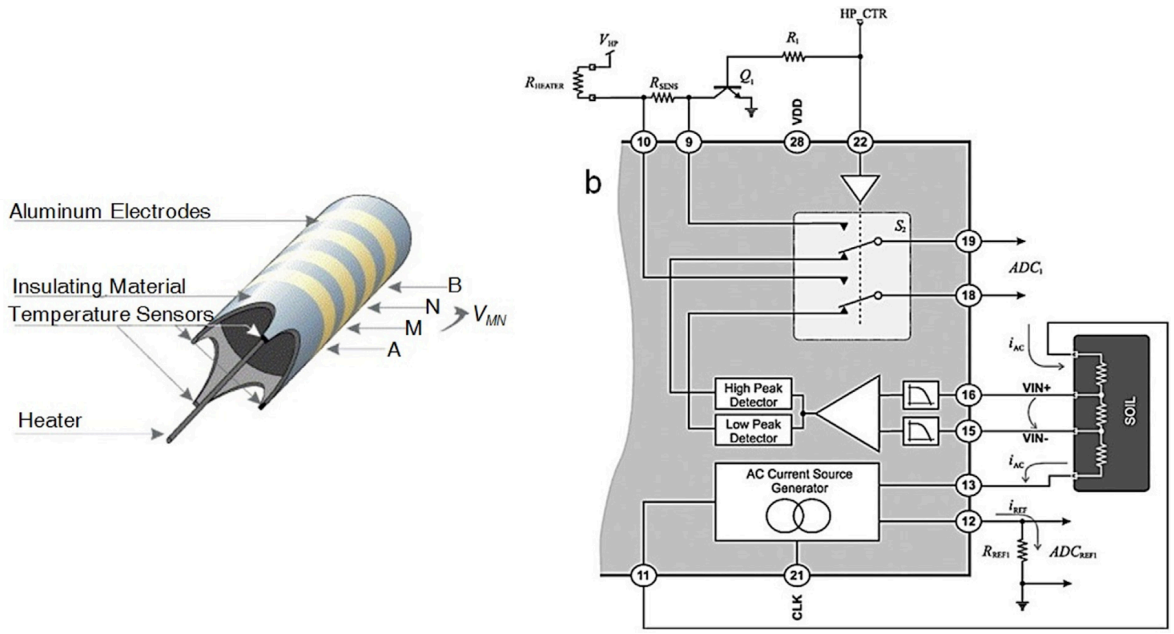

Figure 5. A probe to measure the electrical conductivity and water content of soil. Schematic diagram of (a) a multi-function probe, (b) a Wenner array. Image taken from (Rong et al., 2017).

Rajalakshmi and Mahalakshmi (Rajalakshmi & Devi Mahalakshmi, 2016) proposed an IoT-based automation model for irrigation systems, with the aim of improving the performance of farm-level practices and increasing food production to meet the needs of a growing global population. The model utilises a network of interconnected, internet-connected items to enable the evaluation of agricultural procedures. In the context of irrigation, automation is achieved through the implementation of moisture monitoring sensors, temperature sensors, humidity sensors and light intensity sensors. These sensors collect data which is then transmitted to a web server containing pre-defined standard graphs. An automated program running on the web system evaluates the data and sends the results to the farmer's mobile application. This allows farmers to conveniently assess their crop conditions and remotely control the irrigation system, providing flexibility and efficiency in farm management (Wang et al., 2022) (Mentsiev et al., 2019).

Rao and Sridhar have developed an IoT-based irrigation model using Raspberry Pi that can significantly improve crop production by optimising the use of irrigation water, especially in water-scarce regions. The model includes two types of sensors that measure temperature, humidity and sunshine duration throughout the day. These sensor readings are fed into a database that quantifies the crop's water requirements for the day. Based on this information, the irrigation system (either sprinkler or drip) is automatically activated when the crop needs water. This system effectively minimises water losses during irrigation while ensuring that the crop receives an adequate and optimised amount of water, making it particularly suitable for areas where water is scarce (Wang et al., 2022) (Rajalakshmi & Devi Mahalakshmi, 2016).

Biotic stresses, including insects, pests and diseases, are a major threat to agricultural productivity. Disease prevention is a critical aspect that farmers need to address. A decision

support system (DSS) has been developed to effectively control potato diseases. This system uses sensors to predict environmental conditions and has been successful in controlling fungal diseases in potatoes. High-quality sensors collect climate data, which is transmitted to a database using IoT technology. The collected data is then analysed and evaluated in the cloud IoT framework. The farmer then receives comprehensive information on climatic conditions and specific fungicide application requirements to prevent disease. This system reduces the cost of fungicide applications while ensuring timely disease prevention (Wang et al., 2022) (Rao & Sridhar, 2018).

Scientists and engineers are currently focusing on IoT-based precision agriculture, which uses real-time monitoring systems on farms to improve both the yield and quality of agricultural production–see Figure 6. This approach involves the use of various high-quality sensors to collect data, which is then transmitted to a website database system via IoT technology and internet connectivity. Recent research has introduced data analysis algorithms that optimise energy use in greenhouse systems based on weather conditions (cloudy or sunny days). This system has demonstrated significant effectiveness in managing greenhouse energy systems, resulting in reduced energy costs and minimised production losses (Wang et al., 2022) (Foughali et al., 2018).

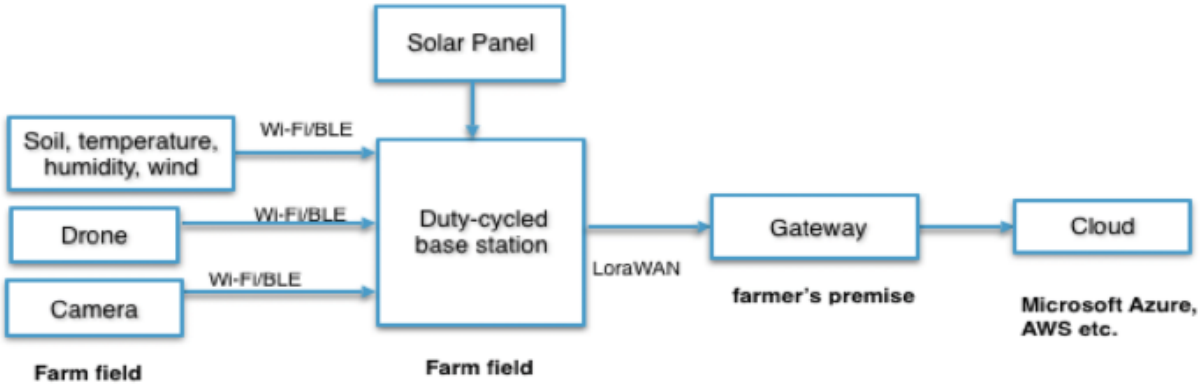

Figure 6. The idea of smart agriculture enabled by IoT. Image taken from (Dhall & Agrawal, 2018).

Manual apple picking, the traditional approach, has significant drawbacks such as high labour costs, labour intensive requirements and challenges in maintaining consistent picking quality (H. Chen et al., 2023) (Perera & Englehardt, 2020). These challenges require the introduction of innovative solutions such as "Automated Apple Picking Sensors" to overcome these limitations. The quality of the picking process plays a critical role in fruit storage, processing, sales and overall economic returns. Optimising the design of the end effector and implementing non-destructive fruit picking techniques are therefore essential. In recent studies, Wang and Yan have developed an innovative apple-picking device inspired by the principles of artificial intelligence and bionics. This device incorporates a negative pressure air suction mechanism that mimics the suction cups of an octopus. It adopts a labour-saving picking mode known as "rotating-pulling". This development has great potential for improving productivity and reducing losses in apple picking (Kuta et al., 2020), see Figure 7.

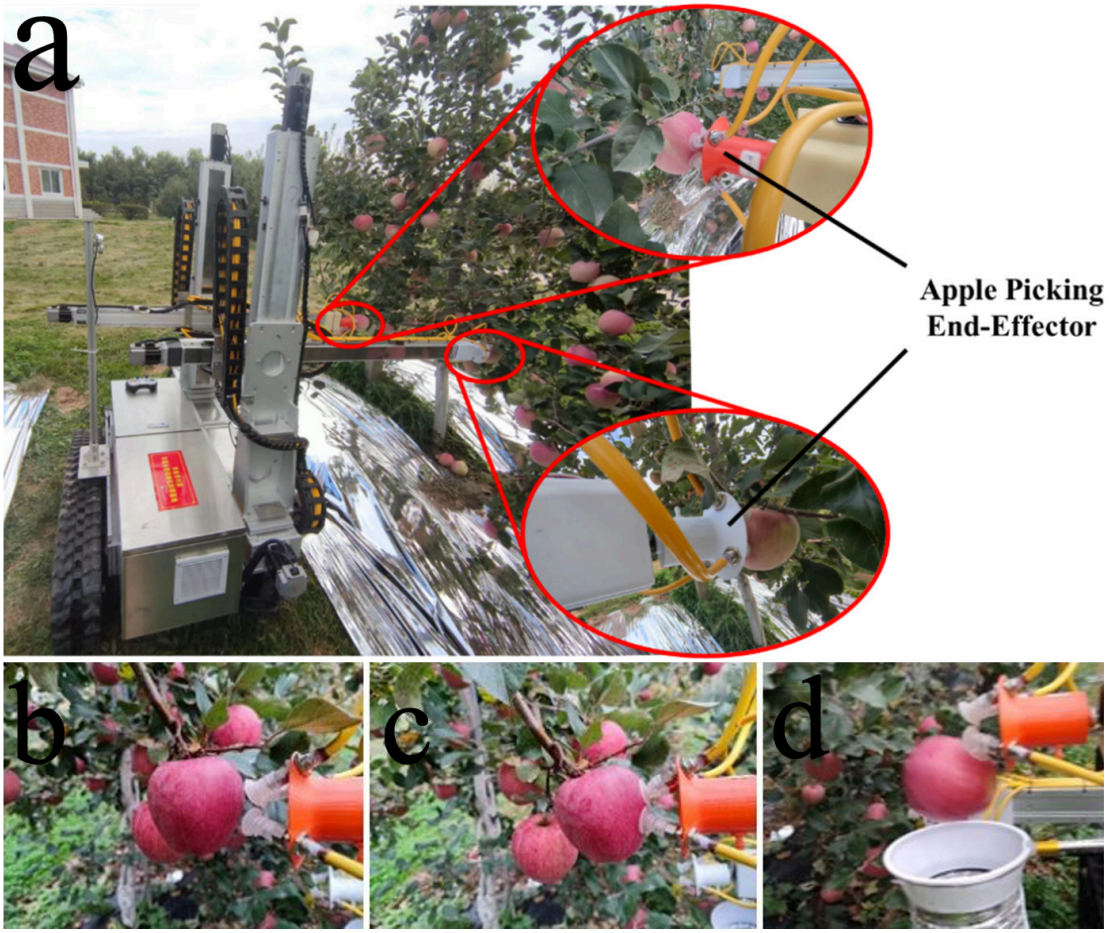

Figure 7. Automated apple picking sensor. (a) Apple picking robot with mechanical hand design, (b) The apple picking robot reaches the apple. (c) The apple picking robot picks the apple, and (d) The apple picking robot releases the apple. (Kuta et al., 2020).

The increasing need for efficient farming practices and the widespread adoption of IoT devices in agriculture have driven the development of specialised micro-electro-mechanical systems (MEMS) sensors for agricultural applications. this section looks at the latest advances in the use of MEMS technology to improve the efficiency of sensors and systems in the agricultural sector:

Today, humidity sensors based on MEMS technology offer advanced capabilities. These sensors incorporate electronic systems for calibration and temperature compensation, allowing digital readout of humidity and temperature measurements. Among the different types of humidity sensors, resistive and capacitive sensors are commonly used in commercial and industrial applications for environmental monitoring. While resistive humidity sensors are easy to manufacture and have simple readout circuits, their limitations include long recovery time and low stability, which limit their applications (Ubudi et al., 2017) (Rittersma, 2002). Capacitive humidity sensors, on the other hand, offer several advantages

such as low power consumption, wide temperature range and long-term stability. However, they may require more complex readout circuits for high-precision applications (Farahani et al., 2014).

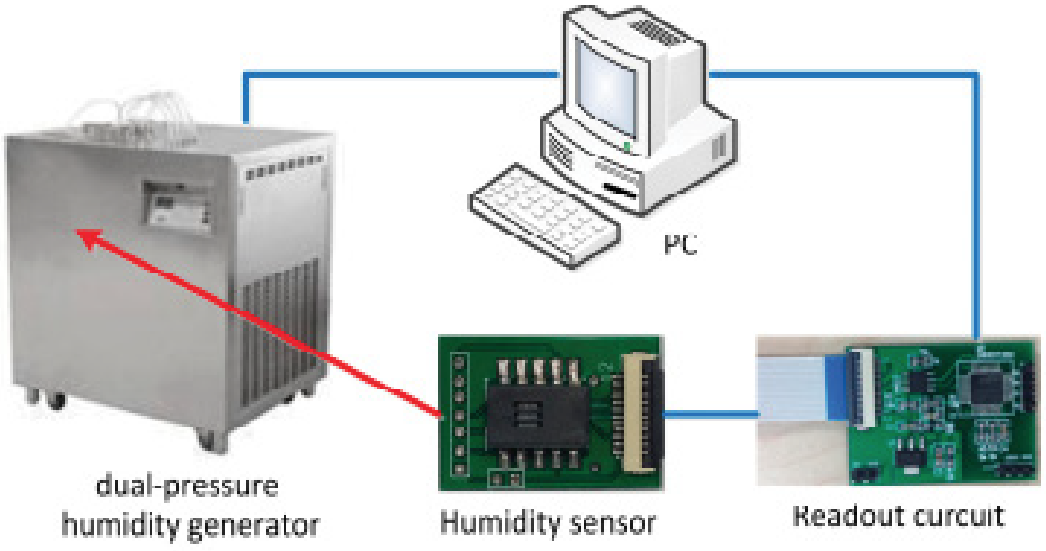

Figure 8. The humidity sensor system for static measurement. Image taken from (Huang et al., 2016).

Measuring soil temperature and moisture using MEMS sensors is critical to understanding the exchange of water and heat energy between the land surface and the atmosphere. These factors, through processes such as evaporation and plant transport, have a significant influence on weather patterns, precipitation and irrigation practices. To capture these parameters, MEMS humidity sensors use micro-machined cantilever beams integrated with a water-sensitive nano polymer and an on-chip piezoresistive temperature sensor. This combination allows simultaneous monitoring of soil temperature and moisture, see figure 8 (Huang et al., 2015).

Wind speed and direction are of paramount importance when assessing the productivity of agricultural land. Traditional sensors used to measure wind, such as mechanical anemometers and ultrasonic sensors, have limitations. However, advances in micro-electro-mechanical systems (MEMS) technology have introduced low cost, miniature and lightweight sensors. MEMS-based wind sensors using cantilever structures have demonstrated their ability to accurately measure wind speed. These sensors consume low power and offer strong competition to other commercially available options. Recently, an octagonal wind sensor with 16 resistors arranged in saltire and cross groups has been developed using a precise two-step MEMS lift-off process on a ceramic substrate (Rong et al., 2017). This newly developed sensor offers improved accuracy and reliability compared to current wind measurement sensors (Dhall & Agrawal, 2018).

When developing MEMS sensors for agriculture, humidity is a critical factor to consider. Humidity sensors are widely used in various industries including pharmaceutical, electronics,

biomedical, semiconductor, metrology and agriculture (Rajalakshmi & Devi Mahalakshmi, 2016). They are categorised into different types based on design considerations, such as resistive, capacitive, hygrometric, optical, gravimetric and positive impedance sensors. Each type has its advantages and limitations. For example, resistive humidity sensors measure humidity by monitoring changes in electrical conductivity, offering fast response, ease of manufacture and high sensitivity. Capacitive humidity sensors, on the other hand, rely on changes in dielectric constant as humidity changes, offering advantages such as low power consumption and condensation tolerance. Recent research (Ahmad et al., 2017) has explored an integrated capacitive and resistive approach using organic nickel phthalocyanine (NiPc) as a humidity sensor. NiPc, which belongs to the category of organic semiconductors, offers advantages in terms of environmental friendliness, cost effectiveness and ease of fabrication–see Figure 9. Organic semiconductor sensors follow a two-step process: first, water vapour is adsorbed or condensed on the sensing layer, and then the resulting change in an electrical property of the organic film is measured to determine the ambient humidity (Farahani et al., 2014) (Dhall & Agrawal, 2018).

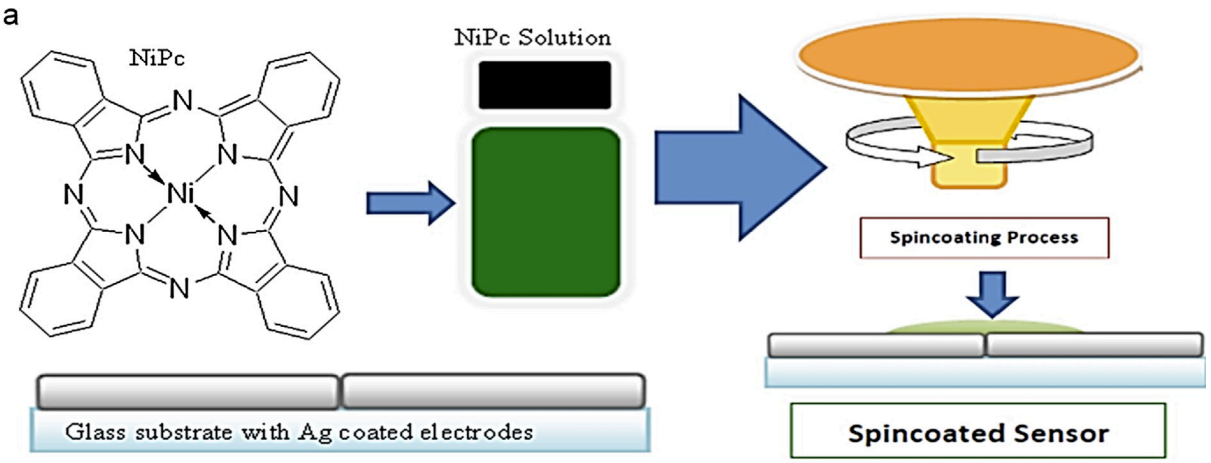

Figure 9. An example of micro/nanotechnology used in smart agriculture. The molecular structures of NiPc and the process of the proposed humidity sensor.Image taken from (Ahmad et al., 2017).

The role played by agriculture in developing sensors using natural fibres

There is an interdependent relationship between agriculture and sensor technology, in the field of smart agriculture. This interdependence is exemplified by the use of natural agricultural fibres in the production of high quality sensors for robotics (Shu et al., 2021). Due to their environmentally friendly nature, these fibres have found application as substitutes for synthetic materials in composite structures and have also been integrated into sensor manufacturing. This integration highlights the interdisciplinary nature of agricultural and technological progress, bridging the previously discussed applications of sensors in agriculture and the emerging role of natural fibres in sensor technology.

Shu and Hu (Shu et al., 2021) have developed a novel non-tensile coaxial piezoresistive fibre sensor with both force sensing and magnetic response properties–see Figure 10. The core of this sensor consists of conductive flax fibre with interwoven silver nanowires (AgNWs) forming a conductive network. The core is surrounded by a soft sheath of magnetorheological elastomer (MRE). The conductive fibre has excellent flexibility, stability and sensing performance, making it suitable for monitoring the movement of various human joints. The high strength of the flax fibre allows the sensor to be non-tensile while remaining sensitive to strain and magnetic fields. The design of the sensor allows for different external shapes, enabling it to act as both a magnetic field actuator and a sensor when deflected at different angles under the influence of a magnetic field. In addition, the conductive flax fibres are woven into a three-dimensional network structure, allowing real-time perception of external pressure stimulation and providing feedback through electrical signals (Shu et al., 2021), see Figure 10.

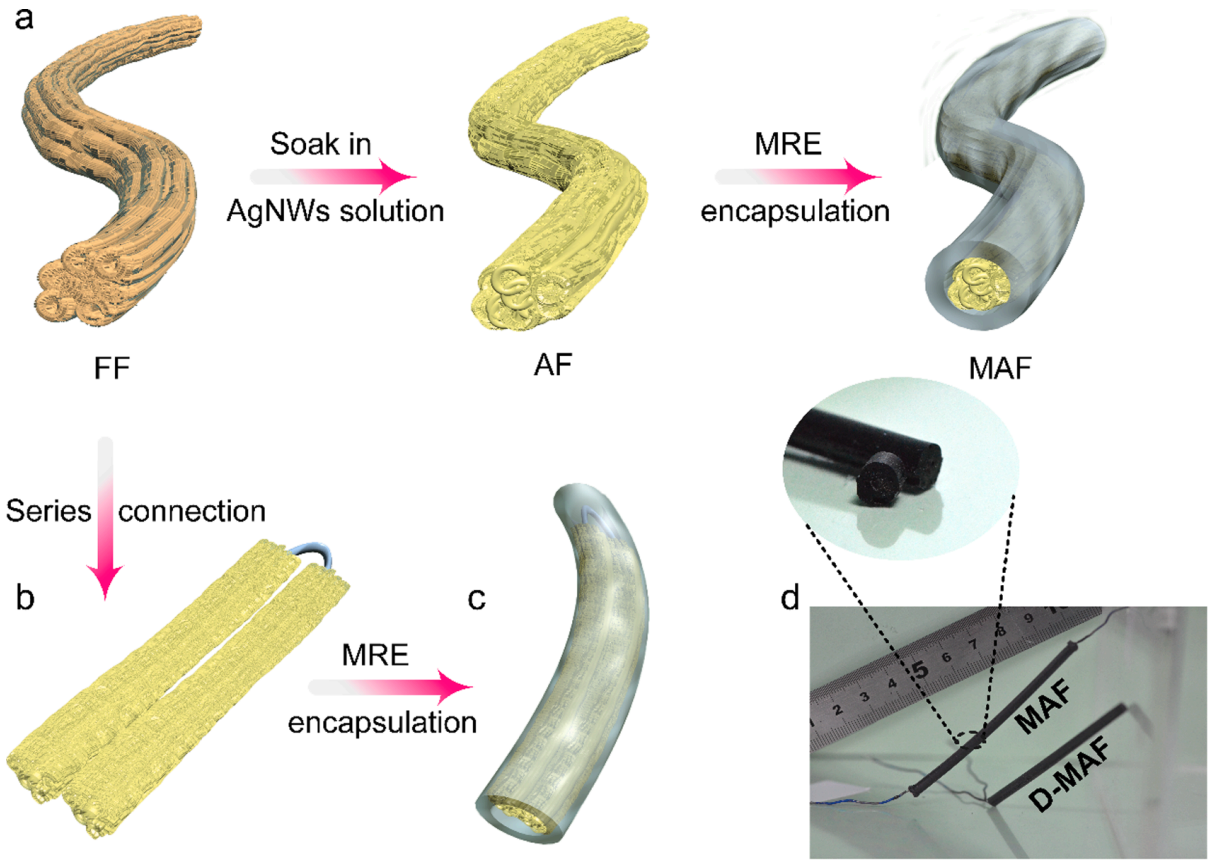

Figure 10. An example of the use of flax fibres as a piezoresistive sensor. The preparation process of (a) the structure of a single MAF, (b) the structure of two AFs and (c) the structure of a D-MAF, (d) the image of the MAF and the D-MAF. Image taken from (Shu et al., 2021).

In conclusion, In the context of Agriculture 4.0, the implementation of precision farming techniques offers a promising approach to improving the sustainability of agricultural practices. This approach aims to deliver multiple benefits, including increased farm profitability, reduced reliance on manual labour and minimise environmental impact. However the integration of Agriculture 4.0, within the broader framework of Industry 4.0,

faces several critical challenges that require attention and resolution to ensure its successful implementation. One of the main challenges is to establish technological standards that facilitate the compatibility and applicability of equipment, especially in rural areas. Achieving seamless data exchange through communication standards that link disparate systems into a cohesive and comprehensive agricultural network is emerging as a key requirement. Another crucial aspect is the financial aspect of farmers, who need to be provided with the means to modernise their production practices. Limited investment capacity and restricted access to credit hamper the adoption of new production tools and technologies associated with Agriculture 4.0. Bridging the gap between traditional and smart agriculture requires additional investment in training farmers to familiarise them with the latest technologies.Currently, communication networks are mainly used in urban areas, but for Agriculture 4.0 to succeed, robust communication networks need to be established in rural areas. The characteristics of farm households, such as education level, family size and gender, play a role in influencing decisions to adopt new technologies in Agriculture 4.0. Farm size also has an impact, as farmers with larger farms are more likely to adopt new technologies, while those with smaller farms may be reluctant due to concerns about increased investment relative to farm returns. Extension services, which include media, meetings and direct contact with extension agents or fellow farmers, have a significant influence on other farmers' adoption of new technologies. If extension services are established in regions where the impact of Industry 4.0 in agriculture is feasible, the adoption of smart agricultural practices is more likely to flourish.

Despite the growing prevalence of smart agriculture and the pervasive integration of technology across different agricultural sectors, the existing literature indicates that smart agriculture is gradually evolving globally. In particular, the field of natural fibres, an important sector within modern agriculture with applications in textiles and composites, has not kept pace with the development of smart agriculture. Natural fibres, including flax, cotton and hemp, have a well-established role in the textile industry due to their diverse properties and sustainability benefits, which include environmental compatibility, cost-effectiveness and ease of processing [39][40]. Taking advantage of their eco-friendly properties, these fibres have been adopted as substitutes for synthetic materials in composite structures and have even found use in sensor manufacturing.

Flax (*Linum usitatissimum* L.) occupies a key position among fibre crops due to its high economic importance. Its exceptional properties, including high tensile strength, favourable biocompatibility, excellent weavability and remarkable flexibility, make flax fibre a prime candidate for applications in textile and thermoplastic materials. Recent investigations have highlighted the key role of flax fibres in sensor development, where they serve as a platform for multifunctional piezoresistive sensors (Shu et al., 2021).

However, in order for flax fibres to be optimally suited for composite and technological applications, their quality must be of the highest standard. The quality of natural fibres is closely linked to extraction methods, which in turn face numerous challenges due to environmental factors. In addition, mechanical extraction methods remain relatively rudimentary, relying on outdated machinery that does not meet today's standards. In this context, Smart agriculture is a powerful strategy to address this major challenge.

To date, no studies have been conducted to demonstrate the integration of smart agriculture into plant fibres. In this section, we look at the importance of flax, an outstanding plant fibre,

including its global market presence, studies conducted, mechanical strength, cultivation practices, and the potential incorporation of smart sensing technology in this area.

The importance of natural fibres

In the current context of increasing demand for sustainable resources, the use of plant fibre reinforcement in various applications has gained significant attention and market traction. Although comprehensive documentation on market volumes is limited, a report by the European Confederation of Flax and Hemp (CELC) and the JEC Group in 2018 indicated that natural fibre composites accounted for 92,000 tonnes in Europe in 2012, representing 15% of the total European market volume when combined with wood plastic composites. Among plant fibres, flax has emerged as a prominent choice, accounting for more than 51% of the total fibre mass used in European automotive applications in 2012 (approximately 29,500 tonnes, excluding wood and cotton). Life cycle analyses have also demonstrated the environmental advantages of flax fibres over glass fibres. However, the wider adoption of plant fibres as an alternative faces a number of challenges, which are explored and discussed in this section. In particular, one of the main obstacles is the accurate prediction of the quality and subsequent mechanical performance of plant fibres, which has implications for their widespread use.

The definition of plant fibres refers to elongated sclerenchyma cells in vascular plants that are organised into bundles . However, the common definition has a broader scope and refers to various types of cells that are elongated, generally have thick walls, tapered ends, are durable and characterised by 'high' tensile strength. Plant fibres can be further classified according to their origin: animal, mineral or vegetable. Of these, plant or biogenic fibres are the most widely used in the biocomposite industry. Among the plant fibres of interest to the biocomposite industry, flax and hemp show interesting similarities (Madsen & Gamstedt, 2013). Research into these fibres has been driven by long-standing industrial interest and their abundance in nature (C. Chen et al., 2020). It is therefore valuable to use the knowledge gained over the past decades on these plant fibres to gain deeper insights into the mechanical behaviour of flax.

The inherent natural properties of plant fibres introduce a wide range of variability at different levels, requiring a comprehensive understanding of their structure-property relationships. As a result, there is a growing demand for accurate structural, biochemical and mechanical descriptions of plant fibres, leading to the development of specialised testing facilities in various scientific fields. However, certain research gaps remain, requiring further advances in the field. For example, innovative coupling techniques to facilitate in situ mechanical testing have yet to be fully developed. In addition, a deeper understanding of the composition and interactions between the biopolymers inherent in the fibre structure, particularly the middle lamella responsible for binding the fibres together, requires more attention and research. Filling these gaps will undoubtedly contribute to a more comprehensive understanding of the behaviour and properties of plant fibres.

In addition, particular emphasis has been placed on the study of defects in plant fibres, with dislocations often inaccurately considered as the sole representation of defects (Hughes, 2012). While it is recognised that defects can lead to reduced mechanical properties at the

composite level (Hughes et al., 2000), their effect at the fibre scale remains an area of research that requires further investigation and attention.

This section presents a comprehensive analysis of flax fibres, covering both their cultural significance and their ultrastructural characteristics. This is followed by an in-depth examination of the flax fibre extraction process, followed by a thorough investigation of the various parameters that influence fibre quality. Finally, the mechanical properties of flax fibres are meticulously elucidated to provide a comprehensive understanding of their behaviour.

Flax cultivation

The interest in the cultivation of flax can be explained by the many advantages of its fibres. First, Flax fibre is mainly grown in temperate and humid regions with moderate temperatures and adequate rainfall, making the coastal areas of Western Europe, such as Belgium, the Netherlands and France, ideal for its cultivation (Xu et al., 2022). This localised production creates opportunities for the development of new materials with potential industrial applications. Moreover, The flax industry involves various stakeholders, including experts in variety selection, knowledgeable farmers, specialists in fibre extraction and marketing, and manufacturers of specific machinery required for different stages of flax processing (Shah, 2013). In addition, Elementary flax fibres have favourable mechanical properties similar to those of E-glass fibres, making them a promising alternative to traditional glass fibres. These properties highlight the interest in their cultivation (Shah, 2013).

Flax cultivation process

Flax cultivation begins with sowing, usually when the top layer of soil reaches a temperature of around 7-9°C, which in France is between 15 March and 15 April (Baley & Bourmaud, 2014). The growth stages of flax can be divided into four main phases: germination, vegetative stage, flowering and seed formation, and senescence (Sultana, 1983), see Figure 11:

1. Germination occurs approximately 5 to 10 days after sowing and is characterised by the emergence of two fully developed cotyledons, characteristic of dicotyledons (Goudenhooft et al., 2019) (Paul-Victor et al., 2017).

2. The vegetative stage is initially slow, with the flax plant growing to a height of about 15 cm within 15 to 20 days of germination. This gradual growth is followed by a period of rapid development lasting about 15-20 days, during which the plant can grow several centimetres per day to reach a height of 80-90 cm. Growth then slows as the plant enters the flowering phase, eventually reaching a final height of about 1 metre (Edwards et al., 1997).

3. Flowering typically begins about 50 days after germination and lasts about 15 days for the whole field, with individual flowers flowering for only one day (Heller et al., 2015).

4. Seed formation begins about 15 days after flowering, with full maturity occurring during the 'late ripening' stage, about 5 to 6 weeks after flowering. Finally, senescence occurs as a natural part of the plant's life cycle.

However, it is important to note that in industrial flax cultivation, plants are harvested at the fibre maturity stage, known as "yellow ripeness", which follows the "green ripeness" or "early ripeness" stage (Du et al., 2015). The entire cultivation process, from sowing to fibre maturity, takes about 100 to 120 days.

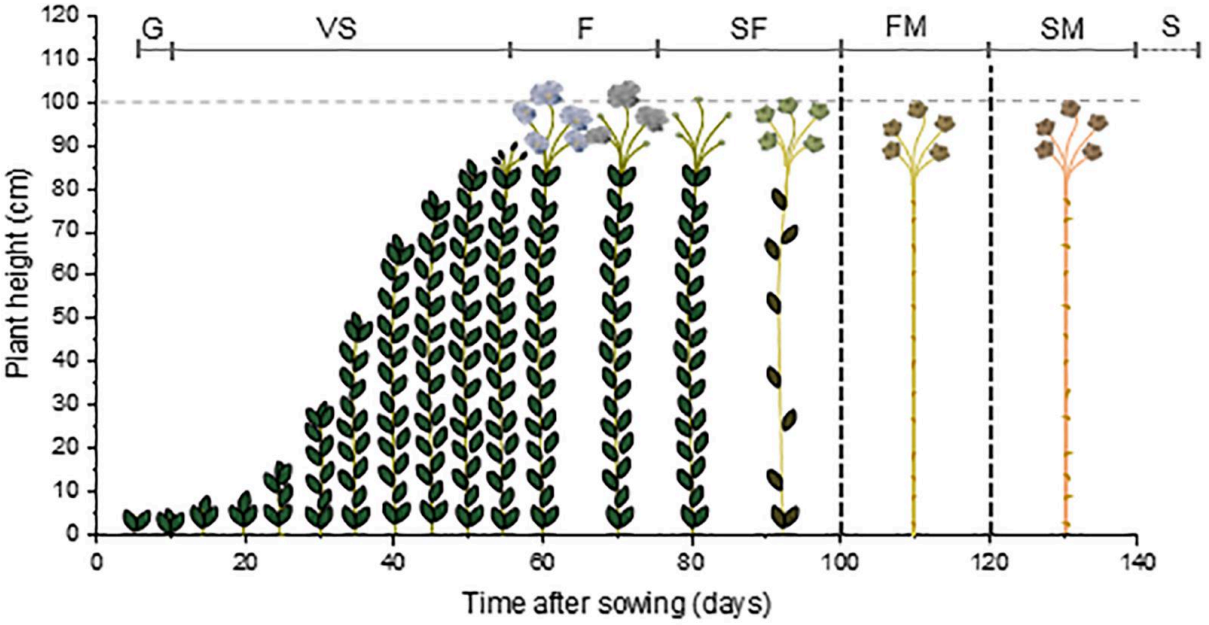

Figure 11. The entire cultivation process of a flax plant, from sowing to plant maturity, takes about 100 to 120 days, taken from (Goudenhooft et al., 2019).

Processes for the extraction of flax fibre; biochemical (retting) and mechanical

The quality of manufactured textiles and natural fibre composites is influenced by the mechanical and chemical properties of the isolated fibre/fibre bundle and the subsequent industrial transformation process (Jonoobi et al., 2011) (J. Müssig, 2010). A major challenge in the processing of plant fibres is the extraction of suitable natural fibres. Following harvest, the breakdown of the pectin-rich regions initiates the separation of the bast fibres from the other components of the stem, including the epidermis and shives. This crucial stage is known as retting. This process involves selective degradation of plant components, and plays a key role in the overall yield and quality of the resulting product (Akin, 2013). Thus the aim of retting is to break down the middle lamella *(ML)* without damaging the primary and secondary cell walls of the fibres.

Therefore, the art of retting is to find the right balance: under-retting can result in coarse technical fibres, consisting of several associated individual fibres and contaminated by wood debris and external tissues (Akin, 2013), while over-retting can reduce the strength of the

fibre by affecting its integral structure (Goodman et al., 2002) (Rosemberg & De França, 1967). Thus understanding and controlling these factors in the retting process is of great importance to ensure the production of high quality flax fibres with desirable mechanical and chemical properties.

Dew retting

There are several methods of retting, including water retting, dew retting, enzymatic retting, chemical retting and mechanical retting. The two main types of retting commonly used are 'water retting' and 'field/dew retting'. In water retting, the flax stalks are harvested, bundled and submerged in water. Traditionally, this process took place in natural basins such as lakes, rivers or dams and lasted 5-7 days. The stalks were then dried on the ground for one to two weeks (Djemiel et al., 2020) . Water retting is primarily based on the activity of anaerobic bacteria that colonise the stalk, resulting in fermentation (Akin, 2010). This method produces high quality flax fibre, but also raises concerns about environmental pollution.

In Europe, flax retting is primarily conducted through dew-/field-retting. In this process, specialised harvesters mechanically uproot (pull) the flax plants, and the stems are arranged in piles on the field to create swathes-see Figure 12.

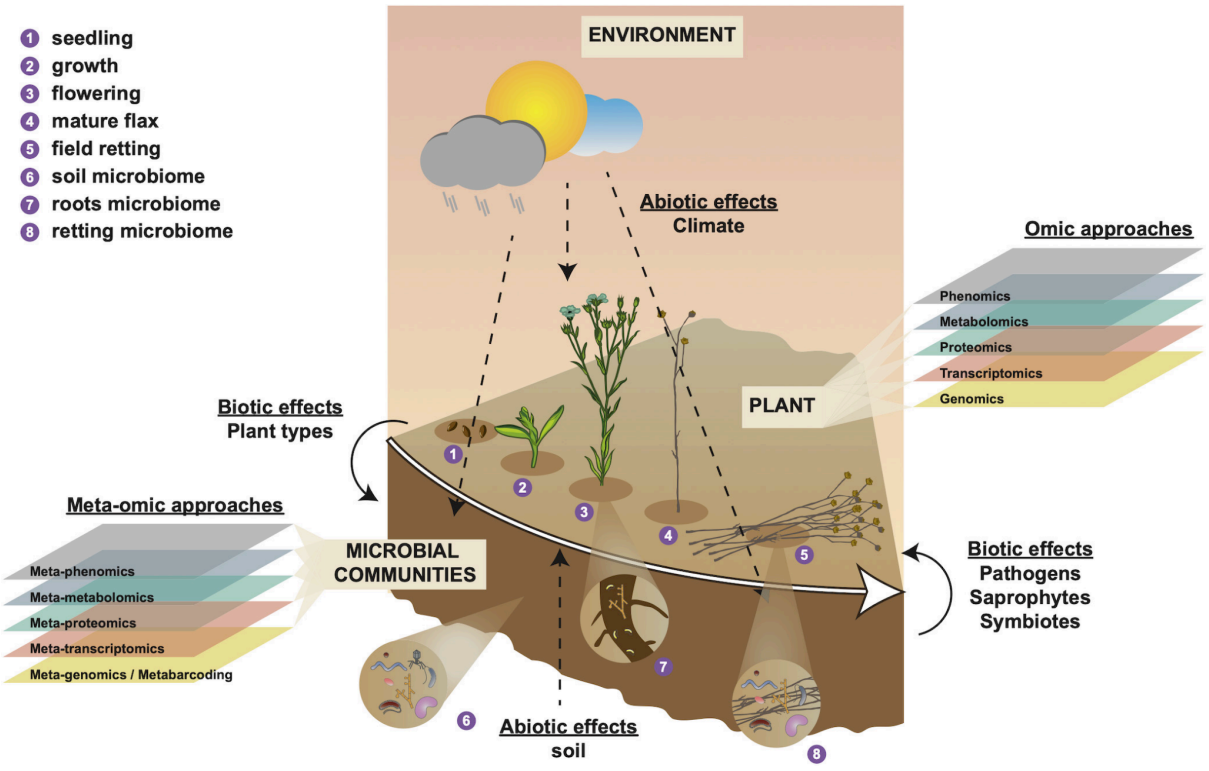

Figure 12. Overview of flax dew-retting process, taken from (Djemiel et al., 2020).

The presence of morning dew and the variation of rainfall and heat contribute to the favourable conditions for the growth of microorganisms, primarily bacteria and fungi, already present on the stems. Additionally, microflora from the soil where the swathes are situated also colonise the stems during this process (Meijer et al., 1995) (Sharma & Faughey, 1999). The enzymes produced by these microorganisms primarily target and degrade specific polysaccharides, such as pectin, a major component forming the pectic cement in the ML, resulting in partial dissociation of the fibre bundles, and individual fibres see Figure 13. Throughout the retting process, the farmer's involvement includes turning the swathes midway through to ensure uniform retting across the entire height of the swathe and monitoring the progress of the process (Djemiel et al., 2017) (Djemiel et al., 2020).

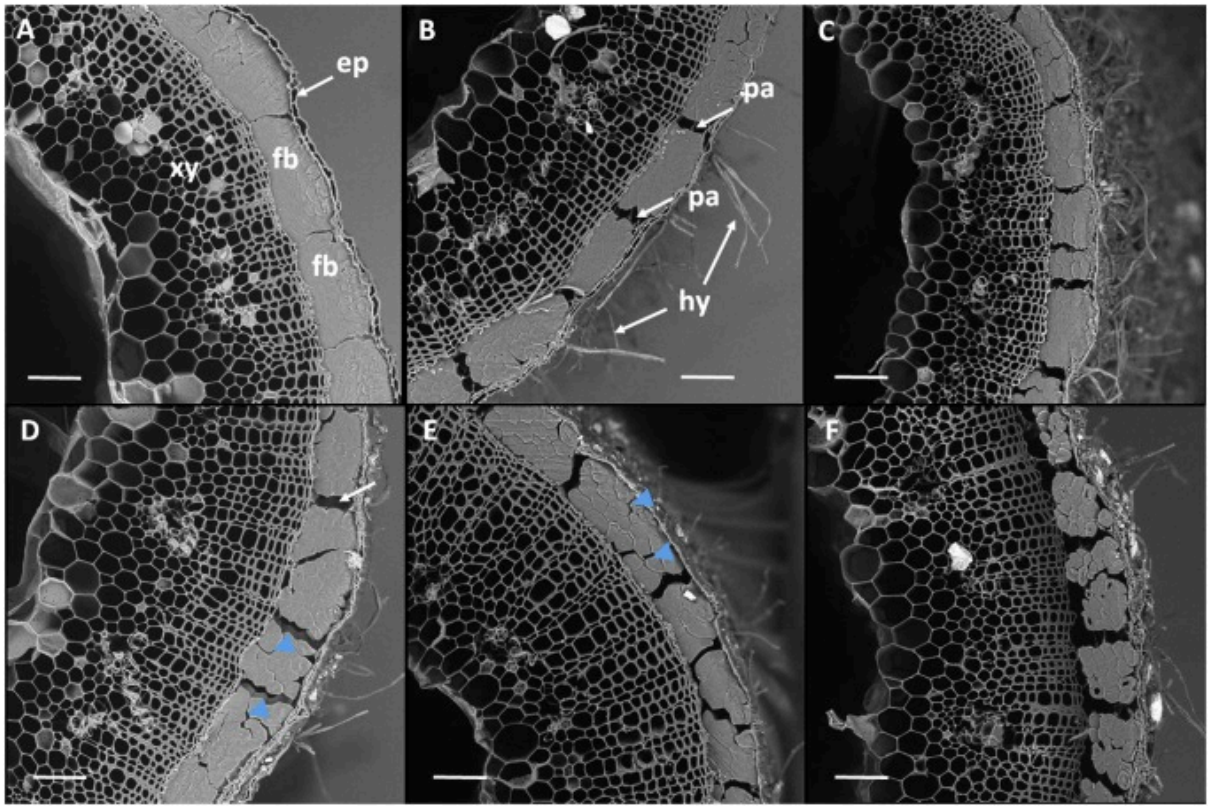

Figure 13. Scanning electron microscopy (SEM) was used to examine transverse sections of flax stems at different stages of retting: (a) R0, (b) R2, (c) R4, (d) R6, (e) R7 and (f) R8. Observed features include xy (xylem), fb (fibre bundles), pa (parenchyma), ep (epidermis) and hy (hypha). In particular, white arrows and blue arrowheads have been used to indicate inter- and intra-bundle dissociation, respectively. The scale bar is set at 100 µm. Image taken from (Chabbert et al., 2020).

The progression of dew retting is accelerated by changes in environmental conditions, including higher humidity and lower temperatures at night and higher temperatures with drier conditions during the day. Seasonal variations, soil structure, mineral elements (e.g. nitrogen, phosphorus and potassium), soil physico-chemical properties, crop rotation and swath thickness also influence the rate and effectiveness of decomposition (Meijer et al., 1995). Together, these exogenous factors contribute to the overall efficiency and quality of

the retting process and influence the final characteristics and properties of the extracted flax fibre.

Mechanical extraction of flax fibre

After retting, mechanical extraction is used to separate the fibres from the shives and epidermis. The first step in mechanical extraction is the breaking process. The straw is passed between grooved rollers in a breaking machine Figure 14a, which effectively breaks the woody core into fragments while maintaining the integrity of the fibres within the stalks figure 14.a. After breaking, the straw undergoes 'scutching', a process that separates unwanted woody material from the fibre. This separation is achieved by beating the straw with blunt wooden or metal blades in a scutching machine-see Figure 14b and Figure 14c. The removed woody material, known as shive, is usually used as fuel, leaving the flax in the form of long strands made up of bundles of individual fibres adhering to each other-see Figure 14d (Gorshkova et al., 1996).

After scutching, the fibres are usually combed or "hackled" by pulling them through sets of pins, with each successive set having finer pins than the previous one. This process separates the coarse fibre bundles into finer ones and aligns the fibres parallel to each other, resulting in long, fine fibres known as 'line'-see Figure 14e . Meanwhile, the tow is subjected to further combing or carding, which accurately aligns the fibres. The aligned fibres are then gathered into a loose rope of fibres known as a 'sliver' or 'rove' (Gorshkova et al., 1996).

Figure 14. Commercial factory mechanical extraction of flax fibres from retted flax stems. (a) The straw is passed between grooved rollers in a breaking machine, (b) and (c) Separation of unwanted woody material from the fibre scutching', a process that separates (d) Leaving the flax in the form of long strands made up of bundles of individual fibres (e) Separation of the coarse fibre bundles into finer ones (f) Further combing or carding.

The environmental conditions during the scutching process, in particular the humidity, have a significant impact on both the tow yield and the average length of the fibre bundles, as well as the likelihood of bundle splitting (Djemiel et al., 2020). In addition, the mechanical parameters of the scutching machines, including straw feed speed, beating rate and grinding intensity, play a crucial role in determining the quality of the tows, which includes their structure, cleanliness and mechanical properties (Djemiel et al., 2020).

Flax structure

Flax stem, fibre cell wall and chemical composition

Flax, like other plants, has plant parts such as stems, leaves and roots, each with a specific function (Gorshkova et al., 1996). Together these plant organs form a continuous system with a common developmental basis. The most important feature of flax is its two main functions: conducting and supporting. Flax can be characterised as a composite system with hierarchical structures ranging from macroscopic to nanoscopic scale (see Figure 15) and can be divided into: the external tissue, also called the epidermal (bark), and the internal tissue also called vascular (xylem). The outer layer, known as the bark, protects against the external elements and stabilises the stem, while the inner layer, known as the xylem, facilitates the movement of water and nutrients from the centre to the fibres in the stem (see Figure 15a).

Flax fibre bundles, also known as technical fibres, are obtained from the inner bark of the flax stalk. These technical fibres have an approximate length of 1 m and consist of approximately 10-40 elementary fibres, also known as single fibres, in their cross-section. On a smaller scale, fibre bundles are formed by several elementary fibres held together by a pectic cement. The elementary flax fibres themselves are typically 10-80 mm long and 10-40 µm in diameter (Jör. Müssig & Martens, 2003) (see Figure 15b). They are characterised by a concentric arrangement of two types of cell walls, the outer primary and the inner secondary, the latter being further divided into three parts of varying thickness and structure. In addition, the fibre has a central hole known as the lumen (see Figure 15c).

a

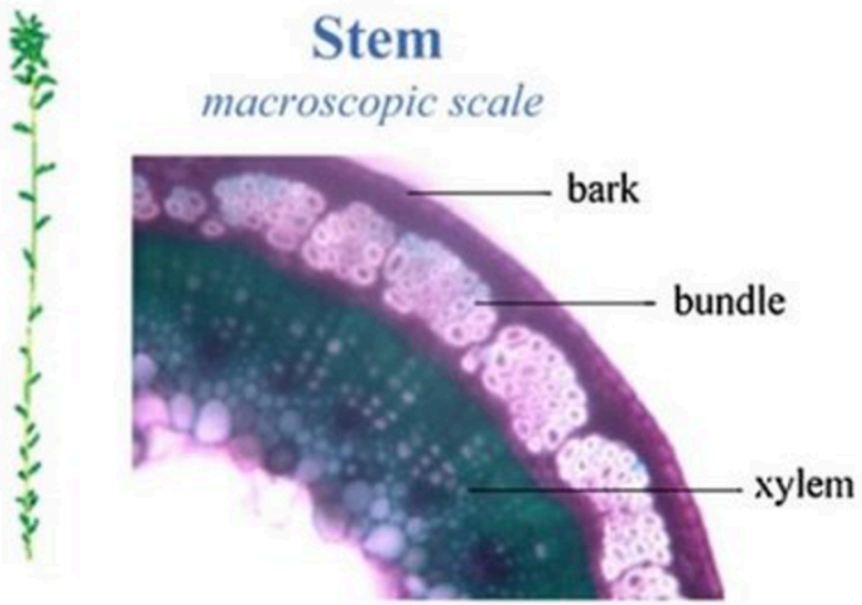

b

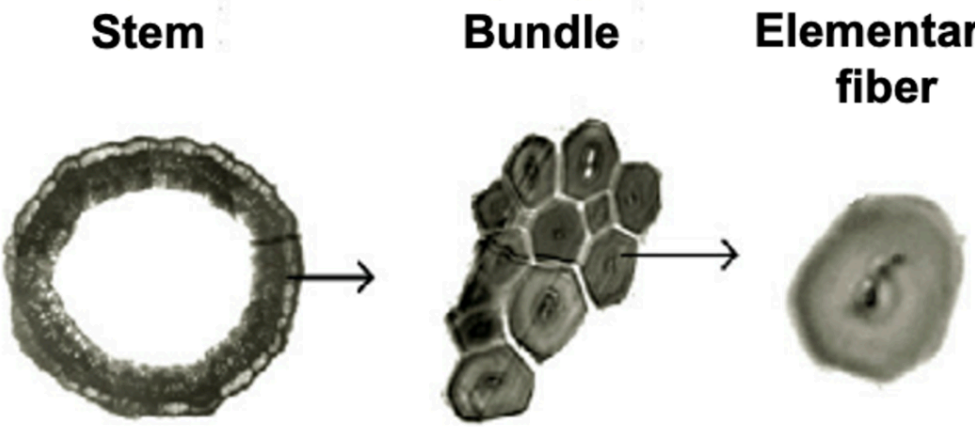

c

d = 2 mm

d = 200 um

d = 20 um

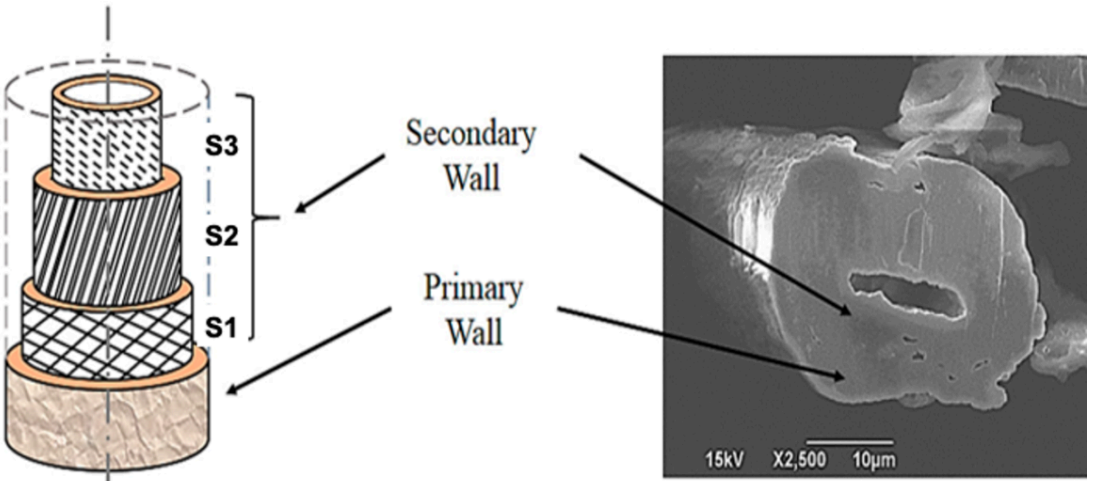

Figure 15: (a) Cross-sections of flax stem, (b) cross-sections and diagrams of flax at various scales, from stalk to cellulose fibrils, and (c) flax fibre cell structure. Image taken from (Zhu et al., 2013)

Structural analysis of a single flax fibre reveals several layers (Hideno et al., 2007) (Easson & Molloy, 1996). The first layer formed during plant growth is the thin primary wall, which contains both cellulose and hemicellulose and has a thickness of approximately 0.2 μm (Akin et al., 2001) (Feleke et al., 2023). This is followed by the secondary cell wall, which makes up the majority of the fibre diameter and is composed mainly of cellulose and hemicelluloses. This secondary wall is further divided into three layers containing helically wound microfibrils of highly crystalline cellulose chains. Each microfibril is composed of 30 to 100 chains of cellulose molecules oriented at an angle of approximately 10° to the fibre axis. According (Van Hazendonk et al., 1996), the secondary wall accounts for up to 70% of the Young's modulus of the fibre, indicating that higher cellulose content corresponds to higher tensile modulus (Van Hazendonk et al., 1996).

Dislocations and kink band structures in the fibre

Certain plant fibres, such as flax, hemp or ramie, have advantageous mechanical properties. However, their application in structural composites is challenged by the presence of defects that affect both the fibre and composite levels. Defects are frequently discussed in the literature, often focusing on well-studied dislocations, as reviewed in detail by (Hughes, 2012). These dislocations are commonly denoted by terms such as slip planes, cell wall folds, wrinkles, kink bands, or zones of microcompression (Hughes, 2012) (Nyholm et al., 2001) . However, the precise differentiations among these terminologies remain ambiguous. (Qi et al., 2019), in their study of ramie fibres, defined knots as transverse circumferential dislocations enveloping the cell wall, while kinks denote areas where the main axis of the fibre turns approximately 20°, and scales represent individual striations. Some researchers differentiate these terms according to the severity of the deformation (Nyholm et al., 2001), with reported dislocation lengths ranging from a few micrometres to 120 μm for wood. Notably, a single-scale dislocation corresponds to a dislocation occurring within a single cell wall, whereas the cross-shaped dislocations may indicate deformation along the entire depth of the cell wall (Nodder, 1922) (Thygesen et al., 2006). However, this classification remains controversial and dislocations are generally defined as regions with a larger microfibril angle than the surrounding areas (Placet et al., 2014).

Mechanical and physical properties of flax fibre

Mechanical testing methods of flax fibre

The mechanical properties of flax fibres and bundles have been extensively studied by several researchers, but a notable limitation is the lack of systematic clarification of the specific scale of investigation. Numerous test methods have been used to evaluate plant fibres, the most common of which can be categorised as global and local test methods,

corresponding to bundle properties and fibre or cell wall properties respectively. In the case of fibre-scale analysis, properties are influenced not only by cell wall properties but also by fibre geometry and cell wall thickness.

Conventional tensile testing is the most widely used method for evaluating the mechanical properties of plant fibres. Originally developed for wood fibres in the 1950s (Eder et al., 2013), this test approach was subsequently adapted to study other plant fibres (Baley, 2002), drawing inspiration from Griffith's pioneering work on glass fibres in the 1920s (‘VI. The Phenomena of Rupture and Flow in Solids’, 1921).

Specific adaptations have been made to the fibre tests in terms of the mode of force transmission and the method of restraining the fibre ends. Griffith's original recommendation was to use wax to allow fibre reorientation and prevent stress concentration at the ends. Currently, the most common practice is to attach the fibres to a paper frame with pre-cut edges prior to tensile testing (Burgert et al., 2003). In addition, in situ imaging techniques can be used in conjunction with tensile testing to gain further insight. In addition, complementary information on compressive properties can be obtained from the elastic loop test, in which individual fibres arranged in a loop are stretched under a microscope (Bos et al., 2002). The compressive strength is determined from the dimensional changes in the loop.

Moreover, the three-point bending method at the stem scale allows the estimation of longitudinal properties at the fibre and bundle scale, giving results that can be compared with those obtained from tensile tests (Réquilé, Goudenhooft, et al., 2018). Studies have used notched specimens under uniaxial tensile loading to study fracture properties (Beaugrand & Guessasma, 2015). In addition, efforts have been made to characterise the time-dependent behaviour of plant fibres using creep/recovery tests (Cisse et al., 2015) (Olsson et al., 2007). These tests are particularly relevant for applications where the identification of viscoelastic properties is important.

Nanoindentation and Atomic Force Microscopy (AFM) are widely used methods at the cell wall scale to determine the longitudinal and transverse mechanical properties of the cell wall (Bourmaud et al., 2018) (Eder et al., 2013). In nanoindentation, the cell wall is loaded by a Berkovich-type indenter at an angle of approximately 25°, providing valuable information on hardness and both longitudinal and transverse modulus. On the other hand, AFM relies on the resonance of a cantilever due to interactions between the tip and the sample, allowing the mapping of surface properties of the cell wall. A promising technique known as peak-force quantitative nanomechanical property mapping (PF-QNM) has been used to investigate possible stiffness gradients of fibres (Arnould et al., 2017). However, comparing AFM results with those obtained from tensile tests is challenging as the longitudinal stiffness of the fibre is underestimated due to the influence of tip geometry, transverse and shear modulus. Nevertheless, this method is valuable for comparing samples and highlighting differences in indentation modulus in multilayered or heterogeneous objects (Eder et al., 2013).

Parameters that influence the fibre mechanical properties

The mechanical properties of flax fibres, particularly at the bundle level, are significantly influenced by the degree of retting and the position of the fibres along the stalk (Charlet et al., 2007) (Bourmaud et al., 2015). Charlet et al.(Charlet et al., 2007) carried out a study showing that fibres extracted from the middle of the stem, where optimum growth conditions exist, have better mechanical properties than those extracted from the top or bottom of the stem.

A study by (Baley & Bourmaud, 2014) investigated the effect of flax variety and year of cultivation on tensile properties. The study involved the analysis of 50 different batches of flax fibre over an 18 year period. The results showed that although there was variability within batches, there was a consistent and uniform performance across all batches, regardless of variety and year grown. The majority of the batches tested showed mechanical properties close to the average calculated values for Young's modulus and tensile strength. Only a few batches showed deviations, suggesting the presence of fibres with exceptional properties, probably benefiting from favourable growth and cultivation conditions.

Major crop incidents, such as pronounced hydric stress or lodging phenomena, could potentially lead to the formation of flax fibres with weaker mechanical properties. However, it should be noted that such extreme events are still rare in practice.

Chemical and physical pre-treatments aimed at improving the adhesion between plant fibres and composite matrices can also affect the mechanical properties of the fibres (Zafeiropoulos et al., 2002). In their study, Bourmaud et al.(Bourmaud et al., 2018) highlighted several experimental uncertainties that could lead to inaccuracies in the results. These uncertainties include determination of the effective cross-sectional area, variability in boundary conditions due to different types and amounts of adhesive used, accurate measurement of total deformation and determination of modulus in non-linear regions. In addition, factors such as gauge length and strain rate can influence the tensile response and require careful consideration before comparing results. To address these issues and promote consistency in testing, efforts have been made to standardise the preparation and tensile test conditions for plant fibres, resulting in the establishment of a standard (AFNOR NF T 25-501). This standard specifies a strain rate of 1 mm/min and gauge lengths of 10 mm for single fibres and 75 mm for fibre bundles.

Several important factors related to fibre testing parameters warrant careful consideration, in particular strain rate, method of cross section measurement and data analysis. These parameters can significantly affect the accuracy and reliability of the results obtained in fibre characterisation. The accurate determination of the cross-sectional area (CSA) of flax fibres remains a subject of ongoing debate. Variations in CSA estimation can significantly affect tensile strength data, with reported discrepancies of up to 300%, as highlighted by Haag et al.(Haag & Müssig, 2016). The conventional approach is to assume a circular cross section and obtain a mean diameter by optical microscopy, calculated as the average of 3 to 6 measurements taken along the fibres and bundles. However, Barbulée (PhD Thesis, Compréhension des effets du défibrage sur la morphologie, les propriétés et le comportement mécanique des faisceaux de fibres de lin. Etude d’un composite dérivé lin-époxyde, Université de Caen Basse-Normandie, 2015) have proposed a more comprehensive method that takes into account variations in the cross-sectional shape of the

fibre along its length. This involves calculating an average of the areas along the fibre, rather than just the diameters, resulting in an average area that provides a more representative estimate of the CSA.

Bensadoun et al.(Bensadoun et al., 2017) drew attention to the importance of the strain range used to determine stiffness. In the context of the rule of mixture, several assumptions, including perfect interface, uniform fibre properties, ideal fibre orientation, presence of voids and process history of the composite, may contribute to the observed discrepancies between experimental and calculated data (Shah et al., 2016).

In addition to the effect of inherent defects in bast fibres, several investigations have shed light on the importance of dislocations in influencing the mechanical properties of fibres. One notable investigation by Bos et al.(Bos et al., 2002) looked at the effect of dislocations on individual flax fibres, comparing standard decorticated fibres with hand-insulated fibres. Through compressive loading via the loop test and tensile testing with varying clamp lengths, it was observed that hand-isolated fibres exhibited higher tensile strength, accompanied by increased variability. In contrast, decorticated fibres showed reduced variability due to the elimination of weaker fibres during the decortication process. Failure during compression was also found to be associated with the formation of kink bands. In a study by Davies et al.(Davies & Bruce, 1998), dislocation quantification was performed qualitatively as a percentage of bright areas observed under polarised light. The research revealed a significant reduction in both static and dynamic tensile modulus and strength of elementary flax fibres with increasing damage. Furthermore, in a study by (Baley, 2004), kink bands were observed in flax fibres during a bending test, mainly on the compression side of the fibre. However, no direct correlation was found between the number or shape of the defects and the resulting tensile strength. Nevertheless, the study observed crack formation in the kink bands, suggesting their role in contributing to fibre failure. Furthermore, Aslan et al.(Aslan et al., 2011) established a correlation between the presence of defects and the shape of the stress-strain curves (linear or nonlinear) in elementary flax fibres. By comparing green and cottonised fibres, they observed that the presence of dislocations increased the occurrence of non-linear behaviour, leading to a decrease in tensile properties. At the composite level,

Hendrickx et al.(Hendrickx et al.(2019). Extraction optimization for and hygroscopic behaviour of flax fibres in composite applications.) conducted a study to investigate the effect of processing history on the mechanical properties of composites. The research showed no discernible differences between the broken, scutched and hackled fibres. It was hypothesised that if kink bands were formed during these processing steps, the lack of effect at the composite scale could be due to reaching the saturation level of damage that could potentially occur during plant growth. In addition, in relation to the composite scale, Rask et al.(Rask et al., 2012) used synchrotron X-ray tomography to observe instances of flax fibre failure in defective regions (e.g. kink bands, knots and scales) that could extend over an entire bundle.

Apart from dislocations, little research has been done to investigate the formation and influence of other types of defects on the mechanical properties of plant fibres. Placet et al.(Placet et al., 2014) carried out a study comparing twisted and untwisted fibres under repeated loading cycles. They observed an additional increase in stiffness for the twisted fibres during the first loading cycle, suggesting a structural change at the cell wall scale. It

was also observed that cracks and interlaminar decohesion showed a preferential occurrence in dislocations, highlighting the significant interdependence between these particular defect types. However, the investigation of surface defects such as impurities and their effect on mechanical properties at the fibre and bundle scale remains relatively scarce in the available literature.

At the composite level, the presence of surface defects has been found to result in reduced interface quality, leading to stress concentrations and early failure (Van De Weyenberg et al., 2003) (Le Duigou et al., 2014). Given the limited existing literature and the importance of these defects in the manufacture of composites, it is vital that specific attention and further research is given to the study of surface defects in the future.

At a smaller level, plant fibres, such as flax, pose a challenge in achieving complete separation on an industrial scale due to the strong cohesive nature of the central lamella. As a result, composite reinforcements are predominantly bundled. There is therefore a growing interest in understanding the mechanical properties at this level. Distinguishing the middle lamella (ML) from the primary walls of adjacent cells is challenging, depending on the scale of observation and whether contrasting techniques are used. Furthermore, isolating the ML in plant cells such as flax, which have a secondary cell wall, is even more difficult. Melelli et al.(Melelli et al., 2020) investigated the mechanical properties of the middle lamella (ML) in various plant fibres using AFM in the PF-QNM mode. They observed an indentation modulus ranging from 6 GPa for date palm leaf sheath to 16 GPa for hemp fibres, with a possible correlation to the organisation of the fibres into bundles. Palm fibres organised in large bundles protected by a lignified outer layer had lower mechanical properties, possibly due to a reduced need for high strength. The inferior mechanical properties observed in bundles compared to single fibres were attributed to premature failure of the middle lamella.

Charlet and breakout (Charlet & Beakou, 2014) carried out a study of the interface between flax fibres within a bundle using mechanical extraction of paired fibres. The aim was to assess interfacial shear properties, such as the force required to break the interface and the displacement at interface failure, by shearing two fibres along each other. The mean lamella thickness was estimated to be between 200 and 800 nm, in agreement with observations made by Melelli et al.(Melelli et al., 2020) for various plant fibres using AFM and by Thuault et al.using TEM methods . Charlet and Beakou (Charlet & Beakou, 2014) reported an interfacial shear modulus of 18.7 kPa ± 10.1 kPa, which is outside the range of pectin shear modulus determined by rheological measurements (about 1 kPa). This discrepancy is attributed to the presence of additional components in the middle lamella and stronger interactions between the fibres and the middle lamella than simple contact. In addition, mechanical extraction of the fibres could lead to the inclusion of 'weak fibres' already in this paired configuration. The mean interfacial strength was found to be 2.9 MPa ± 2.4 MPa, which is lower than most matrix/fibre values typically encountered in composites. These results emphasise the importance of individualising bundles as much as possible prior to composite processing.

In summary, several mechanical characterisation techniques have been successfully adapted to plant fibres. However, very few studies conducted on the bundle scale, in particular the characterisation of the middle lamella, remains a challenging aspect that requires further investigation. The complexity involved in understanding the damage mechanisms leading to fibre and bundle failure underlines the need for the complementary

use of numerical models. In addition, it is important to note that experimental results are often presented in terms of means and associated standard deviations, which may not fully exploit the wealth of information provided by the experiments.

Tensile properties of flax fibres

Flax fibres, derived from the bast of the flax plant, have recently attracted considerable attention due to their exceptional mechanical properties and versatility. This ancient crop has been cultivated for thousands of years, primarily for its integral role in textile production. The importance of flax fibres lies in their unique combination of properties, including high strength, favourable biocompatibility and excellent weaveability, which make them highly suitable for various multifunctional applications, including technical uses such as reinforcement in composite materials. This is in line with the growing focus on sustainable development and the demand for environmentally friendly products. To fully exploit the potential of flax fibres in various applications, a thorough understanding of their mechanical and physical properties is essential.

A comprehensive summary of the results obtained from tensile and compressive tests on individual flax fibres is given in Table 1, which shows a considerable dispersion of values. The Young's modulus ranges from 45 GPa to 70 GPa, showing the variability between the fibres tested. In addition, the tensile strength varies between 850 and 1400 MPa, while the compressive strength is around 1200 MPa (Bos et al., 2002).

Mode of extraction	Young's modulus (GPa)	Tensile strength (MPa)	Failure strain (%)	Reference
Standard and manual extraction	-	1500-1800	-	(Bos et al., 2002)
-	54.08 ± 15.12	1339 ± 486	3.27 ± 0.84	(Baley, 2002)
Manual extraction	50.1 ± 27.2 to 68.2 ± 35.8	854 to 1335	1.8 to 2.2	(Lefeuvre et al., 2014)
-	68.2 ± 35.8	1454 ± 835	2.3 ± 0.6	(Charlet et al., 2007)
-	55.5 ± 20.9	899 ± 461	1.7 ± 0.6	(Pillin et al., 2011)
Manual extraction	54.1 to 68.2	865 to 1454	1.8 to 3.3	(Bourmaud et al., 2013)
Manual	46.9 ± 15.7 to	850 ± 359 to 991	2.14 ± 0.82	(Bourmaud et al.,

extraction	51.2 ± 18.1	± 399	to 2.42 ± 0.99	2016)
-	52.5 ± 8.6	945 ± 200	2.07 ± 0.45	(Baley & Bourmaud, 2014)
-	51.28 ±12.02 to 64.1 ±13.65	1317 ± 529 to 1499 ± 346	2.93 ± 0.74 to 3.34 ± 0.71	(Baley et al., 2012)
-	57.5 ± 0.3	1034 ± 6	2.0 ± 0.1	(Bourmaud et al., 2015)

Table 1. Overview of the mechanical properties of single flax fibres. Taken from various sources in the literature.

Several researchers have observed a decrease in Young's modulus with increasing diameter of unitary flax fibres. (Baley, 2002) suggested that this behaviour could be due to an increase in lumen size. However, Placet et al.(Placet et al., 2012), in their study of the diameter dependence of Young's modulus for elementary hemp fibres, did not experimentally observe a positive correlation between lumen area fraction and fibre diameter. Consequently, the assumption made by (Baley, 2002) only partially explains the modulus-diameter relationship (Baley, 2002). In addition, Charlet et al.(Charlet et al., 2009) found that the modulus/diameter dependence disappeared when the diameter was measured near the break point, further complicating the understanding of this relationship. On the other hand, tensile strength at the fibre scale shows a dependence on gauge length and diameter, consistent with the weakest link theory originally proposed by Griffith (‘VI. The Phenomena of Rupture and Flow in Solids’, 1921) in the context of metallic materials. Strength is limited by critical defects, and longer or larger objects are likely to contain more defects, resulting in lower tensile strength. Therefore, the variation in strength due to size effects can be accurately predicted using a Weibull distribution (Romhány et al., 2003). This illustrates the complexity involved in elucidating the relationship between Young's modulus, tensile strength and fibre diameter in flax fibres.

There also appears to be a correlation between the tensile properties of flax fibres and their biochemical composition. Researchers have found that the cellulose content has a significant effect on the mechanical performance of the fibres. Alix et al.(Alix et al., 2009) demonstrated this relationship, attributing it to a lower interfibrillar spacing when the fibre contains more cellulose and less matrix material. The exceptional mechanical properties of cellulose, with a Young's modulus of approximately 137 GPa (Sakurada et al., 1962), contribute significantly to the overall mechanical performance of the fibres. Goudenhooft et al.(Goudenhooft et al., 2018), in a study combining atomic force microscopy (AFM) and Raman spectroscopy at the cell wall scale, confirmed the role of cellulose in determining the mechanical properties of flax fibres. This highlights the importance of biochemical composition, particularly cellulose content, in influencing the mechanical behaviour of flax fibres.

The mechanical properties of fibres are not only determined by the cellulose content, but also by the orientation of the cellulose microfibrils within the fibre structure. Eder et al.(Eder

et al., 2013) observed a correlation between the stiffness of wood samples and elementary fibres and their initial microfibril angle (MFA). Differences in microfibril orientation contribute to the heterogeneity observed in bast fibres. For example, fibres with a larger MFA, such as sisal and cotton (around 20°), have poorer mechanical properties compared to hemp and flax, which have a smaller MFA (Bourmaud et al., 2018). Bourmaud et al.(Bourmaud et al., 2013) also found a negative correlation (R2 = -0.75) between MFA and Young's modulus in nine flax fibre varieties. They also found that the pectin/hemicellulose ratio correlated with the tensile properties of flax fibres, with pectin acids having a significant effect on Young's modulus and MFA. Lefeuvre et al.(Lefeuvre et al., 2014) provided further confirmation of the importance of the pectin/hemicellulose ratio and hemicellulose content in relation to Young's modulus. A recent study by E. Richely et al. carried out a comprehensive analysis of the tensile behaviour of flax fibres. The cross-sectional areas of the fibres were determined assuming a cylindrical cross-section (Marrot et al., 2013). The experimental results showed a mean Young's modulus of 39.3 ± 12.3 GPa, strain at break of 2.24 ± 0.83% and strength at break of 700 ± 268 MPa. The observed tensile values exhibited comparable strain at break characteristics on average, while the values for Young's modulus and strength at break were at the lower end of the range reported in the existing literature (Richely et al., 2022). These findings highlight the critical role of microfibril organisation within the non-cellulosic polymer matrix in ensuring optimal stress transfer and mechanical performance of plant fibres, in addition to the influence of cellulose in providing high mechanical properties.

Furthermore, a recent study by Kandemir et al. aimed to characterise natural fibres, namely jute, kenaf, curaua, and flax fibres, to evaluate their physical, thermal and mechanical properties in comparison to conventional synthetic fibres. The study showed, both curaua and flax fibres were identified as prime candidates for reinforcement in thermoplastic aligned discontinuous fibre composites ADFRCs, with flax fibres exhibiting superior mechanical performance compared to glass fibres. Flax had the highest Young's modulus (~40 GPa), with curaua in second place (~30 GPa) among the four fibres. Curaua had the highest tensile strength (~660 MPa), while flax ranked second with a value of (~580 MPa). In terms of stiffness and strength, curaua and flax fibres outperformed jute and kenaf fibres. This study highlights the potential application of sustainable ADFRCs in engineering fields, sporting goods, transportation and automotive industries (Kandemir et al., 2020).

Researchers have also sought to develop analytical models to characterise the mechanical properties of flax fibres. A study by Abida et al. (Abida et al., 2020) aimed to analyse the statistical distributions of flax yarn properties based on tensile tests performed on fabric samples using a developed analytical model. The results of the investigation showed that the proposed modelling strategy provided an accurate description of the tensile behaviour of flax fabrics. The mean and standard deviation of Young's modulus, tensile strength and diameter of flax yarns obtained from fabric tensile tests were in good agreement with those obtained experimentally on single yarns. Specifically, the measured mean diameter of unit yarns was found to be 244.4 ± 19.2 µm, while the fitted value was 2474.8 ± 17.4 µm. Similarly, the fitted fracture strength was 292.3 ± 33.4 MPa, in close agreement with the experimental value of 271.2 ± 47.5 MPa. The Young's modulus determined was 9.4 ± 0.9 GPa, slightly lower than the experimental value of 10.8 ± 1.3 GPa.

Explanation of the stress strain diagram

Plant fibres exhibit nonlinear tensile behaviour and Lefeuvre et al.(Lefeuvre et al., 2014) identified three distinct responses in tensile tests on flax unit fibres (see Figure 16a). The first type (TI) exhibits a linear stress-strain curve, while the second type (TII) consists of two linear sections. The most common response is the third type (TIII), characterised by a non-linear section up to a threshold point, followed by an increasing tangent modulus to failure. This type of behaviour is more common in fibres with higher tensile properties and is correlated with cell wall composition. Several explanations have been proposed to explain these different behaviours. Initial hypotheses suggested that the partial reorientation of cellulose microfibrils along the fibre axes during initial stretching contributes to the nonlinearity (Kölln et al., 2005) (Baley, 2002) (Placet et al., 2014). However, this change in microfibril angle alone cannot fully explain the increase in stiffness (Placet et al., 2014). Another contributing phenomenon is the shear strain of amorphous polymers induced by fibre elongation, leading to longitudinal torsion (Placet et al., 2014). In addition, a stick-slip mechanism can occur due to excessive shear stress, causing hydrogen bond breakage and matrix slippage. When the stress is reduced, the microfibrils lock into new positions by reestablishing hydrogen bonds (Kölln et al., 2005) (Placet et al., 2014). The increase in fibre stiffness during loading is also attributed to strain-induced crystallisation of amorphous cellulose. Research by Astley et al.using SAXS and WAXS techniques demonstrated strain induced crystallisation of amorphous flax cellulose, as evidenced by an increase in the (200) peak intensity during deformation. These results complement the stick-slip mechanism proposed by (Placet et al., 2014) and support the scenario (see Figure 16b) for the TIII strain-stress curves of hemp. The initial part of the curve shows linear behaviour due to elastic deformation and irreversible strain from microfibril straightening. Beyond the yield point, the stick-slip mechanism causes both irreversible strain and stiffness reduction. Shear stress caused by fibre twisting in the amorphous regions and at interfaces can partially crystallise paracrystalline cellulose, leading to irreversible stiffening. Microfibril elongation accounts for the time-reversible behaviour and the final part of the curve involves reversible re-orientation of cellulose microfibrils in dislocation zones. Furthermore, Lefeuvre et al.(Lefeuvre et al., 2014) found a significant correlation between the presence of coating polysaccharides, mainly hemicellulose associated with cellulose microfibrils, and the non-linear behaviour observed in the stress-strain curve. These coating polysaccharides appear to have an influence on the second part of the curve, particularly with regard to the increase in tangent modulus.

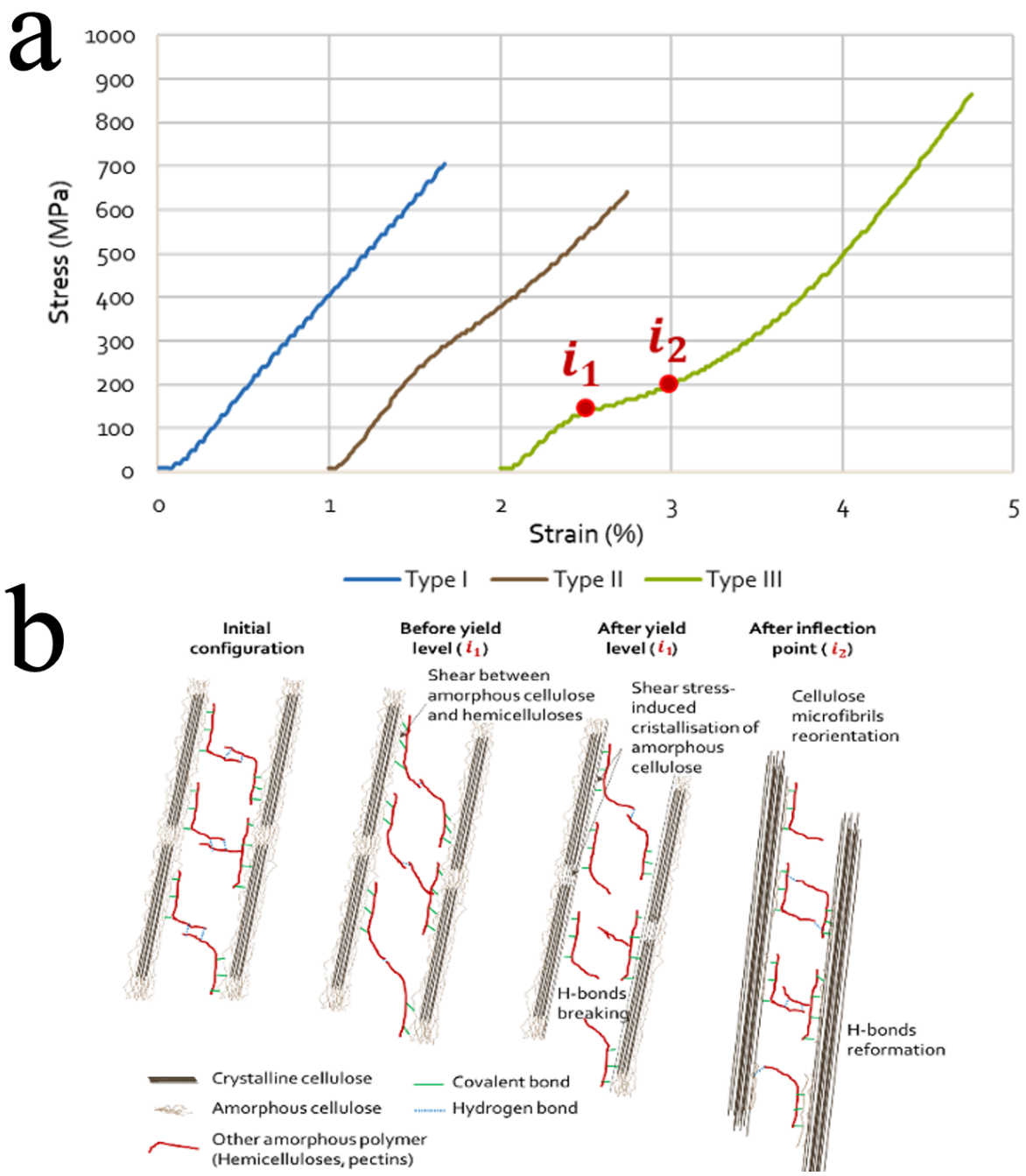

Figure 16. An example of the tensile behaviour of flax fibres. (a) Stress-strain curves of Type I, Type II and Type III (Lefeuvre et al., 2014), (b) Scenario proposed by Placet et al. to explain the Type III complex tensile behaviour of hemp fibres, adapted from (Placet et al., 2014).

Identification of the ‘optimum retting point’

The historical ‘artisanal method’

For centuries artisan farmers have used methods passed down from father to son to determine the optimum period of dew retting of flax stems in the field. The determination of the optimal retting point has been studied for a long time now. In this context early studies published in the 1920's have had the potential to produce tools to identify the optimal retting point. In the period of 1960’s to 1980’s, studies on flax dew retting and its influence on the mechanical properties of flax fibre was of great interest. Several groups worked on designing and producing tools to identify the optimal retting point of flax, for the purpose of obtaining high quality flax fibres for textile industries. However, these studies were paused and neglected after the emergence of plastic fibres. Today, due to the world’s pollution caused by oil sources, the emergence of the renewable energy term drives scientists to rethink about integrating biodegradable green sources in industrial domains. Therefore, in this project we aim to produce a tool to identify the optimal dew-retting point in flax, to obtain high quality fibres for industrial usage. To do this we looked at the literature, and made a bibliographic study on the previous tools that have the potential to identify the optimal retting point. This section summarises the tools that have been designed for this purpose.

Figure 17 shows early drawings from a beautiful book written by Robert L. Davis published in 1923 illustrating how the artisan farmer should use his hands to mechanically test for the optimum retting point of dew retted flax stems. The illustrations and the associated text describe several manual mechanical tests including bending, squeezing, and twisting where the artisan should observe how the exterior tissue reacts to this.

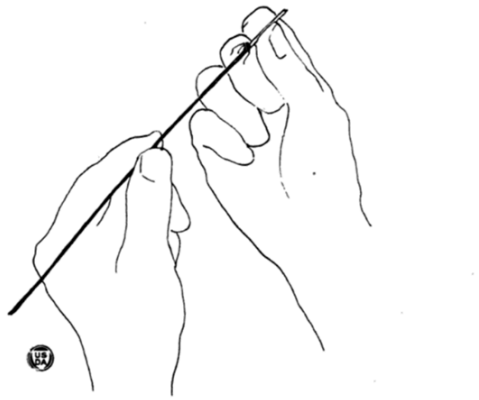

FIG. 14.—Step 1 in the loose-core test of retting flax fibers. The cortex is shoved back from the wooden core so as to leave several centimeters entirely free from fibers.

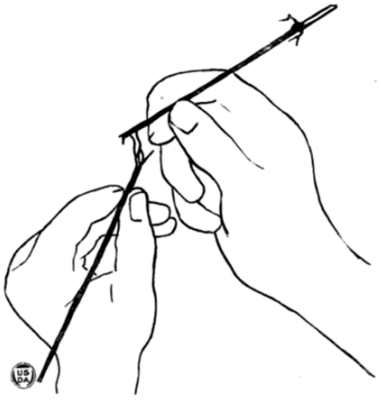

FIG. 15.—Step 2 in the loose-core test of retting flax fibers. The wooden core is broken 6 to 9 inches above the first break where the cortex has been shoved back.

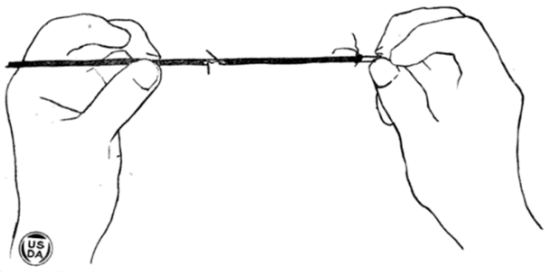

FIG. 16.—Step 3 in the loose-core test of retting flax fibers. One hand holds the stem above the second break in the wooden core, while the other exerts a pull on the exposed lower end.

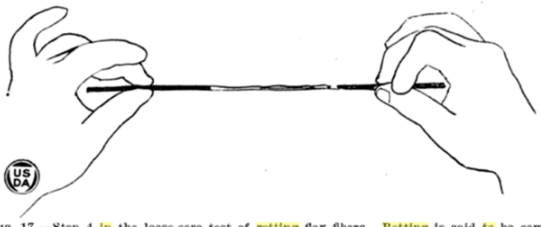

FIG. 17.—Step 4 in the loose-core test of retting flax fibers. Retting is said to be complete if the wooden core slips easily out from the cortex without any of the fibers clinging to it.

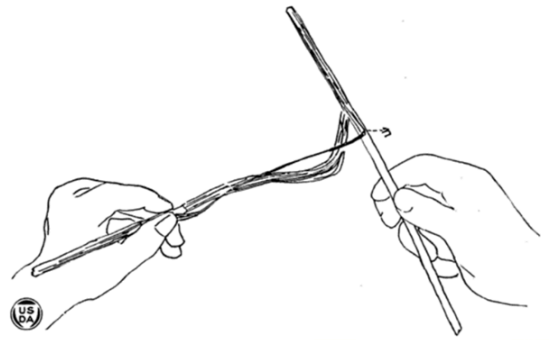

FIG. 19.—Leaf-scar test for the completion of the retting process of flax fibers. Retting is incomplete. Note the fibers clinging at the leaf scar or node (*n*). The sizes of the flax stems in Figures 19 and 21 to 23 are exaggerated as compared with the size of the hands.

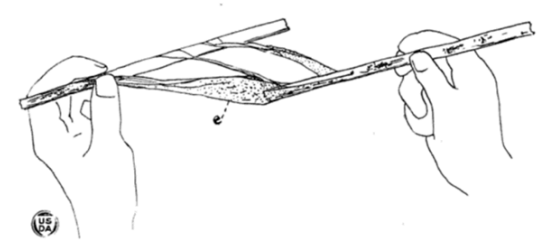

FIG. 21.—Epidermis test in incompletely retted flax. The epidermis (*e*) is clinging to both nodes and internodes in large pieces, showing that the retting process is not complete.

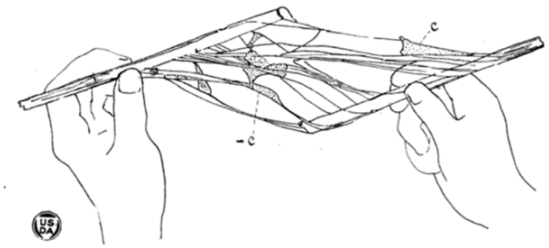

FIG. 22.—Epidermis test of flax fibers when retting is nearly complete. The fibers are well separated and of fine diameter. Pieces of cuticle (*c*) are clinging in spots. When this stage of retting is reached it is necessary to swish the fibers to and fro in water in order to tell whether the epidermis is well loosened.

FIG. 23.—Flax fibers at the completion of the epidermis test. Retting is at the same stage as that shown in Figure 22. The cortex is shown after it has been swished to and fro in water. Retting is almost complete, and the cuticle (*c*) is separated except at the leaf scars (*l*).

Figure 17. Early drawings from a book written by Robert L. Davis published in 1923 illustrating how the artisan farmer should use his hands to mechanically test for the optimum retting point of dew retted flax stems. Taken from (Davis, R. L. (1923). *Flax-stem anatomy in relation to retting* (No. 1185). US Department of Agriculture).

In addition to guidance on the optimum retting period, scientists have measured the mechanical properties of flax fibre in a real-time retting period. Figure 18 shows a 3 years real-time study of the influence of retting of fibre strength from 1926, 1927, and 1928 conducted by Brittain B. Robinson. He was able to control some parameters at that time, where the influence of environmental factors such as the shade and sun time on the fibre strength were studied.

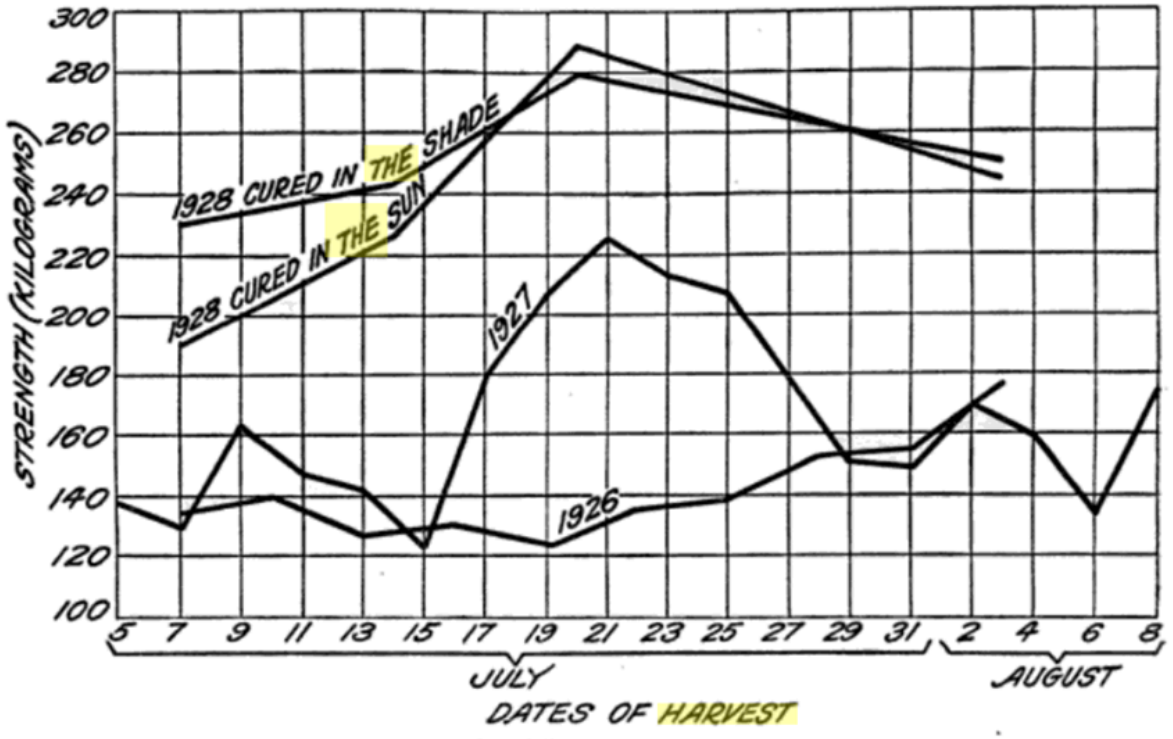

FIGURE 7.—Strength of fiber estimated as kilograms per gram of fiber 15 centimeters in length for different days of harvest in 1926, 1927, and 1928. In 1928, after harvesting a sample of flax, the sample was divided and one half of it was cured in the sun and the other half was cured in the shade

Figure 18. An early example of fibre strength as a function of retting advancement. For 2 years. Taken from (Robinson, B. B. (1931). *The time to harvest fiber flax* (No. 236). US Department of Agriculture).

Tools to identify the optimum retting point

Optical-based methods for tools

Fraser et al.(Fraser et al., 1982) visually documented the structural changes induced by glyphosate treatment, which resulted in uniform drying of flax stems (see Figure 19). To achieve this, they used a methodology that involved embedding flax stems in LR white resin. Cross-sections were then prepared using diamond cutting techniques. These cross-sections were then subjected to staining procedures, followed by microscopic visualisation. The study provides valuable insights into the effects of glyphosate treatment on flax stem morphology and understanding the structural changes induced by this chemical treatment.

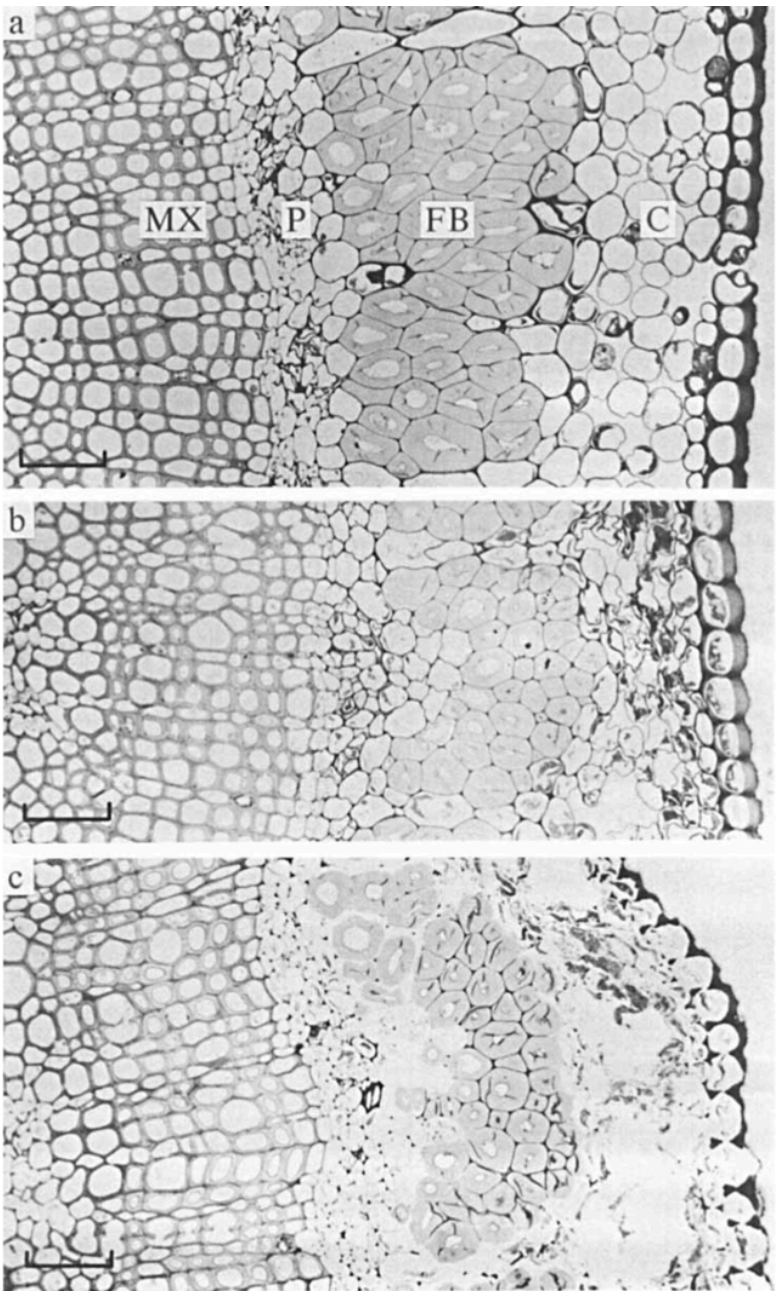

Figure 19. An early example suggesting that retting could be monitored using optical microscopy of stem cross sections. (Fraser et al., 1982)

Mechanical based methods for tools

D. A. Seaby and P. C. Mercer (Seaby & Mercer, 1984) introduced a specially designed tool to replicate the scutching process within the mechanical extraction step of flax fibre–see Figure 20. This innovative tool works by first bending the flax stalk and then using a combination of crushing and shearing forces to release the fibres. The primary objective of this tool is to investigate and identify the optimum conditions for inducing retting in flax, while also providing a means of quickly and accurately assessing the stage of retting progression. The research by Seaby and Mercer represents a novel approach to understanding the

retting process in flax and provides a practical tool for monitoring and evaluating its progress.

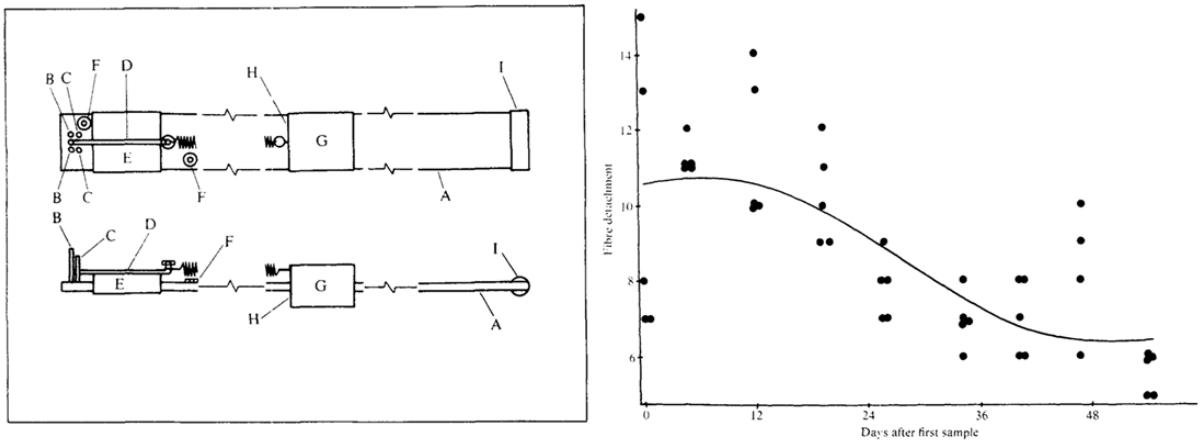

Figure 20. A proposed hand tool to test the degree of retting of flax straw by (Seaby & Mercer, 1984)

A. M. Goodman et al. (Goodman et al., 2002) conducted a study demonstrating the usefulness of peeling tests in measuring mechanical changes at the interface between fibre bundles (primary phloem tissue) and secondary phloem tissue–see Figure 21. This method makes it easier to monitor the progress of retting and allows comparisons to be made to determine the optimum harvesting time for flax. Consequently, the aim of the study was to carry out a series of standardised mechanical tests in the laboratory, following the methods outlined by (Alexander, 1995) and (Wright & Vincent, 1996) to comprehensively investigate the retting process and identify structural changes in flax samples resulting from the application of the herbicide glyphosate and microbial colonisation in a standing crop.

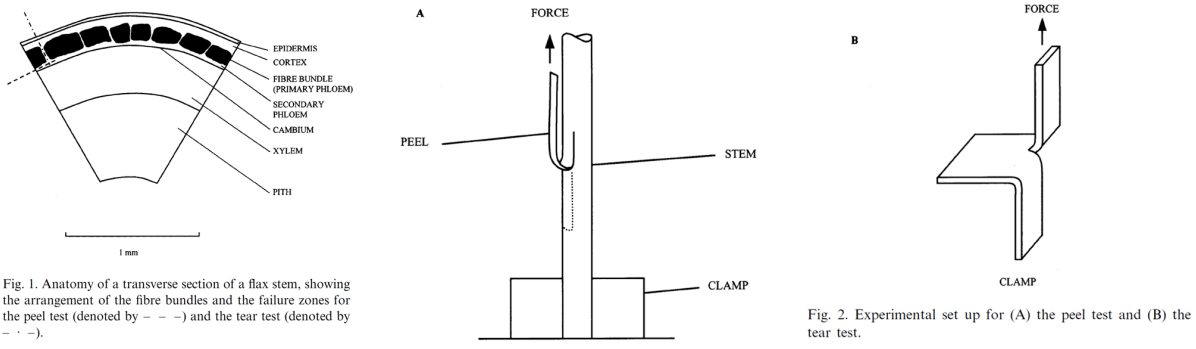

Fig. 1. Anatomy of a transverse section of a flax stem, showing the arrangement of the fibre bundles and the failure zones for the peel test (denoted by – – –) and the tear test (denoted by – · –).

Fig. 2. Experimental set up for (A) the peel test and (B) the tear test.

Figure 21. (Goodman et al., 2002) proposed methods to test the degree of retting of flax stems and suggested quantifiable mechanisms which could form the basis of reliable tools.

Building on the methodology demonstrated by Goodman et al, I. Booth et al. (Booth et al., 2004) used a peeling test approach with a modification of the peeling angle (see Figure 22).

Their aim was to adapt this method for use in the context of hemp cultivation, and they investigated the effect of varying the applied load angle on the work required for peeling. The aim of the research was to determine the most suitable peel test geometry. Their study emphasises that peel tests provide a valuable means of objectively monitoring the reduction in mechanical work required to peel dew-retted hemp stalks, and that this reduction correlates with the progress of retting. Consequently, peel tests emerged as a potential tool for monitoring the influence of various factors on the retting process in hemp, providing valuable insights into this crucial aspect of fibre development.

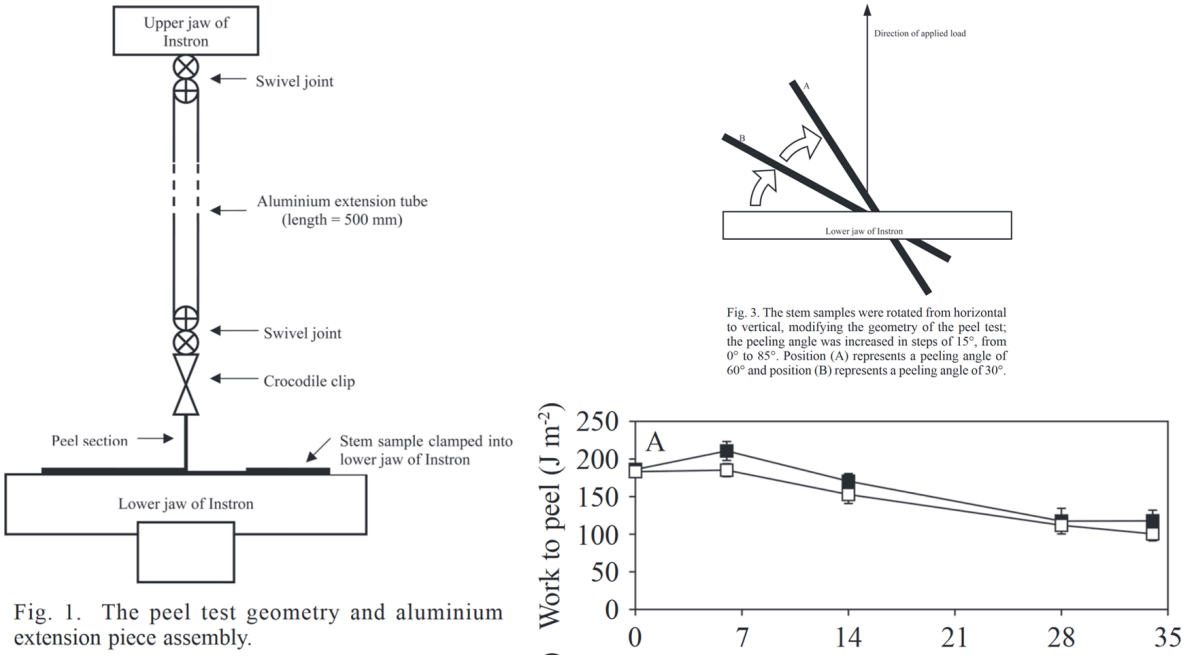

Fig. 1. The peel test geometry and aluminium extension piece assembly.

Fig. 3. The stem samples were rotated from horizontal to vertical, modifying the geometry of the peel test; the peeling angle was increased in steps of 15°, from 0° to 85°. Position (A) represents a peeling angle of 60° and position (B) represents a peeling angle of 30°.

Figure 22. A mechanical peeling tool proposed to monitor the advancement of retting. (Booth et al., 2004)

D. Waldron and J. Harwood (Waldron & Harwood, 2011) carried out a detailed study of the effect of the chemical composition of flax stems on their mechanical properties. They used dynamic mechanical analysis to track changes in stem properties at different stages of plant development (see Figure 23). They also used a sequential chemical extraction approach to analyse the role of individual chemical components. This study provides valuable insights into the mechanical properties of flax stems, which in turn may be a key factor in determining the optimal harvest time for flax crops and the level of mechanical decortication required to achieve optimum fibre separation and cleanliness.

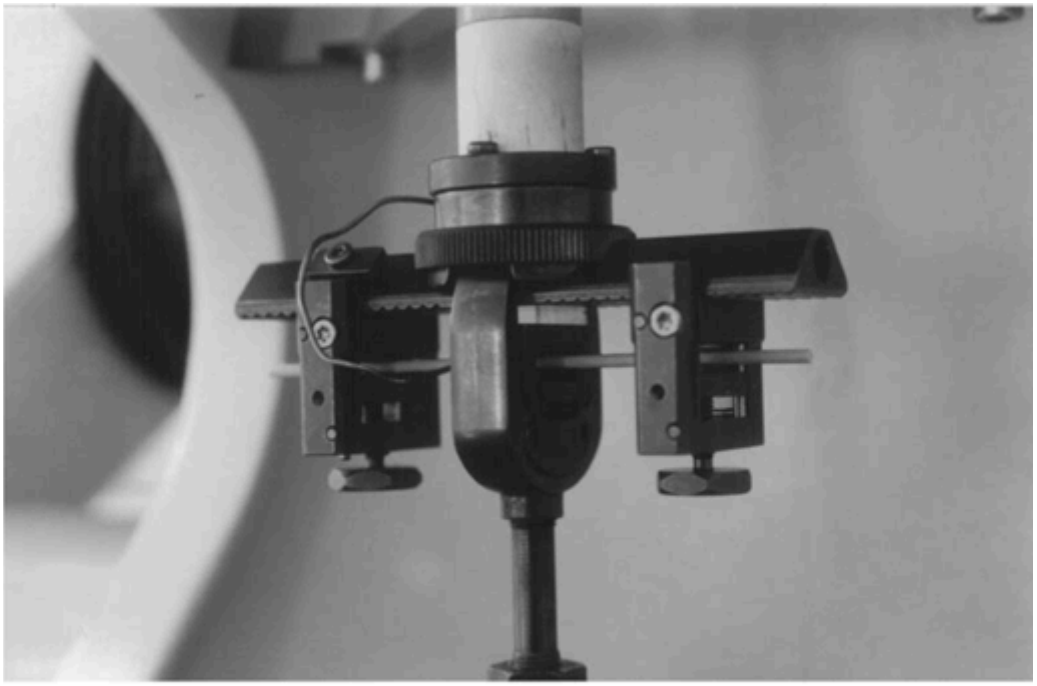

Figure 23. D. Waldron and J. Harwood (Waldron & Harwood, 2011) suggested a tool for measuring the dynamic properties of flax stems. However, the retting evolution was not studied.

More recently, (Réquilé et al., 2018) conducted a comprehensive study with the primary objective of using stem peeling experiments to assess the effect of field retting processes on the tissue cohesion within hemp stems and its subsequent effect on the tensile properties of elementary fibres (see Figure 24). Their experimental approach involved the integration of stem peeling experiments with scanning electron microscopy (SEM) to investigate the influence of varying degrees of retting within the plant material. By examining the evolution of fracture energy at the interface between the fibres and the woody core within the stem, this investigation further explored the mechanisms underlying fracture during peeling experiments. The overall aim was to gain a deeper insight into the progressive changes in fibre bundle cohesion that occur during the retting process.

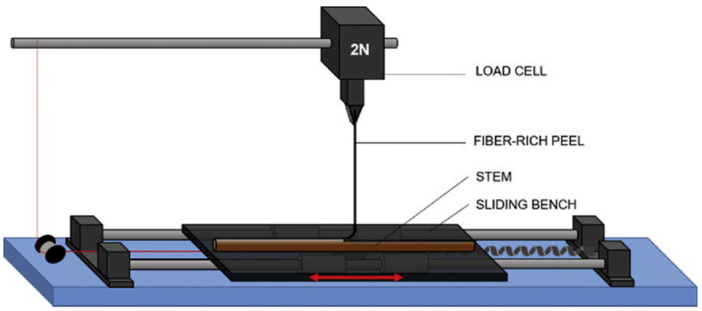

Fig. 2. Peeling test experimental set-up.

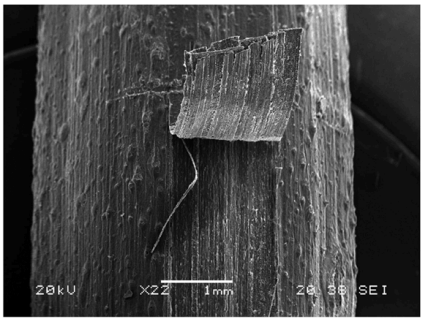

Fig. 3. Scanning electron microscope image of a non-retted hemp stem after peeling test. The peel width is determined to avoid additional bending stresses. For ease of observation, the peel was cut.

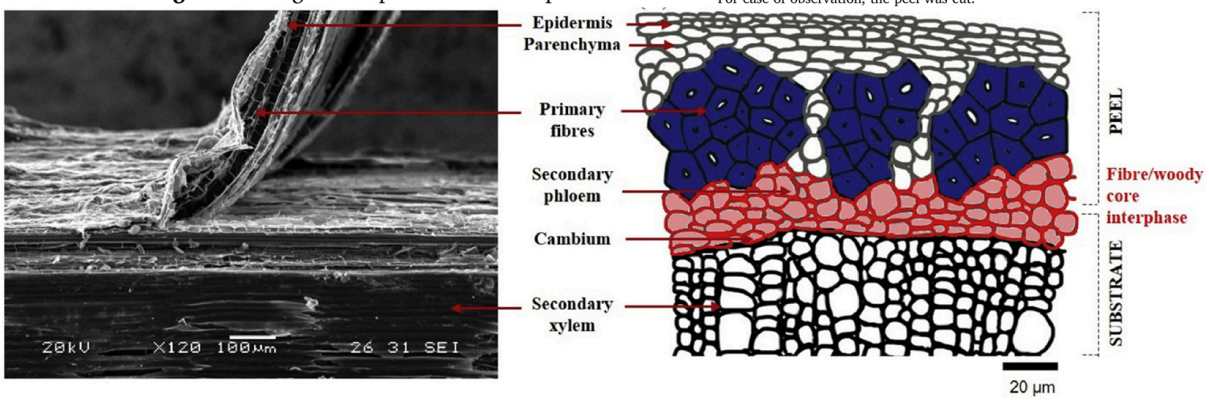

Figure 24. Improved peeling experiments using SEM observation to characterise the advancement of retting. Réquilé et al.(2018). (Réquilé, Le Duigou, et al., 2018)

Using infrared spectroscopy as a tool

H. S. S. Sharma and N. Reinard (Sharma & Reinard, 2004) have made a significant contribution to the field by developing robust visible near-infrared (vis-NIR) calibrations specifically designed to monitor fibre fineness during mechanical processing. These calibrated methods have significant practical relevance for industrial applications, particularly within spinning mills. It is imperative that these calibrations demonstrate the ability to effectively monitor all fibre grades, including water-retted sliver. In addition, the study undertook the essential task of evaluating the precision and accuracy of these calibrations in predicting fibre fineness within the preparation lines, further underlining their practical utility and reliability in an industrial context.

Pectin content approach: potential for a lab-on-chip

W. J. M. Meijer et al. (Meijer et al., 1995) conducted a comprehensive study to investigate the relationship between field and water retting and the pectin content in the stalks–see Figure 25. This research involved assessing readability by quantifying the controlled degradation rate of pectin during water retting. To gain a comprehensive perspective, the study tracked pectin degradation at three specific locations along the stems and in flax samples harvested at four different stages, from flowering to seed ripening. They also looked at how the processes of chopping and drying the straw affected retting in the field. Recognising that the degree of retting has a significant effect on fibre quality, the researchers

used different retting methods on samples of flax with different levels of retting. Through careful analysis, they established correlations between pectin content in retted stalks and key fibre attributes such as tensile strength, fineness and purity.

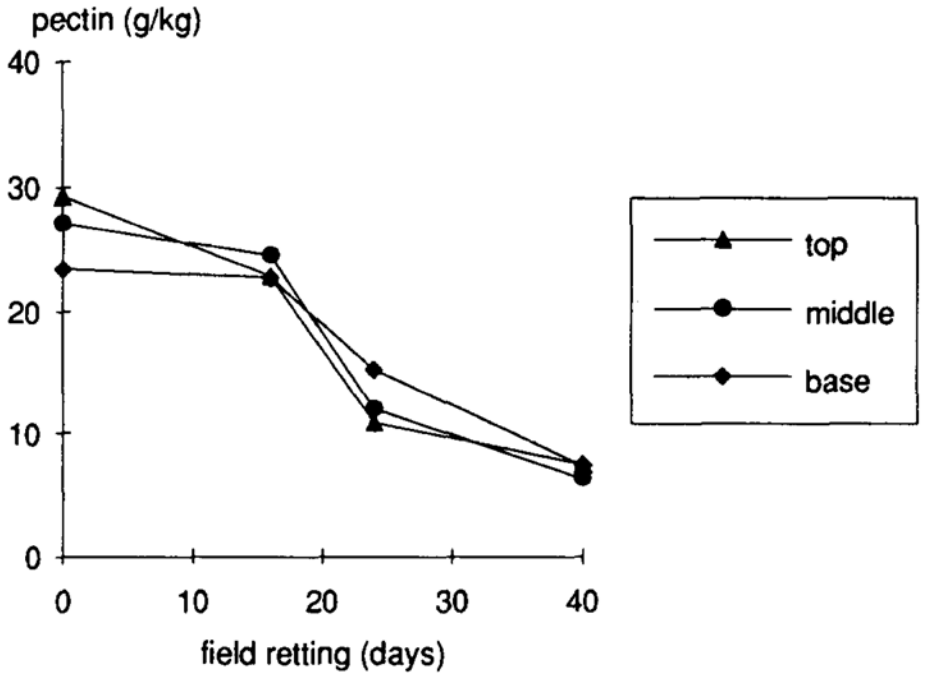

Figure 25. Evolution of the pectin content in fax stems as a function of retting. (Meijer et al., 1995)

Conclusion

Farming, science, and technology (tools) have always been intertwined. For example, the first plough emerged around 5000 BC. Since this, every leap forward that humans have made in science and technology has had an impact on farming. These leaps forward can now be seen at Agriculture 1.0 forward. We are currently living in Agriculture 4.0 whereby the microelectronics and microtechnology revolution is being applied to all sectors of farming. As we have seen, Agriculture 4.0 is also known as Digital Farming, Smart Agriculture, and Smart Farming. One specific area of Agriculture 4.0 is that of using a whole range of sensors for specific purposes in farming. An example of this is to detect the optimum point of something, e.g. ripeness of fruit, maturity of plant etc. To do this, we have seen that there are many physical and chemical properties which can be monitored by existing sensors. In addition to this there are many sensors yet to be developed as commercial apparatus does not exist. This is the case with this PhD. We have see that flax fibre production is an important industry. The use of flax fibre, known for its widespread use in textiles and its emerging presence in thermoplastic materials, is underlined by its remarkable mechanical and tensile properties. Among the many techniques available to evaluate the mechanical properties of fibres, tensile testing remains the most prominent choice. The modulus of flax fibre ranges from 30 to 70 GPa, with considerable variability in

the data obtained. Numerous factors contribute to this variability, including experimental conditions, dimensions such as diameter and length, chemical composition, cellulose orientation within the fibre and the accurate determination of cross-sectional areas is a significant challenge. In addition, environmental factors and inherent structural defects have a complex effect on this value. The research landscape is actively evolving, delving into fibre modelling to improve the accuracy of mechanical property assessment. Studies focusing on the mechanical properties of flax fibres have predominantly relied on macroscopic tensile testing, with microscale assessments yet to be developed. In particular, existing research has predominantly investigated the effect of retting on the mechanical properties of flax fibres only at the optimum retting point. In contrast, there is a lack of research into the influence in a real-time of retting on the mechanical properties of the flax stalk, which encompasses the fibre, and flax fibres. This highlights the need for a comprehensive understanding of the effect of retting on the flax stalk in order to improve mechanical fibre extraction through accurate and real-time determination.

As smart agriculture continues to grow and technology is increasingly integrated into different sectors, the natural fibre sector, particularly flax, has lagged behind in this technological evolution. Despite being a fundamental component of textiles and composites, natural fibres have not fully embraced the potential of smart agriculture. However, achieving optimum flax fibre quality remains a challenge, influenced by factors such as a real-time monitoring of flax dew retting in the field and ability of farmers in accurately predicting the ideal point at which flax is ready. Recognising this critical gap, this PhD programme is strategically designed to address a variety of objectives aimed at bridging this critical gap.

Objectives of the PhD and description of the chapter content

The main goal of the PhD is to demonstrate a mechanical sensor capable of predicting the optimum retting time to enable the high-yield extraction of high quality flax fibres from their parent stems. To do this, the basic fundamental mechanical properties of the flax stems and flax fibres need to be characterised in real time during a full retting period and beyond–such a study has never been conducted in such detail before. Only by doing this can one determine the optimum retting time for high fibre yield extraction. The mechanical properties were gathered using a multiscale approach: macroscopic, microscopic, and nanoscopic mechanical testing using a combination of established and original approaches. These include macroscopic bending, compression, and torsion of the flax stems, flax fibre-based microcantilever measurements (static and dynamic) of single flax fibres, and nanoindentation atomic force microscopy measurements of flax fibre cross sections and surfaces.

Chapter 2 describes the sample gathering enabling the experimentation in the PhD. Seemingly trivial, Chapter 2 details the comprehensive protocol developed to systematically collect samples directly from the field specifically designed for multiscale mechanical testing. As the study was, for the most, a real-time study–a strict experimental timing had to be planned and adhered to.

Chapters 3, 4, and 5 present the macroscopic mechanical characterisation of the flax stems. Detailed descriptions of original experimental setups, methods, and the resulting mechanical parameters are provided, facilitating a comprehensive understanding of the mechanical

behaviour of the stems. The measurements yield interesting results in terms of the evolution of the properties of the stems with retting.

Descending a scale, Chapter 6 presents the microscopic mechanical characterisation of the flax fibres. The microscale experiments, inspired by microelectromechanical (MEMS), include static and dynamic testing conducted on single flax fibres acting as microcantilevers, shedding light on both dynamic and static responses of single flax fibres. This chapter provides a detailed description of the experimental procedures, allowing an in-depth exploration of the micromechanical properties of the fibre. The measurements yield interesting results in terms of the evolution of the properties of the fibres with retting.

Descending another scale, Chapter 7 presents the nanoscopic mechanical characterisation of the flax fibres. Nanoindentation atomic force microscopy (AFM) is used to probe the mechanical modulus of the flax fibres in cross section and on their fibre walls. The measurements also yield interesting results in terms of the evolution of the properties of the fibres with retting.

Finally, Chapter 8 on a more practical note presents a study concerning the drying of flax stems following rainfall. The water content of flax stems has an impact on their mechanical properties. For a sensor-based tool to be reliable, the water content needs to be known. We chose to do this by performing a precise evaporation study of flax stems by simulating rain and then studying evaporation at a typical July/August morning temperature (21°C). The data provides information on when stems could be tested by the tool with confidence.

As we progress through each chapter, the interplay between different scales of mechanical testing converges, ultimately contributing to the overarching goal of this PhD programme - the comprehensive extraction of critical mechanical properties from flax fibres and stalks, advancing our understanding and paving the way for the development of an IoT-based mechanical sensor for real-time prediction of the optimum retting point in flax cultivation.

References

Abida, M., Baklouti, A., Gehring, F., Vivet, A., & Bouvet, C. (2020). Inverse approach for flax yarns mechanical properties identification from statistical mechanical characterisation of the fabric. *Mechanics of Materials*, *151*, 103638. https://doi.org/10.1016/j.mechmat.2020.103638

Ahmad, Z., Touati, F., Zafar, Q., & Shah, M. (2017). Integrated Capacitive and Resistive Humidity Transduction via Surface Type Nickel Phthalocyanine Based Sensor. *International Journal of Electrochemical Science*, *12*(4), 3012–3019. https://doi.org/10.20964/2017.04.21

Akin, D. E. (2010). Flax – Structure, Chemistry, Retting and Processing. In J. Müssig (Ed.), *Industrial Applications of Natural Fibres* (1st ed., pp. 87–108). Wiley. https://doi.org/10.1002/9780470660324.ch4

Akin, D. E. (2013). Linen Most Useful: Perspectives on Structure, Chemistry, and Enzymes

for Retting Flax. *ISRN Biotechnology*, *2013*, 1–23. https://doi.org/10.5402/2013/186534

Akin, D. E., Foulk, J. A., Dodd, R. B., & McAlister, D. D. (2001). Enzyme-retting of flax and characterisation of processed fibers. *Journal of Biotechnology*, *89*(2–3), 193–203. https://doi.org/10.1016/S0168-1656(01)00298-X

Alexander, R. M. (1995). *Biomechanics - Materials: A Practical Approach* . Edited by J. F. V. VINCENT . Pp. 247. IRL Press, Oxford, 1992. £50.00 hardback. ISBN 0 19 963223 5. £27.50 paperback. ISBN 0 19 963222 7. *Experimental Physiology*, *80*(1), 171–171. https://doi.org/10.1113/expphysiol.1998.sp004290

Alix, S., Philippe, E., Bessadok, A., Lebrun, L., Morvan, C., & Marais, S. (2009). Effect of chemical treatments on water sorption and mechanical properties of flax fibres. *Bioresource Technology*, *100*(20), 4742–4749. https://doi.org/10.1016/j.biortech.2009.04.067

Aragón-Briceño, C. I., Pozarlik, A. K., Bramer, E. A., Niedzwiecki, L., Pawlak-Kruczek, H., & Brem, G. (2021). Hydrothermal carbonization of wet biomass from nitrogen and phosphorus approach: A review. *Renewable Energy*, *171*, 401–415. https://doi.org/10.1016/j.renene.2021.02.109

Arnould, O., Siniscalco, D., Bourmaud, A., Le Duigou, A., & Baley, C. (2017). Better insight into the nano-mechanical properties of flax fibre cell walls. *Industrial Crops and Products*, *97*, 224–228. https://doi.org/10.1016/j.indcrop.2016.12.020

Aslan, M., Chinga-Carrasco, G., Sørensen, B. F., & Madsen, B. (2011). Strength variability of single flax fibres. *Journal of Materials Science*, *46*(19), 6344–6354. https://doi.org/10.1007/s10853-011-5581-x

Baley, C. (2002). Analysis of the flax fibres tensile behaviour and analysis of the tensile stiffness increase. *Composites Part A: Applied Science and Manufacturing*, *33*(7), 939–948. https://doi.org/10.1016/S1359-835X(02)00040-4

Baley, C. (2004). Influence of kink bands on the tensile strength of flax fibers. *Journal of Materials Science*, *39*(1), 331–334. https://doi.org/10.1023/B:JMSC.0000007768.63055.ae

Baley, C., & Bourmaud, A. (2014). Average tensile properties of French elementary flax fibers. *Materials Letters*, *122*, 159–161. https://doi.org/10.1016/j.matlet.2014.02.030

Baley, C., Le Duigou, A., Bourmaud, A., & Davies, P. (2012). Influence of drying on the mechanical behaviour of flax fibres and their unidirectional composites. *Composites Part A: Applied Science and Manufacturing*, *43*(8), 1226–1233. https://doi.org/10.1016/j.compositesa.2012.03.005

Beaugrand, J., & Guessasma, S. (2015). Scenarios of crack propagation in bast fibers: Combining experimental and finite element approaches. *Composite Structures*, *133*,

667–678. https://doi.org/10.1016/j.compstruct.2015.07.119

Bensadoun, F., Verpoest, I., Baets, J., Müssig, J., Graupner, N., Davies, P., Gomina, M., Kervoelen, A., & Baley, C. (2017). Impregnated fibre bundle test for natural fibres used in composites. *Journal of Reinforced Plastics and Composites*, *36*(13), 942–957. https://doi.org/10.1177/0731684417695461

Booth, I., Goodman, A. M., Grishanov, S. A., & Harwood, R. J. (2004). A mechanical investigation of the retting process in dew-retted hemp (Cannabis sativa). *Annals of Applied Biology*, *145*(1), 51–58. https://doi.org/10.1111/j.1744-7348.2004.tb00358.x

Bos, H. L., Van Den Oever, M. J. A., & Peters, O. C. J. J. (2002). [No title found]. *Journal of Materials Science*, *37*(8), 1683–1692. https://doi.org/10.1023/A:1014925621252

Bourmaud, A., Beaugrand, J., Shah, D. U., Placet, V., & Baley, C. (2018). Towards the design of high-performance plant fibre composites. *Progress in Materials Science*, *97*, 347–408. https://doi.org/10.1016/j.pmatsci.2018.05.005

Bourmaud, A., Gibaud, M., & Baley, C. (2016). Impact of the seeding rate on flax stem stability and the mechanical properties of elementary fibres. *Industrial Crops and Products*, *80*, 17–25. https://doi.org/10.1016/j.indcrop.2015.10.053

Bourmaud, A., Gibaud, M., Lefeuvre, A., Morvan, C., & Baley, C. (2015). Influence of the morphology characters of the stem on the lodging resistance of Marylin flax. *Industrial Crops and Products*, *66*, 27–37. https://doi.org/10.1016/j.indcrop.2014.11.047

Bourmaud, A., Morvan, C., Bouali, A., Placet, V., Perré, P., & Baley, C. (2013). Relationships between micro-fibrillar angle, mechanical properties and biochemical composition of flax fibers. *Industrial Crops and Products*, *44*, 343–351. https://doi.org/10.1016/j.indcrop.2012.11.031

Burgert, I., Frühmann, K., Keckes, J., Fratzl, P., & Stanzl-Tschegg, S. E. (2003). Microtensile Testing of Wood Fibers Combined with Video Extensometry for Efficient Strain Detection. *Holzforschung*, *57*(6), 661–664. https://doi.org/10.1515/HF.2003.099

Chabbert, B., Padovani, J., Djemiel, C., Ossemond, J., Lemaître, A., Yoshinaga, A., Hawkins, S., Grec, S., Beaugrand, J., & Kurek, B. (2020). Multimodal assessment of flax dew retting and its functional impact on fibers and natural fiber composites. *Industrial Crops and Products*, *148*, 112255. https://doi.org/10.1016/j.indcrop.2020.112255

Chanal, P. M., & Kakkasageri, M. S. (2020). Security and Privacy in IoT: A Survey. *Wireless Personal Communications*, *115*(2), 1667–1693. https://doi.org/10.1007/s11277-020-07649-9

Charlet, K., Baley, C., Morvan, C., Jernot, J. P., Gomina, M., & Bréard, J. (2007). Characteristics of Hermès flax fibres as a function of their location in the stem and

properties of the derived unidirectional composites. *Composites Part A: Applied Science and Manufacturing*, *38*(8), 1912–1921. https://doi.org/10.1016/j.compositesa.2007.03.006

Charlet, K., & Beakou, A. (2014). Interfaces within flax fibre bundle: Experimental characterisation and numerical modelling. *Journal of Composite Materials*, *48*(26), 3263–3269. https://doi.org/10.1177/0021998313508871

Charlet, K., Eve, S., Jernot, J. P., Gomina, M., & Breard, J. (2009). Tensile deformation of a flax fiber. *Procedia Engineering*, *1*(1), 233–236. https://doi.org/10.1016/j.proeng.2009.06.055

Chen, C., Kuang, Y., Zhu, S., Burgert, I., Keplinger, T., Gong, A., Li, T., Berglund, L., Eichhorn, S. J., & Hu, L. (2020). Structure–property–function relationships of natural and engineered wood. *Nature Reviews Materials*, *5*(9), 642–666. https://doi.org/10.1038/s41578-020-0195-z

Chen, H., Yang, G., Xiao, Y., Zhang, G., Yang, G., Wang, X., & Hu, Y. (2023). Effects of nitrogen and phosphorus fertilizer on the eating quality of indica rice with different amylose content. *Journal of Food Composition and Analysis*, *118*, 105167. https://doi.org/10.1016/j.jfca.2023.105167

Chow, Y. W., Pietranico, R., & Mukerji, A. (1975). Studies of oxygen binding energy to hemoglobin molecule. *Biochemical and Biophysical Research Communications*, *66*(4), 1424–1431. https://doi.org/10.1016/0006-291x(75)90518-5

Cisse, O., Placet, V., Guicheret-Retel, V., Trivaudey, F., & Boubakar, M. L. (2015). Creep behaviour of single hemp fibres. Part I: Viscoelastic properties and their scattering under constant climate. *Journal of Materials Science*, *50*(4), 1996–2006. https://doi.org/10.1007/s10853-014-8767-1

Davies, G. C., & Bruce, D. M. (1998). Effect of Environmental Relative Humidity and Damage on the Tensile Properties of Flax and Nettle Fibers. *Textile Research Journal*, *68*(9), 623–629. https://doi.org/10.1177/004051759806800901

Dhall, R., & Agrawal, H. (2018). An Improved Energy Efficient Duty Cycling Algorithm for IoT based Precision Agriculture. *Procedia Computer Science*, *141*, 135–142. https://doi.org/10.1016/j.procs.2018.10.159

Djemiel, C., Goulas, E., Badalato, N., Chabbert, B., Hawkins, S., & Grec, S. (2020). Targeted Metagenomics of Retting in Flax: The Beginning of the Quest to Harness the Secret Powers of the Microbiota. *Frontiers in Genetics*, *11*, 581664. https://doi.org/10.3389/fgene.2020.581664

Djemiel, C., Grec, S., & Hawkins, S. (2017). characterisation of Bacterial and Fungal Community Dynamics by High-Throughput Sequencing (HTS) Metabarcoding during Flax Dew-Retting. *Frontiers in Microbiology*, *8*, 2052.

https://doi.org/10.3389/fmicb.2017.02052

Du, G.-H., Liu, F.-H., & Rowland, G. (2015). Fiber cell development and fiber yield of flax (*Linum usitatissimum* L.) affected by the seasonal temperature pattern. *Canadian Journal of Plant Science*, *95*(6), 1215–1220. https://doi.org/10.4141/cjps-2014-185

Easson, D. L., & Molloy, R. (1996). Retting—A Key Process in the Production of High Value Fibre from Flax. *Outlook on Agriculture*, *25*(4), 235–242. https://doi.org/10.1177/003072709602500405

Eder, M., Arnould, O., Dunlop, J. W. C., Hornatowska, J., & Salmén, L. (2013). Experimental micromechanical characterisation of wood cell walls. *Wood Science and Technology*, *47*(1), 163–182. https://doi.org/10.1007/s00226-012-0515-6

Edwards, H. G. M., Farwell, D. W., & Webster, D. (1997). FT Raman microscopy of untreated natural plant fibres. *Spectrochimica Acta Part A: Molecular and Biomolecular Spectroscopy*, *53*(13), 2383–2392. https://doi.org/10.1016/S1386-1425(97)00178-9

Farahani, H., Wagiran, R., & Hamidon, M. (2014). Humidity Sensors Principle, Mechanism, and Fabrication Technologies: A Comprehensive Review. *Sensors*, *14*(5), 7881–7939. https://doi.org/10.3390/s140507881

Feleke, K., Thothadri, G., Beri Tufa, H., Rajhi, A. A., & Ahmed, G. M. S. (2023). Extraction and characterisation of Fiber and Cellulose from Ethiopian Linseed Straw: Determination of Retting Period and Optimization of Multi-Step Alkaline Peroxide Process. *Polymers*, *15*(2), 469. https://doi.org/10.3390/polym15020469

Fortino, G., Russo, W., Savaglio, C., Shen, W., & Zhou, M. (2018). Agent-Oriented Cooperative Smart Objects: From IoT System Design to Implementation. *IEEE Transactions on Systems, Man, and Cybernetics: Systems*, *48*(11), 1939–1956. https://doi.org/10.1109/TSMC.2017.2780618

Foughali, K., Fathallah, K., & Frihida, A. (2018). Using Cloud IOT for disease prevention in precision agriculture. *Procedia Computer Science*, *130*, 575–582. https://doi.org/10.1016/j.procs.2018.04.106

Fraser, T. W., Courtney, A. D., & Harvey, B. M. R. (1982). Pre-harvest retting of flax: A light microscope study of the effects of glyphosate treatment on the maturation of stem tissues. *Annals of Applied Biology*, *101*(3), 533–537. https://doi.org/10.1111/j.1744-7348.1982.tb00855.x

Friha, O., Ferrag, M. A., Shu, L., Maglaras, L., & Wang, X. (2021). Internet of Things for the Future of Smart Agriculture: A Comprehensive Survey of Emerging Technologies. *IEEE/CAA Journal of Automatica Sinica*, *8*(4), 718–752. https://doi.org/10.1109/JAS.2021.1003925

Goodman, A. M., Ennos, A. R., & Booth, I. (2002). A mechanical study of retting in glyphosate treated flax stems (Linum usitatissimum). *Industrial Crops and Products*,

15(2), 169–177. https://doi.org/10.1016/S0926-6690(01)00108-X

Gorshkova, T. A., Wyatt, S. E., Salnikov, V. V., Gibeaut, D. M., Ibragimov, M. R., Lozovaya, V. V., & Carpita, N. C. (1996). Cell-Wall Polysaccharides of Developing Flax Plants. *Plant Physiology*, *110*(3), 721–729. https://doi.org/10.1104/pp.110.3.721

Goudenhooft, C., Bourmaud, A., & Baley, C. (2019). Flax (Linum usitatissimum L.) Fibers for Composite Reinforcement: Exploring the Link Between Plant Growth, Cell Walls Development, and Fiber Properties. *Frontiers in Plant Science*, *10*, 411. https://doi.org/10.3389/fpls.2019.00411

Goudenhooft, C., Siniscalco, D., Arnould, O., Bourmaud, A., Sire, O., Gorshkova, T., & Baley, C. (2018). Investigation of the Mechanical Properties of Flax Cell Walls during Plant Development: The Relation between Performance and Cell Wall Structure. *Fibers*, *6*(1), 6. https://doi.org/10.3390/fib6010006

Haag, K., & Müssig, J. (2016). Scatter in tensile properties of flax fibre bundles: Influence of determination and calculation of the cross-sectional area. *Journal of Materials Science*, *51*(17), 7907–7917. https://doi.org/10.1007/s10853-016-0052-z

Heller, K., Sheng, Q. C., Guan, F., Alexopoulou, E., Hua, L. S., Wu, G. W., Jankauskienė, Z., & Fu, W. Y. (2015). A comparative study between Europe and China in crop management of two types of flax: Linseed and fibre flax. *Industrial Crops and Products*, *68*, 24–31. https://doi.org/10.1016/j.indcrop.2014.07.010

Hideno, A., Ogbonna, J. C., Aoyagi, H., & Tanaka, H. (2007). Acetylation of loofa (Luffa cylindrica) sponge as immobilization carrier for bioprocesses involving cellulase. *Journal of Bioscience and Bioengineering*, *103*(4), 311–317. https://doi.org/10.1263/jbb.103.311

Huang, J.-Q., Li, B., & Chen, W. (2016). A CMOS MEMS Humidity Sensor Enhanced by a Capacitive Coupling Structure. *Micromachines*, *7*(5), 74. https://doi.org/10.3390/mi7050074

Huang, J.-Q., Li, F., Zhao, M., & Wang, K. (2015). A Surface Micromachined CMOS MEMS Humidity Sensor. *Micromachines*, *6*(10), 1569–1576. https://doi.org/10.3390/mi6101440

Hughes, M. (2012). Defects in natural fibres: Their origin, characteristics and implications for natural fibre-reinforced composites. *Journal of Materials Science*, *47*(2), 599–609. https://doi.org/10.1007/s10853-011-6025-3

Hughes, M., Sèbe, G., Hague, J., Hill, C., Spear, M., & Mott, L. (2000). An investigation into the effects of micro-compressive defects on interphase behaviour in hemp-epoxy composites using half-fringe photoelasticity. *Composite Interfaces*, *7*(1), 13–29. https://doi.org/10.1163/156855400300183551

Jonoobi, M., Khazaeian, A., Tahir, P. Md., Azry, S. S., & Oksman, K. (2011). Characteristics

of cellulose nanofibers isolated from rubberwood and empty fruit bunches of oil palm using chemo-mechanical process. *Cellulose*, *18*(4), 1085–1095. https://doi.org/10.1007/s10570-011-9546-7

Kandemir, A., Pozegic, T. R., Hamerton, I., Eichhorn, S. J., & Longana, M. L. (2020). Characterisation of Natural Fibres for Sustainable Discontinuous Fibre Composite Materials. *Materials*, *13*(9), 2129. https://doi.org/10.3390/ma13092129

Kölln, K., Grotkopp, I., Burghammer, M., Roth, S. V., Funari, S. S., Dommach, M., & Müller, M. (2005). Mechanical properties of cellulose fibres and wood. Orientational aspects *in situ* investigated with synchrotron radiation. *Journal of Synchrotron Radiation*, *12*(6), 739–744. https://doi.org/10.1107/S0909049505011714

Kuta, Ł., Li, Z., Stopa, R., Komarnicki, P., & Słupska, M. (2020). The influence of manual harvesting on the quality of picked apples and the Picker's muscle load. *Computers and Electronics in Agriculture*, *175*, 105511. https://doi.org/10.1016/j.compag.2020.105511

Le Duigou, A., Kervoelen, A., Le Grand, A., Nardin, M., & Baley, C. (2014). Interfacial properties of flax fibre–epoxy resin systems: Existence of a complex interphase. *Composites Science and Technology*, *100*, 152–157. https://doi.org/10.1016/j.compscitech.2014.06.009

Lefeuvre, A., Bourmaud, A., Morvan, C., & Baley, C. (2014). Elementary flax fibre tensile properties: Correlation between stress–strain behaviour and fibre composition. *Industrial Crops and Products*, *52*, 762–769. https://doi.org/10.1016/j.indcrop.2013.11.043

Liu, Y., Ma, X., Shu, L., Hancke, G. P., & Abu-Mahfouz, A. M. (2021). From Industry 4.0 to Agriculture 4.0: Current Status, Enabling Technologies, and Research Challenges. *IEEE Transactions on Industrial Informatics*, *17*(6), 4322–4334. https://doi.org/10.1109/TII.2020.3003910

Madsen, B., & Gamstedt, E. K. (2013). Wood versus Plant Fibers: Similarities and Differences in Composite Applications. *Advances in Materials Science and Engineering*, *2013*, 1–14. https://doi.org/10.1155/2013/564346

Marrot, L., Lefeuvre, A., Pontoire, B., Bourmaud, A., & Baley, C. (2013). Analysis of the hemp fiber mechanical properties and their scattering (Fedora 17). *Industrial Crops and Products*, *51*, 317–327. https://doi.org/10.1016/j.indcrop.2013.09.026

Meijer, W. J. M., Vertregt, N., Rutgers, B., & Van De Waart, M. (1995). The pectin content as a measure of the retting and rettability of flax. *Industrial Crops and Products*, *4*(4), 273–284. https://doi.org/10.1016/0926-6690(95)00041-0

Melelli, A., Arnould, O., Beaugrand, J., & Bourmaud, A. (2020). The Middle Lamella of Plant Fibers Used as Composite Reinforcement: Investigation by Atomic Force Microscopy.

Molecules, *25*(3), 632. https://doi.org/10.3390/molecules25030632

Mentsiev, A. U., Isaev, A. R., Supaeva, K. S., Yunaeva, S. M., & Khatuev, U. A. (2019). Advancement of mechanical automation in the agriculture sector and overview of IoT. *Journal of Physics: Conference Series*, *1399*(4), 044042. https://doi.org/10.1088/1742-6596/1399/4/044042

Müssig, J. (Ed.). (2010). *Industrial Applications of Natural Fibres: Structure, Properties and Technical Applications* (1st ed.). Wiley. https://doi.org/10.1002/9780470660324

Müssig, Jör., & Martens, R. (2003). Quality Aspects in Hemp Fibre Production—Influence of Cultivation, Harvesting and Retting. *Journal of Industrial Hemp*, *8*(1), 11–32. https://doi.org/10.1300/J237v08n01_03

Nodder, C. R. (1922). A Study of Flax and Kindred Fibres. *Journal of the Textile Institute Proceedings and Abstracts*, *13*(9), 161–171. https://doi.org/10.1080/03684504.1922.11673740

Nyholm, K., Ander, P., Bardage, S., & Geoffrey, D. (2001). Dislocations in pulp fibres – their origin, characteristics and importance – a review. *Nordic Pulp & Paper Research Journal*, *16*(4), 376–384. https://doi.org/10.3183/npprj-2001-16-04-p376-384

Olsson, A.-M., Salmén, L., Eder, M., & Burgert, I. (2007). Mechano-sorptive creep in wood fibres. *Wood Science and Technology*, *41*(1), 59–67. https://doi.org/10.1007/s00226-006-0086-5

Patil, T. G., & S. P. Shekhawat. (n.d.). *Industry 4.0 implications on agriculture sector: An overview*. 1512–1524.

Paul-Victor, C., Dalle Vacche, S., Sordo, F., Fink, S., Speck, T., Michaud, V., & Speck, O. (2017). Effect of mechanical damage and wound healing on the viscoelastic properties of stems of flax cultivars (Linum usitatissimum L. cv. Eden and cv. Drakkar). *PLOS ONE*, *12*(10), e0185958. https://doi.org/10.1371/journal.pone.0185958

Perera, M. K., & Englehardt, J. D. (2020). Simultaneous nitrogen and phosphorus recovery from municipal wastewater by electrochemical pH modulation. *Separation and Purification Technology*, *250*, 117166. https://doi.org/10.1016/j.seppur.2020.117166

Pillin, I., Kervoelen, A., Bourmaud, A., Goimard, J., Montrelay, N., & Baley, C. (2011). Could oleaginous flax fibers be used as reinforcement for polymers? *Industrial Crops and Products*, *34*(3), 1556–1563. https://doi.org/10.1016/j.indcrop.2011.05.016

Placet, V., Cissé, O., & Lamine Boubakar, M. (2014). Nonlinear tensile behaviour of elementary hemp fibres. Part I: Investigation of the possible origins using repeated progressive loading with in situ microscopic observations. *Composites Part A: Applied Science and Manufacturing*, *56*, 319–327. https://doi.org/10.1016/j.compositesa.2012.11.019

Placet, V., Trivaudey, F., Cisse, O., Gucheret-Retel, V., & Boubakar, M. L. (2012). Diameter dependence of the apparent tensile modulus of hemp fibres: A morphological, structural or ultrastructural effect? *Composites Part A: Applied Science and Manufacturing*, *43*(2), 275–287. https://doi.org/10.1016/j.compositesa.2011.10.019

Qi, H., Chen, H., Mao, K., Qiu, Z., Zhang, L., & Zhou, J. (2019). Investigation of the structure of ramie fibers by enzymatic peeling. *Cellulose*, *26*(5), 2955–2968. https://doi.org/10.1007/s10570-019-02309-z

Rajak, P., Ganguly, A., Adhikary, S., & Bhattacharya, S. (2023). Internet of Things and smart sensors in agriculture: Scopes and challenges. *Journal of Agriculture and Food Research*, *14*, 100776. https://doi.org/10.1016/j.jafr.2023.100776

Rajalakshmi, P., & Devi Mahalakshmi, S. (2016). IOT based crop-field monitoring and irrigation automation. *2016 10th International Conference on Intelligent Systems and Control (ISCO)*, 1–6. https://doi.org/10.1109/ISCO.2016.7726900

Rao, R. N., & Sridhar, B. (2018). IoT based smart crop-field monitoring and automation irrigation system. *2018 2nd International Conference on Inventive Systems and Control (ICISC)*, 478–483. https://doi.org/10.1109/ICISC.2018.8399118

Rask, M., Madsen, B., Sørensen, B. F., Fife, J. L., Martyniuk, K., & Lauridsen, E. M. (2012). In situ observations of microscale damage evolution in unidirectional natural fibre composites. *Composites Part A: Applied Science and Manufacturing*, *43*(10), 1639–1649. https://doi.org/10.1016/j.compositesa.2012.02.007

Réquilé, S., Goudenhooft, C., Bourmaud, A., Le Duigou, A., & Baley, C. (2018). Exploring the link between flexural behaviour of hemp and flax stems and fibre stiffness. *Industrial Crops and Products*, *113*, 179–186. https://doi.org/10.1016/j.indcrop.2018.01.035

Réquilé, S., Le Duigou, A., Bourmaud, A., & Baley, C. (2018). Peeling experiments for hemp retting characterisation targeting biocomposites. *Industrial Crops and Products*, *123*, 573–580. https://doi.org/10.1016/j.indcrop.2018.07.012

Richely, E., Nuez, L., Pérez, J., Rivard, C., Baley, C., Bourmaud, A., Guessasma, S., & Beaugrand, J. (2022). Influence of defects on the tensile behaviour of flax fibres: Cellulose microfibrils evolution by synchrotron X-ray diffraction and finite element modelling. *Composites Part C: Open Access*, *9*, 100300. https://doi.org/10.1016/j.jcomc.2022.100300

Rittersma, Z. M. (2002). Recent achievements in miniaturised humidity sensors—A review of transduction techniques. *Sensors and Actuators A: Physical*, *96*(2–3), 196–210. https://doi.org/10.1016/S0924-4247(01)00788-9

Romhány, G., Karger-Kocsis, J., & Czigány, T. (2003). Tensile fracture and failure behaviour of technical flax fibers: Technical Flax Fibers. *Journal of Applied Polymer Science*,

90(13), 3638–3645. https://doi.org/10.1002/app.13110

Rong, Q., Guo, T., Bao, W., Shao, Z., Peng, G.-D., & Qiao, X. (2017). Highly sensitive fiber-optic accelerometer by grating inscription in specific core dip fiber. *Scientific Reports*, *7*(1), 11856. https://doi.org/10.1038/s41598-017-12322-6

Rosemberg, J. A., & De França, F. P. (1967). Importance of Galacturonic Acid in Controlling the Retting of Flax. *Applied Microbiology*, *15*(3), 484–486. https://doi.org/10.1128/am.15.3.484-486.1967

Saha, H. N., Roy, R., Chakraborty, M., & Sarkar, C. (2021). Development of IoT‐Based Smart Security and Monitoring Devices for Agriculture. In A. Choudhury, A. Biswas, M. Prateek, & A. Chakrabarti (Eds.), *Agricultural Informatics* (1st ed., pp. 147–169). Wiley. https://doi.org/10.1002/9781119769231.ch8

Sakurada, I., Nukushina, Y., & Ito, T. (1962). Experimental determination of the elastic modulus of crystalline regions in oriented polymers. *Journal of Polymer Science*, *57*(165), 651–660. https://doi.org/10.1002/pol.1962.1205716551

Savanto S. (n.d.). *Tree stem diameter change measurements and sap flow in scots pine.*

Seaby, D. A., & Mercer, P. C. (1984). Development of a hand tool to test the degree of retting of flax straw. *Annals of Applied Biology*, *104*(3), 567–573. https://doi.org/10.1111/j.1744-7348.1984.tb03040.x

Shah, D. U. (2013). Developing plant fibre composites for structural applications by optimising composite parameters: A critical review. *Journal of Materials Science*, *48*(18), 6083–6107. https://doi.org/10.1007/s10853-013-7458-7

Shah, D. U., Nag, R. K., & Clifford, M. J. (2016). Why do we observe significant differences between measured and ‘back-calculated’ properties of natural fibres? *Cellulose*, *23*(3), 1481–1490. https://doi.org/10.1007/s10570-016-0926-x

Sharma, H. S. S., & Faughey, G. J. (1999). Comparison of subjective and objective methods to assess flax straw cultivars and fibre quality after dew-retting. *Annals of Applied Biology*, *135*(2), 495–501. https://doi.org/10.1111/j.1744-7348.1999.tb00879.x

Sharma, H. S. S., & Reinard, N. (2004). Evaluation of Visible and Near-Infrared Spectroscopy as a Tool for Assessing Fiber Fineness during Mechanical Preparation of Dew-Retted Flax. *Applied Spectroscopy*, *58*(12), 1431–1438. https://doi.org/10.1366/0003702042641272

Shu, Q., Hu, T., Xu, Z., Zhang, J., Fan, X., Gong, X., & Xuan, S. (2021). Non-tensile piezoresistive sensor based on coaxial fiber with magnetoactive shell and conductive flax core. *Composites Part A: Applied Science and Manufacturing*, *149*, 106548. https://doi.org/10.1016/j.compositesa.2021.106548

Singh, H., Halder, N., Singh, B., Singh, J., Sharma, S., & Shacham-Diamand, Y. (2023). Smart Farming Revolution: Portable and Real-Time Soil Nitrogen and Phosphorus

Monitoring for Sustainable Agriculture. *Sensors*, *23*(13), 5914. https://doi.org/10.3390/s23135914

Singh, N., & Singh, A. N. (2020). Odysseys of agriculture sensors: Current challenges and forthcoming prospects. *Computers and Electronics in Agriculture*, *171*, 105328. https://doi.org/10.1016/j.compag.2020.105328

Sultana, C. (1983). The cultivation of fibre flax. *Outlook on Agriculture*, *12*(3), 104–110. https://doi.org/10.1177/003072708301200301

Sung, J. (2018). The Fourth Industrial Revolution and Precision Agriculture. In S. Hussmann (Ed.), *Automation in Agriculture—Securing Food Supplies for Future Generations*. InTech. https://doi.org/10.5772/intechopen.71582

Thygesen, L. G., Bilde-Sørensen, J. B., & Hoffmeyer, P. (2006). Visualisation of dislocations in hemp fibres: A comparison between scanning electron microscopy (SEM) and polarized light microscopy (PLM). *Industrial Crops and Products*, *24*(2), 181–185. https://doi.org/10.1016/j.indcrop.2006.03.009

Ubudi, R., Irawan, B., & Saputra, R. E. (2017). Automation system for controlling and monitoring ornamental plants using fuzzy logic method. *2017 International Conference on Control, Electronics, Renewable Energy and Communications (ICCREC)*, 196–201. https://doi.org/10.1109/ICCEREC.2017.8226706

Van De Weyenberg, I., Ivens, J., De Coster, A., Kino, B., Baetens, E., & Verpoest, I. (2003). Influence of processing and chemical treatment of flax fibres on their composites. *Composites Science and Technology*, *63*(9), 1241–1246. https://doi.org/10.1016/S0266-3538(03)00093-9

Van Hazendonk, J. M., Reinerik, E. J. M., De Waard, P., & Van Dam, J. E. G. (1996). Structural analysis of acetylated hemicellulose polysaccharides from fibre flax (Linum usitatissimum L.). *Carbohydrate Research*, *291*, 141–154. https://doi.org/10.1016/S0008-6215(96)00160-7

VI. The phenomena of rupture and flow in solids. (1921). *Philosophical Transactions of the Royal Society of London. Series A, Containing Papers of a Mathematical or Physical Character*, *221*(582–593), 163–198. https://doi.org/10.1098/rsta.1921.0006

Waldron, D., & Harwood, J. (2011). A Preliminary Investigation into the Influence of Chemical Composition on the Dynamic Mechanical Properties of Flax (*Linum usitattisimum*) Straw. *Journal of Natural Fibers*, *8*(2), 126–142. https://doi.org/10.1080/15440478.2011.577596

Wang, M., Yan, B., Zhang, S., Fan, P., Zeng, P., Shi, S., & Yang, F. (2022). Development of a Novel Biomimetic Mechanical Hand Based on Physical Characteristics of Apples. *Agriculture*, *12*(11), 1871. https://doi.org/10.3390/agriculture12111871

Wright, W., & Vincent, J. F. V. (1996). HERBIVORY AND THE MECHANICS OF FRACTURE

IN PLANTS. *Biological Reviews*, *71*(3), 401–413. https://doi.org/10.1111/j.1469-185X.1996.tb01280.x

Xu, J., Zhang, L., Lai, X., Zeng, X., & Li, H. (2022). Wearable RGO/MXene Piezoresistive Pressure Sensors with Hierarchical Microspines for Detecting Human Motion. *ACS Applied Materials & Interfaces*, *14*(23), 27262–27273. https://doi.org/10.1021/acsami.2c06574

Yang, X., Shu, L., Chen, J., Ferrag, M. A., Wu, J., Nurellari, E., & Huang, K. (2021). A Survey on Smart Agriculture: Development Modes, Technologies, and Security and Privacy Challenges. *IEEE/CAA Journal of Automatica Sinica*, *8*(2), 273–302. https://doi.org/10.1109/JAS.2020.1003536

Yang, Z., Liu, S., Xue, F., Zhang, Y., Zhao, X., Miao, J., & Norford, L. K. (2015). Micro anemometer by a MEMS compatible lab-on-a-tube technology. *2015 Transducers - 2015 18th International Conference on Solid-State Sensors, Actuators and Microsystems (TRANSDUCERS)*, 383–386. https://doi.org/10.1109/TRANSDUCERS.2015.7180941

Zafeiropoulos, N. E., Williams, D. R., Baillie, C. A., & Matthews, F. L. (2002). Engineering and characterisation of the interface in flax fibre/polypropylene composite materials. Part I. Development and investigation of surface treatments. *Composites Part A: Applied Science and Manufacturing*, *33*(8), 1083–1093. https://doi.org/10.1016/S1359-835X(02)00082-9

Zhu, J., Zhu, H., Njuguna, J., & Abhyankar, H. (2013). Recent Development of Flax Fibres and Their Reinforced Composites Based on Different Polymeric Matrices. *Materials*, *6*(11), 5171–5198. https://doi.org/10.3390/ma6115171

Chapter 2

Sample gathering

Introduction

The biology of flax plants has been studied and characterised using various techniques for a long time. Specifically, the relation between the microbiology and retting process, explained by the influence of the latter on the enzymatic activity of microorganisms such as bacterias and fungus (Djemiel et al., 2017) (Djemiel et al., 2020).

Gathering flax stems for biological testing is therefore common practice and there are well defined protocols which can be followed (Anderson et al., 1979). Biological testing often involves the refrigerated storage (very low temperatures) of samples for weeks, months, and even years before testing.

When samples intended for biological studies are stored at extremely low temperatures such as -20°C and -80°C, the biological activity of microorganisms tends to slow down significantly or even stop. However, this activity can be reactivated and continued upon thawing. This phenomenon can be very useful in life science and microbiology research, especially when studying the activity of microorganisms. By controlling their activity through freezing and thawing, researchers can make comparisons and gain valuable insights.

However, this approach is not at all suitable for characterising the mechanical properties of a plant with a view to developing a tool. Freezing and then thawing plant samples for mechanical testing can cause significant changes in the strength and stiffness of the samples. This can lead to misleading or inaccurate characterisation of the mechanical properties of the plant material.

In as much, sample gathering for mechanical characterisation of flax stems and fibres over a whole retting period and beyond day-by-day in a real-time study is something new: we therefore had to define a brand new protocol tailored to the objectives of our specific study.

In France, flax cultivation usually starts in March and the entire growth cycle of the flax plant lasts about three months (detailed information on the maturation stages of flax can be found in the section on cultivation in the bibliographical study chapter). When the primary objective of flax cultivation is to extract fibres for the textile industry, the flax plants are usually harvested in early July, but this obviously depends on weather conditions. They are then left in the field for the duration of the retting period, which is a crucial stage in the process of extracting fibre from the flax plants.

The effect of the retting process on the mechanical properties of flax stalks is of great importance in the context of industrial fibre extraction. Optimal fibre yield and quality depends on achieving a precise balance during retting. Inadequate retting will adversely affect mechanical extraction, potentially resulting in poor quality fibres. Conversely, too much retting can lead to similar results. Identifying the ideal point at which flax stalks reach the optimum state for mechanical extraction is therefore a critical consideration in this industrial process.

To effectively address this challenge, it is imperative to determine the precise moment when flax stems reach the optimum state for mechanical extraction. This requires a thorough investigation of how retting affects the mechanical properties of flax stalks in real time. In pursuit of this objective, this Ph.D. research has undertaken a comprehensive real-time

investigation, representing an unprecedented scale of study in this area. To achieve this, a carefully designed sampling protocol was developed to obtain flax samples for real-time mechanical testing with the view of developing a tool for optimised retting prediction. In addition, climatic data, including rainfall and temperature, were carefully monitored in the field to determine whether climatic conditions could influence the degree of retting.

Field location, weather data, and gathering protocol

Field location

Retted flax stem samples (Family: Linaceae, Genus: Linum, Species: L. Usitatissimum, Variety: Felice) were collected from a commercial field near Killem in the *Hauts de France*. The field belongs to the Van Robaeys Frères (VRF) company. Figure x shows a satellite view and a panoramic photo of the flax field used in the study. The world geodetic system (WGS) coordinates of the field are: 50.950244, 2.583505, see Figure 1.

Figure 1. A view of the selected field for the flax sample gathering in Killem north of France. **(**a) present a satellite view of the field. The red colour box presents the area where the samples are gathered. (b) show a panoramic view of the field. The red arrow presents the area where the samples are gathered.

Weather data during summer 2022

It is important to follow the weather day-by-day when gathering plant samples for a real-time mechanical testing during retting, as the mechanical properties of flax stems are highly dependent on environmental conditions. The mechanical properties of the flax stems are affected by factors such as temperature, precipitation, and wind speed. If it is raining, it is best to delay sample gathering until the rain has stopped and the stems have had a chance to naturally dry out. Wet stems become brittle and prone to breakage during the collection process, which can damage the stem and reduce their strength. On the other hand, if the weather is dry and sunny, sampling can be done as the stems are likely dry, making it easier to choose suitable samples for mechanical testing.

In addition, the collection of weather data served as a crucial element in monitoring the effect of environmental conditions on the degree of retting, especially as part of the sample collection took place during a heat wave. This weather data included parameters such as minimum and maximum temperatures (Figure 2a), rainfall (Figure 2b), wind speed (Figure 2c), and duration of direct sunlight with no cloud cover ((Figure 2d) in the field where the samples were gathered–see Figure 2. This data was obtained from France Meteo during the three different phases of the retting process, namely i) the unde-retting phase, ii) the optimal-retting phase and iii) the over-retting phase. The figures below illustrate the variations in weather data as a function of the retting period.

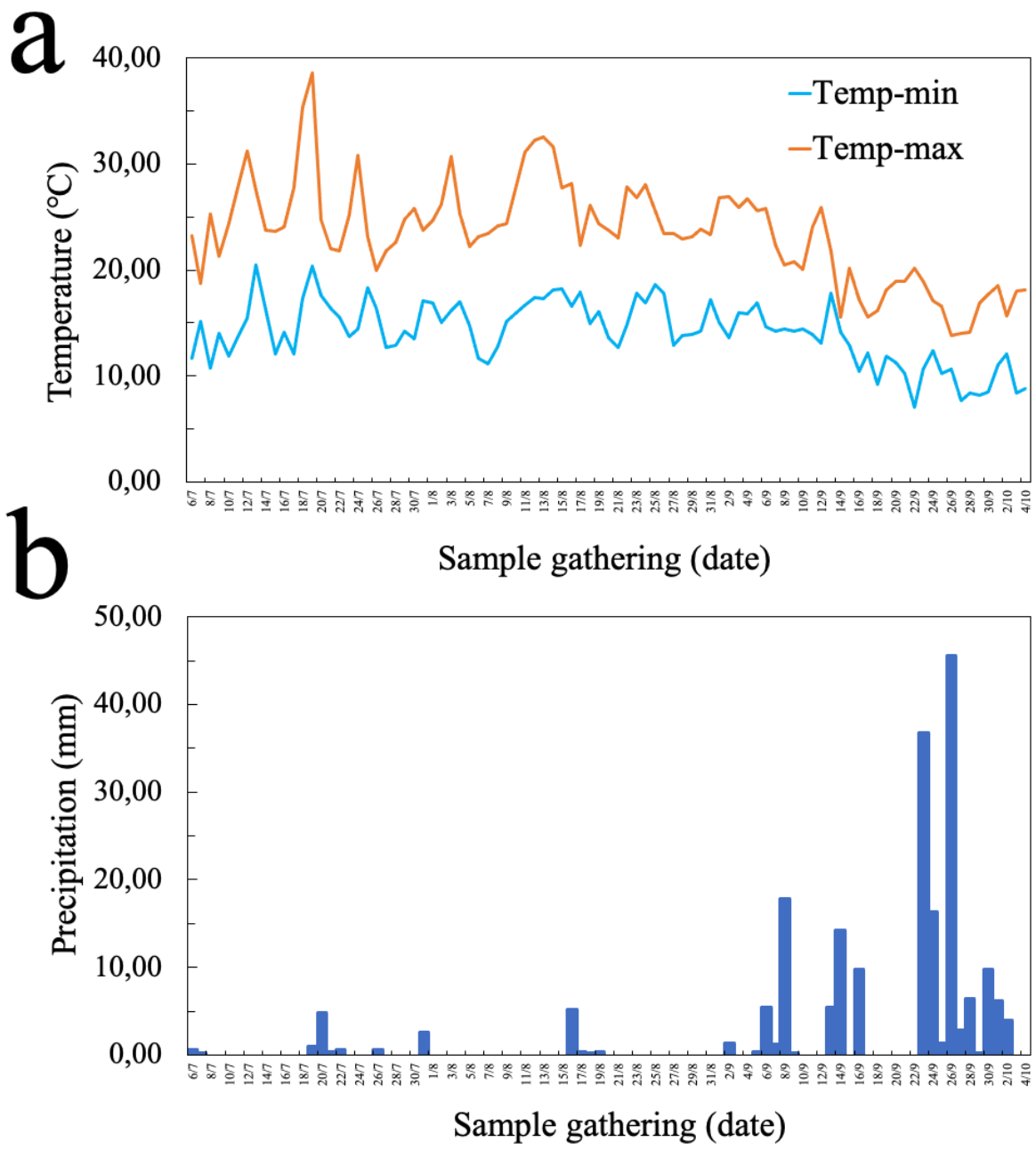
a
40,00
30,00
20,00
10,00
0,00
Temperature (°C)
Temp-min
Temp-max
Sample gathering (date)
b
50,00
40,00
30,00
20,00
10,00
0,00
Precipitation (mm)
Sample gathering (date)

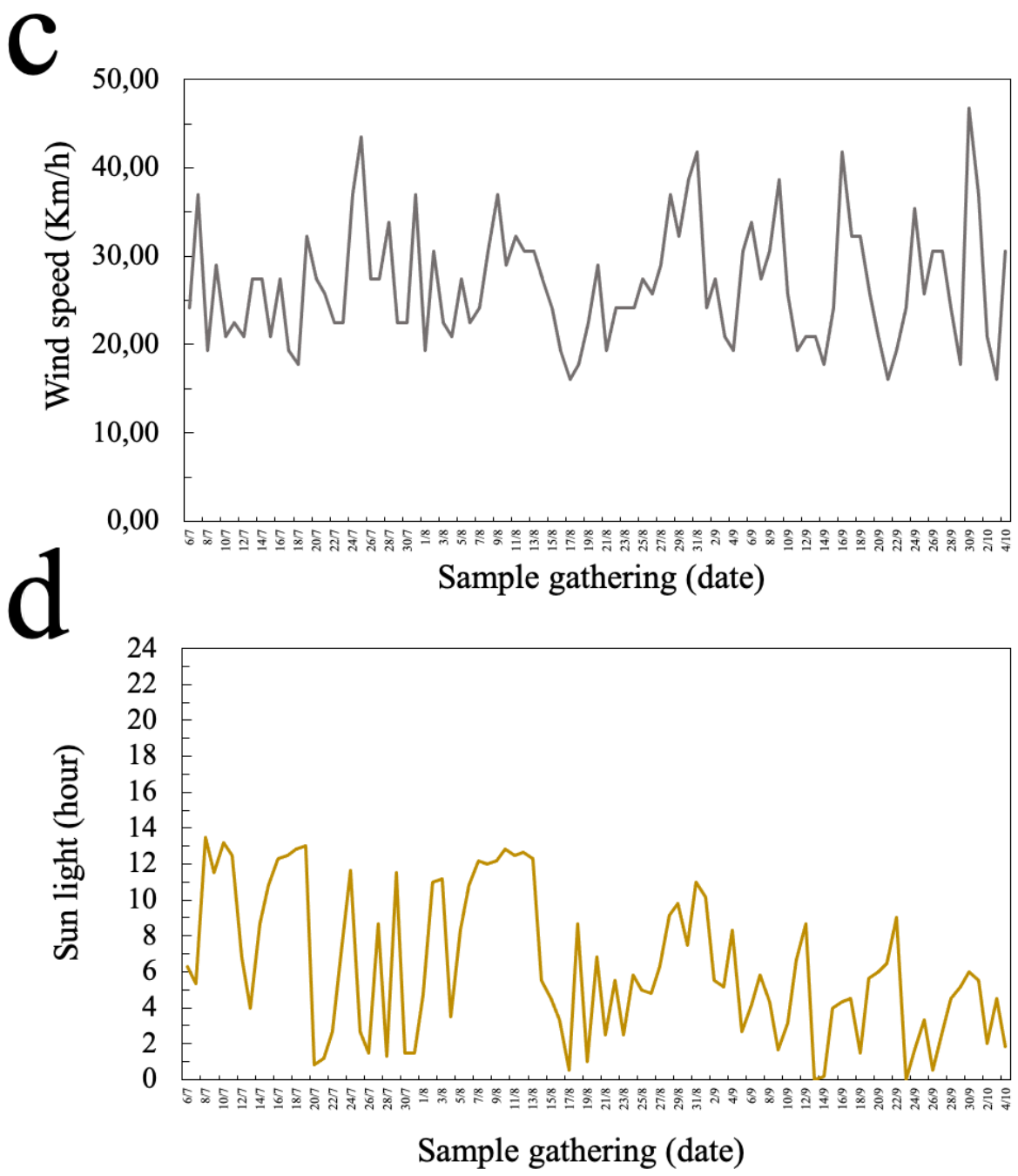

Figure 2. Weather data for Killem, France during the period 6th July to the 1st October. The retting period (as defined by VRF) was from 6th July to the 31st August, from this date to the 1st October is the over-retted period. (a) air temperature, (b) rainfall, (c) wind speed, and (d) direct sunlight (no cloud cover).

Data available on:
https://www.infoclimat.fr/climatologie-mensuelle/000R5/juillet/2022/bergues.html

Sample gathering timing

This PhD was a real-time study. A real time study of the mechanical properties of flax has never been done on the scale that we have attempted here. In addition to this, we decided to gather samples beyond the designated retting period. This had to be negotiated with the farmer so that a portion of the field could be left after harvesting of the retted stems. Like this, we were able to carry on sampling long after retting.

It is well documented that the dew retting period of flax varies from year to year. It can be as short as 2 weeks or as long as 3 months. The total retting time depends on uncontrollable factors (weather, bacteria growth rate) and controllable parameters (choice of field, choice of sampling space in field). In addition to this, it is evidently the farmer (artisan) who decides when the flax plants should be cut, when they should be turned, and when they should be taken from the field for storage (end of dew retting). We had to wait for the farmer (VRF) to tell us when the flax was cut, typically the start of July but this can vary depending on the weather. We had to decide, in advance, how many samplings we should take per week. For example, if we chose 1 sample per week and the retting period was 2 weeks, this would result in only 2 data points for all experiments. In contrast, if we chose 1 sample per day, this requires a journey per day (140 km) to the field and multiple experiments (mechanical) to be carried out in a 24 h period! Another factor is the storage of the stems. Even when cut, 1 sampling per day would generate an enormous volume to be stored in a refrigerator long term for other, complementary experiments. Based on back-of-the-envelope calculations of the time of experiments, we decided to attempt 2 samplings per week (monday and thursday). This allows for experimentation time between the samplings. The timing of the retting was at the period of the closing of our laboratory, special access was required and given for experimentation in exceptional circumstances. The retting period of 2022 started on 6th july and finished on 31st august: a total of 56 days. In addition, samples were gathered on a regular (but less frequently) basis after the designated retted stems were harvested–this we didi until 1st October. In this way the whole real-time evolution of the retting and beyond (post-retting) could be characterised mechanically. This is important for a sensor.

Sample gathering protocol for mechanical characterisation

It is widely recognised that the length of the dew-retting period in flax varies from year to year, from as short as two weeks to as long as three months. The overall retting process is influenced by a combination of biotic and abiotic factors, such as weather conditions and bacterial growth rates, and controllable parameters, such as field selection and the choice of sampling points within the field. In addition, the farmer or artisan plays a key role in determining critical stages in the process, including when to harvest the flax plants, when to turn them (potentially causing mechanical damage to stems) and when to remove them from the field at the end of the dew retting process. Consequently, our ability to collect samples from the field depended on coordination with the farmer.

To ensure that we obtained a representative set of samples, we had to determine the frequency of sampling in advance. For example, choosing to sample once a week would result in only two data points if the retting period was two weeks. Conversely, choosing one sample per day would require daily trips of 140 kilometres to the field and since it is a

real-time study, a large number of sample preparations and experiments, including mechanical tests, to be carried out within a 24-hour window. In addition, storage of the collected stems presented a logistical challenge, especially if frequent daily sampling was aimed, it would generate a huge volume that would require long-term refrigeration and sample storage.

After careful consideration and estimation of the experimental timeframe given the available manpower, we decided on a schedule of two sampling events per week, specifically on Mondays and Thursdays mornings at 10 am. 10am was chosen to enable time to get to the field and also time from the stems to dry out following dew exposure in the night. This approach allowed sufficient time to conduct experiments immediately after sampling and between sampling events. Note that we could not predict the weather when this plan was made. As it was, the 2022 summer heatwave helped us by prolonging the retting period to 2 months allowing many data points to be made. However, we acknowledge also that a heatwave is not typical weather conditions (even though they are occurring more and more with the now apparent climate change in the world) and the study findings must take this into consideration.

It is also noteworthy that the timing of the retting period in 2022 coincided with the closure of the IEMN laboratory. Special access permits have been granted to allow for exceptional circumstances and to facilitate experiments.

In rare exceptional circumstances, we managed to collect samples on rainy days by patiently waiting for the rain to stop. This often resulted in the collection of wet/damp stems. As a result, we established a special drying protocol in our laboratory, which will be described in more detail later.

The retting period in 2022 ran from the 6th of July to the 31th of August, for a total duration of 56 days. During this time we took a total of approximately 6000 samples. In addition, we continued to sample at regular intervals, less frequently, following the removal of the retted stems from the field. Therefore, a marked field area of 10 metres was deliberately left after the removal of optimally retted flax samples, with the specific aim of investigating the effects of over retting on these flax stems. The VRF company kindly allowed us to leave stems in the field and gather them occasionally until the 1st October. This approach allowed us to comprehensively characterise the real-time evolution of the retting process and the post-retting stages, which is of paramount importance for sensor development and mechanical property analysis.

A 10 m area from the field was chosen for the sample gathering. The sample collection requires applying a model directly onto the swath in the field, which takes the form of a rectangular shape measuring 10 metres in length. Figure 3 shows the 10 m area chosen for the gathering protocol and the designed model.

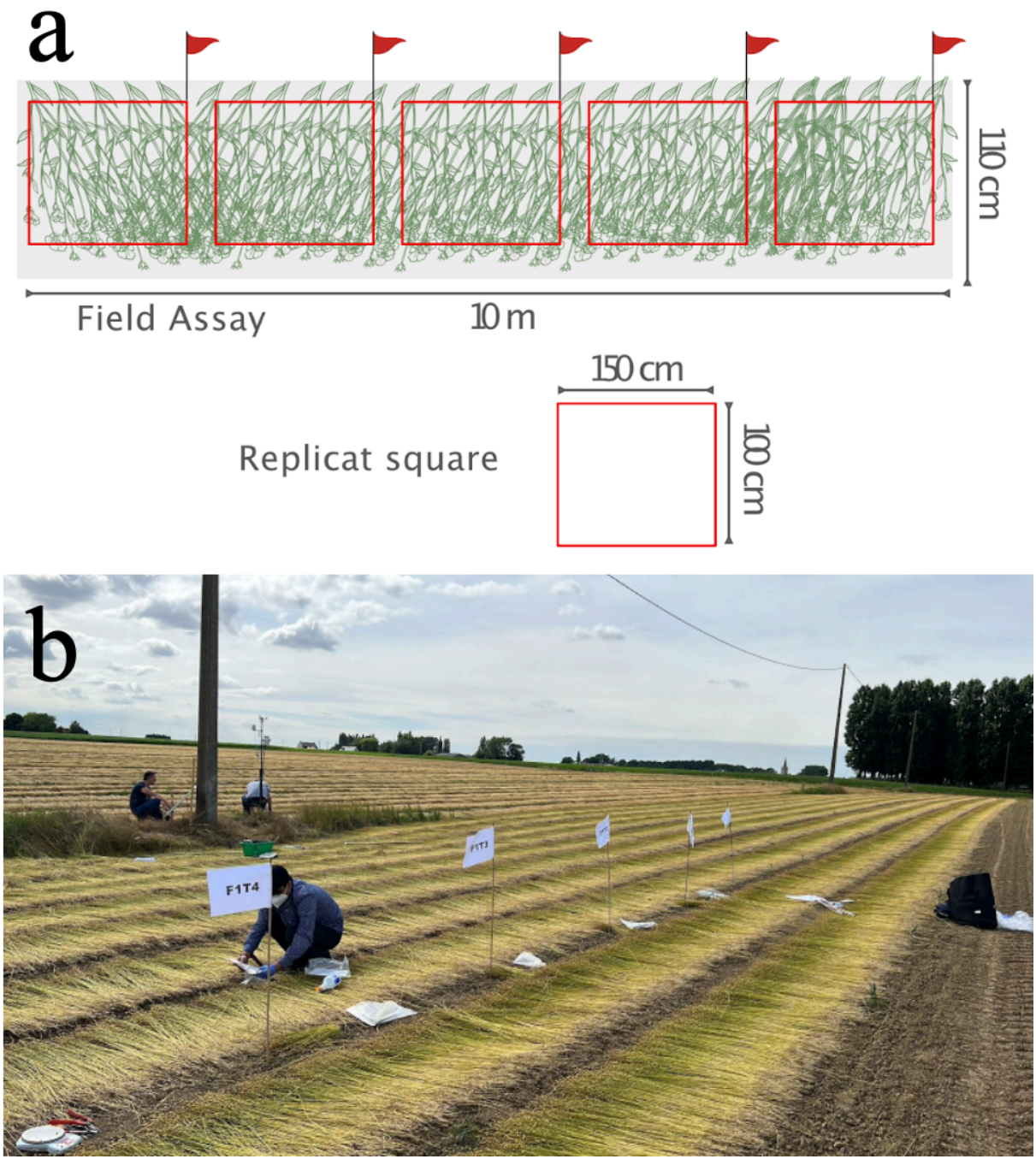

Figure 3. Sampling for flax stems in summer 2022. The 10 m designed area for the sample gathering. (a) The designed protocol for the sample gathering. (b) Shows the 10 m area dedicated for the sample gathering. The photo also shows people from the UGSF (Dr Sebastien Grec and Mr Sujavit Mukherjee) gathering their own flax samples for storage and subsequent biological studies.

Figure 3 shows the delineation of areas corresponding to the sampling. The sampling is performed by defining five replicate squares that span 1.5 metres each, with a slat frame used to mark these areas–see Figure 3a. The frame is moved along the swath, and a marker is placed at the upper corner of each replicate rectangle to enable precise redefinition of

zones during the sampling. To ensure precise and accurate sampling, GPS coordinates are taken for each zone prior to the commencement of the sampling procedure. This step serves to guarantee the proper location of each replicate, mitigating any potential errors during subsequent sampling events.

Flax stems were always taken from the same zone designated by rectangles that span 1.5 metres. Each of these zones consists of a pile of flax stems approximately 10 cm high, therefore to experimentally test all kinds of samples–see Figure 4. Flax stems were taken from the top (T), centre (C), and bottom (B) of these piles - designated T, C, and B.

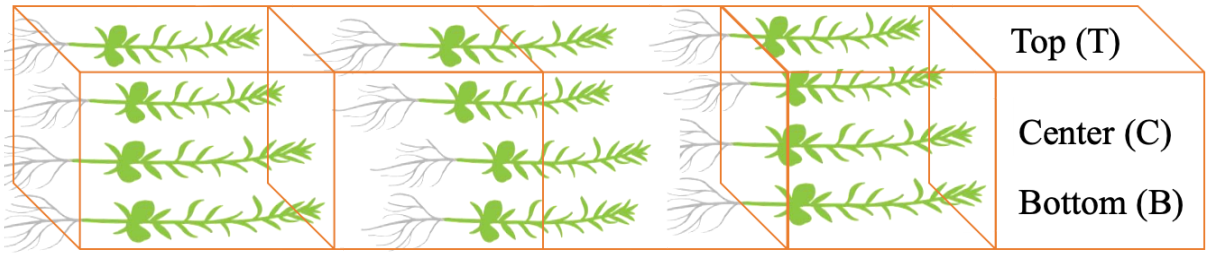

Figure 4. Schematic diagrams showing the flax stem samples were gathered from the Top (T), Center (C) and the Bottom (B).

Knowing that the natural flax stems found in the field do not have the same diameter, and in order to obtain reliable results, we aimed to test samples of different diameters, in this way we try to control some variable diameters of them which is the diameter. Therefore, Different diameter flax stems were selected from each depth, we called these small (S), medium (M), and large (L). The determination of the three noted diameters was achieved by using a vernier calliper. Table 1 shows a range of the average diameters of flax stems gathered.

Stem sample category	Stem diameter range (mm)
Small (**S**)	1-1.5
Medium (**M**)	1.5-2
Large (**L**)	2-3

Table 1. Flax stem diameter ranges gathered from the field. The stems were initially sorted using a standard mechanical calliper.

It is important to note that this sampling process was not random, but rather a deliberate and discerning approach. Flax stalks were carefully examined to determine their suitability for subsequent mechanical testing. Given the limited or almost no guidance available in the existing literature, we had to establish our own set of criteria. We specifically selected stems

that met several key parameters. Samples were taken from the mid-section of the stem, had a consistent and uniform diameter along this mid-section, and had minimal to no visible 'defects'. By 'defects' we refer to (i) stems that appeared to be crushed or broken, possibly due to factors such as turning or trampling by humans or animals, (ii) stems with observable localised irregularities, such as plant growth defects, and (iii) flax stems that were visibly different in some way from the majority of stems in the vicinity, such as exhibiting unusual colour variations or falling outside our defined diameter size categories of small (S), medium (M) and large (L).

After selection of the desired samples, a pair of shears was used to gently remove the leafy part and roots. The stalks were gently tied at three separate positions (top, middle, and bottom) to ensure that they remained straight during transportation, and excluding any potential stress. Finally a white paper is attached to samples indicating the retting stage number. Figure 5 shows an example of the collected samples.

Figure 5. Tools used for the sample collection. A pair of shears was used to cut the middle part of the selected flax stems. Metal threads were used to tighten the flax stems making sure to conserve their straight profile and avoiding any stress.

The stalks were subsequently placed in large plastic bags and stored in a substantially sized container (approximately four times the length of a flax plant) filled with ice to maintain sample freshness during transportation for eventual storage in a fridge at a temperature of 4°C–see Figure 6 (left image).

In the laboratory, flax stems are subjected to a carefully designed protocol using some specially designed tools and equipment to achieve the appropriate size for the mechanical experiments (this protocol is explained in detail in the next chapters), see Figure 6 (right image). The equipment consists of a metallic tool that is drilled by a drill with varying diameters, ranging from 0.5 mm to 3 mm. This tool is used to accommodate different stem sample diameters, avoiding sample damage while cutting with sharp razor blades to attain the desired sample length for the mechanical tests.

After achieving the appropriate length, some of the samples are used fresh for the desired experiments, while the remaining samples are packed in zipped bags of 25 x 20 cm and stored in the fridge at 4°C to ensure their freshness.

Where wet samples were encountered, a specific procedure was followed. These samples were placed on a table in a temperature-controlled room set to mimic field conditions, with a temperature of approximately 19°C, for a period of one night, equivalent to 12 hours. Following this conditioning, the samples were subjected to further manipulation and analysis.

Figure 6. Organised sample storage at 4°C (left images) and mechanical parts used to carefully cut the stems.

Although the work involved in collecting the samples may seem like a pleasant agricultural experience in the field, it was in fact a demanding process. In reality, our timetable put us under considerable time pressure, as we needed to collect, prepare and run the experiments

all on the same day. This was essential to maintain the real-time nature of the experiments and the freshness of the samples.

A seamless workflow was essential, starting with the correct setup of the tools required for sample collection and ending with the completion of the experiments. These tools underwent thorough inspection and sanitation procedures both before and after each sampling event. Ensuring reliable transport was another critical aspect of our operations. We relied on vehicles driven by Steve A, and occasionally Sebastien G, which had to be equipped with an adequate supply of oil. It is worth noting that this took place during a period of fuel shortages in France, which added an extra layer of complexity to our logistical planning.It was also important to carry out the experiments in real time while the samples were still fresh. The timeline outlines the progress of our work throughout the decomposition period. This timeline was meticulously followed from 6 July to 30 September–see Figure 7.

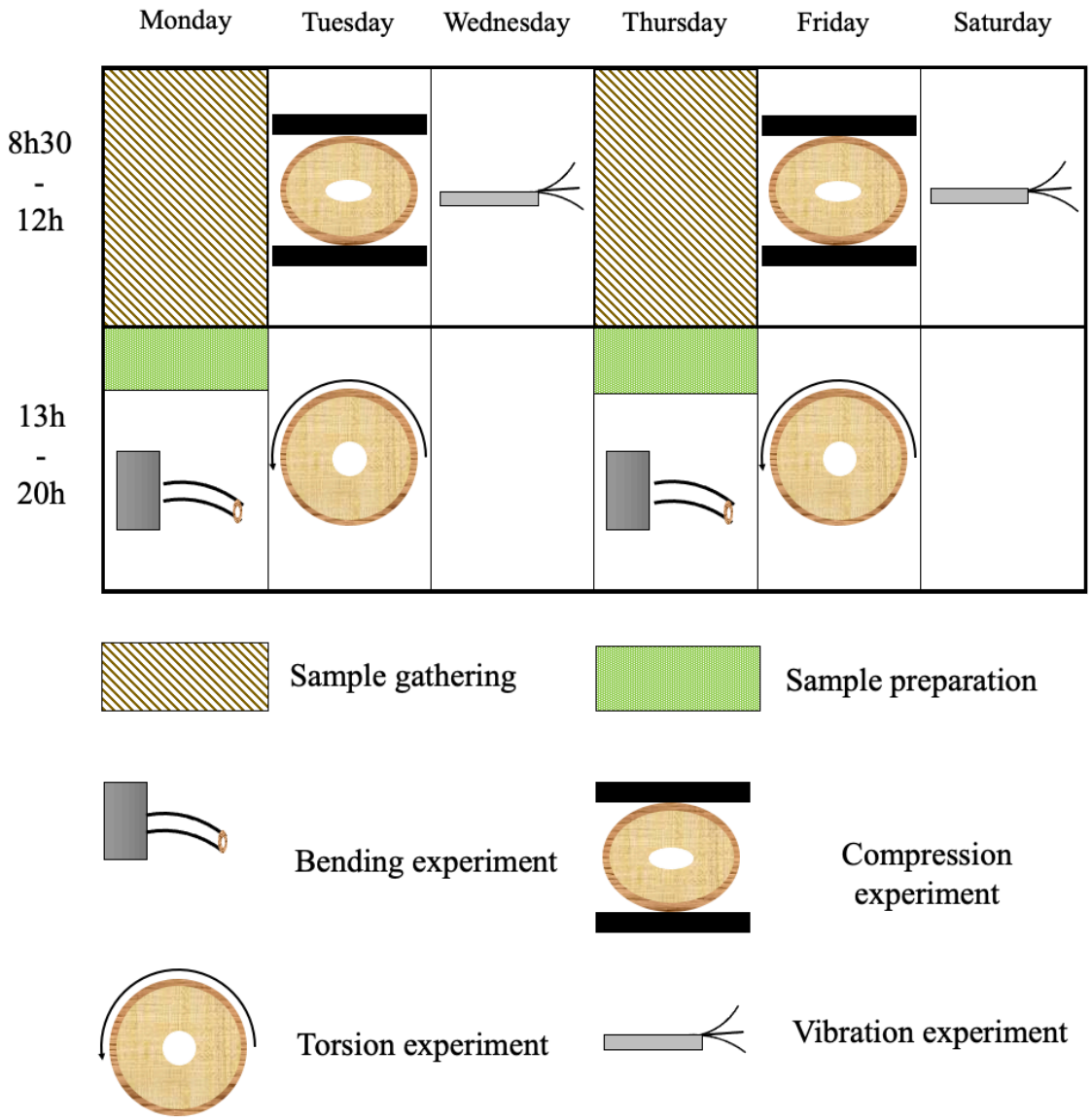

Figure 7. A time chart summarising the planning of the week during the retting period from the 6th july to the 4th of october.

Conclusions

The objective of the work presented in this thesis was to perform a real-time multiscale mechanical characterisation of retting flax stems and tier fibres. By real-time here we mean that samples will be gathered from the field and tested in the laboratory using various tools (existing and those developed for the PhD). Depending on the weather, dew retting can take any time between a few weeks to a few months. As a study of this scale and effort had never been undertaken before in the literature, we therefore had to define a novel protocol for sample gathering–the description of this is presented in this chapter. A key point is that the samples were not to be stored for later testing, as with biological studies. Here, we intended to conduct mechanical testing on flax stem and fibre samples during the retting period and beyond to obtain information without sample aging problems and issues. To do this, we had to devise a new protocol for sample gathering to collect suitable stalks. We had to have enough sampling gathering frequency so as to be able to see potential trends in data. We had to have a sample gathering frequency that allowed mechanical testing in between sample gathering days. Every characterisation tool had to work during the retting period. Every special access to the laboratory had to be asked for during the summer closing. This task was not simple, and this was complicated by the fact that no one had ever conducted such a study before.
Despite this, you will see in the subsequent chapters that the sample gathering protocol worked very well and enabled testing of much material. All characterisation tools and techniques functioned well also and there was enough time between sample gatherings to perform experiments–even if the workload and the pressure was high. In addition, we were helped by mother nature a little in that the summer of 2022 was hot and long. This had the effect of lengthening the retting period out so much data could be gathered.

References

Anderson, D. R., Laake, J. L., Crain, B. R., & Burnham, K. P. (1979). Guidelines for Line Transect Sampling of Biological Populations. *The Journal of Wildlife Management*, *43*(1), 70. https://doi.org/10.2307/3800636

Djemiel, C., Goulas, E., Badalato, N., Chabbert, B., Hawkins, S., & Grec, S. (2020). Targeted Metagenomics of Retting in Flax: The Beginning of the Quest to Harness the Secret Powers of the Microbiota. *Frontiers in Genetics*, *11*, 581664. https://doi.org/10.3389/fgene.2020.581664

Djemiel, C., Grec, S., & Hawkins, S. (2017). characterisation of Bacterial and Fungal Community Dynamics by High-Throughput Sequencing (HTS) Metabarcoding during Flax Dew-Retting. *Frontiers in Microbiology*, *8*, 2052. https://doi.org/10.3389/fmicb.2017.02052

Chapter 3

Macro-mechanical testing: Effect of retting on stem bending

Introduction

The mechanics of plants has been studied for some time now (Gibson, 2012; Shah et al., 2017). Specifically, the bending of plant stems and branches has been performed by many groups over the years to reveal various information about plant science. For example, Caliaro et al.(Caliaro et al., 2013) exposed whole potted plants to drought conditions in a controlled environment. They then performed two-point bending tests to assess the bending stiffness of the plants. Their aim was to investigate the possible relationship between bending stiffness and turgor (cellular water pressure) of parenchyma cells within an intact plant organ. In their research, Henry and Thomas (Henry & Thomas, 2002) conducted a study in a controlled greenhouse environment to investigate how factors such as lateral shade and wind affect the allocation of resources in the herbaceous plant Abutilon theophrasti. They assessed the distribution of resources between stems, leaves and roots, taking into account the mechanical stability of the plant, which they determined by analysing the flexibility of clamped and rooted stems. They also combined stem flexibility data with measurements of leaf area to understand how mechanical stability and wind resistance contribute to stem deflection. Green et al. (Green et al., 2006) conducted bending and compression tests to determine the mechanical properties of 228 mm (about 9 inches) diameter roundwood samples. The aim of Ampofo et al.(Ampofo et al., 2013). was to investigate the mechanical properties, specifically Young's modulus, yield stress and ultimate stress, of three major varieties of plantain pseudostem: Apantu pa, Apem pa and Apem hemaa, all of which are important food sources in Ghana. They used the three-point bending test, also known as the flexural bending test, as the method for their study. The objectives of the Lim et al. (Lim et al., 2011) study were twofold. First, they wanted to gather data on the bending properties of pitch pine timber. Second, they wanted to assess the suitability of pitch pine logs for use as members in safety barrier beams. To achieve this, they performed a static bending test on pitch pine logs and then calculated the modulus of rupture (MOR) at the rupture load using a numerical equation. Christoforo et al. (Luis Christoforo et al., 2012). intend to introduce a non-destructive method for assessing the longitudinal modulus of elasticity in structural round timber beams. This method is based on a three-point static bending test performed under minimum displacement conditions. In their research, Slater and Ennos (Slater & Ennos, 2013) investigated the bending strength of hazel (Corylus avellana L.) forks by analysing the mechanical properties of three different parts within each fork. They performed a three-point bending test and then compared the bending strength of these forks with that of smaller emerging branches of intact specimens. Robertson et al. (Robertson et al., 2015) conducted four types of mechanical tests, specifically three-point bending tests, on bamboo (Phyllostachys aurea), giant reed (Arundo donax) and maize (Zea mays). Their aim was to investigate how different load configurations used in three-point bending experiments affected the test results for septate grass stems. Their ultimate goal was to establish a test protocol that would provide reliable measurements of the bending strength of these plant stems. Lemloh et al. (Lemloh et al., 2014) conducted a three-point flexural test using a universal testing machine. They wanted to assess the stability of sorghum stalks and collect mechanical data from different sorghum lines. This allowed them to study how bending the stalks during growth affected both their morphological and mechanical properties. Recently, the bending of natural plant stems has been performed by very few groups to understand the behaviour of their mechanical properties. There have been some studies concerning the bending of flax stems. For example, Réquilé et al. (Réquilé et al., 2018) investigated the contribution of fibres to the stiffness of dry flax and

hemp stalks. They performed a simple three-point bending test on flax and hemp stem samples (dried samples following the conventional procedure for the industrial processing of flax but without being scutched) and measured the change in bending stiffness between stems with fibres and those from which fibres had been manually removed . Regardless of stem diameter, both hemp and flax stem samples showed a consistent apparent modulus, with values of approximately 10.8 ± 1.4 GPa for hemp and 22.2 ± 2.5 GPa for flax. In addition, the results showed a decrease in apparent modulus for xylem samples, particularly for flax, due to the removal of peripheral tissue. The mean stiffness of the xylem samples was about 6.2 ± 1.8 GPa for hemp and 9.2 ± 1.7 GPa for flax. Goudenhooft et al. (Goudenhooft et al., 2019) studied the stability of flax to understand how this plant can achieve such a slender structure while remaining mechanically stable. To achieve this, they assessed their flexural strength, taking into account variations in stem diameter and mass distribution. They performed a three-point bending test on flax stem samples harvested 100 days after sowing, a period associated with plant maturity. The results of their investigation revealed interesting findings. The apparent flexural modulus varied along the stem, ranging from 8.7 ± 0.5 GPa for the basal segment to 12.9 ± 1.8 GPa for the apical segment.

In the context of these experiments on flax stalks, the literature survey shows that there hasn't been any previous study of the real-time effects of retting on the bending properties of flax stalks. This aspect is of great importance, especially when considering the mechanical extraction of flax fibre.

In this chapter, the following will be presented. This chapter focuses on investigating how retting affects the mechanical bending properties of flax stalks in real-time retting. We achieve this by performing basic macro-mechanical tests on flax stalks taken from the field. By applying mechanical models to these flax stalks, we can calculate their mechanical properties, in particular the flexural modulus and breaking stress. Interpreting the trends observed in flexural modulus and breaking stress as a function of retting time provides valuable insights into how retting affects the mechanical properties of flax stalks in real time. This tells us something about the advancement of the retting. It is important to note that this experimental study is unique and, as far as we know, has not been done before.

Sample preparation, tool design and measurement protocol

Bending experiments on flax stems involve applying a load to the end of the flax stem sample, which causes the stem to bend. In this experiment, this load is applied using a one-point bending test, where the stem is supported on one end in a specially-designed sample holder and a force is applied to the other free end of the stem, causing it to bend. This is effectively a cantilever bending experiment. During the bending experiment, the stem's deflection and load response is recorded using equipment including a DSLR camera (Canon, Japan) and a digital optical microscope (Keyence, France). The photographs are then analysed and the extracted data is used to calculate the mechanical properties of the stem, specifically its flexural modulus and flexural strength.

Overall, The primary objective of conducting bending experiments on flax stems is to acquire a comprehensive understanding of the mechanical behaviour of these natural stems, in a

real time, as a function of the influence retting process, and to create a reliable and comprehensive database of information that can lead to the development of a retting monitoring tool.

Sample preparation

To ensure accurate determination of mechanical properties, it is crucial to control the variables during the sample preparation process. Major challenges of this experiment involve numerous parameters: stem dimensions and uniformity, control of stem defects, applied force, measurement setup, reproducibility from stem to stem. In this study, all samples were standardised to a fixed length of 12 cm and these samples were consistently taken from the middle section of the flax plant. On return to the laboratory, the retted flax samples were carefully removed from the transport container and immediately stored in a refrigerator set at 4°C to preserve their freshness during the two day testing window before testing new stems. The desired length of 12 cm is established using a ruler and a permanent marker. Figure 1 illustrates the first step in the sample preparation. This may seem a trivial point, but correct handling and cutting the stem using a sharp razor blade is important so as not to damage the stem prior to testing.

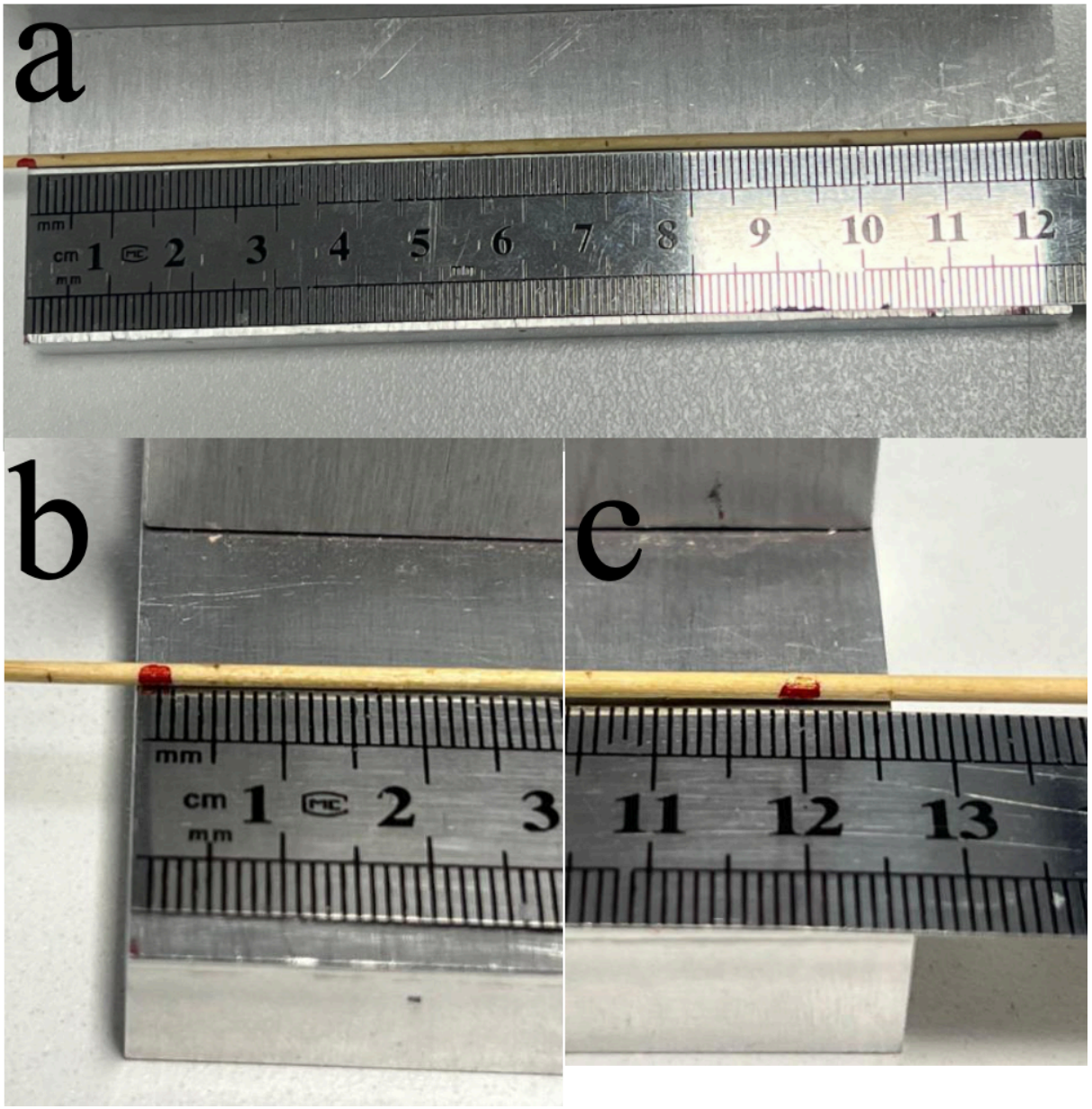

Figure 1. The step to determine the 12 cm length of the flax sample for the bending experiment. (a) shows the complete measured 12 cm length of the flax sample, (b) shows a zoomed image of the ends of the flax sample marked in red.

After marking their length, the flax stem sample has to be cut. A special metal tool was designed in our laboratory, to facilitate the cutting process. This equipment is specifically designed to allow us to cut the flax stems into the desired lengths in a correct and reproducible manner, without causing any damage that could alter their mechanical properties. Figure 2 shows the metal tool used for this step.

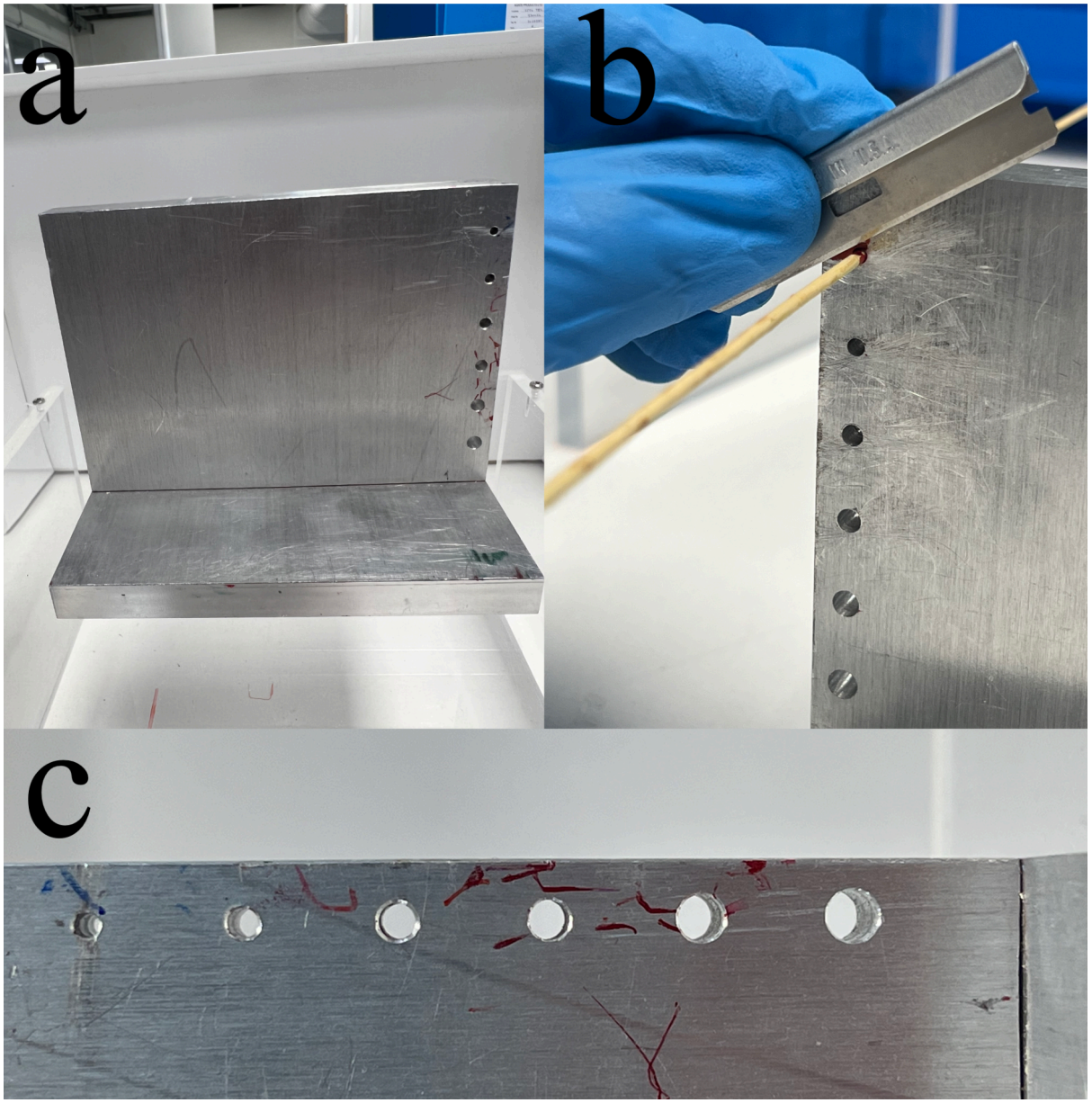

Figure 2. The metal tool used for the cutting process of the flax stems. (a) Shows the different holes of different diameters, (b) Shows the cutting method of the flax stem.

Figure 2a shows the cutting tool contains a series of holes of different diameters ranging from 0.5 mm to 4mm. The stems (of variable diameter) are inserted in the cutting tool based on their diameters, so that each stem of a given diameter can be safely fitted into a corresponding hole of the same diameter and cut using very sharp razor blades as shown in Figure 2b. In this way, the curing tool stops lateral stem deformation due to the mechanical Poisson effect, promoting a good clean cut. Following these steps, a fresh flax stem sample measuring a length of 12 cm is obtained and ready to be tested.

Tool design and measurements protocol

Tool design

After the flax stem sample preparation, the bending experiment is conducted according to a specific measuring protocol that we designed for the PhD. The protocol involves concentrated load at the free end bending of a cantilever experiment of retted flax stem samples, by gradually adding precision weights to the free end. The protocol involves a specific setup that is able to record the flax stem's deflection after each of the applied weights. Figure 3 shows the equipment used for the bending experiment.

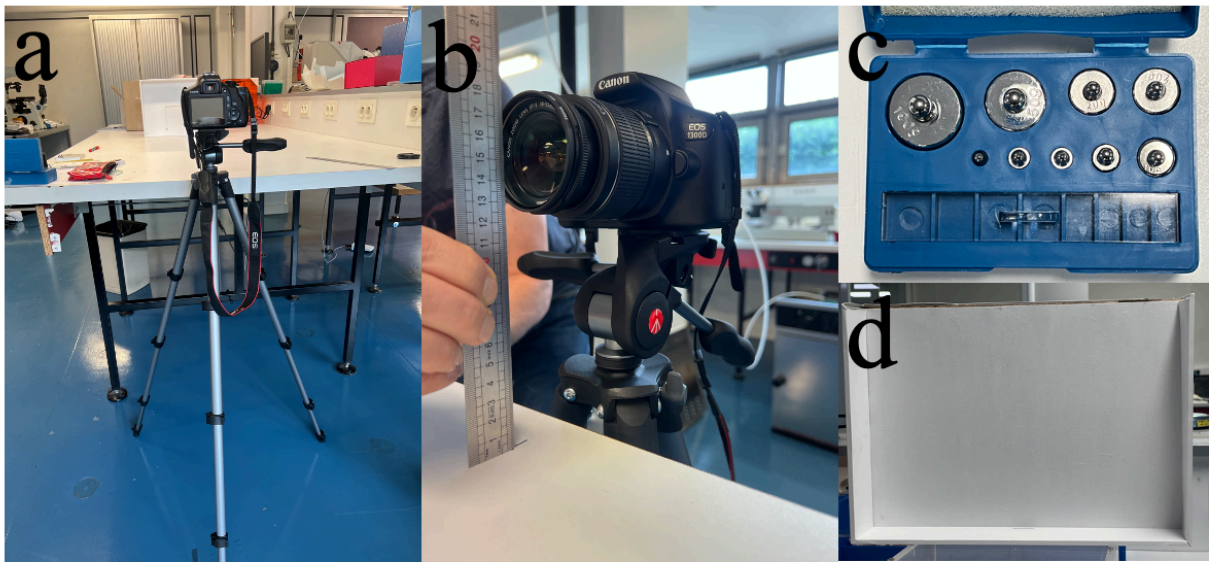

Figure 3. The equipment used for bending experiments of the flax stem samples. (a) overview of the setup and tools used for the bending experiment, including (b) the DSLR camera, (c) precision weights and, (d) the white screen used for the background of the photography.

Figure 3a illustrates the setup where the DSLR camera was positioned on a stable tripod at an appropriate distance and height from the support structure. The distance was set to 2m to reduce any potential effects of perspective distortion when analysing the photographs and extracting the deflection-see Figure 3b. This configuration ensures optimum zoom, lens positioning and high resolution image capture. The precision weights used in the experiment ranged from 1g to 200g (the error is given as +/-0.01g)-see Figure 3c, and a white background was used to minimise contrast of the deflecting stem and to provide a clear, uniform background for the photographs, facilitating accurate image analysis-see Figure 3d.

To hold the weights at the free end of the flax stem, we made a weight holder using polyester paper and cotton. Figure 4 shows the weight holder. Again, this seems like a trivial point but the attachment of the cotton to the stem required some technical solutions. Glueing was not evident given the flax stem’s surface so we decided on a slip knot.

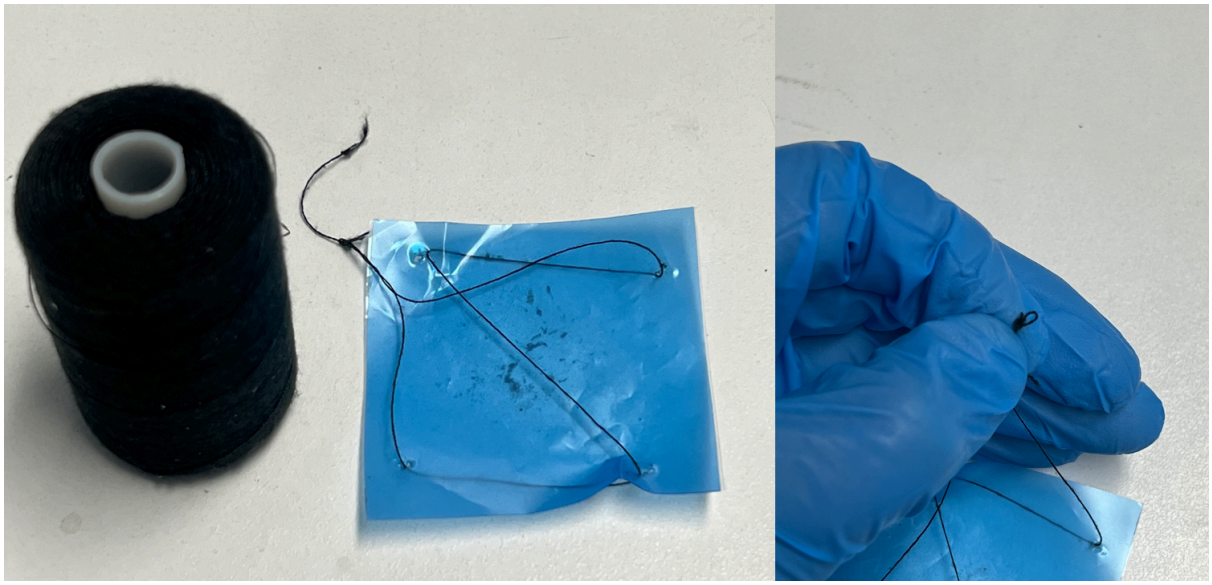

Figure 4. The designed weight holder and the knot to fix the holed to the end of the stem.

The slip knot was used to ensure compatibility with various sample diameters, without requiring frequent adjustments, and to prevent damage to the free end of the sample that may alter the experimental results.

Holding the fixed end is also not as trivial as it seems. For example, in the case of a steel tube mechanical clamping can be used as the base of a steel tube will not be damaged or crushed. In contrast, flax stems are not as robust as steel pipes, we predicted that mechanical clamping would damage the stems at the anchoring point. We therefore designed a simple special holder for the flax stems enabling fixing without clamping. Figure 5 shows the designed sample holder tool.

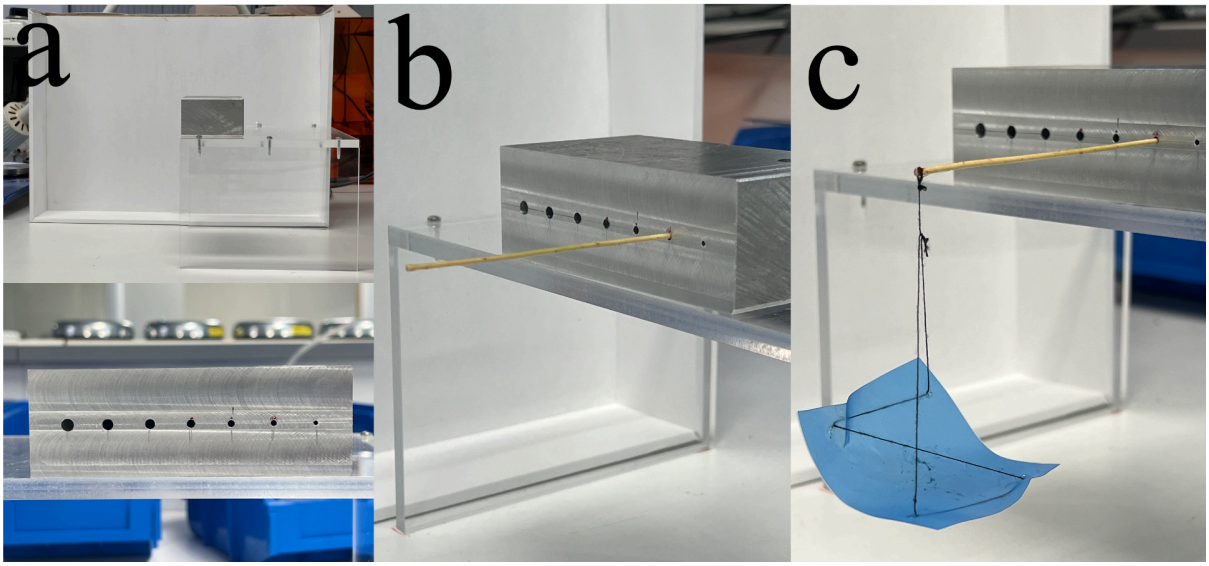

Figure 5. The in-house sample holder designed for the bending experiment. (a) the sample holder metal tool and the inserts corresponding to the different stem diameters (1mm-4mm), (b) shows the sample inserted in the sample holder, (c) shows the sample inserted in the sample holder and the weight holder attached to the free end of the sample.

Figure 5a shows the sample holder, features multiple holes of various stem diameters, and a depth of 3 cm to ensure a secure fit for each stem sample without subjecting it to any mechanical stress that could alter its bending mechanical properties. The sample is inserted snugly into the hole closest to its diameter-see Figure 5b, and the slip knot of the weight holder is suspended at the free end of the stem sample, in order to mount the weight holder onto the flax stem sample-see Figure 5c. Note also that the holes were designed to have a small bevel at their opening, this was done to avoid any stress concentration at the lower part of the stem/tool contact point.

In accordance with the measuring protocol, all flax stem samples, regardless of their retting stages, were subjected to identical procedures. Initially, the samples were classified based on their diameter into three categories, denoted as L (large: 2-3 mm), M (medium: 1.5-2 mm), and S (small: 1-1.5 mm). Nine fresh samples in real-time were tested per each retting stage, with three samples tested from each category. The weight added to the weight holder was increased by 5 grams for the L and M categories, and by 2 grams for the S category. After each weighing, the deflection of the flax sample was captured via the DSLR camera at each added weight. Note that these experiments were repeatedly conducted over a period from 1 July to 10 october–each time the set up needed to be the same. Weights were added until the breaking point of the sample was reached. Subsequently, the tested sample was placed into a special zippered bag and stored at a temperature of 4°C–these samples were used for the stem compression and torsion experiments to be presented in Chapter 4 and Chapter 5.

Figure 6 shows an example of the images captured by the DSLR camera during a bending experiment.

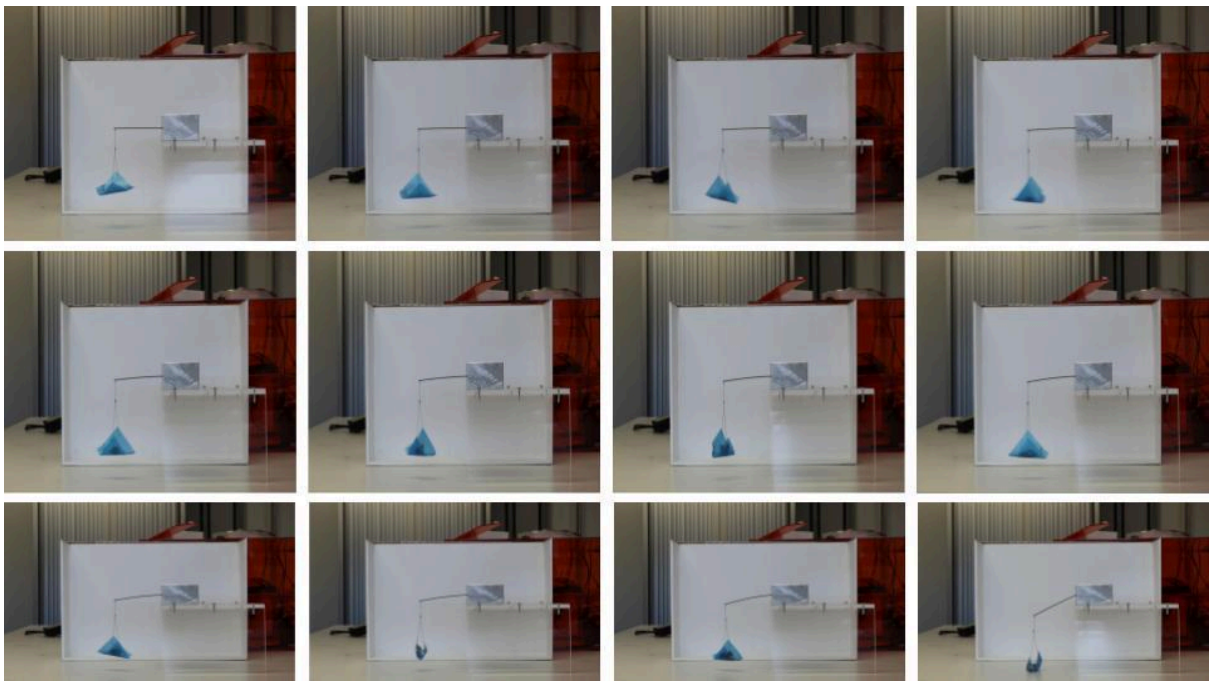

Figure 6. An example of a deflecting flax stem during a point-load cantilever experiment. The deflection of the flax stem sample from its initial state to its breaking point. The flax stem cantilevers are 90 mm in length and have external diameters ranging from 1 to 3 mm

Figure 6 shows an example of how the deflection of a flax stem sample changes as the applied force/weight $F = mg$ increases. These images are then analysed using image analysis software, specifically ImageJ, to extract data on deflection as a function of increasing mass. The results of this analysis are presented in the results section.

Experimental results

The reasoning behind the measurement

The aim of the bending experiment is to compute and monitor the evolution of mechanical properties (flexural modulus and flexural strength) of flax stems during retting.

First, in order to compute the mechanical properties, the flax stems must be modelled. To do this, in a first approximation we chose to approximate the stems to a homogenous, uniform, thin pipe. A bending uniform pipe has an analytical solution based on Euler-Bernoulli beam theory (Timoshenko, 1986, 2010). This solution can be rearranged to give the equation for the flexural modulus.

The analytical model employed for determining the flexural modulus of a flax stem, originates from the Euler-Bernoulli beam theory (Timoshenko, 1986, 2010) and is valid only under low-deflection conditions, where the model incorporates the assumptions and approximations presented in (Timoshenko, 1986, 2010) regarding that the material being analysed is homogeneous and isotropic, and that the deflections are small compared to the length of the beam ($\leq 20\%$). The model takes into account several factors such as the

length of the stem L, the outer diameter d_o, and the inner diameter d_i of the stem. Also the model is established on the basis of the correlation between the force F applied and the vertical deflection and can be mathematically represented as a solution of the Euler-Bernoulli equation as follows:

$$E_f = \frac{F}{\delta}\frac{64\,L^3}{3\pi\left(d_o^{\,4}-d_i^{\,4}\right)} \quad (1)$$

Where F/δ is the linear slope of the results (stiffness), L is the length of the pipe, and do and di are the outer and inner diameters of the pipe.

However, as we have seen in the introduction, flax stems are not uniform homogeneous pipes but rather complex heterogeneous composite structures. Despite this, if we approximate them as 'composite pipes' then we can use the model to extract a composite flexural modulus. More importantly in the context here, by doing this we can directly compare all stems from the same retting stage and also all stems from retting stage to retting stage. The point is that any structural/mechanical changes to the stems caused by up to 3 months lying in a field and exposed to the elements, should be apparent in experimentation. This is a very powerful approach for the development of a technological tool.

As we have said, flax stems are plants and therefore subject to non-uniformities. Therefore, the accuracy of the determination of the flexural modulus may be impacted by variable parameters that are challenging to control, these include: stem diameter (outer and inner), length, geometrical shape, structural uniformity, defects etc. A key point in the experiments is the ability to monitor all these parameters for a single stem. In as much, every stem was meticulously measured in terms of diameters (using digital optical microscopy), length, and uniformity. Indeed, following each experiment, each stem was carefully cut into several parts to enable a control of the diameters (inner and outer) along the whole length of the stem.

Determining the homogeneity and isotropy of the tested material

As mentioned earlier, it is crucial to check the homogeneity of the stem sample to be tested to meet the requirements of the analytical model. This assessment of homogeneity should cover the entire length of the tested sample, rather than focusing on a small portion of it, e.g. the ends. In order to verify the homogeneity of the sample diameters, the 9 cm section of the bent flax stem was cut into multiple equal segments of 1 cm each. Figure 7 and Figure 8 show examples of 1 cm sections from different retting stages captured using a digital optical microscope.

Figure 7. Examples of the cross sections of flax stems from the small category (1-1.5 mm) used for the control of the outer and inner diameters. The images were taken using a digital optical microscope (Keyence, France). The stem here is for retting stage R0 (under-retted stems). A good diameter uniformity was observed along the length of the stem.

Figure 8. Examples of the cross sections of flax stems from the large category (2-2.5 mm) used for the control of the outer and inner diameters. The images were taken using a digital optical microscope (Keyence, France). The stem here is for retting stage R17 (over-retted stems). The scale bar corresponds to 300 µm. A good diameter uniformity was observed along the length of the stem.

Microscopic examination of each 1 cm segment of every stem tested revealed a surprising uniformity in the diameters (inner and outer) along the stems. This results adds weight to our approximation to a thin pipe for extracting the mechanical properties. Figure 9 shows the dimensions of an example of a flax stem sample.

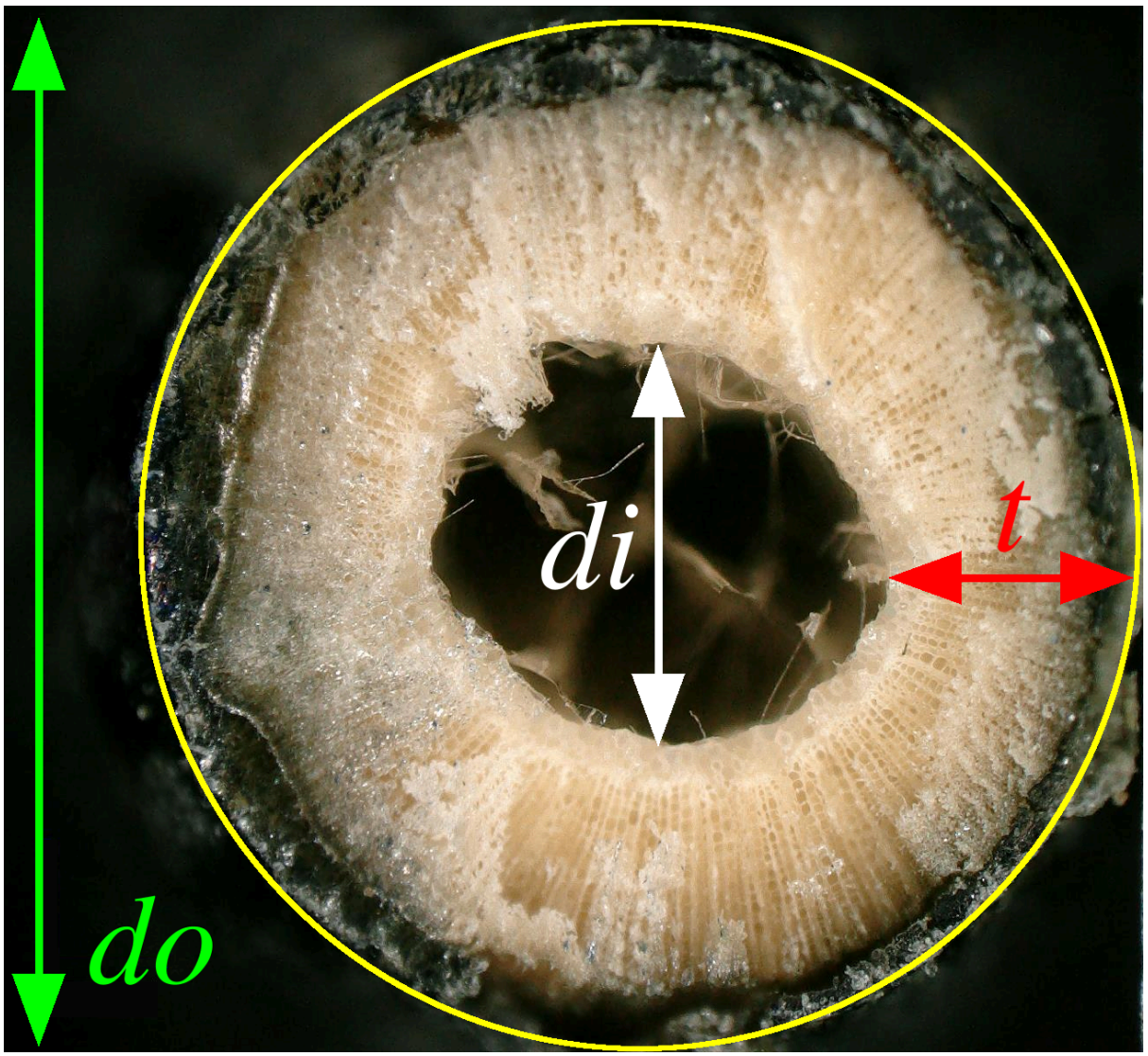

Figure 9. Image showing the outside diameter (green), the inside diameter (white), and the thickness (red) of a typical flax stem used in the study.

Figure 9 shows that the structure of the flax stem section can be fitted to a circular shape as indicated in the yellow circle, having an outer diameter d_o indicated by the green arrow, internal diameter d_i as indicated by the white arrow and a thickness t as indicated with the red arrow. This indicates that the flax stem samples can be approximated by hollow pipes of certain thickness, internal and external diameters.

Further analysis of the flax stalk samples include the determination of the diameter homogeneity along the tested flax stalks samples. This is explained in the following section.

Diameter measurement: 6 diameter method

As flax stalks are plant-based samples, defects are naturally inherited in the stem. This inherent variability can pose a challenge when attempting to accurately measure their diameters. As a result, false diameter measurements can lead to errors in further data analysis. To avoid the potential errors and ensure accurate diameter measurements of these samples, we have implemented an optimised method for this purpose. The diameter of each segment of the bent sample was measured by taking six diameter measurements of different angles for both the outer and inner diameters giving precise attention while determining the end to end point measurement of each diameter. Figure 10 shows the 6 diameter measurement method.

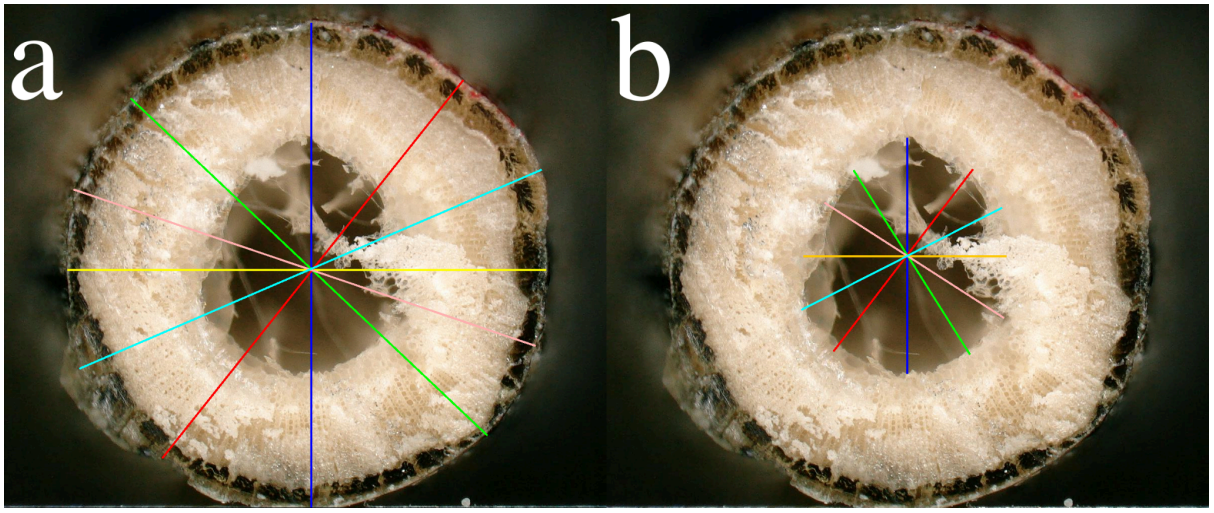

Figure 10. Measurement of the average diameter of each stem section and average diameter for the whole stem. Each colour represents one diameter measurement. (a) shows the measurement method of the outer diameter, and (b) shows the measurement method of the inner diameter.

Then an average diameter representing the final diameter of each single stalk segment is calculated from the 6 measured diameters, and the total average diameter of the complete bent flax stalk sample is then obtained as an average of all average single flax segment diameters. By accurately measuring the diameter in this manner, errors due to variations in diameter, particularly in the outer diameter, can be minimised or eliminated. Table 1 summarises the results of a typical outer diameter measurement of a bent flax stem sample.

Under retted stem (R0-L-Sample1)								
	External Diameter (um)							
Label	S1	S2	S3	S4	S5	S6	S7	S8

D1	2209.9	2272.9	2235.9	2305.5	2220.7	2329.4	2262.0	2253.3
D2	2183.8	2177.3	2205.5	2183.8	2379.4	2288.1	2270.7	2342.4
D3	2252.4	2267.6	2257.2	2287.0	2220.6	2278.8	2263.4	2299.7
D4	2213.3	2302.2	2179.2	2238.8	2379.2	2300.4	2281.2	2313.5
D5	2280.2	2122.6	2238.0	2219.1	2241.4	2306.2	2244.7	2288.0
D6	2164.4	2211.0	2169.2	2207.9	2303.1	2366.6	2240.3	2243.8

Table 1. An example of the measurement of the outer diameter of a single flax stem (Under-retted R0). 180 stems were measured for the study corresponding to 17280 manual diameter measurements.

Table 1 shows that the cut of a 9 cm bent flax sample results in 8 segments of 1 cm length, labelled S1, S2, S3, S4, S5, S6, S7 and S8. From each of these segments, 6 diameter measurements were extracted, labelled D1, D2, D3, D4, D5 and D6. The average outer diameter of the bent flax stalk was found to be 2256.331±56.5 micrometres (μm). These results indicate that the error associated with measuring the average outer diameter along the flax stalk is estimated to be about 2.4%. This suggests that the tested flax stalk has an almost constant outer diameter along its length, and the error resulting from the flax sample diameter in further analysis is negligible. Table 2 summarises the results of a typical inner diameter measurement of a bent flax stem sample.

Under retted stem (R0-L-Sample1)								
	Internal Diameter (μm)							
Label	**P1**	**P2**	**P3**	**P4**	**P5**	**P6**	**P7**	**P8**
D1	1014.7	1060.4	1036.5	1099.5	1177.7	1040.8	997.3	1158.1
D2	956.1	997.3	1032.1	984.3	1032.1	1153.8	953.9	1027.8
D3	944.4	969.1	1054.0	948.2	931.2	1066.1	1026.6	1049.1
D4	975.7	1008.6	993.9	986.8	1050.8	1092.0	1022.5	1112.4
D5	937.3	972.7	1050.6	931.0	960.4	1019.1	922.2	1027.8
D6	954.9	965.67	976.3	1020.8	1063.7	1108.4	927.7	1053.4

Table 2. An example of the measurement of the inner diameter of a single flax stem (Under-retted R0). 180 stems were measured for the study corresponding to 17280 manual diameter measurements.

Table 2 shows the 6 inner diameter measurements, labelled D1, D2, D3, D4, D5 and D6. The average inner diameter d_i of the bent flax stalk was found to be 1017.6±60.7 μm. These results show that the error associated with measuring the average inner diameter along the flax stalk is estimated to be about 5%. This error is negligible, suggesting no influence on further numerical analysis.

In addition, the ratio of the inner diameter to the outer diameter, expressed as $\eta = \frac{d_i}{d_o}$, was calculated to be 0.4. This result suggests that the inner diameter is significantly smaller than the outer diameter and that the outer diameter has a more pronounced and dominant influence in further analyses.

Furthermore, after analysing the diameters of over 180 samples, it was found that the standard deviation $S.D$ resulting from the 6-diameter measurement method for both the outer and inner diameters was extremely small. The importance of the d^4 factor was the very reason why a large experimental effort was made towards evaluating the average diameters of all stems and fibres that were tested. For the stems, this was done by cutting the stems into 1 cm sections and carefully measuring the end diameters of each individual section. The result of this is an average diameter of each tested stem, along the stem. The standard deviation of these diameters indicates the variation of the stem diameter along the stem. This is an important point. The diameter of the stem is never $(d \pm error)^4$ over the whole stem. There is a diameter variation along the stem, but it is the average diameter which governs the mechanical bending of the whole stem, if (and only if) the variation of the diameter can be considered to be small and uniform along the fibre. Based on 2880 diameter measurements, our results show that the average diameter of any stem varies along the stem sample length by less than 5%. This finding suggests that the 9 cm flax stalk samples, taken from the middle part of the flax plant and exposed to various environmental conditions such as wind, rain and moisture for over three months, maintain a consistent diameter along their entire length. This indicates that the numerical model condition regarding the material homogeneity is validated.

Extraction of stem stiffness k from experimental measurements

Based on the model used for calculating the flexural modulus, the determination of the relationship between load and deflection, stiffness, $k = F/\delta$ is crucial for the model validation. According to Newton's 2nd law, the force at the end of the stem can be calculated using:

$$F = mg$$

Where m is the mass added to the free end of the flax stalk sample and g equals 9.81 m/s^2

The deflection δ is extracted from the photographs taken by the camera using image analysis software (ImageJ). Figure 11 illustrates the method used to extract the deflection at the free end of the flax stem sample.

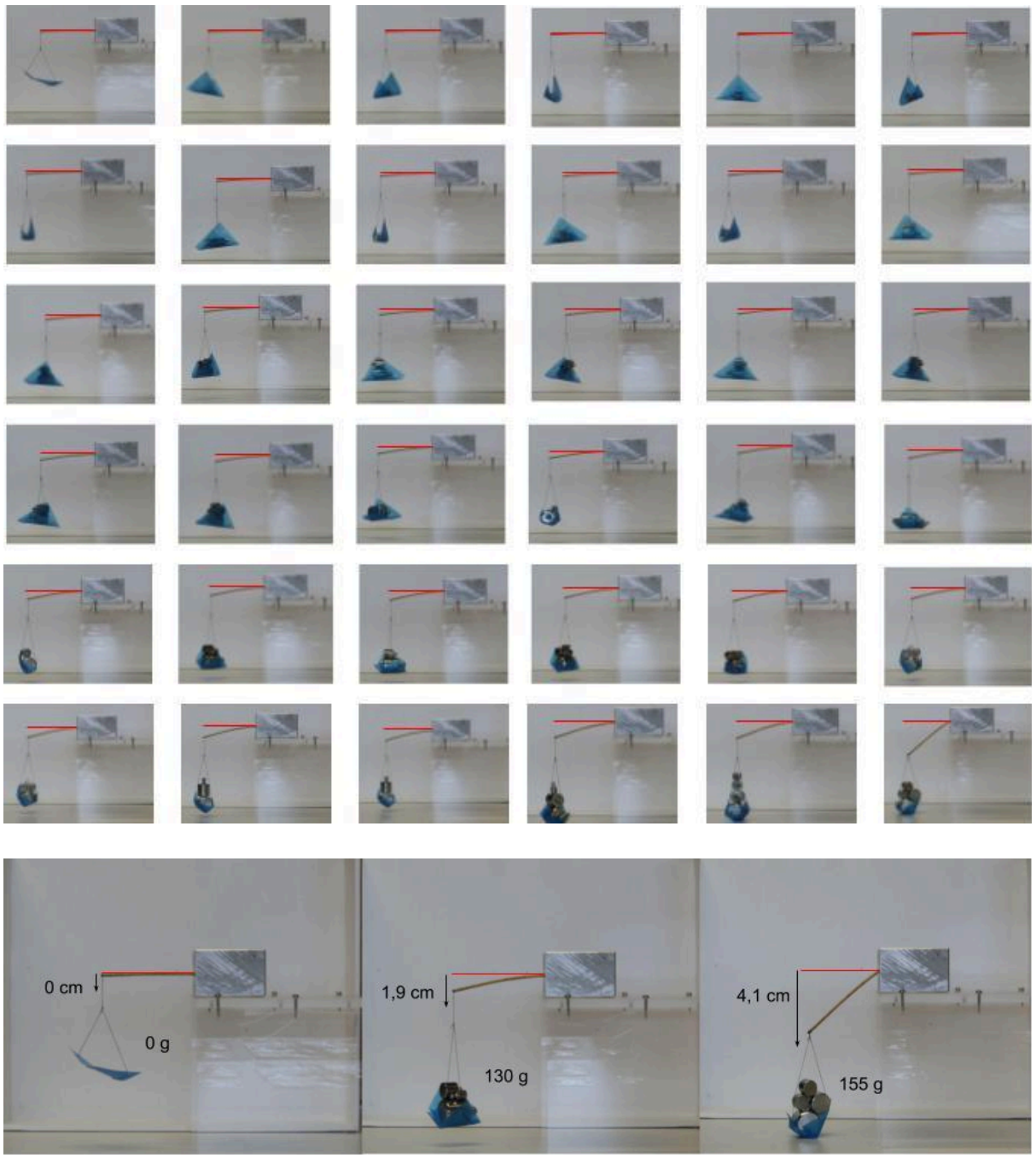

Figure 11. Example of the deflection of a flax stem sample as a function of increasing force. The red line corresponds to undeflected cantilever at $F = 0\,N$.

This experiment was conducted on over 180 fresh flax stem samples in real-time, ie. over a period of three months in summer 2022. To minimise errors associated with initial bending in the resting position, we carefully selected uniform and straight samples for our study (see Chapter 2). The resting state of the flax stem sample is represented by the red line Figure 11. As the force increase at the end of the sample, the deflection δ increases, until it breaks when reaching the breaking force, signifying the breaking point. At this point, the surface stress at the base of the stem (at the top surface of the stem in tension) is equivalent to the

flexural strength of the flax stem. Table 3 gives an example of the results of the flax stem deflection as a function of force of a bending experiment–this example is taken from retting stage R5 (under-retted stems).

Mass (g)	Force (mN)	Deflection (mm)
0	0	0
5	49.05	0.75
10	98.1	1.5
15	147.15	2.47
20	196.2	3.32
25	245.25	4.18
30	294.3	5.26
35	343.35	5.69
40	392.4	7.19
45	441.45	7.51
50	490.5	8.8
55	539.55	9.66
60	588.6	10.95
65	637.65	12.24
70	686.7	13.42
75	735.75	14.39
80	784.8	15.35
85	833.85	17.29
90	882.9	19.97
95	931.95	22.98
100	981	46.07

Table 3. An example of the results of the flax stem deflection as a function of force of a bending experiment–this example is taken from under-retted stems.

In order to carry out a more detailed analysis and to establish the relationship between deflection (in metres) and force (in newtons), the data from Table 3 was plotted. Figure 12 shows the resulting plot of this data.

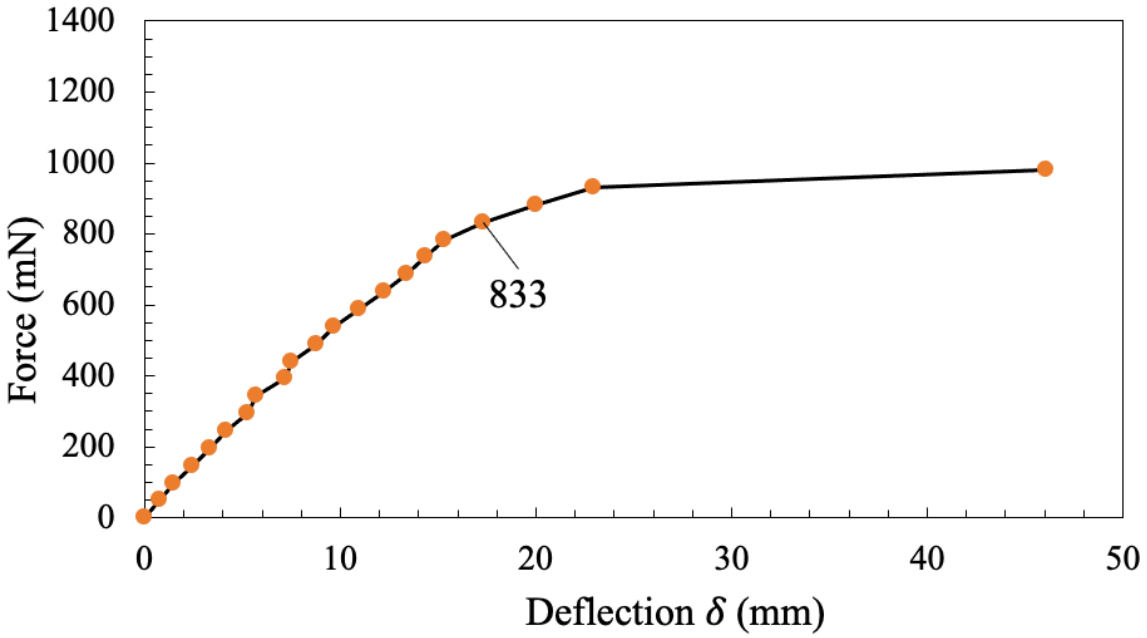

Figure 12. Example of a flax stem deflection δ (in metres) as a function of concentrated load force at the end of the cantilever (in metres). The slope of the linear portion of the data is the stiffness of the cantilever (N/m): this is the value we require to evaluate the flexural modulus.

Figure 12 shows the relationship between the applied force and the resulting deflection of a flax stem, represented by the orange dots. As the applied force increases, so does the deflection until a breaking point is reached at a given breaking force. Closer analysis of the plot reveals two distinct profiles: a linear portion and a nonlinear portion–this was present in all flax stems. This behaviour is very similar to the stress-strain curve typically seen in many materials. The linear profile corresponds to the elastic behaviour of the flax stalk. Here the relationship between force and deflection is linear–this was the case of all flax stems tested. When a force is applied to the end of the flax stem, it responds by deflecting, but without permanent deformation. Importantly, the flax stalk can return to its original state when the force is removed. This elasticity is similar to that of a rubber band, which can stretch and then return to its original shape when released. In contrast, the nonlinear portion represents plastic behaviour. Instead, it shows a constant and steady deflection without a proportional increase in force. This indicates that the flax stem (or part of it) is undergoing permanent deformation in response to the applied force, which will eventually lead to mechanical failure. Once plastic deformation has occurred, the stem cannot return to its initial state, as can be seen from the photographs taken by the camera-see Figure 11

This behaviour mirrors the stress-strain curve of an ideal material, where the linear portion represents elasticity and the constant steady phase represents plasticity. This finding provides further evidence that a retted flax stem sample behaves similarly to an ideal

material in its response to external forces, this further indicates that the discussed analytical model is valid for these plant materials.

According to the analytical model assumptions (Timoshenko, 2010, 1986), the modulus calculation requires the load-deflection relationship F/δ to be established in the low deflection regime, where deflections are assumed to be 20% or less compared to the length of the sample (Timoshenko, 1986, 2010). Therefore, the low deflection regime expressed as δ/L is then determined. Table 4 shows the calculation of the low deflection regime.

Force $F\ (mN)$	**Deflection** δ_y **(mm)**	δ/L
0	0	0.000
49.05	0.75	0.008
98.1	1.5	0.017
147.15	2.47	0.027
196.2	3.32	0.037
245.25	4.18	0.046
294.3	5.26	0.058
343.35	5.69	0.063
392.4	7.19	0.080
441.45	7.51	0.083
490.5	8.8	0.098
539.55	9.66	0.107
588.6	10.95	0.122
637.65	12.24	0.136
686.7	13.42	0.149
735.75	14.39	0.160
784.8	15.35	0.171
833.85	17.29	0.192
882.9	19.97	0.222
931.95	22.98	0.255
981	46.07	0.512

Table 4. The low deflection regime of the stem**.** This is where the deflection/the cantilever length is less than 0.2.

In order to extract the correct value of the stiffness two key issues must be met. First, the deflection in the low deflection regime, $\delta/L = 0.2$: this is a theoretical consideration (Timoshenko, 1986, 2010). Second, the stem must be in the elastic deformation portion of the force vs. deflection curve–this is practical mechanical consideration (Timoshenko, 2010) For each stem, the stiffness was calculated according to these two conditions.

Table 4 confirms that the calculated low deflection regime matches the elastic behaviour observed in the curve shown in Figure 12. In both cases, this match is evident when the applied force reaches 0.833 N for this particular sample. Beyond this force, the sample enters the plastic regime, indicating permanent deformation. Moreover, a comprehensive analysis of more than 180 samples used in the bending experiment consistently shows that the low deflection regime corresponds harmoniously with the elastic behaviour of the sample. This elastic behaviour is represented by the linear segment of the graph. Consequently, this relationship between applied force and deflection, often referred to as stiffness (denoted 'k'), where $k = \frac{F}{\delta}$, can be extracted from the slope of the linear low deflection regime. In simple terms, this regime quantifies how stiff or flexible the flax stem is when subjected to bending forces. Figure 13 shows the plot of the linear part of the curve in figure 12 presenting the low deflection regime/elastic behaviour.

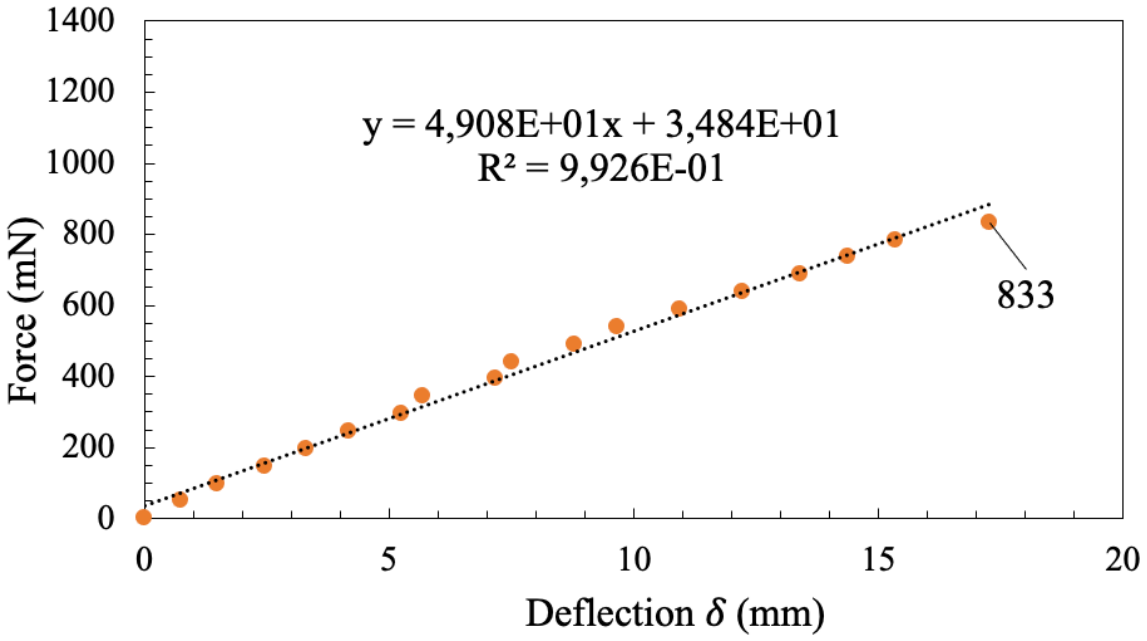

Figure 13. The extraction method of the stiffness k by taking into consideration the two conditions: (i) the low deflection regime $\delta/L < 0.20$ and (ii) the graph must be linear, i.e. elastic behaviour.

Figure 13 shows an example of the method to estimate the stiffness k of all the 9 flax stem samples of retting stage R5 (under-retted sample). In this sample, Figure 13 shows that the stiffness k in the low deflection regime was estimated to be 49.082 N/m , determined by the slope of the linear low deflection regime. Figure 14 shows an example of the load-deflection curve of all the tested samples in R5 (under-retted samples).

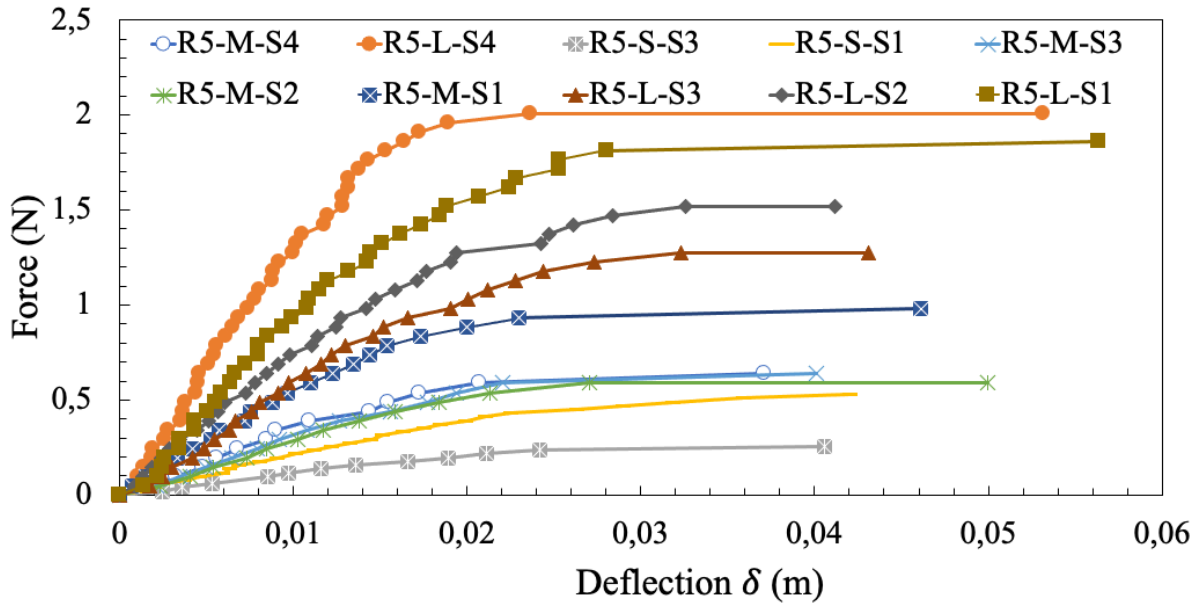

Figure 14. An example of the load-deflection plots of all the tested samples in a single retting stage (under-retted stems from R5 in this case).

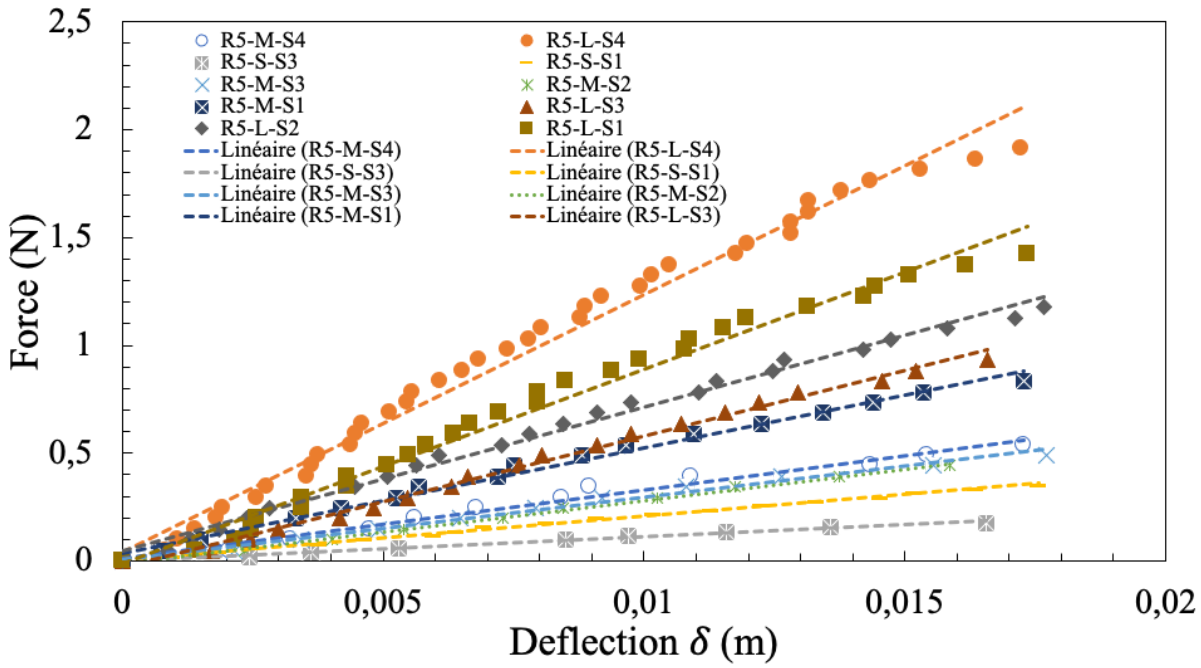

Figure 15. An example of the low deflection linear and elastic deformation regime of each of the tested samples in a single retting stage (under-retted stems from R5 in this case).

Sample	Stiffness k (N/m)
R5-L-S2	66.8
R5-LS4	119.0
R5-L-S1	90.0
R5-M-S3	28.9
R5-M-S4	31.9
R5-M-S1	49.1
R5-M-S2	29.1
R5-L-S3	60.8
R5-S-S1	20.3
R5-S-S3	11.4

Table 5. Shows the slope *k* corresponding to each tested sample in a single retting stage (undet-retted stems from R5 in this case).

Determination of the flexural modulus of flax stems as a function of retting

After conducting the necessary experiments and measurements, all the required variable parameters for calculating the flexural modulus were obtained. The equation for calculating the modulus, as described earlier, incorporates the measured values of length, force, deflection, and diameter. Table 6 presented below summarises an example taken from a retting stage R5 of the experimental data, the necessary calculations, and the corresponding results.

Average outer diameter (µm)	Average internal diameter (µm)	Stiffness k (N/m)	Flexural modulus (GPa)
d_o	d_i	F/δ	E
2318.50	873.10	63.15	11.05

Table 6. presents the key variables extracted from the experimental data that are essential for validating the model. This example concerns a bent flax stalk obtained from the R5 stage of the retting process.

Table 6 gives an example of a bent flax stalk sample taken from the R5 stage of the retting process. It includes various parameters needed to calculate the flexural modulus, such as the average outer and inner diameters and the stiffness (k), which relates load to deflection. It's important to note that the length of all bent flax stalk samples was consistent at 0.09 cm. Applying these data to the analytical model described by equation x, the modulus was determined to be 11.044 GPa. Table x summarises the flexural modulus values for all the samples from the R5 stage of retting.

Sample	Flexural modulus (Gpa)
R5-L-S1	13.99
R5-L-S2	11.68
R5-L-S3	10.14
R5-M-S1	12.39
R5-S-S1	14.75
R5-L-S4	11.21
R5-M-S4	11.21

Table 7. Shows a summary of the flexural modulus of all R5 retting samples tested.

Table 7 gives data on the average flexural modulus for all the samples tested at stage R5. The results show that the average flexural modulus is 12.196 ± 1.646 GPa. It's worth noting that similar calculations were made for each of the 13 retting stages, with 9 samples analysed for each stage, and the corresponding data are also summarised in Table 8.

Retting time (days)	Flexural Modulus (GPa)	ST-Deviation (GPa)
0	13.33	2.67
7	14.65	3.46
14	13.19	2.20
21	12.20	1.65
28	12.67	2.67
35	14.27	3.00

42	13.50	1.92
49	14.00	1.96
56	13.63	3.08
63	14.46	4.12
70	11.77	2.21
77	11.79	1.84
84	10.65	3.65
91	9.63	2.52

Table 8. The average flexural modulus obtained from individual retting stages as a function of the retting period. R0 is on the same day as flax harvesting (day 0). R20 was three months later (day 91).

Table 8 shows the average flexural modulus obtained during the retting process, with an average value of 12.84 ±1.48 GPa. An interesting trend can be seen in the data towards the end of the table. In order to gain a better understanding of how the average flexural modulus changes over the course of retting, these results are plotted against retting time in Figure 16.

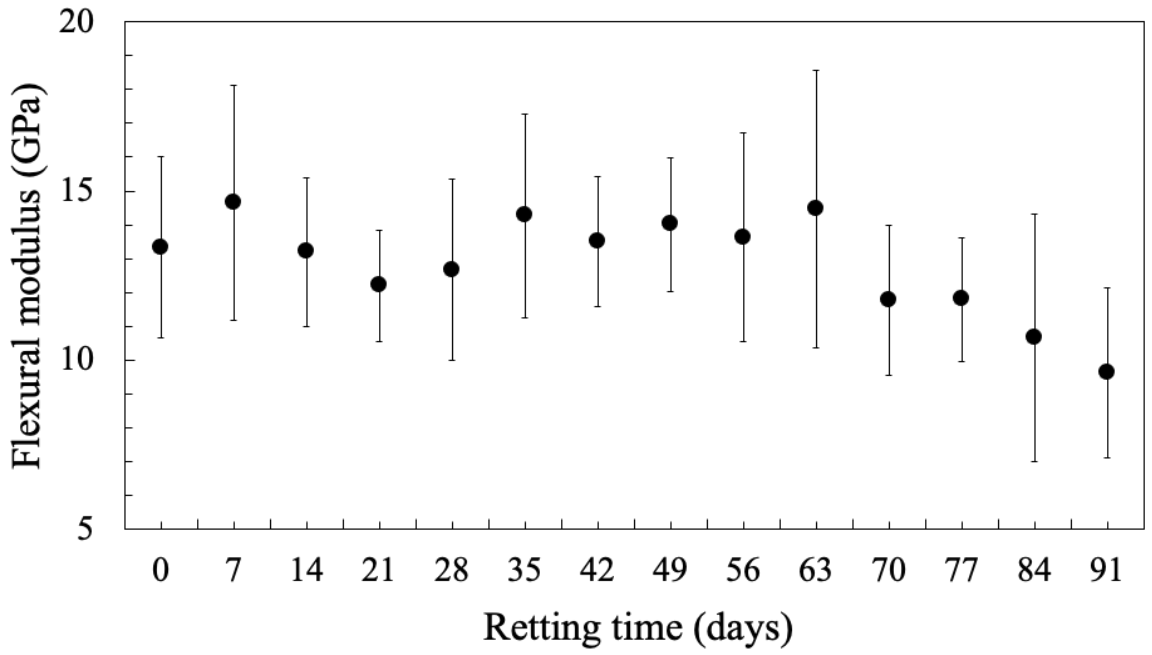

Figure 16. A plot of the evolution of the experimentally-obtained average flexural modulus of flax stems (diameter 1-3 mm) as a function of retting time. This plot is based on 180 flax stem experiments. The results were obtained in real-time during the whole retting period of 2022 and beyond, i.e. 6th July to the 4th October 2022.

Figure 16 shows the relationship between average flexural modulus and retting time. The optimum retting point, as determined by VRF, is marked on the graph (day 56). Prior to reaching this point (under-retting), the stems have a relatively constant flexural modulus. Once the optimum-retting phase is reached, the measured flexural modulus reduces steadily. This trend can provide valuable information on the effect of retting on the mechanical properties of flax stalks.

To gain a deeper understanding of the influence of retting on these properties, we carried out a more detailed analysis of the plot by splitting it into two distinct profiles, as shown in the following figures. Figure 17 shows the behaviour of the average flexural modulus during the under retting period.

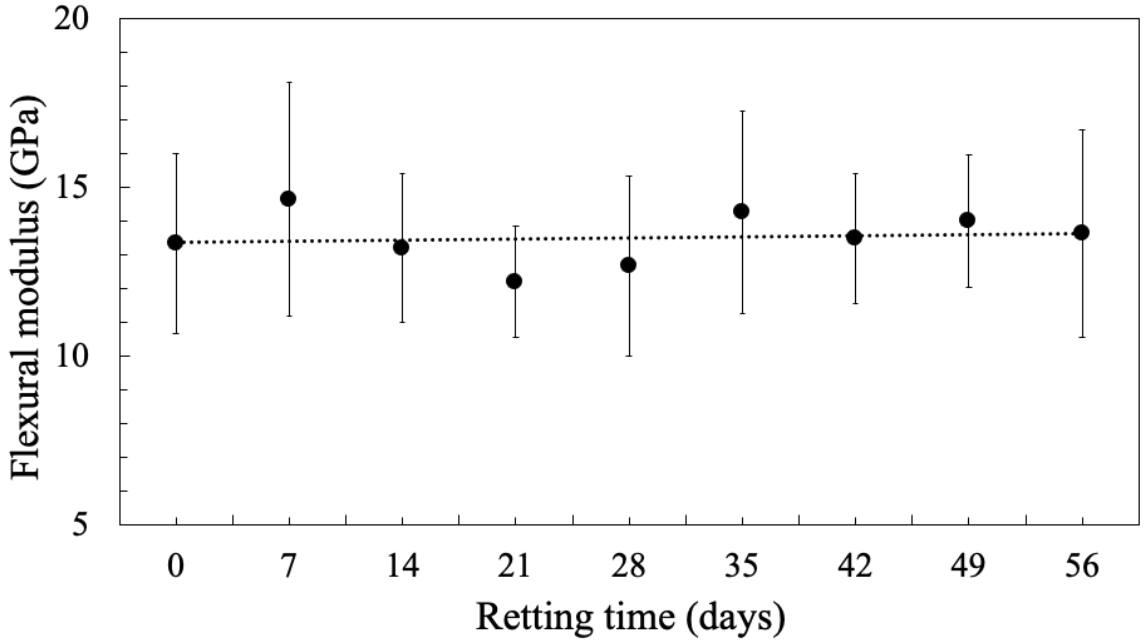

Figure 17. A plot of the average flexural modulus of flax stems during the under-retted period. The flexural modulus increases at approximately 4.6 MPa/day over 56 days prior to the optimum retting time.

Figure 17 shows that during the under-retting period the average flexural modulus remains relatively constant, with only a small increase of 4.6 MPa/day. This increase is considered negligible compared to the actual value of the average flexural modulus, which is approximately 13.49±0.77 GPa (the average over the 56 day retting period).

On the other hand, if we analyse the over-retted period, we observe a different pattern in the behaviour of the average flexural modulus, as shown in Figure 18.

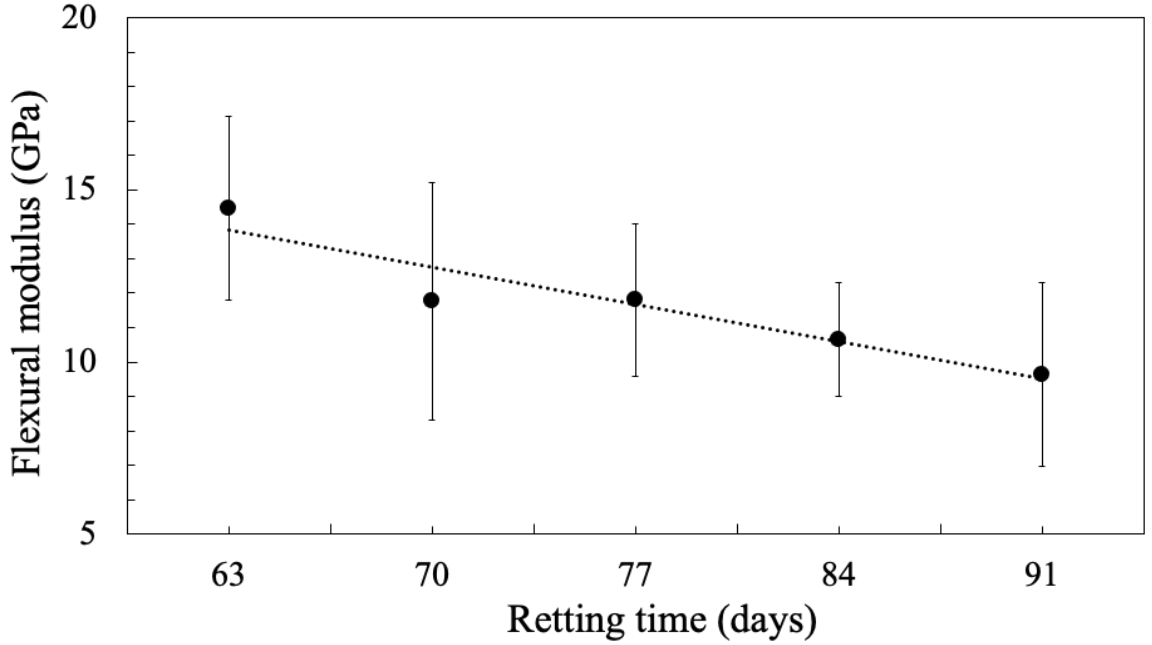

Figure 18. A plot of the average flexural modulus of flex stems during the over-retted period. The flexural modulus reduces at approximately 154 MPa/day ove 28 days following the optimum retting time.

Figure 18 shows that the behaviour of the average flexural modulus during the over-retted period exhibits a significant decreasing trend. The flexural modulus decreases significantly by approximately 5 GPa during this over-retted phase–this is a 35% reduction of the flexural modulus. The flexural modulus reduces at approximately 154 MPa/day over 28 days following the optimum retting time $(R^2 = 0.9)$. This result is clear evidence of the influence of retting on the mechanical properties of the retting flax stems.

Determination of the flexural strength of flax stems as a function of retting

The breaking stress (flexural strength) of flax stems is another important mechanical property that can be extracted from the data obtained in the bending experiments. Extracting the breaking stress from bending experiments provides potentially useful information about the strength and mechanical behaviour of flax stems with the view of making a tool to monitor the advancement of retting. The data could also be coherent with the evolution of flexural modulus–something that does evolve as retting advances. When bending the flax stems by using a concentrated load at the free end of the cantilever, the maximum surface stress (tensile/compressive) will be generated at the base of the cantilever on the top/bottom of the stem. It is apparent from the bending experiments that the flex stems failed at certain levels of force and deflection. These data can be analysed and in order to do so we need a model for the value of the surface stress at the base of a bending pipe.

In this particular section we focus on determining the breaking stress (flexural strength) of flax stems as a function of retting time. The aim was to investigate in real-time the effect of retting on the mechanical strength of flax stalks, and to see if retting plays a role.

Again, by approximating the flax stem to a uniform, homogenous pipe (Timoshenko, 1986, 2010) we have the following relationship for the maximum surface stress as the base of a bending pipe using a concentrated load at the free end of the cantilever:

$$\sigma = \frac{32\, F_b\, d_o}{\pi(d_o^4 - d_i^4)} \tag{2}$$

Where F_b is the breaking breaking, d_o is the outer diameter and d_i is the inner diameter. This equation enables all flax stems in the same retting stage to be compared and stems from retting stage to retting stage to be compared.

The average breaking strength of flax stalks at each stage of retting is determined by measuring the individual breaking stress of flax stem samples throughout the retting period in a real-time experiment. An illustration of the calculated breaking stress values obtained from flax samples at retting stage R5 is given in Table 9:

Sample	Breaking Force (mN)	Flexural strength (MPa)
R5-L-S1	1421	102.38
R5-L-S2	1176	88.32
R5-L-S3	931	67.61
R5-M-S1	833	86.62
R5-M-S2	441	31.32
R5-M-S3	490	38.85
R5-S-S1	353	77.36
R5-S-S3	176	26.28
R5-L-S4	1911	90.46
R5-M-S4	539	68.69

Table 9. Samples tested in retting stage R5 (under-retted sample) of retting, the breaking force and the computed flexural strength, based on Equation 2.

The average breaking stress of the retting stage R5 was determined from 10 samples to be 67.79± 26.81 MPa.

The average breaking stress of each retting stage along all the retting period is calculated in the same manner and the results are summarised in Table 10:

Retting time (days)	Bending Breaking Stress (MPa)	S.D
0	85.79	21.22
7	105.43	29.85
14	108.71	19.03
21	108.97	17.73
28	101.46	14.29
35	101.28	18.77
42	111.13	13.35
49	110.40	11.69
56	87.32	15.13
63	104.30	24.21
70	84.10	12.40
77	83.60	15.31
84	81.45	24.83
91	75.05	14.56

Table 10. The experimentally-determined average flexural strength of all the tested samples as a function of retting time. In total, 180 flax stems were characterised in real-time to achieve this data.

In order to analyse how the average breaking stress varies with the retting time, a graph was made using the data from Table 10. Figure 19 shows the relationship between the average breaking stress observed at each stage of retting as a function of retting days:

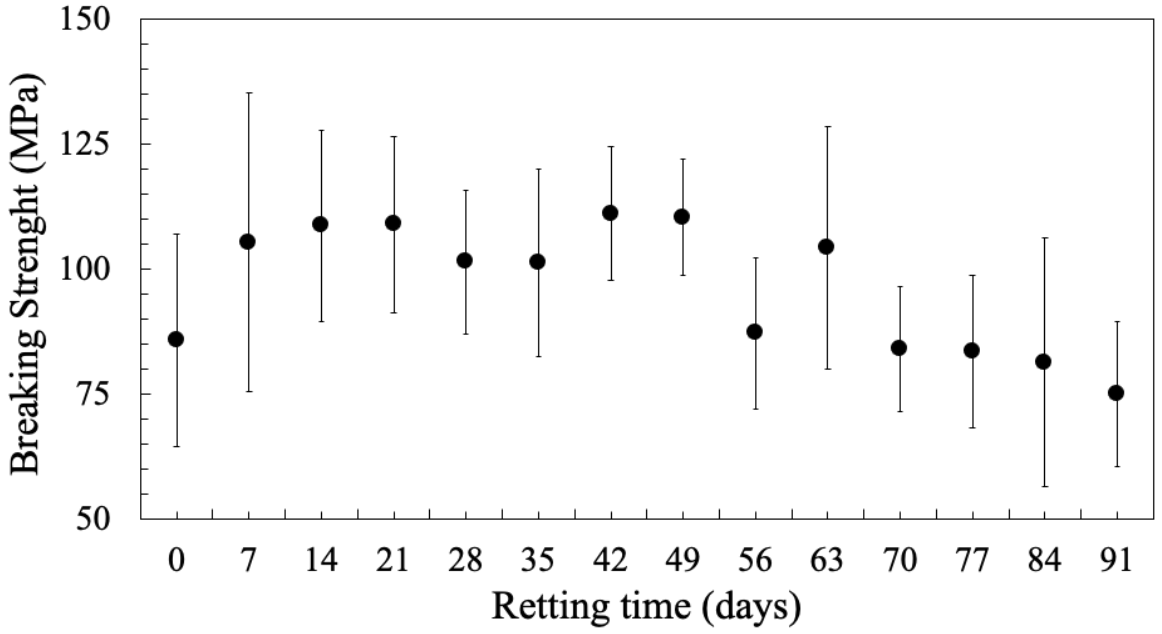

Figure 19. Plot showing the evolution of the average flexural strength of flax stem samples as a function of retting time in days. The optimally-retted time was day 56 (as defined by the VRF company). The results were obtained in real-time during the whole retting period of 2022 and beyond, i.e. 1st July to the 1st October 2022.

Average flexural strength as a function of retting days: 96.4 ±12.7 Gpa. The plot in Figure 19 shows an interesting trend: the average flexural strength, derived from the individual retting stages, remains relatively constant throughout the retting period until it reaches an optimum point (day 56). After this optimum retting stage, the failure stress begins to decrease. This trend is comparable with the trend observed when measuring the flexural modulus during retting. Note that over the whole retting period, the flexural strength of the stems falls by 30 MPa (from day 7); this corresponds to a 29% fall in the value.

To gain a deeper insight into how retting affects the evolution of breaking stress in flax stem samples, we can further analyse the data . We compare the average breaking stress before and after the optimally-retted stage and then determine the overall average breaking stress. Figures 20 illustrate the differences in average breaking stresses at different points in the retting process.

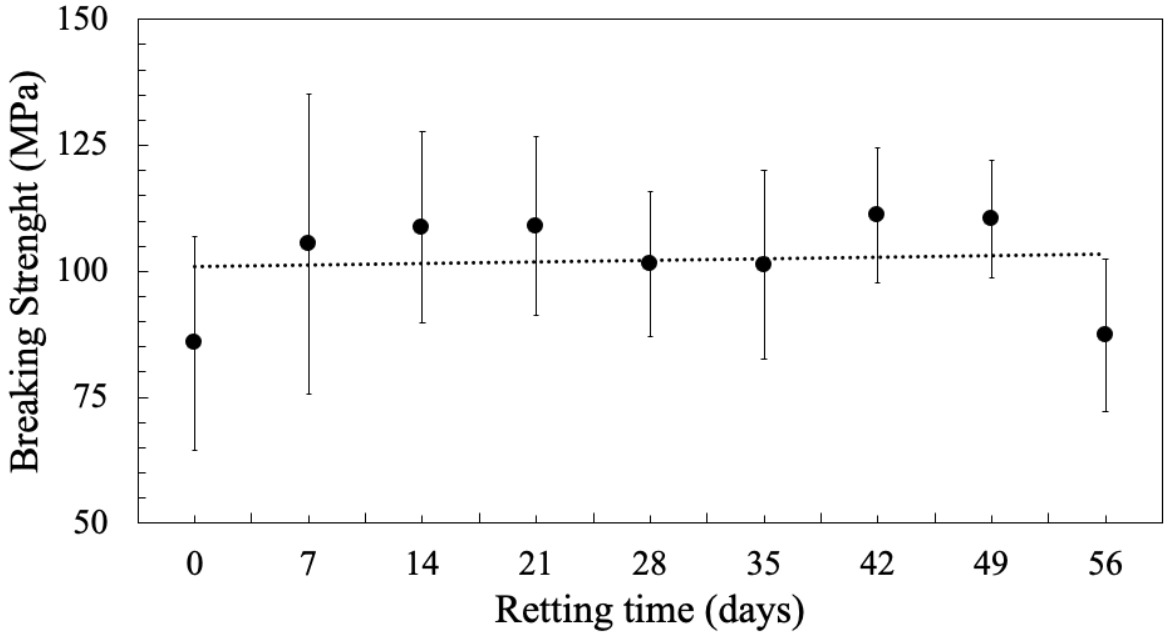

Figure 20. A plot of the average flexural strength of flax stems during the under-retted period. The flexural strength increases at approximately 0.3 MPa/day over 56 days prior to the optimum retting time.

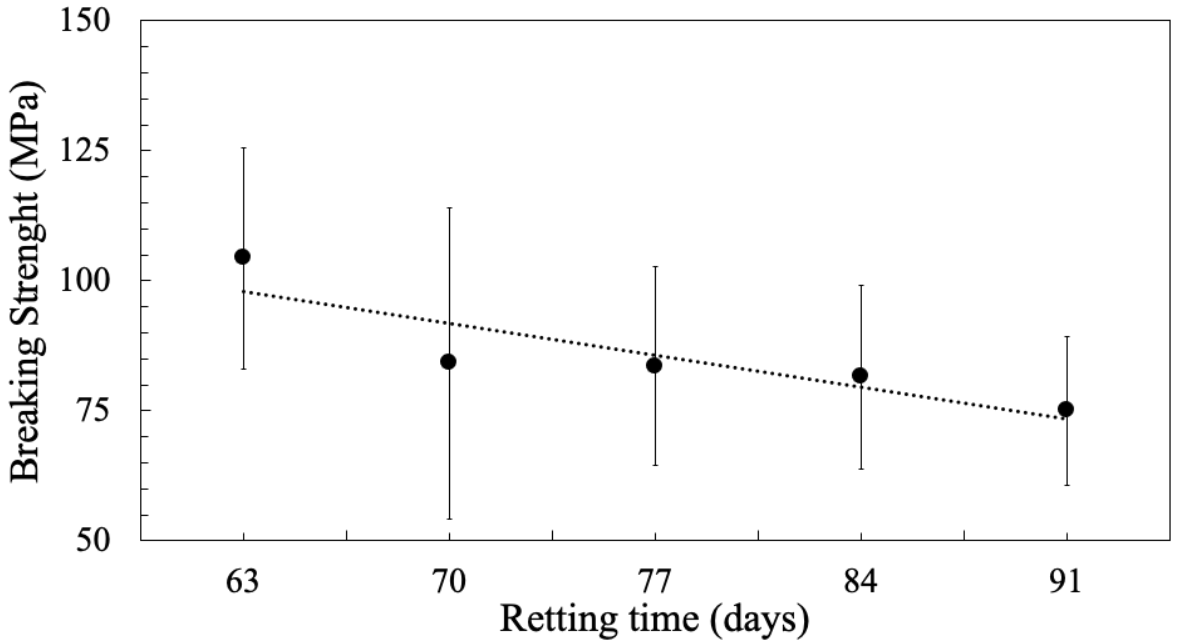

Figure 21. A plot of the average flexural strength of flax stems during the over-retted period. The flexural strength reduces at approximately 0.9 MPa/day ove 28 days following the optimum retting time.

Figure 20 shows that the average breaking stress remains relatively stable during the retting period before reaching the optimum retting stage. There is a slight increase over the whole period. Figure 21, on the other hand, shows the evolution of the average breaking stress after passing the optimum retting point. There is a significant decrease of 0.9 MPa per day over the over-retting period. This decrease suggests that a state of over-retting may be responsible for this reduction in flexural strength, highlighting the obvious influence of the retting process on this parameter during the retting period.

Discussion of this section

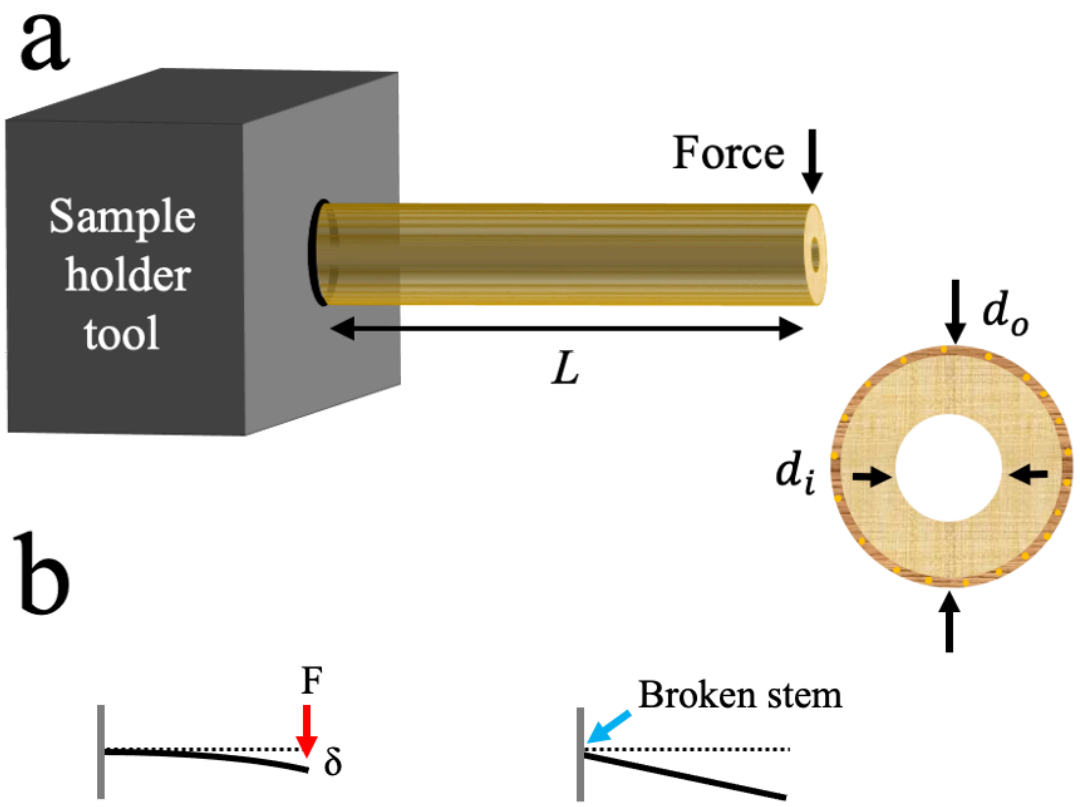

Figure 22. Schematic representation illustrating the bending experiment on flax stems. (a) Schematic presentation showing the status of the flax stem before bending. (b) Schematic representation showing the flax stem during bending and at a breaking point.

Figure 22 shows schematic diagrams of the bending flax stems. When the stem is being bent via a concentrated load at the end–see Figure 22b, the surface stress is maximum at the base. At the base of the cantilever, the stem has a certain cross section–inset to Figure 22. It is this stem cross section position that we will consider in the following discussion.

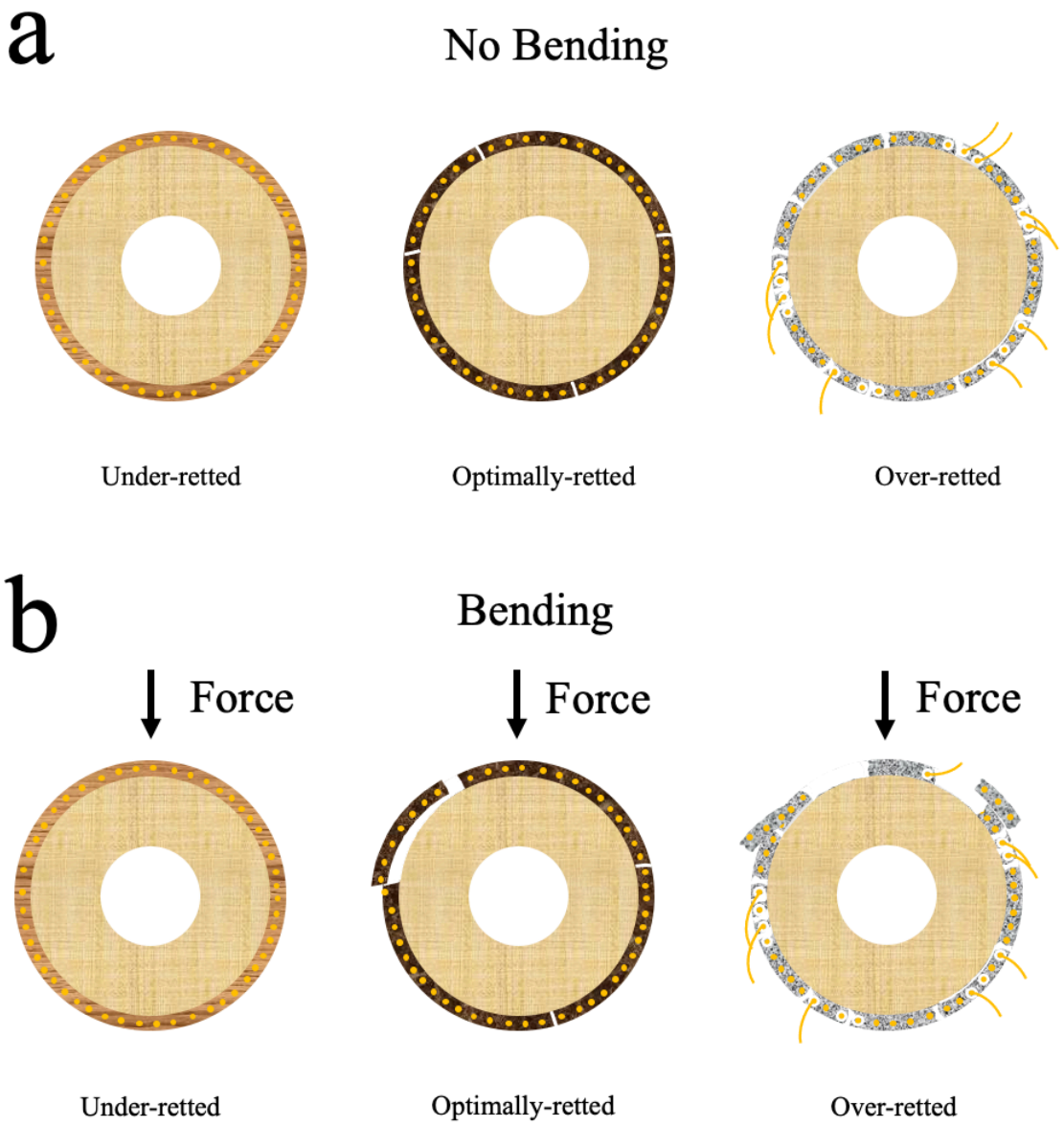

Figure 23. Schematic representation of the flax stems from under-retted, optimally-retted, and over-retted stages before (a) and during bending (b). The schematic diagrams represent flax stem cross sections near to the base of the cantilever where the stress is maximum. The colour of the exterior tissue represents the advancement of the retting. The small yellow dots represent the flax fibres running along the stem. The diagrams are cross sections of a stem. The unchanging inner wood portion 'xylem' is indicated in light brown.

Figure 23 shows schematic representations of the cross sections of the flax stem samples taken from under-retted (left), optimally-retted (middle) and over-retted (right) stages before -see Figure 23a and during-see Figure 23b inducing a bending force. Note that the figures represent schematic cross sections of the stems near to the base of the cantilever where the

stress is maximum. There is an absence of changes in the status of the outer tissue, after bending of all under-retted samples-see Figure 23b. This is not the case for the optimally and over retted samples, where a clear influence of bending and resulting stresses, expressed as delamination and damages, in the tested samples from the optimally and over retting phases.

The results of this study show an interesting pattern. When the under-retted samples are subjected to mechanical bending, there are no observable changes in the stem surface. In this case, the application of mechanical bending (to induce a mechanical stress on the flax composite including the external tissue and the xylem) does not cause damage in the external tissue of the flax stem–for all flax stem samples in all retting stages. This means that the contribution of this layer to the mechanical stiffness of the cantilever remains uncompromised by the bending. This is not the case for the samples from optimally and over-retted phases. The results show that when samples from these stages of retting are subjected to bending force, the external tissue is affected by mechanical stresses. However, this influence is minor in the case of the optimally retted samples (result in slight delamination of the external tissue) while major in the over-retted samples resulting in peeling of the external tissue.

This can be explained as follows: in the optimal retting and beyond, the biochemical degradation of the middle lamella induces the separation of the fibre bundles and the fibres themselves within the bundle in the outer tissue. When the stem samples from these stages were bent, this induced delamination and sliding of the outer tissue including the fibres as represented in schematic diagram of Figure 23b. As a result the tension in the external tissue that results as a response to the bending force is non uniformly distributed in the outer tissue, resulting in the decrease in the flexural modulus as well as the flexural strength.

This matches with the trend in the graphs of the average flexural modulus and the flexural strength extracted from this experiment. We suggest that the decrease in the average value of the modulus and the strength after the optimal retting phase in the tested samples, resulted from delamination and sliding of the external tissue when subjected to the bending force, as illustrated in Figure 23b

These results strongly suggest that the retting process is apparent in a bending mechanical phenomenon. In addition, this experiment opens up a new way of finding out something very interesting about flax stems: the flexural modulus and strength of the flax stem plant. In this context, the average flexural modulus during the under-retting period remains relatively constant, with only a small increase of 4.6 MPa/day. During the over-retted period exhibits a significant decreasing trend. The flexural modulus decreases significantly by approximately 5 GPa during this over-retted phase–this is a 35% reduction of the flexural modulus. The flexural modulus reduces at approximately 154 MPa/day over 28 days following the optimum retting time (the value of $R^2 = 0.9$). Similarly, the average flexural strength remains relatively stable during the retting period before reaching the optimum retting stage. There is a slight increase over the whole period. This could be correlated to the weather conditions during that period. There is a significant decrease of 0.9 MPa per day over the over-retting period. This decrease suggests that a state of over-retting may be responsible for this reduction in flexural strength, highlighting the obvious influence of the retting process on this parameter during the retting period. These novel parameters have remained unknown due to the lack of previous research in this area.

Finally, we can ensure the accuracy and the model validity of the flexural modulus measured here for 180 flax stems. Since numerical modelling is challenging for a complex plant stem, the modelling was verified using bending of homogenous materials such as stainless steel and polypropylene tubes. This work can be found in **Appendix A**. Using stainless steel and polypropylene tubes, the bending modulus was found to be equal and exactly the same value given for these materials in the literature. This suggests that potentially flax stems can take into account anisotropy in their morphology and properties, particularly in its tubular structure.

Microscopy observation of the stem failure at the base of the cantilever

In order to gain a deeper insight into the bending behaviour of the stems, in particular the flexural modulus and breaking stress, and to investigate the influence of retting at the microscopic level, we carried out a bending experiment on the base part of fresh flax stems during the real-time retting process. The flax samples used in this experiment were prepared to match the length and dimensions of those used in the previous bending study. These samples were tested while still fresh and under real-time conditions. The experiment was carried out using a digital optical microscope due to its large working distance, which allowed the sample holder to be positioned to facilitate the experiment. Figure 24 below illustrates the setup used for the microscale bending experiment:

Figure 24. Setup used for the bending experiment under the microscope. (a) shows the sample holder, (b) shows the customised bender by the red arrow, (c) shows the anti-vibration pads by the red box. The objective of this experiment was to observe any potential damage at the base of a bending flax stem.

The sample holder was carefully positioned on the base of the digital optical microscope as shown in Figure 24a. A ruler was used to determine the exact distance between the flax sample in the holder and the support on which the bender tool was placed. The purpose of this initial distance measurement was to determine the appropriate height at which to position the customised bender, indicated by the red arrow in Figure 24b, that will help in controlling the stem deflection value during the experiment.

The experiment involves gradually deflecting the flax stem samples down by 1 cm at a time, taken from different retting stages over the retting period, until an observable break in the stem base can be seen. Note that as we now know the flexural modulus we are able to easily compute the surface stress at the base of the base of the deflecting stem. This observation aims to determine the influence of retting on the mechanical properties of the

flax stalks–with focus on the failure at base of the stem. The results of this experiment are shown in Figure 25.

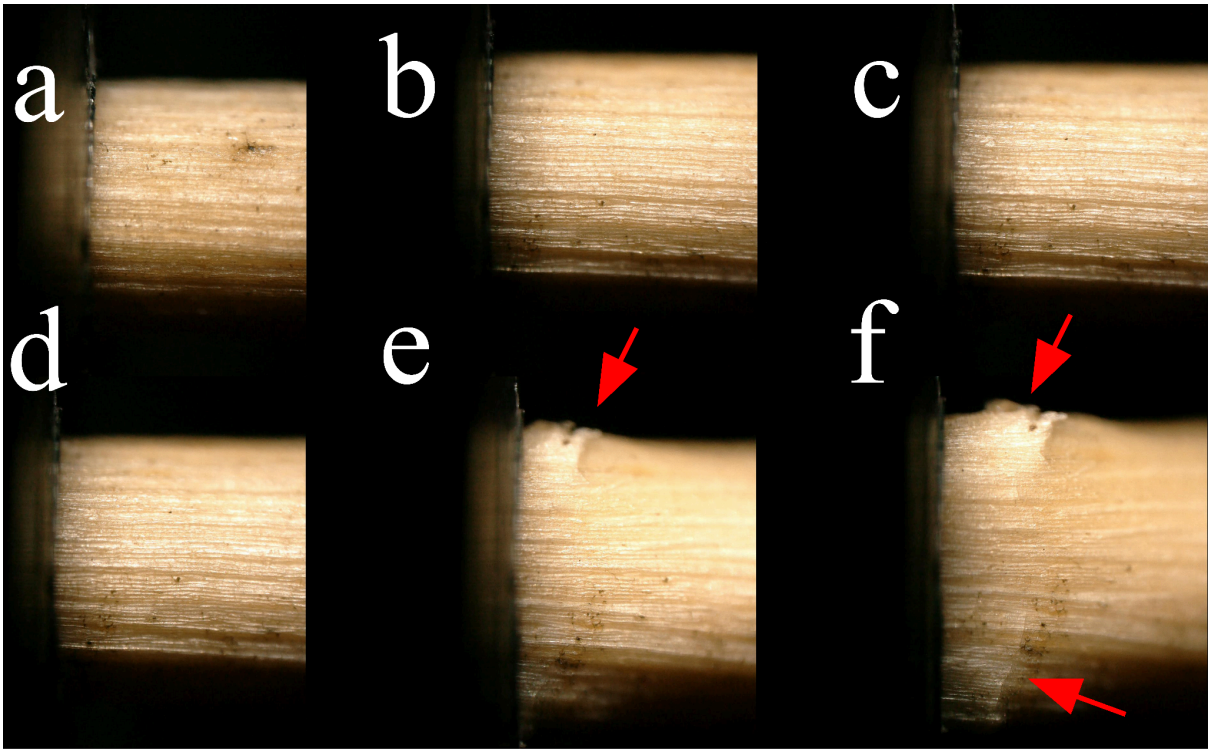

Figure 25. shows the microscope images resulting from the under retting stage. (a) initial state deflection at 0 cm, (b) deflection at 1, (c) deflection at 2 cm, (d) deflection at 3 cm, (e) deflection at 4 cm, (f) deflection at 5 cm.

Figure 25a shows the initial state of the flax stalk sample before any deflection is applied. Subsequently, Figures 25b, 25c and 25d show that no deformation occurs after three successive bends induced when the customised bender height gradually decreases by 1 cm from the initial state. However, when the bender height decreases to 19.7 cm, deformation becomes apparent at the base of the flax stalk samples, as indicated by the red arrow in Figure 25e. With further increases in deflection, the deformation and damage becomes increasingly apparent, as indicated by the red arrow in Figure 25f. Subsequently, the same experiment was applied for samples from retting stage R10. Figure 26 visually shows the results obtained from R10.

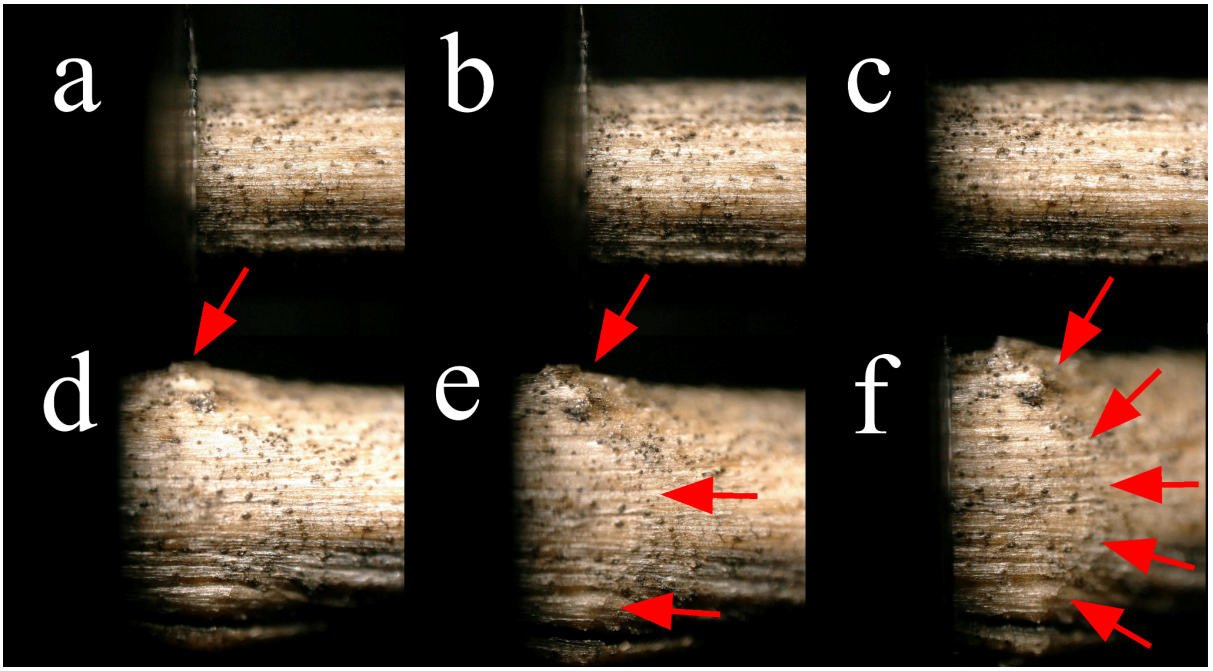

Figure 26. shows the microscopic images of the bending experiment resulting from retting stage R10. (a) initial state deflection at 0 cm, (b) deflection at 1 cm, (c) deflection at 2 cm, (d) deflection at 3 cm, (e) deflection at 4 cm, and (f) deflection at 5 cm.

Figure 26a shows the initial state of the sample with no induced deflection. When the sample is gradually deflected by 1 cm, when the bender height decreases to 22.7 cm as shown in Figures 26b and 21,7 cm as shown in Figure 26c, no significant damage is observed. However, when the deflection reaches 3 cm, damage becomes apparent, as indicated by the red arrow in Figure 26d. With further deflection, the damage becomes increasingly apparent and severe, as shown in Figures 26e and 26f. We continued to test flax stem samples from R15. Figure 27 shows the results of the bending experiment carried out on flax stalk samples obtained at the optimum retting stage R15.

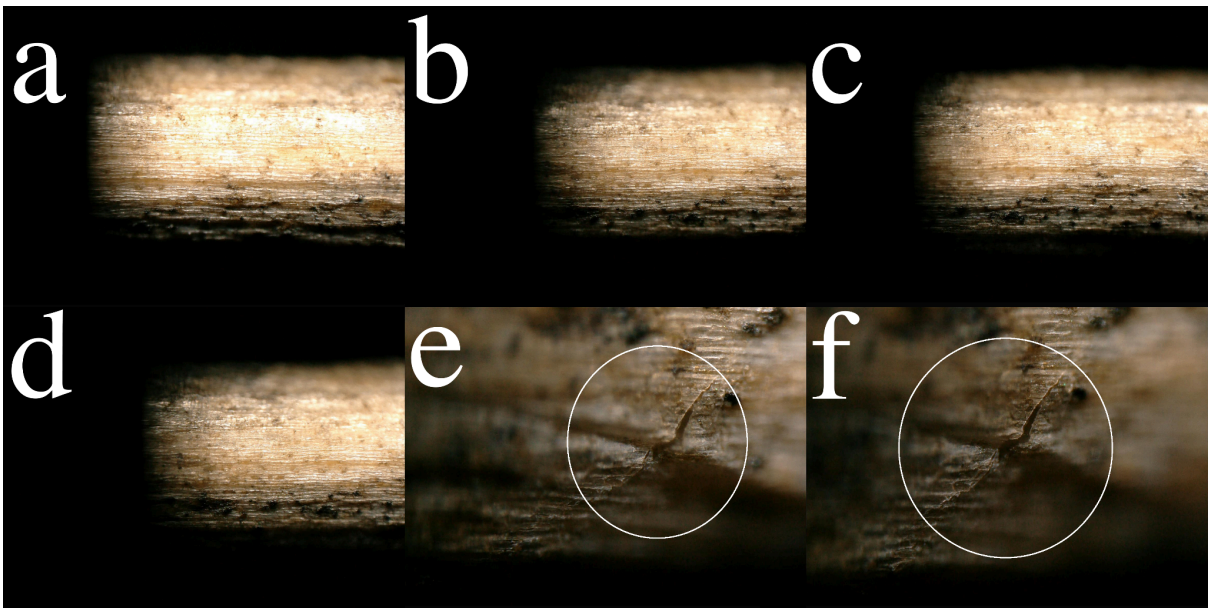

Figure 27. Shows microscopic images of the optimum retting stage. (a) initial state deflection at 0 cm, (b) deflection at 1 cm, (c) deflection at 2 cm, (d) deflection at 3 cm, (e) deflection at 4 cm, (f) deflection at 5 cm.

Figure 27a shows the initial state of the flax stem sample with no induced deflection. After a gradual deflection of 1 cm, as shown in Figures 27b, 27c and 27d, no visible damage is observed. However, after 4 cm and 5 cm of deflection, damage becomes apparent as shown in Figures 27e and 27f. In particular, at this stage, breaks and damage are visible in the outer tissue, as indicated by the white circles. This is in contrast to the previous stages where such damage was not present or visible. This suggests that bending not only affects the woody tissues of the flax stalk, but also has an effect on the external tissues.

In order to gain further insight into the condition of the outer tissue after the optimum retting stage, we carried out the same experiment on samples taken from R20, which was one month after optimum retting. Figure 28 shows the results from retting stage R20.

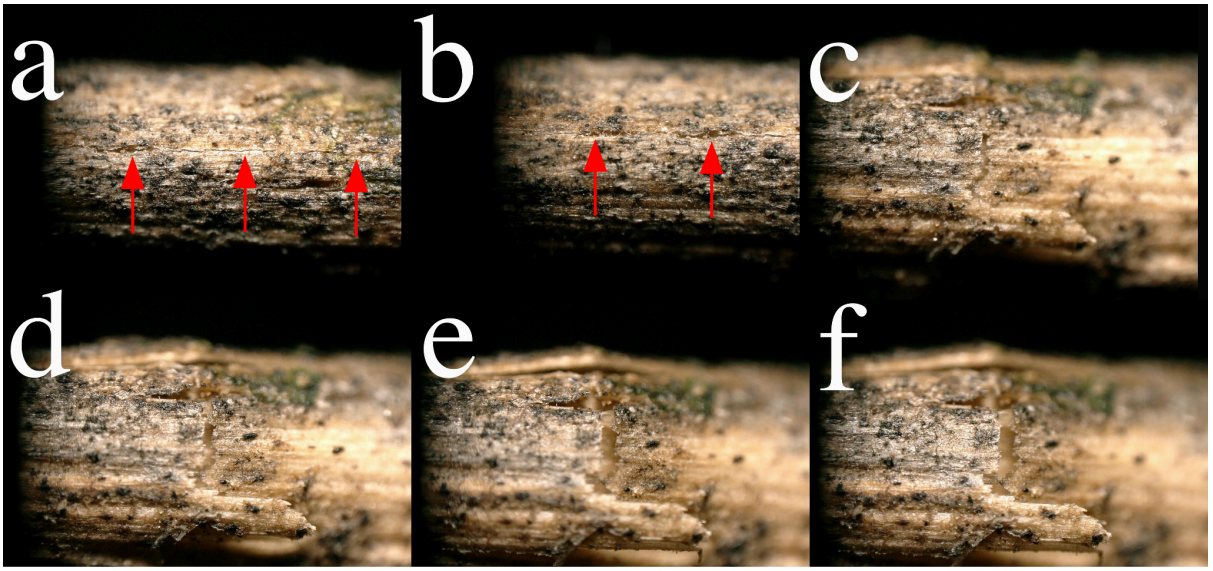

Figure 28. shows the microscopic images from the bending of retting stage R20. (a) initial state deflection 0 cm, (b) deflection at 1 cm, (c) deflection at 2 cm, (d) deflection at 3 cm, (e) deflection at 4 cm, (f) deflection at 5 cm.

Figure 28a shows the initial condition of the sample prior to any bending. In this initial state, prior to any bending, there were already deformations and damage in the outer tissue of the flax stalks noted by the red arrow in Figure 28a. As the deflection is gradually increased by 1 cm, the pre-existing break in the outer tissue widens, as indicated by the red arrows in Figure 28b. With further increases in deflection, the breaks or damage in the outer tissue become more pronounced and extend into the inner tissue, known as the wood of the stalk. This propagation of fracture and damage is clearly shown in Figures 28c, 28d, 28e and 28f.

The presence of the breaks in the external tissue without any mechanical behaviour, could indicate a real influence of the retting on the flax stalks.

Discussion of this section

This experiment provides valuable visual insights into the behaviour of flax stem samples when subjected to bending and having stress concentration and mechanical failure at the base of the bending stem.

A notable observation is that the effect of retting on flax stems is clearly visible during bending, primarily through the breaks observed in the outer tissue as shown in the microscopic images. Prior to the optimum retting point, breaks were only visible in the woody inner tissue and no damage or breaks were observed in the exterior tissue-see Figures 25 and 26. However, after the flax stalk samples were bent at the optimum retting stage, breaks and deformations in the outer tissue became apparent. It is worth noting that the breaks in the external tissue at R20 (4 weeks after optimum retting point) occurred at very low bending. This suggests that these breaks perhaps already present in the outer tissue are a result of the retting process itself.

Furthermore, the microscopic images and results obtained from this experiment are consistent with the results of the previous bending experiments carried out on flax stems samples to determine the flexural modulus and flexural strength. As shown in Figure 20, the breaking stress of the flax stems obtained from the macroscopic image analysis of the bending experiment showed a consistent average value during the retting period, from the start of retting until the optimum retting period. After the optimum retting point was reached, the flexural stress began to decrease. A similar trend was observed for the average flexural modulus as a function of retting time, where the average flexural modulus remained constant from the beginning of the retting process until the optimum retting time, after which it began to decrease.

This suggests that there is a noticeable trend in external tissue breakage as an influence of retting in flax. Perhaps this is not surprising as the point of artisanal retting is to facilitate the extraction of the flax fibres from the exterior tissue. This result has prompted further experimentation, including compression experiments on flax stems samples, to gain a deeper understanding of the effect of retting on the outer tissue and to determine if any trends emerge regarding the influence of retting on the internal tissues, and ultimately to determine which tissues are most affected by the retting process.

Determination of the flexural strength of flax stems with and without the outer tissue as a function of retting

The results of the previous experiments suggest that a trend showing the influence of retting on the flexural modulus and flexural strength of flax composite, especially, on the outer tissue containing the fibres, is observed by bending experiment. Therefore to prove this, 42 flax stems samples collected from different retting stages were tested in real-time before and after peeling the outer tissue.

The sample preparation, including the method and designed tool, as well as the measurement protocol, including the experimental measurements, the 6 diameter measurements method and modelling, used in the section 1 were applied in this experiment. However, each individual sample was tested 2 times. The second time includes real-time testing of the same sample after accurate manual peeling of the outer tissue (resulting in a xylem free of the outer tissue). This generates 84 measurements of the flexural modulus from 42 samples. The results are plotted in Figure 29.

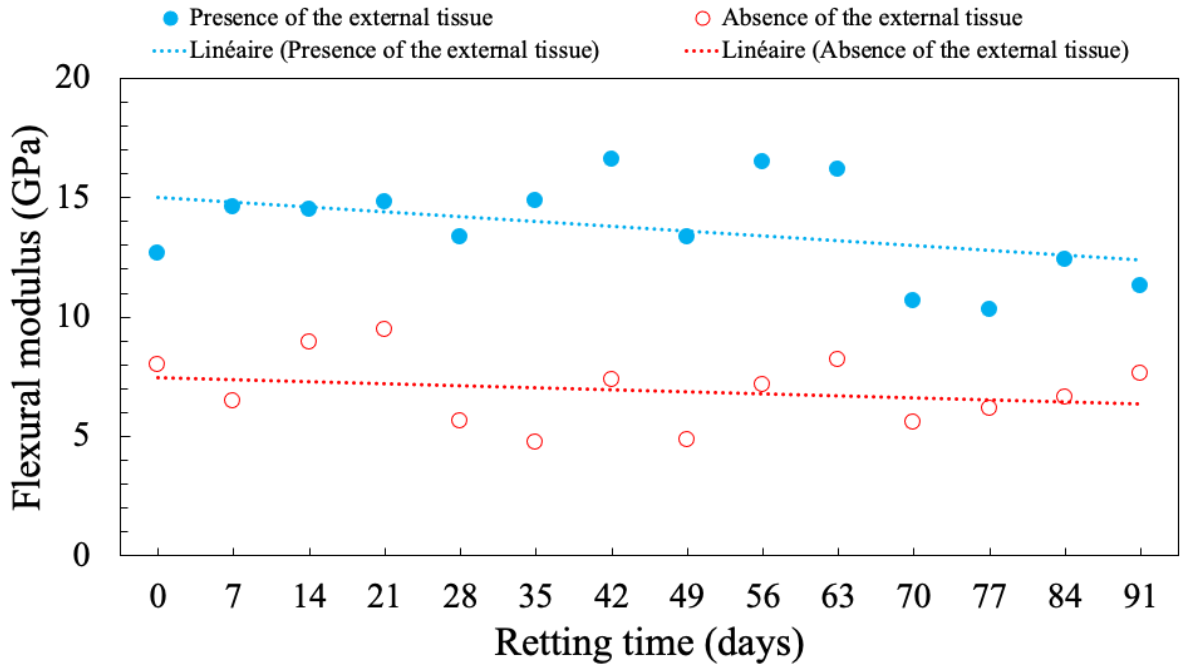

Figure 29. A plot of the evolution of the experimentally-obtained average flexural modulus of flax stems with and without the outer tissue as a function of retting time. This plot is based on 42 tested flax stem samples . The results were obtained in real-time during the whole retting period of 2022.

The plot in Figure 29 shows an interesting trend: the average flexural modulus of the tested samples before removing the external tissue presented by the filled circles, derived from the individual retting stages, remains relatively constant throughout the retting period until it reaches the optimal-retting point at 56 retting days. After this stage, the flexural modulus begins to decrease. The average flexural modulus with the outer tissue measures 13.7±2.1 GPa. The average flexural modulus and the trend observed in this experiment exhibits the same trend observed from the measurement of the flexural modulus determined from the previous bending experiment. However, the average flexural modulus of the tested samples after removing the external tissue presented by the open circles, derived from the individual retting stages, is less than the actual modulus of the stem composite and remains relatively constant over-all the retting period. The average flexural modulus with the outer tissue measures 6.91±1.45 GPa. These results agree with the results (Réquilé et al., 2018). This

indicates that the presence of the fibres in the external tissue plays an important role in the mechanical property of the stem–especially at different stages of retting.

Such results not only prove the importance of the presence of the fibres on the mechanical properties of the flax stem, but also provide a proof on the influence of retting on the stem's mechanical properties. The constant modulus value of the xylem over the retting period indicates no effect of retting on the internal tissue. However, as retting advanced the flexural modulus decreased (period between 56 to 91 days-over retting phase). This decrease indicates that the enzymatic activity of microorganisms resulting from the retting process influences the middle lamella, resulting in separation of the fibres and fibre bundles as discussed before in the discussion part of the bending experiment.

Despite there being an observed correlation between stem bending and the advancement of retting, we conclude that the observations make a tool reliant on bending hard to envisage as the optimal retting phase may be missed by the user. Therefore other complementary macro-mechanical experimentation is required. In the following two chapters we will perform compression and torsion measurements on flax stems as a function of retting. We will see that the evaluation of the flexural modulus in this chapter will be very useful in interpreting the results of the following chapters.

Conclusions

Flax stems can be characterised by bending experiments. This is one of the manual mechanical tests that an artisan (farmer) conducts 'in-the-field' when monitoring the advancement of dew retting of harvested flax stems. The artisan judges qualitative information by hand movement and eye to assess the advancement of the retting of the flax stems. In this chapter, we have attempted to quantify this artisanal bending process in the lab with a view to characterising the flexural modulus and flexural strength of the flax stems as a function of retting.

To do this quantitatively, we have designed a setup which uses the flax stem as a macroscopic cantilever. The experiment enables the controlled, gradual bending (deflection) of a flax stem by applying a precise force to the end of the stem. This force is produced using a set of precise masses. By considering the flax stem to be equivalent to a long, straight homogenous pipe, analytical modelling can be employed to compute the flexural modulus and the flexural strength of the flax stem as a function of retting period. This supposition of the modelling enables all flax stems in the study to be compared with each other: both stems from the same retting stage and stems from retting stage to retting stage. This approach has allowed the quantitative determination of the influence of retting on the flexural modulus and the flexural strength of flax stems.

It is clearly observed that retting has an effect on the both flexural modulus and the flexural strength of flax stems. Both parameters remain constant during the under retting phase and fall during and after the optimal retting point (as defined by the VRF company). This indicates that the influence of retting can be clearly seen in micromechanical experiments such as bending.

The bending tests provided valuable insights. We were able to quantify the daily changes in both average flexural modulus and flexural strength during the 3 months of the retting and

over-retting period. The results show that during the under-retting period the flexural modulus and strength of the stems showed a negligible change. However, after the optimal-retting time and during the over-retting period, there was a significant and large decrease in both flexural modulus and flexural strength of the flex stems. The trend resulting from this experiment shows that the influence of retting is clear in bending. Interestingly, experiments on flax stems in different stages of retting that had the external tissue deliberately removed showed that the flexural modulus and strength of the inner xylem (the 'wood' of the stem) does not change. This result strengthens the hypothesis that it is the retting-induced change in the external tissue of the stem that is causing the mechanical properties of the stems to change.

Finally, a total of 222 flax stems were measured in this chapter. As an example of the workload in this chapter, in the absence of reliable image analysis, the measurement of the external and internal diameters of the cut stem cross sections alone required 17364 manual measurements!

References

Ampofo, J., Ofori, E., & Ibrahim, A. A. (2013). Mechanical properties of plantain pseudostem and implications for susceptibility to lodging. *Journal of Agriculture and Environment for International Development*, *107*(1). https://doi.org/10.12895/jaeid.20131.95

Caliaro, M., Schmich, F., Speck, T., & Speck, O. (2013). Effect of drought stress on bending stiffness in petioles of *Caladium bicolor* (Araceae). *American Journal of Botany*, *100*(11), 2141–2148. https://doi.org/10.3732/ajb.1300158

Gibson, L. J. (2012). The hierarchical structure and mechanics of plant materials. *Journal of The Royal Society Interface*, *9*(76), 2749–2766. https://doi.org/10.1098/rsif.2012.0341

Goudenhooft, C., Alméras, T., Bourmaud, A., & Baley, C. (2019). The remarkable slenderness of flax plant and pertinent factors affecting its mechanical stability. *Biosystems Engineering*, *178*, 1–8. https://doi.org/10.1016/j.biosystemseng.2018.10.015

Green, D. W., Gorman, T. M., Evans, J. W., & Murphy, J. F. (2006). Mechanical Grading of Round Timber Beams. *Journal of Materials in Civil Engineering*, *18*(1), 1–10. https://doi.org/10.1061/(ASCE)0899-1561(2006)18:1(1)

Henry, H. A. L., & Thomas, S. C. (2002). Interactive effects of lateral shade and wind on stem allometry, biomass allocation, and mechanical stability in *Abutilon theophrasti* (Malvaceae). *American Journal of Botany*, *89*(10), 1609–1615. https://doi.org/10.3732/ajb.89.10.1609

Lemloh, M.-L., Pohl, A., Weber, E., Zeiger, M., Bauer, P., Weiss, I. M., & Schneider, A. S. (2014). Structure-property relationships in mechanically stimulated Sorghum bicolor stalks. *Bioinspired Materials*, *1*(1). https://doi.org/10.2478/bima-2014-0001

Lim, J.-A., Yeo, H.-M., & Lee, J.-J. (2011). Study on the Evaluation of Performance for Pitch Pine Round Timbers as Safety Barrier Beam Members. *Journal of the Korean Wood Science and Technology*, *39*(5), 390–397. https://doi.org/10.5658/WOOD.2011.39.5.390

Luis Christoforo, A., Antonio Rocco Lahr, F., Aparecida Martines Morales, E., Luiz Zangiácomo, A., & Hallak Panzera, T. (2012). Influence of Displacements on Calculus of the Longitudinal Modulus of Elasticity of *Pinus Caribaea* Structural Round Timber Beams. *International Journal of Agriculture and Forestry*, *2*(4), 157–160. https://doi.org/10.5923/j.ijaf.20120204.04

Réquilé, S., Goudenhooft, C., Bourmaud, A., Le Duigou, A., & Baley, C. (2018). Exploring the link between flexural behaviour of hemp and flax stems and fibre stiffness. *Industrial Crops and Products*, *113*, 179–186. https://doi.org/10.1016/j.indcrop.2018.01.035

Robertson, D. J., Smith, S. L., & Cook, D. D. (2015). On measuring the bending strength of septate grass stems. *American Journal of Botany*, *102*(1), 5–11. https://doi.org/10.3732/ajb.1400183

Shah, D. U., Reynolds, T. P., & Ramage, M. H. (2017). The strength of plants: Theory and experimental methods to measure the mechanical properties of stems. *Journal of Experimental Botany*, *68*(16), 4497–4516. https://doi.org/10.1093/jxb/erx245

Slater, D., & Ennos, A. R. (2013). Determining the mechanical properties of hazel forks by testing their component parts. *Trees*, *27*(6), 1515–1524. https://doi.org/10.1007/s00468-013-0898-5

Timoshenko, S. (1986). *Strength of materials* (3rd Ed.). CBS Publishers & Distributors.

Timoshenko, S. (2010). *Theory of elasticity* (3rd Ed.). McGraw Hill Education.

Chapter 4

Macro-mechanical testing: Effect of retting on stem compression

Introduction

The two principal conclusions from chapter 3 are (i) the flexural modulus and strength of retting flax stems evolve as retting time proceeds—this is especially true during and after optimal retting point and (ii) the flexural modulus and strength of retting flax stems without their exterior tissue does not significantly evolve during retting. The measurements therefore suggest that the degradation of the exterior tissue (due to retting) is responsible for these observations. Therefore, retting can be ‘seen’ in mechanical testing of flax stalks—opening the way to the possibility of a mechanical sensor.

In order to support these conclusions, in this chapter we have performed experiments to crush flax stems using controlled mechanical compression. In principle, unlike the bending experiments, the role of the exterior tissue should be less apparent. If true, this would strengthen our arguments concerning the mechanisms responsible for the evolution of the flexural modulus and strength during retting.

The mechanical behaviour and properties of plants have been studied for some time now. Specifically, the crushing of plant stems and branches has been performed by many groups over the years to reveal various information about plant science. For example, In their study, Spatz et al. (Spatz et al., 1997) performed a transverse compression test on 2-3.5 cm long segments of Arundo donax. The aim was to assess the variation in stiffness across the radial direction of the tissue. When dealing with thick-walled rings, where shear strains have to be taken into account, the analysis becomes much more complicated and requires numerical treatment. The structural Young's modulus in the tangential direction was then determined by data simulation, using a specific model to interpret the experimental results. In his research, Niklas (Niklas, 1998) investigated how hollow, septate stems fail under mechanical stress. He did this by observing how segments of these stems responded to axial compressive loads strong enough to cause permanent deformation, often referred to as 'critical' compressive loads. The aim was to provide a practical basis for assessing the results of computer simulations designed to reproduce the mechanical behaviour of nodes and internodes within these stems. In their study, Write et al. (Wright et al., 2005) used a compression-based approach. They collected mature biomass that had been harvested and subjected it to testing. The aim was to determine the modulus of elasticity and ultimate strength for the internodal stems of different wheat, barley and corn varieties. The primary objective was twofold: firstly, to create a comprehensive database of biomechanical properties for each variety, and secondly, to investigate whether these properties could distinguish and differentiate individual varieties from each other. The results of this research have improved the understanding of how the biomechanical properties of cellulosic feedstocks are influenced by harvesting and post-harvest handling practices, as well as the molecular biology of the plants. Frese and Blaß (Frese & Blaß, 2014) study had two main aims. Firstly, they wanted to provide a basic understanding of how to better calculate the properties of naturally growing logs. Secondly, they wanted to introduce a modular bolting method. To achieve this, they carried out various tests, including compression tests on natural logs, tests to measure the force required to pull screws out of logs, and tests on screw connections. Using the data from these experiments, they created models to predict compressive strength and screw pull-out resistance. These findings have the potential to expand the possibilities for designing timber structures using naturally grown logs. However, in terms of flax stems, and especially in terms of the evolution of mechanical properties as a

function of retting, published work is null, the literature survey shows that there has not been any previous work in this context.

In this chapter, the following will be presented. This chapter focuses on investigating how retting affects the mechanical compression properties of flax stalks in real-time retting. We achieve this by performing basic macro-mechanical tests on flax stalks taken from the field. By applying mechanical models to these flax stalks, we can calculate their mechanical properties, in particular the flexural modulus and breaking stress. Interpreting the trends observed in flexural modulus and breaking stress as a function of retting time provides valuable insights into how retting affects the mechanical properties of flax stalks in real time. This tells us something about the advancement of the retting. It is important to note that this experimental study is unique and, as far as we know, has not been done before.

Sample preparation, tool design and measurement protocol

Sample preparation

In order to carry out the compression experiments on flax stems a tool was conceived, designed, and built for these purposes. The compression tool (basically a press with a controlled force/pressure) was designed to accommodate 1 cm long flax stems. These flax stems samples were prepared according to the techniques presented in Chapter 3. However, special care was used to ensure a very clean cut that produces a good image on the optical microscope of the cross section of the stems.This approach ensures the reliability and accuracy of the experimental results and allows a comprehensive investigation of the mechanical behaviour of the flax material under compression. It also allows the combination of data from both bending and crushing tests, providing valuable insights and correlations that further enhance the overall analysis of the flax material. The tool applies a force to a 2mm length of the sample, at the end of the sample. These 1 cm flax samples were obtained by cutting them from the 1 cm flax segments of the 9 cm stalks originally used for the bending experiment. Using the same flax samples for both bending and compression experiments has several advantages, including consistent material properties, controlled variables, reduced experimental error, and the ability to directly compare results under different loading conditions. Figure 1 shows the sample preparation for the segments used for the compression test.

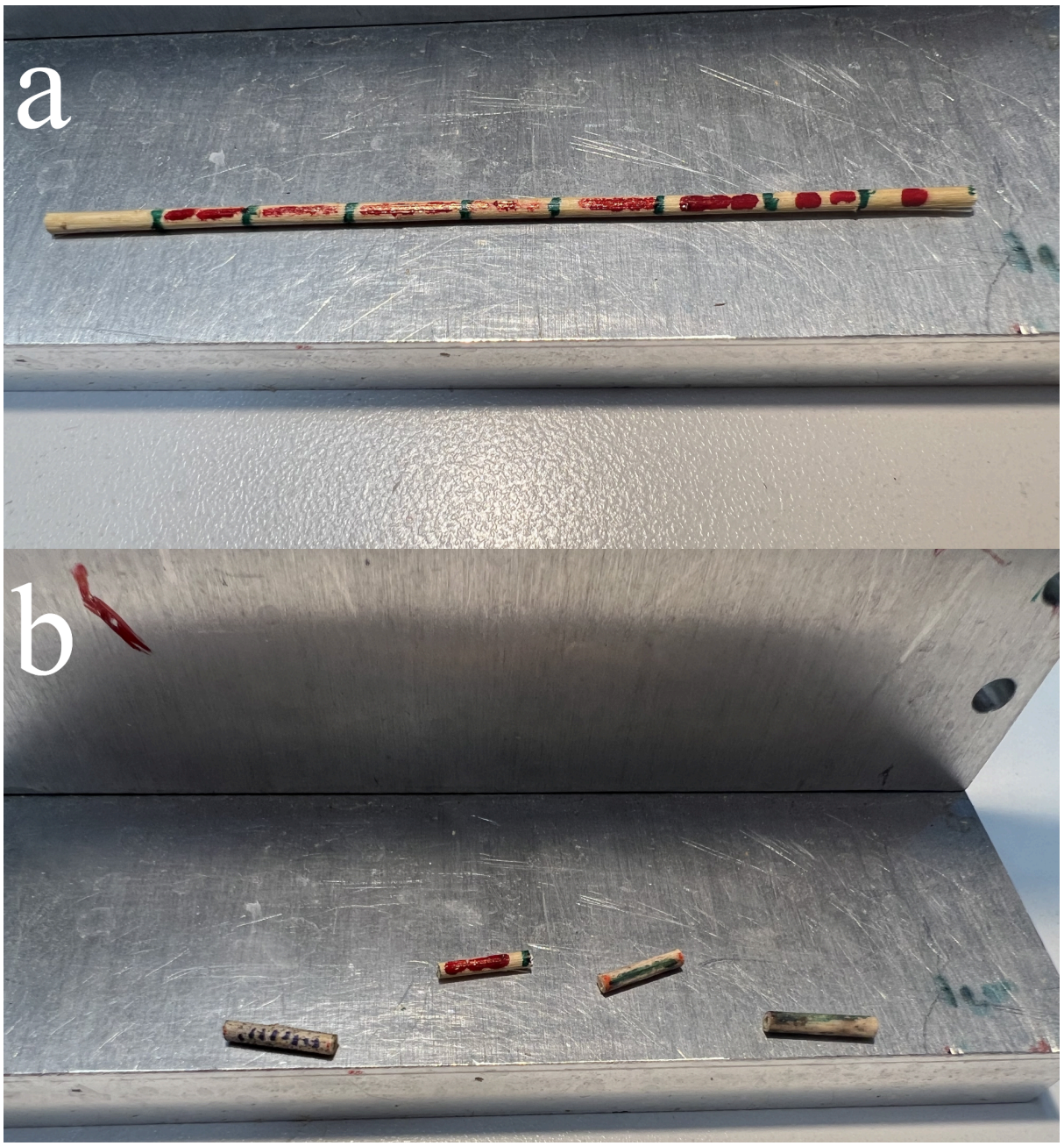

Figure 1. Sample preparation of the flax stalks segment samples used in the compression experiment. (a) Marking of 1 cm flax segment sample. (b) Cutting sample segments of 1 cm in length.

Tool design and measurement protocol

The measuring protocol utilised in the compression test involved incrementally applying weight onto the flax stem sample to induce a compressive force. The experiment was carried out with the aid of a digital optical microscope to capture accurate and precise images of the sample's deformation and displacement.

As previously stated, the sample utilised for the compression experiment comprised a 1 cm long stem sample cut from a larger 9 cm bending sample. The present experiment utilised over 180 flax stem samples (1 cm long) , with more than 9 samples dedicated to each retting stage. As before, these samples were also classified into three size categories of diameter, namely large (2-3 mm), medium (1.5-2), and small (1-1.5 mm). Figure 2 shows a schematic representation of the principle of the designed compression experiment.

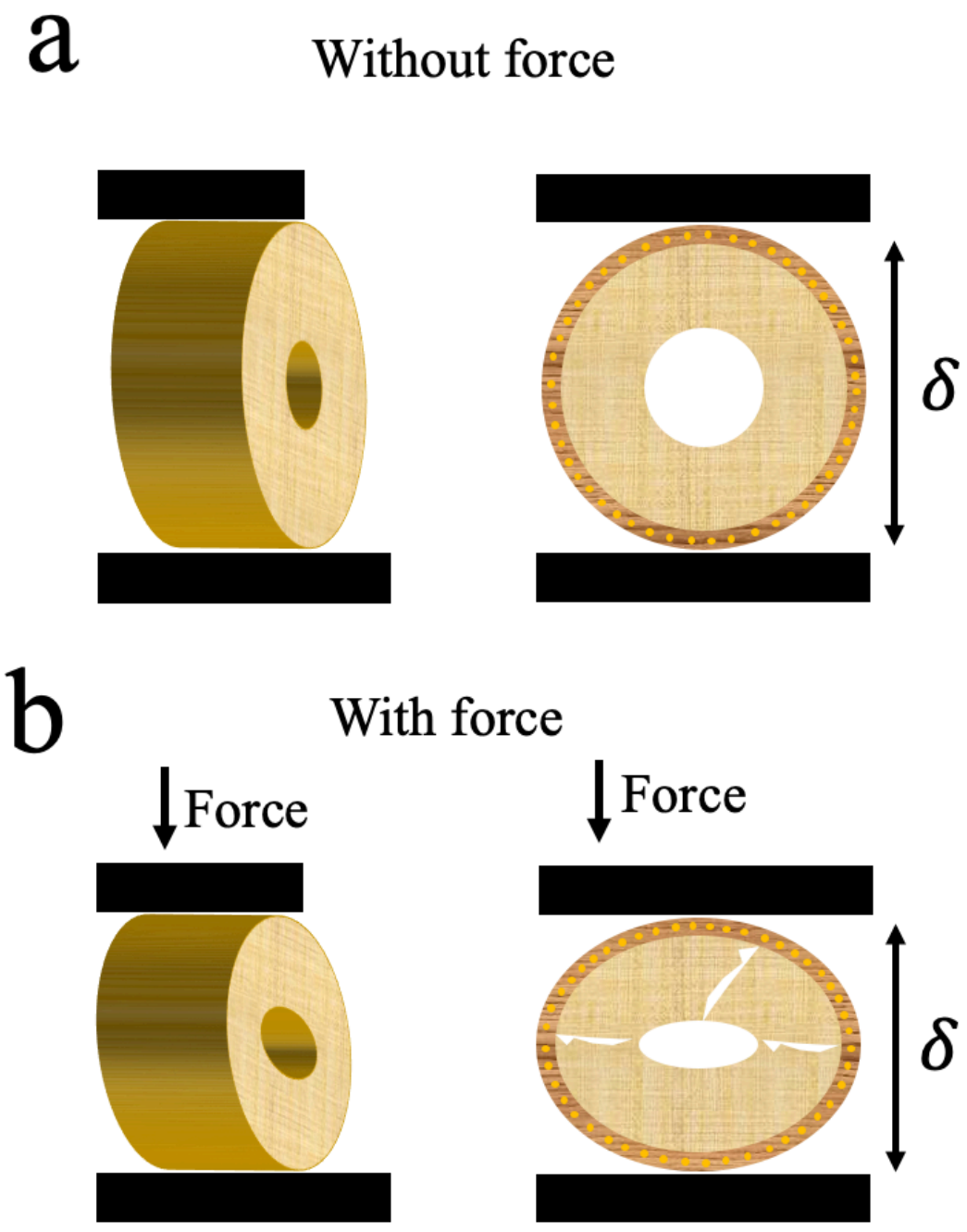

Figure 2. Schematic illustration of the basic principle of the compression experiments on flax stems in different stages of retting. (a) Without and (b) with a compressive force applied to the flax stem. The stem cross section was observed using a digital optical microscope as a function of retting stage and applied force.

A specially designed tool was made and employed for the compression experiment, which consisted of a metallic base plate that provided support for the flax stem sample and a plastic support equipped with a 2 mm wide plastic rim section to induce the compression on the stem, thus the compressed region of this sample was limited to a 2 mm portion. The plastic portion was chosen to be square in shape, allowing for the application of weight to be uniformly distributed and efficiently transferred onto the flax stem sample during the compression test.

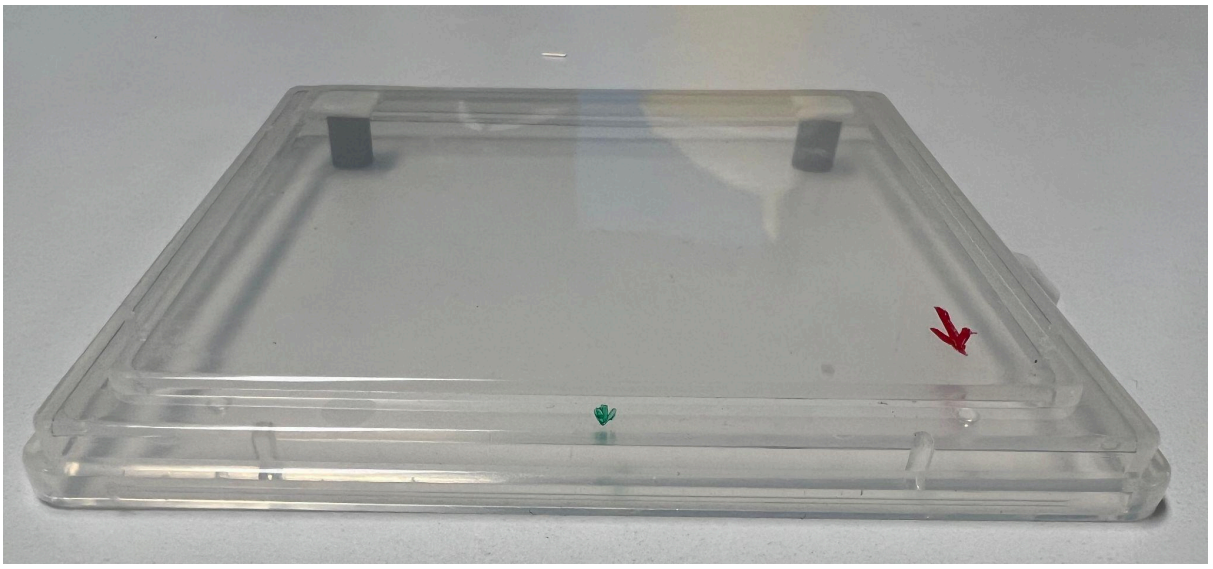

Figure 3. The simple compression tool used for the flax stem compression experiments. The tool enables a 2 mm length of flax stem to be compressed.

The compression tool shown in Figure 3 was securely positioned onto the support of the digital optical microscope, and subsequently, the microscope was adjusted to a 90° tilt to facilitate the accurate recording of the compressive movement. This arrangement enabled the experimental setup to capture high-resolution images of the flax stem sample as it underwent deformation and displacement during the compression test. Figure 4 shows the setup used for the compression tes as well as the tilted microscope.

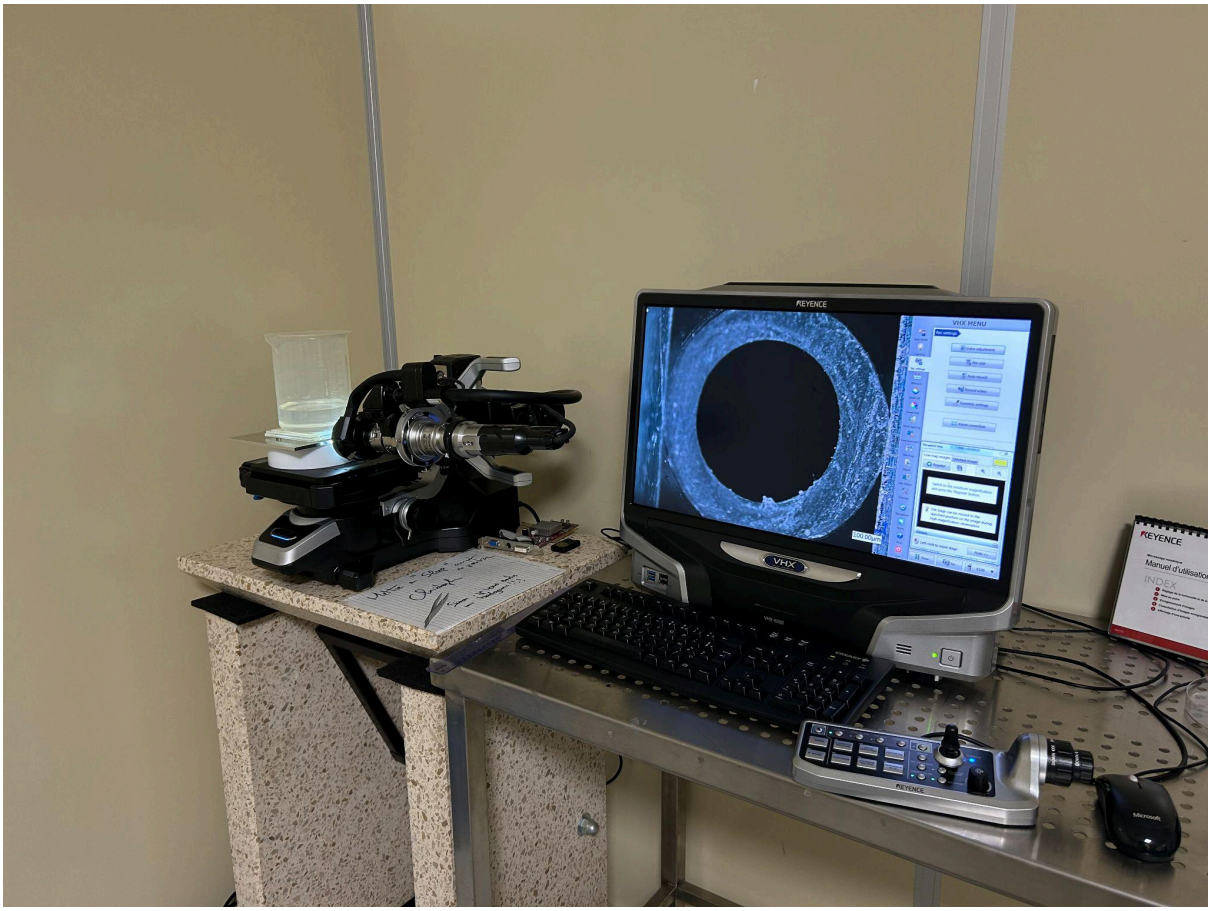

Figure 4. The experimental setup used for the compression experiments on the flax stems. A digital optical microscope (Keyence, france) is used to record the deformation of the flax stem cross sections during compression. The force for compression is carefully controlled using weight $F = mg$ (water poured into a container on top of the press). Although a rudimentary experiment, the results proved to be very meaningful.

The compression process required the application of weight/force to the flax stem sample. However, the use of conventional metal weights presented several challenges, including the potential for damage to the microscope and inaccuracies due to errors introduced when lifting and replacing the weights. The process of exchanging weights for heavier ones often resulted in sample relaxation and errors in the compression measurement. To overcome these issues, we opted to utilise water as a source of weight. The use of water provided a comfortable and accurate solution, as it allowed us to apply weight without the need for weight exchange, thus minimising measurement errors and potential damage to the experimental setup.

In the context of using water as a source of weight, it should be noted that the density of pure water is approximately 1g/ml, thereby allowing for a direct conversion of mass to volume. This resulted in the mass being equal to the volume, converted to kg. Subsequently, the force was calculated by multiplying the mass with gravity $F = mg$, with the force being expressed in newtons.

To facilitate the accurate application of weight, several beakers of varying capacities were utilised, as depicted in Figure 5. First, the weight of the beaker and substrate employed for compression was measured using sensitive and accurate balances, with the values taken into consideration during the load inductionLarge beakers with a capacity exceeding 1000 ml were placed on the plastic substrate to induce the compressive force. Conversely, small beakers with a capacity of 100 ml were employed to gradually add or transfer 100 ml of water to the larger beakers. This approach enabled us to ensure the systematic addition of precise masses of 100 mg to the plastic substrate. Figure 5 shows the methodology for increasing the force in the stem compression tool.

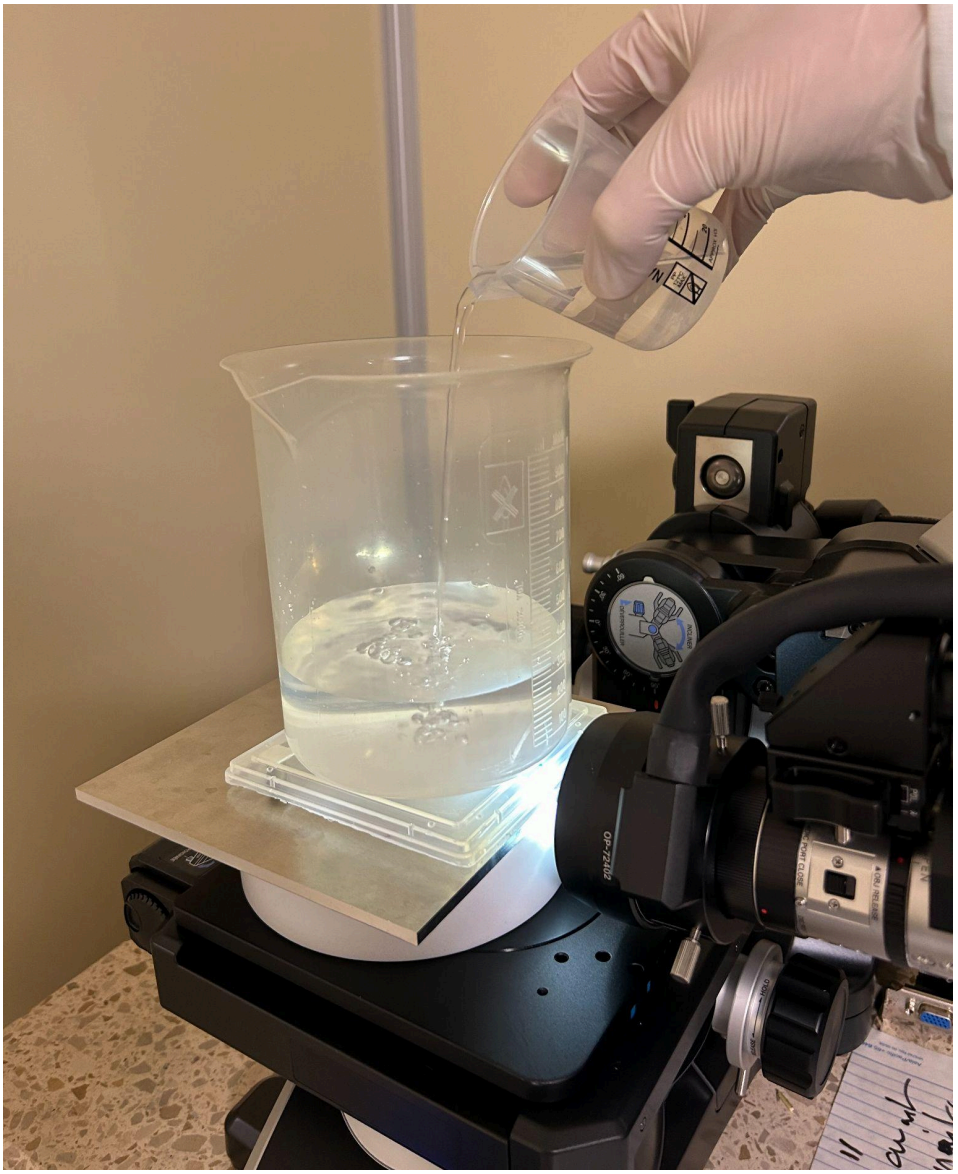

Figure 5. Water being carefully added in a controlled way to increase the force on the stem compression tool.

To document the compression of the sample at each weight increment, digital optical microscope images were taken and recorded for each compression force. The captured images were then analysed for the amount of compression achieved by the sample at each weight increment. Figure 6 shows an example of the captured images.

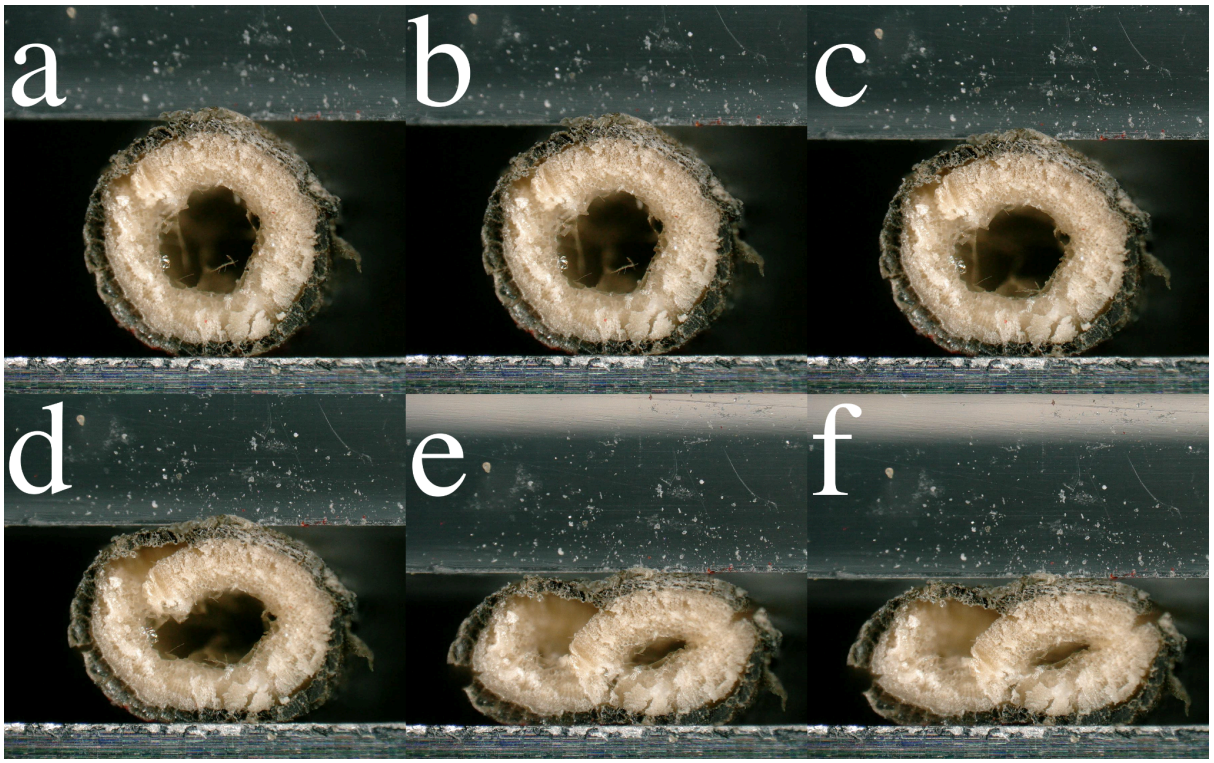

Figure 6. Digital optical microscope images of an example of a flax stem being compressed using the stem compression tool developed for the study. (a) to (f) increasing the compression force.

Three phases of compression are apparent in the data as we will discuss in the experimental results section below: (i) elastic linear deformation, (ii) inelastic nonlinear deformation, and (iii) breaking of the xylem 'wood' portion of the stem

Experimental results

The reasoning behind the measurement.

The bending experiments in the previous chapter (Chapter 3) suggested that both the flexural modulus and the flexural strength of flax stems are modified with progressing retting. As we have seen, this is especially true during and after optimal retting. We also hypothesised and demonstrated (using bending experiments on flax stems with the external tissue, including the fibres, removed) that the mechanical properties of the internal xylem 'wood' of the stem is not modified significantly by retting–even over retting. If this is indeed the case, then compression experiments should reveal no evolution in the mechanical properties of the stems. The reason for this is that under compression the exterior tissue (lamella and fibres)

plays little role in the mechanical structure strength, i.e; the compression behaviour should be dominated by the xylem. As with the bending experiments we have the problem of how we can compare stem samples with different diameters in the same retting stage and from retting stage to retting stage–this being the purpose of the study. As with the bending, this can be achieved by again considering the flax stem to be modelled by a homogenous pipe under compression. Fortunately, the literature contains analytical solutions based on a rigorous mechanical approach . Even though our stems are heterogenous complex structures we make the assumption of a uniform pipe to extract a compressive modulus for the whole sample. We also make the assumption that the compressive deformation is in the elastic part of the deformation–this is the linear part of the deformation. We also assume that the deflection is small compared to the stem diameter.

The compressive modulus E of a length of homogeneous pipe is given by the following formula (Timoshenko, 1986) (Timoshenko, 2010) (Rathnaweera et al., 2011) (DeRuntz & Hodge, 1963):

$$E = 24 \frac{F}{\delta} \frac{r_0^3}{Lt^3} \left(\frac{\pi}{8} - \frac{1}{\pi} \right) \quad (1)$$

F corresponds to the force, δ represents the displacement corresponding to the applied force, r_0 represents the average radius of the sample, L represents the compressed length of the sample, and t represents the thickness of the sample. As with the bending model, this equation enables a ‘normalisation’ of all sample dimensions.

To determine the physical property of compression modulus from the compression test, the model shows that the calculation depends on the relationship between load force and the displacement, as shown in the equation below.

Thus, accurately establishing this relationship between load and displacement is essential to extract the compressive modulus of the flax stems. Furthermore, the equation shows a significant proportionality between Young's modulus and the third root of the thickness, as well as an inverse proportionality with the third root of the average radius.

Specifically, the equation includes $r_0^3 = \left(\frac{d_0}{2}\right)^3$ and $t^3 = \left(\frac{d_0}{2} - \frac{d_i}{2}\right)^3$ This shows that The modulus is highly sensitive to the third power of the average radius and the third power of the difference between the outer and inner diameters. Thus, accurate and controlled measurement of these diameters is essential to avoid any errors that could cause significant variations in the calculated value of the modulus.

The ratio F/δ is obtained from analysis of the experimental results. This is the stiffness of the tube under compression.

Diameter measurement: 6 diameter method

In order to obtain an accurate modulus value from compression tests of flax stems, we have seen from above that it is essential to control the diameter and minimise the errors resulting from the diameter measurements. In this regard, we applied the same six diameter measurement methods used in the bending experiments presented in Chapter 3. This approach aimed to reduce errors and obtain accurate diameter measurements of the compressed section, which would ultimately lead to more accurate modulus values.

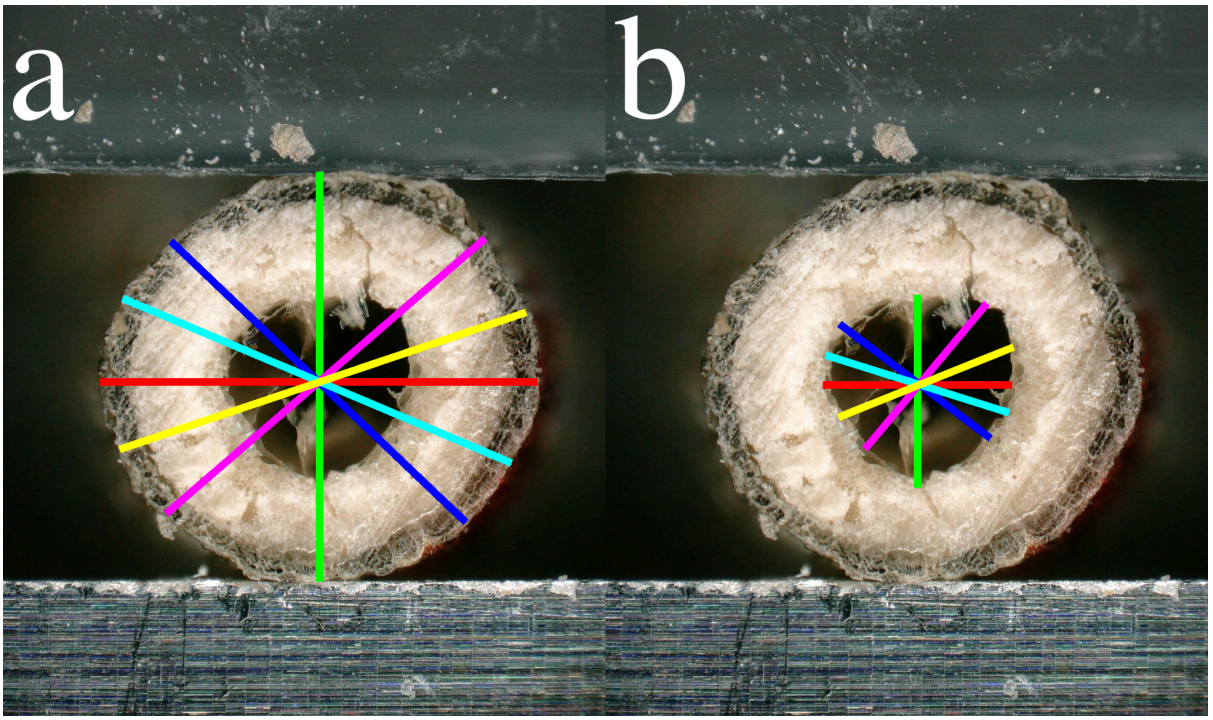

Figure 7. Shows the 6 diameter method used to extract the diameters. (a) shows the method to extract the outer diameter. (b) shows the method used to extract the inner diameter.

Six measurements of different angles were taken for both the internal and external diameters. The average internal and external diameters were calculated as an average of the six measurements for each diameter. An example of the results obtained for one stem section sample is summarised in the table below:

	Under-retted flax stem (R5-L-S2-P2)	
Diameter label	**Outer diameter d_o (um)**	**Inner diameter d_i (um)**
	S1	**S1**
D1	2222.9	888.8
D2	2305.5	871.4

D3	2271.4	833.6
D4	2239.7	851.0
D5	2341.4	794.1
D6	2301.6	889.9

Table 1. An example of the stem section diameter results obtained for one stem section sample (a large diameter, under-retted stem R5 in this case).

The average outer diameter d_o measured 2301.6±44.4 um and the average inner diameter d_i measured 889.9±36.9 um

Extraction of stem stiffness *k* from experimental measurements

Based on the model above, determining the relationship between force and displacement is a critical factor in calculating the modulus, where:

$$Force\ (F) = mg$$

where, m refers to the mass of the object being measured in kilograms, g is the gravity constant at the earth's surface in m/s.

Initially, At a force of $F = 0$, the flax stalk remained in its original resting position with no change in its dimensions. As weight (including the plastic substrate, graduated cups and water) were gradually added, displacement was observed in response to the increasing force applied. Three phases of deformation were observed in the experiments: (i) a linear elastic phase where the displacement was proportional to the force, (ii) a non-linear phase presumably where the stem is in plastic deformation, and (iii) an apparent failure phase where the xylem 'wood' was visibly broken. Figures 8, 9, and 10 below show an example of the three phases in a sample from under-retting stage R5.

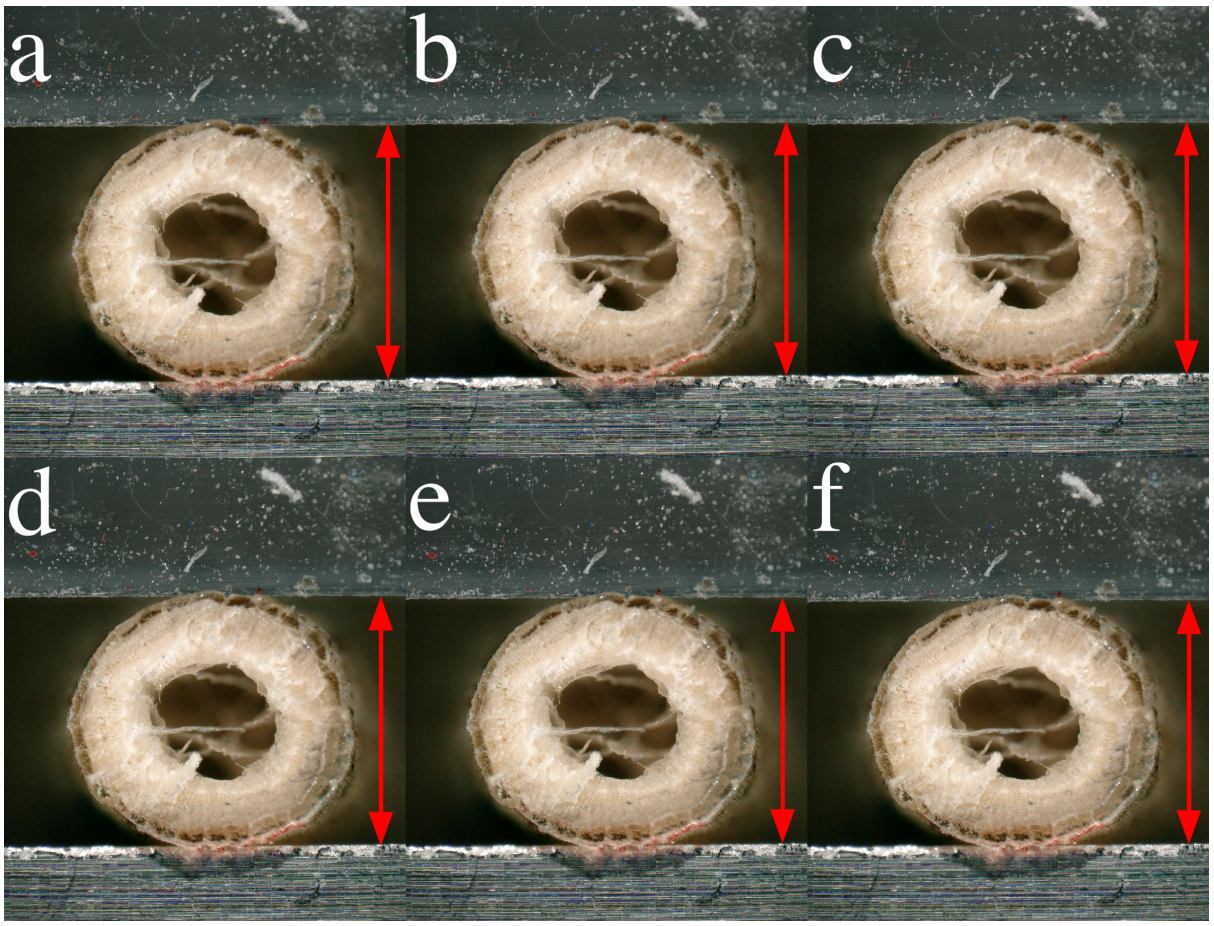

Figure 8. Digital optical microscope images of an example of an elastic linear phase deformation of flax stem being compressed using the stem compression tool developed for the study. The displacement is represented by the red arrow. (a) initially before compression $m = 0$. (b) compressive force $m = 500\,g$. (c) compressive force $m = 600\,g$. d) compressive force $m = 700\,g$. (e) compressive force $m = 800\,g$. (f) compressive force $m = 900\,g$.

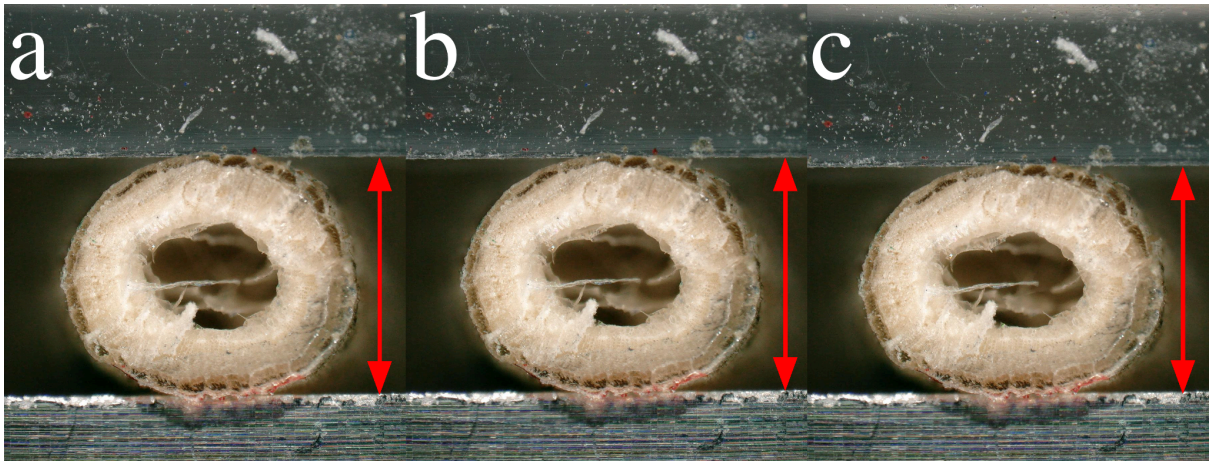

Figure 9. Digital optical microscope images of a **non-linear plastic phase deformation** of flax stem being compressed using the stem compression tool developed for the study. The

displacement is represented by the red arrow. (a) compressive force $m = 1100\ g$. (b) compressive force $m = 1200\ g$. (c) compressive force $m = 1300\ g$.

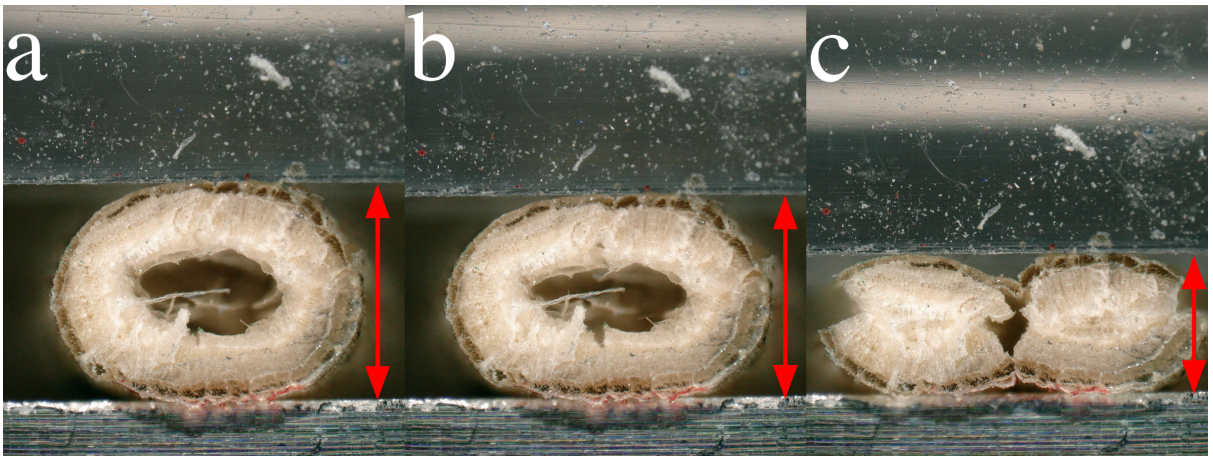

Figure 10. Digital optical microscope images of a **failure phase deformation** of flax stem being compressed using the stem compression tool developed for the study. The displacement is represented by the red arrow. (a) compressive force $m = 1400\ g$. (b) compressive force $m = 1500\ g$. (c) compressive force $m = 1500\ g$.

Image analysis can be used to determine the actual displacement that occurred after each increment of force. The displacement was measured in micrometres

The relationship between weight and displacement was established based on the graph plotted below, where the load value was plotted as a function of displacement.

Based on reference (1), the model used for lateral compression is only applicable in the elastic deflection regime of a pipe. In order to validate the model, it is necessary to establish the relationship between force and displacement F/δ in this regime. The elastic deflection regime can be obtained from the force-displacement curve, where the elastic limit can be identified as the point where the material behaviour transitions from elastic to plastic. This transition point is marked in the plot below.

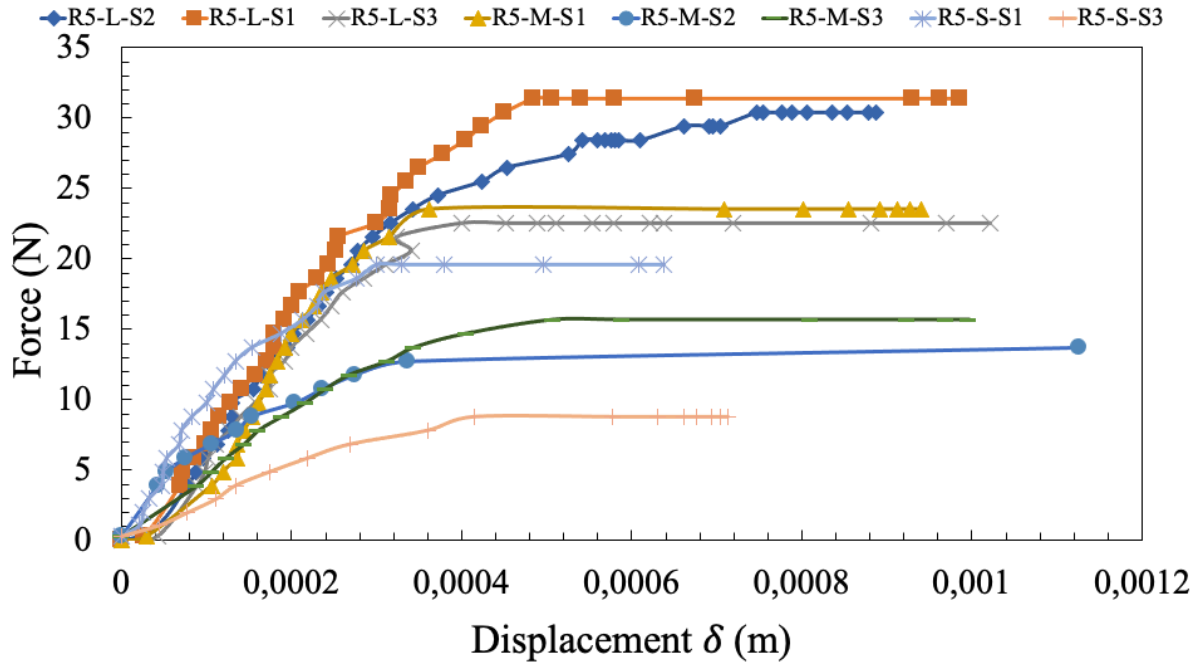

Figure 11. An example showing the plots between the load and the displacement for all the tested samples in an under retting stage (R5).

Therefore, once the elastic region has been identified, the relationship between force and displacement F/δ is established by determining the slope of the linear elastic displacement region, as shown in the plot below:

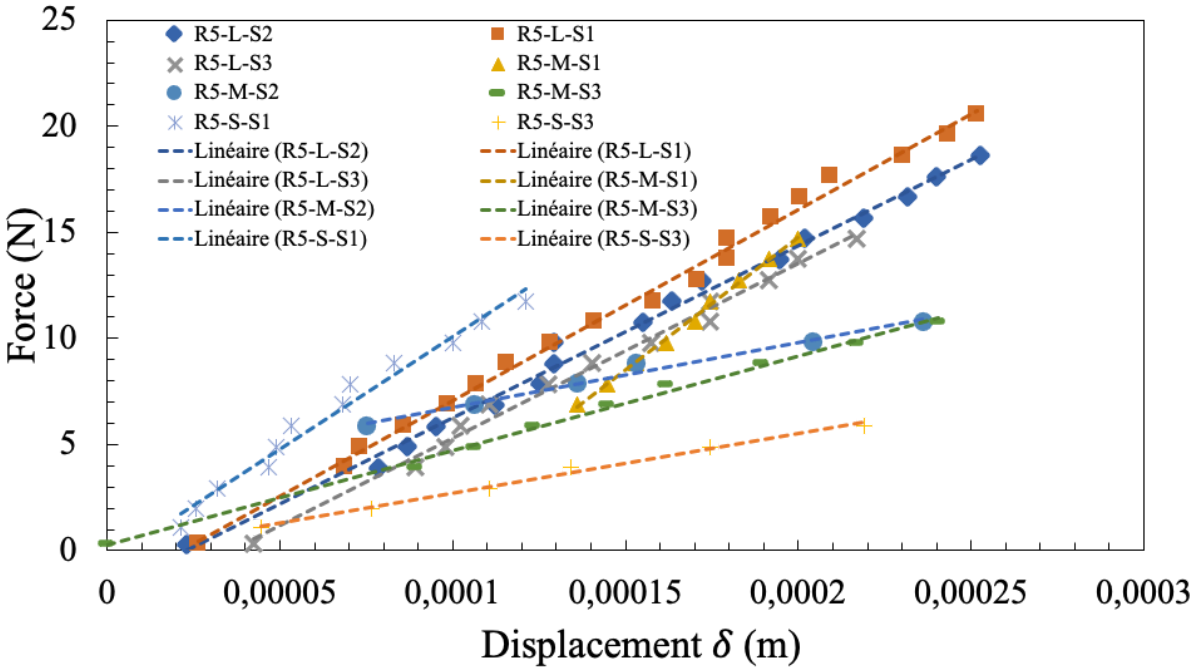

Figure 12. Shows an example of the elastic regime of all the tested samples from under retted stage (R5).

Table 2 below represents the value of the stiffness k, extracted from the plot in Figure 12.

Sample	Stiffness (k) (N/m)
R5-LS2	81182
R5-L-S1	90018
R5-L-S3	82225
R5-M-S1	125273
R5-M-S2	30292
R5-M-S3	44518
R5-S-S1	105665
R5-S-S3	28205

Table 2. Shows an example of the stiffness of the tested samples from under retting R5 stage.

Determination of the compressive modulus of flax stems as a function of retting

Figure 13 shows the experimentally-determined compression modulus of retted flax stems as a function of retting. These results were based on the compression measurement of 180 flax stem sections. The experiments were performed in real time during the 2022 retting period (6th July to 31st August and beyond to 1st October).

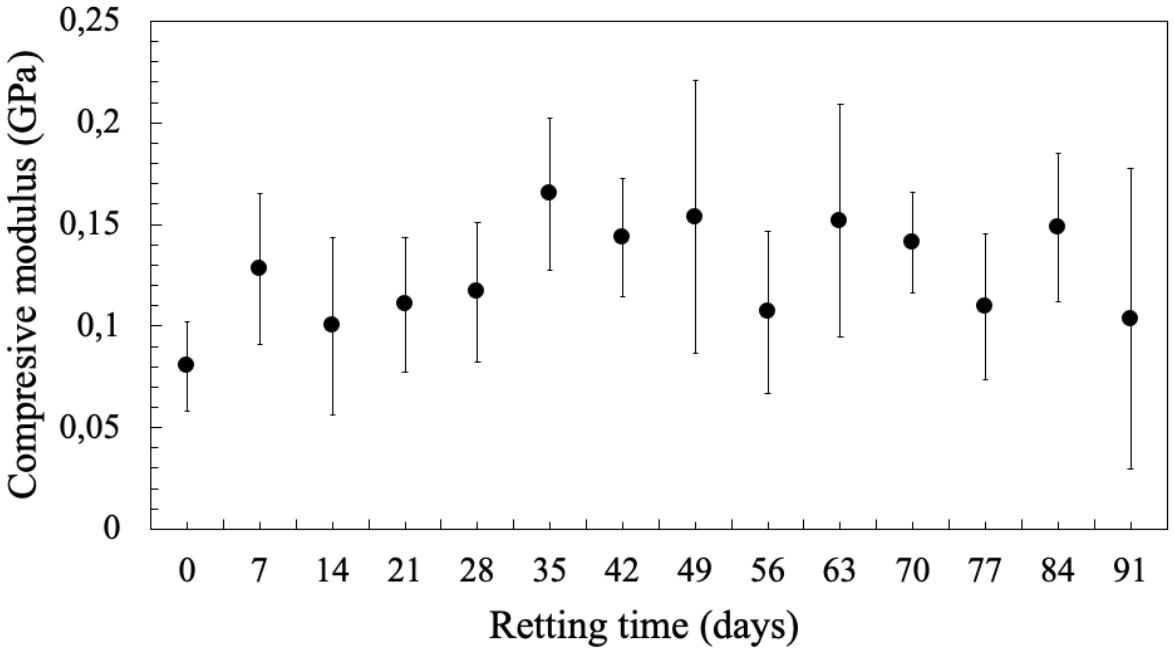

Figure 13. The experimentally-determined compression modulus of retted flax stems as a function of retting. These results are based on the compression of 180 flax stem sections. The results were obtained in real-time during the whole retting period of 2022 and beyond, i.e. 6th July to the 4rth of October 2022. The optimal retting time was 56 days, as defined by the company VRF.

Figure 13 shows an interesting trend of the relation between average compressive modulus and retting time. The optimum retting point, as determined by VRF, is marked on the graph (day 56). Prior to reaching this point (under-retting), the stems have a relatively constant compressive modulus. Once the optimum-retting phase is reached and beyond (over-retting), the measured flexural modulus remains constant. This trend can provide valuable information on the effect of retting on the mechanical properties of flax stalks. The average compressive modulus as a function of retting measured a value of 127.33±25.13 MPa.

Determination of the compressive strength of retted flax stems as a function of retting

Another important physical parameter that can be extracted from our measurements is the compressive strength. The compressive strength of a uniform homogenous tube under compression is given by the following relationship (Liu & Wang, 2019) (Yella Reddy & Reid, 1979) (Timoshenko, 1986) (Timoshenko, 2010):

$$\sigma_{cr} = 6\frac{r_0 F}{\pi l t^2} \quad (2)$$

Where r_0 is the mean radius of the pipe, F is the compressive force at the moment of failure, l is the length of the pipe being compressed, and t is the thickness of the pipe.

By analysing all data, the critical force can be estimated for each stem by identifying the change from elastic to non-elastic behaviour. This was done for every stem sample.

Figure 14 shows the experimentally-determined compression strength of retted flax stems as a function of retting. These results were based on the compression measurement of 180 flax stem sections. The experiments were performed in real time during the 2022 retting period (6th July to 31st August, and beyond to 4th October).

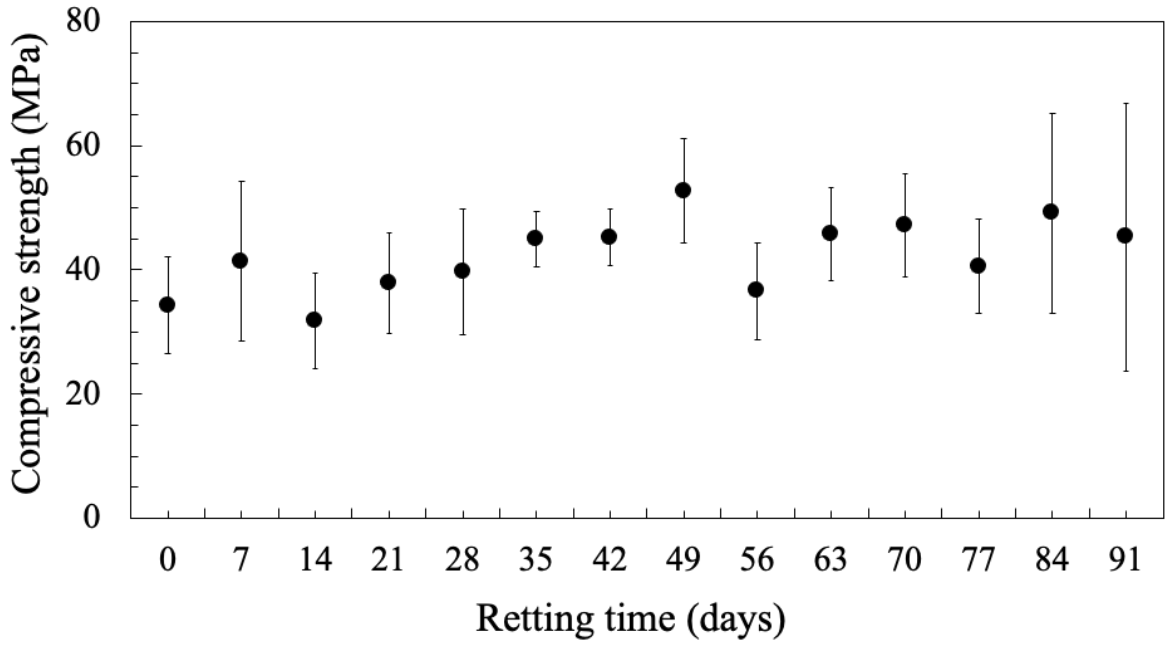

Figure 14. The experimentally-determined compressive strength of retted flax stems as a function of retting. These results are based on the compression of 180 flax stem sections. The results were obtained in real-time during the whole retting period of 2022 and beyond, i.e. 1st July to the 1st October 2022.The optimal retting time was 56 days, as defined by the company VRF.

The plot in Figure 14 shows an interesting trend: the average compressive strength, derived from the individual retting stages, remains relatively constant throughout the retting period, during under, optimal, and over-retting. This trend is comparable with the trend observed when determining the compressive modulus during retting period. The average compressive failure as a function of retting measured a value of 42.32±5.9 MPa.

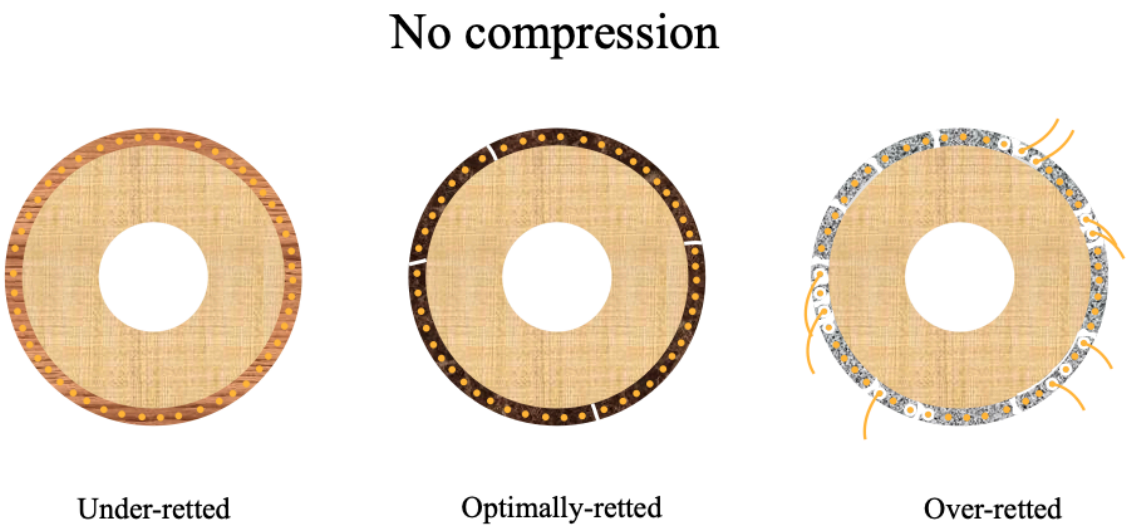

Figure 15. Schematic representation of the flax stems from under-retted, optimally-retted and over-retted stages before compression. The colour of the exterior tissue represents the advancement of the retting. The small yellow dots represent the flax fibres running along the stem. The diagrams are cross sections of a stem. The unchanging inner wood portion 'xylem' is indicated in light brown.

Figure 15 shows schematic representations of the cross sections of the flax stem samples of the under-retted (left), optimally-retted (middle) and over-retted (right) stages before inducing any compressive force externally. The under retted sample shows absence of damages in the outer tissue and the xylem before compression. This is not the case for the optimal and over retted samples, where they show a clear influence of the retting process, expressed as damages, presented by the white areas before compression. In addition the colour change of the exterior tissue represents the retting-induced modification of the exterior tissue, i.e. its mechanical strength becoming less (see Chapter 3).

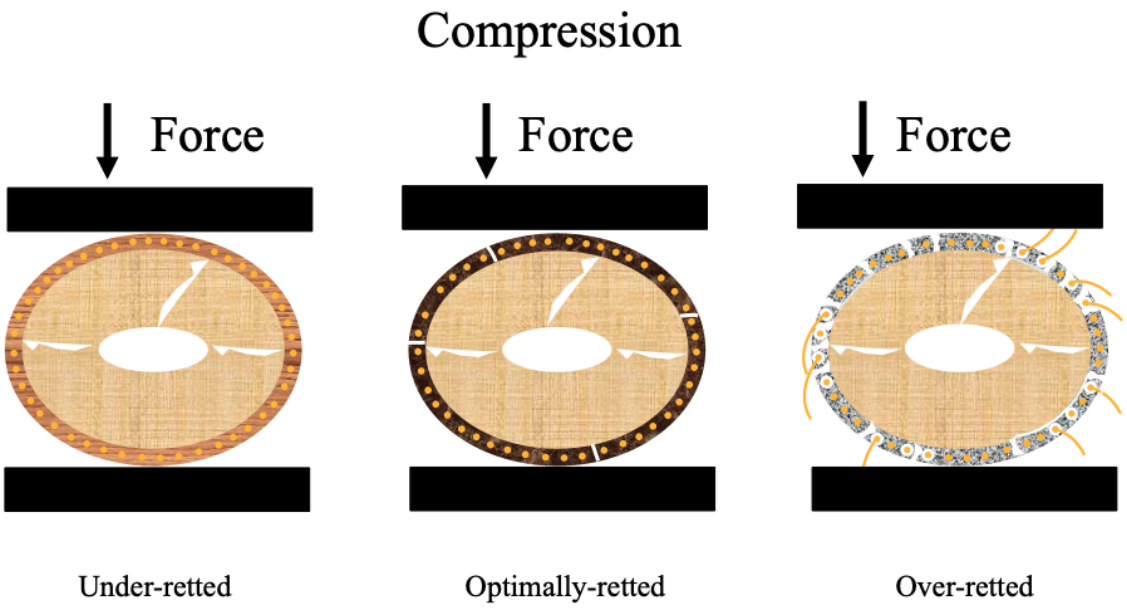

Figure 16. Schematic representation of the flax stems from under-retted, optimally-retted, and over-retted stages during compression. The colour of the exterior tissue represents the advancement of the retting. The small yellow dots represent the flax fibres running along the stem. The diagrams are cross sections of a stem. The unchanging inner wood portion 'xylem' is indicated in light brown.

Figure 16 shows schematic representations of the cross sections of the flax stem samples taken from under-retted (left), optimally-retted (middle) and over-retted (right) stages during application of a compressive force. There is an absence of changes in the status of the outer tissue, after compression of all samples from under-optimal and over-retted stages. This is not the case for the xylem (light brown), where a clear influence of the compressive force, observed as damages, is presented by the white areas in the tested samples from the three retting phases.

The results of this study show an interesting pattern. When the under-optimal and over-retted samples are subjected to mechanical compression, there are no observable changes in the stem surface. In this case, the application of mechanical compression (to induce a mechanical stress on the flax composite including the external tissue and the xylem) does not cause damage in the external tissue of the flax stem–for all flax stem samples in all retting stages. In addition, the microscopic image shows absence of fractures in the outer tissue while presence of fractures in the xylem when a breaking force is reached. The computed value of the average compression modulus as a function of the retting period is constant. Similarly, the computed value of the average compression strength as a function of the retting period is constant. This suggests that the compression modulus and strength values extracted represent the mechanical properties of the xylem, and the sensitivity to mechanical damage of the outer tissue is null.

This seems reasonable as the plant has evolved to have strong fibres running up its length to resist against wind and self-weight due to water absorption during rain. The exterior tissue,

including the fibres, therefore has no role in the compressive behaviour of the stems. As retting only affects the exterior tissue, the advancement of retting will not be apparent on compression tests. This is exactly what is observed in the experiments.

These results strongly suggest that the retting process is not evident in a compression mechanical phenomenon. However, this experiment reveals important information concerning the xylem. When comparing these results with the results of the bending experiment, we can conclude that the outer tissue is influenced by retting (flexural modulus and strength decrease in over-retting stage), which is not the case for the xylem (both compressive modulus and strength remain constant during the three phases of retting)

In addition, this experiment opens up a new way of finding out something very interesting about flax stems: the compressive modulus and compressive failure of the xylem (inner woody component in the flax plant). This novel parameter has remained unknown due to the lack of previous research in this area.

Finally, we can compare the compressive modulus measured here for 180 flax stems with the bending (flexural) modulus of the flax stems, measured in Chapter 3. Clearly they are not the same. In order to verify that this discrepancy is not due to a problem with the modelling, the modelling was verified using bending and compression of polypropylene tubes. This work can be found in **Appendix B**. In terms of the value of compressive modulus, it seems that the value is a bit weird, one can think that the used model is valid only for thin wall tubes, however when the same model is applied to polypropylene tubes (thick wall tubes) the model resulted in an accurate determination of the compressive modulus, this suggests that the model used is valid for a thick walled flax stems and the value is reasonable. Using polypropylene tubes, the bending modulus and the compression modulus were found to be equal and exactly the value given for polypropylene given in the literature. At the time of writing we do not have a clear explanation for this discrepancy, except to invoke a possible anisotropy of the morphology and properties of the xylem tube due to its porous nature.

Conclusions

The mechanical properties of flax stem samples have been characterised using compression measurements. Flax stems in various stages of retting were measured to monitor the effect of retting upon the compression modulus and the compressive strength of the stems. To do so, a simple tool has been developed to apply an accurate progressive force to a small piece of a cut flax stem. To obtain meaningful results, the cut (cross section) had to be high quality for observations by digital optical microscopy. Water weight was successfully used to apply a controlled accurate force to the stems. The results yielded the deformation of the stem cross section as a function of force. Three phases were observed in the data: an elastic regime, plastic deformation, and a rupturing of the stem xylem. By using a model based on the crushing of a uniform homogeneous pipe, we were able to extract the compression modulus and strength of the flax stems in a certain retting stage and directly compare stems in different retting stages. It was observed that the compressive modulus and compressive strength of the stems does not vary significantly with retting. This is in good agreement with bending results of stems presented in chapter 3 where the exterior tissue including fibres had been deliberately removed for measurements. The results and observations from this

Chapter there lend weight to our proposed behaviour of bending flax stems at various stages of retting and how the retting mechanisms damage the external tissue to modify the bending properties of flax stems. In the next chapter we will descend a level and look at the mechanical properties of the flax fibres.

References

DeRuntz, J. A., & Hodge, P. G. (1963). Crushing of a Tube Between Rigid Plates. *Journal of Applied Mechanics*, *30*(3), 391–395. https://doi.org/10.1115/1.3636567

Frese, M., & Blaß, H. J. (2014). Naturally Grown Round Wood – Ideas for an Engineering Design. In S. Aicher, H.-W. Reinhardt, & H. Garrecht (Eds.), *Materials and Joints in Timber Structures* (Vol. 9, pp. 77–88). Springer Netherlands. https://doi.org/10.1007/978-94-007-7811-5_7

Liu, W., & Wang, S. (2019). Analytical prediction of buckling collapse for reinforced thermoplastic pipes based on hoop stress analysis of crushed rings. *Ocean Engineering*, *187*, 106203. https://doi.org/10.1016/j.oceaneng.2019.106203

Niklas, K. (1998). Modes of Mechanical Failure of Hollow, Septate Stems. *Annals of Botany*, *81*(1), 11–21. https://doi.org/10.1006/anbo.1997.0505

Rathnaweera, G., Durandet, Y., Ruan, D., & Kinoshita, S. (2011). characterising the Material Properties of a Tube from a Lateral Compression Test. *International Journal of Protective Structures*, *2*(4), 465–475. https://doi.org/10.1260/2041-4196.2.4.465

Spatz, H.-Ch., Beismann, H., Brüchert, F., Emanns, A., & Speck, Th. (1997). Biomechanics of the giant reed *Arundo donax*. *Philosophical Transactions of the Royal Society of London. Series B: Biological Sciences*, *352*(1349), 1–10. https://doi.org/10.1098/rstb.1997.0001

Timoshenko, S. (1986). *Strength of materials* (3rd Ed.). CBS Publishers & Distributors.

Timoshenko, S. (2010). *Theory of elasticity* (3rd Ed.). McGraw Hill Education.

Wright, C. T., Pryfogle, P. A., Stevens, N. A., Steffler, E. D., Hess, J. R., & Ulrich, T. H. (2005). Biomechanics of Wheat/Barley Straw and Corn Stover. In B. H. Davison, B. R. Evans, M. Finkelstein, & J. D. McMillan (Eds.), *Twenty-Sixth Symposium on Biotechnology for Fuels and Chemicals* (pp. 5–19). Humana Press. https://doi.org/10.1007/978-1-59259-991-2_2

Yella Reddy, T., & Reid, S. R. (1979). On obtaining material properties from the ring compression test. *Nuclear Engineering and Design*, *52*(2), 257–263. https://doi.org/10.1016/0029-5493(79)90055-4

Chapter 5

Macro-mechanical testing: Effect of retting on stem torsion

Introduction

The bending experiments on flax stems at various phases of retting (Chapter 3) showed that retting has an effect on the flexural modulus and the flexural strength of the composite flax stems. We proposed that this was due to the retting-induced degradation of the external stem tissue which effectively leads to a flexural weakening of flex stem as retting time increases. This hypothesis is supported by the compression of flax stems experiments (chapter 4). In compression, no effect of retting is observed on the compressive modulus or breaking strength. We attributed this to the fact that the external tissue (holding together the flax fibres running laterally along the outside of the stem play not part in the structural rigidity in these experiments)

Based on these results and conclusions of the macro-mechanical testing of flax stems (Chapter 3 and Chapter 4) we conceived an original mechanical testing of flax stems based on applying torsion to the stems. Even though skilled artisans perform such a test manually, to do this quantitatively we had to imagine, design, and fabricate an original tool to perform the controlled experiments. The aim of these experiments was to investigate the influence of surface shear stress (due to mechanical torsion) on the external tissue of the flax stems. We anticipated the surface shear stress to cause observable damage (cracking, defect initiation…) on the external tissue. Whereas the artisan uses his/her eye to perceive effects in the retting stems, we decided to make use of a digital optical microscope to record and quantify effects of the applied mechanical torsion.

There are only a handful of scientific works concerned with the twisting of plant stems. In addition to this, and to our knowledge, the torsion of plant stems or branches has never been exploited in a technological way. Applying mechanical torsion to plant stems has been done by groups in the past (Gibson, 2012; Shah et al., 2017). Steven (Vogel, 1992) carried out measurements of two key structural properties, namely resistance to twisting, known as torsional rigidity or torsional stiffness, denoted GJ, and resistance to bending, known as flexural rigidity or flexural stiffness, denoted EI. These measurements were carried out by accomplishing a torsion on a range of herbaceous stems and petioles to provide a comprehensive structural analysis. Niklas (Niklas, 1997) undertook a study aimed at determining two fundamental material properties of stem tissues, namely Young's modulus, denoted as E, and critical shear stress, denoted as τ. His research focused on investigating the mechanical responses of hollow internodes with transverse node septa when subjected to both bending and twisting forces. The primary objective was to assess the agreement between the observed mechanical behaviour and the theoretical predictions derived from the principles of elastic stability, particularly as applied to thin-walled tubes or 'shells'. Spatz et al (Spatz et al., 1997) conducted a study that focused on determining the mechanical properties of various tissues within Arundo donax. Specifically, they examined the Young's modulus in both the longitudinal and tangential directions for these tissues, as well as the shear modulus for the radial-tangential plane. In addition, the study determined the critical strains in both the longitudinal and tangential directions. To achieve these objectives, they used a torsion-based approach over the hypodermal sterome of Arundo donax. The literature survey shows that up to date, no studies done on flax are the first stems. This suggests that we are the first to apply a torque on flax stems.

In this chapter, the following will be presented. An original tool to apply controlled mechanical torsion and surface shear stress to flax stems will be conceived, designed, and fabricated. The protocol of the measurement will be explained, e.g. sample mounting into the tool. The reasoning behind the experiments will be described. The analytical modelling and its relevant assumptions are presented. The mechanical testing of several flax stems at various stages of retting is undertaken. By using the analytical modelling we will show how we are able to extract meaningful, comparable results from the experiments.

Torsion tool design and sample mounting

Torsion tool design

To carry out the twisting experiment and to validate the proposed hypothesis, a custom-designed tool was developed for the PhD. The tool was meticulously designed with specific dimensions, including length, width and thickness, to ensure compatibility with the Keyence digital microscope mounting while meeting working distance and focal length requirements. The twisting tool consists of two ends: a fixed end and an adjustable end, see Figure 1.

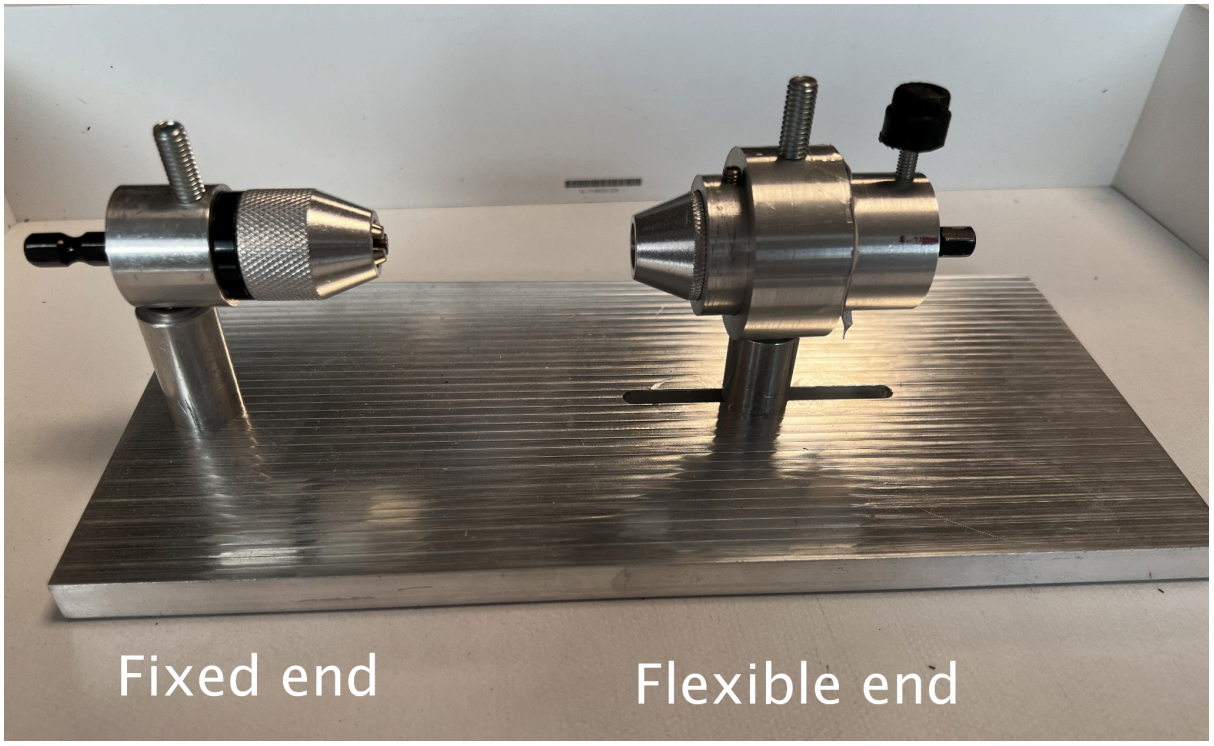

Figure 1. The torsion tool with the fixed end and the adjustable end for flax stem mounting.

The fixed part of the twisting tool consists of a ring with a diameter of 2.5 cm, which is positioned at a distance of 3 cm above the initial tool support, as shown in Figure 1. The purpose of this ring is to act as a support for the sample holder chuck.

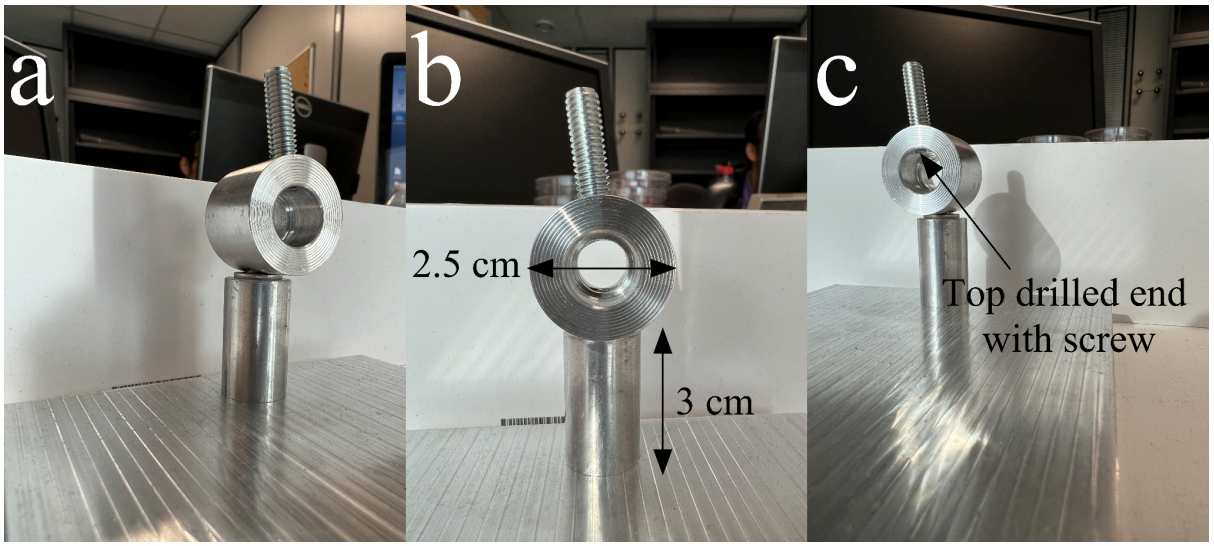

Figure 2. The fixed end holder of the designed tool for the experiment, (a) side view of fixed end, (b) front view of fixed end with dimensions, and (c) side view of the fixed end.

Figure 2 shows the sample holder with the dimensions. The sample holder is essentially a chuck for an electric drill with an adjustable opening from 0 to 6 mm. To control the opening of the chuck and ensure compatibility with the specimen diameter, a long bolt is securely attached to the chuck. Figure 3 shows the dimensions of the chuck used for the tool design.

Figure 3. The chucks used to hold the flax stems in the specially-designed tool for the torsion experiments.

A top-drilled ring is incorporated into the design, and a screw is introduced to securely immobilise the chuck Figure 4a. This arrangement ensures that the chuck remains fixed in position during the sample mounting process as the chuck opening size is adjusted to match that of the sample, specifically as the screwdriver rotates and adjusts the chuck opening, effectively gripping the sample tightly. On the other hand, the flexible end of the tool is designed to facilitate rotation, which is the segment responsible for inducing the twist during the test at various predetermined angles. The flexible end of the twisting tool consists of a ring 4 cm in diameter positioned 2 cm above the tool holder Figure 4b.

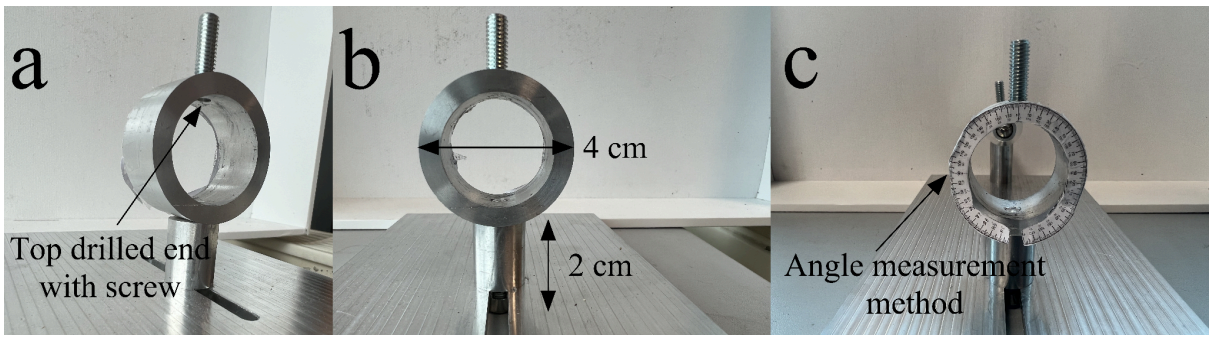

Figure 4. The flexible end holder of the designed tool for the experiment. (a) Side view of flexible end, (b) Front view of flexible end with dimensions and, (c) Side view of flexible end and the simple angle measurement graduations.

This ring serves two purposes: to support the sample holder and to provide a mechanism for controlling the twisting angle. To allow accurate angle induction, a paper strip with a graduated angle scale is attached along the edge of the ring support. In addition, a drill is incorporated into the top of this ring to act as a lock for the sample holder, as shown in Figure 4c.

The sample holder consists of two compartments. Firstly, it contains a drill chuck and a bolt, similar to those discussed in the previous section. Secondly, a large metal roller is incorporated to induce and control the twisting motion. This roller is designed to securely hold the chuck and bold, with both components inserted into it, as shown in Figure 5. In addition, the roller has two upper bores that provide separate locking points for the chuck and bolt, using individual screws, as shown in Figure 5a and 5b. These locking points ensure that the chuck and bolt are independently fixed once the sample has been firmly gripped, preventing them from twisting separately within the roller and eliminating the possibility of false twisting.

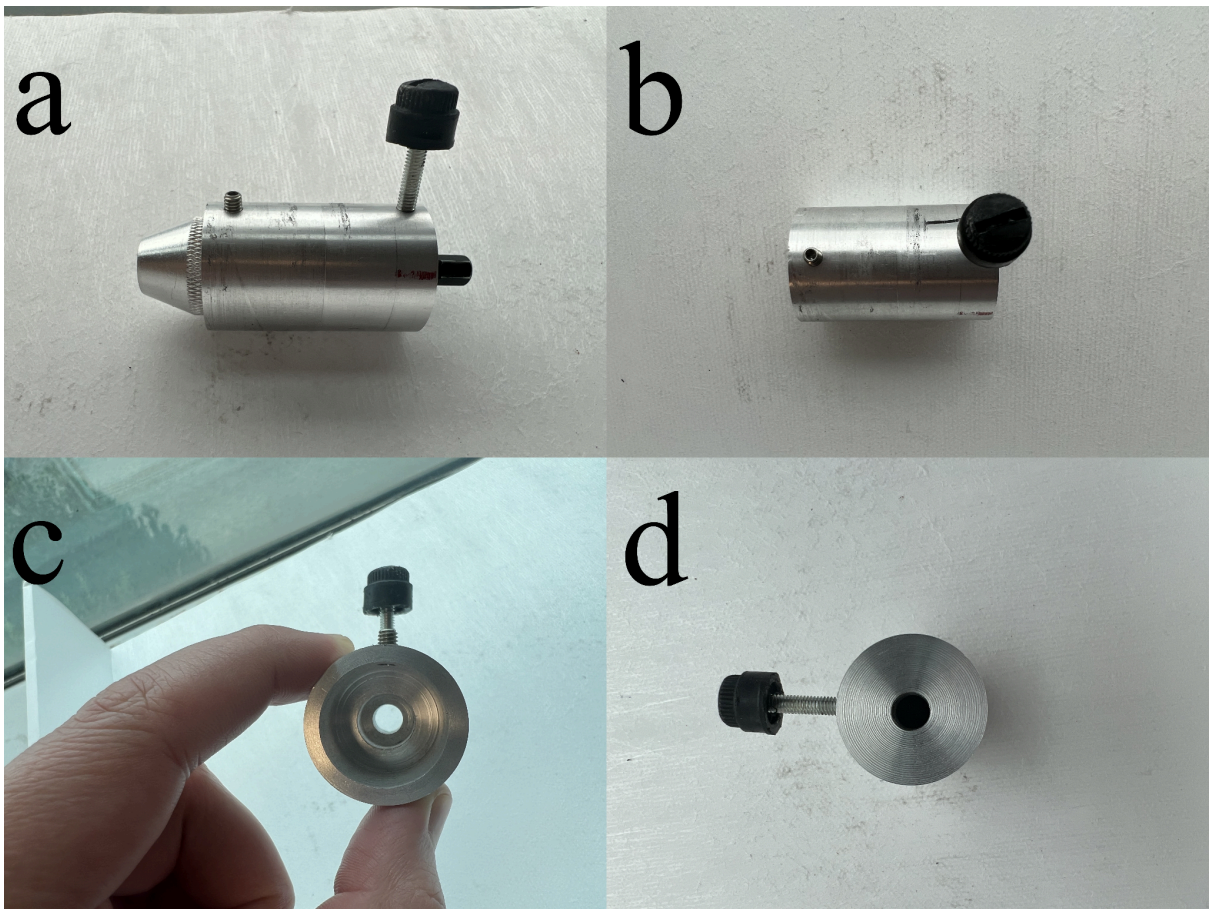

Figure 5. An overview of the flax sample holder (roller), (a) The complete parts of the roller, (b) The top screws acting as blockers, (c) Side view of the roller, (d) Opposite side view of the roller.

By implementing this design, the twisting tool facilitates precise control of the twisting angle using the graduated scale on the ring support and the sample holder, providing a secure grip on the specimen while preventing separate twisting of the chuck and bolt. This arrangement promotes accurate and reliable twisting experiments, reducing any potential sources of error or false twisting. Moreover the careful design, which includes the ring, sample holder with adjustable chuck, and screw fixation, ensures secure placement of the sample and minimises any potential instability or slippage of the sample during twisting operations.

The design also allows for eventual buckling of the stem while applying torsion. The right hand side of the tool can twist and also move laterally to compensate for a length change of the stem due to buckling.

Particular attention was paid to the manipulation of the bolt to achieve secure and damage-free fixation of the stem sample. This meticulous approach aimed to prevent any slippage or instability of the sample throughout the twisting process without causing damage to the stem. The screwdriver was handled with care and precision at both ends to ensure the integrity and reliable fixation of the sample during twisting. The use of blockers further contributed to the success of this approach and resulted in favourable results.

Sample mounting

As explained in Chapter 2, fresh flax stem samples were taken from the field, in collaboration with the VRF company (Killen, France), for the real-time experimental torsion studies. These samples were taken at different retting stages and divided into 3 categories: from the beginning of retting until the optimum point, at the optimum point determined by VRF and after the optimum retting point. The experiment was carried out on fresh samples in real-time conditions.

Specific measures were taken to ensure control of variable parameters that could affect the measurement protocol. The total length of the samples was standardised at 7 cm. Within this length, a segment of 5 cm was reserved exclusively for the portion to apply torsion, while the remaining 2 cm was intended for insertion and fixing into the drill chuck (as described above). A permanent marker was used to clearly mark the boundaries of the 5 cm twisted section and the boundaries of the 7 cm length (including the remaining 1 cm at each end). These markings were shown in Figure 6 to ensure consistent length control for all samples.

Figure 6. Preparation of a flax stem sample for the torsion experiments.

In order to prepare the sample for the torsion experiment, a razor blade and a special cutting tool, described earlier in (Chapter 3-see Figure 2) were used to prepare the samples.

This step, along with measures such as standardised sample lengths and the use of a dedicated cutting tool for precise preparation, was aimed at maintaining a controlled and consistent environment to increase the reliability and reproducibility of the experimental results. To ensure stability and minimise any potential degradation or change in sample properties, the prepared samples were refrigerated at 4 degrees Celsius until the experiment.

Prior to the sample mounting, microscopic images were taken of the cross-sectional ends of each sample. This step was taken to facilitate the measurement of the sample internal and external diameter. To ensure accurate and precise measurements, the average diameter was determined using the six-diameter measurement method as discussed in the **Diameter measurement part of chapter 3.**

Following diameter measurement, the sample was carefully mounted in the torsion tool using the stepwise approach discussed below. First, all screws at the flexible end of the twisting tool are loosened, allowing the sample holder, consisting of roller, chuck and screwdriver, to be displaced in the ring, making space to fit the sample between the ends, as shown in Figure 7a. At the fixed end, the screw is locked to prevent the chuck from slipping during sample mounting. Then the bolt was rotated to its maximum position, causing the drill chuck to reach its widest opening. The sample was then securely inserted into the chuck, ensuring that it reached the limit of the 1cm segment designated for sample fixation within the twist tool, as shown in the Figure 7a. Once the sample was inserted, the bolt was carefully rotated in the opposite direction, gradually closing the chuck to hold the sample firmly in place- see Figure 7b

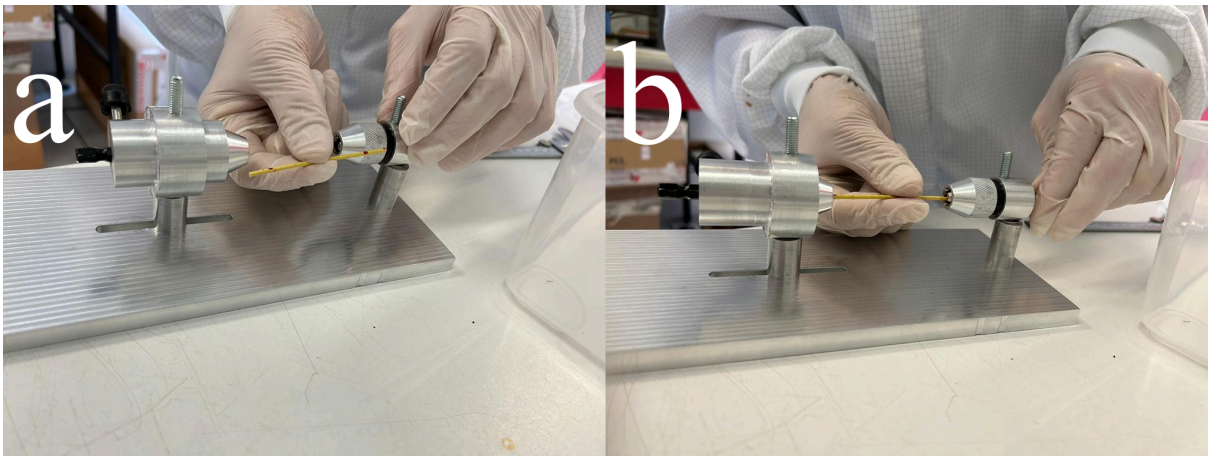

Figure 7. The first step of the mounting process of the flax stem sample into the torsion tool.

Next, at the flexible end of the tool, the bolt attached to the chuck is rotated to its maximum extent, resulting in the widest opening of the chuck.

Figure 8. The second step of the mounting process of the flax stem sample into the torsion tool.

The sample is then inserted into the chuck and the bolt is turned in the opposite direction as far as it will go, firmly securing the stalk in the chuck, and the chuck and screwdriver are replaced in the roller Figure 8. This is followed by tightening all the screws, ensuring that the roller and chuck with the screwdriver are held firmly in place within the ring Figure 9a, 9b, 9c

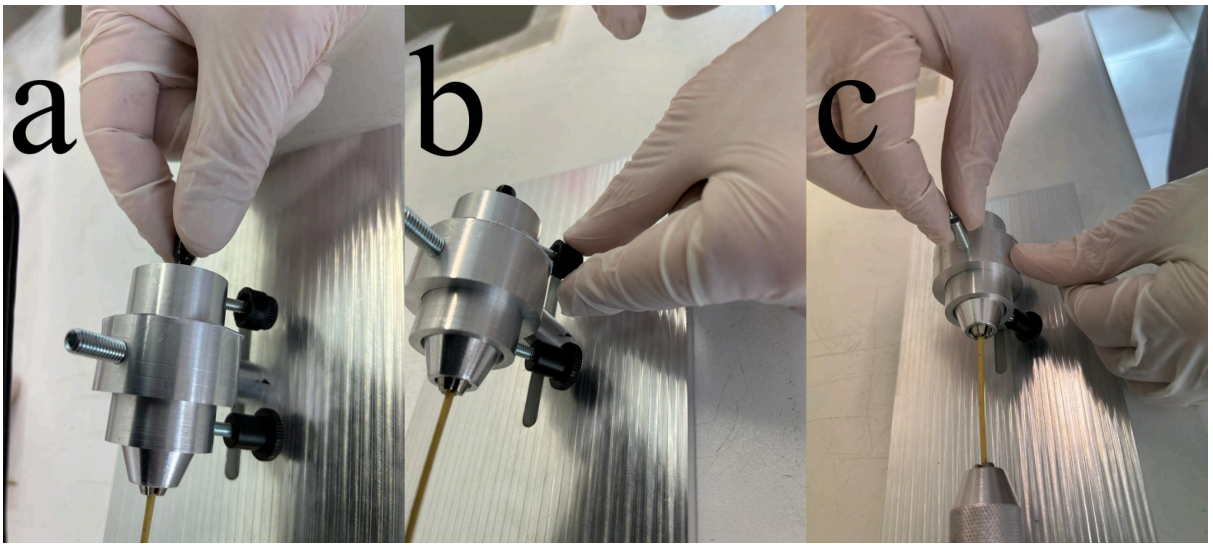

Figure 9. The next steps of the mounting process of the flax stem sample into the torsion tool. Photographs showing the various lock screws used to mount the flax stem into the torsion tool.

The twisting tool was then carefully positioned on the microscope stage as shown in Figure 10.

Figure 10. Photograph of the torsion tool with a flax stem under the digital optical microscope VHX-6000 (Keyence, France).

To overcome the limited range of movement under the microscope lens, a strategy was devised to capture the deformations resulting from the twisting process. Five different locations on the sample were selected as reference points for image acquisition. Using the capabilities of the Keyence digital microscope, a convenient feature allowed these locations to be registered. A simple click allowed a seamless transition between the registered locations. The selected locations were specifically located at different points along the sample, including the fixed end, the middle, the flexible end, and two intermediate positions between the fixed end and the middle, and between the middle and the flexible end.

Experimental results

The main objective of the torsion experiment carried out was to determine the optimum retting stage for flax stalks.This critical stage represents the point at which the outer tissue containing the fibres can be separated from the woody internal structure with minimal mechanical force.

The reasoning behind the measurement

The measurement protocol is as follows. First, a stem of a given retting stage (R0 to R20) is carefully mounted into the tool (as explained above). Note that all stems samples are of different inner and outer diameter (for the same retting stage and from retting stage to retting stage). Second, the tool is placed under the digital optical microscope. As explained above, the design of the tool ensures that no mechanical stress is applied to the stem prior to the experiment (as explained above). Third, five positions along the top of the stem are recorded by the digital microscope's automatic positioning system. These positions will enable stitched and zoomed images to be recorded during the experiment. Fourth, the torsion angle of the stem is increased gradually to give constant values of torque from sample to sample. Note that great care is taken to observe any slippling of the stem, due to poor sample mounting, if this was observed then the experiment was abandoned. The torsion angle of the stem is increased in steps until damage is observed on the external tissue of the stem. The torsion angle is further increased in steps to observe the evolution of this damage. Finally, the experiment is stopped when the wood of the stem breaks. Several stems of different diameters were tested for each retting stage (R0 to R20). In order to compare different size stems from the same retting stage, and also compare results from retting stage to retting stage, a physical parameter needs to be calculated as the torsion angle is meaningless by itself. In order to 'normalise' the different size stem samples, we calculated the torque and surface shear stress for each applied torsion angle. To do this, we approximated the stem to a uniform pipe and used its associated mechanical models (Timoshenko, 2010) (Timoshenko, 1986). We computed the torque (Nm) on each stem and at each torsion angle. We computed the surface shear stress on each stem and at each torsion angle. In this way, using the torque and surface shear stress we could directly compare stems in the same retting stage and stems for retting stage to retting stage.

The following properties are measured for each stem: the inner and outer diameter, the bending modulus E (values calculated in Chapter 3), the shear modulus G (calculated using the Poisson ratio *v* is calculated using an average of similar woods in the literature), and the sample length. The torque T on the stem was computed using the following equation:

$$T = \frac{\pi\theta}{32l}\left(\frac{E}{2(1+\nu)}\right)\left(d_o^4 - d_i^4\right) \quad (1)$$

Where θ is the torsion angle, *l* is the stem length, *E* is the bending modulus of the stem, *v* is the Poisson coefficient of the stem, *d*o and *d*i are the outer and inner diameters of the flax stem.

The surface stress shear σ was calculated using the following formula:

$$\sigma = \frac{\theta G d_o}{2l} \quad (2)$$

Where, θ is the torsion angle, G is the shear modulus, *d*o is the outer diameter, and *l* is the stem length.

Note that these analytical solutions consider that the stem can be approximated to a homogenous straight pipe structure and do not consider buckling of the stem.

Experiments on under-retted flax stems

Figure 11 shows an under-retted flax stem being twisted in the torsion tool. The images are obtained using a digital optical microscope (Keyence, France). The microscope enables large high-resolution stitched images to be obtained as well as magnifications up to x1000, even x5000 if the objective is changed. Although the working distance is reduced somewhat if the x5000 objective is used making some experimentation difficult.

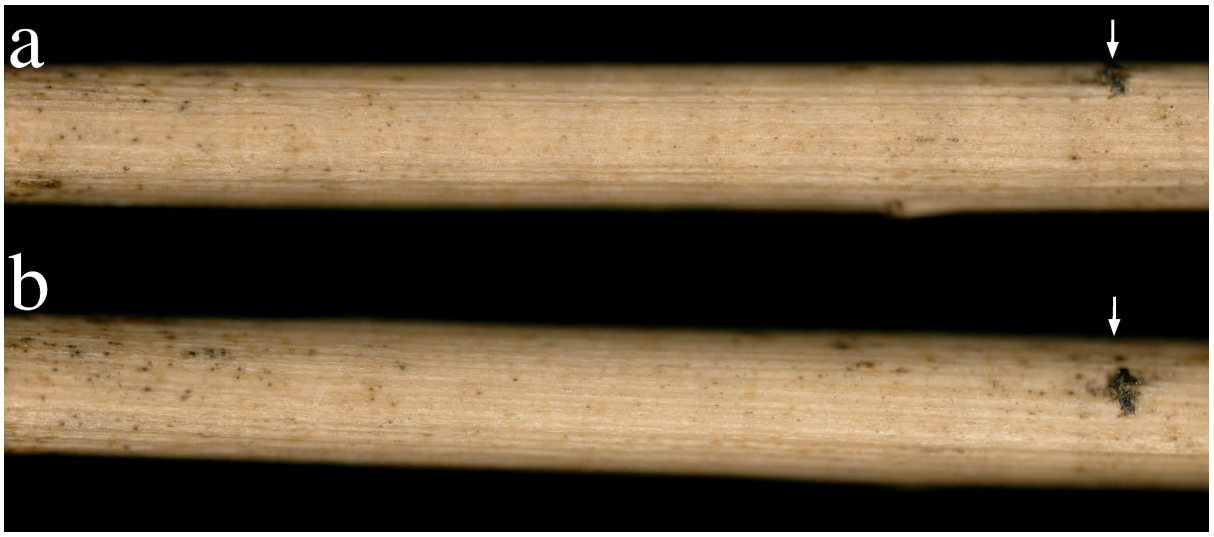

Figure 11. A digital optical microscopy stitched images of the middle section of an under-retted flax stem (a) without and (b) with applied mechanical torsion to the flax stem. This specific stem is taken from an under-retted stage of retting. The torsion angles are 0 degrees (a) and 150 degrees (b). The white arrows indicate the twisting of the stem.

Table 1 provides a comprehensive compilation of the corresponding diameters, torque and shear stress values associated with each different twist angle for a sample before the optimum retting point.

Under-retted flax stem		
Torque (Nm)	**Torsion angle (deg)**	**Surface shear stress (MPa)**
0	0	0
0.04	21	32.43
0.08	42	64.87
0.12	63	97.30
0.16	84	129.74

0.20	105	162.17
0.24	**126**	**194.61**

Table 1. An example of the surface shear stress calculation for under-retted stems. Here the inner and outer diameters were 950 µm and 1881 µm. For these samples no damage in the external tissue was observed. The internal wood failed at a torsion angle of 126 deg equivalent to a surface shear stress of 194.6 MPa (indicated by blue numbers).

Figure 12 Shows the visual representation of the condition of the flax stalk at the five designated locations, from the initial angle of zero degrees to the point of wood breakage.

Figure 12. The effect of torsion on an under-retted flax stem. The lateral images show different positions along the stem. The descending images show the effect of increasing the torsion angle at the right end of the stem. The torsion angles are 0 deg, 20 deg, 60 deg, 100 deg, and 140 deg. No damage to the external tissue was recorded for under-retted stems. The wood failed at a torsion angle of 126 deg corresponding to 194.6 MPa, this is indicated by the blue arrows. The white scale bars are equivalent to 100 µm.

Figures 12a and 12b are taken from the left side and left quarter of the flax stalk respectively. Notably, these images show an absence of twisting of the stalk on these particular sides. This absence of twisting implies that the sample is effectively fixed to the fixed part of the twisting tool, effectively preventing any movement in this region. On the contrary, there is a noticeable twisting phenomenon in the middle part of the flax stalk, with particularly pronounced observations in the right quarter and on the right side-see Figure 12c. At a twisting angle of 60 degrees, the onset of flax stalk twisting becomes apparent, particularly in the middle part, the right quarter and the rightmost end of the stalk. However, it is at the right quarter and right end of the stalk, which is attached to the flexible end of the twisting tool.

When a torsion angle of 140 degrees is reached, the tool can return to the zero angle as the accumulated torsion in the stalk is released, indicating a wood breakage Figure 12d and 12e. The results we observed visually indicated that the stalk was damaged, coinciding with the breakage of the inner woody part of the flax stalk. This breakage occurred within a twisting angle range of 120 to 140 degrees, corresponding to a shear stress range of 194 to 227 MPa. Interestingly, the outer part of the stalk remained undamaged during the twisting process, even when the inner wood broke. This tentatively suggests that the flax stalks are not yet at the optimum retting point. The fact that the outer tissue is still difficult to separate from the inner wood indicates that they aren't ready for industrial mechanical separation.

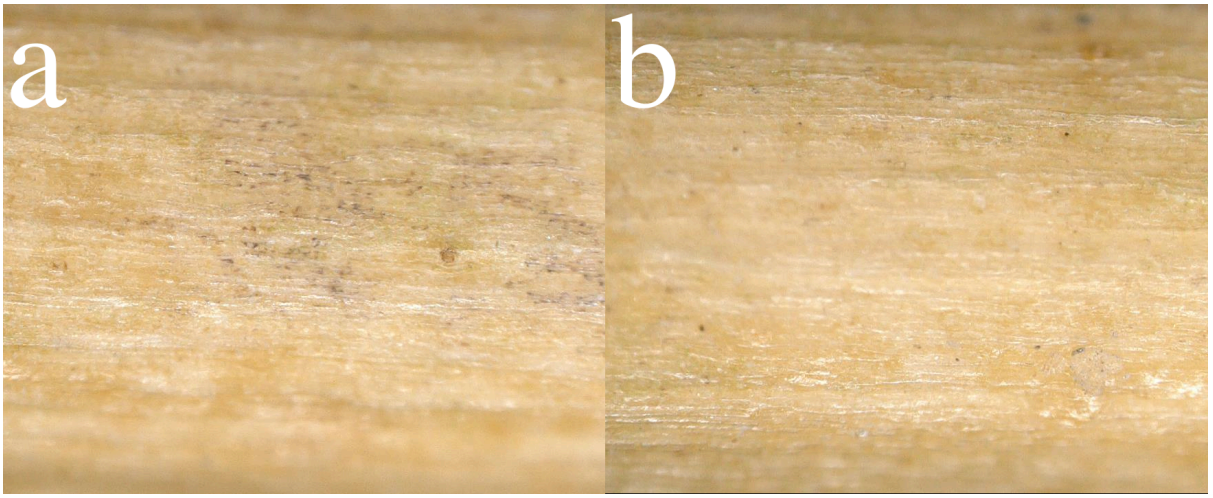

Figure 13. Zoom Appearance of no damage. Digital optical microscopy zoomed images of different parts of an under-retted flax stem under a torsion angle of 126 degrees, equivalent to a surface shear stress of 194.6 MPa. The left image (a) shows no damage or crack-like feature, as well as the right image (b) shows absence of local damage.

Experiments on optimally-retted flax stems

Figure 14. Digital optical microscopy stitched images of the middle sections of an optimally-retted flax stem (R15-S3) during measurement at torsion angles of (a) 20 deg, (b) 40 deg, and (c) 80 deg, equivalent to a surface shear stresses of 33, 66, and 132 MPa.

Figure 14 shows digital optical microscopy stitched images of optimally-retted flax stems during torsion measurements. First, one can observe that the colour of the external tissue of the stems is very different from the under-retted stems presented above. This colour change due to retting is well documented (Pallesen, 1996) and indeed often used by artisans as a guide to the advancement of the stem retting. Figure 14 shows three torsion angles: 20 deg-see Figure 14a, 40 deg-see Figure 14b, and 80 deg-see Figure 14c that have been applied using the tool. For this stem, this corresponds to computed surface shear stresses of 33, 66, and 132 MPa. Straight away, and in contrast to under-retted flax stems, we were able to observe shear stress-induced damage in these optimally-retted samples.

We then examined samples obtained from the optimumaly-retted stage. Before proceeding with the analysis, we measured the diameter using the method described in the bending chapter, using the six-measurement approach. The subsequent calculations focused on determining both the angle and the shear stress values in relation to the constant torque values. Table 2 gives the corresponding angle, torque and shear stress values for this stem.

Optimally-retted flax stem		
Torque (Nm)	**Torsion angle (deg)**	**Surface stress (MPa)**
0	0	0
0.04	10	18.50
0.08	20	37.01
0.12	30	55.52
0.16	40	74.03
0.20	**50**	**92.53**
0.24	60	111.04
0.28	70	129.55
0.32	80	148.05
0.36	90	166.56
0.40	**100**	**185.07**
0.44	110	203.57

Table 2. An example of the surface shear stress calculation for optimum retted stems. Here the inner and outer diameters were 798 μm and 2230 μm. In this sample, the shear stress-induced damage to the external tissue was observed at a shear stress of **92.53** MPa (indicated by red numbers). The internal wood failed at **185.07** MPa (indicated by blue numbers).

Figure 15 shows the twisting process of an example taken from the optimally retting point.

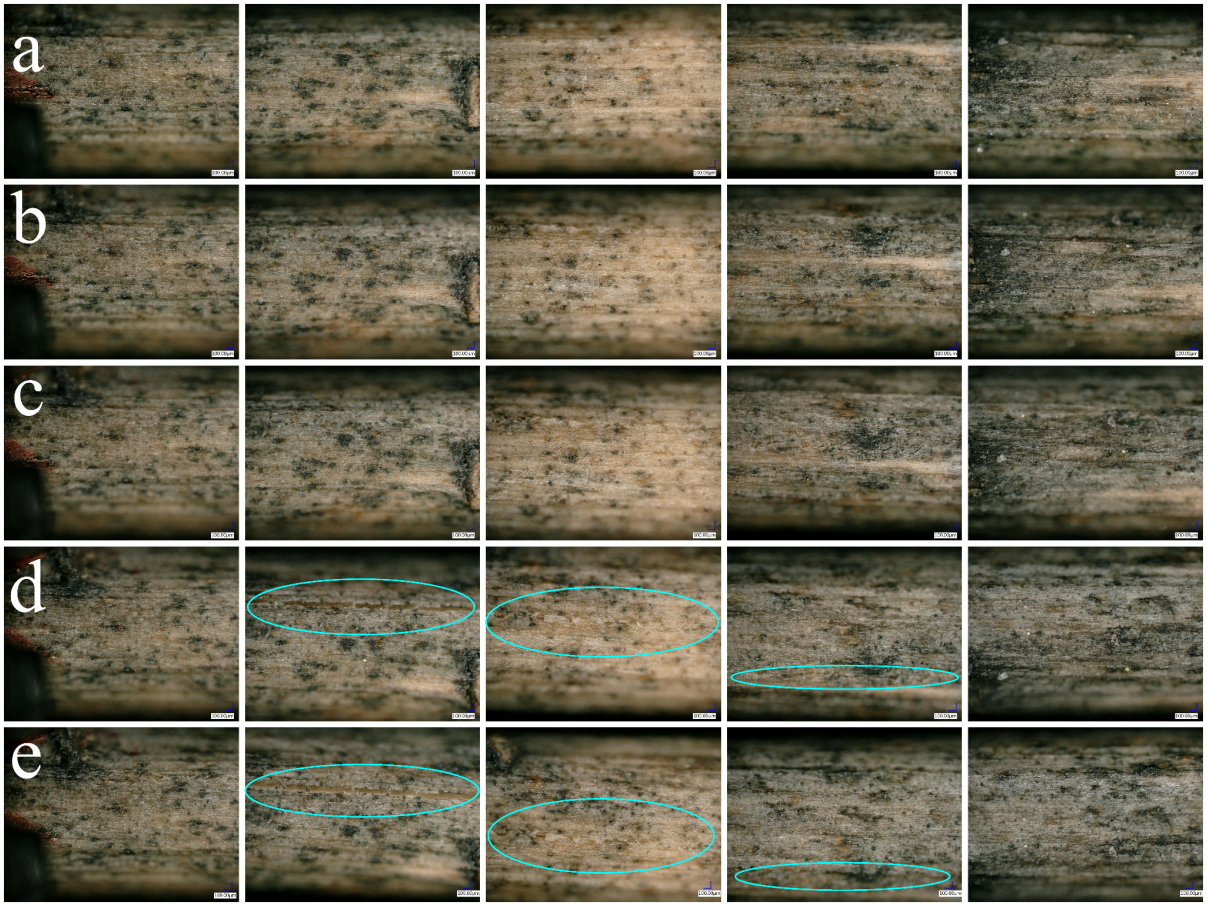

Figure 15. The effect of torsion on an optimally-retted flax stem. The lateral images show different positions along the stem. The descending images show the effect of increasing the torsion angle at the right end of the stem. The torsion angles are (a) 0 deg, (b) 30 deg, (c) 60 deg, (d) 90 deg, and (e) 110 deg (descending images). The external tissue damage appeared for optimally-retted stems at a surface shear stress of 92.53 MPa. The wood failed at a torsion angle of 100 deg corresponding to a surface shear stress of 185.07 MPa. The blue circles and ellipses in (d) and (e) indicate the areas of shear stress-induced damage to the external tissue of the flax stem. The white scale bars are equivalent to 100 μm.

After analysing the photographic data, the visual results are quite revealing. They show that the beginning of surface shear stress-induced damage in the external tissues of the flax stem from the optimum retting stage (as determined by VRF) becomes apparent at a torsion angle of 50 degrees, as shown in Figures 15a-e. This angle corresponds to a computed surface shear stress value of 91.53 MPa for this stem, as shown in Table 2. As the torsion angle is increased, the more severe and extensive the damage to the outer tissue becomes. at an angle of 100 degrees, see Figure 15a-e. An interesting thing happens at this point: the roller can easily return to its original position due to the sudden release of the tension built up in the stem. This means that the inner woody part of the stem breaks at a twisting angle of 100 degrees at a shear stress of 185.07 MPa.

Figure 16 and 17 shows microscopic photos of the damages and deformation in the external tissue at 50 degrees and surface shear stress of 92.5 MPa.

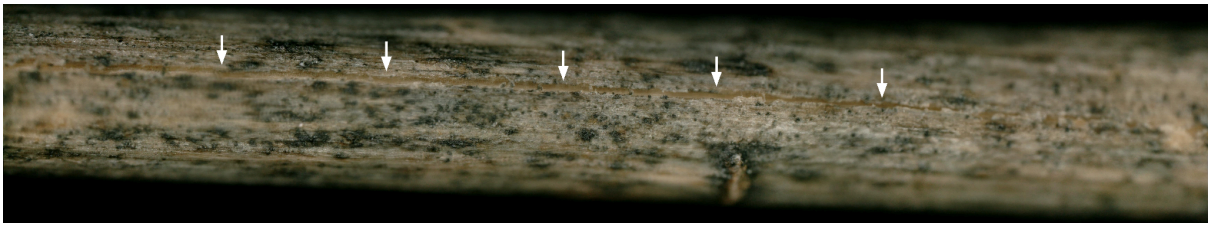

Figure 16. Appearance of damage. A digital optical microscopy stitched image of the middle-left section of an optimally-retted flax stem at a torsion angle of 50 degrees, equivalent to a surface shear stress of **92.5** MPa. The damage in the external tissue of the flax stem is clearly visible using optical microscopy.

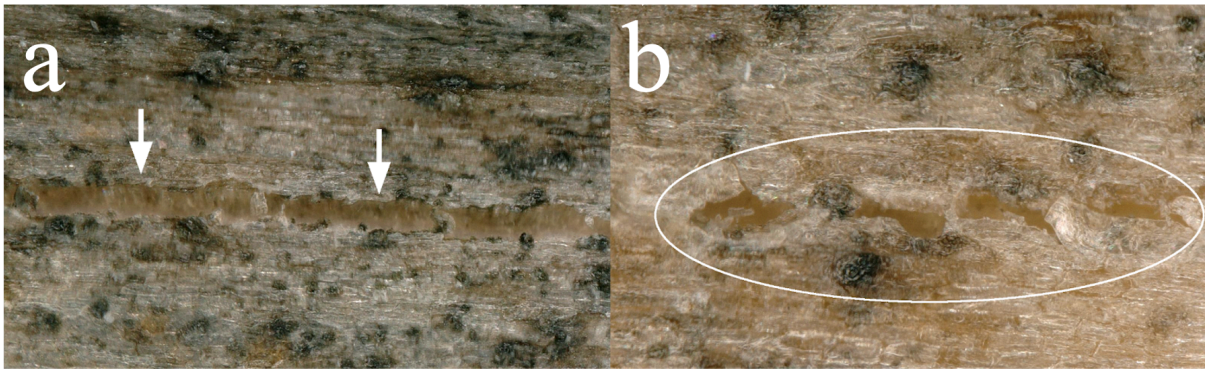

Figure 17. Zoomed images of the appearance of damage in the exterior tissue of a flax stem under torsion. Digital optical microscopy zoomed images of different parts of an optimally-retted flax stem under a torsion angle of 50 degrees, equivalent to a surface shear stress of 92.5 MPa. The left image (a) shows a long crack-like feature, the right image (b) shows the appearance of local damage.

The results show that the outer tissue begins to separate before the inner wood breaks. This means that less force is needed to separate the outer layer. This is an interesting finding because it means that at this stage it is easier to pull the outer tissue away from the wood than at the previous decay stage.

Experiments on over-retted flax stems

We then proceeded to examine the samples obtained after the optimum rotting period–we define these samples as ‘over-retted flax stems’. Following the protocol, we took microscopic images before starting the experiment. These images clearly show significant damage to the outer tissue, with fibre bundles clearly visible even at a zero degree angle. The results are effectively illustrated in Figure 18 below.

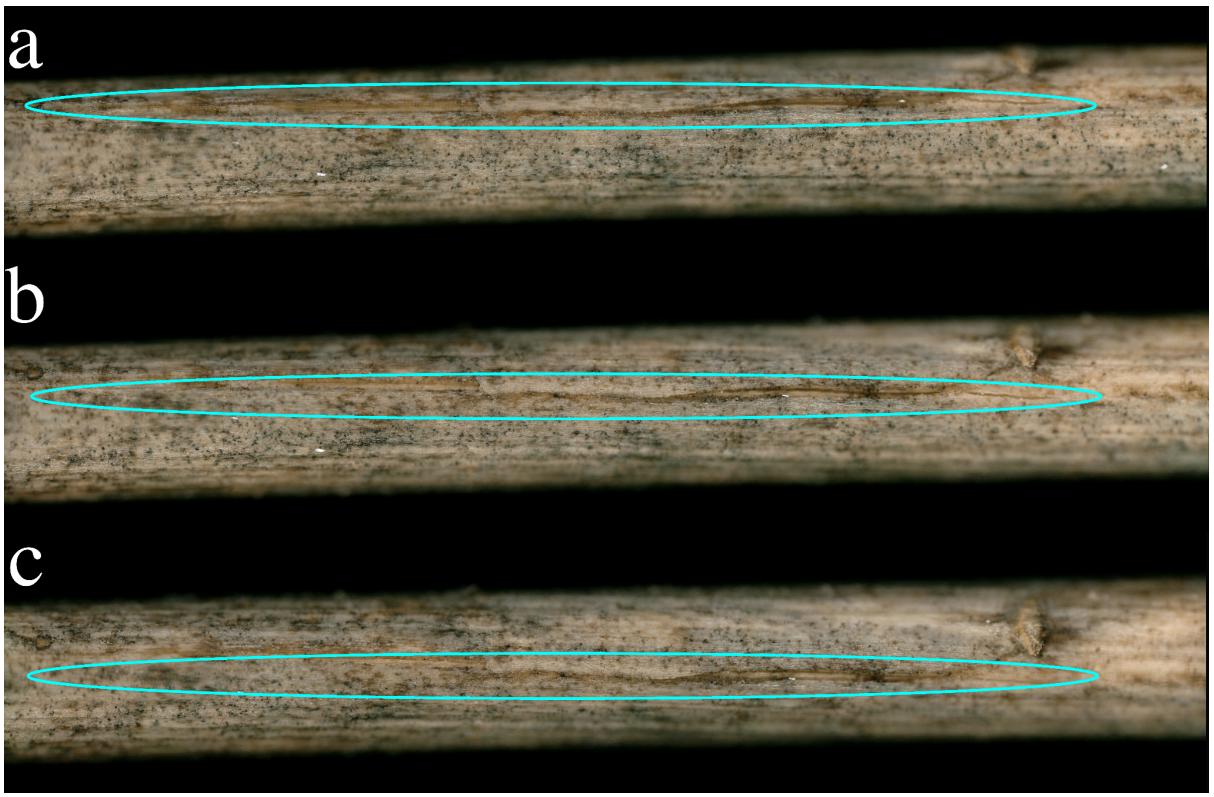

Figure 18. Digital optical microscopy stitched images of the middle sections of an over-retted flax stem (R16-R20) during measurement at torsion angles of (a) 0 deg, (b) 30 deg, and (c) 70 deg, equivalent to a surface shear stresses of 0, 64.1, and 144.3 MPa. The blue ellipses correspond to damage in the external tissue (even present at zero and low values of surface shear stress in these samples).

The visual results we obtained provide an interesting insight. After passing the point of optimal retting as determined by VRF, the outer tissue of the flax stalk shows obvious and significant damage. This is easy to see due to the extensive damage, which makes it clear that the outer tissue can be easily separated without any mechanical effort. In addition, looking at the fibres and fibre bundles under the microscope, it's quite clear that we may have entered an over-retted phase. This observation raises the concern of how retting could affect the quality of the fibre, possibly leading to lower quality. Overall, these results strengthen the credibility of the retting point specified by VRF.

Driven by our curiosity, we decided to continue the experiment at this stage to find out exactly when the wooden part would break. Following the instructions in the protocol, we calculated the angle (theta) and shear stress values corresponding to the specific torque we applied, using equations (1) and (2). We also took diameter measurements and have summarised all these results neatly in the tables below:

Over-retted flax stem		
Torque (Nm)	**Torsion angle (deg)**	**Surface Stress (MPa)**
0	0	0
0.04	**8**	**16.03**
0.08	16	32.06
0.12	24	48.09
0.16	32	64.12
0.20	40	80.15
0.24	48	96.18
0.28	56	112.22
0.32	64	128.25
0.36	72	144.28
0.40	80	160.30
0.44	88	176.34
0.48	**96**	**192.37**
0.51	104	208.40

Table 3: An example of the surface shear stress calculation for over-retted stems. Here the inner and outer diameters were 952 µm and 2347 µm. For these samples damage in the external tissue was observed at a surface shear stress of 16 MPa (indicated by the red numbers). The internal wood failed at 192.4 MPa (indicated by blue numbers).

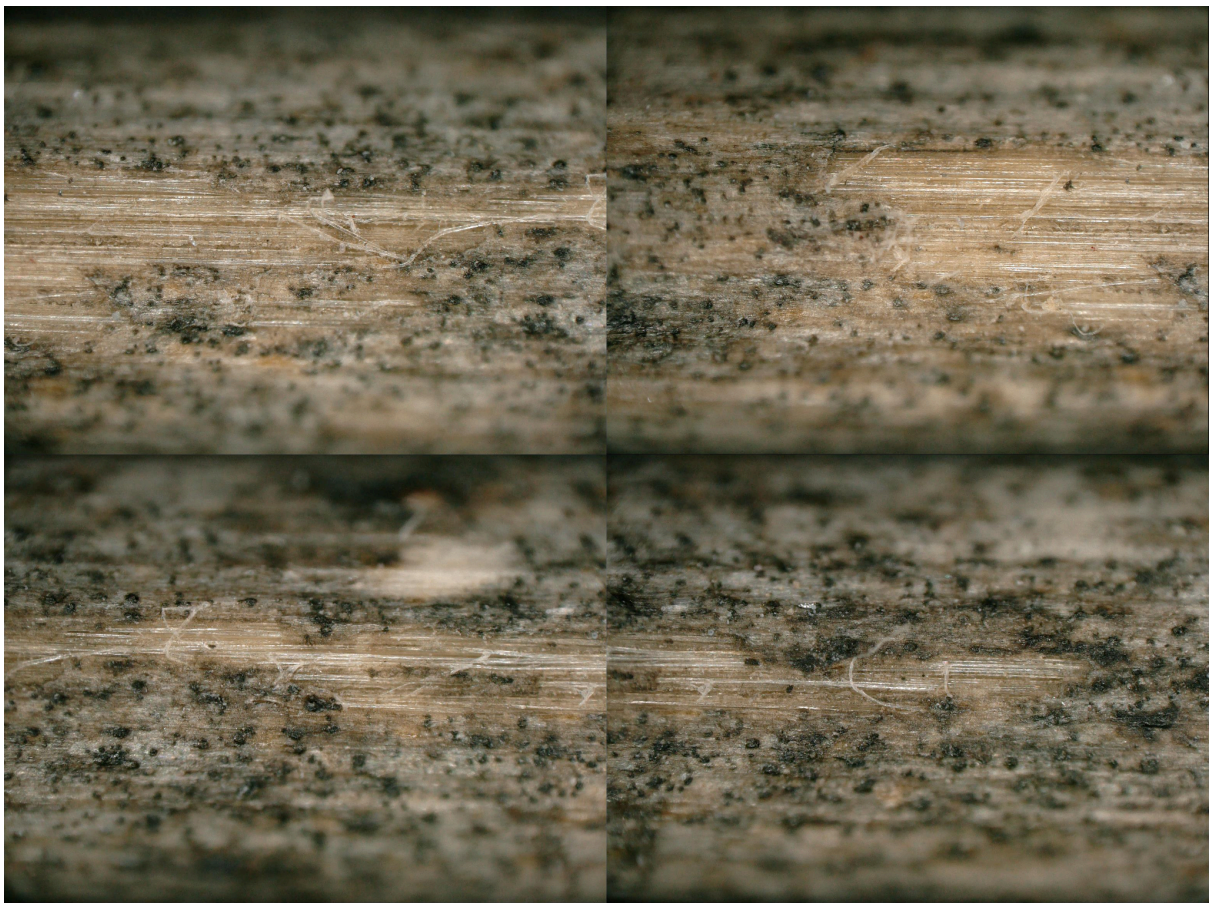

Figure 19. Digital optical microscopy zoomed images of different parts of an over-retted flax stem (R16-R20). Images taken at zero torsion angle. Shows the natural damage of the external tissue due to over retting. These over retted samples are not appropriate for our torsion measurements.

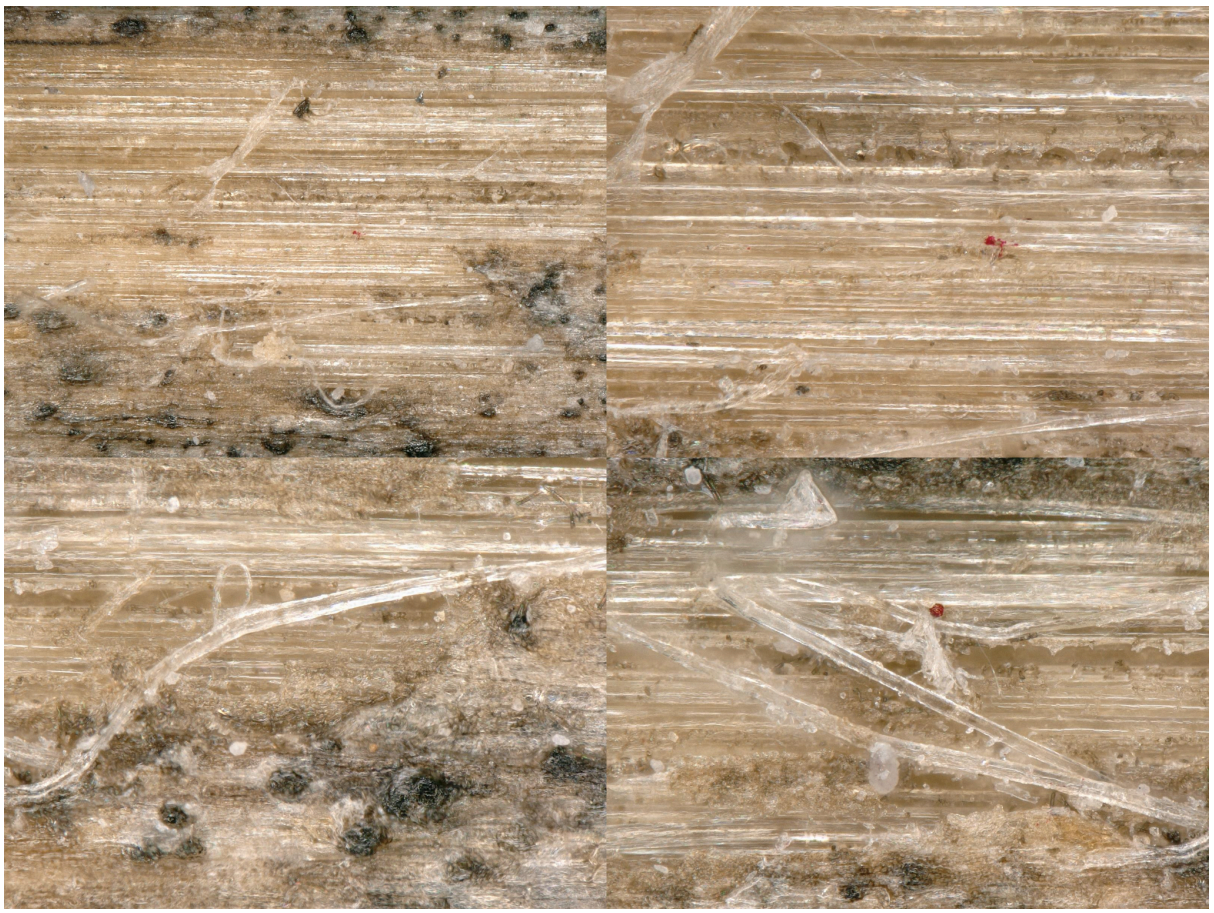

Figure 20. Digital optical microscopy zoomed images of different parts of an over-retted flax stem (R16-R20). Images taken at zero torsion angle. The images clearly indicate the external tissue damage and fibre bundles are visible. These over-retted flax stems are not appropriate for torsion testing as the external tissue damages at very low values of surface shear stress and torque.

Measured property	Surface shear stress (MPa)
Surface shear stress to cause visible damage in optimally-retted samples	91.02±8.87
Surface shear stress to break wood in all samples	180.54±21.70

Table 4. A summary of the results based on all measurements in this chapter.

Table 4 shows a summary of the results based on all measurements in this chapter. These two properties are very important. First, the surface shear stress to cause visible damage in

optimally-retted samples enables the following to be done. Given any stem from any retting stage, the tool user can–at least in principle–measure the stem dimensions, insert the stem into the tool and apply a surface shear stress of 91.02±8.87 MPa to the stems by setting a torsion angle calculated from the dimensions of the stem. If the tool user observes damage occurring in the exterior stem tissue then the flax stem being tested is optimally-retted. If no damage is observed in the exterior stem tissue then the flax stem is in a state of under-retting. Observation of over-retting in the external tissue means that the tool user has not performed enough regular tests and missed the optimum retting point–this is unlikely to happen using this method. The maximum surface shear stress of wood enables the tool user to calculate the maximum torsion angle which can be applied to the flex stem given its dimensions.

These results highlight the effectiveness of the twisting tool in predicting the optimum retting point. This information is very helpful in predicting when the flax stem will break and how to separate the outer tissues containing the flax fibres from the stem by applying torque.

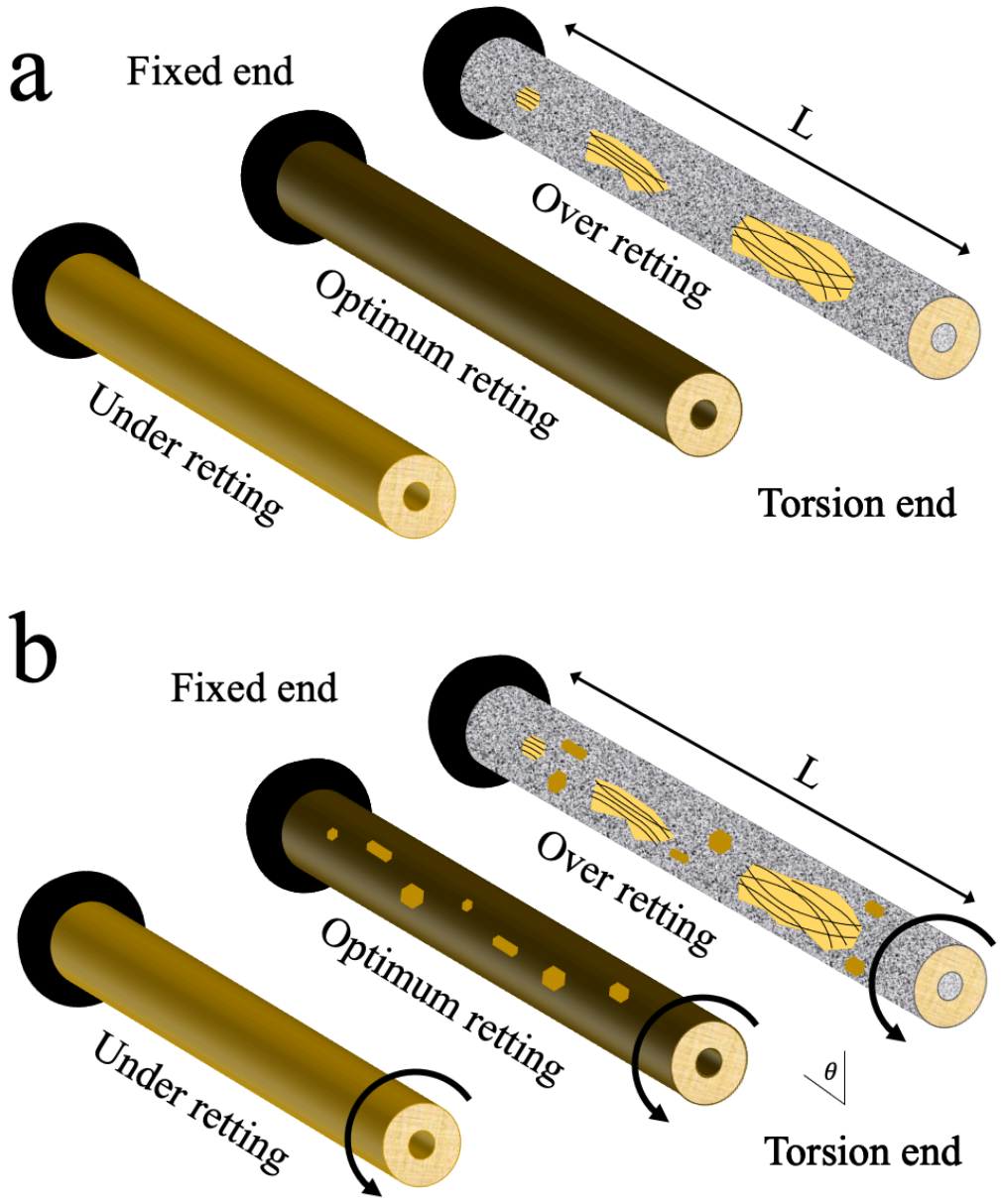

Figure 21. Schematic representations of the flax stems under torsion. (a) before torsion and (b) under torsion. The colour of the exterior tissue represents the advancement of the retting. The small yellow areas represent the damage along the stem. The black lines represent exposed fibres The unchanging inner wood portion 'xylem' is indicated in light brown.

Figure 21 shows schematic representations of the flax stems under torsion. Initially, when no torsion is applied, the optimally-retted stems show very little damage in the exterior tissue–as do the under-retted stems. However, the over-retted stems display very apparent damage in the exterior tissue–this appears soon after the optimum retting time. When torsion is applied to the stems the appearance of damage is very apparent in the optimally-retted samples. This is not the case for the under-retted samples. Some more damage is induced by the

over-retted samples by not as much as the optimally-retted samples. The application of torsion to the stems causes a torque to be induced. This torque causes a uniform surface stress to be induced over the whole of the flax stem. This is why torsion is better as revealing the optimally-retted samples than bending is. As we have seen in Chapter 3, bending induces a maximum surface stress at the base of the stem cantilever–experiments found it difficult to discern the optimally-retted samples using bending, even though it was apparent. In contrast, the induction of a surface stress over *the whole of the stem surface* by using torsion means that torsion-induced damage to the weak exterior tissue in optimally-retted stems is readily apparent to microscopy.

a

Without torsion

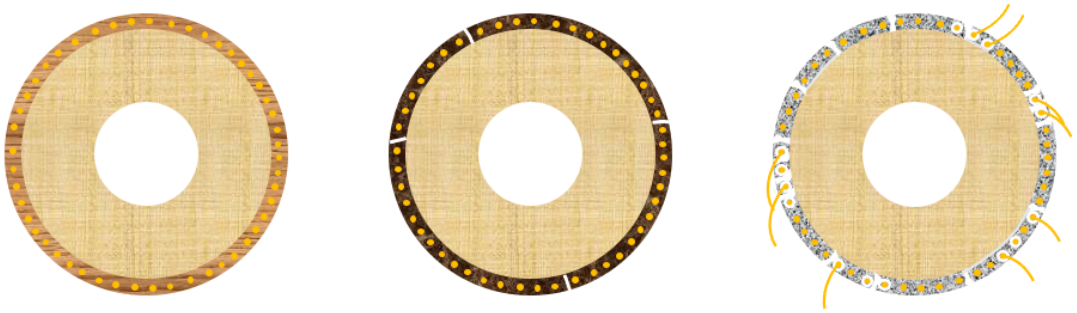

Under-retted | Optimally-retted | Over-retted

b

Low torsion

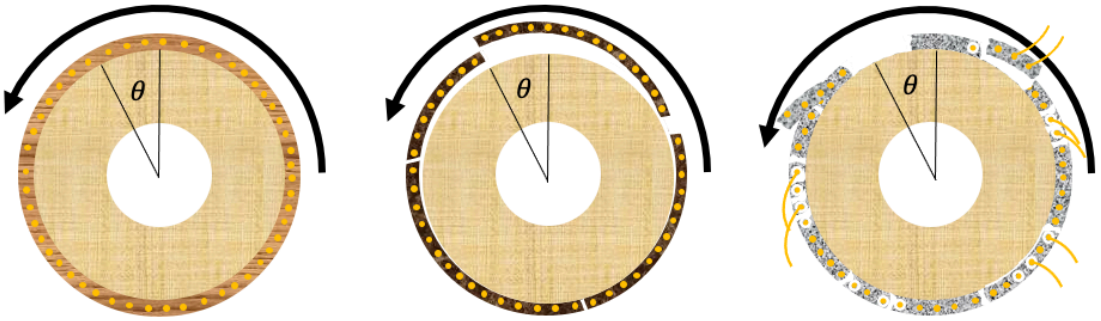

Under-retted | Optimally-retted Good Separation | Over-retted Fibre already exposed

c

High torsion

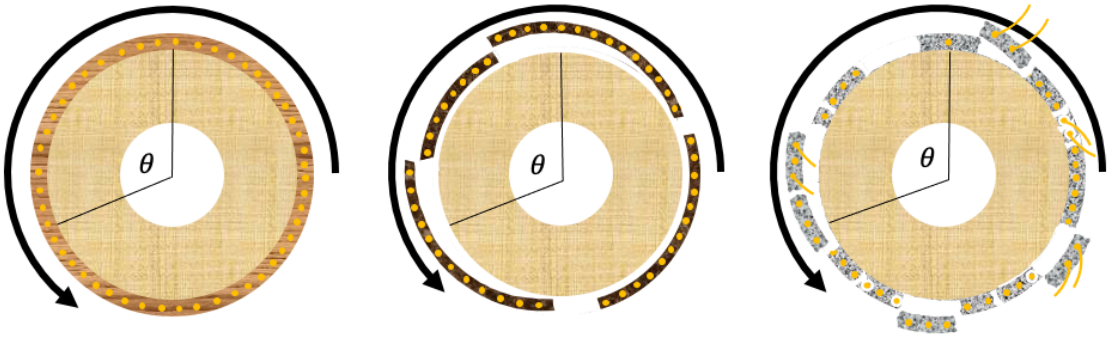

Under-retted | Optimally-retted Good Separation | Over-retted Fibre already exposed

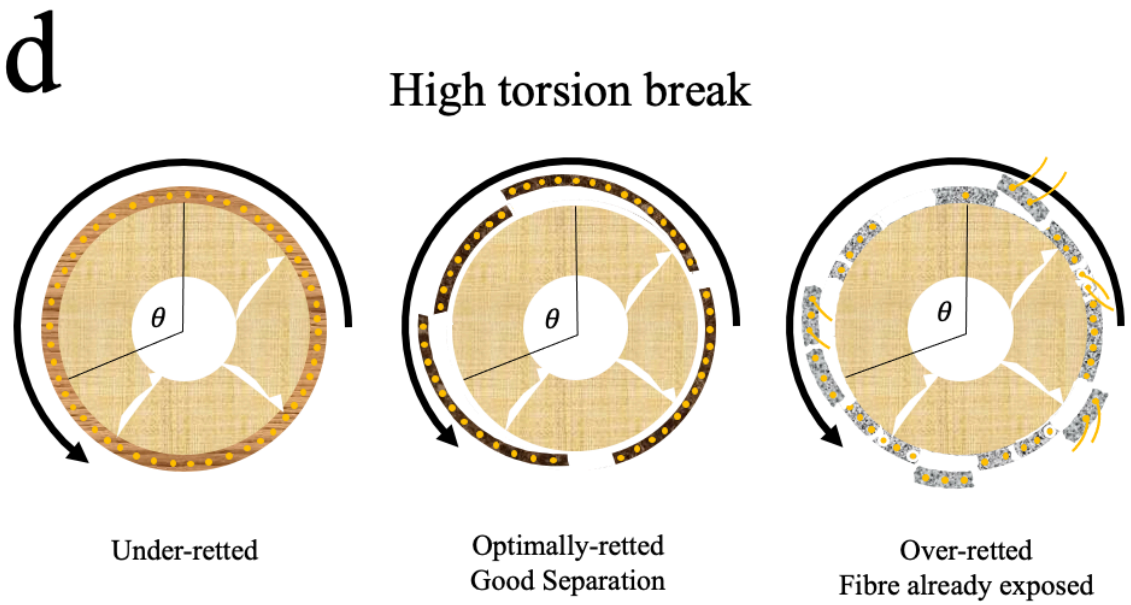

Figure 22. Schematic representation of the flax stems from under-retted, optimally-retted, and over-retted stages before (a), during low torsion (b), during high torsion (c) and during high torsion causing a break (d) . The schematic diagrams represent flax stem cross sections near to the base of the cantilever where the stress is maximum. The colour of the exterior tissue represents the advancement of the retting. The small yellow dots represent the flax fibres running along the stem. The diagrams are cross sections of a stem. The unchanging inner wood portion 'xylem' is indicated in light brown.

Figure 22 shows a schematic representation of the cross sections of flax stems (in three stages of retting) and with applied torsion. In terms of the under-retted samples, the exterior tissue is mechanically robust and strongly attached to the xylem surface. For these samples, torsion has little effect. Indeed, the xylem always breaks before any apparent damage is visible in the exterior tissue. In terms of the over-retted samples, the exterior tissue is already damaged by over-retting and no longer strongly attached to the xylem. In this case application of low torsion leads to visible increase in damage in the already-damaged external tissue. In the case of the optimally-retted samples, the exterior tissue has presumably been damaged by retting, although it is not visible at zero torsion. It is also reasonable to assume that the exterior tissue in an optimally-retted stem is not so strongly attached to the xylem as the under-retted stems. This means that for optimally-retted stems the application of torsion leads to the appearance of damage as a specific value of surface stress. Using multiple experiments it was possible to estimate this value of surface stress and therefore the torque/torsion angle required to cause visible damage for a given stem diameter (outer and inner). Finally, in all samples there is a certain torque which causes the xylem to break. This was found to be approximately the same value in all stems irrespective of the advancement of retting. This agrees well with the results for stem bending presented in Chapter 3.

The results of our study show an interesting pattern. When the samples are subjected to mechanical twisting, there are no observable changes in the stem surface before the optimum retting phase is reached. In this phase, the application of mechanical torsion (to induce a surface shear stress) causes damage in the external tissue of the flax stem–for all flax stem samples in this retting range, the computed value of surface shear stress is constant, 91.02±8.87 MPa. This suggests that the sensitivity to mechanical damage of the outer tissue is significantly increased at this particular point. These results strongly suggest that the biological process of enzymatic separation, which is responsible for removing the outer tissues, is not complete until the optimum retting point has been reached. Interestingly, we also observed obvious damage and deformation in the outer tissues of flax samples taken just after the optimum retting stage. This interesting phenomenon is observed without any requirement for mechanical twisting. Subsequently, in this case, there is the likelihood of over-retting, which potentially affects fibre quality. Furthermore, our observations strongly suggest that the attainment of the optimal retting stage is characterised by a specific condition: the shear stress required to induce shearing of the outer tissue must be significantly lower than the shear stress required to induce fracture in the inner woody tissue of the flax plant. This last point indicates that the dream of a mechanical tool to test the degree of retting in flax stems (Seaby & Mercer, 1984) is at last realisable.

Furthermore, when comparing the results for the surface shear stress and torque required to initiate fracture of the wood/internal tissues in the three phases: ‘under retting’, ‘optimal retting’, and ‘over retting’, it is evident that the shear stress required to initiate fracture of the wood/internal tissues remains constant throughout the retting period. This observation is consistent with the results of the bending experiments without external tissue (Chapter 3) and the compression experiments (Chapter 4), indicating a constant flexural modulus of the internal wood tissue over the course of retting and beyond. This supports the notion that retting predominantly affects the outer tissues while maintaining the stability of the inner woody tissues.

In addition, this experiment opens up a new way of finding out something very interesting about plant fibres: the breaking stress of the inner woody component in the flax plant. This novel parameter has remained unknown due to the lack of previous research in this area. The twisting experiment reveals a value of 180.54±21 MPa for the internal woody tissue of the flax plant.

Conclusions

Flax stems can be characterised by applying mechanical torsion. This is one of the manual mechanical tests that an artisan (farmer) conducts ‘in-the-field’ when monitoring the advancement of dew retting of harvested flax stems. The artisan judges qualitative information by hand movement and eye to assess the advancement of the retting of the flax stems. In this chapter, we have attempted to quantify this artisanal process in the lab with a view to producing a technological tool for monitoring of retting in-the-field.

To do this quantitatively we have developed an original mechanical tool. The tool enables the controlled, gradual twisting (torsion) of a flax stem. By considering the flax stem to be equivalent to a long, straight homogenous pipe, analytical modelling can be employed to compute the torque and the surface shear stress of the flax stem for a given torsion angle. This supposition enables all flax stems in the study to be compared with each other: both stems from the same retting stage and stems from retting stage to retting stage. This approach has allowed the quantitative evaluation of how the application of torsion affects the shear stress-induced damage in the external tissue of the flax stems as the retting proceeds.

It is clearly observed that damage in the external tissue of the flax stems occurs at specific values of surface shear stress for different stages of the retting. For example, in optimally-retired samples (as defined by the VRF company) we observe that a specific surface shear stress value is required for the appearance of damage in the external tissue. For retting stages less than this, no damage is observed at this value of surface shear stress, for retting stages higher than this, damage occurs at values less than this.

The experimental results suggest that a tool based on the application of mechanical torsion and image analysis could be envisaged. The results of this study therefore open up interesting possibilities. The correlation between twisting and retting leads us to consider the development of a real sensor mechanism. Such a tool, based on mechanical torsion/image analysis, could potentially revolutionise the monitoring of dew retting. In addition, this tool could serve as a predictive tool, providing insight into the optimal retting point for flax. This potential innovation promises to improve the efficiency and accuracy of retting processes, thereby contributing to the advancement of flax fibre extraction techniques.

References

Gibson, L. J. (2012). The hierarchical structure and mechanics of plant materials. *Journal of The Royal Society Interface*, *9*(76), 2749–2766. https://doi.org/10.1098/rsif.2012.0341

Niklas, K. (1997). Relative Resistance of Hollow, Septate Internodes to Twisting and Bending. *Annals of Botany*, *80*(3), 275–287. https://doi.org/10.1006/anbo.1997.0452

Pallesen, B. E. (1996). The quality of combine-harvested fibre flax for industrials purposes depends on the degree of retting. *Industrial Crops and Products*, *5*(1), 65–78. https://doi.org/10.1016/0926-6690(95)00049-6

Seaby, D. A., & Mercer, P. C. (1984). Development of a hand tool to test the degree of retting of flax straw. *Annals of Applied Biology*, *104*(3), 567–573. https://doi.org/10.1111/j.1744-7348.1984.tb03040.x

Shah, D. U., Reynolds, T. P., & Ramage, M. H. (2017). The strength of plants: Theory and experimental methods to measure the mechanical properties of stems. *Journal of Experimental Botany*, *68*(16), 4497–4516. https://doi.org/10.1093/jxb/erx245

Spatz, H.-Ch., Beismann, H., Brüchert, F., Emanns, A., & Speck, Th. (1997). Biomechanics of the giant reed *Arundo donax*. *Philosophical Transactions of the Royal Society of*

London. Series B: Biological Sciences, *352*(1349), 1–10. https://doi.org/10.1098/rstb.1997.0001

Timoshenko, S. (1986). *Strength of materials* (3rd Ed.). CBS Publishers & Distributors.

Timoshenko, S. (2010). *Theory of elasticity* (3rd Ed.). McGraw Hill Education.

Vogel, S. (1992). Twist-to-Bend Ratios and Cross-Sectional Shapes of Petioles and Stems. *Journal of Experimental Botany*, *43*(11), 1527–1532. https://doi.org/10.1093/jxb/43.11.1527

Chapter 6

Micro-mechanical testing: Effect of retting on single flax fibres

Introduction

The main conclusion from the macro-mechanical testing of flax stems Chapter 3, chapter 4, and chapter 5 was that the evolution of the properties of the exterior tissue (due to retting) is responsible for the apparent evolution of the mechanical properties of flax stems during retting. Put simply, the exterior tissue of flax stems can be considered to be a retting-enhanced degrading material (positioned between the flax fibres) with the fibres themselves running axially along the flax stem. A good question to answer is the following: do the mechanical properties of the flax fibres evolve as retting progresses? First, the mechanical properties of flax fibres have been studied by numerous groups for over a century–see Chapter 1. To do this, most groups have made use of standard tensile testing. This technique works very well for steel bars but is less accurate in giving results when microscopic diameter fibres are involved. Large error bars mean that comparison of results is different and subtle trends in data may be missed. In this chapter, in an effort to characterise the evolution of the mechanical properties of the fibres, we have developed original micromechanical techniques based on deflecting fibre-based cantilevers (dynamic and static) to reduce measurement error in an effort to observe trends as retting progresses. The results support the idea that it is the retting-induced degradation of exterior tissue between the fibres that is responsible for the evolution of the mechanical properties of the retting stems (observed in Chapter 3 and Chapter 5).
The dynamic response of a structure is a manifestation of its inherent characteristics, including material density, mechanical modulus, thermo- and viscoelastic properties, and geometric properties. Together, these factors influence how the material behaves in dynamic scenarios, dictating its damping properties and behaviour under varying forces. In this study we present a novel approach to accurately determine the flexural (bending) modulus of microscopic diameter natural fibres (flax) using microcantilever vibration analysis. Traditionally, the characterisation of the mechanical properties of fibres has relied on macroscopic methods such as tensile testing, which often results in high scatter in measurement data; furthermore, tensile testing does not accurately represent microscale or dynamic conditions and can be complex in terms of sample preparation and loading. To address this, we have developed a microscale technique involving the fabrication of microcantilevers using flat polypropylene support chips, inspired by microelectromechanical systems (MEMS) approaches. Our approach provides a refined method for accurately characterising the mechanical modulus of flax fibres, with reduced data dispersion compared to traditional macroscopic testing. Furthermore, by reducing the influence of inherent fibre defects and maintaining homogeneity along the length of the fibre, our micro-scale technique provides reliable modulus determination. This work opens up avenues for improved understanding and application of natural and man-made fibres, such as glass and optical fibres, in a variety of fields.

In the field of materials science, the determination of mechanical properties has historically relied on macroscopic vibrational methods to provide insight into various material behaviours. Such methods have been used extensively to investigate the dynamic mechanical properties of composite materials in industrial applications (Qian et al., 1997), structural membranes (Mantena, 1996), and even natural materials such as bone (Bediz et al., 2010). In addition, vibration methods have been widely used to evaluate the sound absorption and vibration damping properties of fibre composites, including glass fibres and natural flax fibres (Prabhakaran et al., 2014). Moreover, numerical models based on natural

frequency measurements from these techniques have been instrumental in assessing physical and mechanical properties, such as Young's modulus, in various materials (Ward & Sweeney, 2013). On a smaller scale, microelectromechanical systems (MEMS) and nanoelectromechanical systems (NEMS) have emerged as powerful tools for characterising mechanical properties at the micro- and nanoscale. These methods have been applied to the study of single crystal silicon, silicon-based materials (Sundararajan & Bhushan, 2002) and diamond (Espinosa et al., 2003). Recent studies using micro-cantilevers have further explored the application of vibration methods to the quantification of the behaviour of representative MEMS devices. For example, microcantilevers have been used to analyse the mechanical properties of single crystal silicon (SSC) using vibration methods (Sheehy et al., 2009). In addition, vibrational methods have found utility in macroscopic cantilevers, allowing the detection of local stiffness variations in materials and structures (Fu et al., 2012). The vibrational modes of atomic force microscope cantilevers have been used to study sample surfaces, adding to the versatility of these methods in materials characterisation (Rabe et al., 1996). Despite the wide applicability of vibration methods, the accurate determination of mechanical properties in fibres, particularly at the microscale, remains a challenge. Macroscale tensile testing has been a common approach to determining fibre properties, but often results in relatively highly scattered experimental results (Baley, 2002; Charlet et al., 2009; Richely et al., 2022; Yan et al., 2014). In particular, there has been a lack of microscale methods capable of accurately assessing the flexural modulus of fibres. Specifically, high speed camera equipment to characterise a vibrating cantilever has been used to determine the mechanical properties of materials on macroscopic (Yoo et al., 2003), microscopic (Sheehy et al., 2009), and nanoscopic scales (Basu et al., 2019) for applications ranging from sport (Pang et al., 2011) to plant mechanics (Shah et al., 2017; Zhang et al., 2022). In terms of characterising plants using cantilever techniques, Schramm *et al.*(Schramm et al., 2019) measured the elastic modulus of a vibrating wheat straw. Shioya *et al.*(Shioya et al., 2019) measured the mechanical properties of long stems of Cyperus malaccensis using high speed camera observation. To our knowledge, there has been no work concerning the transient response (using vibrational studies of cantilevers) of a single fibre-based microcantilever using high speed photography to capture the deflection.

In this chapter, we present a novel approach that overcomes the limitations of macroscopic testing by introducing a microcantilever-based vibration method for single fibres. We demonstrate how this method allows the precise determination of the flexural (bending) modulus of microscopic diameter natural fibres (flax). By taking advantage of the microcantilever technology, we demonstrate the effectiveness of this technique in accurately quantifying the mechanical properties of fibres at the microscale. Our findings contribute to the advancement of microscale material characterisation techniques and pave the way for a deeper understanding of the mechanical behaviour of natural fibres, with potential implications for various applications in industries such as composites, textiles and biomedical materials.

Modelling of vibrating single flax fibres

The resonant frequency f (first mode) of a cantilever is given by (Timoshenko, 2010; Young & Budynas, 2002):

$$f = \frac{\alpha_1^2}{2\pi}\sqrt{\frac{E_f I}{mL^4}} \quad (1)$$

Where α_1 is a constant equal to 1.875104, E_f is the flexural modulus, I is the second moment of area in the direction of the cantilever length, m is the mass per unit length of the cantilever, and L is the cantilever length.

For a cantilever having a hollow circular cross section with an outer diameter d_o and an inner diameter d_i, the second moment of area I is given by:

$$I = \frac{\pi}{64}(d_o^4 - d_i^4) \quad (2)$$

The mass per unit length m is given by:

$$m = \frac{\pi}{4}(d_o^2 - d_i^2)\rho \quad (3)$$

Substituting, simplifying, and rearranging allows us to write the bending modulus E_f of a hollow fibre cantilever as:

$$E_f = \left(\frac{2\pi f}{\alpha_1^2}\right)^2 \frac{16\rho L^4}{d_o^2 + d_i^2} \quad (4)$$

And for a solid fibre cantilever, we have:

$$E_f = \left(\frac{2\pi f}{\alpha_1^2}\right)^2 \frac{16\rho L^4}{d_o^2} \quad (5)$$

Therefore, in principle, if we carefully measure the cantilever's dimensions, its density, and its resonant frequency, we can in principle experimentally determine its flexural modulus.

Experimental

In order to experimentally test the idea of a fibre-based cantilever we chose flax fibres as the test vehicle. Retted flax samples were collected from a field belonging to the company Van Robaeys Frères (Killem, France). To conduct this research, individual flax fibres were carefully removed from the stalk of the flax plant using a methodical manual peeling technique developed by the authors. This involved making a small break at the top of the stalk to separate the outer tissue from the woody inner part. The outer tissue was then carefully peeled off using tweezers. With the aid of a pair of tweezers, straight bundles of fibres were carefully peeled from the outer tissue whilst avoiding bending of the fibres. The extraction of individual flax fibres was then carried out under a Microscope with a large working distance, this facilitates manipulation. Once a single straight flax fibre was identified within the bundle, it was carefully extracted by avoiding bending. The end of the single flax

fibre was held in place with tweezers and the fibre bundle was peeled off. A method developed by the authors was used to carefully position individual flax fibres onto flat polypropylene support chips measuring an average of 6mm x 6mm x 100µm. These polypropylene supports were carefully placed onto the support chip. To ensure secure attachment, small strips (2mm x 2mm) of adhesive tape were used. These strips of tape held the flax fibres in place and, with the aid of the microscope, bonded close to the edge to the polypropylene support, forming cantilevers that extended perpendicularly from the polypropylene support chips. The alignment (<100 µm) was important as this is the crucial 'anchoring' of the cantilever (Davis et al., 2007; Lee et al., 2011). Poorly aligned anchoring could result in spurious results. Figure 1 shows examples of the flax fibre-based cantilevers fabricated for the study.

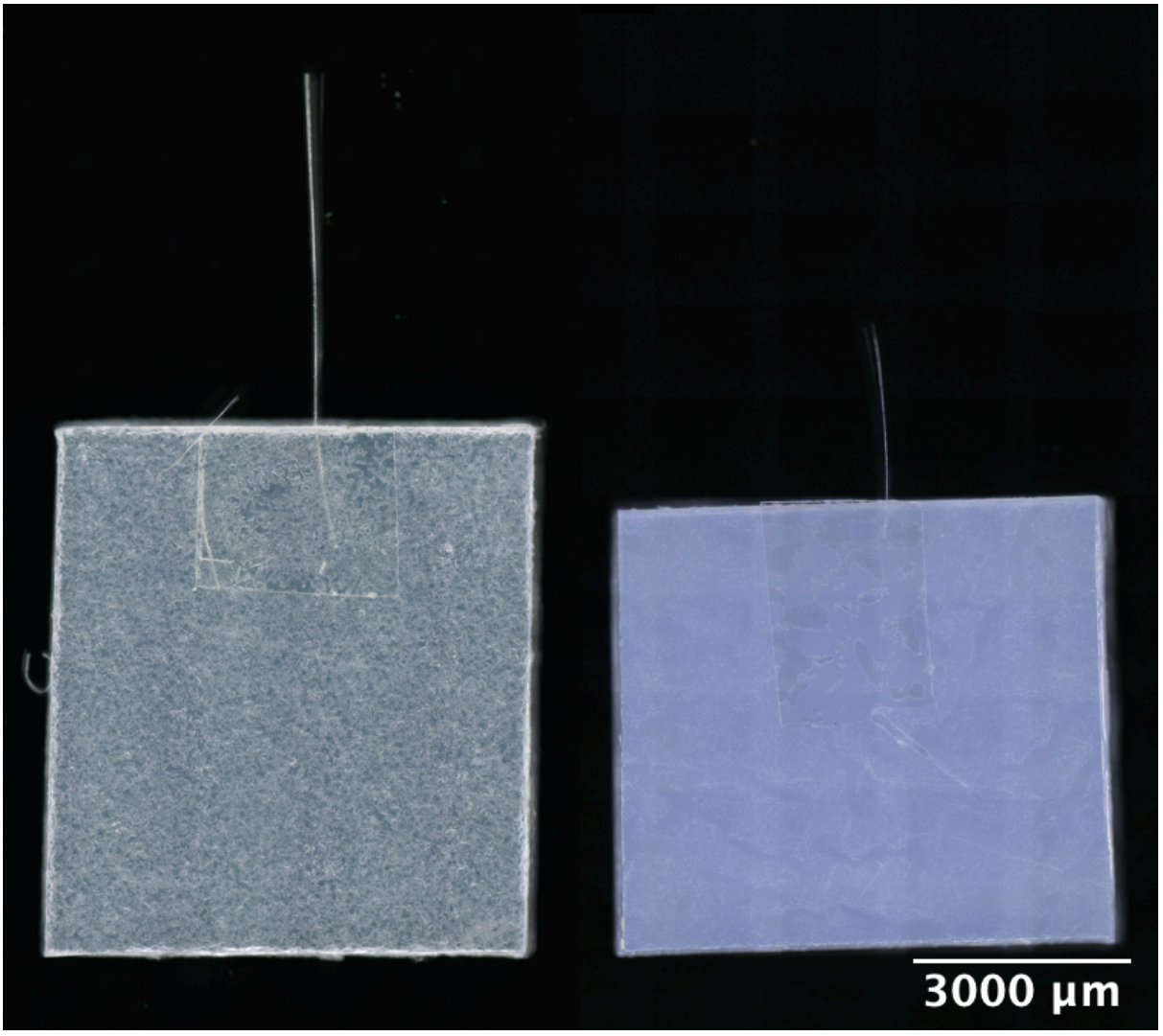

Figure 1. Digital optical microscope (DOM) images of examples of the cantilever/polypropylene support chip ensembles fabricated using our method. Single flax fibre-based cantilevers having a length of (left image) 4752 µm and (right image) 2426 µm. The diameter of the flax fibres tested in the study ranges from 20 µm to 55 µm.

Prior to performing the experiments, and for each sample, the fibre diameter, uniformity, and number of defects along their entire length was painstakingly assessed using a VHX-6000 digital optical microscopy (Keyence, France).

Figure 2 shows digital optical microscopy images of an example of the fabricated fibre-based cantilever. Figure 2(a) shows a top view of the whole fibre. Figure 2(a) and Figure 2(b) show zoomed images of top and lateral views of a single fibre-based cantilever.

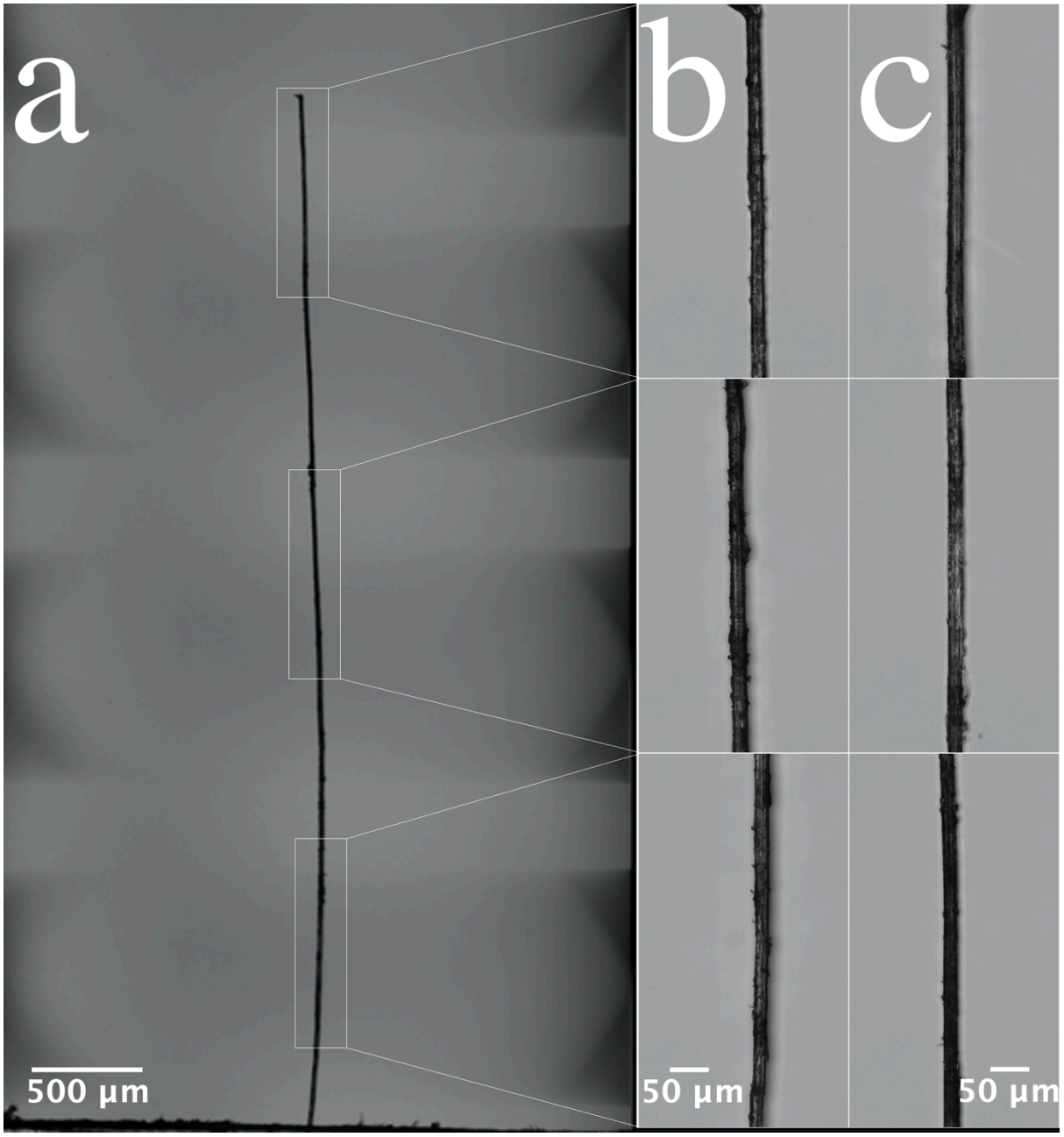

Figure 2. Digital optical microscopy images of an example of a fibre-based cantilever fabricated for the study. (a) Top view of the assembled cantilever showing whole length, (b) zoom of top view of sections and, (c) zooms of side views of sections. The fibre diameter is 20.0±1.8 µm and its length is 4670 µm

The cantilever length in Figure 2 measures 4670 um. Figure 2(b) shows a zoomed top view of the cantilever section taken from the top, centre and the bottom. The microscope objective was then tilted at a 90 degrees angle to assess the fibre diameter uniformity. The lateral section of the top, centre and bottom parts of the cantilever are shown in Figure 2(c). These microscopic images show the homogeneity in the fibre diameter all over its length where the diameter was 20.0±1.8 μm. The measurements suggest that the fibres are quasi-circular in cross sections.

However, more experiments were undertaken to demonstrate this and to quantify the hollowness of the flax fibres—something potentially important in the mechanical model. Given the hollow nature of the flax fibre, it is essential to consider its effect on the mechanical behaviour. In order to investigate this aspect, cross sections of the fibre stems were carefully prepared. Firstly, 1 cm stem samples were embedded in RL white resin and then the sections were cut with a diamond blade method described in Ref. (Goudenhooft et al., 2018). This method minimises any potential damage during the cross-section preparation process and preserves the integrity of the fibre structure. These experiments also enable us to assess the fibre cross section shape to be near circular—as the modelling assumes this to be the case. Indeed, many authors involved with tensile testing of long flax fibres assume a circular cross section.

For each fibres, 15 lateran and 15 top view diameter measurements were taken along the length. Again, The result of this is an average diameter of each tested fibre. The standard deviation of these diameters indicates the variation of the diameter along the fibre. The diameter of the fibre is never $(d \pm error)^4$ over the tested fibre. There is a diameter variation along the fibre, but it is the average diameter which governs the mechanical bending of the fibre, if (and only if) the variation of the diameter can be considered to be small and uniform along the fibre. Based on 30 diameter measurement along the lateral and the top sides of each tested fibre the error was estimated to less than5%.

Figure 3 showing cross-sections of the flax stem, providing a visual insight into the arrangement, distribution, and the cross-sectional shape of fibres within the structure.

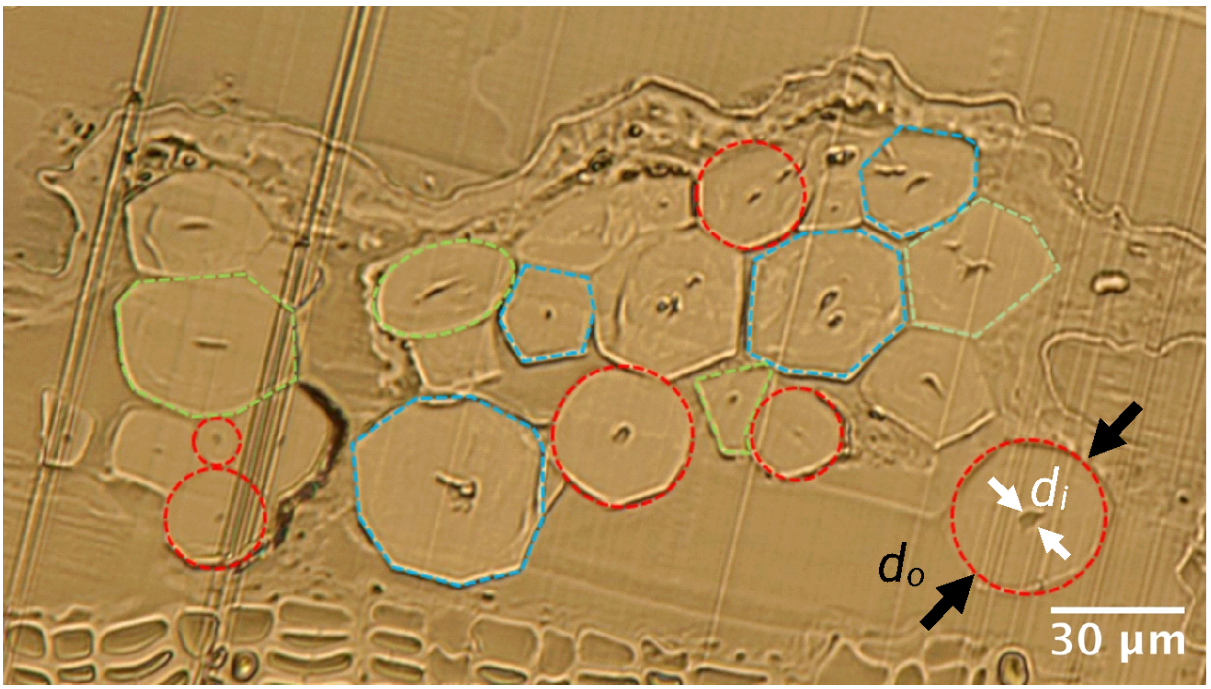

Figure 3. Digital optical microscopy image of cross sections of the flax fibres. The three principal cross-sectional shapes are circular (red), near circular (blue), and irregular (green). The outer and inner diameters of a flax fibre are shown by the black and white arrows.

Figure 3 provides valuable information about the fibre's cross-sectional shape. Figure 3 clearly shows that many fibres have a near circular cross section. Indeed, our analysis enables the identification of three types of cross section: circular (red in Figure 3), polygonal which can be approximated by a circular cross section (blue in Figure 3), and irregular shapes that cannot be approximated by a circular cross section (green in Figure 3). This last category of fibres was excluded from the study by careful observation of mounted cantilever samples. Furthermore, these cross-sectional images provide important quantitative information regarding fibre diameters (outside and inside) for the modelling in order to accurately determine the flexural modulus. Based on 50 measurements of outer and inner diameters from digital microscopy images (see black and white arrows in Figure 3), we observed that the ratio of the inner diameter to the outer diameter is less than 0.12.

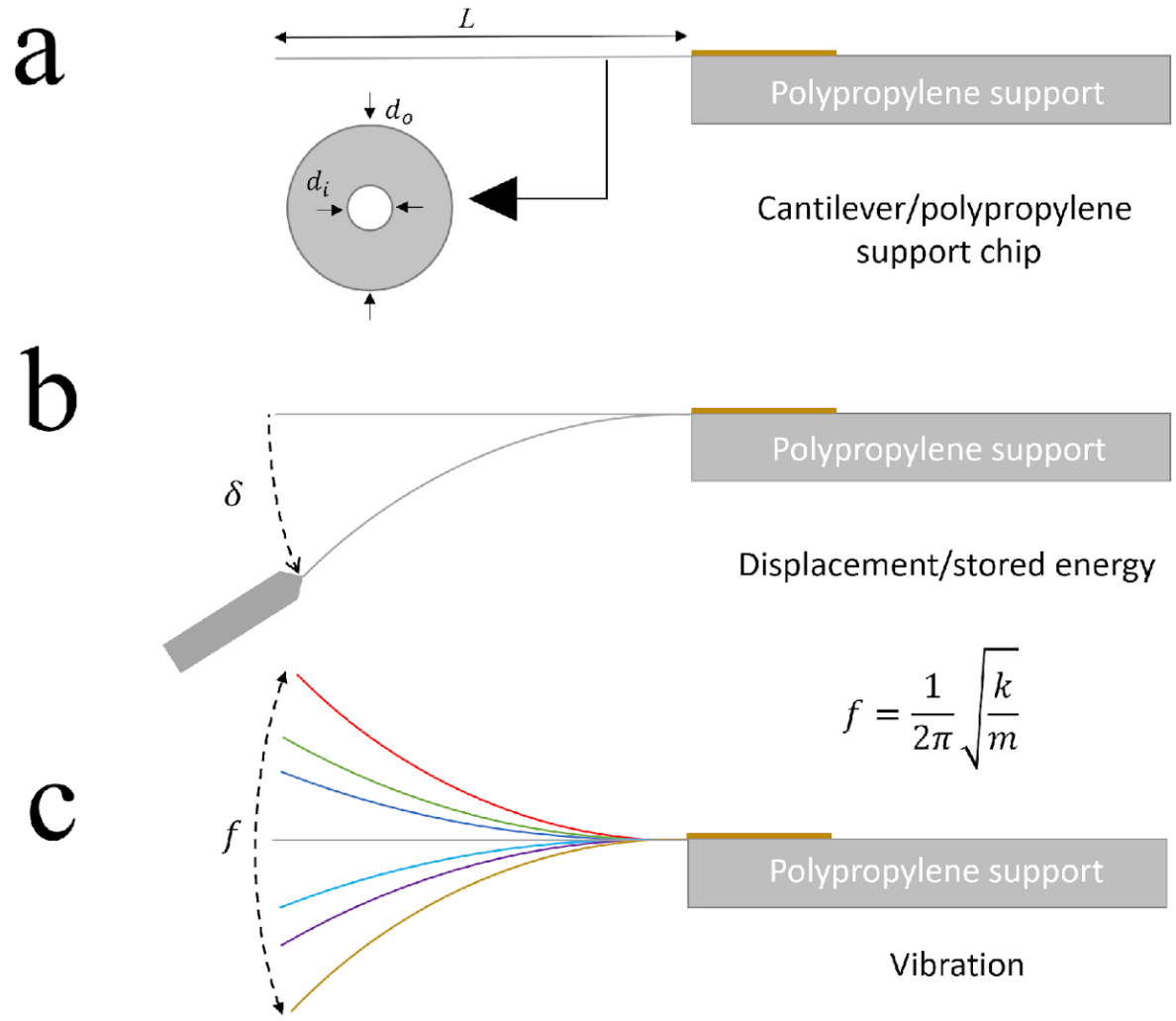

Figure 4. Schematic diagram showing the ideas (a) a hollow cylinder shape fibre-based cantilever is mounted on a polypropylene support chip. (b) a displacement stimulator is used to give the cantilever stored potential energy. (c) upon release the vibrational deflection of the fibre-based cantilever can be captured using high speed photography, analysis of this data gives the transient response of the cantilever.

Figure 4 illustrates the experimental setup used in this particular phase of the study. A single fibre cantilever/support chip configuration is carefully mounted within a high-speed camera setup. The high-speed camera was a 1280×800 pixels, 3260 fps, ISO 7000 (Vision Research, USA). Initially, the sample is positioned horizontally, and perpendicular to the support chip of the setup, in an air environment rather than a vacuum, see Figure 4(a). This configuration ensures negligible initial bending force and deflection, and a straight cantilever profile.

A displacement stimulator is then used to displace the cantilever a few hundred microns away from the central equilibrium position, causing potential stored energy to accumulate within the cantilever, see Figure 4(b). Upon release, the potential stored energy is dissipated, resulting in vibration cycles of the cantilever with diminishing amplitude due to damping (primarily air), see Figure 4(c). The transient response can be determined from the cantilever

deflection data which was captured using the high-speed camera (using frame rate of 3200 fps). The transient response can be fitted with a function to determine the first mode natural frequency. The value of this frequency enables one to determine the flexural modulus of the fibre material

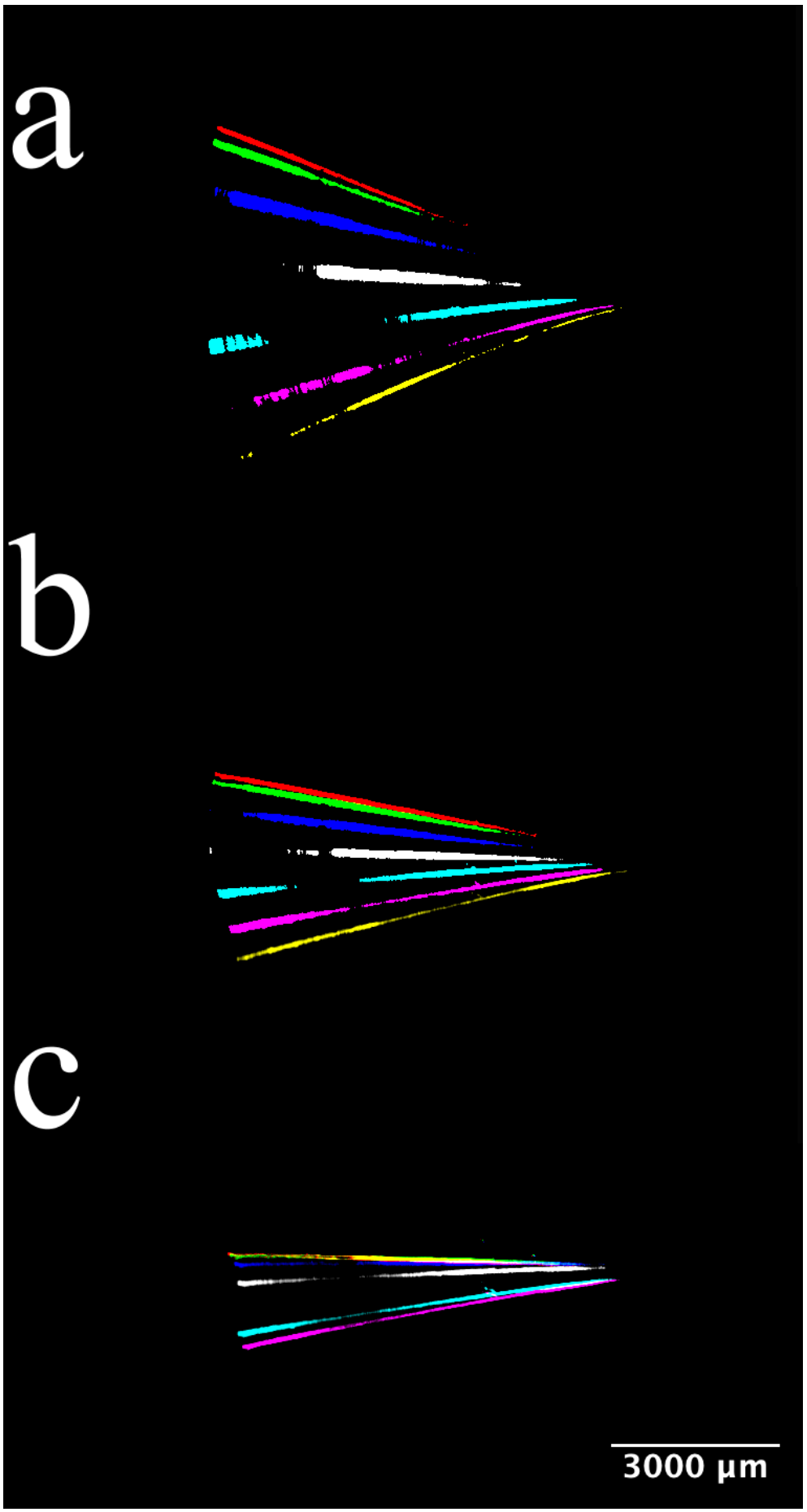
a
b
c
3000 µm

Figure 5. High-speed camera images of a vibrating flax fibre-based cantilever. (a) One half period in high amplitude regime, (b) and (c) one half periods in low amplitude regime. The cantilever has a length of 7547 μm and an average diameter of 20.9 μm. The time between each of the seven deflections shown (colours) is 312 μs.

Figure 5 shows high-speed camera images of a vibrating flax fibre-based cantilever. Damping causes the transition from the high amplitude regime, Figure 5(a), to the low amplitude regime, Figures 5(b) and 5(c). The colours correspond to different deflections of the cantilever during one half cycle—delayed by 312 μs. The deflection is the only variable parameter during damping harmonic vibration of the cantilever. In the high amplitude regime, the amplitude measures 6009 μm, see Figure 5(a). Damping causes the system to move from the high amplitude regime to the low amplitude regime, resulting in a decrease in amplitude to 3373 mm, see Figure 5(b). Towards the end of the vibration, damping causes further reduction in amplitude to 1724 μm Figure 5(c), before returning to its initial state.

Using image analysis software (Image J), video tracking analysis plugins used to extract the data. It should be noted that in Figure 5 the fibre position is sometimes blurred at lower deflections, i.e. higher velocity); in this case the deflection is measured at the centre of the fibre images. The raw data obtained from the videos, assumed to exhibit harmonic behaviour. In order to rigorously validate this assumption, a damped harmonic model is used to fit the raw data. The damped harmonic system is modelled by:

$$A(t) = A_0 e^{-\beta t} cos\,(\omega t + \varphi) \tag{6}$$

This is plotted in red alongside the raw data over the same time span, represented by the open circles.

Figure 6 shows the total transient response of a flax fibre-based cantilever over 36 ms, from the release of the motion simulator to almost the point of fibre relaxation. The data points (open black circles) correspond to measurements of the cantilever deflection extracted from the high-speed camera data. The orange curve is obtained using a numerical fitting method of Equation 6. The best fitting curve minimises the sum of the squares of the differences between the measured and model values and the good fitting of all data to an elastic model suggests that viscoelasticity in the fibers, (keryvin et al., 2015) at this scale, is not dominant.

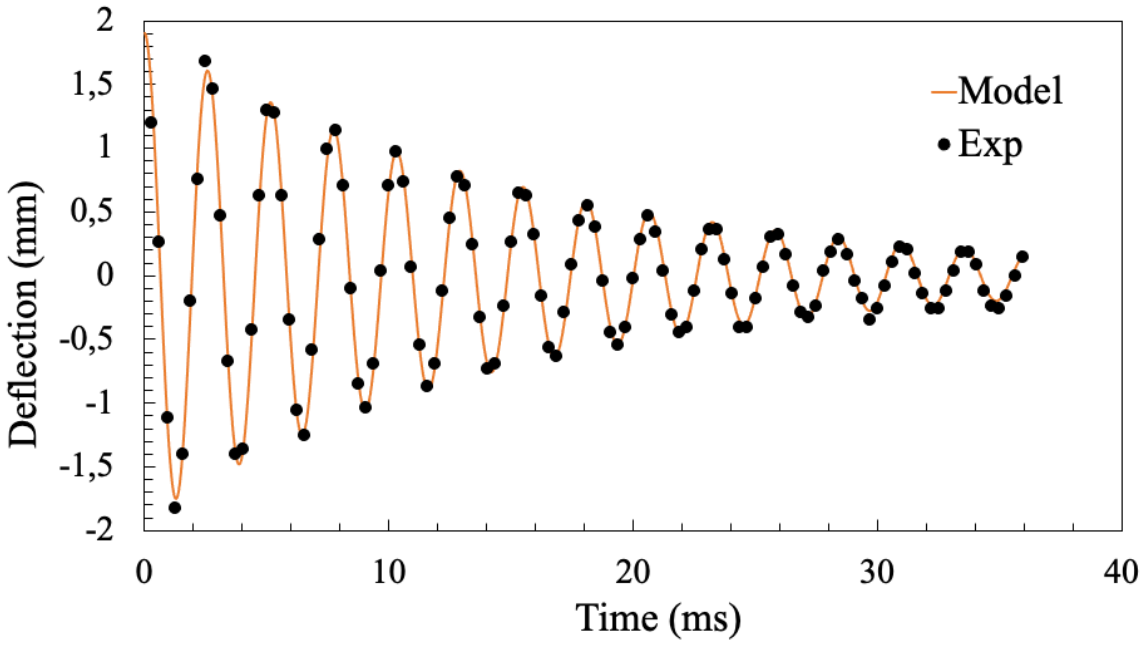

Figure 6. Transient response of the flax fibre-based cantilever. The open circles represent the raw data extracted from data analysis, and the orange curve represents a numerical fitting of the damped simple harmonic motion model in Equation 6.

However, before proceeding in determining the flexural modulus of the flax fibres, we must take two factors into account: (i) adherence to the low deflection regime (where the above solution is valid) and (ii) the contribution of air damping, something that can alter the frequency.

First, the low deflection condition (Timoshenko, 2010; Young & Budynas, 2002) must be met for the modelling to be valid. This means that the following inequality must be applied to the results:

$$\delta \leq 0.2L$$

Where δ is the deflection of the end of the cantilever and L is the length of the cantilever. By assessing the deflection where $\delta \leq 0.2L$, we can locate the low deflection regime in the damped harmonic system, as a function of time. For this particular flax fibre, the analysis revealed that the maximum deflection, relative to $\delta \leq 0.2L$ was 1.6 mm. This marked the beginning of what we defined as the low deflection regime in our study.

Figure 7 shows the transient response of the flax fibre-based cantilever in the low deflection regime.

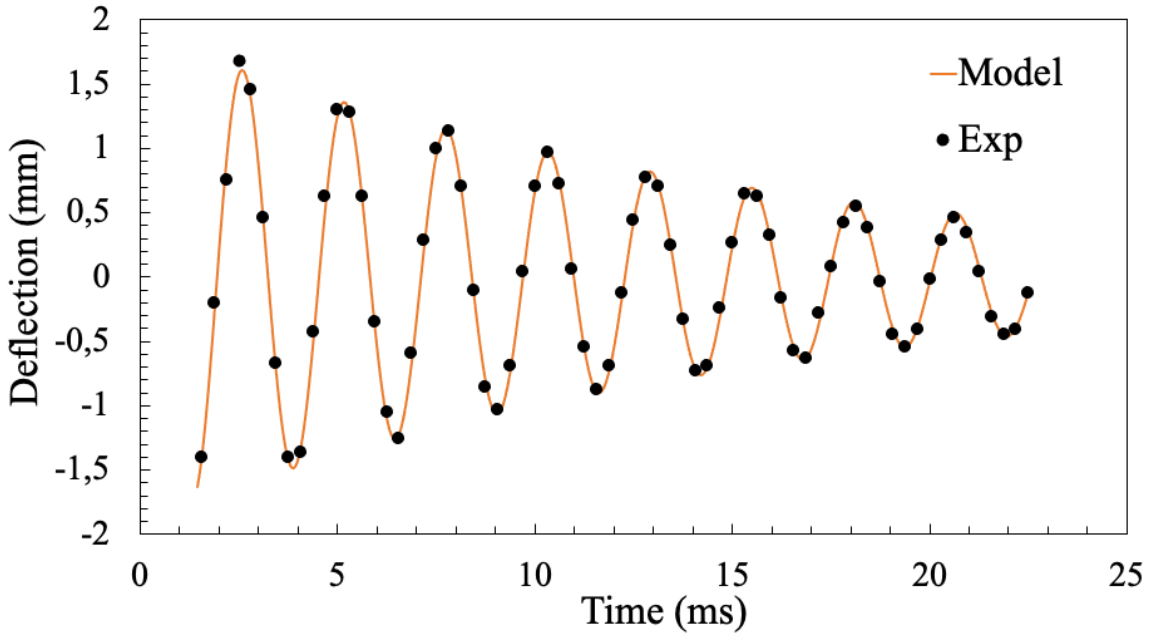

Figure 7. Transient response of the flax fibre-based cantilever in the low deflection regime. The open circles represent the raw data extracted from data analysis, and the orange curve represents a numerical fitting of the damped simple harmonic motion model in Equation 6.

This plot plays a crucial role in determining the harmonic frequency in the low deflection regime. Using the angular frequency value derived from numerically fitting the function in Equation 6 to the raw data, we can accurately determine the first mode harmonic frequency f associated with the damping that occurs in the low deflection regime by the familiar relationship:

$$f = \frac{\omega}{2\pi} \tag{7}$$

Second, air damping results in a shift of the resonant frequency—this is true for macroscopic (Baker et al., 1967) and microscopic (Albrecht et al., 1990) cantilevers. This shift, if non-negligible, would lead to an error in the estimation of the bending modulus. Let us now estimate the shift in frequency due to air damping in our vibrating fibres.

The Reynolds number Re of the system is given by (Batchelor, 2010):

$$Re = \frac{2\pi f \rho_{air} d_o^2}{\mu_{air}} \tag{8}$$

Where ρ and μ are the density and the dynamic viscosity of air. Using commonly known values (ρ_{air} = 1.293 kg m^{-3} and μ_{air} = 1.85×10^{-5} Pa s), an average frequency of the measurements of 264.5 Hz, and an average fibre diameter of 30.7 µm, we have Re = 0.11.

This means that the following equation can be used to estimate the shift in the frequency, and therefore the error in computing the flexural modulus, due to air damping (Sader et al., 1995):

$$f_{air} = f_0\sqrt{1 - \frac{1}{4Q^2}} \tag{9}$$

Where f_{air} is the resonant frequency in the presence of air damping and f_0 is the resonant frequency in the absence of air damping, and Q is the quality factor of the damped harmonic system

$$Q = \frac{\omega}{2\alpha} \tag{10}$$

The experimentally determined average quality factor Q was 8.7, this means that the ratio f_{air}/f_0 = 0.998, i.e. the presence of air damping in the experimentation does not lead to a sizeable shift in the measured resonant frequency and does not lead to a large error (<1%) in the determination of the flexural modulus of the fibres using this method. This means that the following equation is valid to extract the value of the flexural modulus from the experimental measurements:

$$E_f = \left(\frac{2\pi f_{air}}{\alpha_1^2}\right)^2 \frac{16\rho L^4}{d_o^2 + d_i^2} \tag{11}$$

Based on measurements of 18 fibre samples using the described technique, the flexural modulus of the individual flax fibres was determined. Table 1 shows the sample number and corresponding measurements of each sample.

Table 1. Summary of results.

Sample	d_o (µm)	d_i (µm)	f (Hz)	E_f (GPa)	$\frac{\delta}{L}$
S1	46.56	5.59	362.23	15.17	0.19
S2	55.45	6.65	180.60	17.23	0.18
S3	20.08	2.41	190.03	27.87	0.14
S4	36.91	4.43	385.56	18.38	0.14
S5	26.14	3.14	362.23	17.25	0.11
S6	24.55	2.94	180.60	21.61	0.20
S7	30.25	3.63	338.19	27.49	0.19
S8	40.05	4.80	210.14	15.78	0.22
S9	27.54	3.30	148.98	23.88	0.09
S10	22.16	2.66	160.83	26.56	0.13
S11	24.59	2.95	313.69	23.82	0.14
S12	20.93	2.51	276.07	29.92	0.16
S13	33.92	4.07	501.98	14.60	0.30

S14	25.03	3.00	111.47	34.83	0.19
S15	25.03	3.00	214.83	13.98	0.23
S16	35.95	4.31	248.41	28.09	0.12
S17	25.07	3.01	190.03	31.25	0.09
S18	33.20	3.98	385.56	15.75	0.18

As a result, and despite the considerable variation in fibre diameter, ranging from 20 to 55 µm, and a frequency ranging from 111 to 502 Hz, the model was able to accurately determine a flexural modulus of the flax fibres to be 22.41±6.60 GPa. The dispersion in the results is better than that which would be obtained using macro-mechanical testing, e.g. tensile testing. Indeed, our results agree well with previously reported values of the elastic modulus of flax fibres (Faruk et al., 2012; Mohanty et al., 2000), knowing that the value comes from work originally published in 1982 (Sridhar et al., 1982).

Discussion of this part

This study shows that the fabrication and mounting of the samples using polypropylene chips and Scotch tape is straightforward, inexpensive and fast. However, we found that the extraction of single flax fibre samples required careful attention to avoid the presence of multiple fibres, which could affect the accuracy of the measurements. The fabrication process itself is efficient, involving the use of a polypropylene chip and the rigorous attachment of the flax fibre sample perpendicular to the edge of the chip. Microscopic assistance during fabrication was found to be beneficial, ensuring that the fibre was accurately attached to the edge of the chip, thus avoiding any spurious effects due to poor cantilever anchoring.

In terms of measurements, this technique offers a simplified setup compared to macroscopic testing, e.g. tensile tests, requiring only a high-speed camera to record the vibrations and a readily available object to act as a vibration stimulator. Subsequent analysis of the recorded video is straightforward, facilitated by image analysis software that allows us to track the maximum deflection of the tip of the cantilever. Digital optical microscopy enables a measurement of required fibre dimensions, such as diameter and length, to fit the model.

In this study, we found that the flax fibre can be assumed to be very close to a hollow pipe shape, which allowed us to use analytical modelling to accurately estimate the flexural modulus from the natural frequency. Our results successfully validated our assumption and the use of the damped harmonic vibration model, which proved to be highly effective in extracting the flexural modulus of the flax fibre. Importantly, this micro-scale approach allowed us to accurately determine the fibre flexural modulus even for small fibre lengths, resulting in significantly reduced data scatter compared to conventional macro-scale mechanical tests such as tensile testing.

This study demonstrates that the proposed model, initially validated for the low deflection regime, can be reliably extended to accurately extract the modulus even in the high deflection regime. We observed that the performance of the model in the high deflection regime, where the deflections are still relatively small compared to the total fibre length, gave accurate and consistent results. Our results show no frequency shift between the high and

low deflection regimes, indicating that it remains robust and applicable for deflections up to 30% of the fibre length.

Remarkably, the success of our microscale approach extends beyond the precise determination of modulus. It is well known that natural fibres, such as flax, often have numerous surface defects and kinks that can significantly affect their mechanical behaviour. In our approach, we strategically reduced the sample length tested from a few centimetres, as typically used in tensile testing, to a few hundred micrometres. This deliberate reduction effectively minimised the likelihood of encountering defects and ensured a high level of sample homogeneity along the entire length of the fibre. This allowed us to almost eliminate the effect of surface defects on the mechanical behaviour of the fibres. This aspect played a key role in improving the accuracy and reliability of the modulus extraction process. Thus, using our micro-scale method, we achieved good precision with error bars and standard deviations in the narrow range of ±6 GPa, a significant improvement over the wider range often observed in standard traditional tensile tests on longer samples, where large scatter and dispersion in data is seen. The results obtained from our approach thus demonstrate the effectiveness of our strategy inspired by MEMS testing in achieving accurate characterisation of flax fibre properties while minimising the potential disturbances arising from inherent structural irregularities.

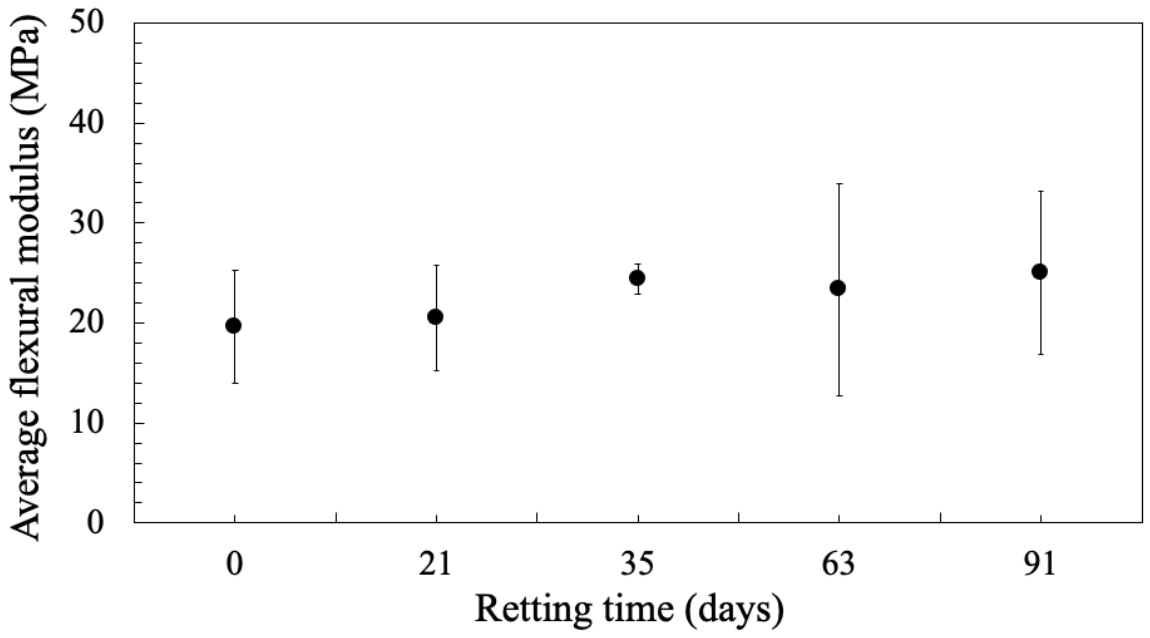

Figure 8. Evolution of the flexural modulus of single flax fibres as a function of retting time.

The flexural modulus of the fibre during the retting period including under, optimal and over retting was determined through testing a data set of 18 samples. These tests result in an average flexural modulus value of 22.41±6.6 GPa. This vibration cantilever-based technique provides a low error and dispersion data when compared to that which may be obtained using macroscopic tensile testing methods.

Our results agree very well with those obtained by (Capron et al., 2017). “Caractérisation mécanique de la paroi cellulaire des fibres végétales par Microscopie à Force Atomique”. In *CFM 2017-23ème Congrès Français de Mécanique*. Capron et al. used (Peak-Force QNM) AFM to semi-quantitatively measure the modulus of cross sections of flax fibres, i.e. a totally different measurement technique to ours. Their results indicate a value of around 20 GPa for the whole fibre.

Verification of the dynamically-measured modulus using a static bending approach

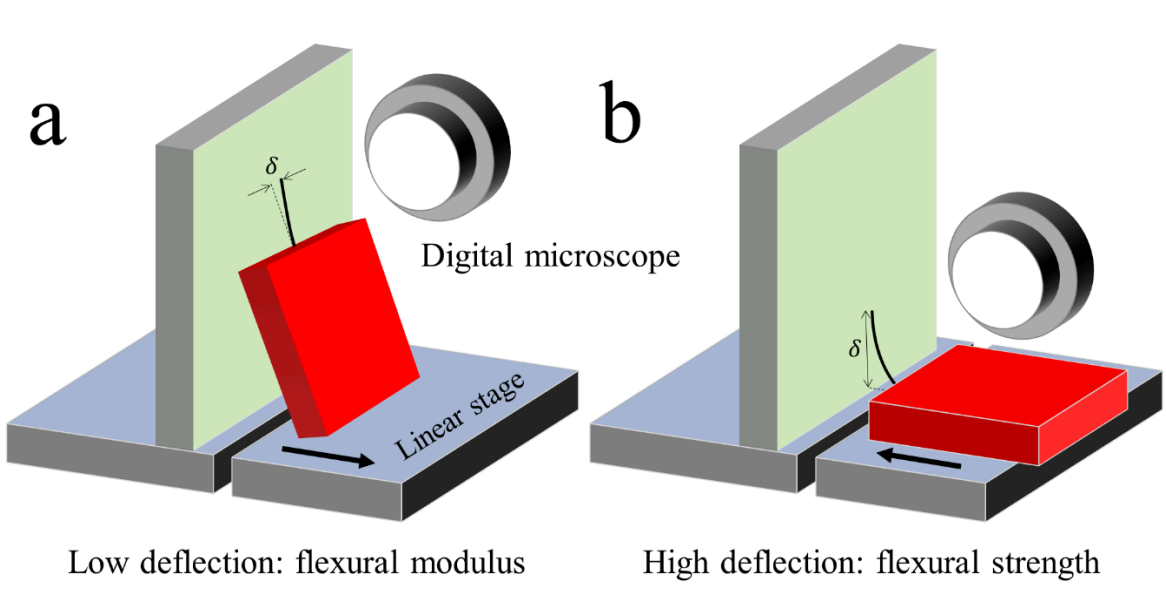

Figure 9. Schematic diagrams showing the two MEMS-inspired measurements developed in the study. (a) Low deflection of a fibre-based microcantilever using the self-weight of the support chip to measure the flexural modulus. (b) High deflection of a fibre-based microcantilever to measure the breaking stress. The support chip (red) is moved using a precision linear stage.

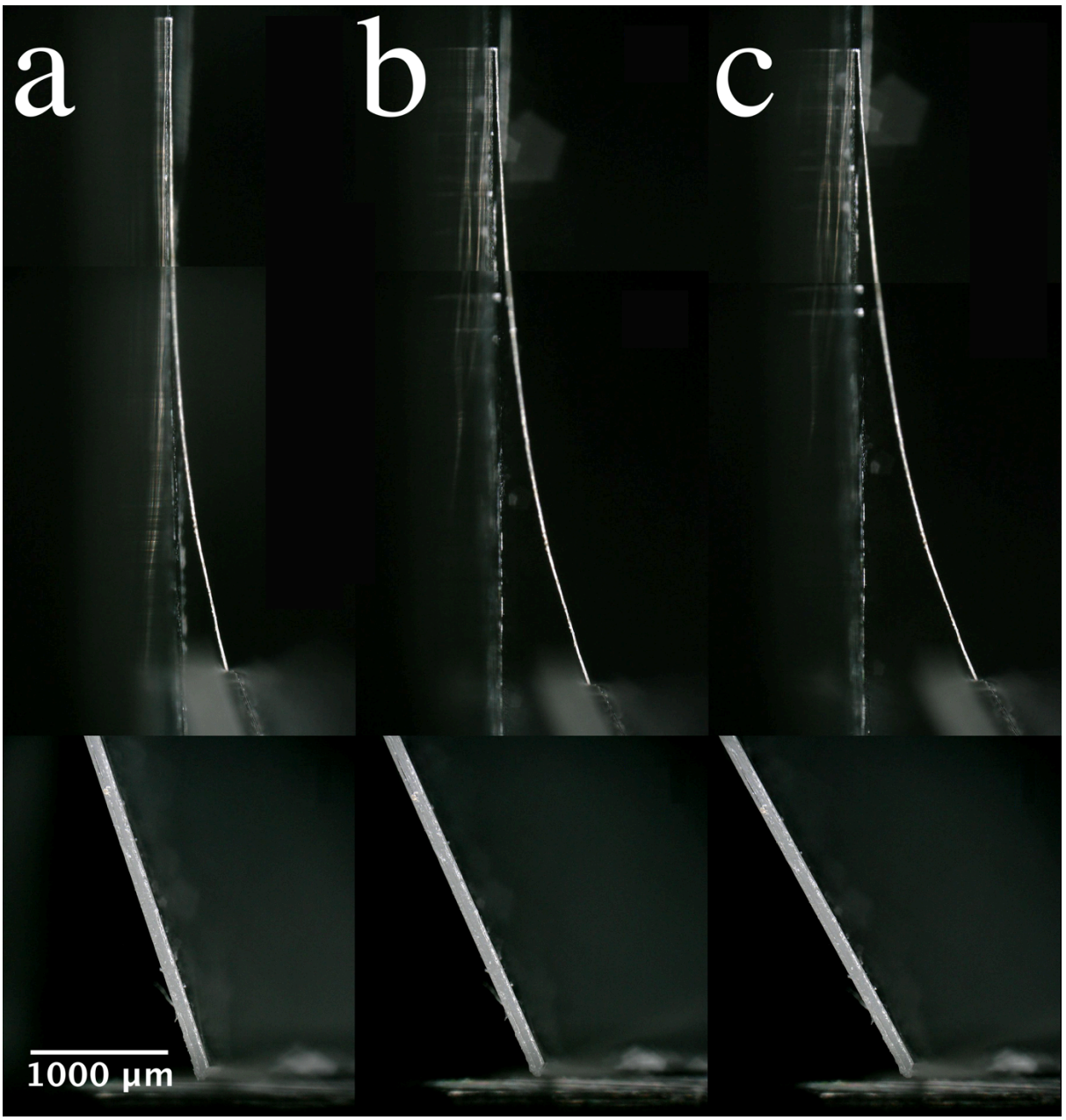

Figure 10. Stitched optical images of deflecting single flax fibre cantilevers obtained using our micromechanical approach and digital optical microscopy. Upper images show the microcantilevers defecting, lower images show the support chip angle varying. The support chip leaning angle is (a) 71.7°, (b), 65.9° and (c) 61.4°. The length of the flax fibre-based cantilever is 4752.6 µm and the diameter is 18.5 µm. The length of the support chip is 7227 µm.

Using these methods, the flexural modulus of flax fibres was evaluated to be 22.9±3.7 GPa. This agrees extraordinarily well with the value of the flexural modulus measured using dynamic methods–a completely different approach.

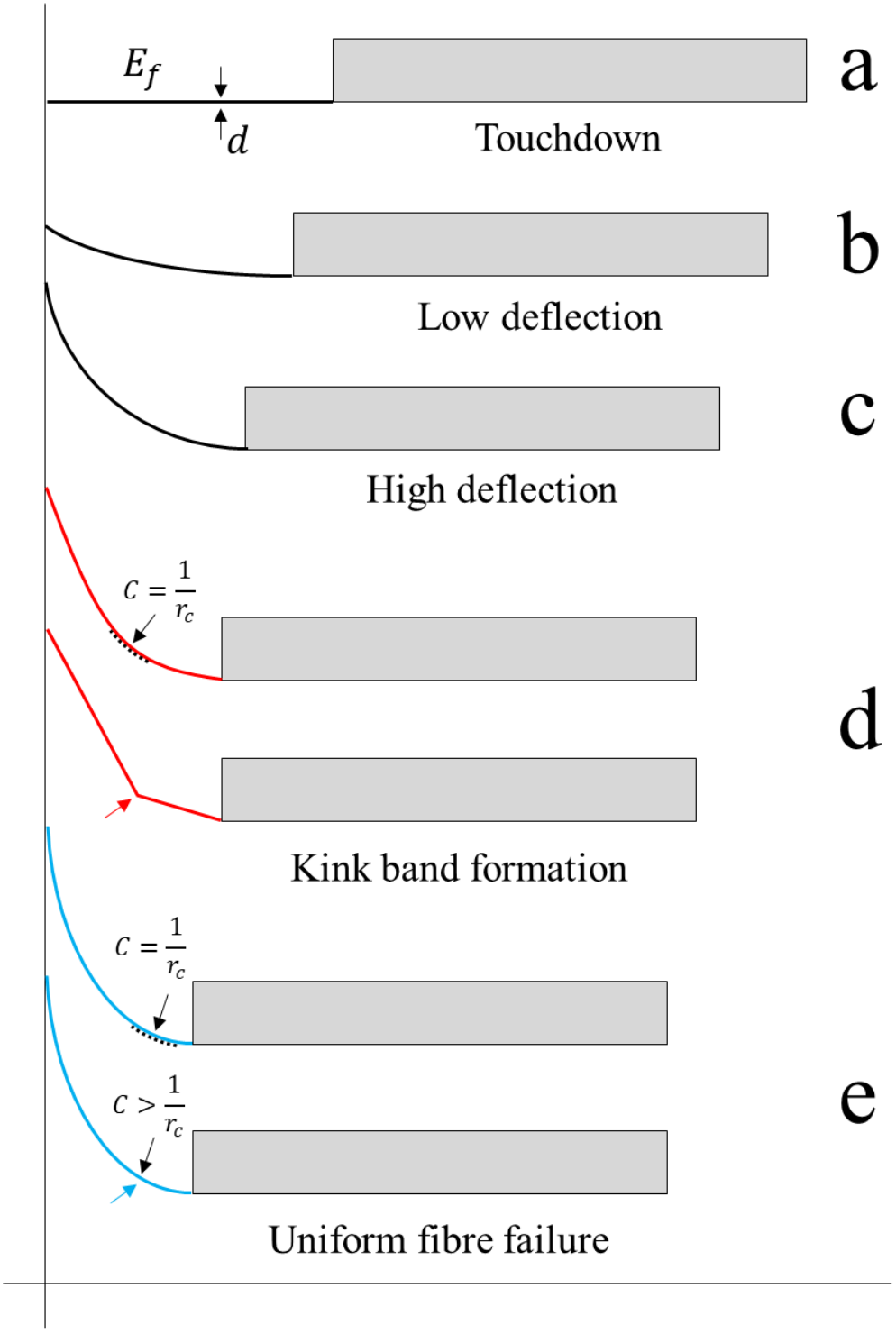

Figure 11. Schematic diagram shows the high deflection micromechanical measurements of the fibre-based cantilevers. (a) Touchdown of the fibre, (b) low deflection causing the tip of the cantilever to skate up the wall, (c) high deflection causing large curvature in parts of the

cantilever, (d) formation of a visible kink band (red arrow), and (e) uniform fibre break (blue arrow) with no kink band formation. The fibres have a diameter d and a flexural modulus E_f. The local curvature C at the breaking point is experimentally measured.

Modelling of the breaking strength of single flax fibres

Based the reasoning of Sinclair(Sinclair, 1950) and Fukuda et al,(Fukuda et al., 1999) the surface strain ε of a bending fibre in is given by the following relationship:

$$\varepsilon = \frac{dC}{2} \tag{13}$$

Where d is the diameter of the fibre and C is the curvature (m^{-1}) of the bending fibre. A positive curvature corresponds to a positive strain (elongation) at the bottom surface of the bending fibre in Figure 10. The top of the fibre has negative curvature and will have negative strain (contraction). Mechanical stress σ is defined as:(Timoshenko, 2010)

$$\sigma = \varepsilon E \tag{14}$$

Where E is the mechanical modulus. We can combine the above equations to give the flexural strength σ_f as:

$$\sigma_f = \frac{d_o C_{max} E_f}{2} \tag{15}$$

Where d_o is the outer diameter of the fibre—see above. C_{max} is the maximum curvature along the bending fibre at breaking, and E_f is the flexural modulus of the fibre. Note that a positive curvature gives a positive (tensile) stress at one surface of the fibre. A negative curvature at the other surface of the fibre corresponds to a negative (compressive) stress. As we will see, fibre failure is evident from the experiments. This results in a very apparent change of fibre deflection shape.

Experiment and results

Uniform single fibre-based microcantilever/polypropylene support chips were fabricated using the methods described above. Again, before measurement the fibres were checked for defects and controlled for their diameter, uniformity, and deflect density (visible kink bands). To obtain a high flexural stress a large curvature is required. This was achieved by high deflection of the cantilever-based samples. The samples were fixed to the mechanical apparatus and the fibre cantilevers deflected by moving the support laterally toward the vertical surface—this is done by moving the precision linear stage—see Figure 1b and Figure 10. The tip of the cantilever makes contact with the surface and skates up the surface causing curvature of the fibre. The curvature of the fibre causes tensile and compressive stresses to be generated—having a maximum at the surface of the fibre and where the curvature is maximum. The process is gradually performed taking multiple high-resolution photographs using digital optical microscopy.

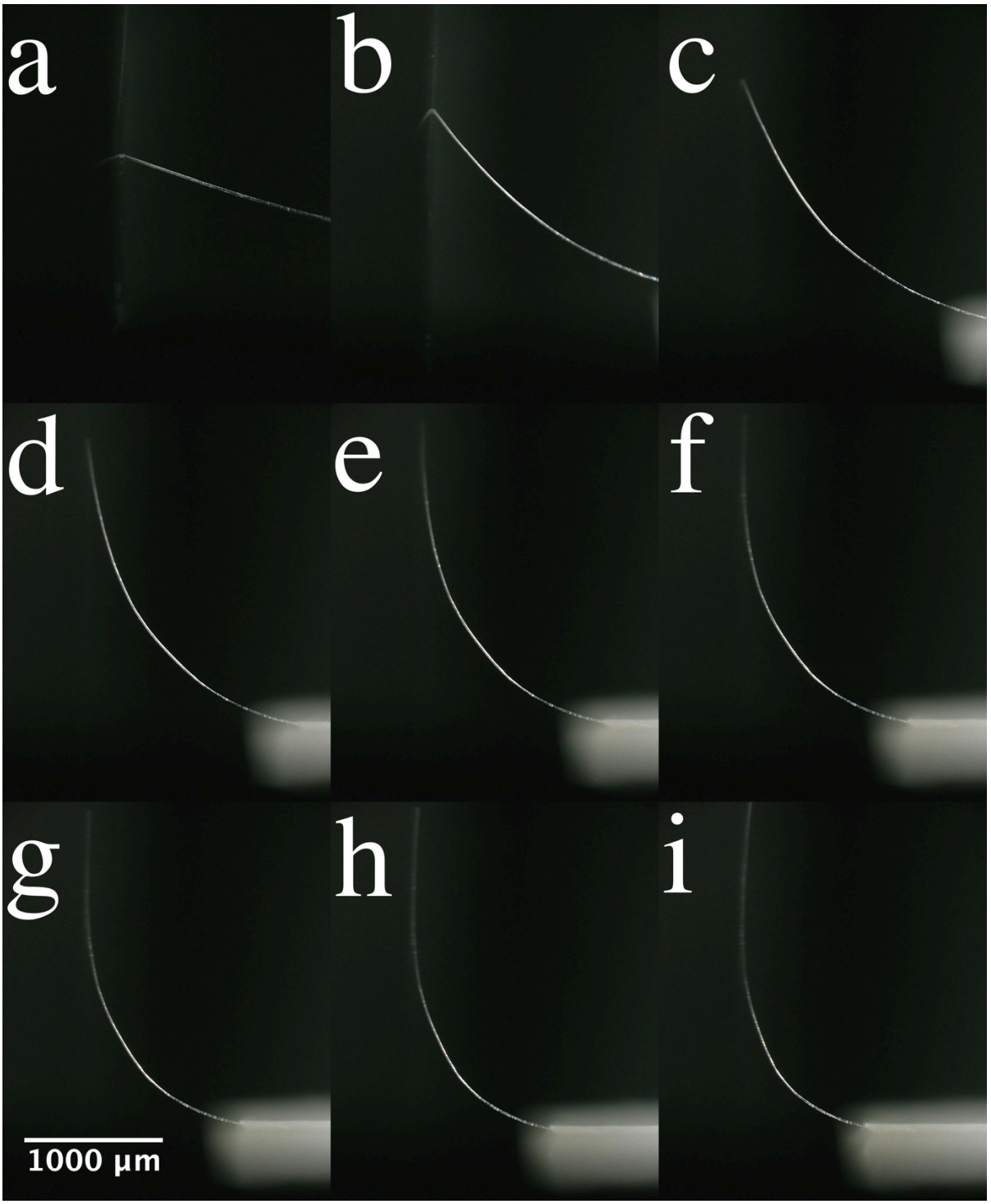

Figure 12. Stitched optical images of highly-deflecting single flax fibre based microcantilevers obtained using our micromechanical approach and digital optical microscopy. The upward skating of the tip and the resulting cantilever bending and local curvature is apparent as the precision linear stage moves the support chip towards the vertical surface.

Figure 11 shows examples of photographs taken sequentially by digital optical microscopy of the deflection profile of the cantilever using our micromechanical technique. Figure 11a shows the initial state of the fibre, without any induced deflection, where it experiences a minimal self-deflection, which is negligible as previously discussed. Subsequently, as the mechanical support of the apparatus undergoes lateral movement, the fibre enters a high deflection regime. This deflection continues progressively, as shown by the sequential progression from Figures 11b to 11i, until a breaking point (fibre mechanical failure) is reached. These microscopic images shown in Figure 11 play a crucial role in clarifying the radius of curvature and hence the precision of the flexural strength of the fibre. The break occurs at the minimum radius of curvature, i.e. the point of maximum curvature, and is extracted from the microscopic images prior to any failure resulting in either the kink band or the uniform fibre section (see methods).

Figure 12 illustrates the process of the extraction of the radius of curvature. This is achieved digitally by fitting a function to the curve traced out by the bending fibre. The software is then able to mathematically compute the maximum curvature along the bending fibre.

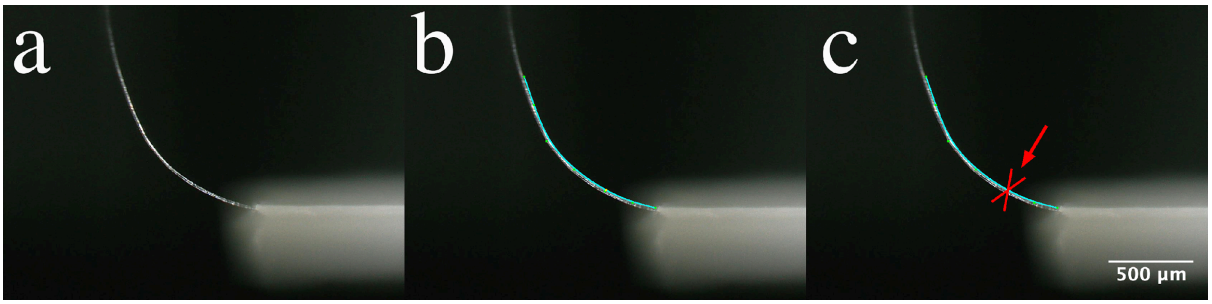

Figure 13. Extraction of the maximum curvature along the deflecting fibre-based cantilever. (a) Digital optical microscopy captures the fibre just prior to failure, (b) a curve is mathematically fitted to the image, and (c) the maximum curvature is computed from the fitting function.

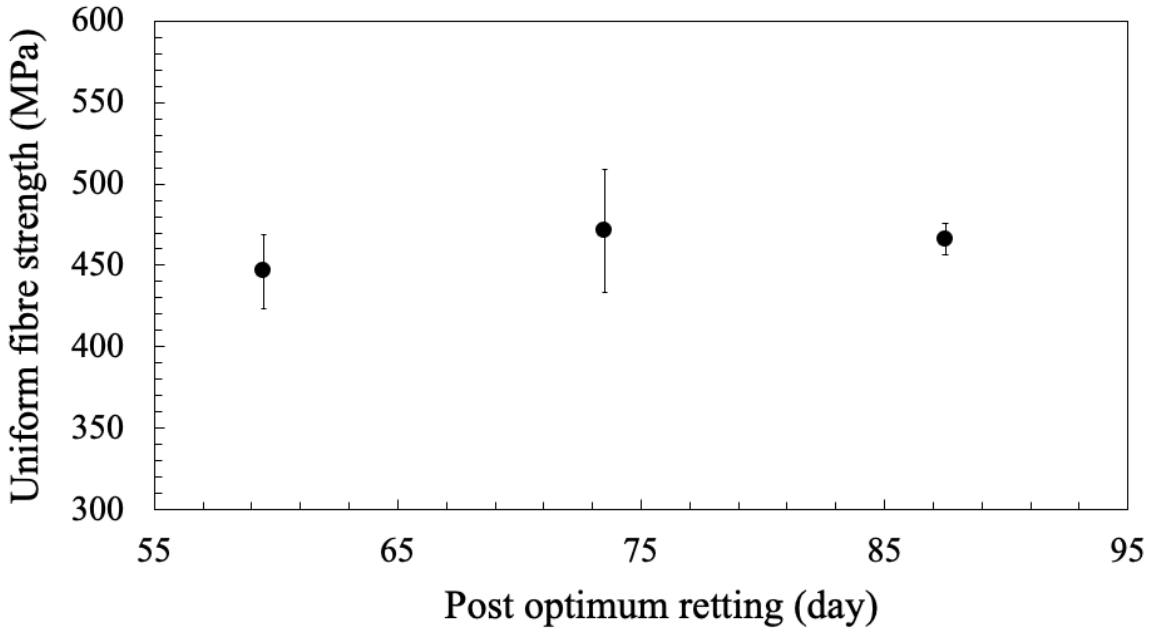

Figure 14. Evolution of the flexural strength of single flax fibres as a function of the retting period.

The exact flexural strength of the fibre was determined through testing a data set of 11 samples. These tests result in an average flexural strength value of 459.03±28.06 MPa. Our original cantilever-based technique provides a low data dispersion data. The error in these measurements is much smaller compared to that which may be obtained using macroscopic tensile testing means.

Figure 15 provides a visual representation of the intricate and heterogeneous structure found within flax fibres. As discussed in the introduction, these fibres are composed of primary and secondary cell walls, each of which has a different chemical composition. This variability in composition contributes to differences in fibre orientation. However, the purpose of mentioning fibre composition at this point is to emphasise the complexity inherent in fibre structure. Our focus here is to emphasise that the flexural modulus measurements obtained from our micromechanical approaches reflect the overall stiffness and strength of this heterogeneous complex composite material. This includes consideration of the cell wall structure and associated chemical composition.

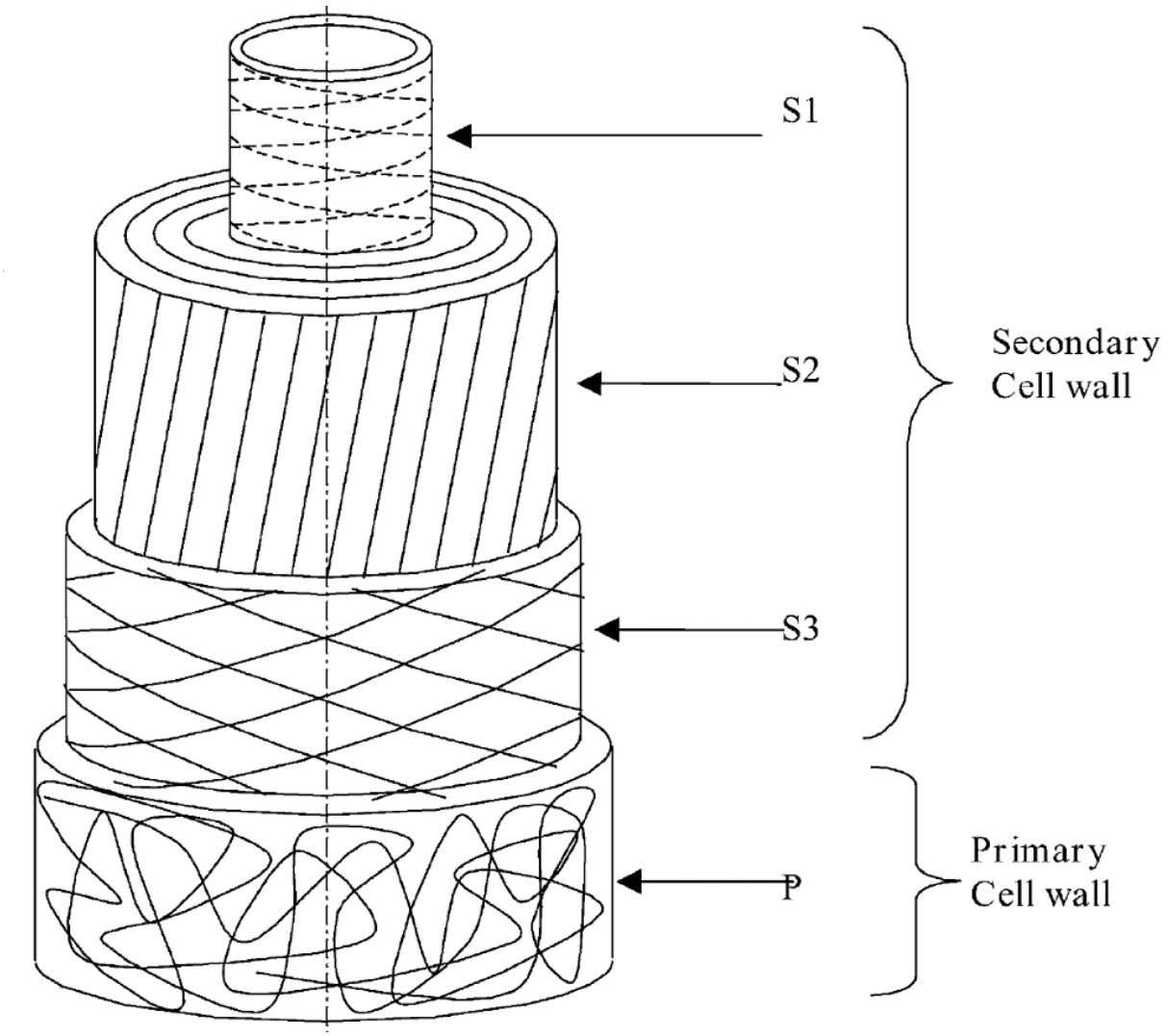

Figure 15. The heterogenous flax fibre structure, taken from (Baley, 2002).

Our results agree very well with those obtained by (Capron et al., 2017). “Caractérisation mécanique de la paroi cellulaire des fibres végétales par Microscopie à Force Atomique”. In *CFM 2017-23ème Congrès Français de Mécanique*. Capron et al. used (Peak-Force QNM) AFM to semi-quantitatively measure the modulus of cross sections of flax fibres, i.e. a totally different measurement technique to ours. Their results indicate a value of around 20 GPa for the whole fibre.

Conclusions

The previous chapters indicate that the mechanical properties (measured using bending and torsion) of flax stems are modified by dew retting. The results of those chapters suggested that it was the retting-induced degradation of the external tissue that was responsible for the modification of the mechanical properties. The external tissue is composed of flax fibres and the material (middle lamella) between the fibres. In order to go further in an understanding of

the macromechanical observations this chapter has presented original micromechanical characterisation of flax fibres at various stages of retting. In order to do this, original approaches for micromechanical measurements of flax fibres were conceived and developed based on MEMS-inspired cantilever techniques. The measurements enabled the flexural modulus and the flexural strength of flax fibres to be evaluated as a function of retting. A key point is the following. Where traditional techniques such as tensile testing can result in very large errors, our micromechanical approaches result in relatively small errors. This means that one can have more confidence in data trends.

The measurements suggest that the mechanical properties of the flax fibres do not change significantly during retting. This implies that the observed modification of the mechanical properties in the flax stems (due to retting) is in fact due to the degradation of the middle lamella material–and it is precisely this degradation which permits an easier extraction of fibres in the factory.

However, like flax stems, flax fibres themselves are heterogeneous, complex structures. Therefore, in the next chapter we decided to conduct nanomechanical characterisation (nanoindentation AFM) on the external tissue of flax fibres. The reasoning behind this is that the retting-induced damage to the middle lamella is present at the surface of the fibres rather than the interior. It seems logical thus to conduct tests on the outside of fibres to see if there is indeed any retting-induced modification of fibre surfaces–especially in over-retted samples.

References

Albrecht, T. R., Akamine, S., Carver, T. E., & Quate, C. F. (1990). Microfabrication of cantilever styli for the atomic force microscope. *Journal of Vacuum Science & Technology A: Vacuum, Surfaces, and Films*, *8*(4), 3386–3396. https://doi.org/10.1116/1.576520

Baker, W. E., Woolam, W. E., & Young, D. (1967). Air and internal damping of thin cantilever beams. *International Journal of Mechanical Sciences*, *9*(11), 743–766. https://doi.org/10.1016/0020-7403(67)90032-X

Baley, C. (2002). Analysis of the flax fibres tensile behaviour and analysis of the tensile stiffness increase. *Composites Part A: Applied Science and Manufacturing*, *33*(7), 939–948. https://doi.org/10.1016/S1359-835X(02)00040-4

Basu, A. K., Sah, A. N., Pradhan, A., & Bhattacharya, S. (2019). BSA Detection on Polymeric Nanocantilever. In M. Kumar, R. K. Pandey, & V. Kumar (Eds.), *Advances in Interdisciplinary Engineering* (pp. 589–594). Springer Singapore. https://doi.org/10.1007/978-981-13-6577-5_56

Batchelor, G. K. (2010). *An Introduction to fluid dynamics*. Cambridge Univ. Press.

Bediz, B., Nevzat Özgüven, H., & Korkusuz, F. (2010). Vibration measurements predict the mechanical properties of human tibia. *Clinical Biomechanics*, *25*(4), 365–371. https://doi.org/10.1016/j.clinbiomech.2010.01.002

Charlet, K., Eve, S., Jernot, J. P., Gomina, M., & Breard, J. (2009). Tensile deformation of a flax fiber. *Procedia Engineering*, *1*(1), 233–236. https://doi.org/10.1016/j.proeng.2009.06.055

Davis, Z. J., Svendsen, W., & Boisen, A. (2007). Design, fabrication and testing of a novel MEMS resonator for mass sensing applications. *Microelectronic Engineering*, *84*(5–8), 1601–1605. https://doi.org/10.1016/j.mee.2007.01.199

Espinosa, H. D., Prorok, B. C., Peng, B., Kim, K. H., Moldovan, N., Auciello, O., Carlisle, J. A., Gruen, D. M., & Mancini, D. C. (2003). Mechanical properties of ultrananocrystalline diamond thin films relevant to MEMS/NEMS devices. *Experimental Mechanics*, *43*(3), 256–268. https://doi.org/10.1007/BF02410524

Faruk, O., Bledzki, A. K., Fink, H.-P., & Sain, M. (2012). Biocomposites reinforced with natural fibers: 2000–2010. *Progress in Polymer Science*, *37*(11), 1552–1596. https://doi.org/10.1016/j.progpolymsci.2012.04.003

Fu, J., Lin, L., Zhou, X., Li, Y., & Li, F. (2012). A macroscopic non-destructive testing system based on the cantilever-sample contact resonance. *Review of Scientific Instruments*, *83*(12), 123707. https://doi.org/10.1063/1.4770123

Goudenhooft, C., Siniscalco, D., Arnould, O., Bourmaud, A., Sire, O., Gorshkova, T., & Baley, C. (2018). Investigation of the Mechanical Properties of Flax Cell Walls during Plant Development: The Relation between Performance and Cell Wall Structure. *Fibers*, *6*(1), 6. https://doi.org/10.3390/fib6010006

Lee, J. E.-Y., Yan, J., & Seshia, A. A. (2011). Study of lateral mode SOI-MEMS resonators for reduced anchor loss. *Journal of Micromechanics and Microengineering*, *21*(4), 045010. https://doi.org/10.1088/0960-1317/21/4/045010

Mantena, P. R. (1996). Frequency Domain Vibration Analysis For characterising The Dynamic Mechanical Properties Of Materials. *1996 Annual Conference Proceedings*, 1.222.1-1.222.7. https://doi.org/10.18260/1-2--6064

Mohanty, A. K., Misra, M., & Hinrichsen, G. (2000). Biofibres, biodegradable polymers and biocomposites: An overview. *Macromolecular Materials and Engineering*, *276–277*(1), 1–24. https://doi.org/10.1002/(SICI)1439-2054(20000301)276:1<1::AID-MAME1>3.0.CO;2-W

Pang, T. Y., Subic, A., & Takla, M. (2011). Finite element analysis of impact between cricket ball and cantilever beam. *Procedia Engineering*, *13*, 258–264. https://doi.org/10.1016/j.proeng.2011.05.082

Prabhakaran, S., Krishnaraj, V., Kumar, M. S., & Zitoune, R. (2014). Sound and Vibration Damping Properties of Flax Fiber Reinforced Composites. *Procedia Engineering*, *97*, 573–581. https://doi.org/10.1016/j.proeng.2014.12.285

Qian, G.-L., Hoa, S. V., & Xiao, X. (1997). A vibration method for measuring mechanical properties of composite, theory and experiment. *Composite Structures*, *39*(1–2), 31–38. https://doi.org/10.1016/S0263-8223(97)00034-2

Rabe, U., Janser, K., & Arnold, W. (1996). Vibrations of free and surface-coupled atomic force microscope cantilevers: Theory and experiment. *Review of Scientific Instruments*, *67*(9), 3281–3293. https://doi.org/10.1063/1.1147409

Richely, E., Bourmaud, A., Placet, V., Guessasma, S., & Beaugrand, J. (2022). A critical review of the ultrastructure, mechanics and modelling of flax fibres and their defects. *Progress in Materials Science*, *124*, 100851. https://doi.org/10.1016/j.pmatsci.2021.100851

Sader, J. E., Larson, I., Mulvaney, P., & White, L. R. (1995). Method for the calibration of atomic force microscope cantilevers. *Review of Scientific Instruments*, *66*(7), 3789–3798. https://doi.org/10.1063/1.1145439

Schramm, M., Tekeste, M. Z., Plouffe, C., & Harby, D. (2019). Estimating bond damping and bond Young's modulus for a flexible wheat straw discrete element method model. *Biosystems Engineering*, *186*, 349–355. https://doi.org/10.1016/j.biosystemseng.2019.08.003

Shah, D. U., Reynolds, T. P., & Ramage, M. H. (2017). The strength of plants: Theory and experimental methods to measure the mechanical properties of stems. *Journal of Experimental Botany*, *68*(16), 4497–4516. https://doi.org/10.1093/jxb/erx245

Sheehy, M., Punch, J., Goyal, S., Reid, M., Lishchynska, M., & Kelly, G. (2009). The Failure Mechanisms of Micro-Scale Cantilevers Under Shock and Vibration Stimuli. *Strain*, *45*(3), 283–294. https://doi.org/10.1111/j.1475-1305.2008.00610.x

Shioya, M., Myoga, A., Kitagawa, A., Tokunaga, Y., Hayashi, H., Kogo, Y., Shimada, H., & Satake, S. (2019). Analysis of deflection and dynamic plant characteristics of *Cyperus malaccensis* Lam. *Plant Production Science*, *22*(2), 242–249. https://doi.org/10.1080/1343943X.2019.1588075

Sridhar, M. K., Basavarajappa, G., Kasturi, S. G., & Balasubramanian, N. (1982). *Evaluation of jute as a reinforcement in composites*. *7*, 87–92.

Sundararajan, S., & Bhushan, B. (2002). Development of AFM-based techniques to measure mechanical properties of nanoscale structures. *Sensors and Actuators A: Physical*, *101*(3), 338–351. https://doi.org/10.1016/S0924-4247(02)00268-6

Timoshenko, S. (2010). *Theory of elasticity* (Third edition). McGraw-Hill Education.

Ward, I. M., & Sweeney, J. (2013). *Mechanical properties of solid polymers* (Third edition). Wiley.

Yan, L., Chouw, N., & Jayaraman, K. (2014). Flax fibre and its composites – A review. *Composites Part B: Engineering*, *56*, 296–317. https://doi.org/10.1016/j.compositesb.2013.08.014

Yoo, W.-S., Lee, J.-H., Park, S.-J., Sohn, J.-H., Dmitrochenko, O., & Pogorelov, D. (2003). Large Oscillations of a Thin Cantilever Beam: Physical Experiments and Simulation Using the Absolute Nodal Coordinate Formulation. *Nonlinear Dynamics*, *34*(1/2), 3–29. https://doi.org/10.1023/B:NODY.0000014550.30874.cc

Young, W. C., & Budynas, R. G. (2002). *Roark's formulas for stress and strain* (7th ed). McGraw-Hill.

Zhang, C., Zhou, H., Xu, L., Ru, Y., Ju, H., & Chen, Q. (2022). Measurement of morphological changes of pear leaves in airflow based on high-speed photography. *Frontiers in Plant Science*, *13*, 900427. https://doi.org/10.3389/fpls.2022.900427

Chapter 7

Nano-mechanical testing: Effect of retting on single fibre surface

Introduction

The main conclusion from the micromechanical testing of flax fibres as a function of retting (Chapter 6) was that the flexural modulus and strength of the fibres do not significantly evolve during a retting cycle and beyond. These results lend weight to the idea that it is the retting-induced damage to the external tissue (between the fibres) that is responsible for the observation of the retting-induced modification of the mechanical properties of the flax stems. This idea is most apparent in the macro-mechanical torsion characterisation–which we believe could be the basis of a tool to monitor the advancement of retting. In order to go further in an understanding of this, one can perform nanomechanical experiments using atomic force microscopy (AFM).

The AFM has proven to be a highly effective and reliable tool for investigating the mechanics of nanofibers. Of the three most widely used approaches in this field - namely AFM-based tensile testing, three-point deformation testing and nanoindentation - AFM techniques have demonstrated a clear advantage over conventional tensile testing in many cases, although this superiority is not universal (Neugirg et al., 2016). In their research, (Rico et al., 2005) had two main objectives. The first was to formulate a contact model for a blunted pyramidal tip, and the second was to evaluate the suitability of AFM pyramidal tips for investigating the mechanical properties of soft biopolymer gels and living cells. To achieve these goals, they first established a contact model for a blunted regular pyramid interacting with an elastic half-space. They then carried out experiments to study soft samples, including agarose gels and living human alveolar epithelial cells. In these experiments, they used pyramidal tips according to the blunt pyramidal model and spherical tips according to the spherical Hertz model. This allowed them to make a comparative assessment between the two models, particularly in terms of estimating Young's modulus (E) and complex shear modulus (G^*) for the materials studied.

There have been some studies concerning the young’s modulus of flax stems using AFM (Muraille, L., et al (2017). Many experimenters have used near-field microscopy to measure the mechanical properties (mostly the local modulus) of cross sections of flax fibres. In order to do this they must imbue a flax stem with a liquid resin which solidifies, enabling one to make a clean cut (using a diamond saw) for a high-quality surface which can be used in AFM. For example, (Melelli et al., 2021) highlight the significant role played by intrinsic fibre porosity, commonly referred to as 'lumen', which is thought to be a key variable in the composting ageing process. To gain a deeper insight into the mechanisms underlying the ageing process during garden composting, they carried out microstructural investigations using AFM-PF-QNM technology. This technique allowed a detailed examination of the microstructure of the composite material. In addition, the mechanical properties of this composite material were assessed both before and after the composting process. Furthermore, (Melelli et al., 2020) used AFM PF-QNM technology to investigate the characteristics of the middle lamellae at the cell wall level. The aim of this investigation was to gain valuable insight into the indentation modulus of these middle lamellae. To achieve this, they carried out a comprehensive analysis involving a wide range of plant fibres typically used in biocomposite applications. These included flax, hemp, jute, kenaf, stinging nettle and date palm leaf sheath fibres. The result of this research has been the development of a comprehensive database detailing the modulus of indentation of the centre lamella of these different plant fibres. The development of this database serves as a

valuable resource contributing to a deeper understanding of the mechanical properties of this critical layer within plant fibres. It also provides a fundamental resource for future research efforts, particularly in the area of computational modelling and the advancement of knowledge in this field.
(Bourmaud & Baley, 2012) carried out a comprehensive study using nanoindentation on sections of flax fibre. The study can be divided into two distinct phases: In the first phase, following a careful validation process of their methodology, the researchers embarked on an investigation aimed at delineating the Young's modulus and hardness profiles across a cross-section of a flax fibre. The aim was to reveal the intricate structural characteristics and multi-layered composition of the fibre. The second phase of their research was then dedicated to the mechanical evaluation of flax fibres, taking into account their specific locations within a fibre bundle. This phase was particularly important as flax fibres exhibit variations in properties as one moves from the outer to the inner sections of the bundle, mainly due to differences in maturity. These results provided valuable insights into the effect of the extraction process on the mechanical properties of the fibres. This was achieved by making comparisons with nanoindentation results obtained from manually extracted fibres.

However, the embedding approach is time consuming and not compatible with a real-time approach–as is the objective here. In addition to this it has been noted by several authors (Wimmer & Lucas, 1997) (Ren et al., 2015) (Richely et al., 2021) that the resin itself can perturb results using this approach. In contrast we took a different approach here. The micromechanical experiments suggested that the flexural modulus and strength of the fibres (taken as a composite structure) did not evolve with retting and beyond. It is well known that the main cause of retting is to break down (through enzyme activity) the middle lamella material between the fibres (Melelli et al., 2020)–and in the extreme case of over-retting the secondary cell wall of the fibres (Akin et al., 1998) (Akin et al., 1997) (Pallesen, 1996) (Richely et al., 2022).

It seems reasonable therefore to see if it is possible to measure the outside of the fibres using near-field microscopy (nanoindentation AFM) to see if any evolution of the fibres' primary cell wall properties evolve with retting. The techniques developed in the PhD to do this and the results are presented in this chapter.

Nanoindentation AFM: Measurement principle and extraction of modulus

Measurement principle

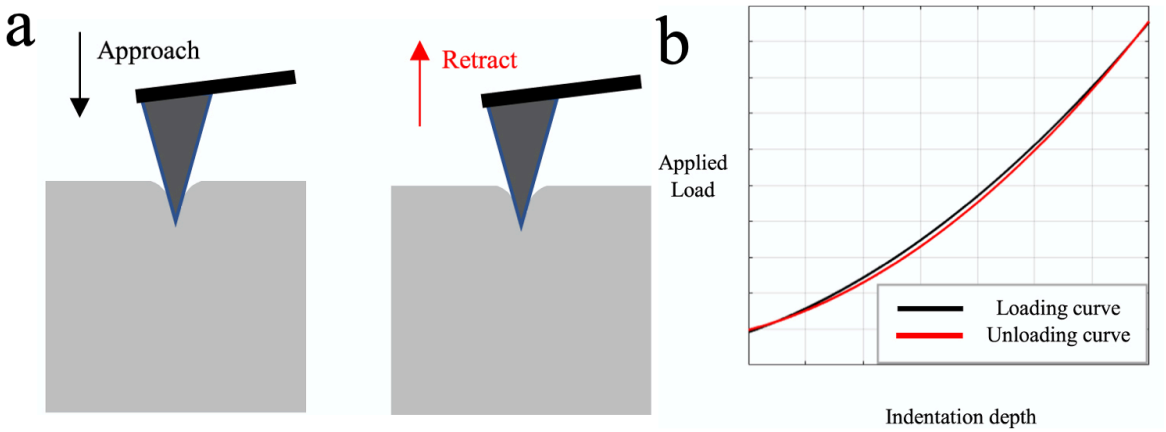

Figure 1. Schematic diagram showing (a) the measurement principle of nanoindentation 'contact-force' AFM and (b) typical displacement vs. force curves.

In nanoindentation AFM the AFM tip indents the soft sample and a load displacement curve is recorded. The same procedure is performed on a hard reference sample. The values of indentation are calculated from the difference in the piezo-displacement between the hard and the soft sample for the same value of applied load force. This results in a load force/indentation curve for the soft material. The curve consists of a loading part (tip moving towards the sample) and an unloading part (tip moving away from the sample). The mechanical modulus of the soft material can be obtained by analysis of this data using mechanical contact models.

In practice, a hard reference material is required, e.g. silicon or silicon dioxide, and the properties of the AFM tip (stiffness, tip radius) have to be known–this can be obtained from the tip supplier or measured in the laboratory.

Extraction of modulus: Model

In order to extract the modulus from the contact-force AFM measurement we used the most commonly-used basic model proposed by Hertz (Johnson, 1982) (Hunter, 1960) (S.-V. Kontomaris, 2018) (S. V. Kontomaris & Malamou, 2020). The assumptions of this model are that the AFM tip has a spherical shape and the indentation depth is much smaller than the tip radius If this is the case, then the load force/indentation curves can be fitted using the following equation (S.-V. Kontomaris, 2018):

$$F = \frac{4}{3}\frac{E}{1-\nu^2}R^{\frac{1}{2}}h^{\frac{3}{2}} \quad (1)$$

Where F is the load force, E is the modulus, ν is the Poisson coefficient of the material,R is the tip radius, and h is the indentation depth. Note that if ν is not known then the effective modulus is measured:

$$E^* = \frac{E}{1-\nu^2} \quad (2)$$

The Hertz theory of contact mechanics makes the following assumptions. First, the strains are small and fall in the elastic limit. Second, the surfaces are continuous and smooth. Third, the area of contact is much smaller than the characteristic dimensions of the contacting parts. Fourth, each material can be considered an elastic half-space. Finally, the surfaces are frictionless. If the materials are not smooth and adhesion forces need to be taken into account then more sophisticated models are needed (‘Contact of Nominally Flat Surfaces’, 1966) (‘Surface Energy and the Contact of Elastic Solids’, 1971) (Muller et al., 1983). As we will see, the nanoindentation data we gathered here fits extremely well with the Hertzian model.

The conditions of the Hertz model are: The sample should be homogeneous, the matter should be isotropic, and possess a linear elastic response. Most biological samples do not meet these criteria, flax fibres are no exception. However, there is mounting evidence in the literature that if small forces are used resulting in small indentation then the force/indentation curves follow the Hertz model. In addition to this, life sciences often involve multiple samples where a trend in data is required. In this case, a precise value of the modulus may not be required but rather a noticeable trend in the evolution of the modulus. This is the case of the study in this chapter where we are looking for a potential evolution of the modulus of the outer surface of the fibres as a function of the retting stage. As a counterexample to this, if one sought to improve knowledge of the modulus of silicon, a very precise and accurate value of the modulus would be required–this would necessitate a very accurate fitting of the model to the data.

Nanoindentation AFM measurements on flax fibre cross sections: flax stems imbued with resin to enable cutting

Sample preparation

Flax stalk samples were collected from flax growing fields belonging to the VRF company, located in Northern France. A full description of the sampling protocol is given in Chapter 3.

Back in the laboratory, 1 to 2 cm long segments were carefully cut from the stems using a sharp razor blade (these methods are detailed in Chapter 4). These samples were immediately placed in a solution of ethanol and deionised water having a 1:1 ratio, and stirred for several days at a temperature of 4°C.

Subsequently, the flax stem samples were treated with a series of ethanol and deionised water solutions, gradually increasing the concentration of ethanol (50%, 75%, 90% and finally 100%). After this preparation phase, the samples were embedded in a composite mixture consisting of increasing proportions of London Resin (LR) white acrylic resin and ethanol (25%, 50%, 75% and pure resin at 100%). To ensure consolidation of the resin, the entire assembly underwent a final polymerisation phase in an oven maintained at a temperature of 60°C for an overnight period (Goudenhooft et al., 2018). Figure 2a provides a visual representation of the embedded flax sample encapsulated in resin.

Following this, the embedded samples were shaped into a pyramidal configuration to reduce their cross-sectional area to fit in the AFM-sample holder. This process was carried out using an ultramicrotome equipped with diamond blades for precision cutting. Figure 2b provides a visual representation of the embedded flax sample held in the AFM-sample holder after cutting using a diamond blade.

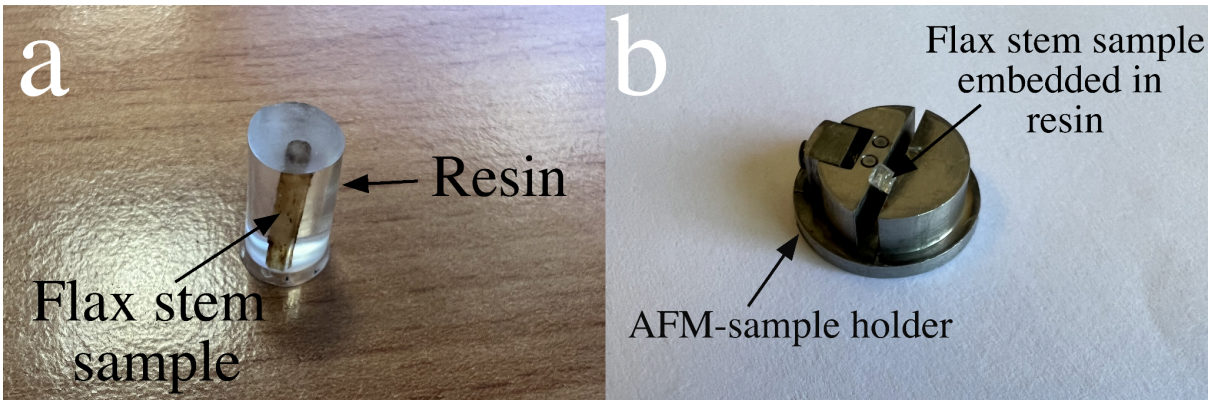

Figure 2. Sample preparation steps to make flax stem cross sections enabling surfaces of high enough quality for nanoindentation AFM. (a) Photograph of part of a flax stem embedded in resin. (b) Photograph of part of a flax stem embedded in resin held in the AFM sample holder.

Note that sample preparation prior to embedding is a critical step as it can affect cell wall properties (S.-V. Kontomaris, 2018) (Meng et al., 2013). The choice of LR-White resin is based on its minimal effect on cell wall properties, particularly when considering the abbreviated embedding process used in this study (Konnerth et al., 2008) (Wagner et al., 2014). This preparation technique serves to reduce artefacts due to sample surface irregularities and boundary effects, thus ensuring accurate measurement (Arnould & Arinero, 2015). It also avoids structural disruption of the cell wall and prevents detachment or collapse of the cell wall layers due to stress release during microtome sectioning by effectively embedding and filling the fibre lumens (Clair et al., 2005).

Experimental setup

Atomic force microscopy (AFM) measurements were carried out using multimode AFM equipment (Bruker, USA). Before starting the measurements of the flax cross section, nanoindentation measurements were made on the mounting resin. These measurements acted as a control mechanism for the calibration of the tip and cantilever, and subsequently provided information on the accuracy of the AFM measurements.

The probing mechanism involves a step-by-step procedure: first, the cross-sectional area is systematically scanned until a fibre bundle becomes visible. Next, a specific flax fibre is selected and the cantilever is positioned to take measurements. This procedure is shown schematically in Figure 3.

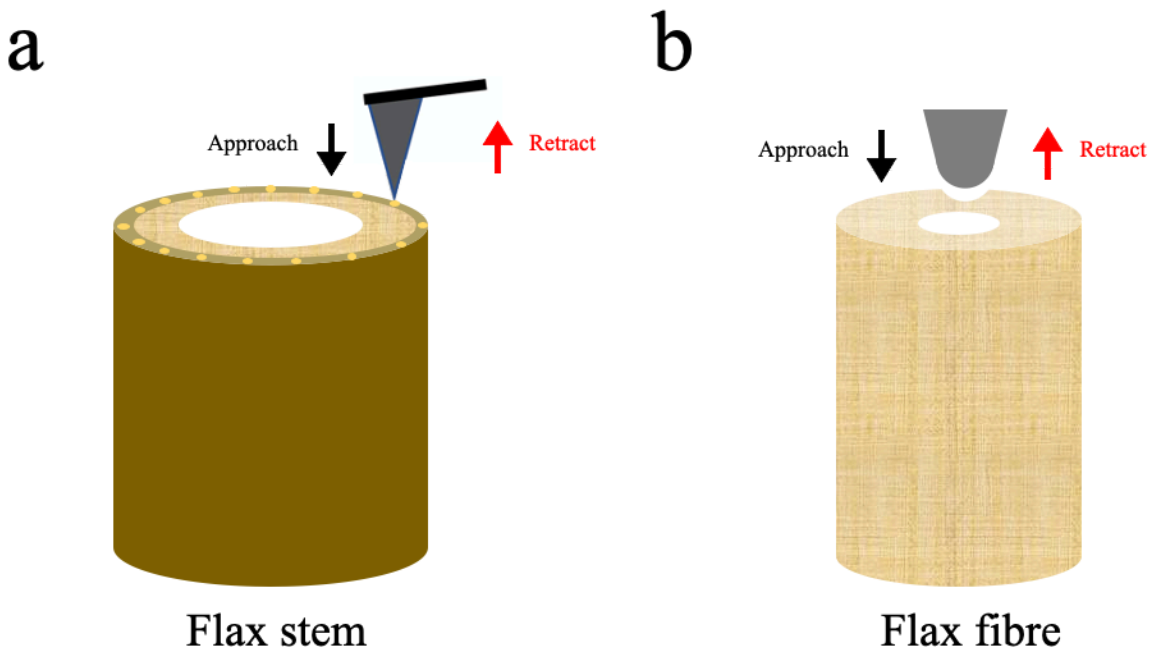

Figure 3. Schematic diagram of experimental setup: nanoindentation AFM. (a) Nanoindentation on flax stem cross section, (b) Zoomed diagram on the nanoindentation of the flax fibre in the external tissue of the flax stem.

Results for cross section oriented single flax fibre using resin imbuing

After calibration, measurements were done on the flax-resin embedded cross section. Figure 4 shows the AFM cantilever-tip before scanning the cross section surface.

The results from this approach release a constant modulus of 30 GPa always along all the samples and in any area of the indentation. This value corresponds to the LR white resin modulus. Knowing that the LR white resin is hard to remove and require special treatment to dissolve it, causing a challenge, this result indicates that the resin was occupying all the surface of the flax cross section, and indenting the modulus of the flax fibre by using this method is impossible. This conclusion guides us to invent a new method which is a resin free method to determine the indent of the modulus. The following discusses this method.

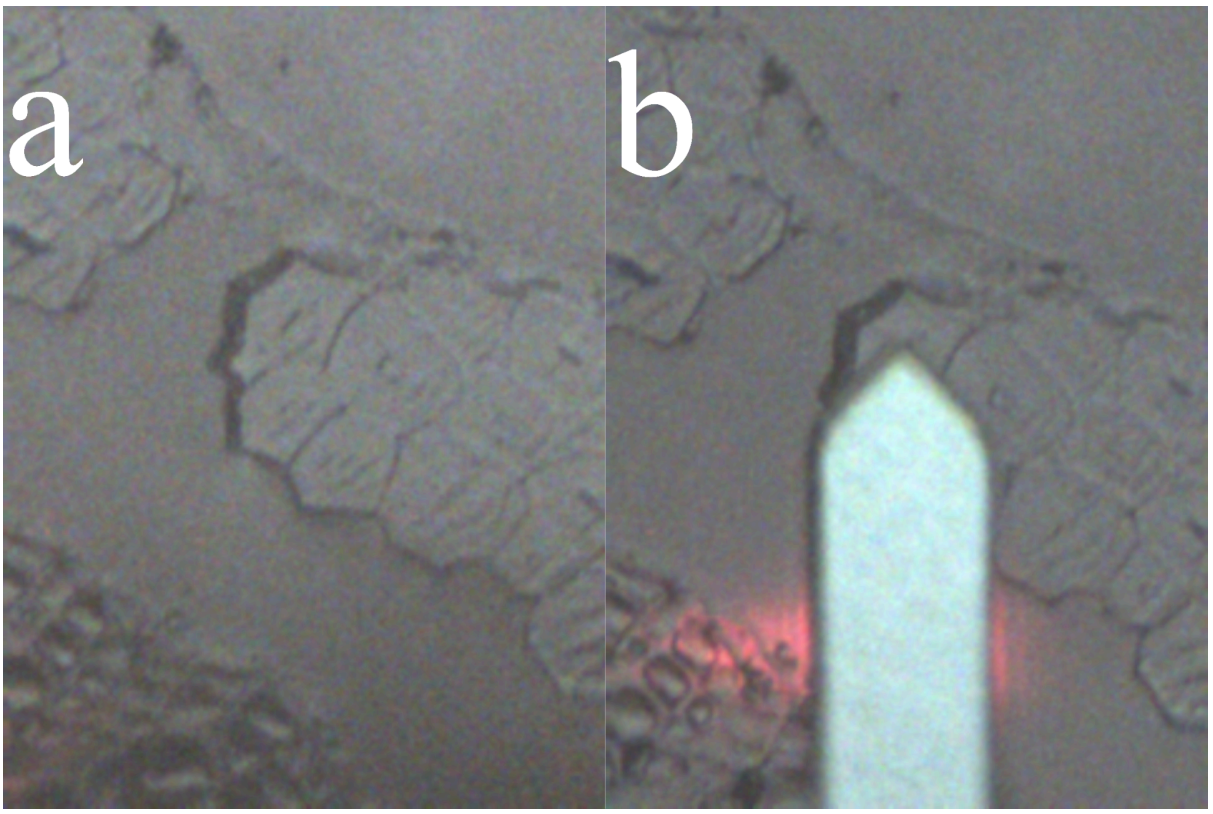

Figure 4. AFM photograph of a nanoindentation test on the flax stem cross section. (a) AFM photograph of the tested cross section flax stem showing the fibre bundle. (b) AFM photograph of the AFM tip when indenting the flax fibres.

Discussion

Embedding flax stalks in resin has long been a conventional approach to studying the nanoscale mechanical properties of flax fibres. However, the disadvantages of this method often outweigh its advantages. One notable challenge is the polymerisation step in resin embedding, where the curing time affects the hardness of the resin. As a result, the choice of diamond blade used to prepare the section becomes critical, and these blades can be prohibitively expensive. Careful handling is also essential to avoid breakage during sectioning.

In addition, despite existing protocols, resin removal requires a high level of skill and expertise, making it inaccessible to everyone. In many cases, the resin tends to cover the entire surface of the cross section, limiting the contact of the cantilever tip with the actual fibre surface. This leads to uncertainty as to whether the measured modulus reflects the properties of the flax fibres or the resin itself.

Furthermore, this method may not effectively reveal the influence of retting on the mechanical properties of the fibre. This is because the effects of retting are primarily observed in the middle lamella, which interfaces with the lateral outer cell wall of the primary cell wall of the fibre. Logically, if the central part of the fibre remains unaffected, a real-time study to observe the nanoscale effects of retting is somewhat redundant.

However, for a more complete understanding of the influence of retting in real time, it seems more rational to make indentations on the lateral surface of the fibre, particularly in the region facing the middle lamella, where the influence of retting is most pronounced. Based on these considerations, and recognising that retting mainly involves the breakdown of the mid-lamellar material between the fibres, and in extreme cases even the secondary cell wall, it is reasonable to propose the use of near-field microscopy, such as nanoindentation AFM, to investigate the influence of retting on the lateral surface of the fibres. This approach is likely to provide valuable insight into the effect of retting on the mechanical properties of flax fibres at the nanoscale. This section summarises the developed technique.

Nanoindentation AFM measurements on single flax fibre sides: no resin used in this process

Sample preparation

Due to the real-time nature of this test, which involves indenting the modulus while studying the effect of retting on flax fibres, the use of this newly developed method is advisable. By using this technique, any possible influence of retting can be accurately identified. This is due to the fact that any effects of retting would be localised on the surface attached to the external tissues of the flax stalk when laid horizontally in the field; logically, this refers to the lateral surface of a flax tissues, as opposed to the hidden vertical surface within a sample cross-section.

Based on the results of the resin embedding technique, a novel approach was developed in the laboratory to study in real time the influence of retting at the nanoscale, probably on the middle lamella, and to assess the nanoscale modulus of flax fibres. This innovative technique is based on the horizontal fixation of a single flax fibre to silicon chips measuring 1 x 1 cm². This configuration allows a direct interface between the lateral or horizontal plane of the single flax fibre and the atomic force microscope (AFM) probe. The main objective of this method is to analyse the surface properties of individual flax fibres, free from resin or extraneous compounds. In addition, this technique significantly increases the surface area available for indentation, allowing the AFM probe to traverse and indent a larger area along the length of the flax fibre. As a result, this innovation effectively mitigates the limitations associated with resin-based methods and produces precision results.

The flax stalks were collected from the flax fields of the VRF located in the north of France. Figure 5 shows the steps to extract a single fibre.

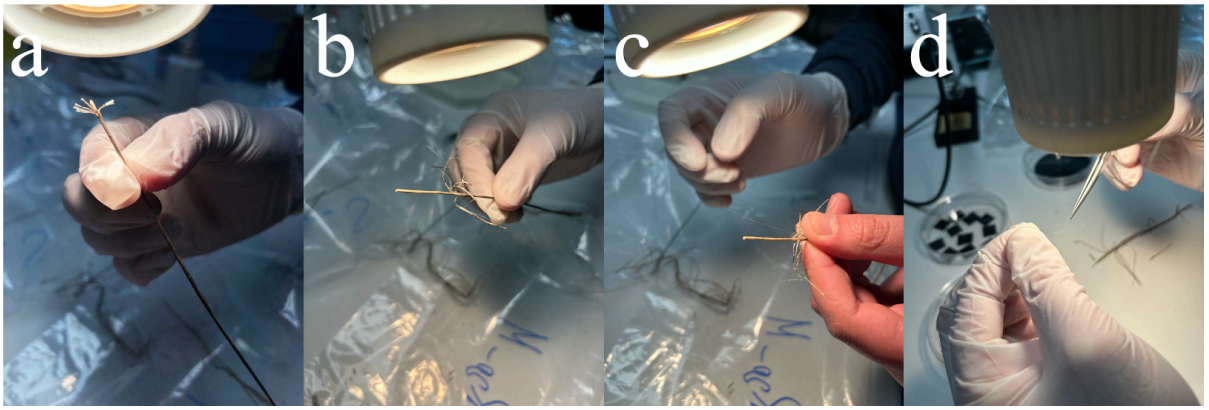

Figure 5. The different steps used to extract a single fibre. a) break in the top of the stem. b) peeling of the external tissue. c) Identification of the fibre bundle. c) Single fibre extraction.

individual flax fibres were carefully extracted from the flax stalks manually. First, a slight incision was made near the top of the stem to facilitate observation of the outermost layer, known as the outer tissue Figure 5a. The outer tissue was then peeled from the flax stalk Figure 5b. Using a pair of tweezers and aided by the illumination of a lamp, the fibre bundle was then carefully separated from the outer tissue Figure 5c. Finally, using a pair of tweezers, the identified single fibres were peeled from the bundle for further analysis Figure 5d.

The preparation of the chip/fibre support involves several steps. Figure 6 shows a schematic representation of the steps involved for the preparation.

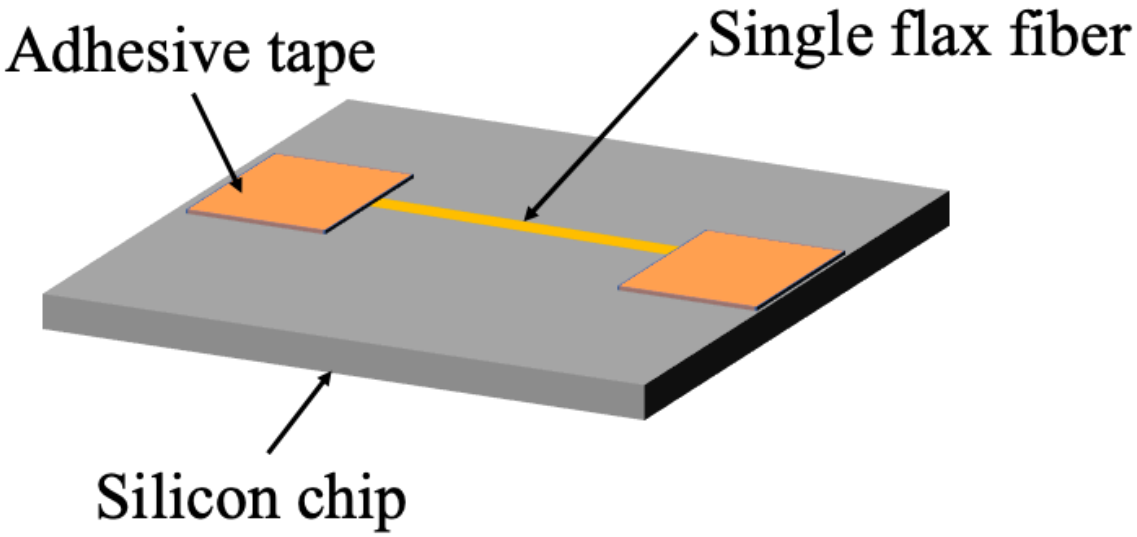

Figure 6. Schematic diagram of a fibre/chip sample.

First, 1cm x 1cm silicon chips are cut from silicon wafers (400 µm thick). These chips are then cleaned with isopropanol in a controlled environment (a class ISO6 cleanroom). Following the chip preparation, the individual flax fibres previously extracted are placed on

the silicon chips. The ends of these flax fibres are fixed to the chips with adhesive tape. After this assembly, the Fibre/chip sample is examined under a digital microscope (Keyence, France). The purpose of this microscopic evaluation is to verify the precise alignment of the fibre on the chip. It is essential that the fibre has a linear orientation on the chip surface, without any curvature. This is due to the need to achieve a straight, tension-induced fibre profile during the subsequent test process, as opposed to a curved configuration. Any deviation from a linear orientation could potentially introduce inaccuracies in the determination of the indentation modulus. Figure 7 shows a photograph of the sample used for the lateral indentation.

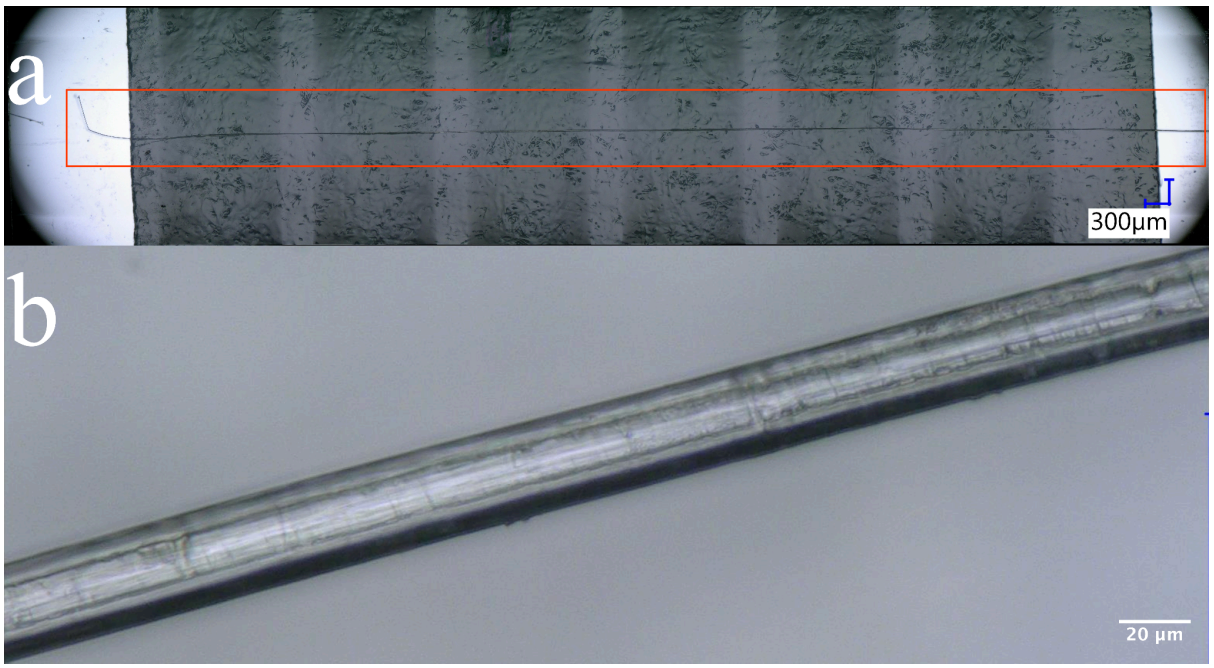

Figure 7. optical microscopic image of the prepared planar oriented flax fibre. a) optical microscopy image showing the flax fibre (red box) attached to the silicon chip. b) Zoomed microscopic image of the flax fibre to be tested.

Experimental setup

Before starting the indentation on the fibre horizontal surface, nanoindentation measurements were made on a silicon chip. These measurements acted as a control mechanism for the calibration of the tip and cantilever, and subsequently provided information on the accuracy of the AFM measurements. Nanoindentation measurements were carried out using a Multimode AFM from Bruker, USA. The imaging mode used, employed with a TAP525A probe with a spring constant of 122 N/m and a tip radius in the range of 100 nm.

The samples used in these experimental studies were extracted from stalks of different stages of the retting process, designated R0 (start of retting), R5, R10, R15 (optimum retting stage) and R20 (over-retting stage). The intervals between these stages were spaced at 2 weeks between R0 and R5, 2 weeks between R5 and R10, 2 weeks between R10 and R15,

and 4 weeks between R15 and R20. Measurements were taken at four different locations on the flax fibres. These locations included both end zones (right and left) of the fibres and two intermediate zones along the length of the fibre. Figure 8 shows an AFM photography of the indented zones at the surface of the fibre.

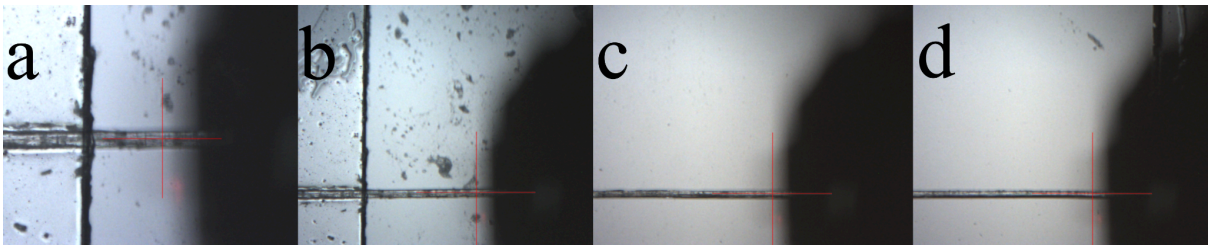

Figure 8. Typical examples of AFM-image of the different indenting zones for the planar-oriented flax fibre samples from R15. a) Zone 1, b) zone 2, c) Zone 3, d) Zone 4.

The indenting mechanism includes approaching the cantilever tip to the lateral surface of the flax fibre sample. The tip indents a depth of 10 nm at the surface of the fibre and then retracts. Figure 9 shows a schematic representation of the experimental setup.

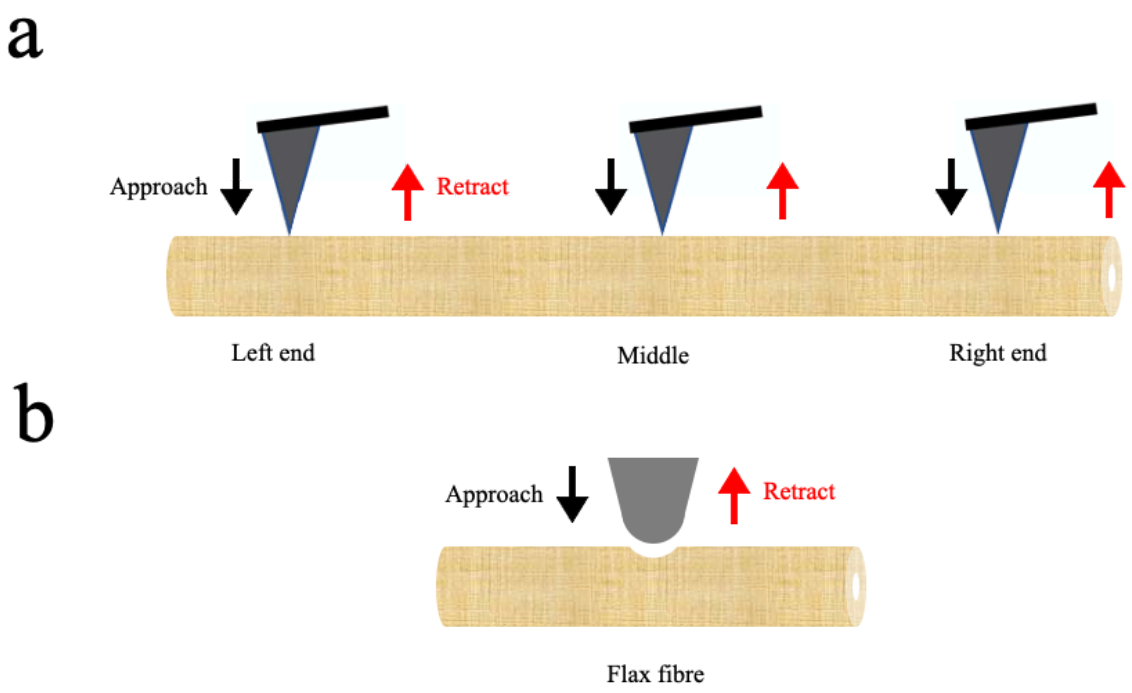

Figure 9. Schematic diagram of experimental setup: AFM. a) Schematic representation showing the different indentation locations. b) A scheme showing a zoomed representation of the indented location.

The experimental force-displacement curves derived from the indentation tests were analysed using Nanoscope and bruker's mountains software. The resulting results and findings are detailed in the following section

Results for planar-oriented single flax fibres

Following the experiments, the data derived from the load-displacement curve was subjected to manual fitting with the Hertzian model using Nanoscope software. For accuracy and speed, automatic fitting was also performed using Bruker's Mountain software. It is noteworthy that both fitting methods produced consistent results, and for this particular experiment the manual fitting approach is specifically considered. During the fitting process, care was taken to record the coefficient of determination of the fit, denoted as R2, while extracting the effective modulus from the fitted data.

As an illustrative example, Figure 10 shows a typical load-displacement curve obtained from the nanoindentation process, accompanied by the corresponding Hertzian fit.

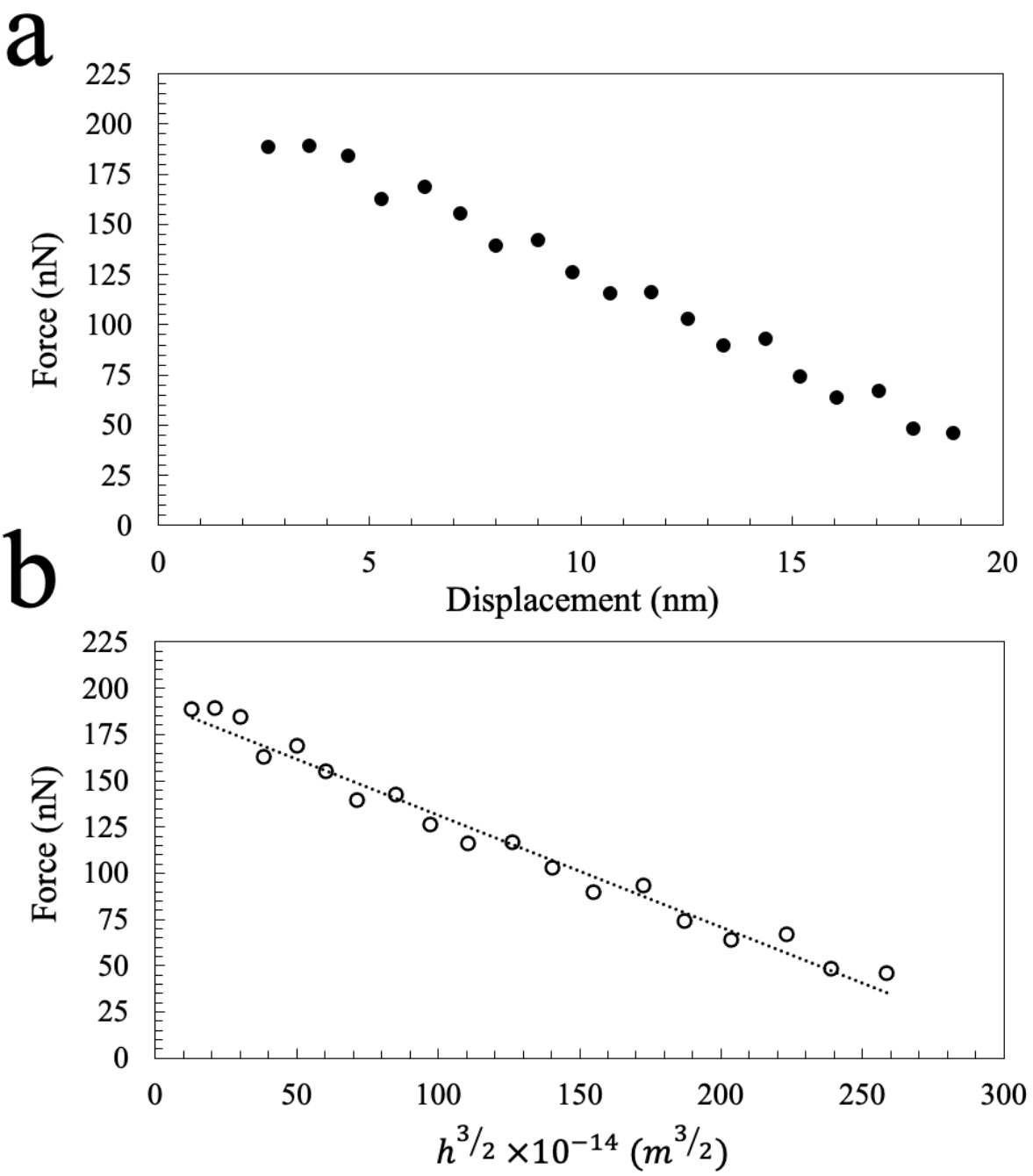

Figure 10. Typical examples of force versus indentation depth data obtained for the planar-oriented flax fibre samples, taken from the optimal-retted stage in this case. (a) Raw data extracted from the AFM measurements. (b) Data fitted to the Hertzian model.

Figure 10a is a representative plot of the load-displacement curve resulting from the nanoindentation experiment using a flax fibre obtained from the optimum retted phase. The data presented in the graph shows a linear relationship between the applied force and the displacement. Typically, the effective modulus is determined by calculating the slope of the portion of this curve that fits the Hertzian model.

To verify the modelling, we attempted to fit the data manually to the Hertzian model to assess the accuracy of the software. Figure 10b shows the result of the Hertzian fit. The plot shows a linear relationship between force (F) and displacement ($h^{\frac{3}{2}}$), consistent with the model's equation where force and displacement are directly proportional.

All data were then manually processed using Nanoscope software, including manual fitting of the Hertzian model.

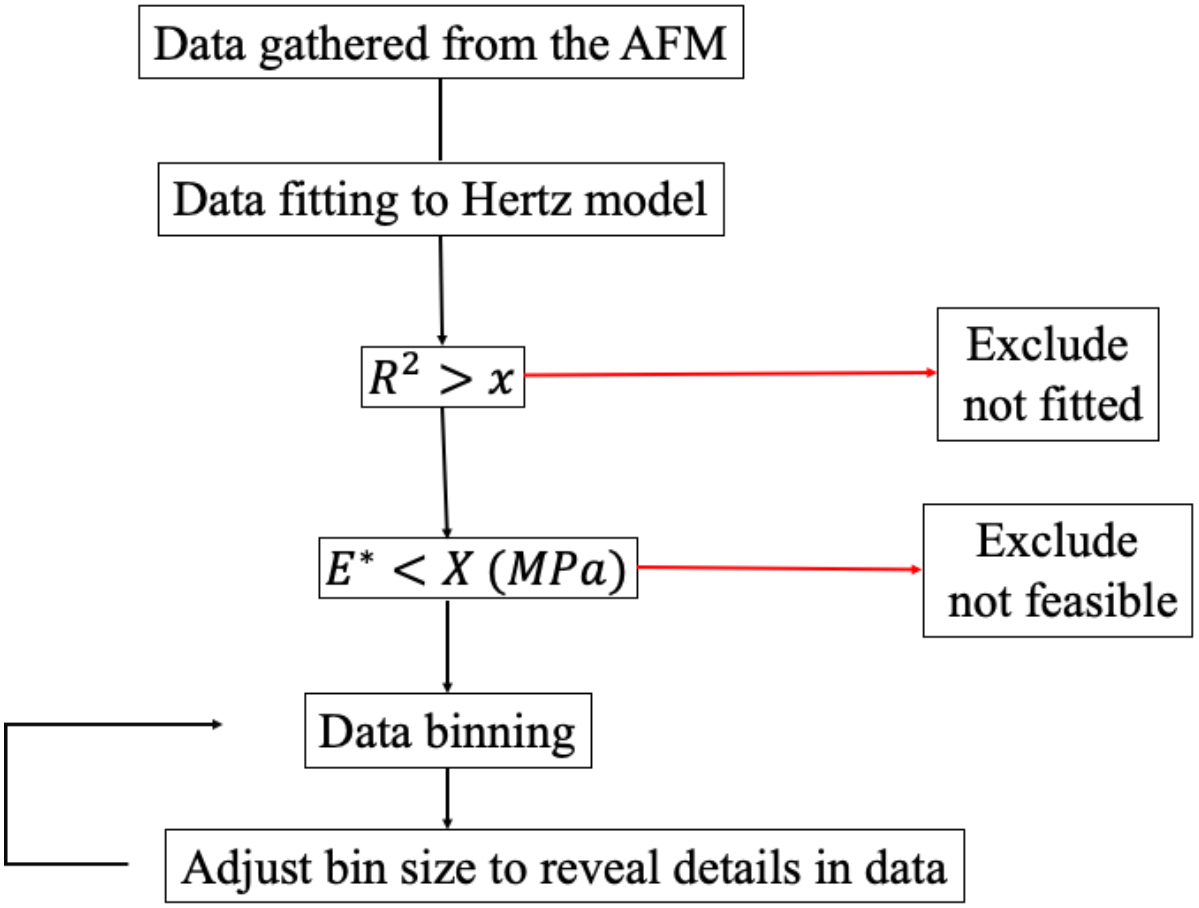

Figure 11. A schematic chart showing the data analysis protocol.

A data sorting process, shown in Figure 11, was performed on the fitted data to produce results which were (i) uniquely Hertzian and (ii) were reasonable values. First, the fitted data was sorted by ensuring that the coefficient of determination (R^2) exceeded a given threshold (e.g. R2 > 0.99) to enable a sufficient amount of data to have a statistical analysis. It is important to note that only data conforming to the Hertzian model was used in this way. Any data that did not meet this criterion, with an (R^2) value below 0.96, was systematically excluded from the analysis.

Out of a total of 1015 measurements carried out on samples obtained from the three stages of retting 676 measurements were consistent with the Hertzian model and met the (R^2) threshold.

The data were then further categorised according to their values of modulus. Whilst the majority of values fell within the range of 100 to 2000 MPa, a few outliers had exceptionally high values which were not meaningful to interpret and were therefore excluded. As a result, a total of 650 of the original 676 measurements were included in the subsequent statistical analysis.

To facilitate further comprehensive analysis and presentation, the data was also organised into bins. This binning process simplified the creation of histograms that effectively represent the distribution of E^* values and their corresponding frequency. The choice of bin determines how apparent trends and details are in the results. If the bin is too large, details are missed; if the bin is too small, the data becomes noisy and difficult to understand. We therefore modified and optimised the bin size to make the details of the data apparent.

Figure 12, 13, and 14 give a visual representation of the histograms showing the distribution of the extracted *E** values that conformed to the Hertzian model, using 650 measurements from the three phases of retting.

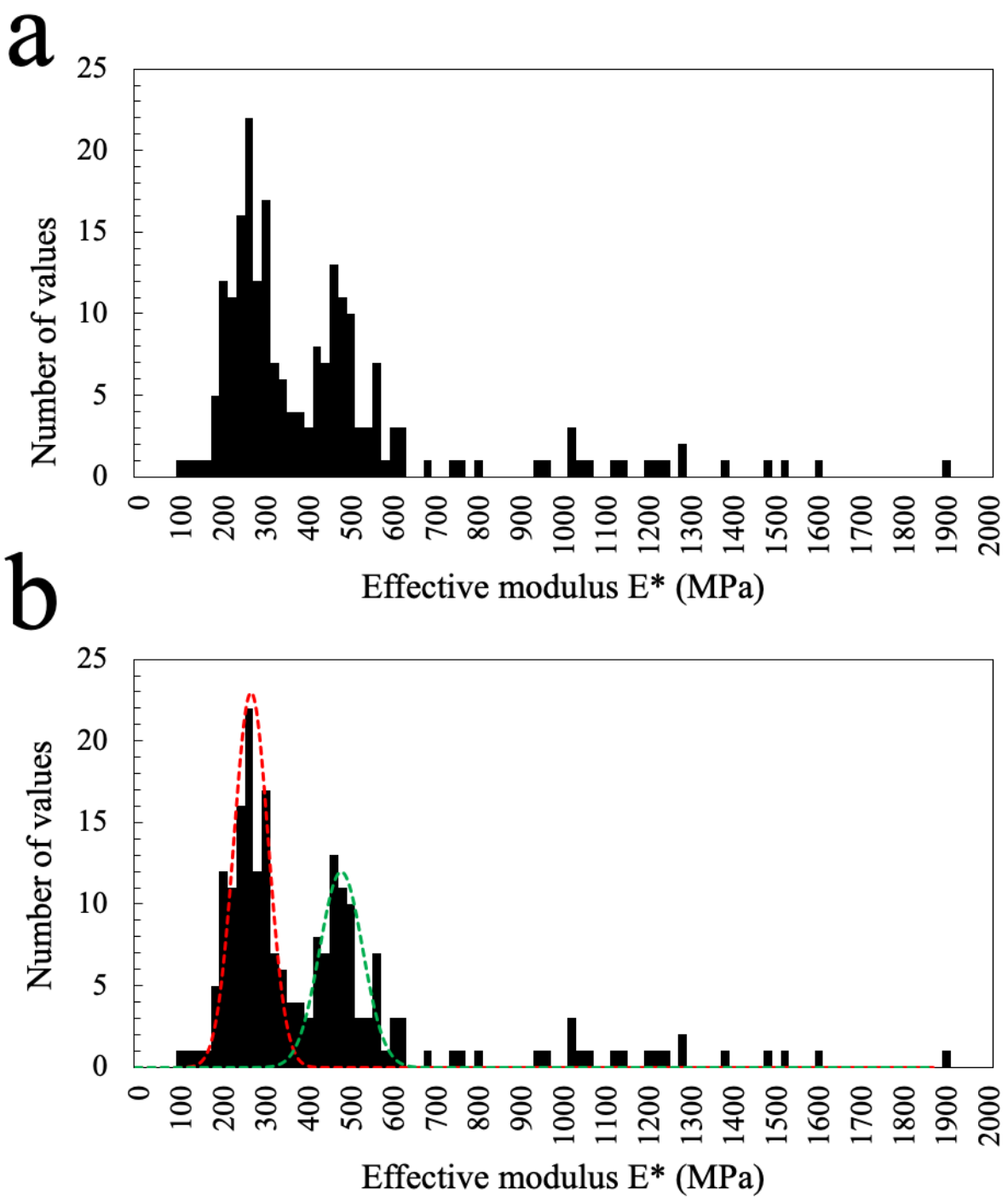

Figure 12. Histograms of the extracted effective modulus of the flax fibres from an under-retted phase. (a) Histogram of the sorted values fitting the Hertzian model, (b) Histogram of the sorted values fitting the Hertzian model with a Gaussian fit.

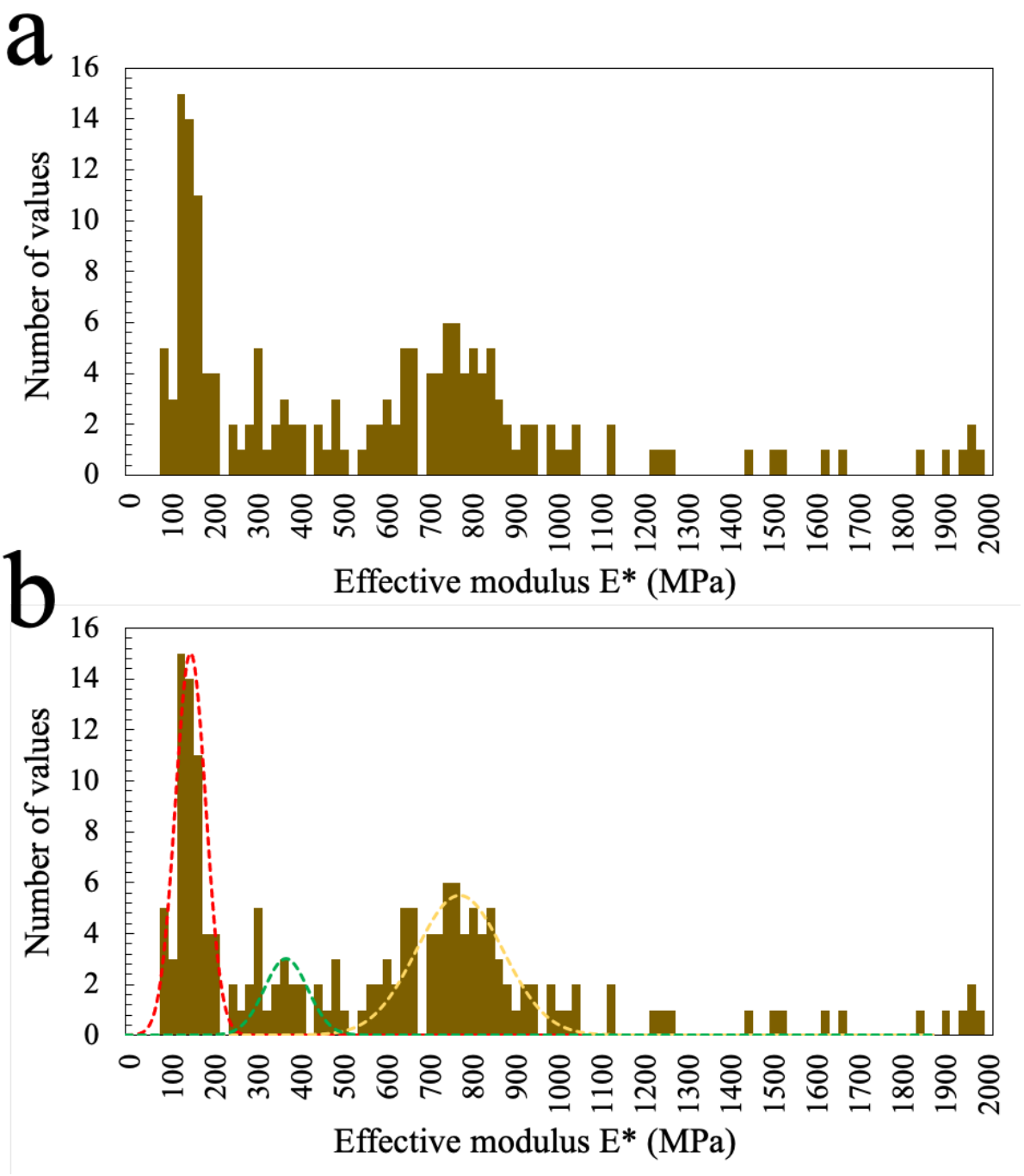

Figure 13. Histograms of the extracted effective modulus of the flax fibres from an optimal-retted phase. (a) Histogram of the sorted values fitting the Hertzian model, (b) Histogram of the sorted values fitting the Hertzian model with a Gaussian fit.

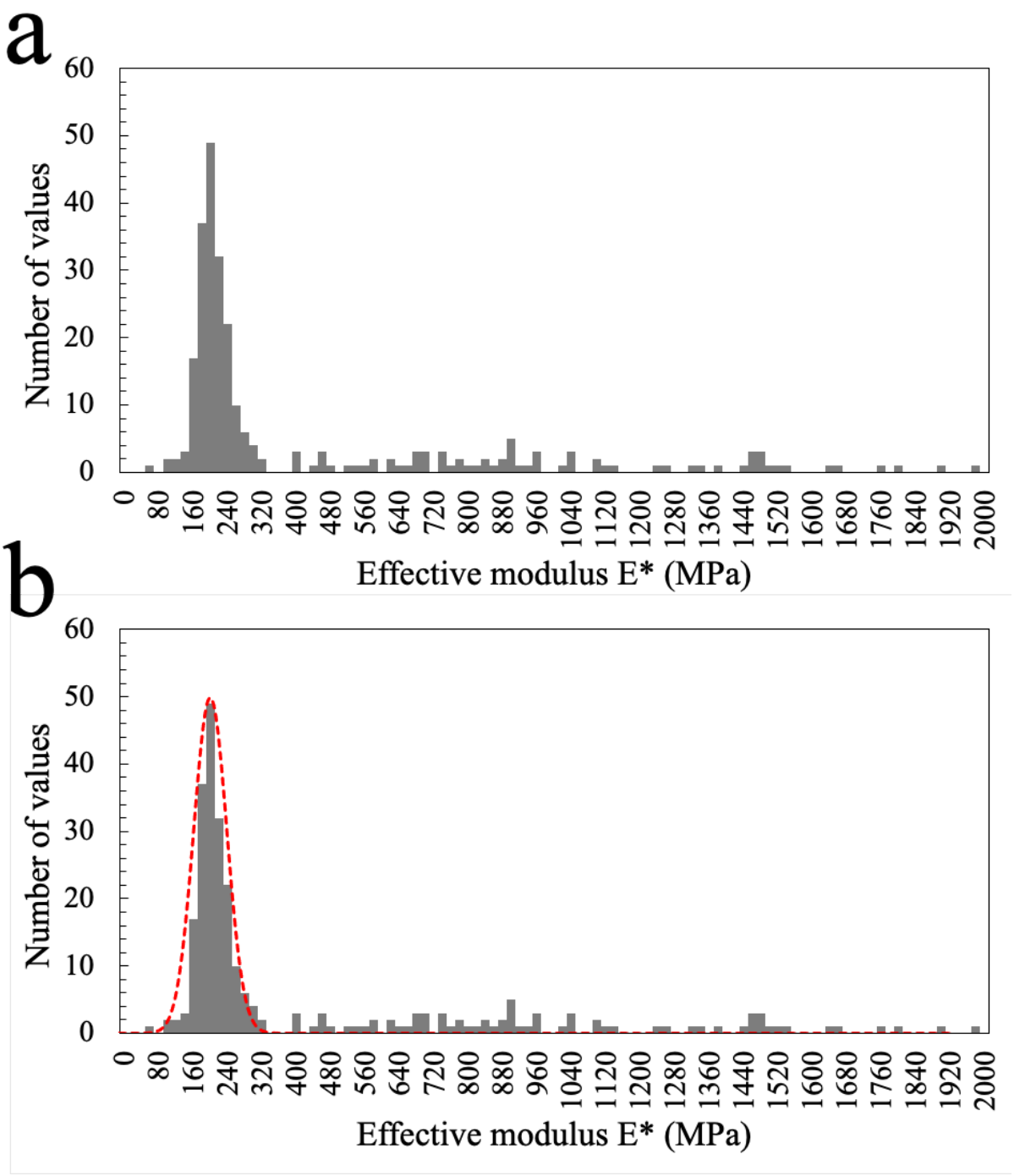

Figure 14. Histograms of the extracted effective modulus of the flax fibres from an over-retted phase. (a) Histogram of the sorted values fitting the Hertzian model, (b) Histogram of the sorted values fitting the Hertzian model with a Gaussian fit.

Figure 12 shows histograms of the data for the under-retted phases. Figure 12a represents the raw data and shows two distinct peaks - one at 250 MPa and another at 480 MPa. To gain a deeper understanding of these results, the histograms were fitted with Gaussian functions, as shown in Figure 12b. The red fit corresponds to the peak at 250 MPa, while the green fit corresponds to the peak at 480 MPa.

As the retting process progresses and the optimum retting point is reached, there is a noticeable shift in the data patterns–see Figure 13a. This transformation is particularly evident in the left histogram of Figure 13b. The red peak undergoes a significant shift towards a lower value and is now recorded at 150 MPa. The green peak remains relatively stable but experiences a reduction in the number of measurements within this peak compared to the under-retting stage. At the same time, a new peak characterised by the yellow colour appears at around 760 MPa, as shown in the right histograms of Figure 13b.

However, as retting progresses beyond the optimum phase, all peaks converge to a value of 220 MPa, as shown in the histogram of Figure 14a and 14b. These results strongly suggest that there is significant variation at the fibre surface, indicating the influence of retting at different stages on the fibre surface. To gain a more complete understanding of the effect of retting time on the fibre surface, further analysis will focus on the E^* values corresponding to these peaks. Therefore, the values corresponding to the peak positions are plotted as a function of retting time. Figure 15 shows the resulting plot.

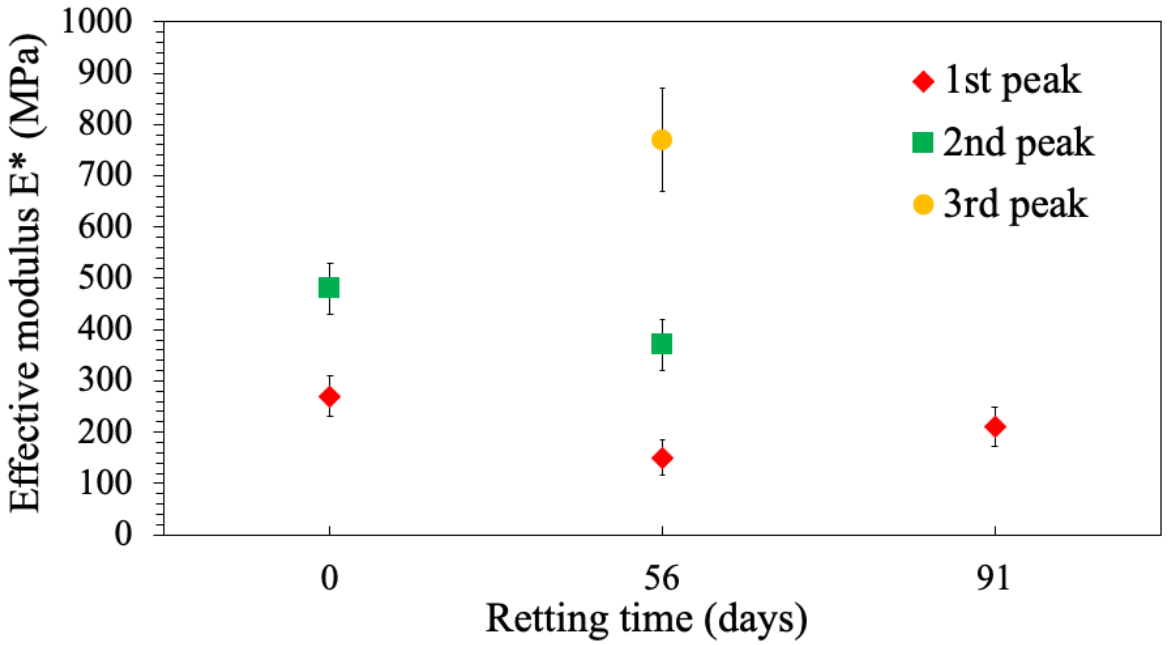

Figure 15. Plot of the average effective modulus of the single flax fibre sides extracted using nanoindentation AFM as a function of the retting stage.

Figure 15 shows a plot of the behaviour of the peak mean effective modulus as a function of retting time. The results show a peak with a value between 150 and 250, which is constant as a function of the 3 retting phases, as represented by the red diamonds. The second peak appears in the early retting phase at a value of 480 MPa, represented by the green squares. As retting progresses, this peak also appears at the optimum retting point at 360 MPa, represented by the green square. However, this peak disappears beyond the optimum retting point. Despite the indented values, this result indicates that nanoindentation has been

able to indent the surface of the flax fibre and produce a trend that obviously and clearly shows the influence of retting on the surface of the flax fibre as a function of the retting time.

Discussion

Let us consider Figure 16. In the previous chapter, the modulus of the entire heterogeneous flax fibre was measured. Figure 16a shows the heterogeneous nature of a single flax fibre. The micromechanical measurements were unable to discern between the mechanical properties of the individual components of the fibres. In contrast, nanoindentation AFM of planar-oriented flax fibres are able to measure the modulus of the outer surface (primary cell wall) of the flax fibres–see Figure 16b. As it is this surface that is 'exposed' to retting, it seems reasonable to measure the evolution of this surface as a function of retting. Before continuing the discussion, let us remember that the micromechanical measurements suggested that the heterogenous modulus of the flax fibres did not significantly change with retting,even over retting. In addition, the nanoindentation AFM experimentation of planar-oriented flax fibres in various stages of retting and over retting do show a change in their outer surface.

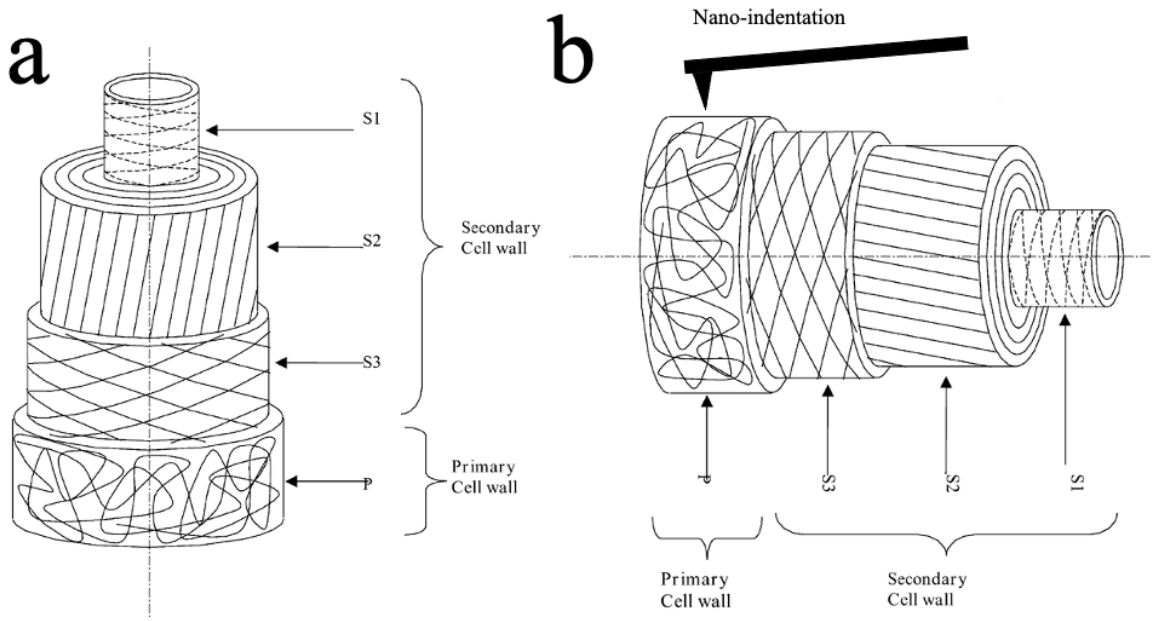

Figure 16. The heterogeneous complex structure of the flax fibre composite material.

Figure 16 provides a visual representation of the intricate and heterogeneous structure of the flax fibre, reinforcing its classification as a complex composite material. In particular, Figure 16a illustrates the internal complexity of this material. The flax fibre composite is composed of both primary and secondary cell walls, a concept that has been explored previously. Within the secondary cell wall there are three distinct layers referred to as S1, S2 and S3. the presence of these layers makes the secondary cell wall stiffer, and they are recognisably characterised by the orientation of the fibres and have a diverse composition of

polysaccharides, specifically including pectin, lignin, and hemicellulose, as elaborated by (Goudenhooft et al., 2019).

Furthermore, it is worth noting that the chemical composition of the fibre cell wall is strikingly similar to that of the middle lamella. This parallel in composition underlines the intricate interplay of components within the structural make-up of the flax fibre. The middle lamella is a critical adhesive material that binds fibre bundles and individual fibres within those bundles. Numerous previous studies, (Melelli et al., 2020), have thoroughly investigated and documented the effect of retting on the middle lamella. Given its important role, it is plausible that the influence of retting could extend to the interphase between the fibre and the middle lamella. This interphase essentially corresponds to the outer surface of the fibre, referred to as the primary cell wall.

Considering similarity in the chemical composition and the enzymatic activities of microorganisms during retting, it is possible then that the influence of retting on the fibre cell wall can be observed at the molecular level, particularly with regard to the sugars present in this region.

In order to gain a deeper insight into this phenomenon, we used AFM nanoindentation resin free approach, to investigate the mechanical properties of the flax fibre surface, with a particular focus on the primary cell wall. This choice is based on the understanding that the primary cell wall is the first structural element within the fibre at the interphase with the middle lamela to undergo changes if there is influence of retting on this zone. Figure 16b provides a visual representation of the method used in our study. This method focuses on indenting the lateral surface of the flax fibre, precisely providing mechanical insight into the primary cell wall components as shown in Figure 16b. What sets our approach apart is its ability to perform real-time indentation, which, unlike previous methods that use resin and vertical orientation, allows us to effectively demonstrate the influence of retting on the fibre surface.

It's worth noting that the Hertz model used here, although not perfectly suited to such samples, was used in our study. This decision was motivated by the potential to reveal trends in the data. These trends do not aim to precisely quantify the nanoscale modulus, but serve the qualitative purpose of observing a trend, illustrating the influence of retting on the mechanical properties of the fibre in real time. However, we were also able to obtain quantitative measurements at the nanoscale. The results show an interesting trend of three different peaks, representing three different values of the effective modulus, as a function of retting period. Given the lack of previous research and investigation in this specific area, particularly in relation to the indentation of the lateral surface of the fibre, we are faced with the challenge of accurately identifying the exact material subjected to indentation. However, while a definitive identification remains elusive, we can propose possible hypotheses. One such hypothesis relates to the modulus of the polysaccharides found in the primary cell wall of the flax fibre. It is conceivable that the nanoindentation measurements indent the mechanical properties of these polysaccharides. Alternatively, the measurements may include some polysaccharides that are either persistently attached to the fibre-middle lamella interface or are exposed after degraded by enzymatic activity during the retting process. Further research and analysis is required to clarify this intriguing aspect of the study.

However, it is worth noting that the trend obtained by nanoindentation does not agree with the modulus obtained by the micromechanical approach. This discrepancy is due to the fact that the nanoindentation value only represents the modulus from the fibre surface as described in Figure 16b. Knowing that the thickness of the Primary cell wall is 0.2 um (Goudenhooft et al., 2019) (Bos et al., 2002), in this nanoindentation test a depth of only 10 nanometres is indented. It is therefore clear that this measurement is specific to the surface of the primary cell wall and does not encompass the entirety of the fibre cell wall, and even the fibre as a whole heterogeneous composite.

The measurements here can be readily compared with work by (Capron et al., 2017). 'Caractérisation mécanique de la paroi cellulaire des fibres végétales par Microscopie à Force Atomique', in *CFM 2017-23ème Congrès Français de Mécanique*. Capron et al. used Peak Force QNM AFM measurements to semi-quantitatively measure the modulus of cross sections of flax fibres embedded in resin. First, they clearly show that the resin is present in the lumen part of the fibres. Second they report a modulus of around 20 GPa for the whole fibre, which agrees very well with our micro-mechanical measurements. Third, they report a much lower modulus in the tissue between the fibres, where the resin is unlikely to reach. This lower value <<1 GPa seems to agree with our observations at the lateral wall of the fibre here.

Conclusions

Near field microscopy (nanoindentation AFM) can be used to study the cross section and sides of single flax fibres. In addition this can be done as a function of the advancement of retting. Nanoindentation AFM can be used to measure the mechanical modulus locally on part of a flax fibre. Initially, a standard sample preparation method was used to prepare cross sections of flax stems to enable near field microscopy of their flax fibres in various stages of retting. The mechanical modulus was extracted from these measurements using nanoindentation AFM by applying the Hertz model. The standard sample preparation method involves imbuing the flax stem with a resin. The nanoindentation AFM measurements revealed some interesting observations. The modulus could be extracted from probing of the fibre cross sections-as others have done. However, tests were also conducted in other zones of the flax stem cross section, notably the xylem regions and their pores. Interestingly, the modulus in the zone was similar to that measured in the fibre zones-suggesting that the resin had imbued many parts of the stem.

In an effort to avoid the use of the resin, and also to probe only the outer part of the fibres, we developed an original planar mounting approach to perform AFM on single fibres lying flat on a host chip. We were able to mount several single fibres like this from different retting stages. AFM was performed on several zones along the surface of a single fibre–this is another advantage of this sample mounting along with the absence of resin. The total number of measurements was 650. AFM revealed some interesting results for the modulus at the surface of the fibres as a function of retting. However these results do not agree with the micromechanical results.

Firstly, it is important to note that the modulus obtained by nanoindentation using Atomic Force Microscopy (AFM) was significantly lower than that obtained by the micromechanical

approach. The micromechanical technique gave an average effective modulus in the range of 150 to 770 MPa, while the microindentation method gave a modulus of 22 GPa for the whole fibre. This difference in measurement is attributed to the following reasons. The micromechanical approach provides an assessment of the modulus for the whole fibre, including the primary and secondary cell walls, their layers and polysaccharides. In contrast, AFM nanoindentation only penetrates to a depth of just 10 nm. Notably, the depth of the primary cell wall in the fibre composite is approximately 200 nm, as supported by the reference. This suggests that the nanoindentation technique is primarily concerned with the surface of the primary cell wall. The results from this technique show three interesting peaks, each characterised by different modulus values in relation to the retting time. The evolution of these peaks over the course of retting shows a compelling trend: The first peak has a constant value and remains stable as retting progresses. The second peak experiences a decrease at the optimum retting point and then disappears beyond this point, The third peak appears exclusively at the optimum retting point.

Whilst there are no previous studies to act as a reference point to conclusively identify the material being indented, the observed trend clearly demonstrates the influence of retting on the fibre surface. This observation is consistent with the understanding that prolonged enzyme activity during over-retting is known to have a detrimental effect on the primary cell wall of the fibres and the resulting effective modulus could be attributed to the mechanical properties of biochemical structures such as lignin, pectin and hemicelluloses present in the fibre cell walls, in particular the primary cell wall.

Finally, we note that the planar mounting approach is not to the exclusion of the cross section mounting approach but rather a complimentary technique which can be added to the researchers toolbox—as indeed are the other original techniques and approaches developed in the PhD.

References

Akin, D. E., Morrison, W. H., Gamble, G. R., Rigsby, L. L., Henriksson, G., & Eriksson, K.-E. L. (1997). Effect of Retting Enzymes on the Structure and Composition of Flax Cell Walls. *Textile Research Journal*, *67*(4), 279–287. https://doi.org/10.1177/004051759706700407

Akin, D. E., Rigsby, L. L., Henriksson, G., & Eriksson, K.-E. L. (1998). Structural Effects on Flax Stems of Three Potential Retting Fungi. *Textile Research Journal*, *68*(7), 515–519. https://doi.org/10.1177/004051759806800708

Arnould, O., & Arinero, R. (2015). Towards a better understanding of wood cell wall characterisation with contact resonance atomic force microscopy. *Composites Part A: Applied Science and Manufacturing*, *74*, 69–76. https://doi.org/10.1016/j.compositesa.2015.03.026

Bos, H. L., Van Den Oever, M. J. A., & Peters, O. C. J. J. (2002). [No title found]. *Journal of Materials Science*, *37*(8), 1683–1692. https://doi.org/10.1023/A:1014925621252

Bourmaud, A., & Baley, C. (2012). Nanoindentation contribution to mechanical characterisation of vegetal fibers. *Composites Part B: Engineering*, *43*(7), 2861–2866. https://doi.org/10.1016/j.compositesb.2012.04.050

Clair, B., Gril, J., Baba, K., Thibaut, B., & Sugiyama, J. (2005). Precautions for the Structural Analysis of the Gelatinous Layer in Tension Wood. *IAWA Journal*, *26*(2), 189–195. https://doi.org/10.1163/22941932-90000110

Contact of nominally flat surfaces. (1966). *Proceedings of the Royal Society of London. Series A. Mathematical and Physical Sciences*, *295*(1442), 300–319. https://doi.org/10.1098/rspa.1966.0242

Goudenhooft, C., Bourmaud, A., & Baley, C. (2019). Flax (Linum usitatissimum L.) Fibers for Composite Reinforcement: Exploring the Link Between Plant Growth, Cell Walls Development, and Fiber Properties. *Frontiers in Plant Science*, *10*, 411. https://doi.org/10.3389/fpls.2019.00411

Goudenhooft, C., Siniscalco, D., Arnould, O., Bourmaud, A., Sire, O., Gorshkova, T., & Baley, C. (2018). Investigation of the Mechanical Properties of Flax Cell Walls during Plant Development: The Relation between Performance and Cell Wall Structure. *Fibers*, *6*(1), 6. https://doi.org/10.3390/fib6010006

Hunter, S. C. (1960). The Hertz problem for a rigid spherical indenter and a viscoelastic half-space. *Journal of the Mechanics and Physics of Solids*, *8*(4), 219–234. https://doi.org/10.1016/0022-5096(60)90028-4

Johnson, K. L. (1982). One Hundred Years of Hertz Contact. *Proceedings of the Institution of Mechanical Engineers*, *196*(1), 363–378. https://doi.org/10.1243/PIME_PROC_1982_196_039_02

Konnerth, J., Harper, D., Lee, S.-H., Rials, T. G., & Gindl, W. (2008). Adhesive penetration of wood cell walls investigated by scanning thermal microscopy (SThM). *Hfsg*, *62*(1), 91–98. https://doi.org/10.1515/HF.2008.014

Kontomaris, S. V., & Malamou, A. (2020). Hertz model or Oliver & Pharr analysis? Tutorial regarding AFM nanoindentation experiments on biological samples. *Materials Research Express*, *7*(3), 033001. https://doi.org/10.1088/2053-1591/ab79ce

Kontomaris, S.-V. (2018). The Hertz Model in AFM Nanoindentation Experiments: Applications in Biological Samples and Biomaterials. *Micro and Nanosystems*, *10*(1), 11–22. https://doi.org/10.2174/1876402910666180426114700

Melelli, A., Arnould, O., Beaugrand, J., & Bourmaud, A. (2020). The Middle Lamella of Plant Fibers Used as Composite Reinforcement: Investigation by Atomic Force Microscopy. *Molecules*, *25*(3), 632. https://doi.org/10.3390/molecules25030632

Melelli, A., Pantaloni, D., Balnois, E., Arnould, O., Jamme, F., Baley, C., Beaugrand, J., Shah, D. U., & Bourmaud, A. (2021). Investigations by AFM of Ageing Mechanisms

in PLA-Flax Fibre Composites during Garden Composting. *Polymers*, *13*(14), 2225. https://doi.org/10.3390/polym13142225

Meng, Y., Wang, S., Cai, Z., Young, T. M., Du, G., & Li, Y. (2013). A novel sample preparation method to avoid influence of embedding medium during nano-indentation. *Applied Physics A*, *110*(2), 361–369. https://doi.org/10.1007/s00339-012-7123-z

Muller, V. M., Derjaguin, B. V., & Toporov, Yu. P. (1983). On two methods of calculation of the force of sticking of an elastic sphere to a rigid plane. *Colloids and Surfaces*, *7*(3), 251–259. https://doi.org/10.1016/0166-6622(83)80051-1

Neugirg, B. R., Koebley, S. R., Schniepp, H. C., & Fery, A. (2016). AFM-based mechanical characterisation of single nanofibres. *Nanoscale*, *8*(16), 8414–8426. https://doi.org/10.1039/C6NR00863A

Pallesen, B. E. (1996). The quality of combine-harvested fibre flax for industrials purposes depends on the degree of retting. *Industrial Crops and Products*, *5*(1), 65–78. https://doi.org/10.1016/0926-6690(95)00049-6

Ren, D., Wang, H., Yu, Z., Wang, H., & Yu, Y. (2015). Mechanical imaging of bamboo fiber cell walls and their composites by means of peakforce quantitative nanomechanics (PQNM) technique. *Holzforschung*, *69*(8), 975–984. https://doi.org/10.1515/hf-2014-0237

Richely, E., Bourmaud, A., Placet, V., Guessasma, S., & Beaugrand, J. (2022). A critical review of the ultrastructure, mechanics and modelling of flax fibres and their defects. *Progress in Materials Science*, *124*, 100851. https://doi.org/10.1016/j.pmatsci.2021.100851

Richely, E., Durand, S., Melelli, A., Kao, A., Magueresse, A., Dhakal, H., Gorshkova, T., Callebert, F., Bourmaud, A., Beaugrand, J., & Guessasma, S. (2021). Novel Insight into the Intricate Shape of Flax Fibre Lumen. *Fibers*, *9*(4), 24. https://doi.org/10.3390/fib9040024

Rico, F., Roca-Cusachs, P., Gavara, N., Farré, R., Rotger, M., & Navajas, D. (2005). Probing mechanical properties of living cells by atomic force microscopy with blunted pyramidal cantilever tips. *Physical Review E*, *72*(2), 021914. https://doi.org/10.1103/PhysRevE.72.021914

Surface energy and the contact of elastic solids. (1971). *Proceedings of the Royal Society of London. A. Mathematical and Physical Sciences*, *324*(1558), 301–313. https://doi.org/10.1098/rspa.1971.0141

Wagner, L., Bader, T. K., & De Borst, K. (2014). Nanoindentation of wood cell walls: Effects of sample preparation and indentation protocol. *Journal of Materials Science*, *49*(1), 94–102. https://doi.org/10.1007/s10853-013-7680-3

Wimmer, R., & Lucas, B. N. (1997). Comparing Mechanical Properties of Secondary Wall and Cell Corner Middle Lamella in Spruce Wood. *IAWA Journal*, *18*(1), 77–88. https://doi.org/10.1163/22941932-90001463

Chapter 8

Water content: Impact on tool performance

Introduction

The work presented in this chapter differs from the previous chapters as it studies the water content of the flax stems, specifically due to rain. Flax stems, like many plant structures, contain water by nature. They can also contain water because of dew exposure and also rainfall. The amount of water in the flax stems has a critical influence on their mechanical properties. Any child who has played with wet straw knows this. In the context of this PhD, variations in water content can significantly affect stiffness and strength of flax stems, complicating the task of real-time tools (potentially working in the field) used to monitor the influence of retting on the mechanical extraction of flax fibres. The variable nature of water content in flax stems introduces a level of complexity that must be considered when using sensors in the field, as it could lead to incorrect determination of the optimum retting point. The variable water content of the flax stems comes predominantly from two sources (i) dew exposure and (ii) rainfall. In order to develop a reliable tool, an in-depth investigation of the behaviour of water content in flax stems is therefore essential. Such an investigation has the potential to refine the operation and timing of sensors used in the field.

However, in this context, the literature survey shows that there has been previous study of the real-time measurement of water content of fruity plants (Ayensu, 1997) (Karathanos & Belessiotis, 1999) (Akpinar et al., 2003) (Diamante & Munro, 1993) (Midilli & Kucuk, 2003) but very few on green flax. Recently, Gibaud et al.(Gibaud et al., 2015) carried out a study to determine the differences between the characteristics of a flax stem in its green state and the same stem when dried, thus investigating the effects of water variation. In this context, the variation in weight can be addressed to the reduction in water content originally present in the stem. The final water content was quantified using Thermogravimetric Analysis (TGA) and gave a consistent value of approximately 6.15% for both the lower and middle sections of the stem. With knowledge of the initial mass of the stem, it is possible to calculate the initial water content retained within the stem.

Therefore, it is viable to develop an approach to measuring water content in flax stems. Is possible by quantifying water loss by comparative weighing during the drying process. This allows the moisture content to be determined as a function of the weight of the stem. In addition, this method can be used to determine the rate at which water content evaporates during the drying period

In this chapter, we have attempted to simulate two different types of rain under controlled conditions that reflect field weather conditions during precipitation events. These simulated scenarios are a 5 minute light rain, which mimics a light rain shower in the field, and a 12 hour soaking experiment, which replicates the effects of prolonged, heavy rain in the field. The knowledge gained from such experiments is invaluable in determining the ideal timing for sensor operation following rain events, thus reducing the risk of false sensor readings. In as much, the work presented in this chapter is of great practical use but also reveals some interesting scientific data which can be compared to the work of others.

Sample preparation and measurement protocol

Retted flax plants are collected from agricultural fields belonging to the VRF company, located in the north of France. The collection protocol is described in detail in Chapter 2.

Initial experiments on bundles of flax stems.

Before the precision experiments, a rudimentary experiment was carried out on long flax stems. The flax stems (taken from the field) were initially weighed and then subjected to a 5 minute shower to simulate a light summer rain. During the shower, the stems were a little spread out rather than in a tight collection bundle–again to simulate field conditions. The flax stems were then weighed again to estimate their water absorption. Following this, the weight of the stems was recorded as a function of time. The scales had a precision of 0.1g. Note that some stems are in contact with each other–as would be the case in the field. Figure 1 shows the flax stem bundle being weighed.

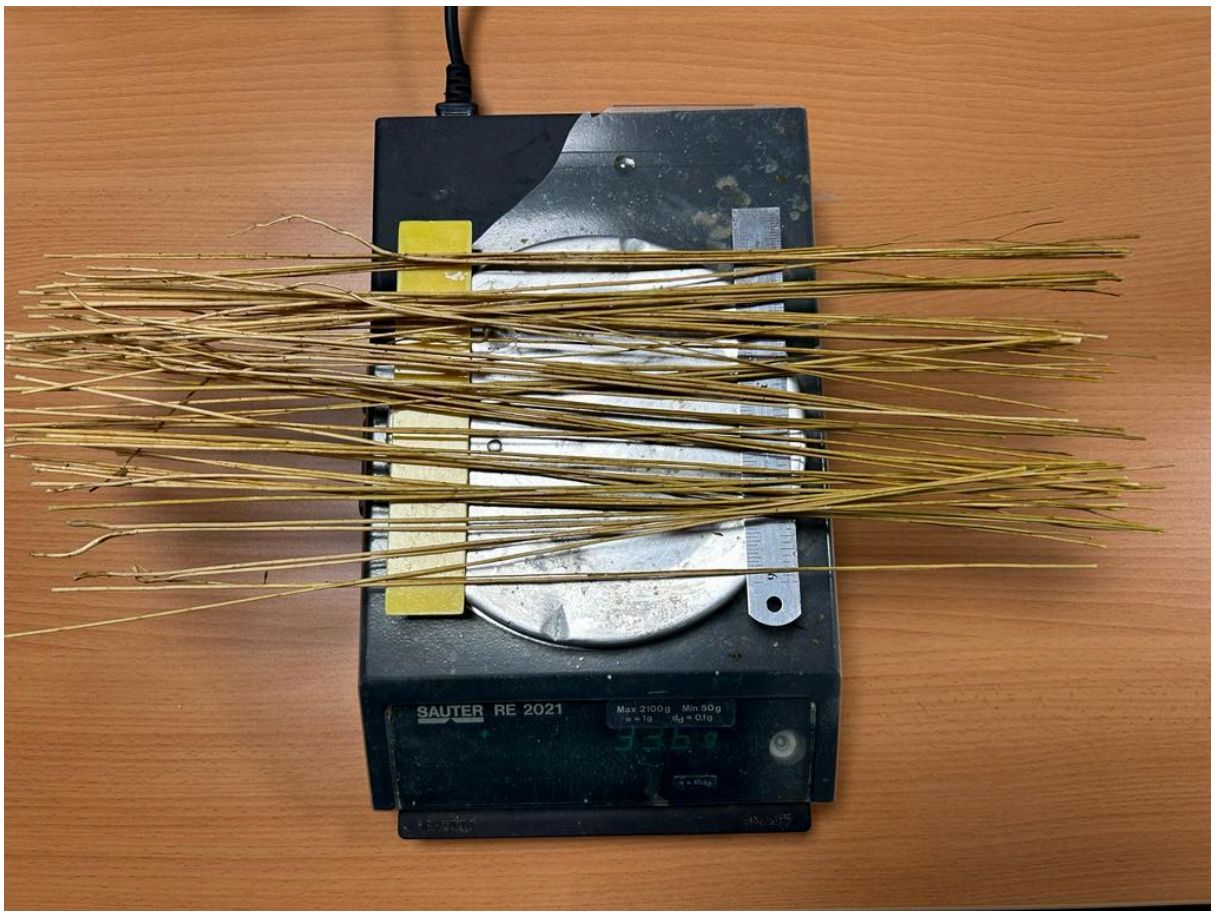

Figure 1. Water absorption and evaporation experiment on long flax stems. The room temperature was measured to be 17°C.

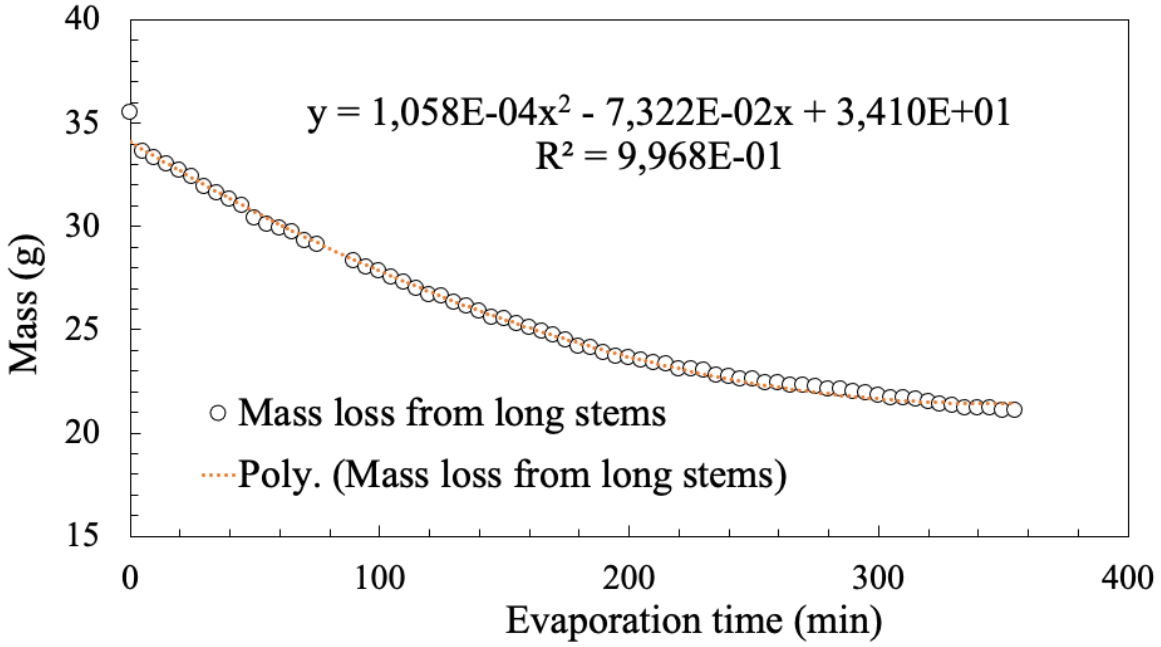

Figure 2. A plot of the weight of the stems as a function of time. There were 77 stems used in this experiment.

The initial dry weight was 19.6g. Following a 5 minute shower this rises to 34.5g. This corresponds to a ratio of 1.76, indicating that the stems absorb water through their surface. In terms of the evaporation, if one wished to extract the evaporation rate (mass loss/time/unit area) from this type of result one would be faced with the problem of evaluating the precise surface area of the stem bundle–this would be challenging. In addition, a tool would use a single isolated flax stem not a bundle.

Therefore, following the reasoning of this experiment we decided to do a more precise experiment on flax stems having well defined dimensions. In this way, the surface area of each sample could be estimated. In addition, the use of precise scales would be needed.

Precise experiments on small samples

In this experiment the samples used are taken from the same plan stems, where samples for the bending experiment were taken. Segments of 1 cm flax stem samples were cut from flax

stem sample of different retting stages, identified as follows: R0 denotes the initial stage of retting immediately after harvesting; R5 corresponds to a point three weeks after harvesting and the beginning of retting; R10 denotes a period five weeks after harvesting; R15 represents the optimum retting time, as determined by Van Robaeys Frères, which occurs eight weeks after harvesting; finally, R20 denotes a stage thirteen weeks after harvesting, characterised by an advanced stage of retting or as over retting. Figure 3 shows the retted flax segments used for the experiment.

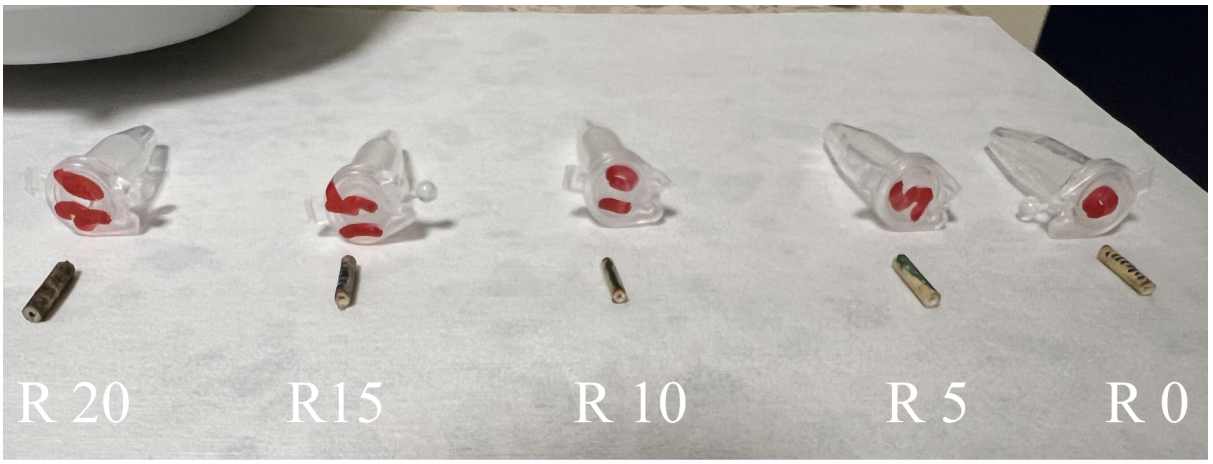

Figure 3. Examples of 1 cm long retted flax stem segments taken from the retted flax stem samples at different stages of retting. These samples are to be used for the water content study.

First, the mass of each individual segment from different retting stages is weighted when the sample is fresh using precision balances, (Mettler Toledo, France). These scales are accurate to 0.2 µg. Figure 4 shows the method used to weight the samples.

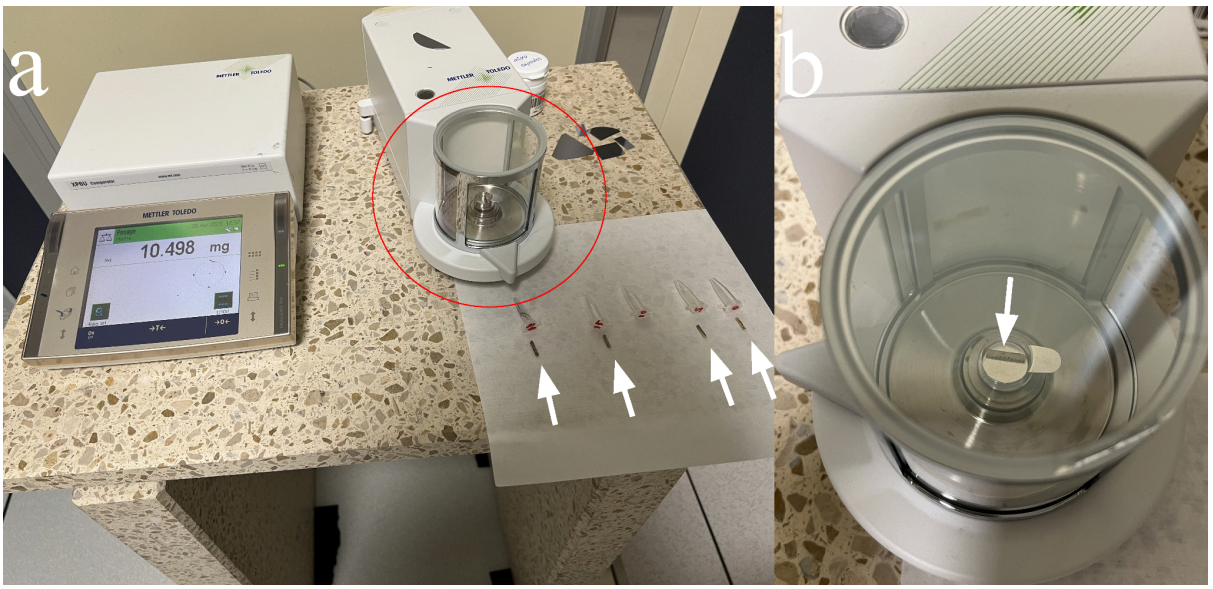

Figure 4. (a) The precision scales used to measure the precise weight of the flax stem segments (indicated by white arrows) prior to and after exposure to water. (b) example of a 1 cm stem segment being measured. The experiments were carried out in a cleanroom (ISO6, temperature 21±1°C, RH 40±5%).

Figure 4 illustrates the equipment used to weigh the samples. Figure 4a shows the precision scales registering a weight of 10.5 milligrams when weighing sample R10. The samples are indicated by white arrows and the sample holder of the balance is indicated by a red circle. Figure 4b is a close-up, highlighting the precise positioning of sample R10 in the holder, as indicated by the white arrow.

After accurately measuring the masses of the samples, we carried out two different experiments. In the first experiment, we used a special cleanroom hand shower to gently spray the prepared samples. The idea was to mimic the light summer rain found in nature. This was done for 5 minutes at cleanroom temperature 21°C. A temperature of 21°C is suitable for the experiment as this would be a typical daytime temperature in July/August in flax growing climates. After spraying, we took the samples out and weighed them every 5 minutes while they dried at room temperature and the mass was recorded. Figure 5 shows the described experiment.

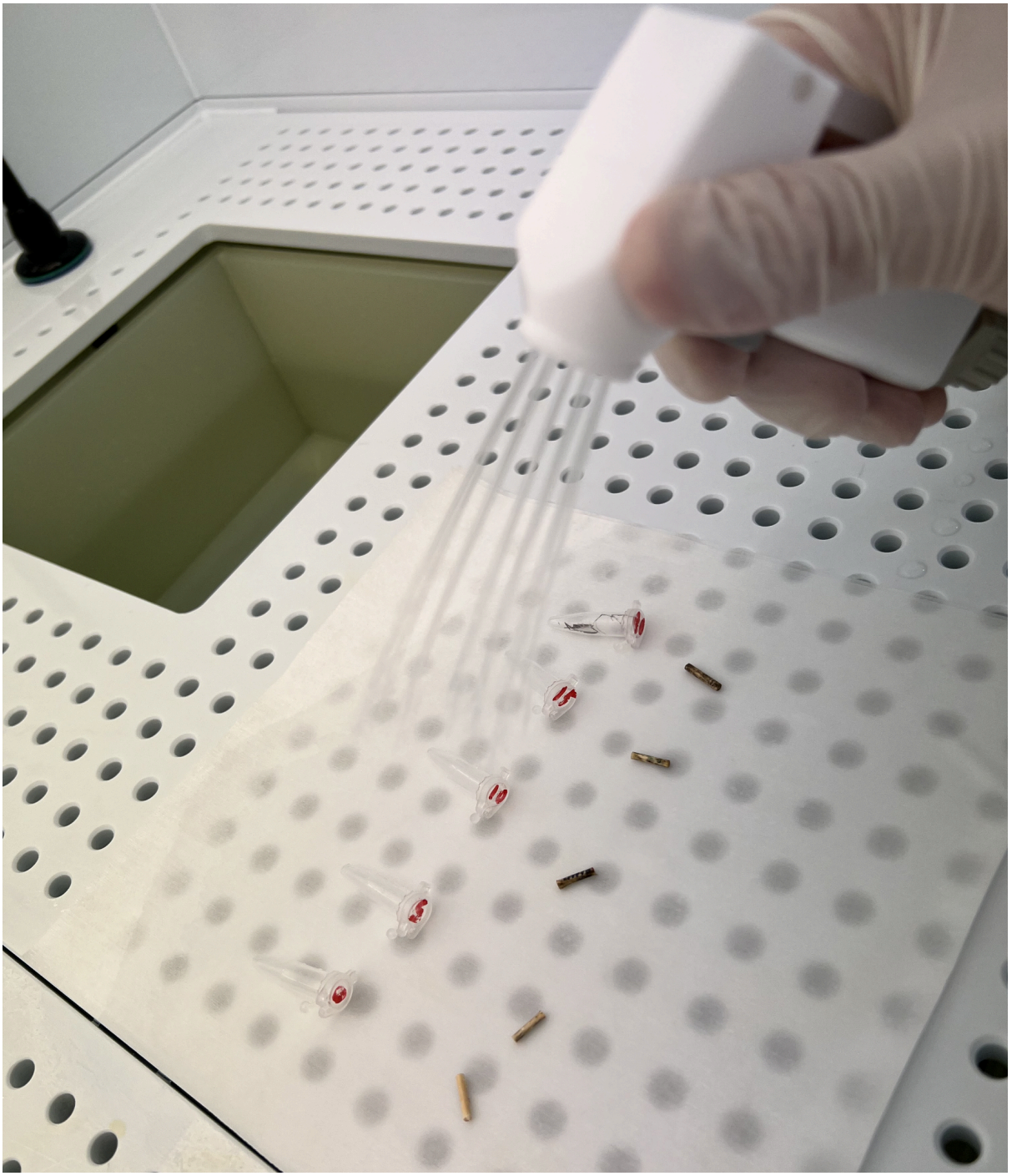

Figure 5. Experiment simulating light (5 minute long) rainfall on the flax stem segments. This would be a typical light ‘sun shower’ in the field.

Figure 5 shows the 5 minutes showering experiment done on 1 cm length flax segments of different retting stages.

For the second experiment, we waited until the samples from the first experiment were completely dry (when the mass of the sample went back to the initial mass weighted before conducting the experiment). These dried samples were then soaked in 1000 µl volume

falcon tubes for one night. This experiment resembles a heavy rain that lasts about 12 hours as in the field. After soaking, the samples were taken out and left to dry again at room temperature. As before, the weight of the samples was measured and manually recorded every 5 minutes as they dried. Figure 6 shows the described experiment.

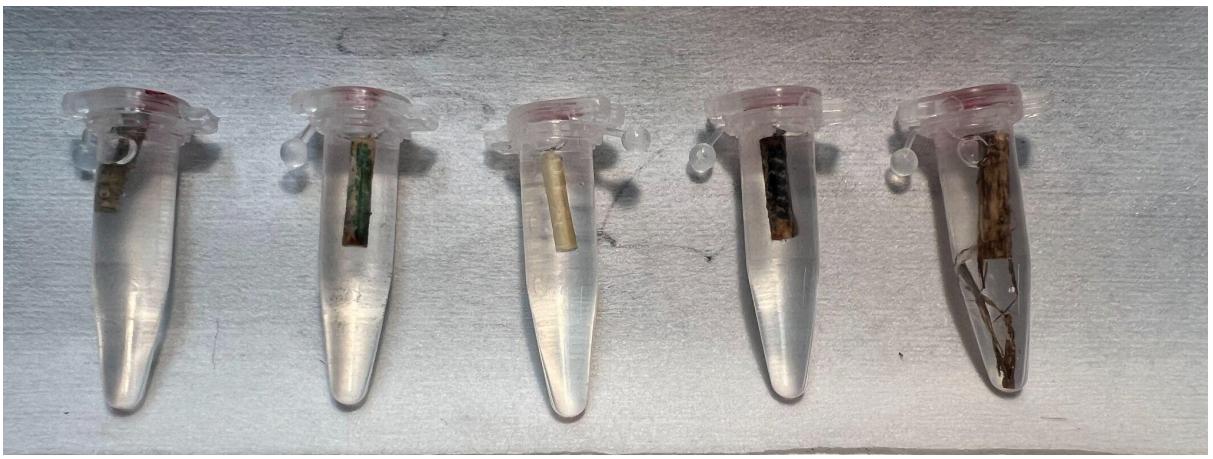

Figure 6. Experiment simulating heavy (12 hour long) rainfall on the flax stem segments. This would be an atypical heavy rainfall in the field during summer Although rare, it can happen.

Following the recording of mass variations over time at room temperature, the data obtained was plotted and analysed to extract the relevant information.

The reasoning behind the measurement

We wish to approximate the time required for the flax stems to dry in a natural field environment and to determine the point at which a potential sensor can resume its operational functionality. To achieve this objective, it is essential to determine the average rate of evaporation of the water content in the flax stems. This average evaporation rate can be calculated as the average mass loss rate of stalks at different stages of retting, per unit surface area.

First, the mass m of the wet stems changes with time. Remember that each stem has a constant length $(1\ cm)$ but a different diameter (d). The variation of wet stem mass m is first plotted as a function of time (t). Curves are numerically fitted to the data to give functions $m(t)$ for each stem. It was discovered that polynomials (quadratic functions) fit the data with a coefficient of determination near to unity. These quadratic fits were then differentiated to obtain linear functions and plotted as a function of time (t). In order to normalise the data with respect to the diameter of the stems used in the experiments, we divided the values of the mass loss rate by the surface area of the stems segments. These values are the

evaporation rate of the flax stems in units of mass/time/unit area. The evaporation rate of the flax stems v is given by:

$$v = \frac{1}{A}\frac{dm(t)}{dt} \quad (1)$$

Assuming that the fibre structure is cylindrical (described earlier) and considering the two sides of the segment, the surface area of this cylinder can be approximated as:

$$A = \pi\, l\, d + \frac{1}{2}\pi d^2 \quad (2)$$

Where d is the flax sample diameter and l is the sample length. Consequently, the evaporation rate v can be expressed as follows:

$$v = \frac{1}{\pi\, l\, d}\frac{dm(t)}{dt} \quad (3)$$

To determine the evaporation rate, it is essential to (i) measure the mass loss as a function of evaporation time and (ii) determine the dimensions of the stems used.

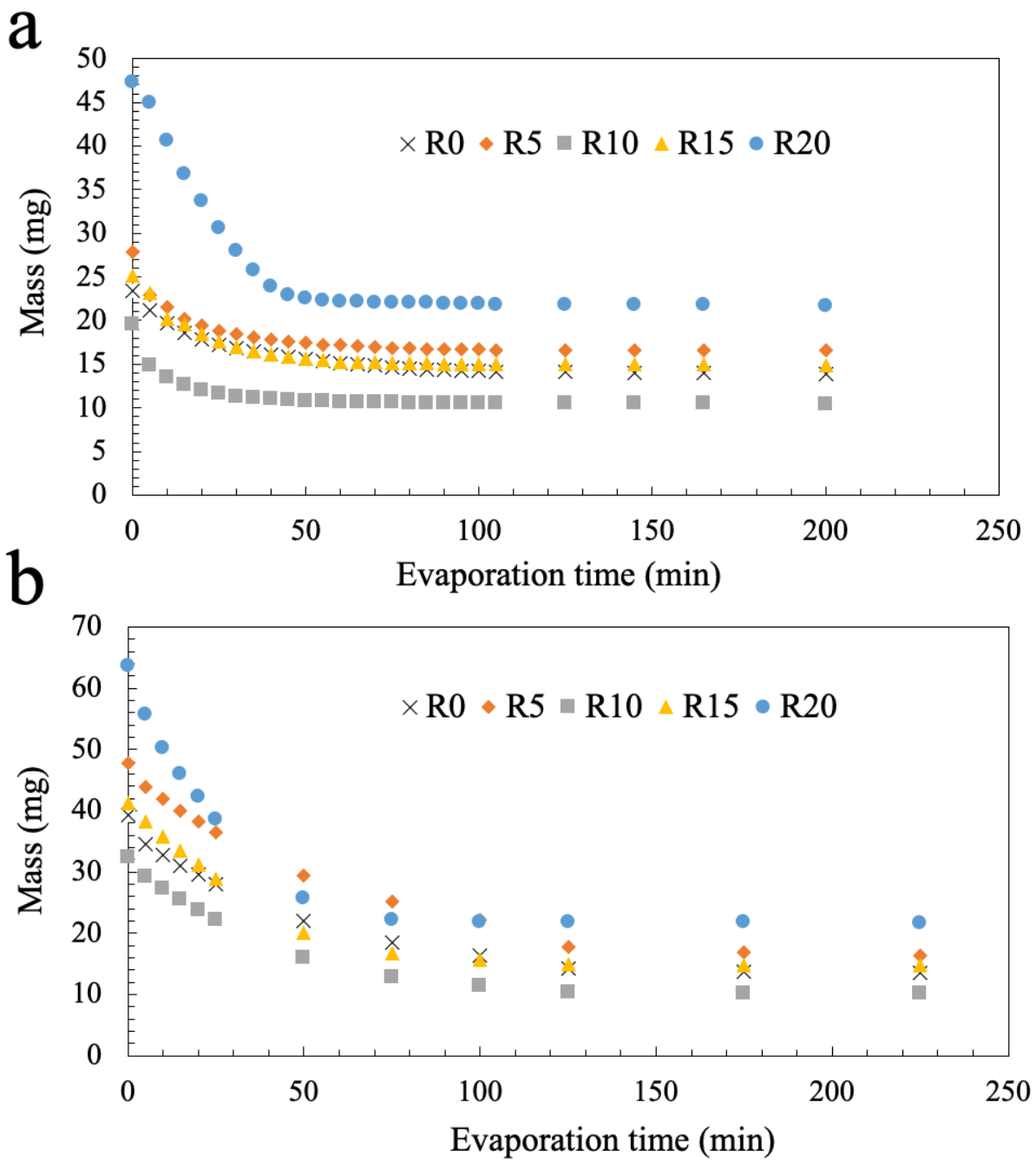

Figure 7. Plot of the mass of the wet flax stems as a function of time. (a) Data for a light rain (5 min) on the stems segments and (b) data for a heavy rain (12 hours) on the stems segments. Measurements performed in an ISO6 cleanroom (T = 21±10C, RH = 40±5%).

Figure 7 shows the evolution of the wet flax stem masses as a function of time following a simulated 5 min shower-see Figure 7a and 12 hours of heavy rain-see Figure 7b. The plots are divided into two distinct parts. First, a portion where the mass of the stems decreases smoothly with time. Secondly, a portion where the mass of the flax stems is relatively constant. The observations suggest that the rate of mass loss is not uniform throughout the

evaporation period, meaning the evaporation rate is not constant. Let us now focus on the portion of the data where the mass of the wet stems reduces smoothly to see if we can fit a curve to the data.

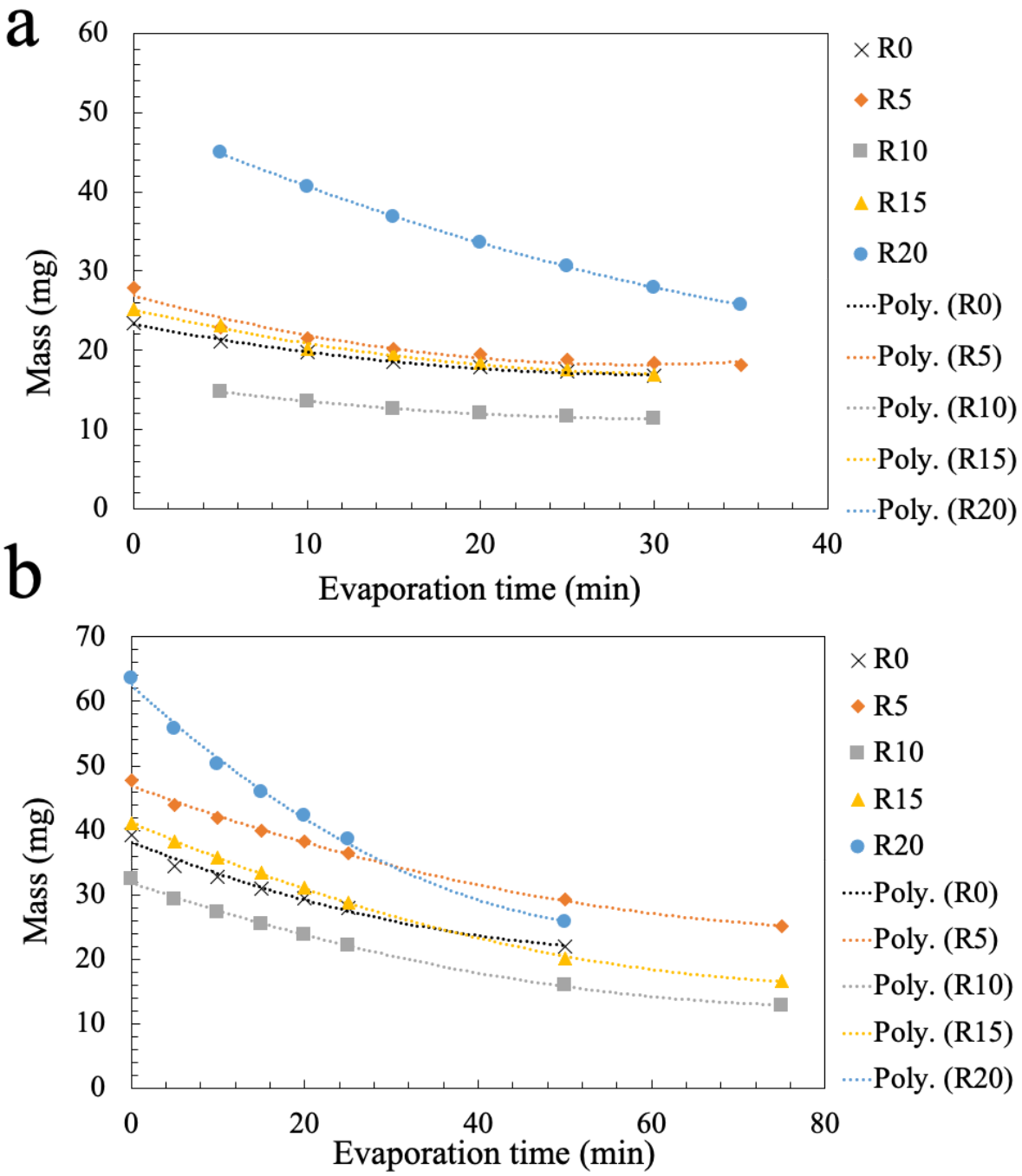

Figure 8. Plot of the mass of the wet flax stems as a function of time in the part of the data where the mass varies (t < 40 min). (a) Data for a light rain (5 min) on the stems segments and (b) data for a heavy rain (12 hours) on the stems segments. The curves correspond to polynomial (quadratic) fits to the raw data.

In Figure 8, it is evident that the data (for all retting samples and both light and heavy rain) adheres very well to fitting with second order polynomial functions, which can be expressed as:

$$m(t) = A(t)^2 + B(t) + C \quad (4)$$

Where, $m(t)$ represents the mass at time t, and A, B, and C are constants which can be obtained from the experimental results. In order to extract the rate of mass loss for each sample at each retting stage, we plot the derivative of the fitted polynomial equation:

$$\frac{dm}{dt} = 2A(t) + B \quad (5)$$

This can be plotted as a function of the evaporation time.

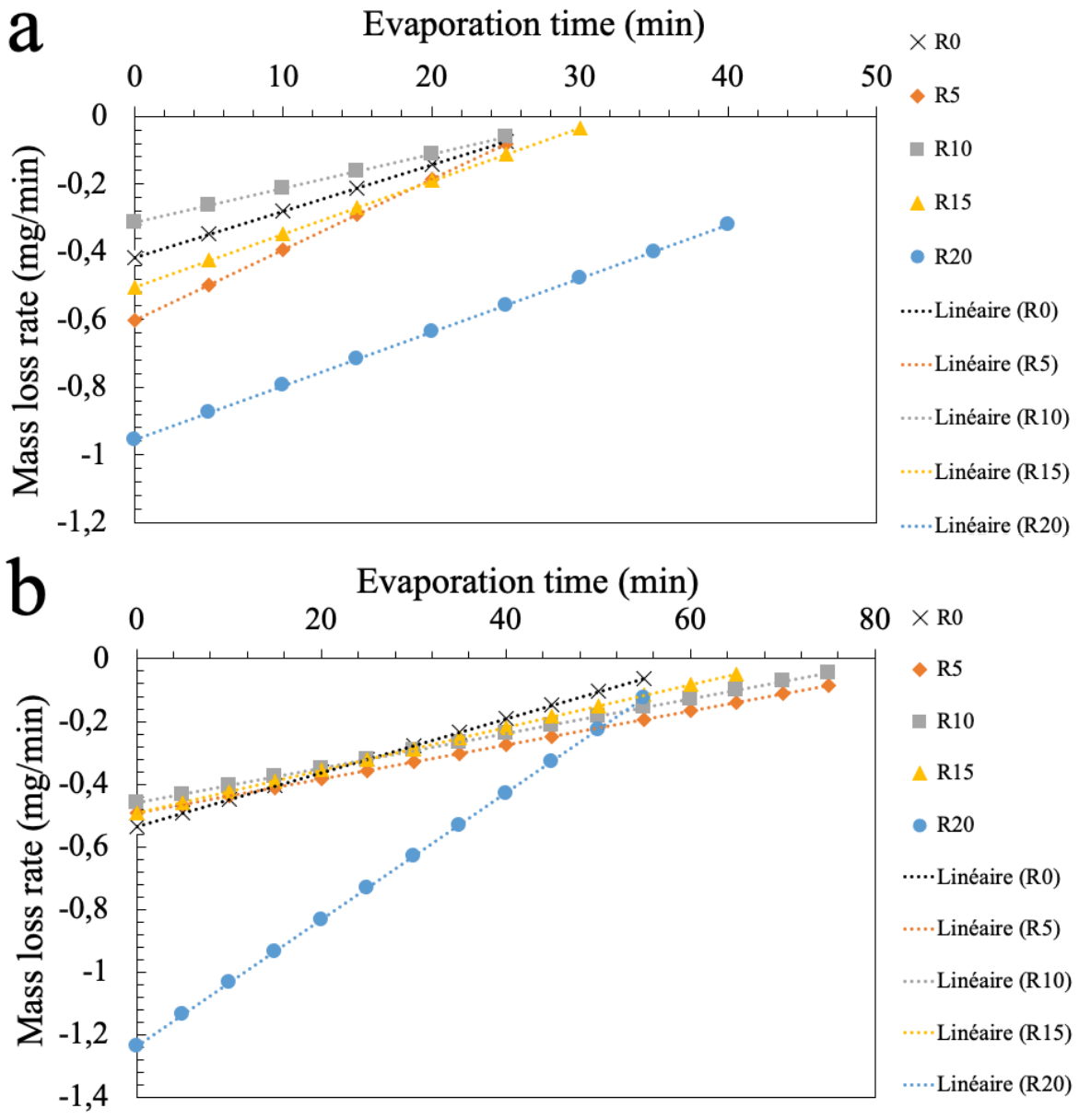

Figure 9. Plot of the mass loss rate (mg/min) of the wet flax stems as a function of time. (a) Data for a light rain (5 min) on the stems segments and (b) data for a heavy rain (12 hours) on the stems segments.

Figure 9 shows the relationship between the mass loss rate (mass/time) as a function of time following a simulated 5 min shower-see Figure 9a and 12 hours of heavy rain-see Figure 9b. Not surprisingly, the mass loss rate shows a linear decrease with increasing evaporation time. In other words, less water is evaporated from the stems as time goes by. At this point, the data has not yet been 'normalised' with respect to the diameters of the stems, i.e. the different surface areas of the stems. This can be done by dividing the fitted data curves by the individual surface areas of the stems.

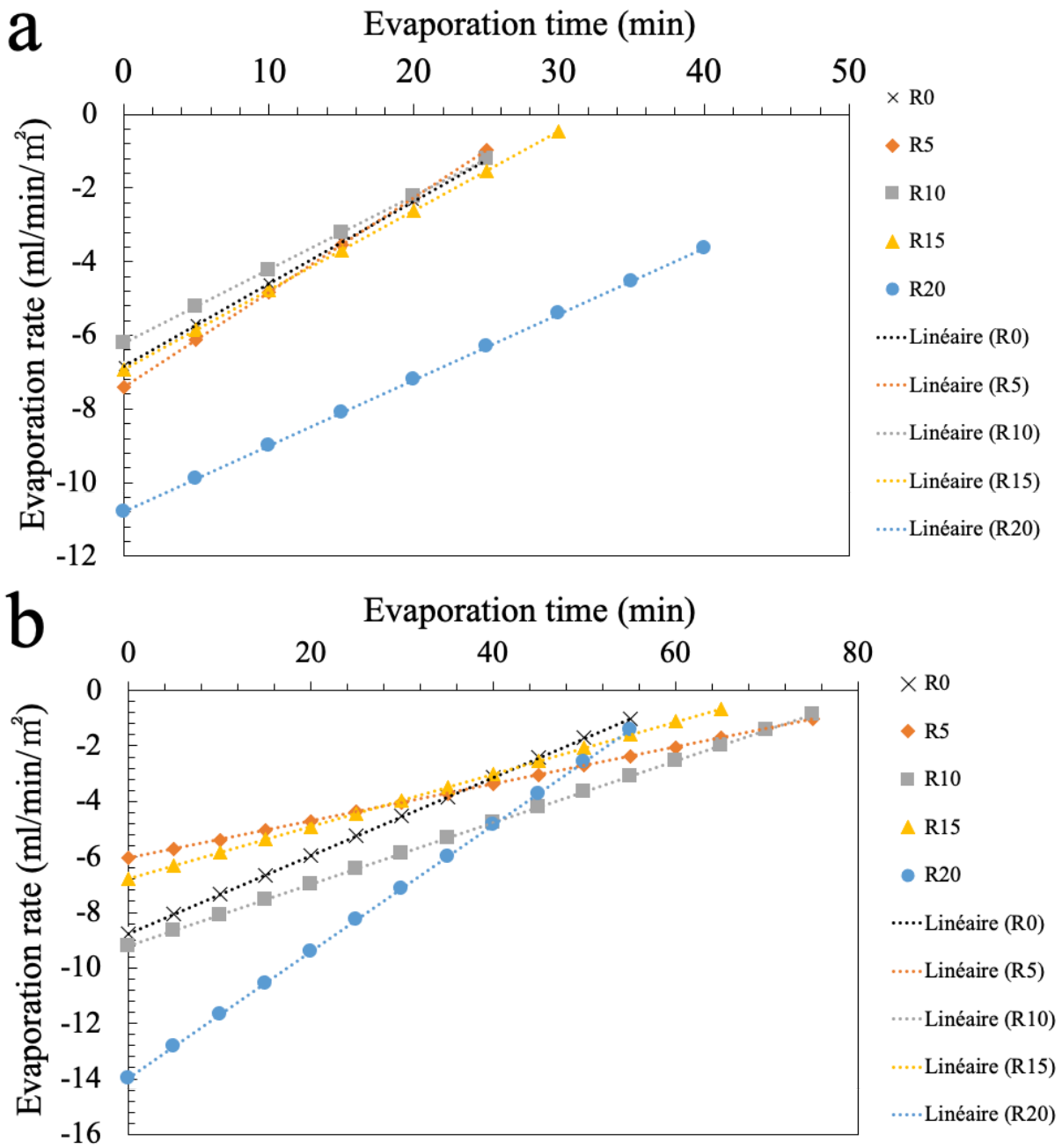

Figure 10. Plot of the evaporation rate (ml//min/m2) of the wet flax stems as a function of time. (a) Data for a light rain (5 min) on the stems segments and (b) data for a heavy rain (12 hours) on the stems segments.

Figure 10 plots the evaporation rate (mass loss/time/unit surface area in this case mg/min/m2) as a function of evaporation time for a simulated 5 min shower-see Figure 10a and 12 hours of heavy rain-see Figure 10b. These plots show that the evaporation rate of the stems decreases with time. The evaporation rates for R0 to R15 are similar. However, for R20 over-retted samples (little or no exterior tissue) the evaporation rates are higher. If we consider that the evaporation rates are not a function of retting from R0 to R15 then it is possible to extract an average evaporation rate for these flax stems from the experimental data.

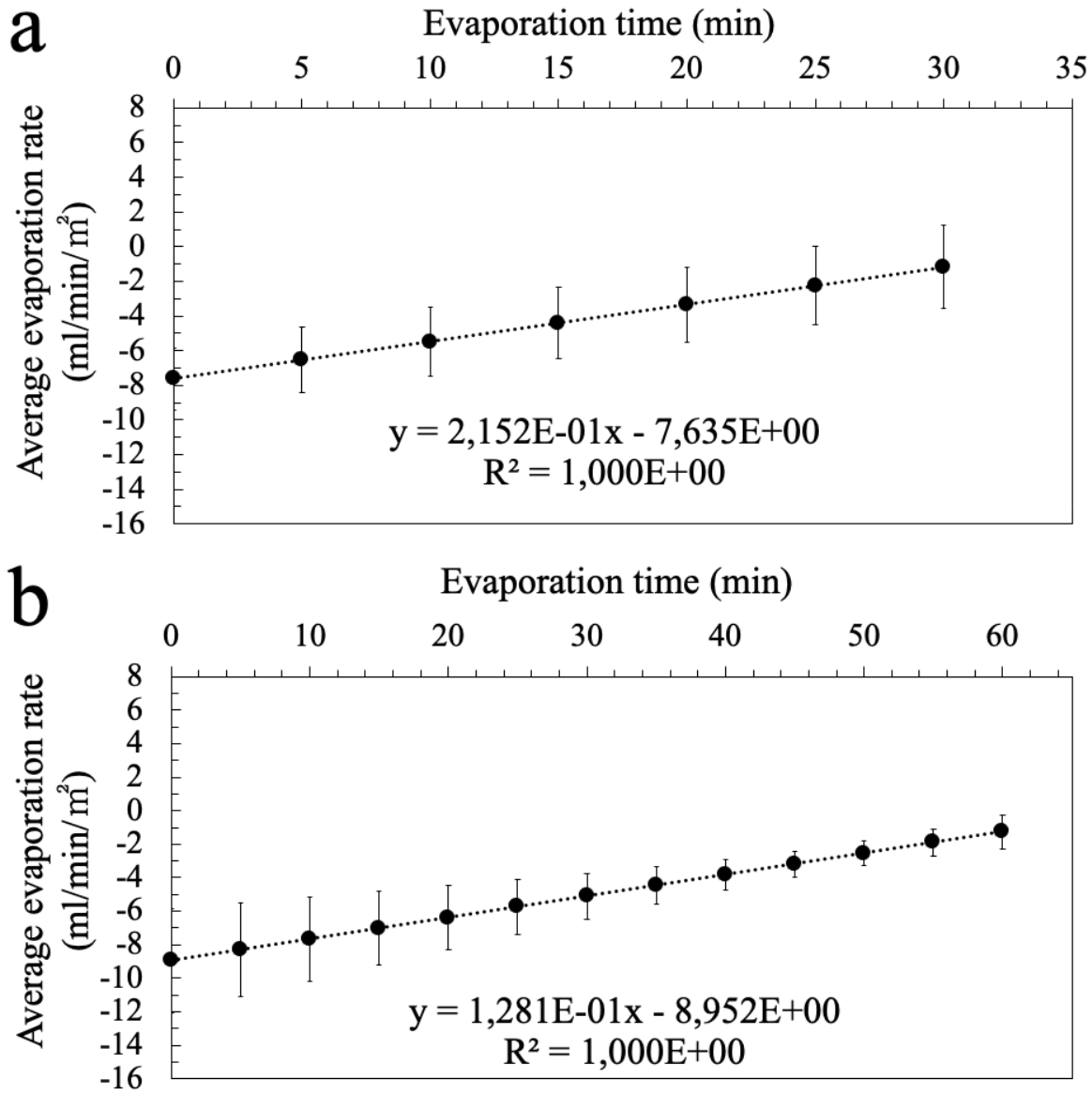

Figure 11. Plot of the average volume evaporation rate (ml/min/m2) of the wet flax stems versus time.(a) Data for a light rain (5 min) on the stems segments and (b) data for a heavy rain (12 hours) on the stems segments.

Figure 11 shows a plot of the average evaporation rate of retting flax stems as a function of time following a simulated 5 min shower-see Figure 11a and 12 hours of heavy rain-see Figure 11b. These are very useful graphs and enable a prediction of the drying time of flax in the field.

Observations and discussions

Let us now discuss the results. First, the stem segments absorb water. This is true for a 5 min light shower and a 12 hour heavy rain. The stem segments absorb more water after a 12 hour soak than a 5 minute shower. At time zero, these ratios are 1.88±0.23 and 3.02±0.15 respectively.

Second, the stem segments lose weight via evaporation of adsorbed water. This mass loss is not linear with time, unlike for example evaporation from a surface of water. The mass loss is also different for each stem, this is because each stem has a different diameter.

Third, the mass loss versus time can be fitted using a polynomial function for all stems. These polynomials can be differentiated with respect to time and plotted as linear functions. These linear functions can be divided by the surface areas of the individual stems to ‘normalise’ the data and compute the evaporation rate of the water from the stems. When this is plotted the evaporation rate of the stems appears to be very comparable from stem to stem. In addition to this, the evaporation rates (and their slopes i.e. the rate of change of the evaporation rates with time) are very comparable for light rain and for heavy rain.

The phenomenon of mass loss, average mass loss rate and average evaporation rate shows a greater acceleration in the R20 samples. This phenomenon can be attributed to the absence of the outer tissues in the R20 samples, where advanced retting leads to degradation of the outer tissues (illustrated in the macro-mechanical chapter), thus exposing the inner tissues. As a result, the rate of water uptake by the outer tissues as well as the woody parts is almost null, resulting in faster water evaporation from the wood surface.

The observed variable evaporation rate of flax stems is interesting. The evaporation rate reduces linearly as time progresses. This indicates a mass flow related issue. A nonlinear drying of flax straw has been previously observed and several groups have been modelled (Nair et al., 2012). Out polynomial fittings agree with the modelling of (Midilli & Kucuk, 2003).

Model name	*Equation*	*Reference*	*Equation no.*
Newton	$MR = e^{-kt}$	Ayensu (1997)	(2)
Page	$MR = e^{-kt^n}$	Karathanos and Belessiotis (1999)	(3)
Henderson and Pabis	$MR = a\, e^{-kt}$	Akpinar et al. (2003)	(4)
Modified Page	$MR = e^{(-kt)^n}$	Diamante and Munro(1993)	(5)
Logarithmic	$MR = a\, e^{-kt^n} + c$	Midilli and Kucuk (2003)	(6)
Wang and Singh	$MR = 1 + at + bt^2$	Midilli and Kucuk (2003)	(7)

Table 12. Various models for the drying of flax stems found in the literature. K is the drying rate constant (min-1), other parameters are constants defined in the references, and MR is the moisture ratio. Table taken from (Nair et al., 2012)

Finally, our data indicates that in a worst case scenario, i.e. large diameter stems (3 mm) subjected to 12 hours of heavy rain, one would need to wait 4 hours to be sure that the stems are dry enough to test mechanically.

Conclusions

It was possible to precisely measure the evaporation rate of water of flax stems which had absorbed water through simulated rainfall. Two types of simulated rainfall were used: a 5 minute light shown and a 12 hour heavy rain. The evaporation rates were measured for flax stems in various stages of retting: from day one to 3 months later. It was observed that the evaporation rates were comparable for all stems (all retting stages) which still contained their exterior tissue. For stems that no longer had the exterior tissue (R20/3 months retting in the field), the evaporation rates were clearly different: they were larger. The evaporation rates of all stems were observed to decrease with time. This is consistent with evaporation from a porous material. The results were also in agreement with observations by others. In addition to this, the evaporation rates were seen to decrease linearly with time. This implies a quadratic decrease of the mass as a function of time, and this is what we observed in the experiments. This agrees with a proposed model for the evaporation of water from wet flax stems. Finally, and in practical terms, this experiment produced a significant result: the ability to determine the drying time of flax stalks in the field. The maximum drying time observed for individual flax stems was 75 minutes, i.e. stems which would be used for a tool. This important finding means that the sensor can resume operation after just 75 minutes of sunny weather at a temperature of 21°C following a period of rain. Regardless of the retting stage or the diameter of the sample, the results show a constant evaporation rate throughout the retting process. This suggests that all samples in the field, regardless of diameter or moisture content, have the same evaporation rate. This finding is promising as it suggests that the sensor can be used effectively on a wide range of samples in the field, regardless of their size or moisture content.

References

Akpinar, E. K., Bicer, Y., & Yildiz, C. (2003). Thin layer drying of red pepper. *Journal of Food Engineering*, *59*(1), 99–104. https://doi.org/10.1016/S0260-8774(02)00425-9

Ayensu, A. (1997). Dehydration of food crops using a solar dryer with convective heat flow. *Solar Energy*, *59*(4–6), 121–126. https://doi.org/10.1016/S0038-092X(96)00130-2

Diamante, L. M., & Munro, P. A. (1993). Mathematical modelling of the thin layer solar drying of sweet potato slices. *Solar Energy*, *51*(4), 271–276. https://doi.org/10.1016/0038-092X(93)90122-5

Gibaud, M., Bourmaud, A., & Baley, C. (2015). Understanding the lodging stability of green flax stems; The importance of morphology and fibre stiffness. *Biosystems Engineering*, *137*, 9–21. https://doi.org/10.1016/j.biosystemseng.2015.06.005

Karathanos, V. T., & Belessiotis, V. G. (1999). Application of a Thin-Layer Equation to Drying Data of Fresh and Semi-dried Fruits. *Journal of Agricultural Engineering Research*, *74*(4), 355–361. https://doi.org/10.1006/jaer.1999.0473

Midilli, A., & Kucuk, H. (2003). Mathematical modelling of thin layer drying of pistachio by using solar energy. *Energy Conversion and Management*, *44*(7), 1111–1122. https://doi.org/10.1016/S0196-8904(02)00099-7

Nair, G. R., Liplap, P., Gariepy, Y., & Raghavan, G. S. V. (2012). Effect of microwave and hot air drying on flax straw at controlled temperatures. *International Journal of Postharvest Technology and Innovation*, *2*(4), 355. https://doi.org/10.1504/IJPTI.2012.050982

Chapter 9

General conclusions and future work

Farming, science, and technology (tools) have always been intertwined. For example, the first plough emerged around 5000 BC. Since this, every leap forward that humans have made in science and technology has had an impact on farming. These leaps forward can now be seen at Agriculture 1.0 forward. We are currently living in Agriculture 4.0 whereby the microelectronics and microtechnology revolution is being applied to all sectors of farming. As we have seen, Agriculture 4.0 is also known as Digital Farming, Smart Agriculture, and Smart Farming. One specific area of Agriculture 4.0 is that of using a whole range of sensors for specific purposes in farming. An example of this is to detect the optimum point of something, e.g. ripeness of fruit, maturity of plant etc. To do this, we have seen that there are many physical and chemical properties which can be monitored by existing sensors. In addition to this there are many sensors yet to be developed as commercial apparatus does not exist. This is the case with this PhD. We have seen that flax fibre production is an important industry. The use of flax fibre, known for its widespread use in textiles and its emerging presence in thermoplastic materials, is underlined by its remarkable mechanical and tensile properties. Among the many techniques available to evaluate the mechanical properties of fibres, tensile testing remains the most prominent choice. The modulus of flax fibre ranges from 30 to 70 GPa, with considerable variability in the data obtained. Numerous factors contribute to this variability, including experimental conditions, dimensions such as diameter and length, chemical composition, cellulose orientation within the fibre and the accurate determination of cross-sectional areas is a significant challenge. In addition, environmental factors and inherent structural defects have a complex effect on this value. The research landscape is actively evolving, delving into fibre modelling to improve the accuracy of mechanical property assessment. Studies focusing on the mechanical properties of flax fibres have predominantly relied on macroscopic tensile testing, with microscale assessments yet to be developed. In particular, existing research has predominantly investigated the effect of retting on the mechanical properties of flax fibres only at the optimum retting point. In contrast, there is a lack of research into the influence in a real-time of retting on the mechanical properties of the flax stalk, which encompasses the fibre, and flax fibres. This highlights the need for a comprehensive understanding of the effect of retting on the flax stalk in order to improve mechanical fibre extraction through accurate and real-time determination. As smart agriculture continues to grow and technology is increasingly integrated into different sectors, the natural fibre sector, particularly flax, has lagged behind in this technological evolution. Despite being a fundamental component of textiles and composites, natural fibres have not fully embraced the potential of smart agriculture. However, achieving optimum flax fibre quality remains a challenge, influenced by factors such as a real-time monitoring of flax dew retting in the field and ability of farmers in accurately predicting the ideal point at which flax is ready. Recognising this critical gap, this PhD programme is strategically designed to address a variety of objectives aimed at bridging this critical gap.

In Chapter 2, a new sample gathering/mechanical measurements protocol was designed and implemented for this novel study. The objective of the work presented in this thesis was to perform a real-time multiscale mechanical characterisation of retting flax stems and tier fibres. By real-time here we mean that samples will be gathered from the field and tested in the laboratory using various tools (existing and those developed for the PhD). Depending on the weather, dew retting can take any time between a few weeks to a few months. As a study of this scale and effort had never been undertaken before in the literature, we

therefore had to define a novel protocol for sample gathering–the description of this is presented in this chapter. A key point is that the samples were not to be stored for later testing, as with biological studies. Here, we intended to conduct mechanical testing on flax stem and fibre samples during the retting period and beyond to obtain information without sample ageing problems and issues. To do this, we had to devise a new protocol for sample gathering to collect suitable stalks. We had to have enough sampling gathering frequency so as to be able to see potential trends in data. We had to have a sample gathering frequency that allowed mechanical testing in between sample gathering days. Every characterisation tool had to work during the retting period. Every special access to the laboratory had to be asked for during the summer closing. This task was not simple, and this was complicated by the fact that no one had ever conducted such a study before.
Despite this, you will see in the subsequent chapters that the sample gathering protocol worked very well and enabled testing of much material. All characterisation tools and techniques functioned well also and there was enough time between sample gatherings to perform experiments–even if the workload and the pressure was high. In addition, we were helped by mother nature a little in that the summer of 2022 was hot and long. This had the effect of lengthening the retting period out so much data could be gathered.

In Chapter 3, flax stems in various stages of retting were characterised by bending experiments. As we saw in Chapter 1, this is one of the manual mechanical tests that an artisan (farmer) conducts ‘in-the-field’ when monitoring the advancement of dew retting of harvested flax stems. The artisan judges qualitative information by hand movement and eye to assess the advancement of the retting of the flax stems. In this chapter, we have attempted to quantify this artisanal bending process in the lab with a view to characterising the flexural modulus and flexural strength of the flax stems as a function of retting. To do this quantitatively, we have designed a setup which uses the flax stem as a macroscopic cantilever. The experiment enables the controlled, gradual bending (deflection) of a flax stem by applying a precise force to the end of the stem. This force is produced using a set of precise masses. By considering the flax stem to be equivalent to a long, straight homogenous pipe, analytical modelling can be employed to compute the flexural modulus and the flexural strength of the flax stem as a function of retting period. This supposition of the modelling enables all flax stems in the study to be compared with each other: both stems from the same retting stage and stems from retting stage to retting stage. This approach has allowed the quantitative determination of the influence of retting on the flexural modulus and the flexural strength of flax stems. It is clearly observed that retting has an effect on the both flexural modulus and the flexural strength of flax stems. Both parameters remain constant during the under retting phase and fall during and after the optimal retting point (as defined by the VRF company). This indicates that the influence of retting can be clearly seen in micromechanical experiments such as bending. The bending tests provided valuable insights. We were able to quantify the daily changes in both average flexural modulus and flexural strength during the 3 months of the retting and over-retting period. The results show that during the under-retting period the flexural modulus and strength of the stems showed a negligible change. However, after the optimal-retting time and during the over-retting period, there was a significant and large decrease in both flexural modulus and flexural strength of the flex stems. The trend resulting from this experiment shows that the influence of retting is clear in bending. Interestingly, experiments on flax stems in different stages of retting that

had the external tissue deliberately removed showed that the flexural modulus and strength of the inner xylem (the ‘wood’ of the stem) does not change. This result strengthens the hypothesis that it is the retting-induced change in the external tissue of the stem that is causing the mechanical properties of the stems to change.

In Chapter 4, the mechanical properties of flax stem samples in various stages of retting were characterised using compression measurements. Flax stems in various stages of retting were measured to monitor the effect of retting upon the compression modulus and the compressive strength of the stems. To do so, a simple tool has been developed to apply an accurate progressive force to a small piece of a cut flax stem. To obtain meaningful results, the cut (cross section) had to be high quality for observations by digital optical microscopy. Water weight was successfully used to apply a controlled accurate force to the stems. The results yielded the deformation of the stem cross section as a function of force. Three phases were observed in the data: an elastic regime, plastic deformation, and a rupturing of the stem xylem. By using a model based on the crushing of a uniform homogeneous pipe, we were able to extract the compression modulus and strength of the flax stems in a certain retting stage and directly compare stems in different retting stages. It was observed that the compressive modulus and compressive strength of the stems does not vary significantly with retting. This is in good agreement with bending results of stems presented in Chapter 3 where the exterior tissue including fibres had been deliberately removed for measurements. The results and observations from this Chapter there lend weight to our proposed behaviour of bending flax stems at various stages of retting and how the retting mechanisms damage the external tissue to modify the bending properties of flax stems. In the next chapter we will descend a level and look at the mechanical properties of the flax fibres.

In Chapter 5, flax stems in various stages of retting were characterised by applying mechanical torsion. This is also one of the manual mechanical tests that an artisan (farmer) conducts ‘in-the-field’ when monitoring the advancement of dew retting of harvested flax stems–this was explained in Chapter 1. The artisan judges qualitative information by hand movement and eye to assess the advancement of the retting of the flax stems. In this chapter, we have attempted to quantify this artisanal process in the lab with a view to producing a technological tool for monitoring of retting in-the-field. To do this quantitatively we have developed an original mechanical tool. The tool enables the controlled, gradual twisting (torsion) of a flax stem. By considering the flax stem to be equivalent to a long, straight homogenous pipe, analytical modelling can be employed to compute the torque and the surface shear stress of the flax stem for a given torsion angle. This supposition enables all flax stems in the study to be compared with each other: both stems from the same retting stage and stems from retting stage to retting stage. This approach has allowed the quantitative evaluation of how the application of torsion affects the shear stress-induced damage in the external tissue of the flax stems as the retting proceeds. It is clearly observed that damage in the external tissue of the flax stems occurs at specific values of surface shear stress for different stages of the retting. For example, in optimally-retired samples (as defined by the VRF company) we observe that a specific surface shear stress value is required for the appearance of damage in the external tissue. For retting stages less than this, no damage is observed at this value of surface shear stress, for retting stages higher than this,

damage occurs at values less than this. The experimental results suggest that a tool based on the application of mechanical torsion and image analysis could be envisaged. The results of this study therefore open up interesting possibilities. The correlation between twisting and retting leads us to consider the development of a real sensor mechanism. Such a tool, based on mechanical torsion/image analysis, could potentially revolutionise the monitoring of dew retting. In addition, this tool could serve as a predictive tool, providing insight into the optimal retting point for flax. This potential innovation promises to improve the efficiency and accuracy of retting processes, thereby contributing to the advancement of flax fibre extraction techniques.

In Chapter 6, single flax fibres in various stages of retting were characterised using novel micro-mechanical approaches developed for the PhD. The previous chapters indicate that the mechanical properties (measured using bending and torsion) of flax stems are modified by dew retting. However, unlike the previous chapters, this is a length scale that is not accessible to the artisan farmer. The results of those chapters suggested that it was the retting-induced degradation of the external tissue that was responsible for the modification of the mechanical properties. The external tissue is composed of flax fibres and the material (middle lamella) between the fibres. In order to go further in an understanding of the macromechanical observations this chapter has presented original micromechanical characterisation of flax fibres at various stages of retting. In order to do this, original approaches for micromechanical measurements of flax fibres were conceived and developed based on MEMS-inspired cantilever techniques. The measurements enabled the flexural modulus and the flexural strength of flax fibres to be evaluated as a function of retting. A key point is the following. Where traditional techniques such as tensile testing can result in very large errors, our micromechanical approaches result in relatively small errors. This means that one can have more confidence in data trends. The measurements suggest that the mechanical properties of the flax fibres do not change significantly during retting. This implies that the observed modification of the mechanical properties in the flax stems (due to retting) is in fact due to the degradation of the middle lamella material–and it is precisely this degradation which permits an easier extraction of fibres in the factory. However, like flax stems, flax fibres themselves are heterogeneous, complex structures. Therefore, in the next chapter we decided to conduct nanomechanical characterisation (nanoindentation AFM) on the external tissue of flax fibres. The reasoning behind this is that the retting-induced damage to the middle lamella is present at the surface of the fibres rather than the interior. It seems logical thus to conduct tests on the outside of fibres to see if there is indeed any retting-induced modification of fibre surfaces–especially in over-retted samples.

In Chapter 7, near field microscopy (nanoindentation AFM) was used to study the cross section and sides of single flax fibres. In addition this can be done as a function of the advancement of retting. Again, unlike chapters 3, 4, and 5, this is certainly a length scale that is not accessible to the artisan farmer! Nanoindentation AFM can be used to measure the mechanical modulus locally on part of a flax fibre. Initially, a standard sample preparation method was used to prepare cross sections of flax stems to enable near field microscopy of their flax fibres in various stages of retting. The mechanical modulus was extracted from these measurements using nanoindentation AFM by applying the Hertz model. The standard

sample preparation method involves imbuing the flax stem with a resin. The nanoindentation AFM measurements revealed some interesting observations. The modulus could be extracted from probing of the fibre cross sections-as others have done. However, tests were also conducted in other zones of the flax stem cross section, notably the xylem regions and their pores. Interestingly, the modulus in the zone was similar to that measured in the fibre zones-suggesting that the resin had imbued many parts of the stem. In an effort to avoid the use of the resin, and also to probe only the outer part of the fibres, we developed an original planar mounting approach to perform AFM on single fibres lying flat on a host chip. We were able to mount several single fibres like this from different retting stages. AFM was performed on several zones along the surface of a single fibre–this is another advantage of this sample mounting along with the absence of resin. The total number of measurements was 650. AFM revealed some interesting results for the modulus at the surface of the fibres as a function of retting. However these results are in contrast with the micromechanical results. Firstly, it is important to note that the modulus obtained by nanoindentation using Atomic Force Microscopy (AFM) was significantly lower than that obtained by the micromechanical approach. The micromechanical technique gave an average effective modulus in the range of 150 to 770 MPa, while the microindentation method gave a modulus of 22 GPa for the whole fibre. This difference in measurement is attributed to the following reasons. The micromechanical approach provides an assessment of the modulus for the whole fibre, including the primary and secondary cell walls, their layers and polysaccharides. In contrast, AFM nanoindentation only penetrates to a depth of just 10 nm. Notably, the depth of the primary cell wall in the fibre composite is approximately 200 nm, as supported by the reference. This suggests that the nanoindentation technique is primarily concerned with the surface of the primary cell wall. The results from this technique show three interesting peaks, each characterised by different modulus values in relation to the retting time. The evolution of these peaks over the course of retting shows a compelling trend: The first peak has a constant value and remains stable as retting progresses. The second peak experiences a decrease at the optimum retting point and then disappears beyond this point, The third peak appears exclusively at the optimum retting point. Whilst there are no previous studies to act as a reference point to conclusively identify the material being indented, the observed trend clearly demonstrates the influence of retting on the fibre surface. This observation is consistent with the understanding that prolonged enzyme activity during over-retting is known to have a detrimental effect on the primary cell wall of the fibres and the resulting effective modulus could be attributed to the mechanical properties of biochemical structures such as lignin, pectin and hemicelluloses present in the fibre cell walls, in particular the primary cell wall. Finally, we note that the planar mounting approach is not to the exclusion of the cross section mounting approach but rather a complimentary technique which can be added to the researchers toolbox—as indeed are the other original techniques and approaches developed in the PhD.

Finally in Chapter 8, it was shown that it was possible to precisely measure the evaporation rate of water of flax stems which had absorbed water through simulated rainfall. Two types of simulated rainfall were used: a 5 minute light shown and a 12 hour heavy rain. The evaporation rates were measured for flax stems in various stages of retting: from day one to 3 months later. It was observed that the evaporation rates were comparable for all stems (all retting stages) which still contained their exterior tissue. For stems that no longer had the exterior tissue (R20/3 months retting in the field), the evaporation rates were clearly different:

they were larger. The evaporation rates of all stems were observed to decrease with time. This is consistent with evaporation from a porous material. The results were also in agreement with observations by others. In addition to this, the evaporation rates were seen to decrease linearly with time. This implies a quadratic decrease of the mass as a function of time, and this is what we observed in the experiments. This agrees with a proposed model for the evaporation of water from wet flax stems. Finally, and in practical terms, this experiment produced a significant result: the ability to determine the drying time of flax stalks in the field. The maximum drying time observed for individual flax stems was 75 minutes, i.e. stems which would be used for a tool. This important finding means that the sensor can resume operation after just 75 minutes of sunny weather at a temperature of 21°C following a period of rain. Regardless of the retting stage or the diameter of the sample, the results show a constant evaporation rate throughout the retting process. This suggests that all samples in the field, regardless of diameter or moisture content, have the same evaporation rate. This finding is promising as it suggests that the sensor can be used effectively on a wide range of samples in the field, regardless of their size or moisture content.

Future work

There are three main avenues for future work which can be envisaged after the PhD: (i) the development of a commercial tool for flax and an extension of the approach to other crops, (ii) numerical modelling of flax stems and fibres, and (iii) going further with the techniques developed in the PhD.

A commercial tool?

The results of the mechanical testing in the PhD suggest that a tool which can monitor the advancement of dew retting flax stems is feasible. The basis of this tool is torsion-induced damage to the exterior tissue of retting flax stems. When the stems are optimally-retted, a certain quantifiable surface shear stress (induced by mechanical torsion) induces observable damage which can be analysed by image processing. Image processing and analysis would be a key point. In the current work, the image analysis was performed manually. If one was to use multiple sensors ‘in-the-field’ one would need to investigate and employ reliable image analysis to identify mechanical-induced damage. One could envisage such a tool or tools being deployed autonomously in the field and being linked wirelessly in the context of the IOT. An important factor is weather, as this governs the rate of retting. The weather can easily be obtained using an in-the-field weather station. However, and it is a big however, the data presented in this thesis, albeit original and large, is for only one single retting period (summer 2022), one particular variety of flax, one set of weather conditions (Killem 2022), one particular field type. In order to validate the mechanical data, we conclude that a 10 year study would need to be carried out to do this. This work would need a major investment in terms of money, time, effort, and willingness. This would also need a long partnership between a public research laboratory and a private company. At the time of writing, it is not evident how such financing could be found. Beyond flax, using mechanical properties for sensing in Agriculture 4.0 could be useful for other crops. It is well known that the mechanical properties of plants evolve with their growth and maturity. It is possible that approaches

inspired by the work presented here could have an impact in the optimisation of other stem-based crops.

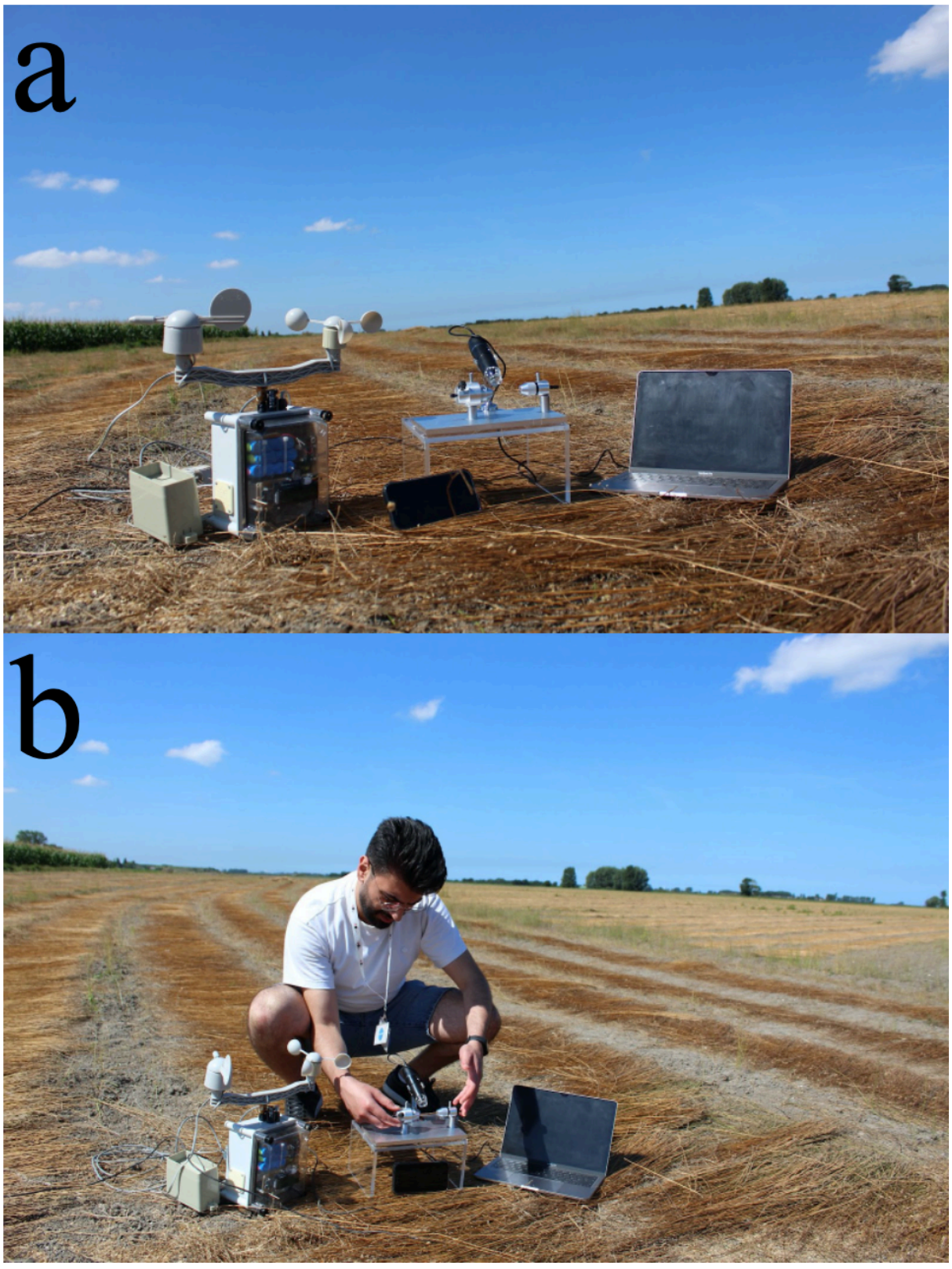

Figure 1. In-field prototype tool assessment during flax dew retting of summer 2023. (a) portable weather station (left), optimised retting tool, microscope, mobile phone (middle), and PC (right). Note that the portable weather station was designed and built by Sebastien Grec (UGSF, Univ. Lille), David Delacrois, and Redha Kassi (IEMN, Univ. Lille). (b) Manual testing of the tool.

Figure 1 shows In the field prototype an assessment during flax dew retting of summer 2023. The setup includes a portable weather station, an optimised retting tool, a microscope, a mobile phone and PC wirelessly connected. The portable weather station (rain, wind, temperature, and field probes) was designed and built by Sebastien Grec (UGSF, Univ. Lille), David Delacrois, and Redha Kassi (IEMN, Univ. Lille). The portable microscope enables visualisation of the stem surface under controlled torsion. The weather station is left in the field and the portable tool could be used daily.

Numerical modelling

In this thesis all the experimental mechanical characterisation (macro, micro, and nano) of flax stems and fibres has been modelled using analytical approaches. Indeed, in a first approximation this has been relatively successful to extract the mechanical modulus and strength of stems and fibres. The analytical models used for this assume a perfect, elastic, homogenous structure. Evidently flax stems and fibres are not perfect and they are certainly not homogeneous structures. In as much, analytical modelling can only extract the composite modulus and strength of a heterogeneous structure–in other words the stems and fibres are like black boxes. Both stems and fibres are very much heterogeneous structures having complex inner structures composed of many different things. In order to go beyond the very rudimentary modelling (albeit relatively successful) used in this thesis, one would need to turn to numerical modelling. Such an approach could be done using commercial software such as Comsol Multiphysics. It is anticipated that such a study would be very involved as many of the mechanical properties of the heterogeneous components of flax stems and fibres are still not well known. Despite this, a study could be performed and compared with experimental results.

Extending the techniques developed in the PhD

As we have seen, the nanoindentation AFM work in the PhD revealed some interesting results and trends in terms of the values of mechanical modulus of the surface of the single flax fibres and their evolution as retting progresses. First, this work could be repeated another year for validation. Second, single fibre extraction methods could be modified and refined to control the surface that is being measured. This could involve chemical means that were not used in the current work. Third, other near field microscopy techniques could be employed–going beyond the nanoindentation used in the current study. For example, commercial techniques such as Bruker's Peak-Force and Peak-Force Tapping mode AFM provide nanomechanical properties, such as modulus and adhesion, whilst simultaneously imaging sample topography at high resolution. Results using these modes could be compared with nanoindentation AFM. In addition to this abundance of physical information,

parallel biological testing of the same flax fibres may provide information to interpret and understand the physical results.

In terms of the techniques developed for the micromechanical measurements, these techniques could be applied to a whole host of other micrometre-diametre fibres, e.g. hairs, to reveal physical properties.

Appendices

Appendix A

Validation of bending model of a pipe

We have calculated the flexural modulus of a complex heterogeneous composite flax stem with the use of an analytical model based on a homogenous thin uniform pipe and making some assumptions. Even though the analytical model is well documented (Timoshenko), model validation is a crucial step to ensure the model's accuracy and reliability in predicting real systems. Failure to validate a model can lead to erroneous predictions and unreliable results. Validating a bending model for flax stems poses significant challenges, as flax stems are complex structures–as discussed before. We decided to verify the analytical model using a pipe with known material properties. To do this, steel and polypropylene pipes were purchased and measured in the same setup and under the same conditions. If the modelling predicts the behaviour of bending steel pipes, then this adds weight to the computation of the composite flexural modulus of flex stems. The following explains these experiments.

Diameter control

To validate the model, two different homogeneous materials were used: 304 grade steel pipes and polypropylene pipes were purchased from a commercial supplier. 304 grade steel has a Young's modulus ranging between 193 and 200 GPa, while the Young's modulus of polypropylene is 1325 MPa. The steel pipes have an inner diameter d_i of 2 mm and an outer diameter d_o of 3 mm, while the external and internal diameters of the polypropylene pipes were measured to be 3 mm and 2 mm, respectively. Figure 1 shows a schematic representation of the steel and polypropylene pipes.

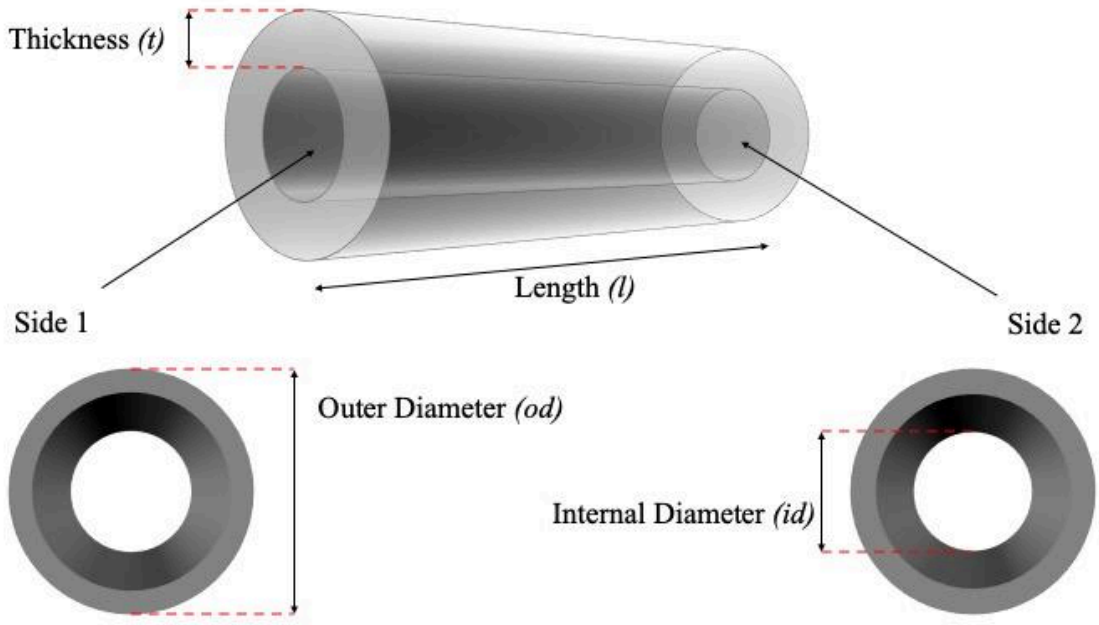

Figure 1. Shows a schematic representation of the dimensions of steel and polypropylene pipes used for the model validation experiment.

To ensure experimental accuracy, the same diameter measurement protocol was used for the steel and polypropylene pipes. Six diameter measurements of different angles were taken on the 2 opposite sides of each pipe and the average diameter was calculated from these six measurements. Figure 2 shows the average diameter extraction method of the stainless steel 403 pipe.

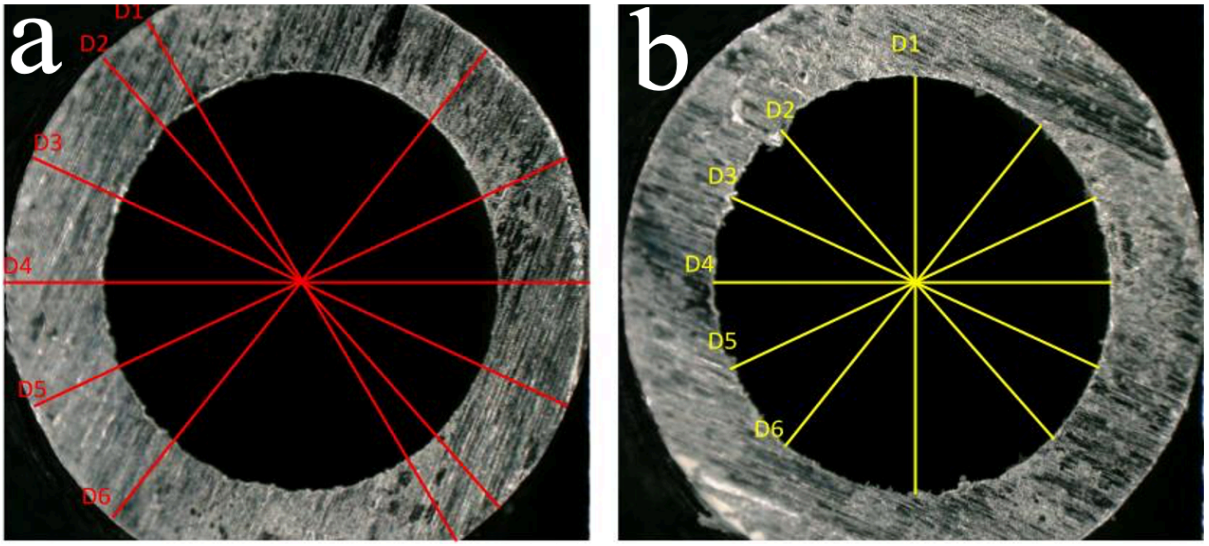

Figure 2. Shows the 6 diameter method used to extract the diameters of the stainless steel 403 pipe. a) shows the 6 diameter extraction method of the outer diameter. b) shows the 6 diameter extraction method of the inner diameter.

The values of the diameter measurements of the stainless steel 304 pipe are summarised in Table 1.

Stainless Steel 304				
Diameter	**Outer diameter d_o (um)**		**Internal diameter d_i (um)**	
Label	**Side 1**	**Side 2**	**Side 1**	**Side 2**
D1	2964.70	2975.42	2023.03	2018.69
D2	2967.08	2970.97	2031.03	2054.32
D3	2968.59	2984.04	2015.05	2010.19
D4	2976.36	2946.91	2002.27	2034.31
D5	2972.62	2950.89	2020.10	1999.83
D6	2962.16	2987.00	2018.69	2016.51

Table 1. Shows 6 diameter measurement values and the average diameter values of the outer and inner diameters of the stainless steel 403 pipe at different angles from both sides.

The same method was used for the extraction of the average outer and inner diameters of the polypropylene pipe illustrated in Figure 3.

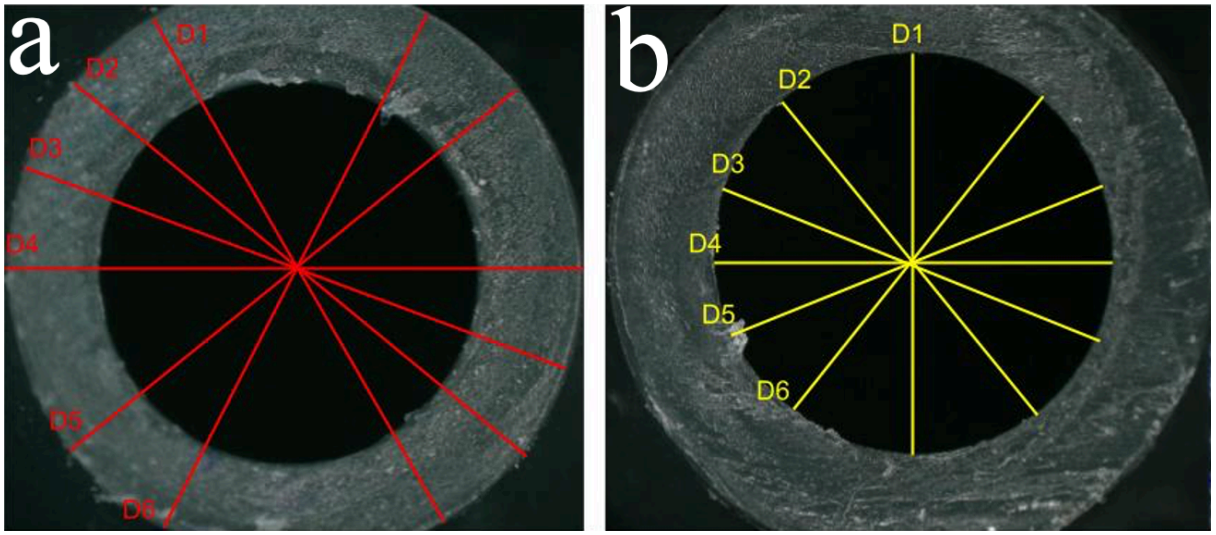

Figure 3. Shows the 6 diameter method used to extract the diameters of the polypropylene pipe. a) shows the 6 diameter extraction method of the outer diameter. b) shows the 6 diameter extraction method of the inner diameter.

The values of the diameter measurements of polypropene pipe are summarised in Table 2.

Polypropylene				
Diameter	**Outer diameter d_o (um)**		**Internal diameter d_i (um)**	
Label	**S1**	**S2**	**S1**	**S2**
D1	2859.63	2990.01	1894.83	1981.75
D2	2886.86	3017.60	1883.71	1979.57
D3	2859.22	3039.24	1886.14	1989.13
D4	2838.22	3008.43	1878.86	1975.86
D5	2869.92	2998.21	1893.35	1985.39
D6	2856.50	3039.82	1894.64	1974.24

Table 2. Shows 6 diameter measurement values and the average diameter values of the outer and inner diameters of the polypropylene pipe at different angles from both sides.

Based on the measurements tabulated in Table 1 and 2 regarding the average outside and inside diameters, along with their respective standard deviations, it is evident that the errors

resulting from the average outside and inside diameters of the 403 stainless steel pipe are 4 and 7 (mm).

Extraction of the tube stiffness k from the experimental measurements

The second key variable required to validate the numerical model, as described in equation (1), is the stiffness parameter (k). As explained earlier, this parameter defines the relationship between the applied load and the resulting deflection. Since these materials exhibit homogeneity and isotropy, the stiffness (k) is determined from the linear region of the load-deflection curve presenting the low deflection regime. With this in mind, we deliberately worked within the low deflection range by avoiding reaching the breaking point and ensuring that all recorded deflection measurements remained within this low deflection regime. The bending experiment applied on both the stainless steel 403 and the polypropylene pipes follows the same measurement protocol as that applied for the flax stalk samples. Figure 4 shows the bending experiment applied on the stainless steel 403 and polypropylene pipe used to validate the model.

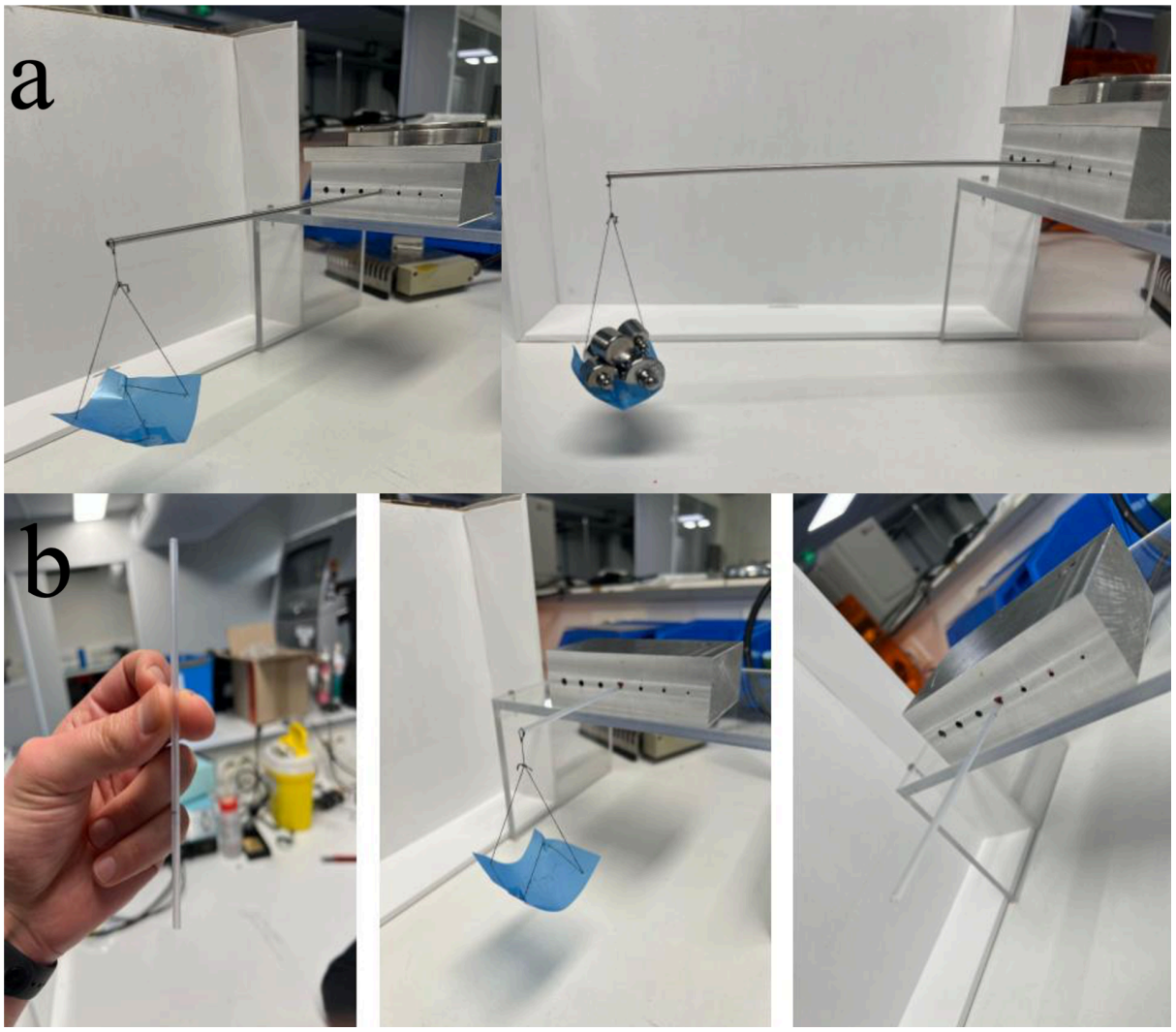

Figure 4. Shows the stainless steel 403 and polypropylene pipes used in the model validation experiment. a) shows the initial state and a bent state of the stainless steel pipe at a given force, b) shows the polypropylene pipe used for the model validation bending experiment, in its initial state before any induced force.

Figure 4 shows the measurement protocol of the model validation bending experiment of the stainless steel 403 and polypropylene pipe. Figure 4 shows that the bending experiment started by fixing the pipes in the holes of the corresponding diameter of the sample holder followed by gradually adding a constant mass of 10 g for the steel pipes and 5 g for the polypropylene pipes, where the weight was manually recorded and the deflection was recorded using the same camera

The acquired images were analysed using ImageJ software, allowing the determination of the deflection after each added mass. The corresponding force for each added mass was then calculated. Table 3 provides a summary of the results obtained from the bending of the steel pipe experiment.

Stainless Steel 304		
Mass (kg)	**Force (N)**	**Deflection (m)**
0	0	0
0.01	0.098	0.00087
0.02	0.196	0.00153
0.03	0.294	0.00219
0.04	0.392	0.00285
0.05	0.49	0.00394
0.06	0.588	0.00438
0.07	0.686	0.00482
0.08	0.784	0.00526
0.09	0.882	0.00658
0.1	0.98	0.00734
0.11	1.078	0.00745
0.12	1.176	0.00822
0.13	1.274	0.00833
0.14	1.372	0.00964
0.15	1.47	0.0103

0.16	1.568	0.01096
0.17	1.666	0.0114
0.18	1.764	0.01206
0.19	1.862	0.01271
0.2	1.96	0.01348

Table 3. Shows the results extracted from the image analysis of bending the stainless steel 403 pipe, including the mass, force and deflection.

Table 4 provides a summary of the results obtained from the bending experiment on the polypropylene pipe.

Polypropylene		
Mass (kg)	**Force (N)**	**Deflection (m)**
0	0	0
0.005	0.049	0.00326
0.01	0.098	0.00674
0.015	0.147	0.01098
0.02	0.196	0.01413
0.025	0.245	0.01815

Table 4. Shows the results extracted from the image analysis of bending the polypropylene pipe, including the mass, force and deflection.

After extracting the experimental data of the force and the deflection, the force F was then plotted as a function of the deflection. Figure 5 shows the plot of the force as a function of deflection resulting from the bending experiments of the stainless steel 403 and polypropylene pipe.

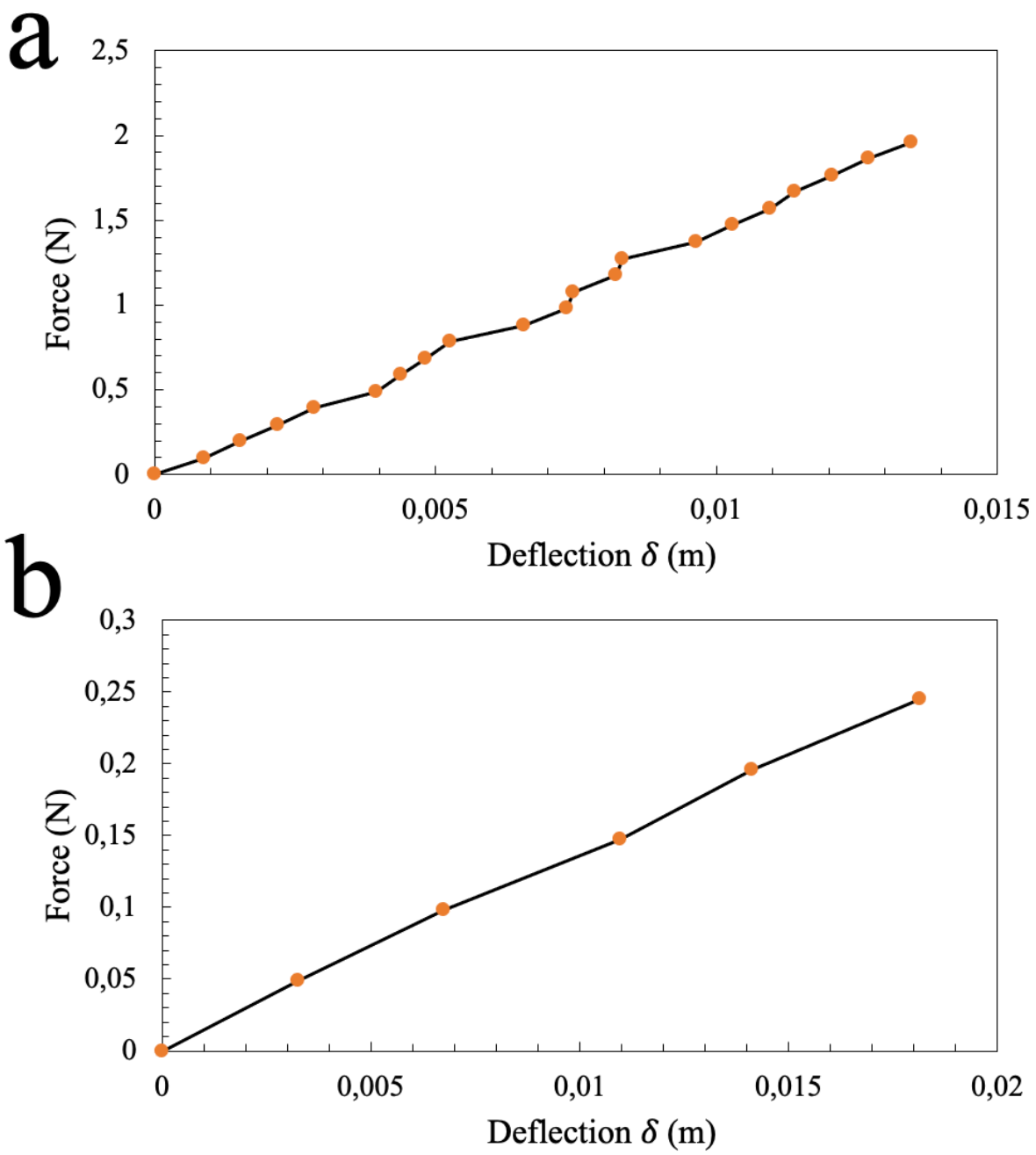

Figure 5. Shows the bending behaviour of the stainless steel 403 and polypropylene pipe. a) shows the plot of the force as a function of deflection of the stainless steel pipe, b) shows the plot of the force as a function of deflection of the polypropylene pipe.

Before further analysis of the graphs in Figure 5, the low deflection regime expressed as δ/L is calculated, to ensure the accuracy in the results. Table 5 shows the low deflection calculations resulted from both experiments. Table 6 Shows the low deflection regime calculation for the stainless steel and the polypropylene pipe.

Stainless Steel 304		Polypropylene	
Deflection δ (cm)	δ/L	**Deflection δ (cm)**	δ/L
0	0	0	0
0.087	0.00905307	0.326	0.033922997
0.153	0.015920916	0.674	0.070135276
0.219	0.022788762	1.098	0.114255983
0.285	0.029656608	1.413	0.147034339
0.394	0.040998959	1.815	0.188865765
0.438	0.045577523		
0.482	0.050156087		
0.526	0.054734651		
0.658	0.068470343		
0.734	0.076378772		
0.745	0.077523413		
0.822	0.0855359		
0.833	0.086680541		
0.964	0.100312175		
1.03	0.107180021		
1.096	0.114047867		
1.14	0.118626431		
1.206	0.125494277		
1.271	0.132258065		
1.348	0.140270552		

Table 5. The low deflection regime corresponds to the deflection of each pipe. The last point corresponding to the low deflection regime is marked in grey.

Table 6 shows that the low deflection regime values expressed by the equation δ/L obtained from the experimental model validation for stainless steel and polypropylene pipes, are 14% and 18% respectively. The deflection values corresponding to these values marked by the grey colour in Table 5, represent the maximum deflection of the pipes relative to their total

length, as indicated in the plots in Figure 6. In both cases, these results indicate that the maximum deflection remains below 20% of the total length of the pipes. This confirmation ensures that the maximum deflection is in the low deflection range and allows the stiffness parameter k to be obtained from the linear relationship between load and deflection, expressed by the slope of the linear curve. Figure 6 shows the method of extraction of the relation between the force and deflection δ.

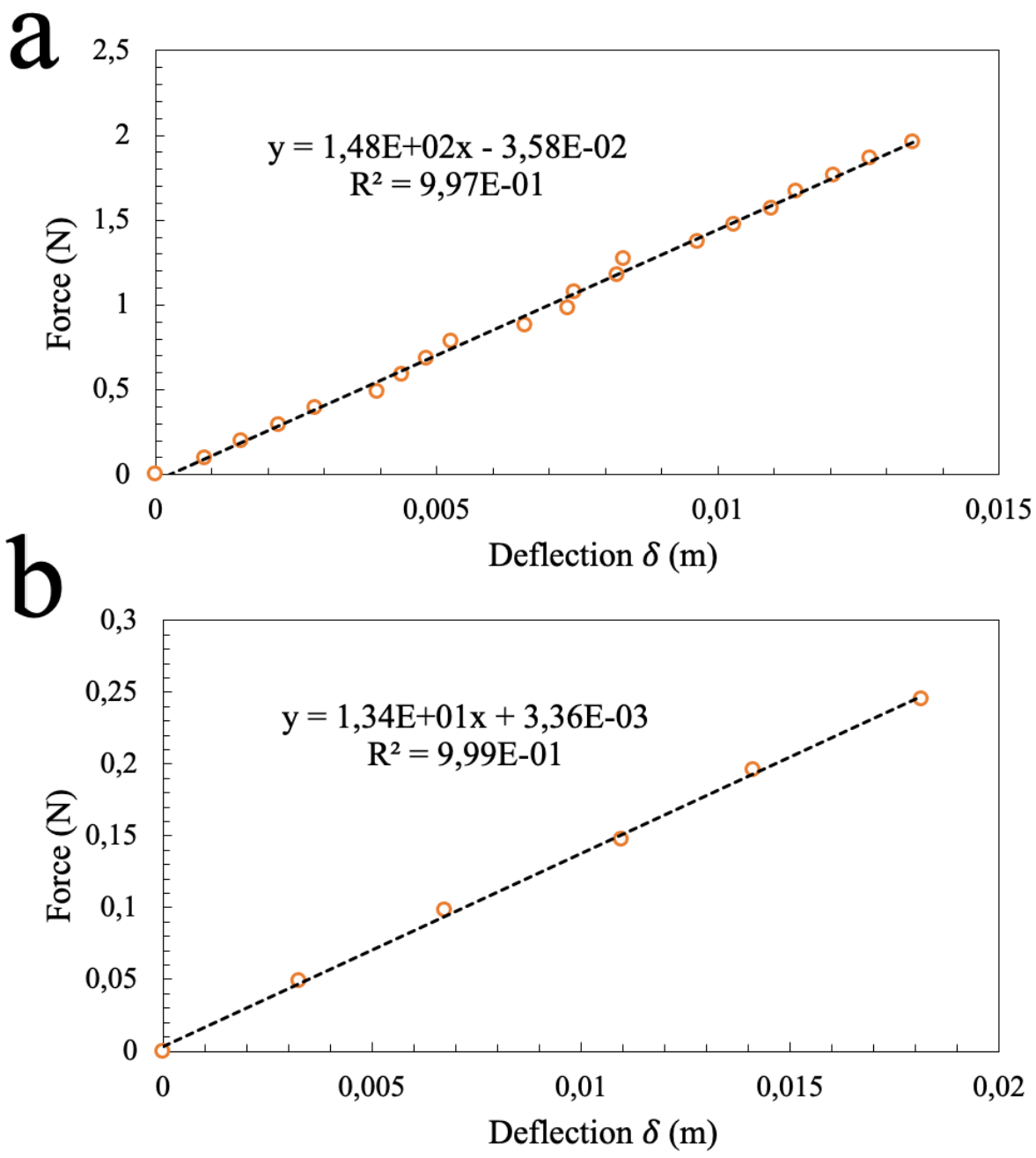

Figure 6. Shows the extraction method of the stiffness k parameter expressed as the slope of the linear part of the plot showing the relation between the force and the deflection. a) shows the linear low deflection regime and the extraction method of the stiffness of the stainless steel 403 pipe. b) shows the linear low deflection regime and the extraction method of the stiffness of the polypropylene pipe.

Figure 6 shows the stiffness values for the 403 stainless steel pipe, which was determined to be 147.82 N/m, and the polypropylene pipe, which had a stiffness of 13.422 N/m. These stiffness values are then applied to the analytical model to validate the flexural modulus of the pipes.

Determination of the tube's flexural modulus

The calculation of flexural modulus in this experiment follows the same procedure as in the previous analysis of flax stems, using the equation presented in the Experimental part of Chapter 3. A summary of all the parameters required for the calculation of Young's modulus is presented in Table 6.

Stainless Steel 304				
Outer diameter (m)	**Internal Diameter (m)**	**Stiffness (N/m)**	**Flexural Modulus (N/m2)**	**Flexural Modulus (GPa)**
d_o	d_i	$\frac{F}{\delta}$	E	E
0.002968899	0.002020339	147.82	1.95033E+11	**195.033**
Polypropylene				
Outer Diameter (m)	**Internal Diameter (m)**	**Stiffness (N/m)**	**Flexural Modulus (N/m2)**	**Flexural Modulus (MPa)**
d_o	d_i	$\frac{F}{\delta}$	E	E
0.002020339	0.001934794	13.422	1336366439	**1336.366**

Table 6. Shows a summary for the variables required for the young's modulus calculation and the value of the stainless steel and polypropylene young's modulus.

According to the data in Table 6, the calculated Young's modulus for the 304 steel pipe and the polypropylene pipe are 195.033 GPa and 1336.366 MPa respectively. These values are within the range of the true Young's modulus of the two materials (widely accepted values). This suggests that the model used to calculate Young's modulus is valid for these homogeneous materials as well as the flax stalks. Furthermore, the consistency of the model results with the mechanical properties of the steel and polypropylene pipes also indicates that the flax stalks, which have been exposed to various environmental factors for more than three months, have retained their mechanical properties and behave as a homogeneous material.

Appendix B

Validation of compression model of a pipe

Although simulations are valuable for exploring theoretical scenarios and making predictions, the inclusion of experimental validation using known materials adds an additional level of confidence and applicability to the model's predictions. Validating a model through experimental testing on a known material is widely considered to be advantageous over relying solely on simulations for several compelling reasons. First and foremost, experimental validation allows direct measurement and observation of the material's behaviour under specified conditions, facilitating the acquisition of real experimental data that can be directly compared with the model's predictions. This comparison allows a more accurate assessment of the accuracy and reliability of the model. In addition, experimental testing allows for the consideration of various factors that can influence the material's response, including variations in material properties, environmental conditions and boundary conditions. By taking these factors into account during experiments, researchers can gain a comprehensive understanding of the material's behaviour and validate the model's ability to accurately capture such complexities.

In order to validate the flax stalk compression model, a compression test was performed on the same polypropylene specimen used in the bending experiment. The objective was to evaluate the ability of the model to accurately predict the behaviour of flax stalks under compression. The experimental conditions were meticulously maintained, including the use of a 2 mm sample size, the same diameter measurement method and the identical compression setup used in the compression testing of the flax segments.

Extraction of the tube stiffness k from the experimental measurements

The relationship between force and displacement is determined by analysing the elastic region of the force-displacement curve-see Figure 1 below:

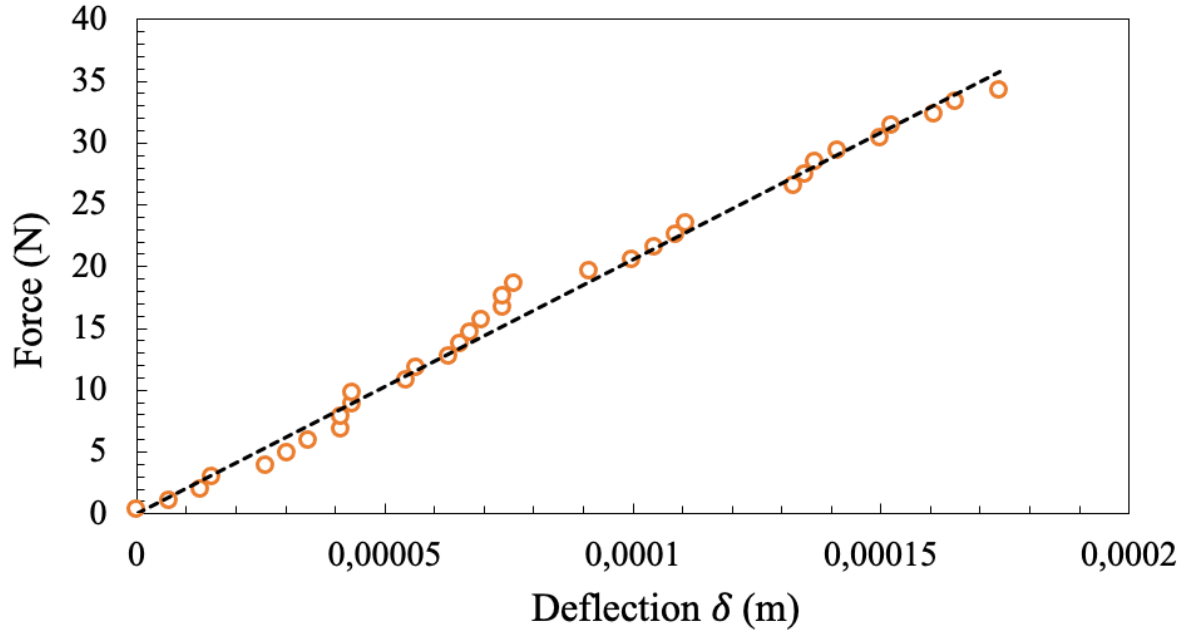

Figure 1. Shows the extraction method of the stiffness k parameter expressed as the slope of the linear part of the plot showing the relation between the force and the deflection.

Determination of the tube's flexural modulus

The parameters required to obtain from the compression test are summarised in the table below.

Stiffness (N/m)	Outer Diameter (m)	Internal Diameter (m)	length (2 mm)	Thickness (m)
k	d_o	d_i	l	t
127768	0.003015558	0.001980995	0.002	0.000517281

Table 1. Shows a summary for the variables required for the compressive modulus calculation

The modulus of the polypropylene material was calculated using the equation (1) given in the Compression Chapter. The results of these calculations are presented in the tables below:

Compressive Modulus E (N/m)	Compressive Modulus E (MPa)
1309594379	1309.59

Table 2. Shows a summary of the obtained compressive modulus.

Based on the results obtained, the modulus derived from the polypropylene compression test is approximately 1309.59 MPa. These results are consistent with the modulus value of 1336 MPa obtained from the bending test. The consistency of these accurate results provides strong evidence for the validity of the model in characterising the homogeneity of the material, as well as the accuracy of the measurement methods and experimental protocol used.

Appendix C

Version condensée de la thèse en français

Résumé

L'agriculture 4.0, également connue sous plusieurs pseudonymes tels que "agriculture numérique", "agriculture intelligente" et "agriculture électronique", se développe actuellement rapidement en termes de recherche, de développement et d'applications commerciales. Comme pour l'agriculture 1.0, 2.0 et 3.0, l'objectif de l'agriculture 4.0 est d'utiliser la technologie pour améliorer tous les domaines de l'agriculture. Dans l'agriculture 4.0, il s'agit de l'application de la microélectronique et des microtechnologies. Contrairement à ce qui se passait auparavant, ces technologies apportent des éléments tels que l'internet des objets, les données massives, les télécommunications, les nouveaux capteurs, le retour d'information rapide, l'analyse des données, la connectivité, l'intelligence artificielle, etc. En principe, tous ces domaines devraient entraîner une modernisation massive de l'agriculture en termes d'organisation, de rendement, d'efficacité et de qualité des produits. Cependant, l'agriculture 4.0 est tellement vaste que si l'on veut y contribuer, même de façon mineure, il faut choisir un domaine spécifique. Le domaine choisi pour l'étude de ce doctorat est la production de fibres de lin. Les fibres de lin sont des fibres naturellement solides qui peuvent être extraites des tiges de lin. Les tiges de lin ont évolué pour avoir des fibres robustes d'un diamètre de l'ordre du micromètre qui courent le long de l'extérieur de la tige et sont maintenues en place dans le tissu externe de la tige. Une fois extraites et isolées, les fibres de lin ont de nombreuses applications, allant des textiles aux matériaux composites. Afin de faciliter l'extraction mécanique des fibres de lin de leurs tiges mères, les tiges subissent un processus connu sous le nom de « rouissage ». Le rouissage entraîne la décomposition du tissu externe (appelé lamelle moyenne) entre les fibres. Une forme courante de rouissage est connue sous le nom de « rouissage de rosée ». Dans le rouissage de la rosée, des processus naturels tels que les bactéries et les champignons produisent des enzymes qui décomposent la lamelle centrale et séparent progressivement les grappes de fibres et les fibres des grappes. La durée du rouissage dépend fortement des conditions météorologiques. Un rouissage insuffisant entraîne une extraction difficile des fibres dans l'usine, tandis qu'un rouissage excessif peut compromettre la qualité des fibres. On sait depuis longtemps qu'il existe un point de rouissage optimal - même les anciens le savaient. Certains agriculteurs artisans qualifiés sont capables de juger ce point par une combinaison de manipulation manuelle des tiges, d'observation des dommages causés aux tissus externes par cette manœuvre, et aussi d'observation de la couleur et de l'odeur des tiges au cours de ce test très habile, mais artisanal. Il est clair que l'artisan effectue des tests de laboratoire rudimentaires littéralement « sur le terrain ». Il semblerait donc logique d'essayer de quantifier ces tests et de voir si un outil fiable peut être mis au point pour aider l'artisan. Et c'est exactement ce que d'autres ont tenté de faire. L'introduction de la thèse donne des exemples de tentatives de fabrication d'outils de rouissage optimal dans les années 1980 et suivantes. Inspirés par ces premiers travaux, les travaux de cette thèse tentent une caractérisation mécanique multi-échelle complète des tiges et des fibres de lin pendant un cycle de rouissage (été 2022) et, de manière quelque peu ambitieuse, réalisée en temps réel - à notre connaissance pour la première fois. La caractérisation mécanique comprend des essais mécaniques macroscopiques (flexion, écrasement et torsion de la tige), ainsi que des essais mécaniques microscopiques inédits sur des fibres de lin individuelles à l'aide de nouvelles méthodes inspirées des systèmes microélectromécaniques (MEMS). En outre, les propriétés mécaniques nanoscopiques de la paroi cellulaire primaire des fibres de lin en cours de rouissage ont été caractérisées à l'aide de la microscopie à force atomique (AFM) par nanoindentation. Au fur et à mesure que le travail expérimental, l'analyse via la

modélisation analytique et l'interprétation descendent en échelle, de la macro au nano en passant par le micro, nous en apprenons un peu plus sur la manière dont le rouissage affecte les tiges, leurs propriétés et leurs fibres. En plus de l'apprentissage, un résultat très positif du doctorat est que l'on est capable de suggérer un mécanisme de dommage induit mécaniquement dans les tiges, qui pourrait être la base d'un outil. On peut cependant noter que la nature multiparamétrique incontrôlable du sujet, par exemple le temps, signifie que plusieurs études seraient nécessaires pour confirmer sans aucun doute les observations d'un seul cycle de rouissage.

Chapitre 1

Introduction

L'émergence de l'agriculture 4.0

L'agriculture est un secteur fondamental qui fournit à l'homme des aliments et des matières premières indispensables. Première source de nourriture dans le monde, l'agriculture a joué un rôle central dans le progrès des civilisations tout au long de l'histoire de l'humanité. Selon l'ONU, la population mondiale devrait augmenter d'environ 2 milliards de personnes d'ici à 2050, pour atteindre un total d'environ 11 milliards à la fin du siècle. Il est donc urgent d'augmenter la production alimentaire mondiale pour répondre à la demande de cette population croissante. Toutefois, selon l'ONU pour l'alimentation et l'agriculture (FAO), l'impératif d'atténuer la faim et de garantir la sécurité alimentaire ne nécessite pas nécessairement une augmentation significative de la production agricole, même jusqu'à 50 %, à condition que les systèmes de production agricole adoptent des mesures de durabilité plus importantes.

Dans le monde d'aujourd'hui, caractérisé par des avancées technologiques significatives dans un large éventail de domaines, l'intégration de la technologie et des efforts de recherche sera la clé de la réalisation d'une agriculture durable. Dans ce contexte, l'agriculture de précision revêt une importance capitale pour garantir la sécurité alimentaire d'une population mondiale croissante.

L'agriculture numérique, également appelée « Smart Agriculture », « Smart Farming », « Digital Agriculture » ou « Agriculture 4.0 », vise à optimiser la productivité, l'efficacité et la durabilité dans le secteur agricole. Cela implique l'utilisation de technologies telles que la microélectronique, les micro- et nanotechnologies, les communications, l'internet des objets (IoT), l'informatique en nuage, la robotique et l'intelligence artificielle (IA) pour améliorer divers aspects des pratiques agricoles. Par conséquent, les données numériques jouent un rôle important dans l'agriculture, y compris la communication électronique entre les fournisseurs et les clients finaux.

L'agriculture intelligente émerge en tant que produit d'une révolution agricole qui est entrelacée avec la trajectoire de la révolution industrielle. Cette relation symbiotique découle du rôle central de l'industrie, des machines et de la technologie dans le façonnement du paysage de l'agriculture intelligente. La révolution industrielle, avec son impact transformateur, est la pierre angulaire sur laquelle la révolution agricole se construit et évolue. Cette transformation a également eu un impact profond sur divers aspects de la société.

La confluence de ces révolutions a ouvert une ère où les avancées technologiques s'harmonisent avec les pratiques agricoles, conduisant à l'émergence de l'agriculture intelligente comme une force puissante et fédératrice. Aujourd'hui, grâce à ces révolutions, l'agriculture intelligente et l'intégration de la technologie numérique apparaissent comme des tendances dominantes dans le secteur agricole des pays européens. Le nombre

d'agriculteurs utilisant les technologies numériques dans leurs exploitations est en constante augmentation. Ce changement de paradigme promet d'accroître la productivité, de réduire les dommages causés aux cultures et d'optimiser l'utilisation des ressources telles que l'eau, le carburant et les engrais grâce au potentiel offert par les pratiques agricoles de précision.

Pourquoi l'agriculture 4.0 ?

Tout au long de l'histoire, plusieurs révolutions industrielles ont façonné l'industrie et introduit des mécanismes visant à améliorer l'efficacité de la production.

La première révolution, connue sous le nom d'Industrie 1.0, a commencé au milieu du XVIIe siècle avec l'avènement de la machine à vapeur, qui a ouvert la voie à l'intégration des machines dans les processus de production. La deuxième révolution, Industrie 2.0, a eu lieu à la fin du XIXe siècle et s'est caractérisée par l'utilisation généralisée de l'électricité à des fins domestiques et industrielles. La troisième révolution, l'industrie 3.0, s'est déroulée tout au long du XXe siècle et s'est caractérisée par l'introduction des robots et de l'automatisation dans les processus industriels. Nous sommes actuellement dans la quatrième révolution industrielle, communément appelée « industrie 4.0 ». Cette ère est caractérisée par le concept d'entreprise intelligente, dans lequel des machines et des systèmes interconnectés visent à atteindre l'efficacité et l'adaptabilité des systèmes de production. Dans ce contexte, la collecte d'informations joue un rôle central dans les processus de production. Les capteurs et autres technologies déployées collectent des données dans l'ensemble de la zone de production, ce qui nécessite une capacité importante de stockage, de traitement et d'analyse des données afin de les transformer en informations exploitables qui améliorent les performances.

La prolifération de l'industrie et de l'innovation technologique s'est accompagnée d'une vague de changements dans l'agriculture. Cette confluence a marqué le début d'une révolution agricole, une période caractérisée par l'assimilation des principes et des technologies industriels dans les processus agricoles. L'agriculture est une industrie manufacturière à grande échelle et toutes les révolutions industrielles mentionnées ci-dessus ont eu un impact sur la manière dont elle est produite aujourd'hui.

L'évolution du développement agricole peut être retracée à travers quatre révolutions distinctes. Ces révolutions sont les suivantes : Agriculture 1.0, l'ère de l'agriculture traditionnelle, qui reposait sur la main-d'œuvre humaine et animale. L'ère de l'agriculture 2.0, parallèlement à l'industrie 2.0, des progrès significatifs ont été réalisés avec l'introduction de la machine à vapeur et de l'électricité dans l'agriculture. Le tracteur à vapeur a joué un rôle crucial dans l'augmentation de la capacité de production, en particulier dans les processus post-récolte. Le XXe siècle a vu l'émergence de l'agriculture 3.0, qui a marqué un tournant important vers l'automatisation des processus agricoles. Cette époque a vu l'intégration de machines complexes capables d'effectuer diverses tâches tout au long du cycle agricole, notamment la plantation, la récolte, la fertilisation et le triage de base.

Au moment de la rédaction de cette thèse (2023), nous sommes au début de la quatrième révolution agricole. L'ère actuelle de l'agriculture, connue sous le nom de « Digital Farming » ou Agriculture 4.0, mais aussi familièrement sous le nom de « Smart Farming », se

caractérise par l'intégration de technologies de pointe et d'approches axées sur les données dans les opérations agricoles. Cette révolution bénéficiera de deux technologies : l'intelligence artificielle, qui aidera à la prise de décision, et le Big Data, qui permet d'analyser de vastes données statistiques collectées par diverses techniques.

Ces technologies ont été développées par diverses organisations de pointe dans le secteur de l'agriculture intelligente. Ces secteurs jouent un rôle central dans diverses opérations agricoles, englobant des tâches essentielles telles que l'analyse de l'humidité du sol, l'évaluation de la santé des cultures, la prédiction précise des périodes optimales de récolte et la planification stratégique des activités de lutte contre les ravageurs. Grâce à la technologie-cadre de l'internet des objets (IoT), les systèmes agricoles peuvent désormais être contrôlés à distance via des appareils mobiles, ce qui facilite la surveillance en temps réel de paramètres vitaux tels que la température, l'humidité et l'exposition à la lumière du soleil dans les fermes de production. En outre, l'intégration de la « technologie blockchain » dans le secteur agricole, notamment par la mise en œuvre d'actions automatiques ou de « contrats intelligents », facilite le stockage sécurisé et la traçabilité des données tout au long de la chaîne d'approvisionnement, garantissant l'authenticité et la provenance de chaque transaction. Cela a le potentiel de réduire les cas de malhonnêteté et de pratiques frauduleuses parmi les différents partenaires impliqués dans la chaîne d'approvisionnement. L'utilisation de la technologie analytique des drones contribue à cette avancée technologique en capturant des images haute résolution des cultures. Ces images sont ensuite soumises à une analyse approfondie à l'aide de techniques d'intelligence artificielle (IA), ce qui permet d'obtenir des informations précieuses sur les modèles de rendement et les performances des cultures. Le terme « big data » fait référence au stockage et à l'analyse de très grands volumes de données collectées par les technologies de l'information et de la communication (TIC). L'accumulation et l'analyse rapide des données permettent de prendre des décisions en temps opportun, ce qui se traduit en fin de compte par une augmentation de la productivité dans l'agriculture. Cette intégration de ces technologies de pointe permet non seulement d'accroître la productivité agricole, mais aussi d'ajouter de la valeur au processus agricole.

En outre, la notion d'agriculture intelligente englobe l'évolution vers des pratiques agricoles intelligentes, ce qui implique la modernisation et l'amélioration des outils agricoles traditionnels. Le vieillissement de ces outils a rendu nécessaire leur intégration dans le domaine numérique. Le paysage actuel exige des outils à la fois robustes et universellement interopérables, sans qu'il soit nécessaire de suivre une formation spécialisée pour les utiliser. La robotique agricole a trouvé des applications dans divers domaines, notamment la production, la transformation, la distribution et la consommation. Dans le secteur agricole, des robots ont été intégrés dans une série d'équipements à des fins telles que la sélection des produits et la distribution précise des pesticides. Cette approche technologique s'étend aux véhicules aériens utilisés pour surveiller systématiquement l'état de santé des fruits, des légumes et du bétail dans l'environnement agricole. Spécifiquement adaptés à la révolution de l'agriculture 4.0, les systèmes robotiques peuvent être divisés en trois catégories distinctes. La première catégorie comprend les robots de plein champ, déployés stratégiquement pour des tâches telles que l'irrigation et la culture des récoltes. Dans la deuxième, les robots d'installation jouent un rôle clé dans l'évaluation des rendements et la régulation des activités agricoles. La troisième classification concerne les robots d'élevage, qui sont conçus pour veiller au bien-être des animaux qui font partie intégrante du domaine

agricole. Cette intégration diversifiée des robots dans les pratiques agricoles souligne leur potentiel à révolutionner et à accroître l'efficacité des processus agricoles modernes. En outre, face au défi posé par l'infrastructure de télécommunications limitée dans les zones rurales, le développement des outils de l'agriculture 4.0 a introduit des solutions capables de fonctionner de manière transparente même dans les zones sans couverture de téléphonie mobile, et couvrant différents secteurs des régions en croissance.

Ces dernières années, des progrès considérables ont été réalisés dans l'automatisation des équipements mécaniques utilisés dans les pratiques agricoles, ce qui a permis d'augmenter la production agricole. La capacité de collecter des données en temps réel sur divers facteurs environnementaux, les paramètres de croissance des plantes et la santé des cultures a permis aux agriculteurs et aux chercheurs de prendre des décisions éclairées, d'optimiser l'affectation des ressources et d'atténuer les risques potentiels. Des progrès considérables ont ainsi été réalisés dans la gestion des cultures, ce qui a permis d'améliorer les rendements, de réduire l'impact sur l'environnement et d'améliorer la qualité des produits. Cette section examine les dernières avancées dans l'utilisation de la technologie IoT pour améliorer l'efficacité des équipements et systèmes mécaniques dans le secteur agricole.

Compte tenu de ce contexte, il est donc très clair qu'une question clé de l'agriculture intelligente est celle des technologies des capteurs. Examinons maintenant ce domaine en pleine évolution.

Le développement de capteurs pour l'agriculture 4.0

La classification des capteurs en fonction du domaine

Il est évident, même pour l'amateur, qu'il existe une myriade de paramètres impliqués dans chaque aspect de l'agriculture. Jusqu'à l'avènement de l'agriculture 4.0, la plupart de ces paramètres étaient mesurés de manière très rudimentaire ou simplement « jugés » par l'agriculteur artisanal. La détection technologique permet d'envisager la quantification des paramètres agricoles comme jamais auparavant.

Les capteurs utilisés dans l'agriculture intelligente ont une taxonomie basée sur les zones agricoles spécifiques qu'ils surveillent. Par exemple, les capteurs optiques montés sur des véhicules, des satellites, des drones ou des robots peuvent utiliser la lumière pour évaluer les propriétés du sol et capturer des données sur la couleur des plantes, tout en mesurant également des attributs tels que la teneur en argile et l'humidité. Les capteurs électrochimiques, montés sur des traîneaux spécialisés, contribuent à la collecte de données chimiques, y compris les niveaux de nutriments et le pH, avec des mesures sans erreur facilitées par des électrodes sélectives d'ions. Les capteurs mécaniques mesurent le compactage du sol en évaluant les forces exercées lors de la pénétration du sol. Les capteurs diélectriques mesurent la teneur en eau du sol sur la base de la constante diélectrique, ce qui est particulièrement utile lorsque la végétation est clairsemée. Les capteurs de localisation, semblables aux stations météorologiques agricoles, utilisent les satellites GPS pour déterminer les données de position dans les champs. Des capteurs électroniques fixés à l'équipement de terrain surveillent les opérations et transmettent les

données par l'intermédiaire de systèmes de communication. Les capteurs de flux d'air, qui produisent des signatures uniques influencées par les différentes propriétés du sol, mesurent l'infiltration de l'air dans le sol. Avec l'avènement de l'IoT, les capteurs agricoles fournissent désormais des données en temps réel couvrant divers paramètres tels que la température de l'air et du sol, la pluviométrie, la vitesse du vent, la teneur en chlorophylle et la pression atmosphérique. Ces classifications de capteurs contribuent de manière significative au développement et à la réalisation de systèmes agricoles intelligents, augmentant la productivité et la durabilité.

Par conséquent, l'intégration de capteurs pour l'agriculture de précision permet aux agriculteurs d'accéder à des informations vitales sur divers aspects de leurs cultures, notamment le calendrier des récoltes, l'utilisation de l'eau, la santé du sol et la nécessité de recourir à des intrants supplémentaires. Ces données sont systématiquement mesurées et enregistrées à intervalles réguliers, ce qui permet de prendre des décisions en connaissance de cause et d'optimiser les pratiques agricoles. Le large éventail de capteurs utilisés dans l'agriculture, collectivement appelés capteurs de l'internet des objets IoT) ou solutions d'agriculture intelligente, est très prometteur pour l'industrie agricole. Grâce à l'utilisation de capteurs pour l'agriculture de précision, la production agricole peut être considérablement améliorée, l'introduction de variétés de cultures résistantes aux parasites et à haut rendement peut être facilitée, et la demande mondiale de denrées alimentaires, en constante augmentation, peut être satisfaite plus efficacement.

L'importance des fibres naturelles

Dans le contexte actuel de demande croissante de ressources durables, l'utilisation de renforts en fibres végétales dans diverses applications a fait l'objet d'une attention significative et d'une traction sur le marché. Bien que la documentation complète sur les volumes de marché soit limitée, un rapport de la Confédération européenne du lin et du chanvre (CELC) et du groupe JEC en 2018 indique que les composites à base de fibres naturelles représentaient 92 000 tonnes en Europe en 2012, soit 15 % du volume total du marché européen lorsqu'ils sont combinés avec les composites bois-plastique. Parmi les fibres végétales, le lin s'est imposé comme un choix de premier plan, représentant plus de 51 % de la masse totale de fibres utilisées dans les applications automobiles européennes en 2012 (environ 29 500 tonnes, à l'exclusion du bois et du coton). Les analyses du cycle de vie ont également démontré les avantages environnementaux des fibres de lin par rapport aux fibres de verre. Cependant, l'adoption plus large des fibres végétales comme alternative se heurte à un certain nombre de défis, qui sont explorés et discutés dans cette section. En particulier, l'un des principaux obstacles est la prédiction précise de la qualité et des performances mécaniques ultérieures des fibres végétales, ce qui a des implications pour leur utilisation à grande échelle.

La définition des fibres végétales fait référence aux cellules allongées du sclérenchyme des plantes vasculaires qui sont organisées en faisceaux. Toutefois, la définition commune a une portée plus large et fait référence à divers types de cellules allongées, généralement dotées de parois épaisses, d'extrémités effilées, durables et caractérisées par une résistance à la traction « élevée ». Les fibres végétales peuvent être classées en fonction de leur origine :

animale, minérale ou végétale. Les fibres végétales ou biogènes sont les plus utilisées dans l'industrie des biocomposites. Parmi les fibres végétales présentant un intérêt pour l'industrie des biocomposites, le lin et le chanvre présentent des similitudes intéressantes. La recherche sur ces fibres a été motivée par un intérêt industriel de longue date et par leur abondance dans la nature. Il est donc intéressant d'utiliser les connaissances acquises au cours des dernières décennies sur ces fibres végétales pour mieux comprendre le comportement mécanique du lin.

Les propriétés naturelles inhérentes aux fibres végétales introduisent un large éventail de variabilité à différents niveaux, ce qui nécessite une compréhension approfondie de leurs relations structure-propriété. Par conséquent, la demande de descriptions structurelles, biochimiques et mécaniques précises des fibres végétales ne cesse de croître, ce qui a conduit à la mise en place d'installations d'essai spécialisées dans divers domaines scientifiques. Toutefois, certaines lacunes dans la recherche subsistent, ce qui nécessite de nouvelles avancées dans ce domaine. Par exemple, des techniques de couplage innovantes pour faciliter les essais mécaniques in situ doivent encore être développées. En outre, une compréhension plus approfondie de la composition et des interactions entre les biopolymères inhérents à la structure de la fibre, en particulier la lamelle centrale responsable de la liaison des fibres entre elles, nécessite plus d'attention et de recherche. Combler ces lacunes contribuera sans aucun doute à une compréhension plus complète du comportement et des propriétés des fibres végétales.

En outre, un accent particulier a été mis sur l'étude des défauts dans les fibres végétales, les dislocations étant souvent considérées à tort comme la seule représentation des défauts. S'il est reconnu que les défauts peuvent entraîner une réduction des propriétés mécaniques au niveau du composite, leur effet à l'échelle de la fibre reste un domaine de recherche qui nécessite davantage d'investigations et d'attention.

Cette section présente une analyse complète des fibres de lin, couvrant à la fois leur importance culturelle et leurs caractéristiques ultrastructurales. Elle est suivie d'un examen approfondi du processus d'extraction des fibres de lin, puis d'une étude approfondie des différents paramètres qui influencent la qualité des fibres. Enfin, les propriétés mécaniques des fibres de lin sont méticuleusement élucidées afin de fournir une compréhension complète de leur comportement.

La culture du lin

L'intérêt pour la culture du lin s'explique par les nombreux avantages de ses fibres. Tout d'abord, la fibre de lin est principalement cultivée dans des régions tempérées et humides, avec des températures modérées et des précipitations adéquates, ce qui rend les zones côtières de l'Europe occidentale, telles que la Belgique, les Pays-Bas et la France, idéales pour sa culture. Cette production localisée crée des opportunités pour le développement de nouveaux matériaux ayant des applications industrielles potentielles. En outre, l'industrie du lin implique divers acteurs, notamment des experts en sélection de variétés, des agriculteurs avertis, des spécialistes de l'extraction et de la commercialisation des fibres et des fabricants de machines spécifiques nécessaires aux différentes étapes de la transformation du lin, En outre, les fibres de lin élémentaire présentent des propriétés mécaniques favorables

similaires à celles des fibres de verre E, ce qui en fait une alternative prometteuse aux fibres de verre traditionnelles. Ces propriétés soulignent l'intérêt de leur culture.

Les processus de culture du lin

La culture du lin commence par le semis, généralement lorsque la couche supérieure du sol atteint une température d'environ 7-9°C, soit en France entre le 15 mars et le 15 avril. Les stades de croissance du lin peuvent être divisés en quatre phases principales : la germination, le stade végétatif, la floraison et la formation des graines, et la sénescence :

- La germination se produit environ 5 à 10 jours après le semis et se caractérise par l'émergence de deux cotylédons entièrement développés, caractéristiques des dicotylédones

- Le stade végétatif est d'abord lent, le plant de lin atteignant une hauteur d'environ 15 cm dans les 15 à 20 jours suivant la germination. Cette croissance progressive est suivie d'une période de développement rapide d'environ 15 à 20 jours, au cours de laquelle la plante peut croître de plusieurs centimètres par jour pour atteindre une hauteur de 80 à 90 cm La croissance ralentit ensuite lorsque la plante entre dans la phase de floraison, pour atteindre finalement une hauteur d'environ 1 mètre

- La floraison commence généralement environ 50 jours après la germination et dure environ 15 jours pour l'ensemble du champ, les fleurs individuelles ne fleurissant qu'un jour

- La formation des graines commence environ 15 jours après la floraison, et la maturité complète se produit pendant la phase de « maturation tardive », environ 5 à 6 semaines après la floraison. Enfin, la sénescence fait partie intégrante du cycle de vie de la plante

Cependant, il est important de noter que dans la culture industrielle du lin, les plantes sont récoltées au stade de maturité de la fibre, appelé « maturité jaune », qui suit le stade de « maturité verte » ou « maturité précoce ». L'ensemble du processus de culture, du semis à la maturité des fibres, prend environ 100 à 120 jours.

Le rouissage de lin à la rosée

Il existe plusieurs méthodes de rouissage, dont le rouissage à l'eau, le rouissage à la rosée, le rouissage enzymatique, le rouissage chimique et le rouissage mécanique. Les deux principaux types de rouissage couramment utilisés sont le « rouissage à l'eau » et le « rouissage au champ/à la rosée ». Dans le cas du rouissage à l'eau, les tiges de lin sont récoltées, mises en bottes et immergées dans l'eau. Traditionnellement, ce processus se déroulait dans des bassins naturels tels que des lacs, des rivières ou des barrages et durait de 5 à 7 jours. Les tiges sont ensuite séchées sur le sol pendant une à deux semaines. Le rouissage à l'eau repose principalement sur l'activité de bactéries anaérobies qui colonisent les tiges et provoquent une fermentation. Cette méthode permet de produire des fibres de lin

de haute qualité, mais soulève également des inquiétudes quant à la pollution de l'environnement.

En Europe, le rouissage du lin est principalement effectué par le biais du rouissage à la rosée/au champ. Dans ce processus, des moissonneuses spécialisées déracinent (arrachent) mécaniquement les plants de lin, et les tiges sont disposées en piles sur le champ pour créer des andains. La présence de rosée matinale et la variation des précipitations et de la chaleur contribuent à créer des conditions favorables à la croissance des micro-organismes, principalement des bactéries et des champignons, déjà présents sur les tiges. De plus, la microflore du sol où se trouvent les andains colonise également les tiges au cours de ce processus.

Les enzymes produites par ces micro-organismes ciblent et dégradent principalement des polysaccharides spécifiques, tels que la pectine, un composant majeur formant le ciment pectique dans la ML, ce qui entraîne une dissociation partielle des faisceaux de fibres, et des fibres individuelles. Tout au long du processus de rouissage, l'implication de l'agriculteur comprend le retournement des andains à mi-parcours pour assurer un rouissage uniforme sur toute la hauteur de l'andain et le suivi de l'avancement du processus.

La progression du rouissage de la rosée est accélérée par les changements des conditions environnementales, notamment une humidité plus élevée et des températures plus basses pendant la nuit et des températures plus élevées et des conditions plus sèches pendant la journée. Les variations saisonnières, la structure du sol, les éléments minéraux (par exemple l'azote, le phosphore et le potassium), les propriétés physico-chimiques du sol, la rotation des cultures et l'épaisseur de l'andain influencent également la vitesse et l'efficacité de la décomposition. Ensemble, ces facteurs exogènes contribuent à l'efficacité et à la qualité globales du processus de rouissage et influencent les caractéristiques et les propriétés finales de la fibre de lin extraite.

L’extraction mécanique de la fibre de lin

Après le rouissage, l'extraction mécanique permet de séparer les fibres des anas et de l'épiderme. La première étape de l'extraction mécanique est le cassage. La paille est passée entre des rouleaux rainurés dans une machine à briser, qui brise efficacement le noyau ligneux en fragments tout en préservant l'intégrité des fibres à l'intérieur des tiges. Après le bris, la paille subit un « teillage », un processus qui sépare la matière ligneuse indésirable de la fibre. Cette séparation est réalisée en battant la paille avec des lames émoussées en bois ou en métal dans une teilleuse. La matière ligneuse enlevée, connue sous le nom d'anas, est généralement utilisée comme combustible, laissant le lin sous la forme de longs brins constitués de faisceaux de fibres individuelles adhérant les unes aux autres.

Après le teillage, les fibres sont généralement peignées ou « décortiquées » en les tirant à travers des ensembles de broches, chaque ensemble successif ayant des broches plus fines que le précédent. Ce processus sépare les faisceaux de fibres grossières en faisceaux plus fins et aligne les fibres parallèlement les unes aux autres, ce qui donne des fibres longues et fines. Entre-temps, l'étoupe est soumise à un nouveau peignage ou cardage, qui

aligne les fibres avec précision. Les fibres alignées sont ensuite rassemblées en un cordon de fibres lâches appelé « sliver » ou « rove ».

Les conditions environnementales pendant le processus de teillage, en particulier l'humidité, ont un impact significatif sur le rendement des étoupes et la longueur moyenne des faisceaux de fibres, ainsi que sur la probabilité de division des faisceaux. En outre, les paramètres mécaniques des teilleuses, notamment la vitesse d'alimentation de la paille, le rythme de battage et l'intensité du broyage, jouent un rôle crucial dans la détermination de la qualité des étoupes, qui comprend leur structure, leur propreté et leurs propriétés mécaniques.

La structure du lin

La composition chimique de la paroi cellulaire de la tige et de la fibre de lin

Le lin, comme les autres plantes, possède des parties végétales telles que les tiges, les feuilles et les racines, chacune ayant une fonction spécifique. Ensemble, ces organes végétaux forment un système continu avec une base de développement commune. La caractéristique la plus importante du lin réside dans ses deux fonctions principales : conduire et soutenir. Le lin peut être caractérisé comme un système composite avec des structures hiérarchiques allant de l'échelle macroscopique à l'échelle nanoscopique et peut être divisé en : le tissu externe, également appelé épidermique (écorce), et le tissu interne également appelé vasculaire (xylème). La couche externe, appelée écorce, protège contre les éléments extérieurs et stabilise la tige, tandis que la couche interne, appelée xylème, facilite le mouvement de l'eau et des nutriments du centre vers les fibres de la tige.

Les faisceaux de fibres de lin, également appelés fibres techniques, sont obtenus à partir de l'écorce interne de la tige de lin. Ces fibres techniques ont une longueur approximative de 1 m et sont constituées d'environ 10 à 40 fibres élémentaires, également appelées fibres simples dans leur section transversale. À plus petite échelle, les faisceaux de fibres sont formés de plusieurs fibres élémentaires maintenues ensemble par un ciment pectique. Les fibres élémentaires de lin elles-mêmes ont généralement une longueur de 10 à 80 mm et un diamètre de 10 à 40 µm. Elles se caractérisent par une disposition concentrique de deux types de parois cellulaires, la primaire externe et la secondaire interne, cette dernière étant elle-même divisée en trois parties d'épaisseur et de structure variables. En outre, la fibre présente un trou central appelé lumen

L'analyse structurelle d'une seule fibre de lin révèle plusieurs couches. La première couche formée pendant la croissance de la plante est la paroi primaire mince, qui contient à la fois de la cellulose et de l'hémicellulose et a une épaisseur d'environ 0,2 µm. Vient ensuite la paroi cellulaire secondaire, qui représente la majeure partie du diamètre de la fibre et se compose principalement de cellulose et d'hémicelluloses. Cette paroi secondaire est ensuite divisée en trois couches contenant des microfibrilles enroulées en hélice et constituées de chaînes de cellulose hautement cristallines. Chaque microfibrille est composée de 30 à 100 chaînes de molécules de cellulose orientées à un angle d'environ 10° par rapport à l'axe de

la fibre. La paroi secondaire représente jusqu'à 70 % du module d'Young de la fibre, ce qui indique qu'une teneur élevée en cellulose correspond à un module de traction plus élevé.

l’identification du « point de rouissage optimal ».

La "méthode artisanale" historique

Depuis des siècles, les agriculteurs artisanaux utilisent des méthodes transmises de père en fils pour déterminer la période optimale de rouissage des tiges de lin dans les champs. La détermination du point de rouissage optimal est étudiée depuis longtemps. Dans ce contexte, les premières études publiées dans les années 1920 ont eu le potentiel de produire des outils permettant d'identifier le point de rouissage optimal. Dans les années 1960 à 1980, les études sur le rouissage de la rosée de lin et son influence sur les propriétés mécaniques de la fibre de lin ont suscité un grand intérêt. Plusieurs groupes ont travaillé à la conception et à la production d'outils permettant d'identifier le point de rouissage optimal du lin, dans le but d'obtenir des fibres de lin de haute qualité pour les industries textiles. Toutefois, ces études ont été interrompues et négligées après l'apparition des fibres plastiques. Aujourd'hui, en raison de la pollution mondiale causée par les sources de pétrole, l'émergence du terme d'énergie renouvelable pousse les scientifiques à repenser l'intégration des sources vertes biodégradables dans les domaines industriels. Par conséquent, dans ce projet, nous visons à produire un outil permettant d'identifier le point de rosée optimal dans le lin, afin d'obtenir des fibres de haute qualité pour l'utilisation industrielle. Pour ce faire, nous avons examiné la littérature et réalisé une étude bibliographique sur les outils antérieurs susceptibles d'identifier le point de rouissage optimal. Cette section résume les outils qui ont été conçus à cette fin.

La figure 1 montre les premiers dessins d'un beau livre écrit par Robert L. Davis et publié en 1923, illustrant la manière dont l'agriculteur artisanal devrait utiliser ses mains pour tester mécaniquement le point de rouissage optimal des tiges de lin rouies. Les illustrations et le texte associé décrivent plusieurs tests mécaniques manuels, notamment la flexion, la compression et la torsion, au cours desquels l'artisan doit observer la réaction du tissu extérieur.

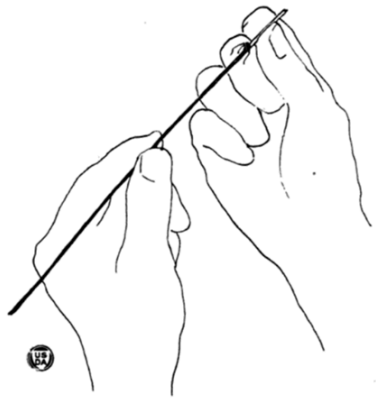

FIG. 14.—Step 1 in the loose-core test of retting flax fibers. The cortex is shoved back from the wooden core so as to leave several centimeters entirely free from fibers.

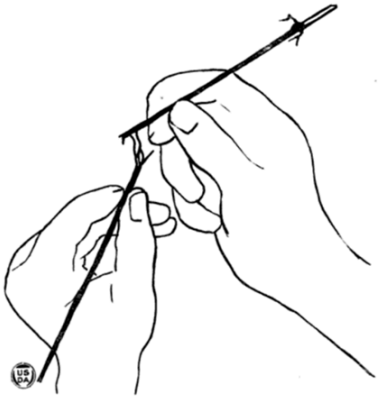

FIG. 15.—Step 2 in the loose-core test of retting flax fibers. The wooden core is broken 6 to 9 inches above the first break where the cortex has been shoved back.

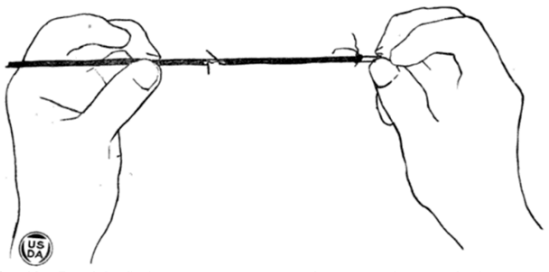

FIG. 16.—Step 3 in the loose-core test of retting flax fibers. One hand holds the stem above the second break in the wooden core, while the other exerts a pull on the exposed lower end.

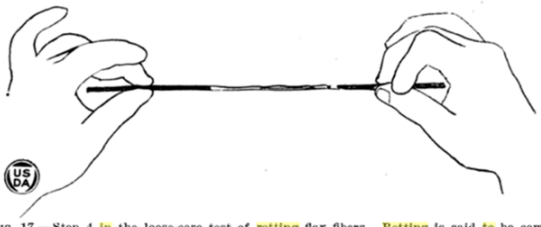

FIG. 17.—Step 4 in the loose-core test of retting flax fibers. Retting is said to be complete if the wooden core slips easily out from the cortex without any of the fibers clinging to it.

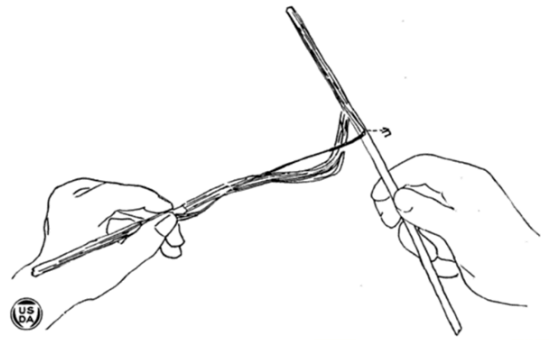

FIG. 19.—Leaf-scar test for the completion of the retting process of flax fibers. Retting is incomplete. Note the fibers clinging at the leaf scar or node (*n*). The sizes of the flax stems in Figures 19 and 21 to 23 are exaggerated as compared with the size of the hands.

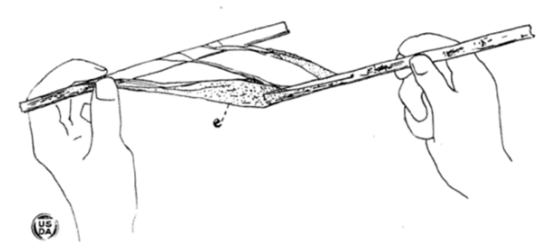

FIG. 21.—Epidermis test in incompletely retted flax. The epidermis (*e*) is clinging to both nodes and internodes in large pieces, showing that the retting process is not complete.

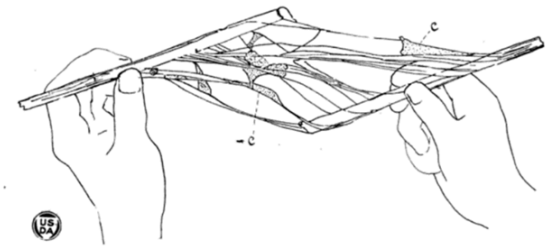

FIG. 22.—Epidermis test of flax fibers when retting is nearly complete. The fibers are well separated and of fine diameter. Pieces of cuticle (*c*) are clinging in spots. When this stage of retting is reached it is necessary to swish the fibers to and fro in water in order to tell whether the epidermis is well loosened.

FIG. 23.—Flax fibers at the completion of the epidermis test. Retting is at the same stage as that shown in Figure 22. The cortex is shown after it has been swished to and fro in water. Retting is almost complete, and the cuticle (*c*) is separated except at the leaf scars (*l*).

Figure 1. Premiers dessins tirés d'un livre écrit par Robert L. Davis publié en 1923, illustrant comment l'artisan agriculteur doit utiliser ses mains pour tester mécaniquement le point de rouissage optimal des tiges de lin rouies par la rosée. Tiré de [Davis, RL (1923). Anatomie

de la tige de lin en relation avec le rouissage (n° 1185). Département américain de l'Agriculture.]

Outre les conseils sur la période de rouissage optimale, les scientifiques ont mesuré les propriétés mécaniques des fibres de lin au cours d'une période de rouissage en temps réel. Une étude en temps réel sur trois ans de l'influence du rouissage sur la résistance des fibres, a été réalisée en 1926, 1927 et 1928 par Brittain B. Robinson. Il a pu contrôler certains paramètres à cette époque, où l'influence des facteurs environnementaux tels que l'ombre et le temps d'ensoleillement sur la résistance des fibres a été étudiée.

Les outils permettant d'identifier le point de rouissage optimal

Les méthodes optiques

Fraser et al. ont documenté visuellement les changements structurels induits par le traitement au glyphosate, qui ont entraîné un séchage uniforme des tiges de lin. Pour ce faire, ils ont utilisé une méthodologie qui consistait à noyer les tiges de lin dans de la résine blanche LR. Des coupes transversales ont ensuite été préparées à l'aide de techniques de coupe au diamant. Ces coupes transversales ont ensuite été soumises à des procédures de coloration, suivies d'une visualisation au microscope. L'étude fournit des informations précieuses sur les effets du traitement au glyphosate sur la morphologie des tiges de lin et permet de comprendre les changements structurels induits par ce traitement chimique.

Les méthodes mécaniques

En 1984 D. A. Seaby et P. C. Mercer ont introduit un outil spécialement conçu pour reproduire le processus de teillage lors de l'étape d'extraction mécanique des fibres de lin, voir la figure 2.

Cet outil innovant fonctionne en pliant d'abord la tige de lin, puis en utilisant une combinaison de forces d'écrasement et de cisaillement pour libérer les fibres. L'objectif premier de cet outil est d'étudier et d'identifier les conditions optimales pour induire le rouissage du lin, tout en fournissant un moyen d'évaluer rapidement et précisément le stade de progression du rouissage. Les recherches de Seaby et Mercer représentent une nouvelle approche pour comprendre le processus de rouissage du lin et fournissent un outil pratique pour contrôler et évaluer sa progression.

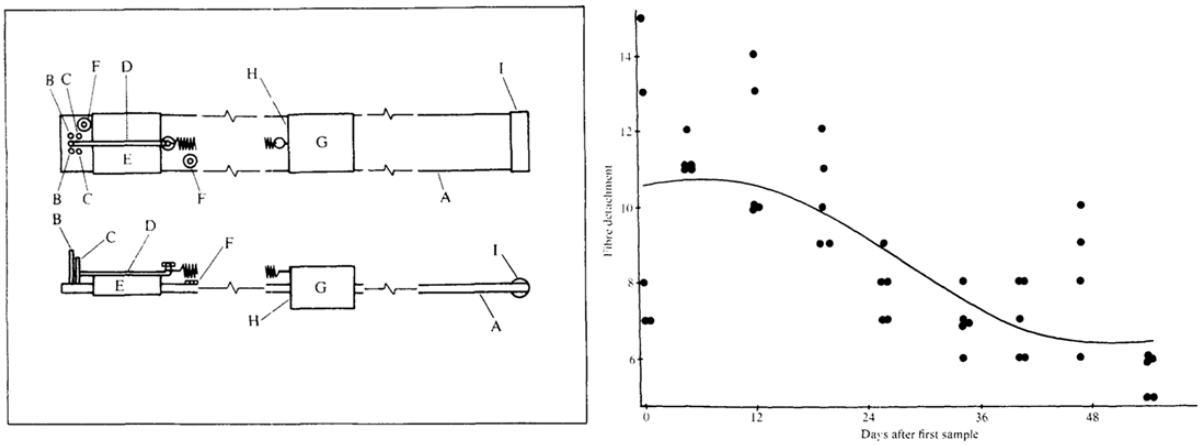

Figure 2. A proposed hand tool to test the degree of retting of flax straw by (Seaby & Mercer, 1984)

A.M. Goodman et al. ont mené une étude démontrant l'utilité des tests d'épluchage pour mesurer les changements mécaniques à l'interface entre les faisceaux de fibres (tissu phloémien primaire) et le tissu phloémien secondaire, voir la figure 3.

Cette méthode facilite le suivi de l'évolution du rouissage et permet des comparaisons pour déterminer le moment optimal de récolte du lin. Par conséquent, l'objectif de l'étude était d'effectuer une série d'essais mécaniques standardisés en laboratoire, en suivant les méthodes décrites afin d'étudier de manière exhaustive le processus de rouissage et d'identifier les changements structurels dans les échantillons de lin résultant de l'application de l'herbicide glyphosate et de la colonisation microbienne dans une culture sur pied.

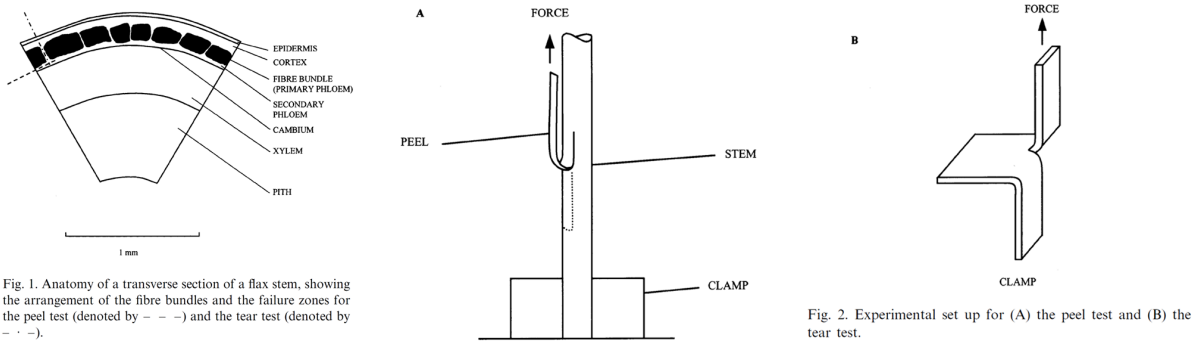

Fig. 1. Anatomy of a transverse section of a flax stem, showing the arrangement of the fibre bundles and the failure zones for the peel test (denoted by – – –) and the tear test (denoted by – · –).

Fig. 2. Experimental set up for (A) the peel test and (B) the tear test.

Figure 3. (Goodman et al., 2002) propose des méthodes pour tester le degré de rouissage des tiges de lin et suggère des mécanismes quantifiables qui pourraient constituer la base d'outils fiables.

S'appuyant sur la méthodologie démontrée par Goodman et al., I. Booth et al. ont utilisé une approche de test d'épluchage avec une modification de l'angle d'épluchage, voir la figure 4.

Leur objectif était d'adapter cette méthode au contexte de la culture du chanvre et ils ont étudié l'effet de la variation de l'angle de la charge appliquée sur le travail requis pour l'épluchage. L'objectif de la recherche était de déterminer la géométrie de test de pelage la plus appropriée. Leur étude souligne que les tests de pelage constituent un moyen précieux de contrôler objectivement la réduction du travail mécanique nécessaire pour peler les tiges de chanvre rouies par la rosée, et que cette réduction est en corrélation avec l'évolution du rouissage. Par conséquent, les tests de pelage sont apparus comme un outil potentiel pour surveiller l'influence de divers facteurs sur le processus de rouissage du chanvre, fournissant des informations précieuses sur cet aspect crucial du développement des fibres.

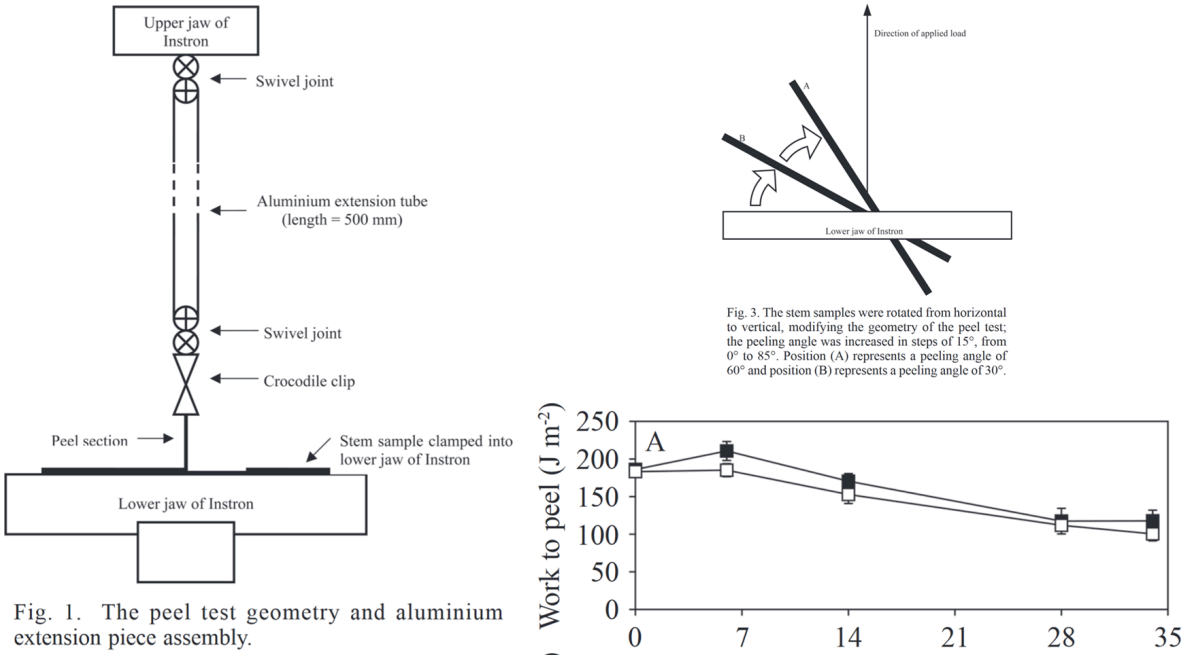

Figure 4. Un outil mécanique de pelage proposé pour suivre l'avancement du rouissage. (Booth et al., 2004)

D. Waldron et J. Harwood ont réalisé une étude détaillée de l'effet de la composition chimique des tiges de lin sur leurs propriétés mécaniques, voir la figure 5. Ils ont utilisé l'analyse mécanique dynamique pour suivre les changements dans les propriétés des tiges à différents stades du développement de la plante. Ils ont également utilisé une approche d'extraction chimique séquentielle pour analyser le rôle des composants chimiques individuels. Cette étude fournit des informations précieuses sur les propriétés mécaniques des tiges de lin, qui peuvent à leur tour constituer un facteur clé pour déterminer le moment optimal de la récolte des cultures de lin et le niveau de décortication mécanique requis pour obtenir une séparation et une propreté optimales des fibres.

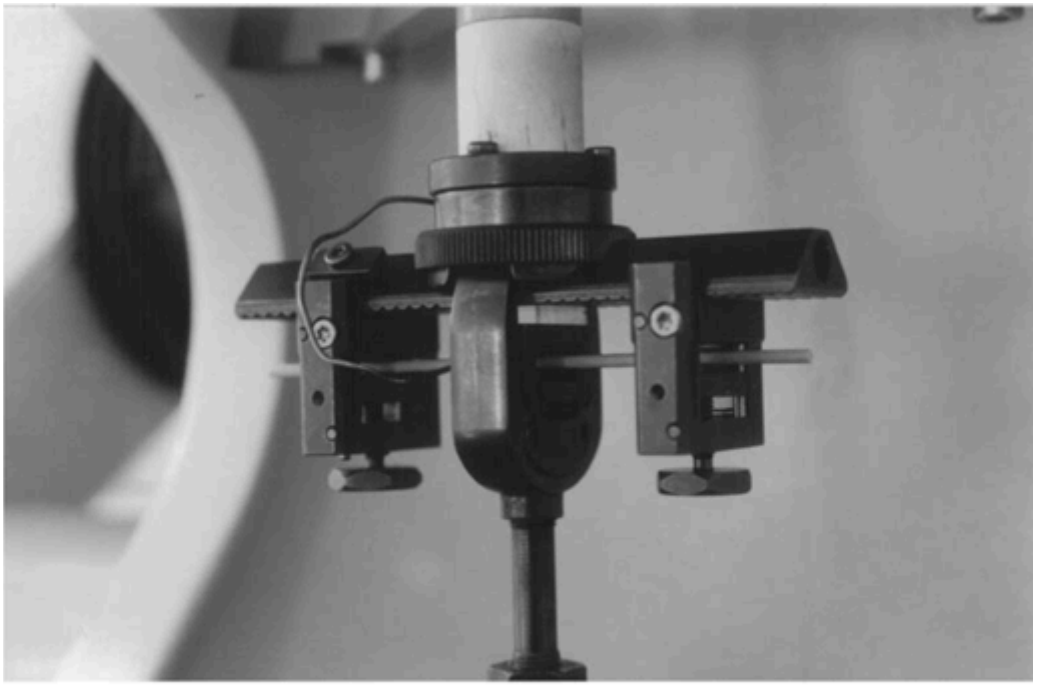

La figure 5. D. Waldron et J. Harwood (Waldron & Harwood, 2011) ont proposé un outil pour mesurer les propriétés dynamiques des tiges de lin. Cependant, l'évolution du rouissage n'a pas été étudiée.

Plus récemment, Réquilé et al. ont mené une étude complète dont l'objectif principal était d'utiliser des expériences de pelage des tiges pour évaluer l'effet des processus de rouissage sur le terrain sur la cohésion des tissus à l'intérieur des tiges de chanvre et son effet ultérieur sur les propriétés de traction des fibres élémentaires, voir la figure 6.

Leur approche expérimentale comprenait l'intégration d'expériences de pelage de tiges avec la microscopie électronique à balayage (MEB) pour étudier l'influence de différents degrés de rouissage dans le matériel végétal. En examinant l'évolution de l'énergie de rupture à l'interface entre les fibres et le cœur ligneux de la tige, cette étude a permis d'approfondir les mécanismes sous-jacents à la rupture lors des expériences de pelage. L'objectif global était de mieux comprendre les changements progressifs de la cohésion des faisceaux de fibres qui se produisent au cours du processus de rouissage.

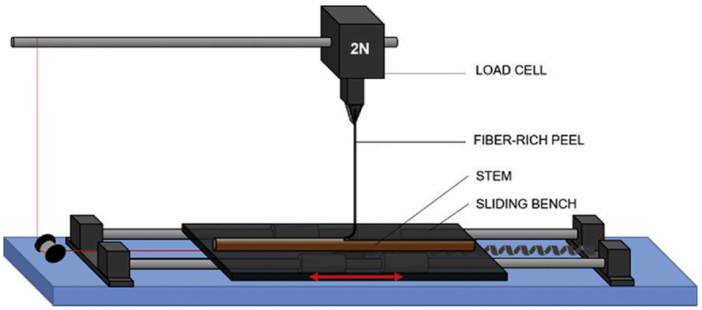

Fig. 2. Peeling test experimental set-up.

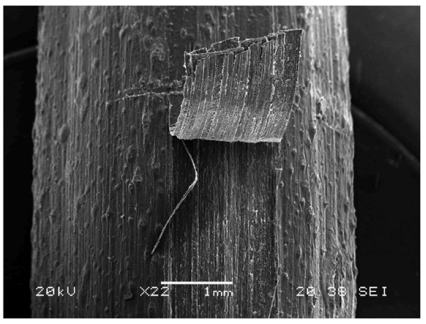

Fig. 3. Scanning electron microscope image of a non-retted hemp stem after peeling test. The peel width is determined to avoid additional bending stresses. For ease of observation, the peel was cut.

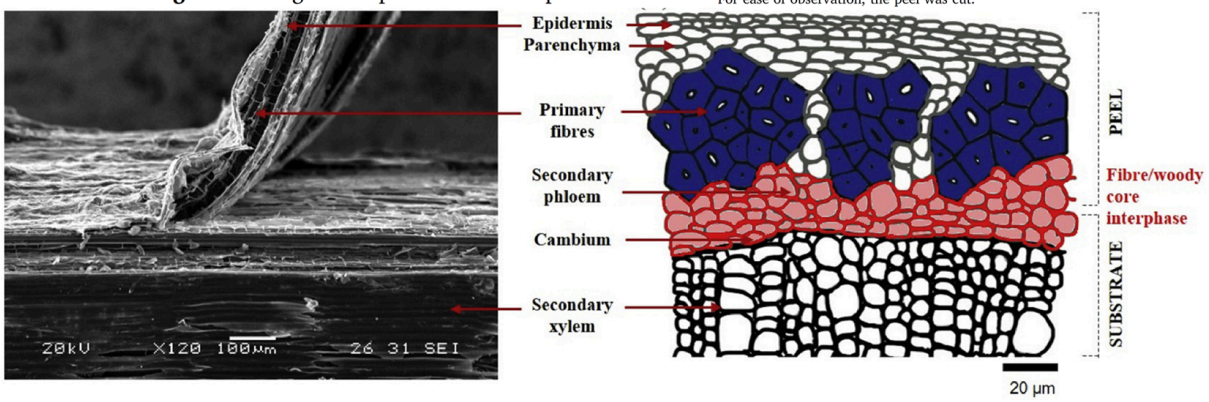

Figure 6. Expériences de pelage améliorées utilisant l'observation SEM pour caractériser l'avancement du rouissage. Réquilé et al (2018). (Réquilé, Le Duigou, et al., 2018)

La spectroscopie infrarouge comme outil

H. S. S. Sharma et N. Reinard ont apporté une contribution significative dans ce domaine en développant des calibrations robustes dans le visible et le proche infrarouge (vis-NIR) spécialement conçues pour contrôler la finesse des fibres au cours du traitement mécanique. Ces méthodes calibrées présentent un intérêt pratique significatif pour les applications industrielles, en particulier dans les filatures. Il est impératif que ces étalonnages démontrent leur capacité à contrôler efficacement toutes les qualités de fibres, y compris celles qui sont altérées par l'eau. En outre, l'étude a entrepris la tâche essentielle d'évaluer la précision et l'exactitude de ces étalonnages pour prédire la finesse des fibres dans les lignes de préparation, soulignant ainsi leur utilité pratique et leur fiabilité dans un contexte industriel.

La teneur en pectine : potentiel pour un laboratoire sur puce

W. J. M. Meijer et al. ont mené une étude approfondie pour examiner la relation entre le rouissage au champ et à l'eau et la teneur en pectine des tiges. Cette recherche a consisté à évaluer la lisibilité en quantifiant le taux de dégradation contrôlée de la pectine pendant le rouissage à l'eau. Pour obtenir une perspective globale, l'étude a suivi la dégradation de la

pectine à trois endroits spécifiques le long des tiges et dans des échantillons de lin récoltés à quatre stades différents, de la floraison à la maturation des graines. Les chercheurs ont également examiné comment les processus de broyage et de séchage de la paille affectent le rouissage sur le terrain. Reconnaissant que le degré de rouissage a un effet significatif sur la qualité des fibres, les chercheurs ont utilisé différentes méthodes de rouissage sur des échantillons de lin présentant différents degrés de rouissage. Grâce à une analyse minutieuse, ils ont établi des corrélations entre la teneur en pectine des tiges rouies et les principales caractéristiques des fibres, telles que la résistance à la traction, la finesse et la pureté.

Les conclusions du Chapitre 1

L'agriculture, la science et la technologie (outils) ont toujours été étroitement liées. Par exemple, la première charrue est apparue vers 5000 avant JC. Depuis lors, chaque progrès scientifique et technologique réalisé par l'homme a eu un impact sur l'agriculture. Ces avancées sont désormais visibles dans Agriculture 1.0. Nous vivons actuellement dans une Agriculture 4.0 dans laquelle la révolution de la microélectronique et de la microtechnologie s'applique à tous les secteurs de l'agriculture. Comme nous l'avons vu, l'Agriculture 4.0 est également connue sous les noms d'agriculture numérique, d'agriculture intelligente et d'agriculture intelligente. Un domaine spécifique de l'Agriculture 4.0 est celui de l'utilisation de toute une gamme de capteurs à des fins spécifiques dans l'agriculture. Un exemple de ceci est de détecter le point optimal de quelque chose, par ex. maturité du fruit, maturité de la plante etc. Pour ce faire, nous avons vu qu'il existe de nombreuses propriétés physiques et chimiques qui peuvent être suivies par les capteurs existants. En plus de cela, de nombreux capteurs restent encore à développer car il n'existe pas d'appareil commercial. C'est le cas de ce doctorat. Nous avons constaté que la production de fibre de lin est une industrie importante. L'utilisation de la fibre de lin, connue pour son utilisation généralisée dans le textile et sa présence émergente dans les matériaux thermoplastiques, est soulignée par ses remarquables propriétés mécaniques et de traction. Parmi les nombreuses techniques disponibles pour évaluer les propriétés mécaniques des fibres, les essais de traction restent le choix le plus important. Le module des fibres de lin varie de 30 à 70 GPa, avec une variabilité considérable dans les données obtenues. De nombreux facteurs contribuent à cette variabilité, notamment les conditions expérimentales, les dimensions telles que le diamètre et la longueur, la composition chimique, l'orientation de la cellulose dans la fibre et la détermination précise des surfaces transversales constitue un défi important. De plus, les facteurs environnementaux et les défauts structurels inhérents ont un effet complexe sur cette valeur. Le paysage de la recherche évolue activement et s'intéresse à la modélisation des fibres pour améliorer la précision de l'évaluation des propriétés mécaniques. Les études axées sur les propriétés mécaniques des fibres de lin se sont principalement appuyées sur des essais de traction macroscopique, les évaluations à l'échelle microscopique restant à développer. En particulier, les recherches existantes ont principalement étudié l'effet du rouissage sur les propriétés mécaniques des fibres de lin uniquement au point de rouissage optimal. En revanche, les recherches sur l'influence en temps réel du rouissage sur les propriétés mécaniques de la tige de lin, qui englobe la fibre, et des fibres de lin manquent. Cela met en évidence la nécessité d'une compréhension

globale de l’effet du rouissage sur la tige de lin afin d’améliorer l’extraction mécanique des fibres grâce à une détermination précise et en temps réel.

Alors que l’agriculture intelligente continue de croître et que la technologie est de plus en plus intégrée dans différents secteurs, le secteur des fibres naturelles, en particulier le lin, est à la traîne dans cette évolution technologique. Bien qu’elles constituent un élément fondamental des textiles et des composites, les fibres naturelles n’ont pas encore pleinement exploité le potentiel de l’agriculture intelligente. Cependant, atteindre une qualité optimale de fibre de lin reste un défi, influencé par des facteurs tels que la surveillance en temps réel du rouissage du lin dans les champs et la capacité des agriculteurs à prédire avec précision le moment idéal auquel le lin est prêt. Reconnaissant cette lacune critique, ce programme de doctorat est stratégiquement conçu pour répondre à une variété d'objectifs visant à combler cette lacune critique.

Les objectifs du doctorat et description du contenu du chapitre

L'objectif principal de la thèse est de démontrer un capteur mécanique capable de prédire le temps de rouissage optimal pour permettre l'extraction à haut rendement de fibres de lin de haute qualité à partir de leurs tiges parentales. Pour ce faire, les propriétés mécaniques fondamentales des tiges et des fibres de lin doivent être caractérisées en temps réel pendant une période de rouissage complète et au-delà – une telle étude n’a jamais été menée de manière aussi détaillée auparavant. Ce n'est qu'ainsi que l'on peut déterminer le temps de rouissage optimal pour une extraction à haut rendement en fibres. Les propriétés mécaniques ont été recueillies à l'aide d'une approche multi-échelle : tests mécaniques macroscopiques, microscopiques et nanoscopiques utilisant une combinaison d'approches établies et originales. Ceux-ci comprennent la flexion macroscopique, la compression et la torsion des tiges de lin, les mesures microcantilever à base de fibres de lin (statiques et dynamiques) de fibres de lin simples et les mesures par microscopie à force atomique par nanoindentation des sections transversales et des surfaces des fibres de lin.

Le chapitre 2 décrit le prélèvement d'échantillons permettant l'expérimentation en thèse. En apparence trivial, le chapitre 2 détaille le protocole complet développé pour collecter systématiquement des échantillons directement sur le terrain, spécialement conçus pour les essais mécaniques multi-échelles. Comme l’étude était pour l’essentiel une étude en temps réel, un calendrier expérimental strict devait être planifié et respecté.

Les chapitres 3, 4 et 5 présentent la caractérisation mécanique macroscopique des tiges de lin. Des descriptions détaillées des configurations expérimentales originales, des méthodes et des paramètres mécaniques qui en résultent sont fournies, facilitant une compréhension globale du comportement mécanique des tiges. Les mesures donnent des résultats intéressants en termes d'évolution des propriétés des tiges au rouissage.

En descendant une échelle, le chapitre 6 présente la caractérisation mécanique microscopique des fibres de lin. Les expériences à micro-échelle, inspirées des systèmes micro électro-mécaniques (MEMS), comprennent des tests statiques et dynamiques menés sur des fibres de lin simples agissant comme des micropoutres, mettant en lumière les réponses dynamiques et statiques des fibres de lin simples. Ce chapitre fournit une description détaillée des procédures expérimentales, permettant une exploration

approfondie des propriétés micromécaniques de la fibre. Les mesures donnent des résultats intéressants en termes d'évolution des propriétés des fibres au rouissage.

En descendant une autre échelle, le chapitre 7 présente la caractérisation mécanique nanoscopique des fibres de lin. La microscopie à force atomique par nanoindentation (AFM) est utilisée pour sonder le module mécanique des fibres de lin en section transversale et sur leurs parois fibreuses. Les mesures donnent également des résultats intéressants en termes d'évolution des propriétés des fibres au rouissage.

Enfin, le chapitre 8 sur une note plus pratique présente une étude concernant le séchage des tiges de lin suite à une pluie. La teneur en eau des tiges de lin a un impact sur leurs propriétés mécaniques. Pour qu'un outil basé sur des capteurs soit fiable, la teneur en eau doit être connue. Nous avons choisi de le faire en réalisant une étude précise de l'évaporation des tiges de lin en simulant la pluie puis en étudiant l'évaporation à une température matinale typique de juillet/août (21°C). Les données fournissent des informations sur le moment où les tiges peuvent être testées en toute confiance par l'outil.

Au fur et à mesure que nous progressons dans chaque chapitre, l'interaction entre les différentes échelles d'essais mécaniques converge, contribuant finalement à l'objectif primordial de ce programme de doctorat : l'extraction complète des propriétés mécaniques critiques des fibres et des tiges de lin, faisant progresser notre compréhension et ouvrant la voie à la développement d'un capteur mécanique basé sur l'IoT pour la prédiction en temps réel du point de rouissage optimal dans la culture du lin.

Chapitre 2

Collecte d'échantillons

Les principaux résultats du Chapitre 2

La biologie des plantes de lin a été étudiée et caractérisée à l'aide de différentes techniques depuis longtemps. En particulier, la relation entre la microbiologie et le processus de rouissage, expliquée par l'influence de ce dernier sur l'activité enzymatique des micro-organismes tels que les bactéries et les champignons. La collecte de tiges de lin pour des tests biologiques est donc une pratique courante et il existe des protocoles bien définis qui peuvent être suivis. Les tests biologiques impliquent souvent le stockage réfrigéré (à très basse température) des échantillons pendant des semaines, des mois, voire des années avant l'analyse. Lorsque les échantillons destinés aux études biologiques sont conservés à des températures extrêmement basses, telles que -20°C et -80°C, l'activité biologique des micro-organismes a tendance à ralentir considérablement, voire à s'arrêter. Toutefois, cette activité peut être réactivée et poursuivie lors de la décongélation. Ce phénomène peut être très utile dans la recherche en sciences de la vie et en microbiologie, notamment pour l'étude de l'activité des micro-organismes. En contrôlant leur activité par la congélation et la décongélation, les chercheurs peuvent faire des comparaisons et obtenir des informations précieuses. Cependant, cette approche n'est pas du tout adaptée à la caractérisation des propriétés mécaniques d'une plante en vue du développement d'un outil. La congélation et la décongélation d'échantillons de plantes pour les essais mécaniques peuvent entraîner des changements significatifs dans la résistance et la rigidité des échantillons. Cela peut conduire à une caractérisation trompeuse ou inexacte des propriétés mécaniques du matériel végétal.

Dans la mesure où la collecte d'échantillons pour la caractérisation mécanique des tiges et des fibres de lin pendant toute une période de rouissage et au-delà, jour après jour, dans le cadre d'une étude en temps réel, est quelque chose de nouveau : nous avons donc dû définir un tout nouveau protocole adapté aux objectifs de notre étude spécifique.

La période de rouissage en 2022 s'est déroulée du 6 juillet au 31 août, pour une durée totale de 56 jours. Au cours de cette période, nous avons prélevé un total d'environ 6 000 échantillons. En outre, nous avons continué à prélever des échantillons à intervalles réguliers, moins fréquemment, après l'enlèvement des tiges rouies du champ. Par conséquent, une zone de champ marquée de 10 mètres a été délibérément laissée après l'enlèvement des échantillons de lin roui de manière optimale, dans le but spécifique d'étudier les effets d'un rouissage excessif sur ces tiges de lin. L'entreprise VRF nous a aimablement autorisés à laisser les tiges dans le champ et à les ramasser occasionnellement jusqu'au 1er octobre. Cette approche nous a permis de caractériser de manière exhaustive l'évolution en temps réel du processus de rouissage et des étapes post-rouissage, ce qui est d'une importance capitale pour le développement de capteurs et l'analyse des propriétés mécaniques. Une zone de 10 m du champ a été choisie pour la collecte des échantillons. La collecte d'échantillons nécessite l'application d'un modèle directement sur l'andain dans le champ, qui prend la forme d'une forme rectangulaire

mesurant 10 mètres de long. La figure 1 montre la zone de 10 m choisie pour le protocole de collecte et le modèle conçu.

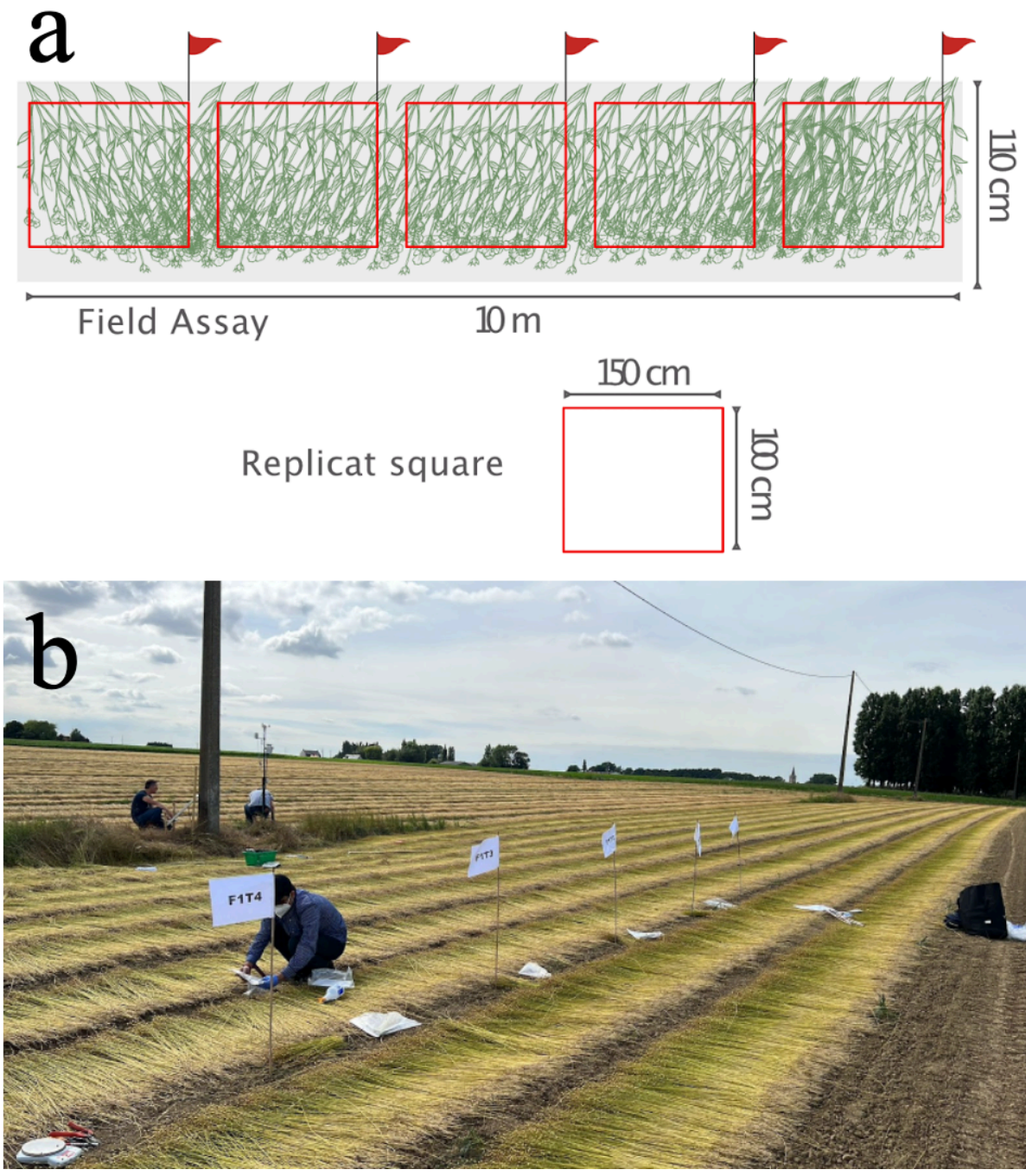

Figure 1. Échantillonnage des tiges de lin au cours de l'été 2022. La zone de 10 m prévue pour la collecte des échantillons. (a) Protocole conçu pour la collecte d'échantillons. (b) Montre la zone de 10 m dédiée à la collecte de l'échantillon. La photo montre également des personnes de l'UGSF (Dr Sebastien Grec et Mr Sujavit Mukherjee) collectant leurs propres échantillons de lin pour le stockage et les études biologiques ultérieures.

Sachant que les tiges de lin naturelles trouvées sur le terrain n'ont pas le même diamètre, et afin d'obtenir des résultats fiables, nous avons cherché à tester des échantillons de différents diamètres, de cette façon nous essayons de contrôler certains diamètres variables d'entre eux, qui est le diamètre. Par conséquent, des tiges de lin de différents diamètres ont été sélectionnées à chaque profondeur, nous les avons appelées petites (S), moyennes (M) et grandes (L). La détermination des trois diamètres notés a été réalisée à l'aide d'un pied à coulisse. Le tableau 1 montre une gamme de diamètres moyens des tiges de lin récoltées.

Stem sample category	**Stem diameter range (mm)**
Small (**S**)	1-1.5
Medium (**M**)	1.5-2
Large (**L**)	2-3

Tableau 1. Gammes de diamètres des tiges de lin récoltées sur le terrain. Les tiges ont été initialement triées à l'aide d'un pied à coulisse mécanique standard.

Bien que le travail de collecte des échantillons puisse sembler être une expérience agricole agréable sur le terrain, il s'agit en fait d'un processus exigeant. En réalité, notre emploi du temps nous a soumis à une pression considérable, car nous devions collecter, préparer et réaliser les expériences le même jour. C'était essentiel pour maintenir la nature en temps réel des expériences et la fraîcheur des échantillons.
Un flux de travail continu était essentiel, commençant par l'installation correcte des outils nécessaires à la collecte des échantillons et se terminant par l'achèvement des expériences. Ces outils ont fait l'objet de procédures d'inspection et d'assainissement approfondies avant et après chaque échantillonnage. Assurer un transport fiable était un autre aspect critique de nos opérations. Nous nous sommes appuyés sur des véhicules conduits par Steve A, et occasionnellement par Sébastien G, qui devaient être équipés d'une réserve d'huile suffisante. Il convient de noter que cette opération s'est déroulée pendant une période de pénurie de carburant en France, ce qui a ajouté une couche supplémentaire de complexité à notre planification logistique. La chronologie présente l'avancement de nos travaux tout au long de la période de décomposition. Ce calendrier a été méticuleusement suivi du 6 juillet au 30 septembre, voir la figure 2.

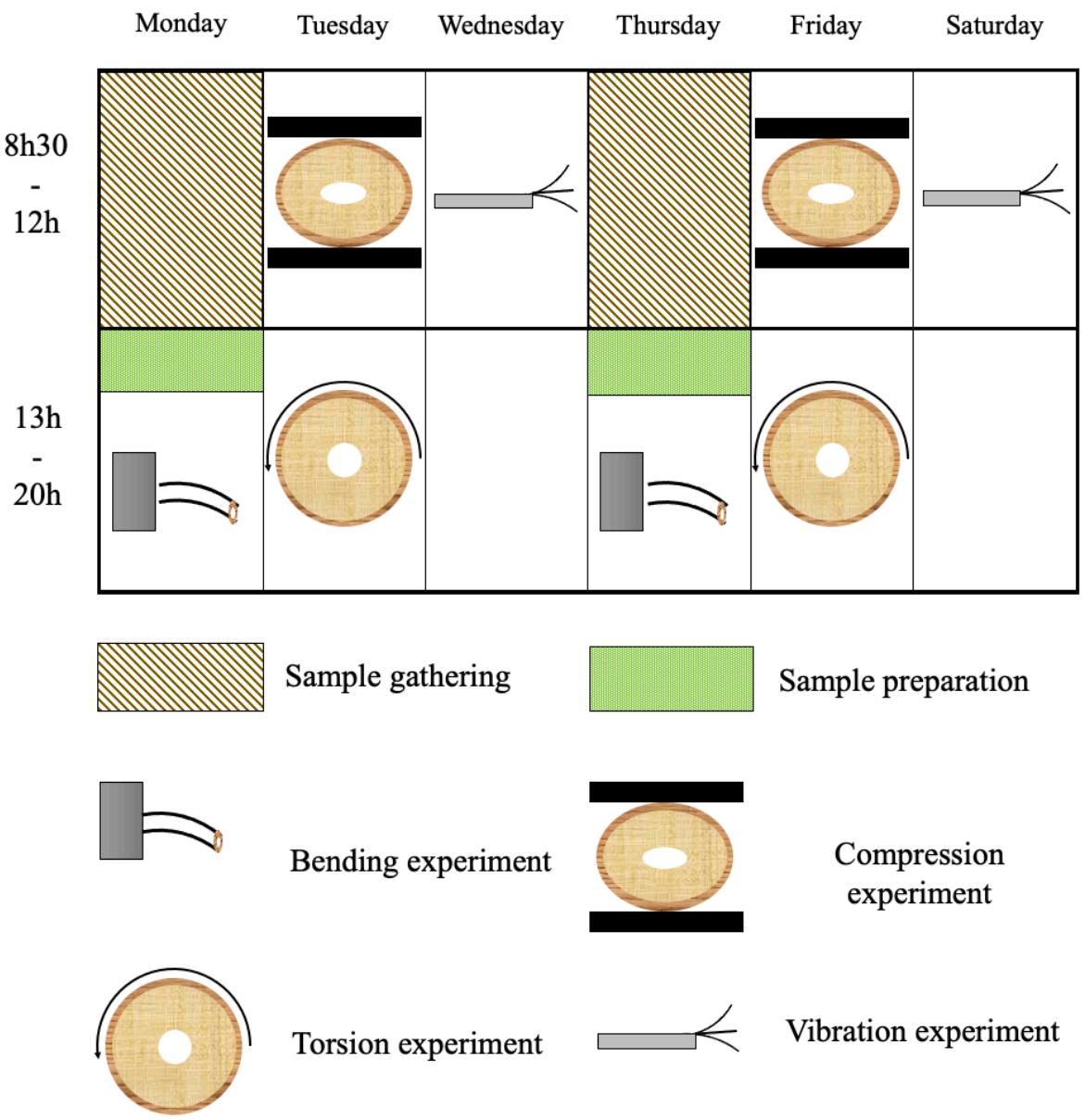

Figure 2. Diagramme temporel résumant la planification de la semaine pendant la période de rouissage du 6 juillet au 4 octobre.

Les conclusions du Chapitre 2

L'objectif du travail présenté dans cette thèse est de réaliser une caractérisation mécanique multi-échelle en temps réel des tiges de lin en cours de rouissage et des fibres de l'étage. Par temps réel, nous entendons ici que les échantillons seront prélevés sur le terrain et testés en laboratoire à l'aide de divers outils (existants et développés pour la thèse). En fonction des conditions météorologiques, le rouissage de la rosée peut durer de quelques semaines à quelques mois. Une étude de cette ampleur et de cet effort n'ayant jamais été entreprise dans la littérature, nous avons donc dû définir un nouveau protocole de collecte d'échantillons, dont la description est présentée dans ce chapitre. Un point essentiel est que

les échantillons ne devaient pas être stockés en vue de tests ultérieurs, comme c'est le cas pour les études biologiques. Il s'agit ici de réaliser des essais mécaniques sur des échantillons de tiges et de fibres de lin pendant la période de rouissage et au-delà, afin d'obtenir des informations sans problèmes de vieillissement des échantillons. Pour ce faire, nous avons dû élaborer un nouveau protocole de collecte d'échantillons afin de recueillir des tiges appropriées. Nous devions avoir une fréquence de collecte d'échantillons suffisante pour être en mesure de voir les tendances potentielles dans les données. Nous devions avoir une fréquence de collecte d'échantillons qui permette des essais mécaniques entre les jours de collecte d'échantillons. Chaque outil de caractérisation devait fonctionner pendant la période de rouissage. Tout accès spécial au laboratoire devait être demandé pendant la fermeture estivale. Cette tâche n'était pas simple, d'autant plus que personne n'avait jamais mené une telle étude auparavant.

Malgré cela, vous verrez dans les chapitres suivants que le protocole de collecte des échantillons a très bien fonctionné et a permis de tester de nombreux matériaux. Tous les outils et techniques de caractérisation ont également bien fonctionné et il y avait suffisamment de temps entre les collectes d'échantillons pour réaliser des expériences, même si la charge de travail et la pression étaient élevées. En outre, nous avons été un peu aidés par Dame Nature : l'été 2022 a été chaud et long. Cela a eu pour effet d'allonger la période de rouissage, ce qui a permis de recueillir beaucoup de données.

Chapitre 3

Caractérisation macro-mécanique : Effet de rouissage sur la flexion des tiges

Les principaux résultats du Chapitre 3

Dans ce chapitre, les éléments suivants seront présentés. Ce chapitre se concentre sur l'étude de la manière dont le rouissage affecte les propriétés mécaniques de flexion des tiges de lin dans le cadre d'un rouissage en temps réel. Pour ce faire, nous effectuons des tests macro-mécaniques de base sur des tiges de lin prélevées sur le terrain. En appliquant des modèles mécaniques à ces tiges de lin, nous pouvons calculer leurs propriétés mécaniques, en particulier le module de flexion et la contrainte de rupture. L'interprétation des tendances observées dans le module de flexion et la contrainte de rupture en fonction du temps de rouissage fournit des indications précieuses sur la manière dont le rouissage affecte les propriétés mécaniques des tiges de lin en temps réel. Cela nous renseigne sur l'avancement du rouissage. Il est important de noter que cette étude expérimentale est unique et, à notre connaissance, n'a jamais été réalisée auparavant.

Les deux principales conclusions du chapitre 3 sont (i) le module de flexion et la résistance des tiges de lin rouies évoluent avec le temps de rouissage - ceci est particulièrement vrai pendant et après le point de rouissage optimal et (ii) le module de flexion et la résistance des tiges de lin rouies sans leur tissu extérieur n'évoluent pas significativement au cours du rouissage. Les mesures suggèrent donc que la dégradation du tissu extérieur (due au rouissage) est responsable de ces observations. Par conséquent, le rouissage peut être "vu" lors d'essais mécaniques sur des tiges de lin, ce qui ouvre la voie à la possibilité d'un capteur mécanique. Afin d'étayer ces conclusions, nous avons réalisé dans ce chapitre des expériences de broyage de tiges de lin par compression mécanique contrôlée. En principe, contrairement aux expériences de flexion, le rôle du tissu extérieur devrait être moins apparent. Si c'est le cas, cela renforcerait nos arguments concernant les mécanismes responsables de l'évolution du module de flexion et de la résistance au cours du rouissage.

La figure 1 montre un exemple de l'évolution de la déflexion d'un échantillon de tige de lin en fonction de l'augmentation de la force/du poids appliqué F = mg. Ces images sont ensuite analysées à l'aide d'un logiciel d'analyse d'images, en particulier ImageJ, afin d'extraire des données sur la déflexion en fonction de l'augmentation de la masse. Les résultats de cette analyse sont présentés dans la section des résultats**.**

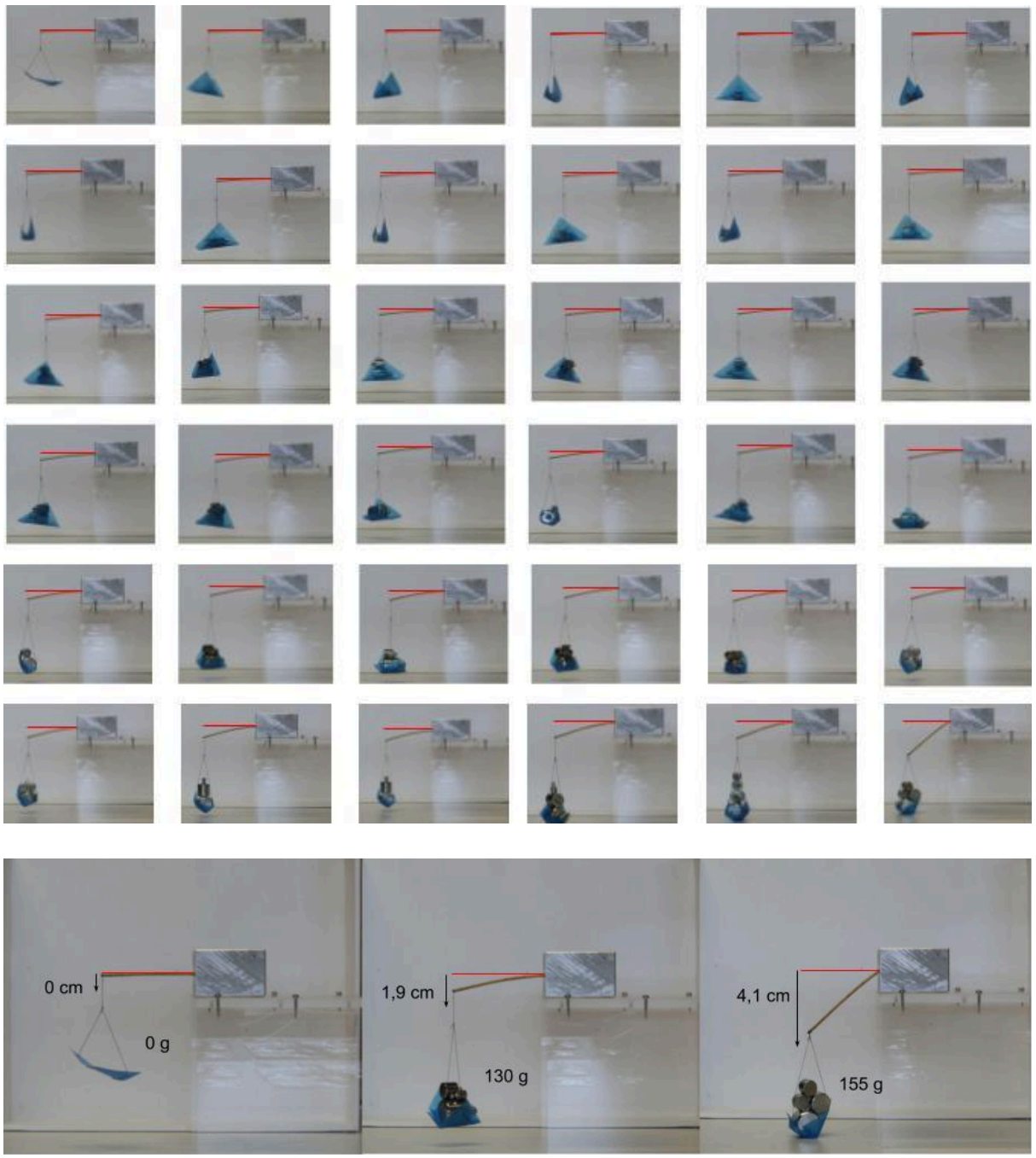

Figure 1. Exemple d'une tige de lin déformée lors d'une expérience de charge ponctuelle en porte-à-faux. La déviation de l'échantillon de tige de lin depuis son état initial jusqu'à son point de rupture. Les cantilevers de tiges de lin ont une longueur de 90 mm et des diamètres extérieurs allant de 1 à 3 mm.

Les résultats de ce chapitre montrent la relation entre le module de flexion moyen et le temps de rouissage. Le point de rouissage optimal, déterminé par VRF, est indiqué sur le graphique (jour 56). Avant d'atteindre ce point (sous rouissage), les tiges ont un module de flexion relativement constant. Une fois la phase de rouissage optimal atteinte, le module de

flexion mesuré diminue régulièrement. Cette tendance peut fournir des informations précieuses sur l'effet du rouissage sur les propriétés mécaniques des tiges de lin.

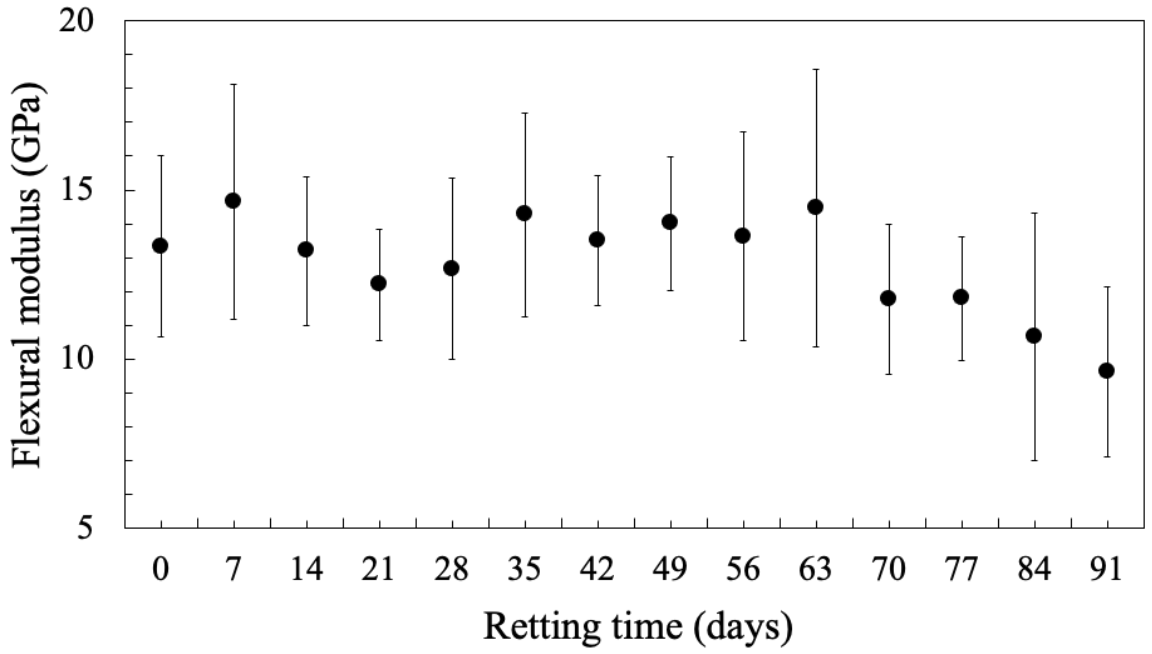

Figure 2. Graphique de l'évolution du module de flexion moyen obtenu expérimentalement pour les tiges de lin (diamètre 1-3 mm) en fonction du temps de rouissage. Ce graphique est basé sur 180 expériences de tiges de lin. Les résultats ont été obtenus en temps réel pendant toute la période de rouissage de 2022 et au-delà, c'est-à-dire du 6 juillet au 4 octobre 2022.

Pour mieux comprendre l'influence du rouissage sur ces propriétés, nous avons effectué une analyse plus détaillée du graphique en le divisant en deux profils distincts, comme le montrent les figures suivantes. La figure 2 montre le comportement du module de flexion moyen pendant la période de rouissage.

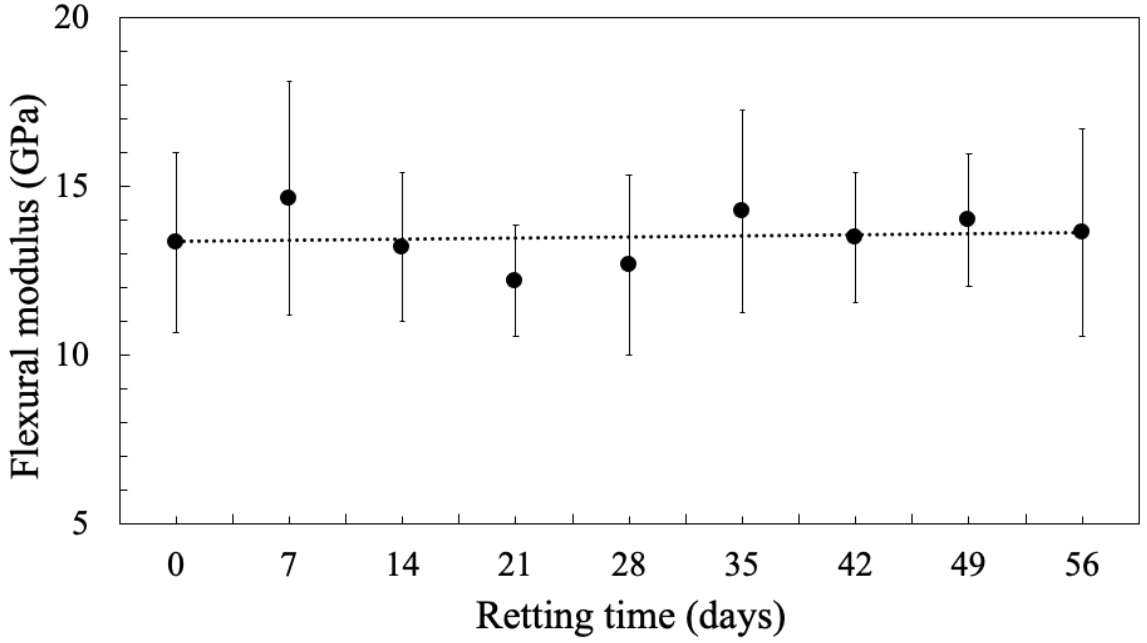

Figure 3. Tracé du module de flexion moyen des tiges flexibles pendant la période de rouissage insuffisant. Le module de flexion augmente d'environ 4,6 MPa/jour pendant 56 jours avant le temps de rouissage optimal.

La figure 3 montre que pendant la période de rouissage insuffisant, le module de flexion moyen reste relativement constant, avec seulement une légère augmentation de 4,6 MPa/jour. Cette augmentation est considérée comme négligeable par rapport à la valeur réelle du module de flexion moyen, qui est d'environ 13,49±0,77 GPa (la moyenne sur la période de rouissage de 56 jours).

D'autre part, si nous analysons la période de rouissage excessif, nous observons un modèle différent dans le comportement du module de flexion moyen, comme le montre la figure 4.

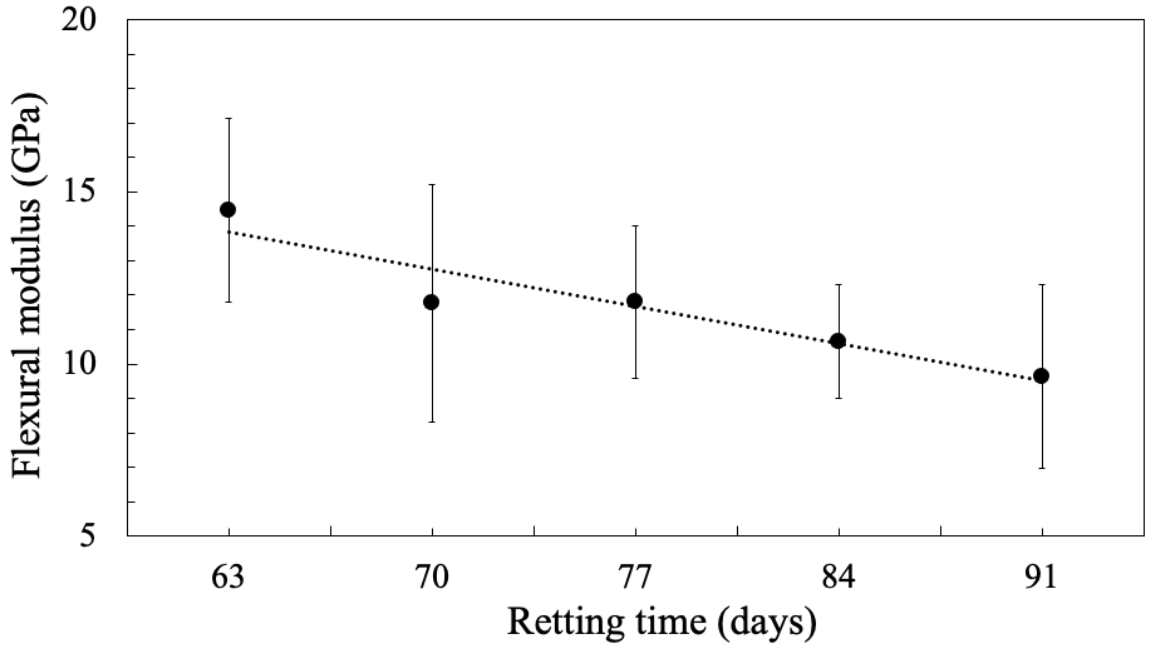

Figure 4. Tracé du module de flexion moyen des tiges flexibles pendant la période de surcreusement. Le module de flexion diminue d'environ 154 MPa/jour pendant 28 jours après le temps de rouissage optimal.

La figure 4 montre que le comportement du module de flexion moyen pendant la période de surcreusement présente une tendance significative à la baisse. Le module de flexion diminue de manière significative d'environ 5 GPa au cours de cette phase de sur-rouissage, ce qui représente une réduction de 35 % du module de flexion. Le module de flexion diminue d'environ 154 MPa/jour sur 28 jours après le temps de rouissage optimal (R2 = 0,9). Ce résultat démontre clairement l'influence du rouissage sur les propriétés mécaniques des tiges de lin rouies.

La figure 5 montre la relation entre la contrainte de rupture moyenne observée à chaque stade du rouissage en fonction du nombre de jours de rouissage :

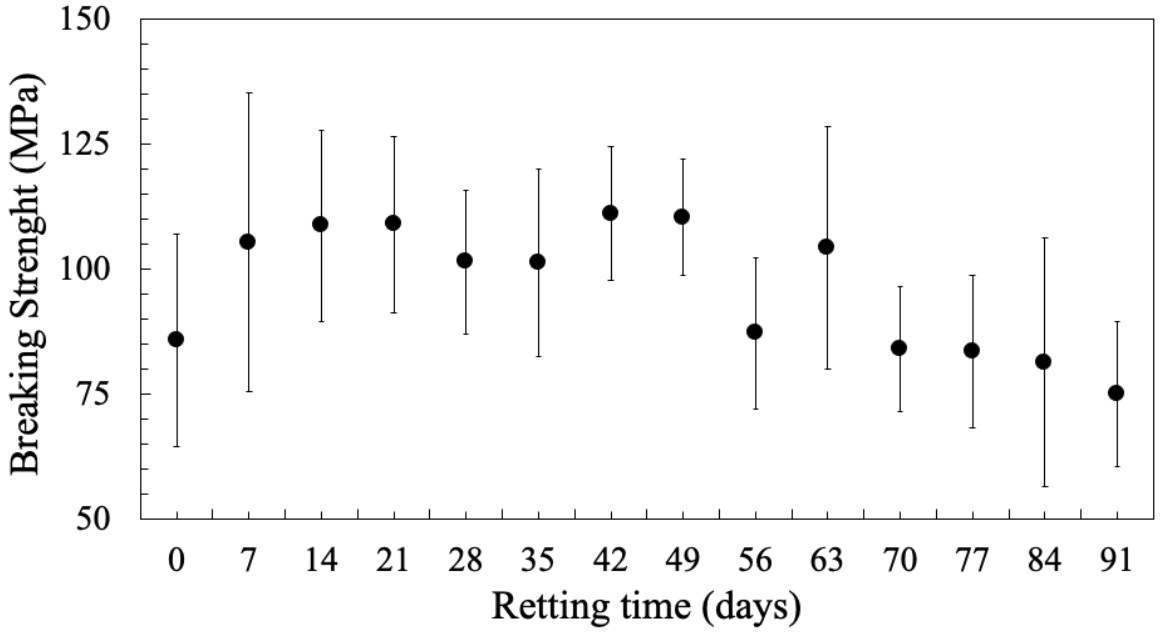

Figure 5. Graphique montrant l'évolution de la résistance moyenne à la flexion des échantillons de tiges de lin en fonction du temps de rouissage en jours. Le temps de rouissage optimal était le jour 56 (tel que défini par l'entreprise VRF). Les résultats ont été obtenus en temps réel pendant toute la période de rouissage de 2022 et au-delà, c'est-à-dire du 1er juillet au 1er octobre 2022.

Le graphique de la figure 5 montre une tendance intéressante : la résistance moyenne à la flexion, dérivée des différentes étapes de rouissage, reste relativement constante tout au long de la période de rouissage jusqu'à ce qu'elle atteigne un point optimal (jour 56). Après ce stade de rouissage optimal, la contrainte de rupture commence à diminuer. Cette tendance est comparable à celle observée lors de la mesure du module de flexion pendant le rouissage. Notons que sur l'ensemble de la période de rouissage, la résistance à la flexion des tiges diminue de 30 MPa (à partir du 7ème jour), ce qui correspond à une baisse de 29% de la valeur.

Pour mieux comprendre comment le rouissage affecte l'évolution de la contrainte de rupture dans les échantillons de tiges de lin, nous pouvons analyser les données plus en détail. Nous comparons la contrainte de rupture moyenne avant et après le stade de rouissage optimal et déterminons ensuite la contrainte de rupture moyenne globale.

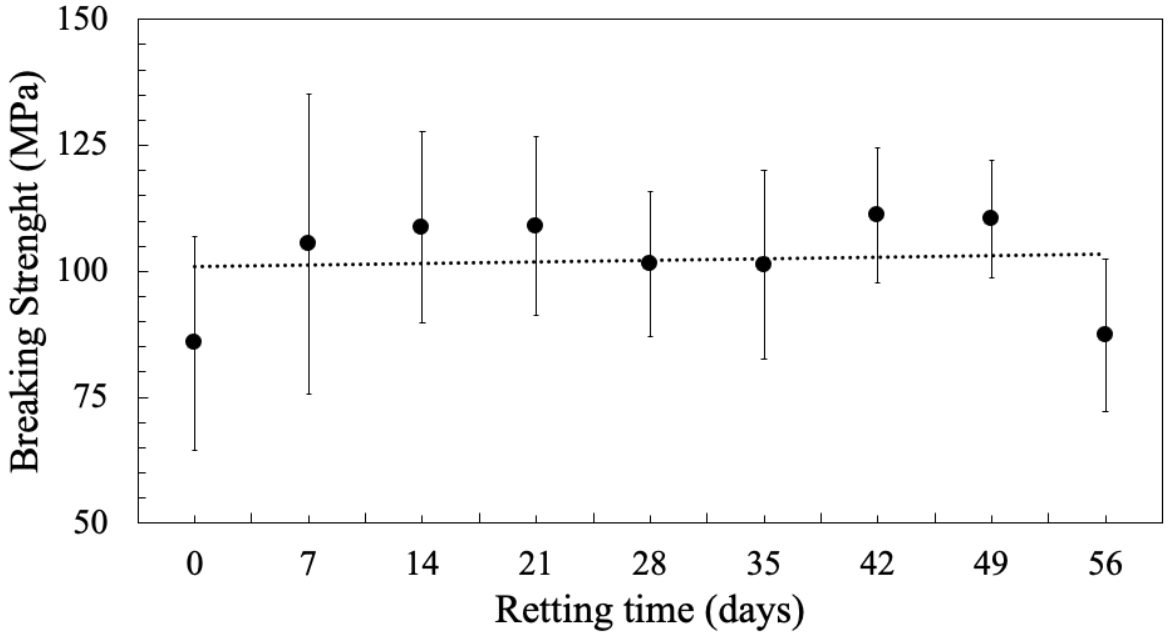

Figure 6. Tracé de la résistance moyenne à la flexion des tiges de lin pendant la période de rouissage insuffisant. La résistance à la flexion augmente d'environ 0,3 MPa/jour pendant 56 jours avant le temps de rouissage optimal.

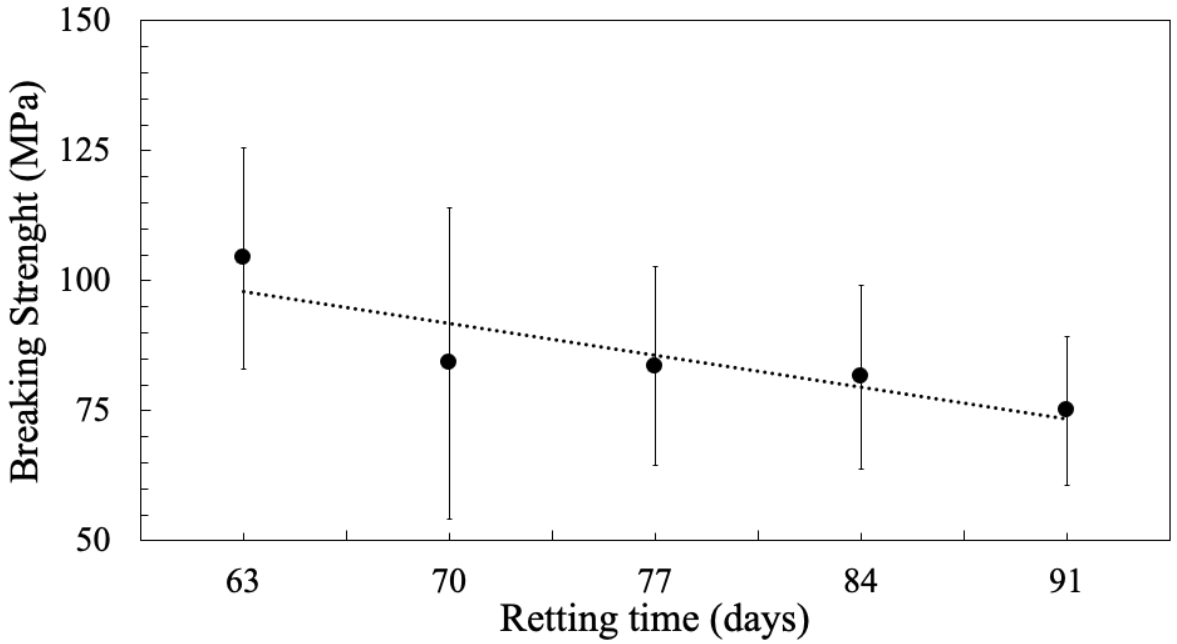

Figure 7. Tracé de la résistance moyenne à la flexion des tiges de lin pendant la période de rouissage excessif. La résistance à la flexion diminue d'environ 0,9 MPa/jour pendant 28 jours après le temps de rouissage optimal.

La figure 6 montre que la contrainte de rupture moyenne reste relativement stable pendant la période de rouissage avant d'atteindre le stade optimal de rouissage. On observe une légère augmentation sur l'ensemble de la période. La figure 7, par contre, montre l'évolution de la contrainte de rupture moyenne après avoir passé le point de rouissage optimal. On observe une diminution significative de 0,9 MPa par jour au cours de la période de sur-rouissage. Cette diminution suggère qu'un état de rouissage excessif peut être responsable de cette réduction de la résistance à la flexion, soulignant l'influence évidente du processus de rouissage sur ce paramètre pendant la période de rouissage.

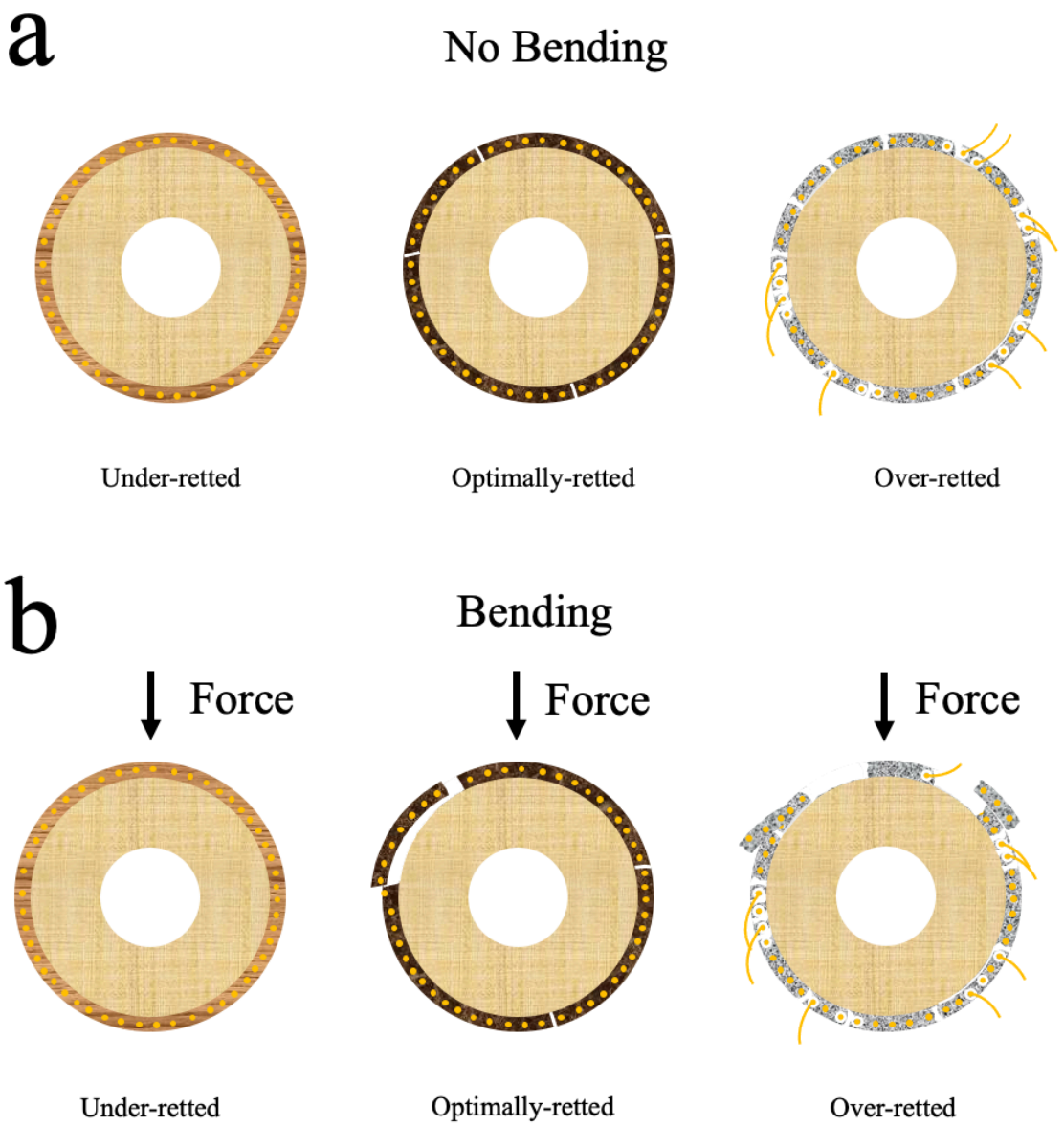

Figure 8. Représentation schématique du lin provenant des étapes de sous-rouissage, de rouissage optimal et de sur-rouissage avant (a) et pendant le cintrage (b). Les diagrammes

schématiques représentent des coupes transversales de tiges de lin près de la base du porte-à-faux là où la contrainte est maximale. La couleur du tissu extérieur représente l'avancement du rouissage. Les petits points jaunes représentent les fibres de lin qui courent le long de la tige. Les diagrammes sont des coupes transversales d'une tige. La partie intérieure du bois, immuable, le « xylème », est indiquée en brun clair.

La figure 8 montre des représentations schématiques des sections transversales des échantillons de tiges de lin prélevés à des stades de rouissage insuffisant (à gauche), de rouissage optimal (au milieu) et de rouissage excessif (à droite) avant - voir la figure 8a - et pendant - voir la figure 8b - l'induction d'une force de flexion. Notez que les figures représentent des sections transversales schématiques des tiges près de la base du porte-à-faux où la contrainte est maximale. Il n'y a pas de changement dans l'état du tissu extérieur, après la flexion de tous les échantillons sous-retardés - voir figure 8b. Ce n'est pas le cas pour les échantillons ayant subi un rouissage optimal et un rouissage excessif, où l'on constate une nette influence de la flexion et des contraintes qui en résultent, exprimées sous forme de délamination et de dommages, dans les échantillons testés provenant des phases de rouissage optimal et excessif.

Les résultats de cette étude montrent un schéma intéressant. Lorsque les échantillons sous-retardés sont soumis à une flexion mécanique, il n'y a pas de changements observables à la surface de la tige. Dans ce cas, l'application de la flexion mécanique (pour induire une contrainte mécanique sur le composite de lin, y compris le tissu externe et le xylème) ne provoque pas de dommages dans le tissu externe de la tige de lin - pour tous les échantillons de tige de lin à tous les stades de rouissage. Cela signifie que la contribution de cette couche à la rigidité mécanique du cantilever n'est pas compromise par la flexion. Ce n'est pas le cas pour les échantillons issus des phases de rouissage optimal et excessif. Les résultats montrent que lorsque les échantillons de ces stades de rouissage sont soumis à une force de flexion, le tissu externe est affecté par des contraintes mécaniques. Cependant, cette influence est mineure dans le cas des échantillons ayant subi un rouissage optimal (légère délamination du tissu externe), tandis qu'elle est majeure dans le cas des échantillons ayant subi un rouissage excessif, ce qui entraîne un décollement du tissu externe.

Cela peut s'expliquer comme suit : au cours du rouissage optimal et au-delà, la dégradation biochimique de la lamelle centrale induit la séparation des faisceaux de fibres et des fibres elles-mêmes à l'intérieur du faisceau dans le tissu extérieur. Lorsque les échantillons de tiges de ces stades sont pliés, cela induit une délamination et un glissement du tissu externe, y compris des fibres, comme le montre le diagramme schématique de la figure 8b. En conséquence, la tension dans le tissu externe qui résulte de la réponse à la force de flexion n'est pas uniformément répartie dans le tissu externe, ce qui entraîne une diminution du module de flexion ainsi que de la résistance à la flexion.

Cela correspond à la tendance des graphiques du module de flexion moyen et de la résistance à la flexion extraits de cette expérience. Nous suggérons que la diminution de la valeur moyenne du module et de la résistance après la phase optimale de rouissage dans les échantillons testés, résulte de la délamination et du glissement du tissu externe lorsqu'il est soumis à la force de flexion, comme illustré dans la Figure 8b.

Ces résultats suggèrent fortement que le processus de rouissage se manifeste par un phénomène mécanique de flexion. En outre, cette expérience ouvre une nouvelle voie pour découvrir quelque chose de très intéressant sur les tiges de lin : le module de flexion et la résistance de la plante de la tige de lin. Dans ce contexte, le module de flexion moyen pendant la période de sous-retrait reste relativement constant, avec seulement une petite augmentation de 4,6 MPa/jour. Pendant la période de sur-retrait, on observe une tendance significative à la baisse. Le module de flexion diminue de manière significative d'environ 5 GPa pendant cette phase de sur-retrait, ce qui représente une réduction de 35 % du module de flexion. Le module de flexion diminue d'environ 154 MPa/jour pendant 28 jours après le temps de rouissage optimal (valeur de R2=0,9).

De même, la résistance moyenne à la flexion reste relativement stable pendant la période de rouissage avant d'atteindre le stade optimal de rouissage. On observe une légère augmentation sur l'ensemble de la période. Cela pourrait être lié aux conditions météorologiques pendant cette période. On observe une diminution significative de 0,9 MPa par jour au cours de la période de rouissage excessif. Cette diminution suggère qu'un état de rouissage excessif peut être responsable de cette réduction de la résistance à la flexion, soulignant l'influence évidente du processus de rouissage sur ce paramètre pendant la période de rouissage. Ces nouveaux paramètres sont restés inconnus en raison du manque de recherches antérieures dans ce domaine.

Enfin, nous pouvons nous assurer de la précision et de la validité du modèle du module de flexion mesuré ici pour 180 tiges de lin. La modélisation numérique étant difficile pour une tige végétale complexe, la modélisation a été vérifiée en utilisant la flexion de matériaux homogènes tels que des tubes en acier inoxydable et en polypropylène. Ce travail se trouve à l'annexe 1. En utilisant des tubes en acier inoxydable et en polypropylène, le module de flexion s'est avéré égal et exactement la même valeur que celle donnée pour ces matériaux dans la littérature. Cela suggère que les tiges de lin peuvent potentiellement prendre en compte l'anisotropie dans leur morphologie et leurs propriétés, en particulier dans leur structure tubulaire.

Les conclusions du Chapitre 3

Les tiges de lin peuvent être caractérisées par des expériences de flexion. Il s'agit de l'un des tests mécaniques manuels qu'un artisan (agriculteur) effectue "sur le terrain" lorsqu'il contrôle l'avancement du rouissage des tiges de lin récoltées. L'artisan juge des informations qualitatives par le mouvement de la main et l'œil pour évaluer l'avancement du rouissage des tiges de lin. Dans ce chapitre, nous avons tenté de quantifier ce processus de pliage artisanal en laboratoire afin de caractériser le module de flexion et la résistance à la flexion des tiges de lin en fonction du rouissage.

Pour ce faire, nous avons conçu un dispositif qui utilise la tige de lin comme un cantilever macroscopique. L'expérience permet de contrôler la flexion progressive d'une tige de lin en appliquant une force précise à l'extrémité de la tige. Cette force est produite à l'aide d'un ensemble de masses précises. En considérant la tige de lin comme équivalente à un long tuyau droit et homogène, la modélisation analytique peut être utilisée pour calculer le module de flexion et la résistance à la flexion de la tige de lin en fonction de la période de rouissage.

Cette hypothèse de modélisation permet de comparer toutes les tiges de lin de l'étude entre elles : à la fois les tiges du même stade de rouissage et les tiges d'un stade de rouissage à l'autre. Cette approche a permis de déterminer quantitativement l'influence du rouissage sur le module de flexion et la résistance à la flexion des tiges de lin.

On observe clairement que le rouissage a un effet sur le module de flexion et la résistance à la flexion des tiges de lin. Les deux paramètres restent constants pendant la phase de rouissage et chutent pendant et après le point de rouissage optimal (tel que défini par l'entreprise VRF). Cela indique que l'influence du rouissage peut être clairement observée dans des expériences micromécaniques telles que la flexion.

Les essais de flexion ont fourni des informations précieuses. Nous avons pu quantifier les changements quotidiens du module de flexion moyen et de la résistance à la flexion pendant les trois mois de la période de rouissage et de sur-rouissage. Les résultats montrent qu'au cours de la période de rouissage insuffisant, le module de flexion et la résistance des tiges ont subi un changement négligeable. Cependant, après le temps de rouissage optimal et pendant la période de sur-rouissage, il y a eu une diminution significative et importante du module de flexion et de la résistance à la flexion des tiges flexibles. La tendance résultant de cette expérience montre que l'influence du rouissage est évidente en flexion. Il est intéressant de noter que les expériences menées sur des tiges de lin à différents stades de rouissage et dont le tissu externe a été délibérément enlevé ont montré que le module de flexion et la résistance du xylème interne (le "bois" de la tige) ne changent pas. Ce résultat renforce l'hypothèse selon laquelle c'est le changement induit par le rouissage dans le tissu externe de la tige qui entraîne une modification des propriétés mécaniques des tiges.

Enfin, un total de 222 tiges de lin ont été mesurées dans ce chapitre. A titre d'exemple de la charge de travail de ce chapitre, en l'absence d'une analyse d'image fiable, la mesure des diamètres externes et internes des sections transversales des tiges coupées a nécessité à elle seule 17364 mesures manuelles !

Chapitre 4

Caractérisation macro-mécanique : Effet de rouissage sur la compression des tiges

Les principaux résultats du Chapitre 4

Initialement, à une force de F=0, la tige de lin est restée dans sa position de repos originale sans modification de ses dimensions. Au fur et à mesure de l'ajout de poids (y compris le substrat en plastique, les gobelets gradués et l'eau), un déplacement a été observé en réponse à l'augmentation de la force appliquée. Trois phases de déformation ont été observées au cours des expériences : (i) une phase élastique linéaire où le déplacement était proportionnel à la force, (ii) une phase non linéaire où la tige subit vraisemblablement une déformation plastique, et (iii) une phase de rupture apparente où le "bois" du xylème était visiblement cassé. Les figures ci-dessous montrent un exemple des trois phases dans un échantillon du stade de sous-retrait R5.

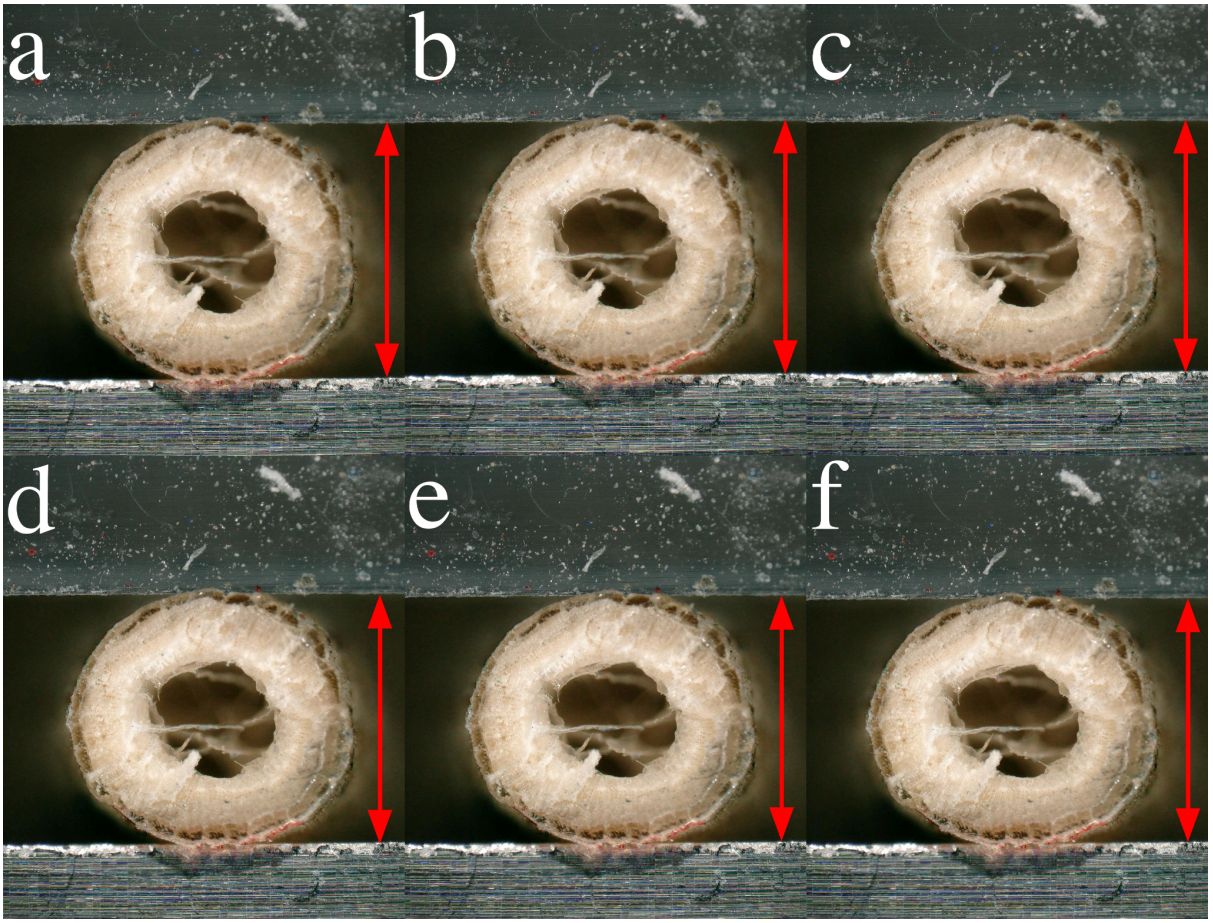

Figure 1. Images au microscope optique numérique d'un exemple de déformation élastique en phase linéaire d'une tige de lin comprimée à l'aide de l'outil de compression de tige mis au point pour l'étude. Le déplacement est représenté par la flèche rouge. (a) initialement

avant la compression m=0. (b) force de compression m=500 g. (c) force de compression m=600 g. d) force de compression m=700 g. (e) force de compression m=800 g.(f) force de compression m=900 g.

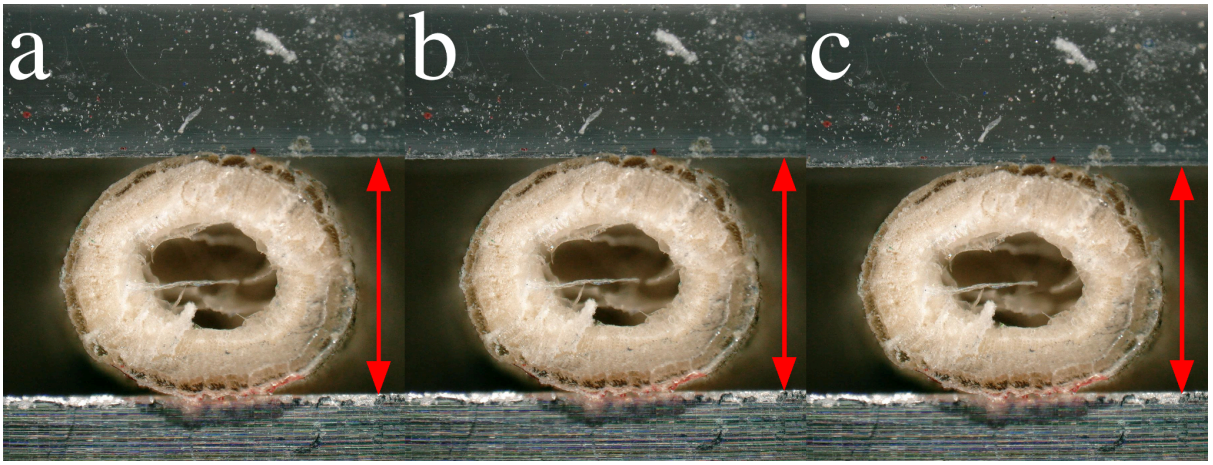

Figure 2. Images au microscope optique numérique d'une déformation en phase plastique non linéaire d'une tige de lin comprimée à l'aide de l'outil de compression de tige développé pour l'étude. Le déplacement est représenté par la flèche rouge. (a) force de compression m=1100 g. (b) force de compression m=1200 g. (c) force de compression m=1300 g.

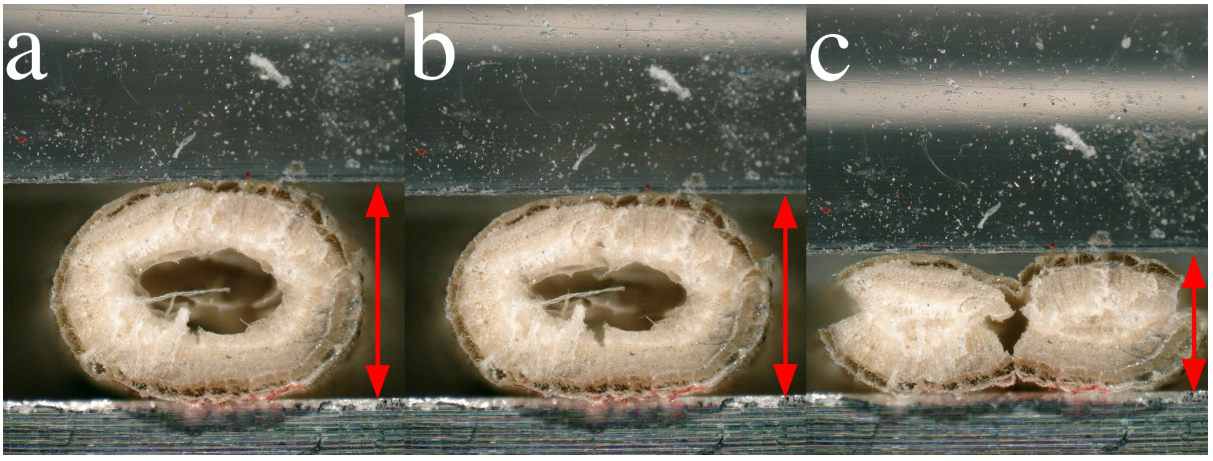

Figure 3. Images au microscope optique numérique d'une déformation en phase de rupture d'une tige de lin comprimée à l'aide de l'outil de compression de tige mis au point pour l'étude. Le déplacement est représenté par la flèche rouge. (a) force de compression m=1400 g. (b) force de compression m=1500 g. (c) force de compression m=1500 g.

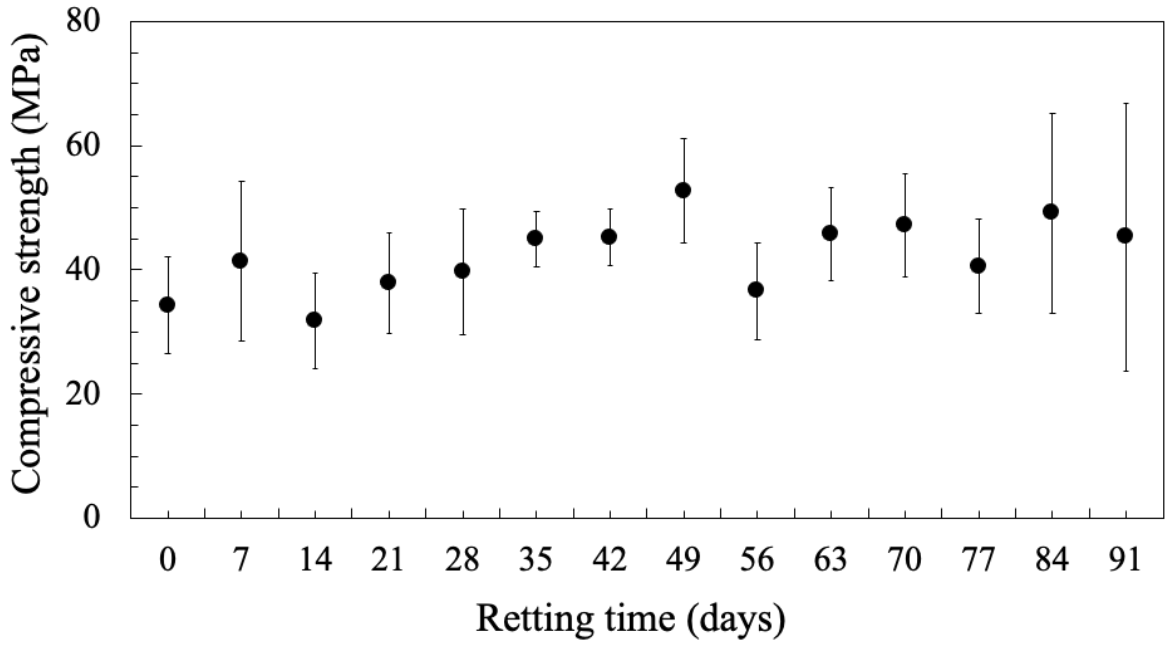

Figure 4. Résistance à la compression des tiges de lin rouies, déterminée expérimentalement, en fonction du rouissage. Ces résultats sont basés sur la compression de 180 sections de tiges de lin. Les résultats ont été obtenus en temps réel pendant toute la période de rouissage de 2022 et au-delà, c'est-à-dire du 1er juillet au 1er octobre 2022. La durée optimale de rouissage était de 56 jours, comme défini par l'entreprise VRF.

Le graphique de la figure 4 montre une tendance intéressante : la résistance moyenne à la compression, dérivée des étapes individuelles de rouissage, reste relativement constante tout au long de la période de rouissage, pendant le rouissage insuffisant, optimal et excessif. Cette tendance est comparable à celle observée lors de la détermination du module de compression pendant la période de rouissage. La défaillance moyenne en compression en fonction du rouissage a mesuré une valeur de 42.32±5.9 MPa.

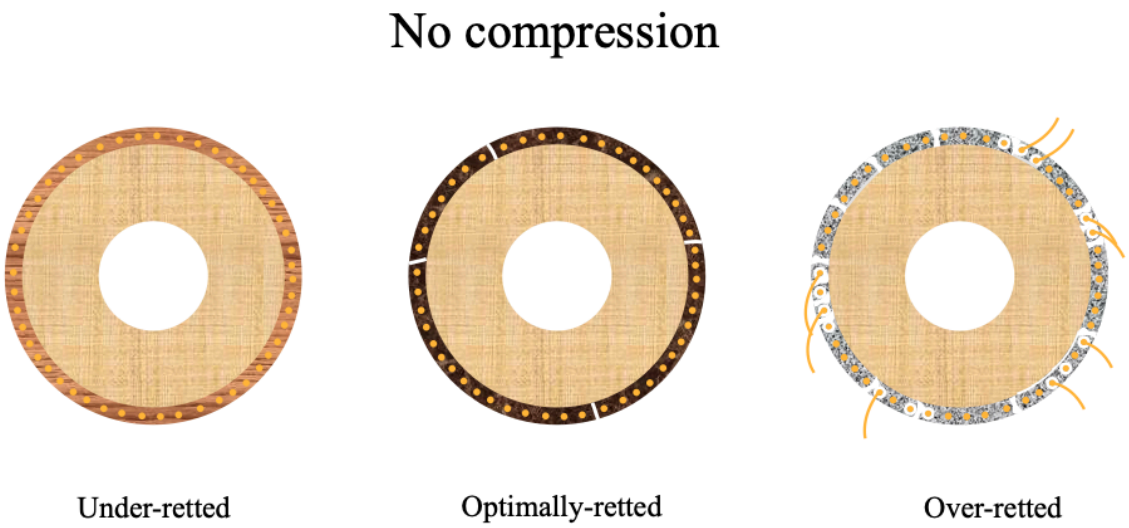

Figure 5. Représentation schématique du lin provenant des étapes de sous-rouissage, de rouissage optimal et de sur-rouissage avant compression. La couleur du tissu extérieur représente l'avancement du rouissage. Les petits points jaunes représentent les fibres de lin qui courent le long de la tige. Les diagrammes sont des coupes transversales d'une tige. La partie intérieure du bois, immuable, le « xylème », est indiquée en brun clair.

La figure 5 montre des représentations schématiques des sections transversales des échantillons de tiges de lin aux stades de rouissage insuffisant (à gauche), de rouissage optimal (au milieu) et de rouissage excessif (à droite) avant l'induction d'une force de compression externe. L'échantillon insuffisamment roui montre l'absence de dommages dans le tissu externe et le xylème avant la compression. Ce n'est pas le cas pour les échantillons à rouissage optimal et excessif, qui montrent une influence évidente du processus de rouissage, exprimée par des dommages, présentés par les zones blanches avant la compression. En outre, le changement de couleur du tissu extérieur représente la modification induite par le rouissage du tissu extérieur, c'est-à-dire la diminution de sa résistance mécanique (voir chapitre 3).

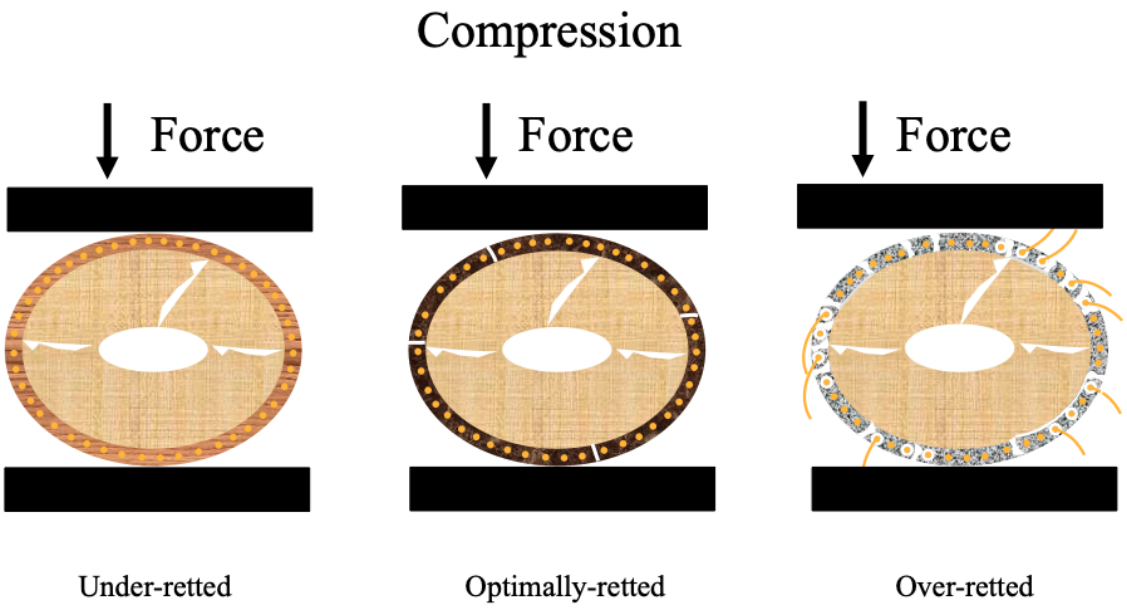

Figure 6. Représentation schématique du lin provenant des étapes de sous-rouissage, de rouissage optimal et de sur-rouissage pendant la compression. La couleur du tissu extérieur représente l'avancement du rouissage. Les petits points jaunes représentent les fibres de lin qui courent le long de la tige. Les diagrammes sont des coupes transversales d'une tige. La partie intérieure du bois, immuable, le « xylème », est indiquée en brun clair.

La figure 6 montre des représentations schématiques des sections transversales des échantillons de tiges de lin prélevés à des stades de rouissage insuffisant (à gauche), de rouissage optimal (au milieu) et de rouissage excessif (à droite) pendant l'application d'une force de compression. Il n'y a pas de changement dans l'état du tissu externe après la compression de tous les échantillons provenant de stades sous-optimaux et sur-retardés. Ce n'est pas le cas pour le xylème (brun clair), où une influence claire de la force de compression, observée sous forme de dommages, est présentée par les zones blanches dans les échantillons testés des trois phases de rouissage.
Les résultats de cette étude montrent un schéma intéressant. Lorsque les échantillons sous-optimaux et sur-retardés sont soumis à une compression mécanique, il n'y a pas de changements observables à la surface de la tige. Dans ce cas, l'application d'une compression mécanique (pour induire une contrainte mécanique sur le composite de lin, y compris le tissu externe et le xylème) ne provoque pas de dommages dans le tissu externe de la tige de lin - pour tous les échantillons de tige de lin à tous les stades de rouissage. En outre, l'image microscopique montre l'absence de fractures dans le tissu externe et la présence de fractures dans le xylème lorsqu'une force de rupture est atteinte. La valeur calculée du module de compression moyen en fonction de la période de rouissage est constante. De même, la valeur calculée de la résistance moyenne à la compression en fonction de la période de rouissage est constante. Ceci suggère que les valeurs de module de compression et de résistance extraites représentent les propriétés mécaniques du xylème, et que la sensibilité aux dommages mécaniques du tissu extérieur est nulle.
Cela semble raisonnable car la plante a évolué pour avoir des fibres solides sur toute sa longueur afin de résister au vent et au poids propre dû à l'absorption d'eau en cas de pluie. Le tissu extérieur, y compris les fibres, ne joue donc aucun rôle dans le comportement en

compression des tiges. Comme le pourrissement n'affecte que le tissu extérieur, l'avancement du pourrissement ne sera pas apparent lors des tests de compression. C'est exactement ce que l'on observe dans les expériences.
Ces résultats suggèrent fortement que le processus de rouissage n'est pas évident dans un phénomène mécanique de compression. Cependant, cette expérience révèle des informations importantes concernant le xylème. En comparant ces résultats avec ceux de l'expérience de flexion, nous pouvons conclure que le tissu extérieur est influencé par le rouissage (le module de flexion et la résistance diminuent dans la phase de rouissage excessif), ce qui n'est pas le cas pour le xylème (le module de compression et la résistance restent constants pendant les trois phases du rouissage).
En outre, cette expérience ouvre une nouvelle voie pour découvrir un aspect très intéressant des tiges de lin : le module de compression et la rupture par compression du xylème (composant ligneux interne de la plante de lin). Ce nouveau paramètre est resté inconnu en raison du manque de recherches antérieures dans ce domaine.
Enfin, nous pouvons comparer le module de compression mesuré ici pour 180 tiges de lin avec le module de flexion des tiges de lin, mesuré au chapitre 3. Il est clair qu'ils ne sont pas identiques. Afin de vérifier que cette divergence n'est pas due à un problème de modélisation, la modélisation a été vérifiée en utilisant la flexion et la compression de tubes en polypropylène. Ce travail se trouve à l'annexe 2. En utilisant des tubes de polypropylène, le module de flexion et le module de compression se sont avérés égaux et correspondent exactement à la valeur donnée pour le polypropylène dans la littérature. Au moment où nous écrivons ces lignes, nous n'avons pas d'explication claire pour cette divergence, si ce n'est d'invoquer une possible anisotropie de la morphologie et des propriétés du tube de xylème en raison de sa nature poreuse.

Les conclusions du Chapitre 4

Les propriétés mécaniques des échantillons de tiges de lin ont été caractérisées par des mesures de compression. Des tiges de lin à différents stades de rouissage ont été mesurées pour contrôler l'effet du rouissage sur le module de compression et la résistance à la compression des tiges. Pour ce faire, un outil simple a été développé pour appliquer une force progressive précise à un petit morceau d'une tige de lin coupée. Pour obtenir des résultats significatifs, la coupe (section transversale) devait être de haute qualité pour permettre des observations par microscopie optique numérique. Le poids de l'eau a été utilisé avec succès pour appliquer une force précise et contrôlée aux tiges. Les résultats ont permis d'obtenir la déformation de la section transversale de la tige en fonction de la force. Trois phases ont été observées dans les données : un régime élastique, une déformation plastique et une rupture du xylème de la tige. En utilisant un modèle basé sur l'écrasement d'un tube uniforme et homogène, nous avons pu extraire le module de compression et la résistance des tiges de lin à un certain stade de rouissage et comparer directement des tiges à différents stades de rouissage. Il a été observé que le module de compression et la résistance à la compression des tiges ne varient pas de manière significative avec le rouissage. Ceci est en accord avec les résultats de flexion des tiges présentés dans le chapitre 3 où le tissu extérieur, y compris les fibres, a été délibérément enlevé pour les mesures. Les résultats et les observations de ce chapitre donnent du poids à notre proposition de comportement de flexion des tiges de lin à différents stades de rouissage et à la façon dont les mécanismes de rouissage endommagent le tissu externe pour modifier les

propriétés de flexion des tiges de lin. Dans le chapitre suivant, nous descendrons d'un niveau et examinerons les propriétés mécaniques des fibres de lin.

Chapitre 5

Caractérisation macro-mécanique : Effet de rouissage sur la torsion des tiges

Les principaux résultats du Chapitre 5

Les expériences de flexion sur des tiges de lin à différentes phases de rouissage (chapitre 3) ont montré que le rouissage a un effet sur le module de flexion et la résistance à la flexion des tiges de lin composites. Nous avons proposé que cela était dû à la dégradation du tissu externe de la tige induite par le rouissage, qui conduit effectivement à un affaiblissement de la flexion de la tige à mesure que le temps de rouissage augmente. Cette hypothèse est confirmée par les expériences de compression des tiges de lin (chapitre 4). En compression, aucun effet du rouissage n'est observé sur le module de compression ou la résistance à la rupture. Nous avons attribué cela au fait que le tissu externe (qui maintient ensemble les fibres de lin qui courent latéralement le long de l'extérieur de la tige) ne joue aucun rôle dans la rigidité structurelle dans ces expériences. Pour réaliser l'expérience de torsion et valider l'hypothèse proposée, un outil sur mesure a été mis au point pour le doctorat. L'outil a été méticuleusement conçu avec des dimensions spécifiques, y compris la longueur, la largeur et l'épaisseur, pour assurer la compatibilité avec le montage du microscope numérique Keyence tout en respectant les exigences de distance de travail et de longueur focale. L'outil de torsion se compose de deux extrémités : une extrémité fixe et une extrémité réglable. La partie fixe de l'outil de torsion consiste en un anneau qui est positionné au-dessus du support initial de l'outil, comme le montre la figure 1. Cet anneau sert de support au mandrin du porte-échantillon. Sur la base de ces résultats et des conclusions des essais macro-mécaniques des tiges de lin (chapitres 3 et 4), nous avons conçu un essai mécanique original des tiges de lin basé sur l'application d'une torsion aux tiges. Même si des artisans qualifiés effectuent ce type de test manuellement, nous avons dû imaginer, concevoir et fabriquer un outil original pour réaliser les expériences contrôlées. L'objectif de ces expériences était d'étudier l'influence de la contrainte de cisaillement superficielle (due à la torsion mécanique) sur le tissu externe des tiges de lin. Nous nous attendions à ce que la contrainte de cisaillement superficielle provoque des dommages observables (fissuration, apparition de défauts...) sur le tissu externe. Alors que l'artisan utilise son œil pour percevoir les effets dans les tiges de rouissage, nous avons décidé d'utiliser un microscope optique numérique pour enregistrer et quantifier les effets de la torsion mécanique appliquée.

Figure 1. Photographie de l'outil de torsion avec une tige de lin sous le microscope optique numérique VHX-6000 (Keyence, France).

Les figures 2 et 3 montrent des photos microscopiques des dommages et de la déformation du tissu externe à 50 degrés et à une contrainte de cisaillement de surface de 92,5 MPa.

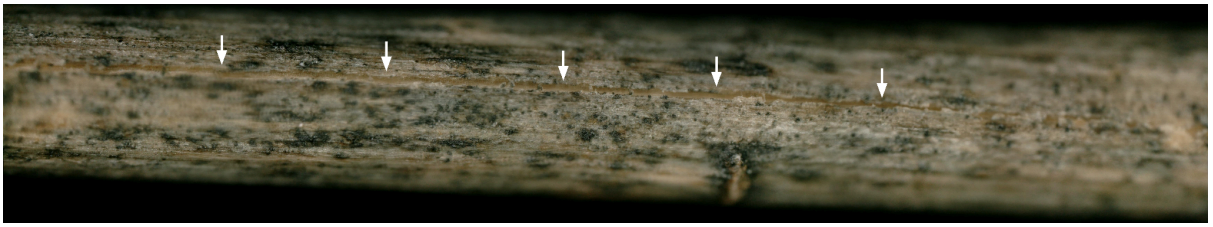

Figure 2. Apparence des dommages. Image piquée en microscopie optique numérique de la section centrale gauche d'une tige de lin ayant subi un rouissage optimal à un angle de torsion de 50 degrés, ce qui équivaut à une contrainte de cisaillement superficielle de 92,5 MPa. L'endommagement du tissu externe de la tige de lin est clairement visible au microscope optique.

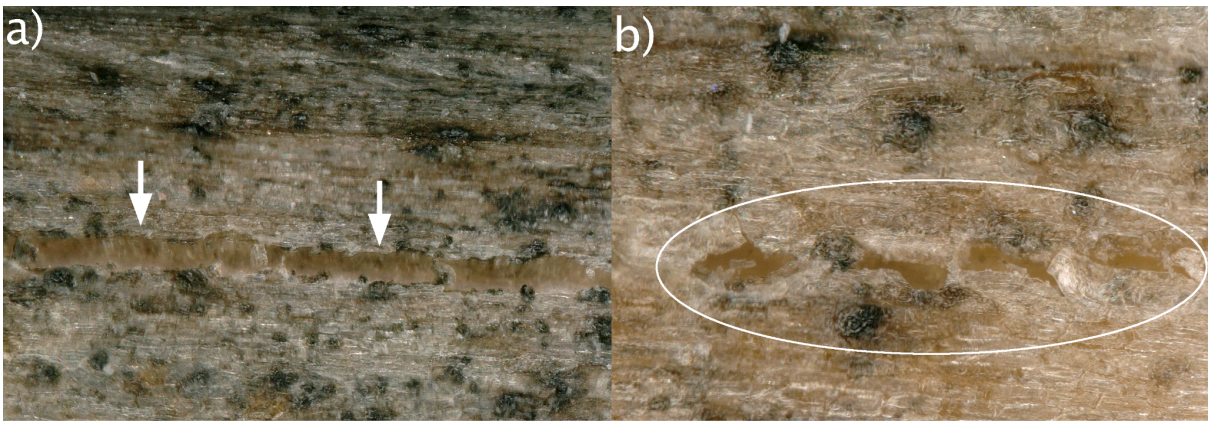

Figure 3. Images zoomées de l'apparition de dommages dans le tissu extérieur d'une tige de lin soumise à une torsion. Images zoomées en microscopie optique numérique de différentes parties d'une tige de lin ayant subi un rouissage optimal sous un angle de torsion de 50 degrés, ce qui équivaut à une contrainte de cisaillement de surface de 92,5 MPa. L'image de gauche (a) la figure montre une longue fissure, l'image de droite (b) montre l'apparition de dommages locaux.

Les résultats montrent que le tissu extérieur commence à se séparer avant que le bois intérieur ne se brise. Cela signifie qu'une force moindre est nécessaire pour séparer la couche externe. Cette constatation est intéressante car elle signifie qu'à ce stade, il est plus facile d'arracher le tissu externe du bois qu'au stade de décomposition précédent.

Measured property	Surface shear stress (MPa)
Surface shear stress to cause visible damage in optimally-retted samples	91.02±8.87
Surface shear stress to break wood in all samples	180.54±21.70

Tableau 1. Résumé des résultats obtenus sur la base de toutes les mesures effectuées dans ce chapitre.

Le tableau 1 présente un résumé des résultats obtenus sur la base de toutes les mesures effectuées dans ce chapitre. Ces deux propriétés sont très importantes. Tout d'abord, la contrainte de cisaillement superficielle qui provoque des dommages visibles dans les échantillons rouis de manière optimale permet de faire ce qui suit. L'utilisateur de l'outil peut

- du moins en principe - mesurer les dimensions de n'importe quelle tige à n'importe quel stade de rouissage, insérer la tige dans l'outil et appliquer une contrainte de cisaillement superficielle de 91,02±8,87 MPa aux tiges en réglant un angle de torsion calculé à partir des dimensions de la tige. Si l'utilisateur de l'outil observe des dommages dans le tissu extérieur de la tige, cela signifie que la tige de lin testée a subi un rouissage optimal. Si aucun dommage n'est observé dans le tissu extérieur de la tige, la tige de lin se trouve dans un état de sous-retrait. L'observation d'un rouissage excessif dans le tissu extérieur signifie que l'utilisateur de l'outil n'a pas effectué suffisamment de tests réguliers et qu'il a manqué le point de rouissage optimal, ce qui ne risque pas de se produire avec cette méthode. La contrainte de cisaillement superficielle maximale du bois permet à l'utilisateur de l'outil de calculer l'angle de torsion maximal qui peut être appliqué à la tige flexible compte tenu de ses dimensions.

Ces résultats mettent en évidence l'efficacité de l'outil de torsion pour prédire le point de rouissage optimal. Cette information est très utile pour prédire le moment où la tige de lin se brisera et comment séparer les tissus extérieurs contenant les fibres de lin de la tige en appliquant un couple de torsion.

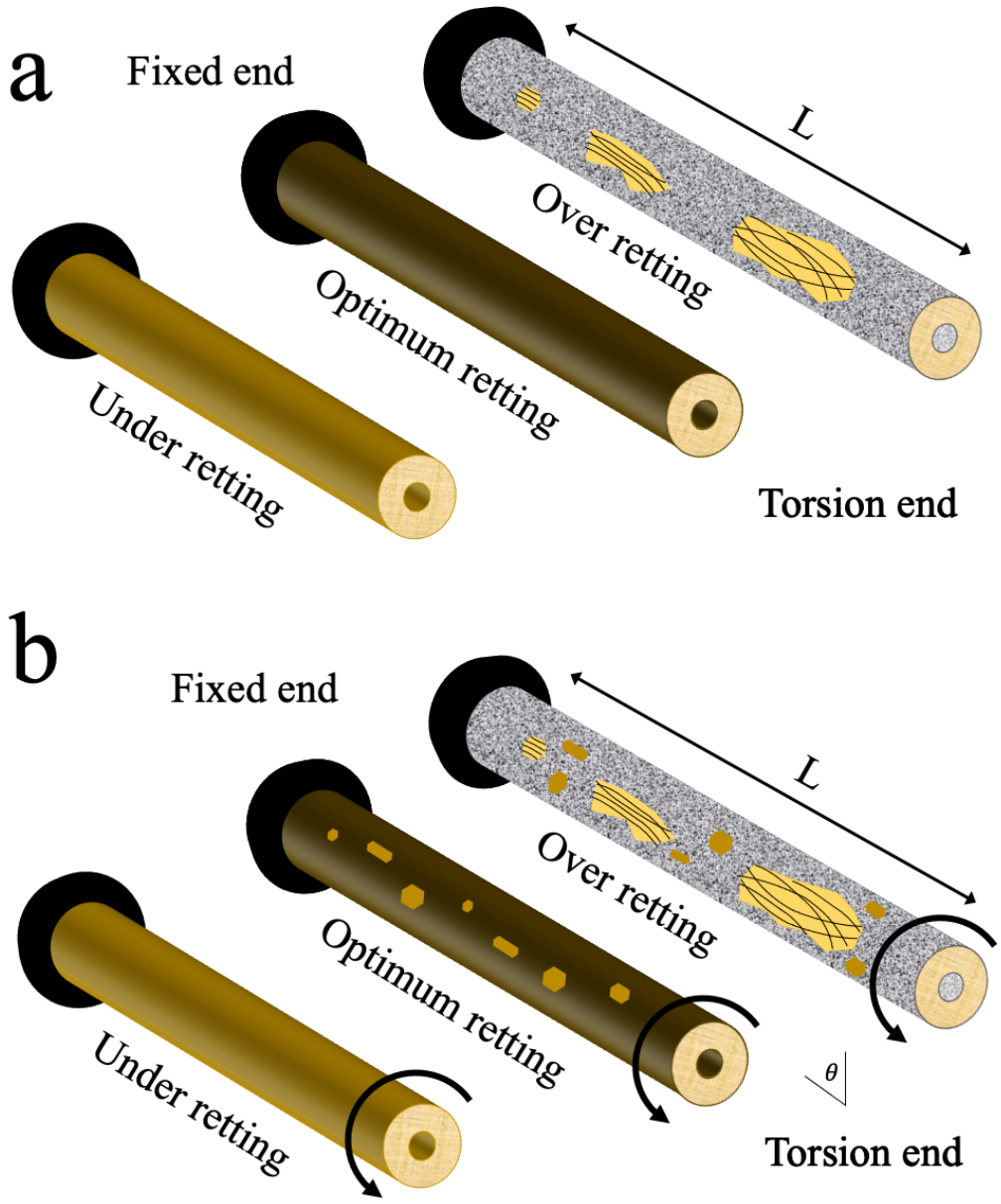

Figure 4. Représentations schématiques des tiges de lin sous torsion. (a) avant torsion et (b) sous torsion. La couleur du tissu extérieur représente l'avancement du rouissage. Les petites zones jaunes représentent les dommages le long de la tige. Les lignes noires représentent les fibres exposées. La partie interne immuable du bois, le "xylème", est indiquée en marron clair.

La figure 4 montre des représentations schématiques des tiges de lin soumises à une torsion. Au début, lorsqu'aucune torsion n'est appliquée, les tiges prétéritées de manière optimale présentent très peu de dommages dans le tissu extérieur, tout comme les tiges insuffisamment prétéritées. Cependant, les tiges trop rouies présentent des dommages très apparents dans le tissu extérieur, qui apparaissent peu de temps après le temps de rouissage optimal. Lorsque la torsion est appliquée aux tiges, l'apparence des dommages est très apparente dans les échantillons rouis de façon optimale. Ce n'est pas le cas pour les

échantillons insuffisamment rouis. Les échantillons trop rouis induisent un peu plus de dégâts, mais pas autant que les échantillons rouis de manière optimale. L'application d'une torsion aux tiges induit un couple. Ce couple induit une contrainte superficielle uniforme sur l'ensemble de la tige de lin. C'est pourquoi la torsion révèle mieux que la flexion les échantillons à frettage optimal. Comme nous l'avons vu au chapitre 3, la flexion induit une contrainte superficielle maximale à la base du cantilever de la tige - les expériences ont montré qu'il était difficile de discerner les échantillons à frettage optimal à l'aide de la flexion, même s'ils étaient apparents. En revanche, l'induction d'une contrainte superficielle sur l'ensemble de la surface de la tige par l'utilisation de la torsion signifie que les dommages induits par la torsion sur le tissu extérieur faible dans les tiges soumises à un rouissage optimal sont facilement visibles au microscope.

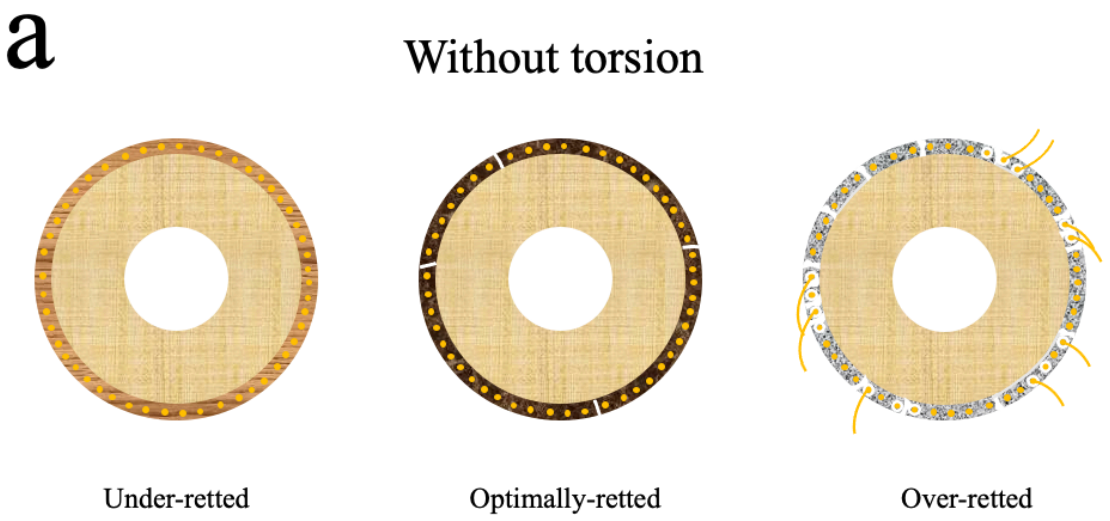
a
Without torsion
Under-retted
Optimally-retted
Over-retted
b
Low torsion
θ
θ
θ
Under-retted
Optimally-retted
Good Separation
Over-retted
Fibre already exposed
c
High torsion
θ
θ
θ
Under-retted
Optimally-retted
Good Separation
Over-retted
Fibre already exposed

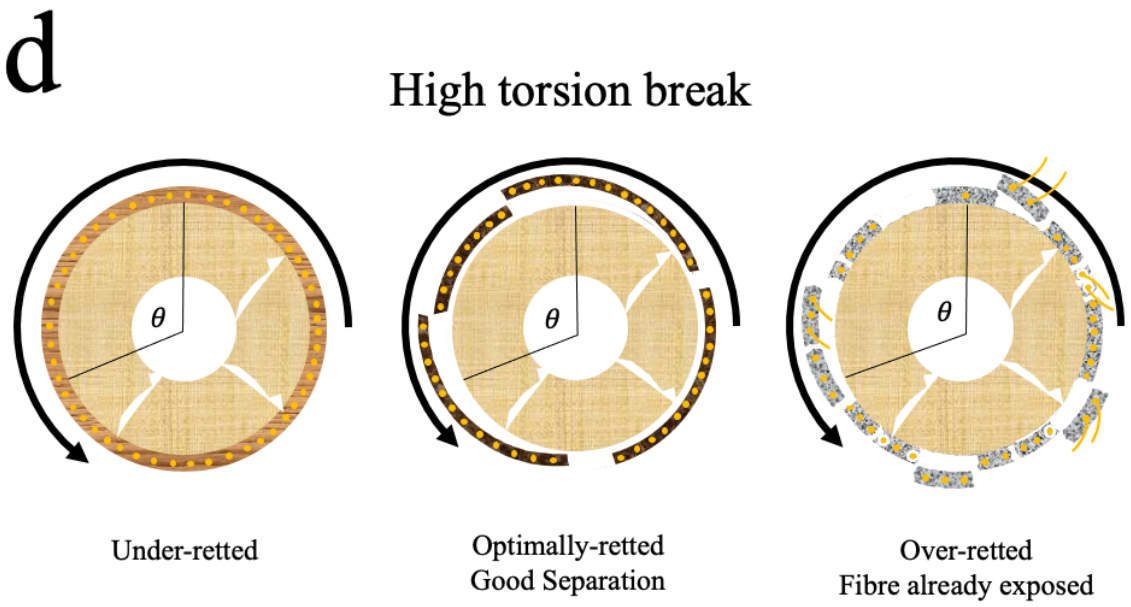

Figure 5. Représentation schématique des tiges de lin issues des étapes de sous-rouissage, de rouissage optimal et de sur-rouissage avant (a), lors d'une faible torsion (b), lors d'une forte torsion (c) et lors d'une forte torsion provoquant une cassure (d) . Les diagrammes schématiques représentent des coupes transversales de tiges de lin près de la base du porte-à-faux là où la contrainte est maximale. La couleur du tissu extérieur représente l'avancement du rouissage. Les petits points jaunes représentent les fibres de lin qui courent le long de la tige. Les diagrammes sont des coupes transversales d'une tige. La partie intérieure du bois, immuable, « xylème », est indiquée en marron clair.

La figure 5 montre une représentation schématique des sections transversales de tiges de lin (en trois étapes de rouissage) et avec torsion appliquée. En ce qui concerne les échantillons sous-rouis, le tissu extérieur est mécaniquement robuste et fortement attaché à la surface du xylème. Pour ces échantillons, la torsion a peu d'effet. En effet, le xylème se brise toujours avant qu'un quelconque dommage apparent ne soit visible dans les tissus extérieurs. En ce qui concerne les échantillons trop rouis, le tissu extérieur est déjà endommagé par le rouissage excessif et n'est plus fortement attaché au xylème. Dans ce cas, l'application d'une faible torsion entraîne une augmentation visible des dommages dans les tissus externes déjà endommagés. Dans le cas des échantillons rouis de manière optimale, le tissu extérieur a probablement été endommagé par le rouissage, bien qu'il ne soit pas visible en cas de torsion nulle. Il est également raisonnable de supposer que le tissu extérieur d'une tige au rouissage optimal n'est pas aussi fortement attaché au xylème que les tiges sous-rouies. Cela signifie que pour des tiges rouies de manière optimale, l'application d'une torsion conduit à l'apparition d'endommagements sous la forme d'une valeur spécifique de contrainte superficielle. Grâce à plusieurs expériences, il a été possible d'estimer cette valeur de contrainte de surface et donc l'angle de couple/torsion nécessaire pour provoquer des dommages visibles pour un diamètre de tige donné (extérieur et intérieur). Enfin, dans tous les échantillons, il existe un certain couple qui provoque la rupture du xylème. Cette valeur

s'est avérée approximativement la même dans toutes les tiges, quel que soit l'avancement du rouissage. Cela concorde bien avec les résultats de flexion des tiges présentés au chapitre 3.

Les résultats de notre étude montrent une tendance intéressante. Lorsque les échantillons sont soumis à une torsion mécanique, aucun changement observable dans la surface de la tige n'est observé avant que la phase de rouissage optimale ne soit atteinte. Dans cette phase, l'application d'une torsion mécanique (pour induire une contrainte de cisaillement superficielle) provoque des dommages aux tissus externes de la tige de lin. Pour tous les échantillons de tiges de lin dans cette plage de rouissage, la valeur calculée de la contrainte de cisaillement superficielle est constante, 91.02 ± 8.87 MPa. Ceci suggère que la sensibilité aux dommages mécaniques du tissu externe est considérablement augmentée à ce stade particulier. Ces résultats suggèrent fortement que le processus biologique de séparation enzymatique, responsable de l'élimination des tissus externes, n'est pas terminé tant que le point de rouissage optimal n'a pas été atteint. Fait intéressant, nous avons également observé des dommages et des déformations évidents dans les tissus externes des échantillons de lin prélevés juste après l'étape de rouissage optimale. Ce phénomène intéressant s'observe sans aucune nécessité de torsion mécanique. Par la suite, dans ce cas, il existe un risque de rouissage excessif, ce qui pourrait affecter la qualité de la fibre. De plus, nos observations suggèrent fortement que l'atteinte du stade optimal de rouissage est caractérisée par une condition spécifique : la contrainte de cisaillement requise pour induire le cisaillement du tissu externe doit être significativement inférieure à la contrainte de cisaillement requise pour induire une fracture dans le tissu ligneux interne du la plante de lin. Ce dernier point indique que le rêve d'un outil mécanique pour tester le degré de rouissage des tiges de lin est enfin réalisable.

De plus, lorsque l'on compare les résultats de la contrainte de cisaillement superficielle et du couple requis pour initier la fracture du bois/des tissus internes dans les trois phases : « sous rouissage », « rouissage optimal » et « surrouissage », il est évident que le cisaillement la contrainte nécessaire pour initier la fracture du bois/des tissus internes reste constante tout au long de la période de rouissage. Cette observation est cohérente avec les résultats des expériences de flexion sans tissu externe (Chapitre 3) et des expériences de compression (Chapitre 4), indiquant un module de flexion constant du tissu interne du bois au cours du rouissage et au-delà. Cela conforte l'idée selon laquelle le rouissage affecte principalement les tissus externes tout en maintenant la stabilité des tissus ligneux internes. En outre, cette expérience ouvre une nouvelle voie pour découvrir quelque chose de très intéressant sur les fibres végétales : la contrainte de rupture du composant ligneux interne de la plante de lin. Ce nouveau paramètre est resté inconnu en raison du manque de recherches antérieures dans ce domaine. L'expérience de torsion révèle une valeur de 180.4 ± 21 MPa pour le tissu ligneux interne de la plante de lin.

Les conclusions du Chapitre 5

Les tiges de lin peuvent être caractérisées par l'application d'une torsion mécanique. Il s'agit de l'un des tests mécaniques manuels qu'un artisan (agriculteur) effectue "sur le terrain" lorsqu'il contrôle l'avancement du rouissage des tiges de lin récoltées. L'artisan juge les informations qualitatives par le mouvement de la main et l'œil pour évaluer l'avancement du rouissage des tiges de lin. Dans ce chapitre, nous avons tenté de quantifier ce processus artisanal en laboratoire en vue de produire un outil technologique pour le suivi du rouissage sur le terrain.

Pour ce faire, nous avons développé un outil mécanique original. L'outil permet la torsion progressive et contrôlée d'une tige de lin. En considérant la tige de lin comme l'équivalent d'un long tuyau droit et homogène, une modélisation analytique permet de calculer le couple et la contrainte de cisaillement superficielle de la tige de lin pour un angle de torsion donné. Cette hypothèse permet de comparer toutes les tiges de lin de l'étude entre elles : à la fois les tiges du même stade de rouissage et les tiges d'un stade de rouissage à l'autre. Cette approche a permis d'évaluer quantitativement la façon dont l'application de la torsion affecte les dommages induits par la contrainte de cisaillement dans le tissu externe des tiges de lin au fur et à mesure du rouissage.

On observe clairement que les dommages dans le tissu externe des tiges de lin se produisent à des valeurs spécifiques de contrainte de cisaillement de surface pour différents stades du rouissage. Par exemple, dans les échantillons ayant subi un rouissage optimal (tel que défini par la société VRF), nous observons qu'une valeur spécifique de contrainte de cisaillement de surface est nécessaire pour l'apparition de dommages dans le tissu externe. Pour les stades de rouissage inférieurs à cette valeur, aucun dommage n'est observé à cette valeur de contrainte de cisaillement de surface, pour les stades de rouissage supérieurs à cette valeur, des dommages apparaissent à des valeurs inférieures à cette valeur.

Les résultats expérimentaux suggèrent qu'un outil basé sur l'application de la torsion mécanique et l'analyse d'images pourrait être envisagé. Les résultats de cette étude ouvrent donc des perspectives intéressantes. La corrélation entre la torsion et le rouissage nous amène à envisager le développement d'un véritable mécanisme de détection. Un tel outil, basé sur une analyse mécanique torsion/image, pourrait potentiellement révolutionner le suivi du rouissage de la rosée. En outre, cet outil pourrait servir d'outil prédictif, fournissant un aperçu du point de rouissage optimal pour le lin. Cette innovation potentielle promet d'améliorer l'efficacité et la précision des processus de rouissage, contribuant ainsi à l'avancement des techniques d'extraction des fibres de lin.

Chapitre 6

Caractérisation micro-mécanique : Effet de rouissage sur les fibres de lin uniques

Les principaux résultats du Chapitre 6

La principale conclusion des essais macro-mécaniques des tiges de lin (chapitres 3, 4 et 5) est que l'évolution des propriétés du tissu extérieur (due au rouissage) est responsable de l'évolution apparente des propriétés mécaniques des tiges de lin au cours du rouissage. En d'autres termes, le tissu extérieur des tiges de lin peut être considéré comme un matériau dont la dégradation est favorisée par le rouissage (placé entre les fibres de lin), les fibres elles-mêmes s'étendant axialement le long de la tige de lin. Une bonne question à laquelle il convient de répondre est la suivante : les propriétés mécaniques des fibres de lin évoluent-elles au fur et à mesure que le rouissage progresse ? Tout d'abord, les propriétés mécaniques des fibres de lin ont été étudiées par de nombreux groupes depuis plus d'un siècle - voir chapitre 1. Pour ce faire, la plupart des groupes ont utilisé des essais de traction standard. Cette technique fonctionne très bien pour les barres d'acier mais donne des résultats moins précis lorsqu'il s'agit de fibres de diamètre microscopique. De grandes barres d'erreur signifient que la comparaison des résultats est différente et que des tendances subtiles dans les données peuvent être manquées. Dans ce chapitre, afin de caractériser l'évolution des propriétés mécaniques des fibres, nous avons développé des techniques micromécaniques originales basées sur la déflexion de cantilevers à base de fibres (dynamiques et statiques) afin de réduire l'erreur de mesure et d'observer les tendances au fur et à mesure de l'évolution du rouissage.Les résultats soutiennent l'idée que c'est la dégradation du tissu extérieur entre les fibres, induite par le rouissage, qui est responsable de l'évolution des propriétés mécaniques des tiges rouies (observée dans les chapitres 3 et 5).

Afin de tester expérimentalement l'idée d'un cantilever à base de fibres, nous avons choisi des fibres de lin comme véhicule d'essai. Des échantillons de lin roui ont été collectés dans un champ appartenant à la société Van Robaeys Frères (Killem, France). Pour mener à bien cette recherche, les fibres de lin individuelles ont été soigneusement retirées de la tige de la plante de lin à l'aide d'une technique d'épluchage manuel méthodique mise au point par les auteurs. Cette technique consiste à faire une petite entaille au sommet de la tige pour séparer le tissu extérieur de la partie intérieure ligneuse. Le tissu extérieur a ensuite été soigneusement détaché à l'aide de pinces. À l'aide d'une paire de pinces, des faisceaux droits de fibres ont été soigneusement détachés du tissu extérieur tout en évitant de plier les fibres. L'extraction des fibres de lin individuelles a ensuite été effectuée sous un microscope à grande distance de travail, ce qui facilite la manipulation. Une fois qu'une seule fibre de lin droite a été identifiée dans le faisceau, elle a été extraite avec précaution en évitant de la plier. L'extrémité de la fibre de lin unique a été maintenue en place à l'aide de pinces et le faisceau de fibres a été détaché. Une méthode développée par les auteurs a été utilisée pour positionner soigneusement les fibres de lin individuelles sur des supports plats en

polypropylène mesurant en moyenne 6 mm x 6 mm x 100 µm. Ces supports en polypropylène ont été soigneusement placés sur la puce de support. Pour assurer une bonne fixation, de petites bandes (2 mm x 2 mm) de ruban adhésif ont été utilisées. Ces bandes de ruban adhésif ont maintenu les fibres de lin en place et, à l'aide du microscope, se sont collées près du bord du support en polypropylène, formant des cantilevers qui s'étendaient perpendiculairement aux puces de support en polypropylène. L'alignement (<100 µm) était important car il s'agit de l'ancrage crucial du cantilever (Davis et al., 2007 ; Lee et al., 2011). Un ancrage mal aligné pourrait entraîner des résultats erronés. La figure 1 montre des exemples de leviers (cantilevers) à base de fibres de lin fabriqués pour l'étude.

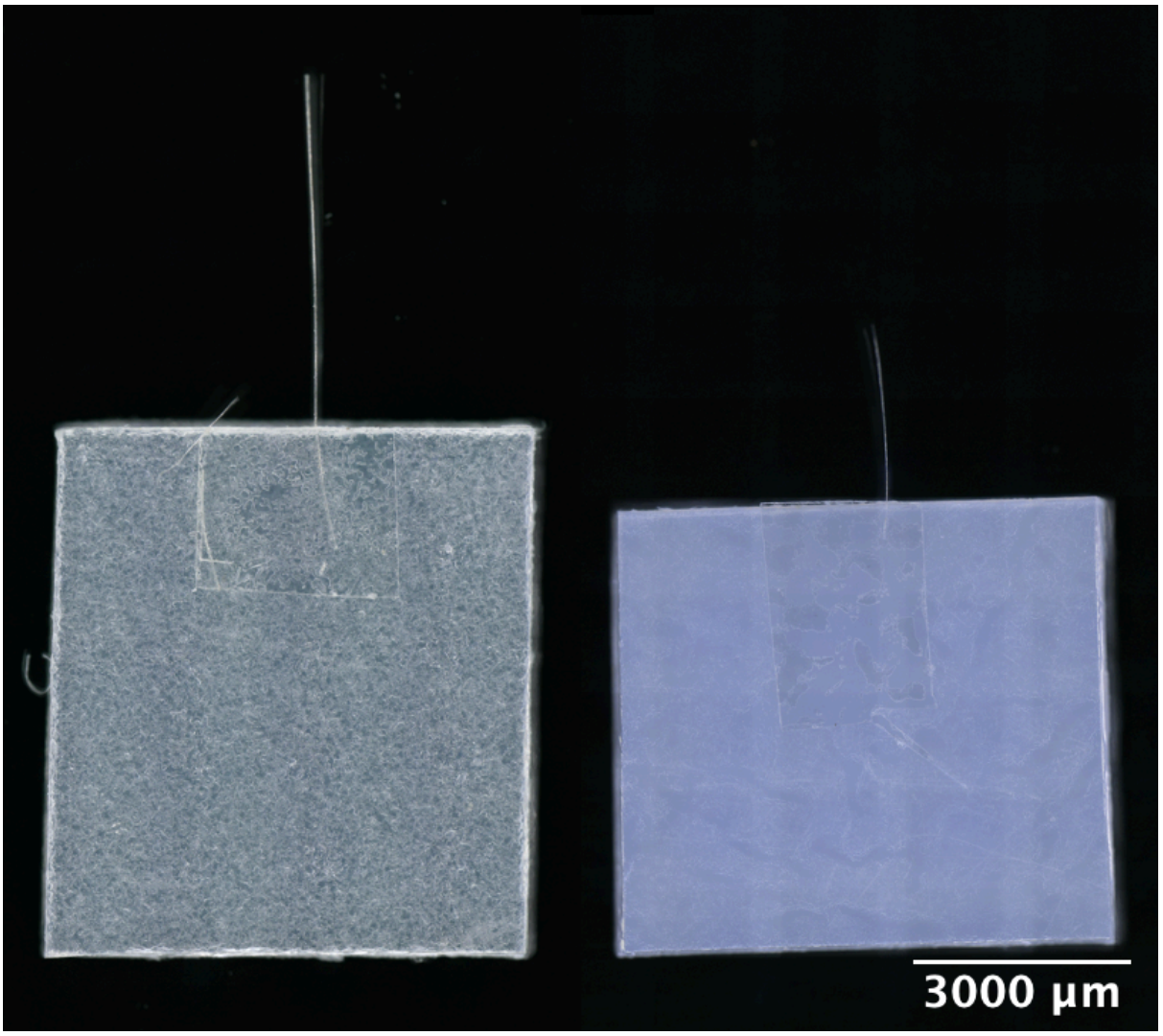

Figure 1. Images au microscope optique numérique d'exemples d'ensembles cantilever/puce de support en polypropylène fabriqués à l'aide de notre méthode. Cantilevers simples à base de fibres de lin d'une longueur de 4752 µm (image de gauche) et de 2426 µm (image de droite). Le diamètre des fibres de lin testées dans l'étude varie de 20 µm à 55 µm.

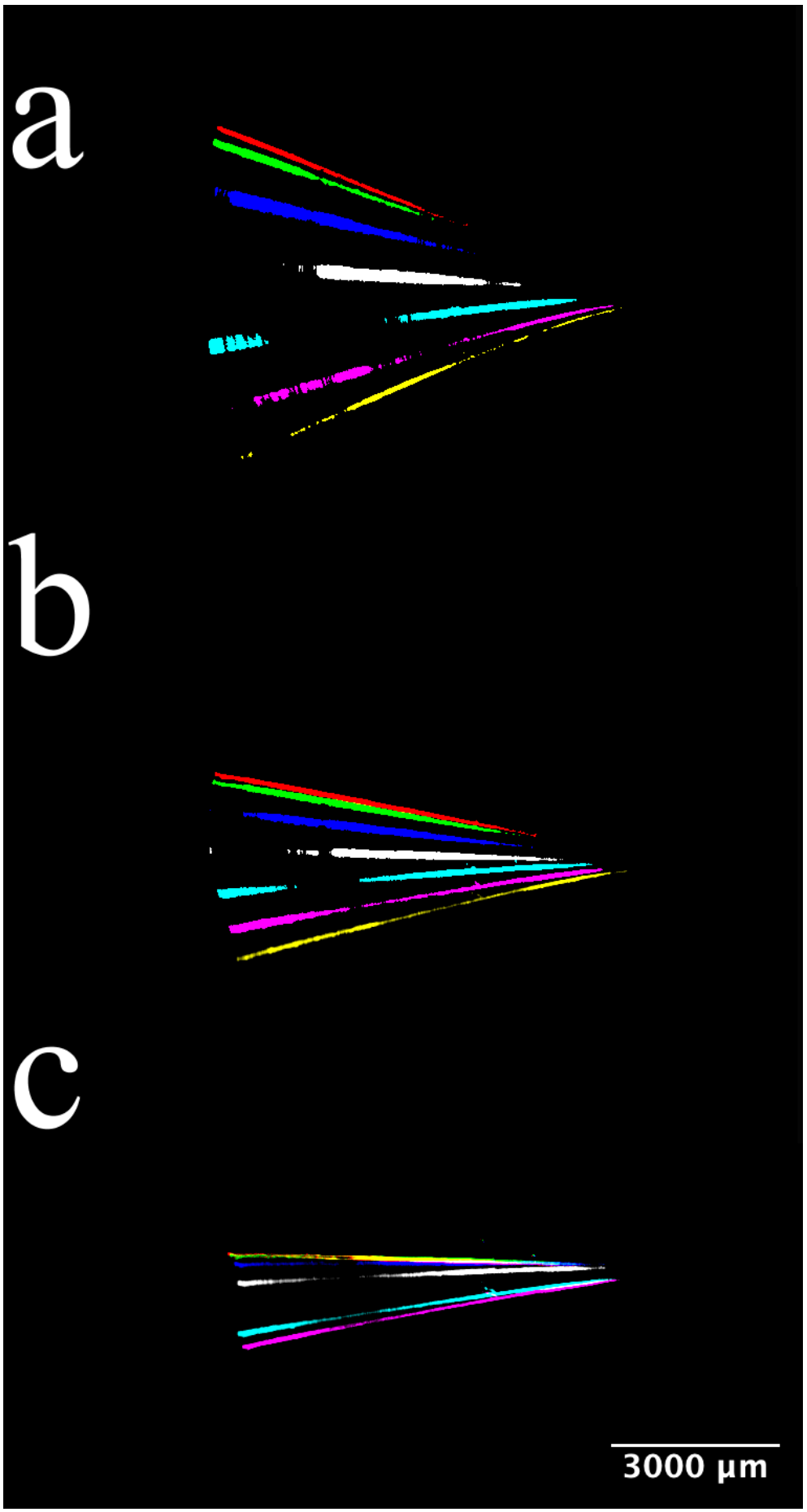
a
b
c
3000 µm

Figure 2. Images d'un cantilever vibrant à base de fibres de lin prises par une caméra à grande vitesse. (a) Une demi-période en régime d'amplitude élevée, (b) et (c) une demi-période en régime d'amplitude faible. Le cantilever a une longueur de 7547 µm et un diamètre moyen de 20,9 µm. Le temps entre chacune des sept déflexions représentées (couleurs) est de 312 µs.

La figure 2 montre des images prises par une caméra à grande vitesse d'un cantilever vibrant à base de fibres de lin. L'amortissement provoque la transition du régime de grande amplitude, figure 2(a), au régime de faible amplitude, figures 2(b) et 2(c). Les couleurs correspondent à différentes déviations du cantilever pendant un demi-cycle - retardé de 312 µs. La déflexion est le seul paramètre variable pendant l'amortissement de la vibration harmonique du cantilever. Dans le régime de forte amplitude, l'amplitude mesure 6009 µm, voir figure 2(a). L'amortissement fait passer le système du régime de haute amplitude au régime de basse amplitude, ce qui entraîne une diminution de l'amplitude à 3373 mm (voir figure 2(b)). Vers la fin de la vibration, l'amortissement entraîne une nouvelle réduction de l'amplitude à 1 724 µm (figure 2(c)), avant de revenir à l'état initial.

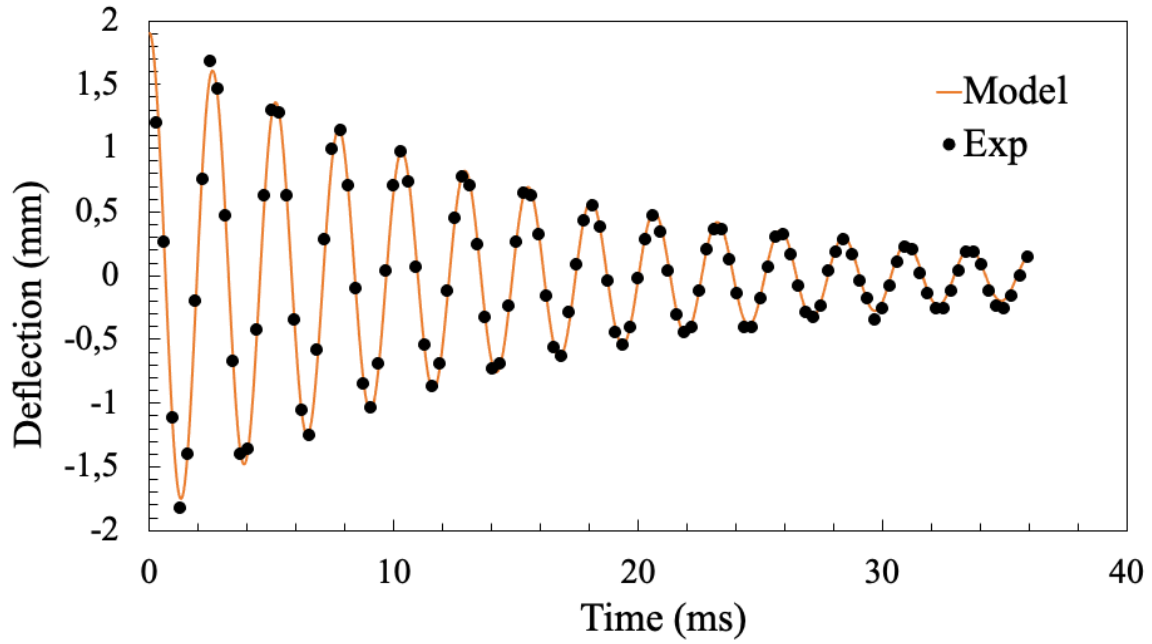

Figure 3. Réponse transitoire du cantilever à base de fibres de lin. Les cercles ouverts représentent les données brutes extraites de l'analyse des données, et la courbe orange représente un ajustement numérique du modèle de mouvement harmonique simple amorti.

La figure 3 montre la réponse transitoire totale d'un cantilever à base de fibres de lin sur 36 ms, depuis le déclenchement du simulateur de mouvement jusqu'au point de relaxation des fibres. Les points de données (cercles noirs ouverts) correspondent aux mesures de la déviation du cantilever extraites des données de la caméra à grande vitesse. La courbe

orange est obtenue à l'aide d'une méthode d'ajustement numérique de l'équation 6. La meilleure courbe d'ajustement minimise la somme des carrés des différences entre les valeurs mesurées et les valeurs du modèle.

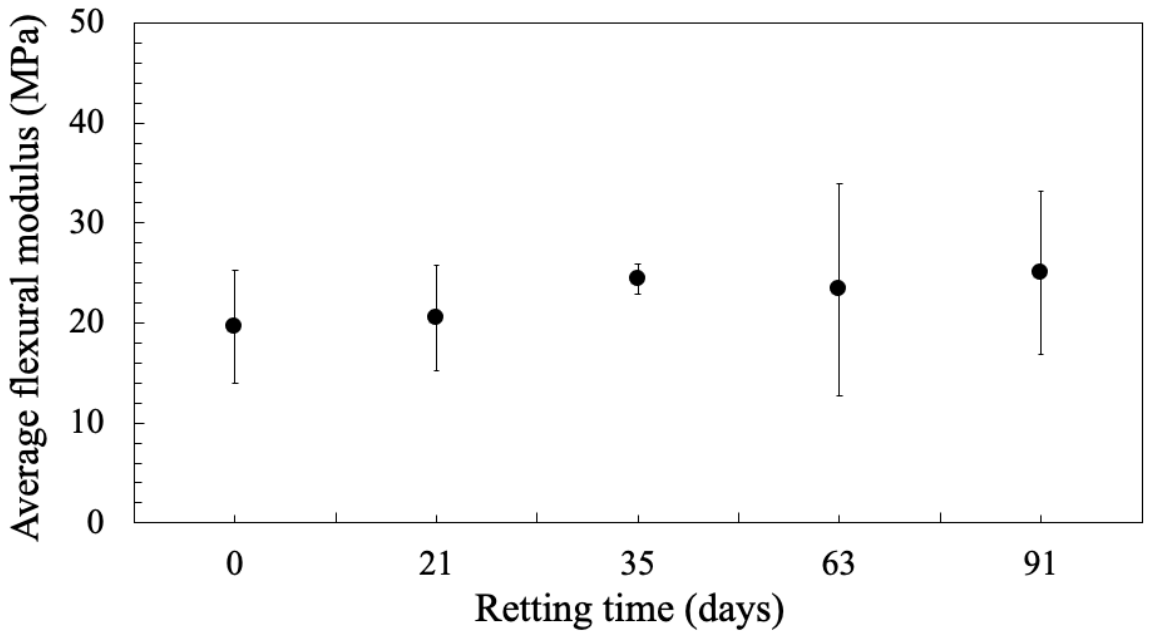

Figure 4. Évolution du module de flexion des fibres de lin simples en fonction du temps de rouissage.

Le module de flexion de la fibre pendant la période de rouissage, y compris le rouissage insuffisant, optimal et excessif, a été déterminé en testant un ensemble de données de 18 échantillons. Ces tests ont donné une valeur moyenne de module de flexion de 22,41±6,6 GPa. Cette technique basée sur un cantilever vibrant fournit des données à faible erreur et dispersion par rapport à celles qui peuvent être obtenues en utilisant des méthodes d'essai de traction macroscopiques.

Des microporteurs uniformes à base de fibres simples et des puces de support en polypropylène ont été fabriqués à l'aide des méthodes décrites ci-dessus. Une fois de plus, avant la mesure, les fibres ont été vérifiées pour détecter les défauts et contrôlées pour leur diamètre, leur uniformité et leur densité de déflexion (bandes de plis visibles). Pour obtenir une contrainte de flexion élevée, il faut une grande courbure. Celle-ci a été obtenue par une forte déflexion des échantillons en porte-à-faux. Les échantillons ont été fixés à l'appareil mécanique et les cantilevers en fibre ont été déviés en déplaçant le support latéralement vers la surface verticale–ce qui est fait en déplaçant l'étage linéaire de précision. La pointe du cantilever entre en contact avec la surface et glisse le long de celle-ci, ce qui provoque la courbure de la fibre. La courbure de la fibre génère des contraintes de traction et de compression qui atteignent leur maximum à la surface de la fibre et à l'endroit où la courbure est maximale. Le processus est réalisé progressivement en prenant de multiples photographies à haute résolution à l'aide de la microscopie optique numérique.

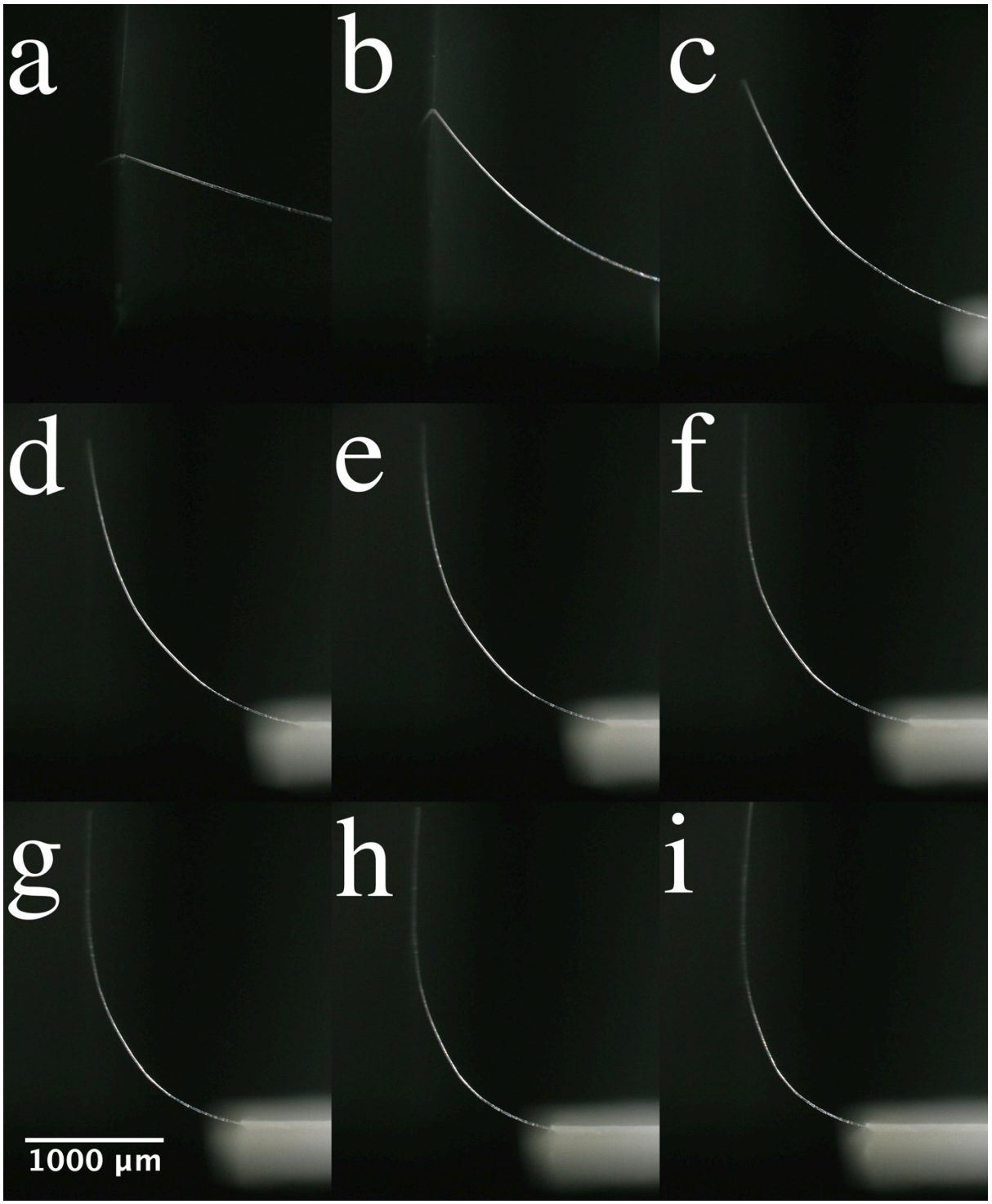

Figure 5. Images optiques assemblées de microcantilevers à base de fibres de lin uniques hautement déviantes, obtenues à l'aide de notre approche micromécanique et de la microscopie optique numérique. Le patinage vers le haut de la pointe, la flexion du cantilever et la courbure locale qui en résultent sont apparents lorsque la platine linéaire de précision déplace la puce de support vers la surface verticale.

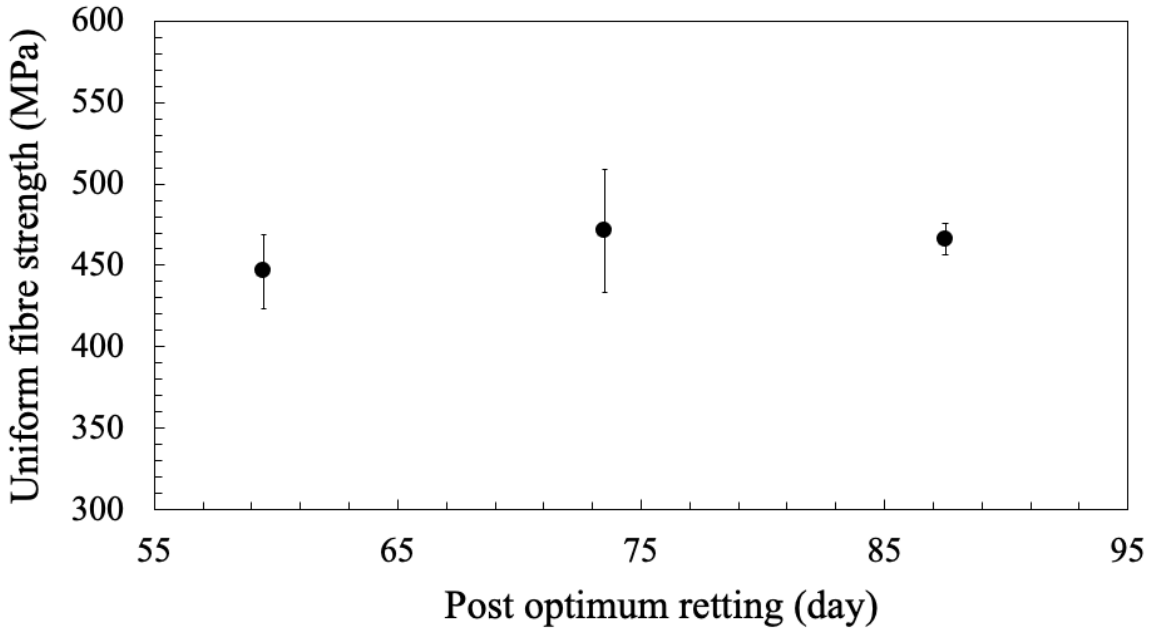

Figure 6. Évolution de la résistance à la flexion de fibres de lin simples en fonction de la période de rouissage.

La résistance à la flexion exacte de la fibre a été déterminée en testant un ensemble de données de 11 échantillons. Ces tests ont donné une valeur moyenne de résistance à la flexion de 459,03±28,06 MPa. Notre technique originale basée sur le cantilever fournit des données à faible dispersion. L'erreur dans ces mesures est beaucoup plus faible que celle qui peut être obtenue en utilisant des moyens d'essai de traction macroscopiques.

La figure 7 fournit une représentation visuelle de la structure complexe et hétérogène trouvée dans les fibres de lin. Comme indiqué en introduction, ces fibres sont composées de parois cellulaires primaires et secondaires, chacune ayant une composition chimique différente. Cette variabilité de composition contribue aux différences d'orientation des fibres. Cependant, le but de mentionner la composition des fibres à ce stade est de souligner la complexité inhérente à la structure des fibres. Notre objectif ici est de souligner que les mesures de module de flexion obtenues à partir de nos approches micromécaniques reflètent la rigidité et la résistance globales de ce matériau composite complexe hétérogène. Cela inclut la prise en compte de la structure de la paroi cellulaire et de la composition chimique associée.

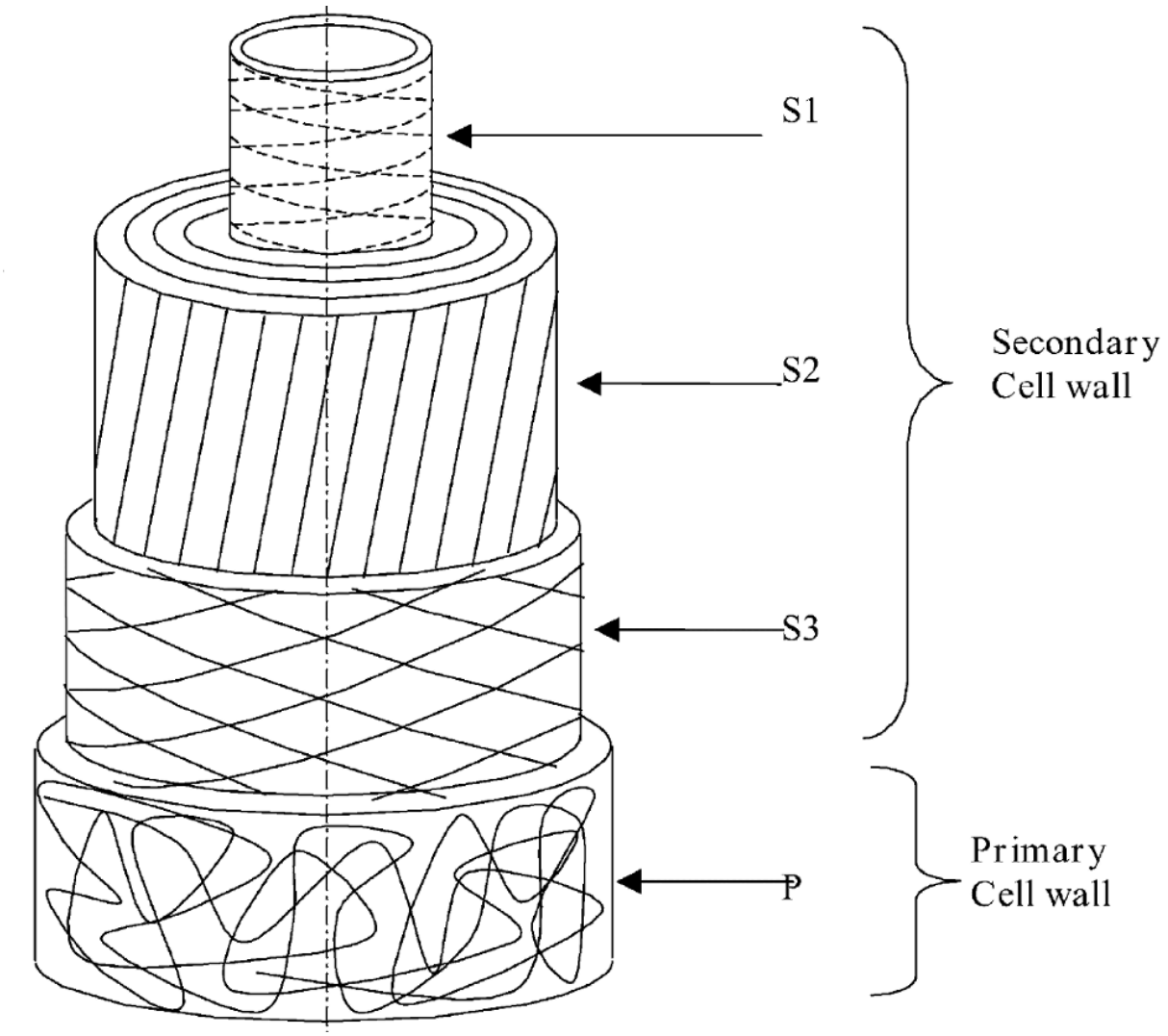

Figure 7. La structure hétérogène des fibres de lin.

Nos résultats concordent très bien avec ceux obtenus par Capron et al., 2017. « Caractérisation mécanique de la paroi cellulaire des fibres végétales par Microscopie à Force Atomique ». Au CFM 2017-23ème Congrès Français de Mécanique. Capron et coll. utilisé (Peak-Force QNM) AFM pour mesurer de manière semi-quantitative le module des sections transversales des fibres de lin, soit une technique de mesure totalement différente de la nôtre. Leurs résultats indiquent une valeur de l'ordre de 20 GPa pour l'ensemble de la fibre.

Les conclusions du Chapitre 6

Les chapitres précédents indiquent que les propriétés mécaniques (mesurées par flexion et torsion) des tiges de lin sont modifiées par le rouissage à la rosée. Les résultats de ces chapitres suggèrent que c'est la dégradation du tissu externe induite par le rouissage qui est responsable de la modification des propriétés mécaniques. Le tissu externe est composé des fibres de lin et du matériau (lamelle moyenne) entre les fibres. Afin d'aller plus loin dans la compréhension des observations macro-mécaniques, ce chapitre a présenté une caractérisation micromécanique originale des fibres de lin à différents stades de rouissage. Pour ce faire, des approches originales de mesures micromécaniques des fibres de lin ont été conçues et développées sur la base de techniques de cantilever inspirées des MEMS. Les mesures ont permis d'évaluer le module de flexion et la résistance à la flexion des fibres de lin en fonction du rouissage. Le point clé est le suivant. Alors que les techniques traditionnelles telles que les essais de traction peuvent entraîner des erreurs très importantes, nos approches micromécaniques permettent d'obtenir des erreurs relativement faibles. Cela signifie que l'on peut avoir davantage confiance dans les tendances des données.Les mesures suggèrent que les propriétés mécaniques des fibres de lin ne changent pas de manière significative au cours du rouissage. Cela implique que la modification observée des propriétés mécaniques des tiges de lin (due au rouissage) est en fait due à la dégradation du matériau de la lamelle centrale - et c'est précisément cette dégradation qui permet une extraction plus facile des fibres dans l'usine.

Cependant, comme les tiges de lin, les fibres de lin sont elles-mêmes des structures hétérogènes et complexes. C'est pourquoi, dans le chapitre suivant, nous avons décidé de procéder à une caractérisation nanomécanique (nanoindentation AFM) du tissu externe des fibres de lin. Le raisonnement sous-jacent est que les dommages induits par le rouissage sur la lamelle centrale sont présents à la surface des fibres plutôt qu'à l'intérieur. Il semble donc logique d'effectuer des tests sur l'extérieur des fibres pour voir s'il y a effectivement une modification de la surface des fibres due au rouissage, en particulier dans les échantillons sur-routeux.

Chapitre 7

Caractérisation nano-mécanique : Effet de rouissage sur la surface de fibres de lin uniques

Les principaux résultats du Chapitre 7

La principale conclusion des essais micromécaniques des fibres de lin en fonction du rouissage (chapitre 6) est que le module de flexion et la résistance des fibres n'évoluent pas significativement au cours d'un cycle de rouissage et au-delà. Ces résultats donnent du poids à l'idée que c'est l'endommagement du tissu externe (entre les fibres) induit par le rouissage qui est responsable de l'observation de la modification des propriétés mécaniques des tiges de lin induites par le rouissage. Cette idée est particulièrement évidente dans la caractérisation macro-mécanique de la torsion qui, selon nous, pourrait constituer la base d'un outil permettant de suivre l'évolution du rouissage. Pour aller plus loin dans la compréhension de ce phénomène, il est possible de réaliser des expériences nano-mécaniques en utilisant la microscopie à force atomique (AFM).

La préparation du support puce/fibre comporte plusieurs étapes. La figure 1 montre une représentation schématique des étapes de la préparation.

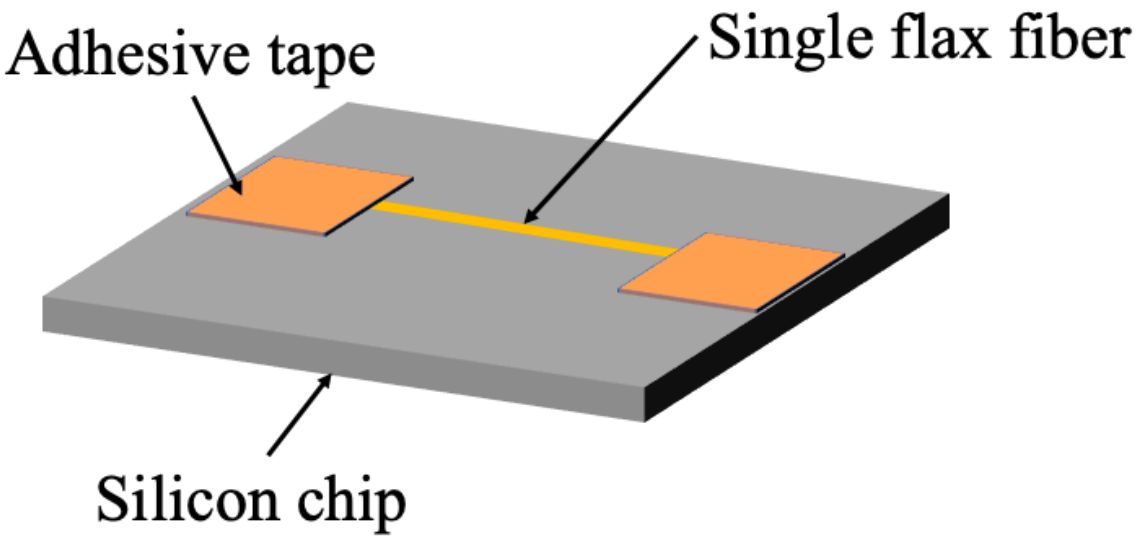

Figure 1. Schéma d'un échantillon fibre/puce en <<montage planaire>>.

Tout d'abord, des puces de silicium de 1 cm x 1 cm sont découpées dans des plaquettes de silicium. Ces puces sont ensuite nettoyées à l'isopropanol dans un environnement contrôlé, la salle blanche. Après la préparation des puces, les différentes fibres de lin précédemment extraites sont placées sur les puces de silicium. Les extrémités de ces fibres de lin sont

fixées aux puces à l'aide d'un ruban adhésif. Après cet assemblage, l'échantillon fibre/puce est examiné au microscope numérique (Keyence, France). Le but de cette évaluation microscopique est de vérifier l'alignement précis de la fibre sur la puce. Il est essentiel que la fibre ait une orientation linéaire sur la surface de la puce, sans aucune courbure. En effet, il est nécessaire d'obtenir un profil de fibre droit, induit par la tension, au cours du processus d'essai ultérieur, par opposition à une configuration courbée. Tout écart par rapport à une orientation linéaire pourrait potentiellement introduire des inexactitudes dans la détermination du module d'indentation. La figure 2 montre une photographie de l'échantillon utilisé pour l'indentation latérale.

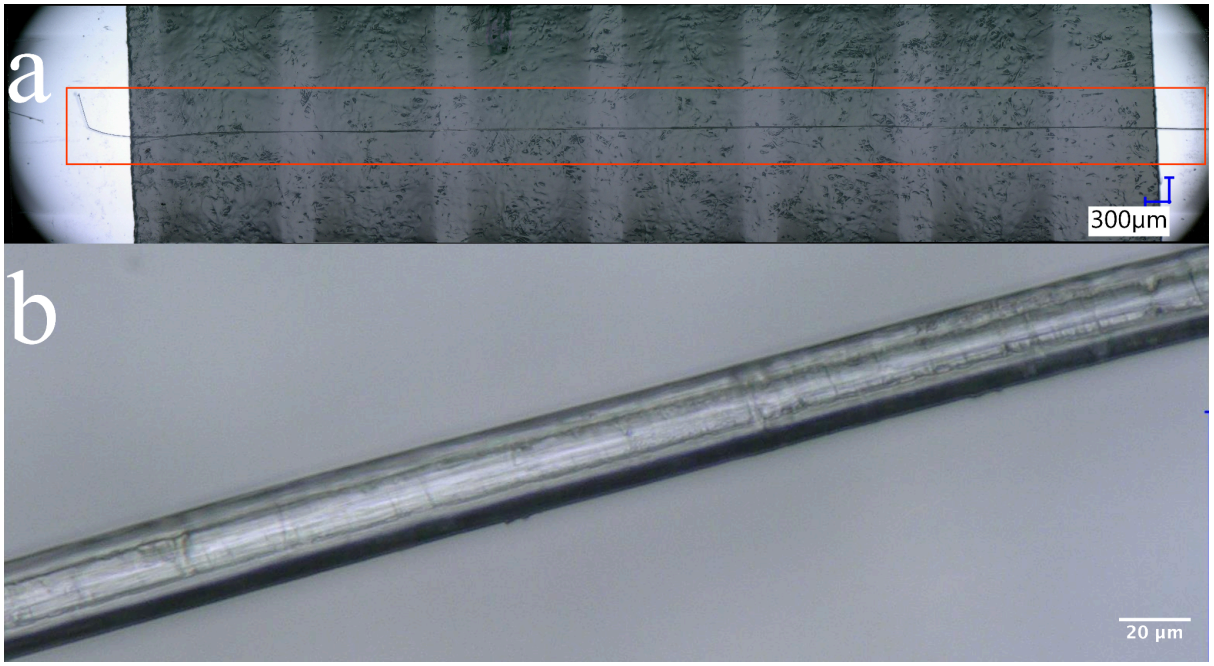

Figure 2. Image au microscope optique de la fibre de lin en montage <<planaire>>. a) Image au microscope optique montrant la fibre de lin (boîte rouge) fixée à la puce de silicium. b) Image au microscope zoomée de la fibre de lin à tester.

Les échantillons utilisés dans ces études expérimentales ont été extraits de tiges à différents stades du processus de rouissage, désignés R0 (début du rouissage), R5, R10, R15 (stade de rouissage optimal) et R20 (stade de rouissage excessif). Les intervalles entre ces stades ont été espacés de 2 semaines entre R0 et R5, de 2 semaines entre R5 et R10, de 2 semaines entre R10 et R15, et de 4 semaines entre R15 et R20. Les mesures ont été prises à quatre endroits différents sur les fibres de lin. Ces endroits comprenaient les deux zones d'extrémité (droite et gauche) des fibres et deux zones intermédiaires sur la longueur de la fibre. La figure 3 montre une photographie AFM des zones dentelées à la surface de la fibre.

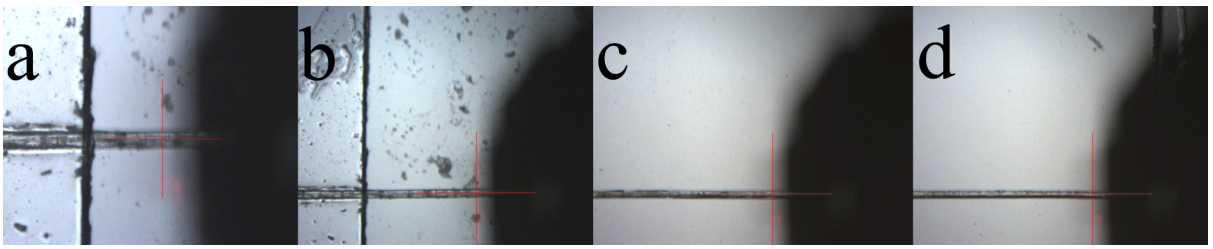

Figure 8. Exemples typiques d'images AFM des différentes zones d'indentation pour les échantillons de fibres de lin orientées en plan de R15. a) Zone 1, b) Zone 2, c) Zone 3, d) Zone 4.

Les figures 4, 5 et 6 donnent une représentation visuelle des histogrammes montrant la distribution des valeurs E^* extraites qui sont conformes au modèle hertzien, en utilisant 650 mesures provenant des trois phases de rouissage.

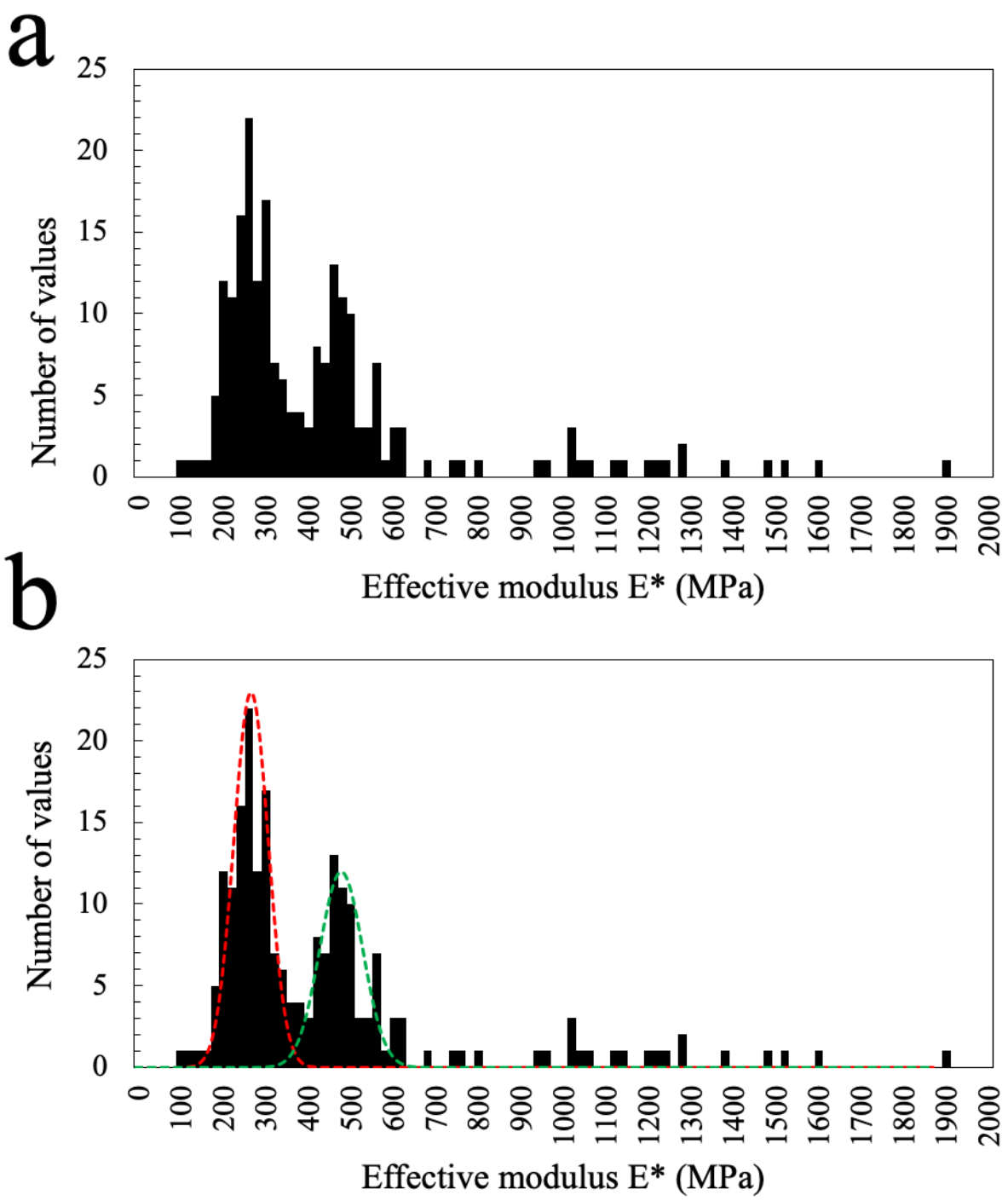

Figure 4. Histogrammes du module effectif extrait des fibres de lin provenant d'une phase de sous-retrait. (a) Histogramme des valeurs triées correspondant au modèle hertzien, (b) Histogramme des valeurs triées correspondant au modèle hertzien avec un ajustement gaussien.

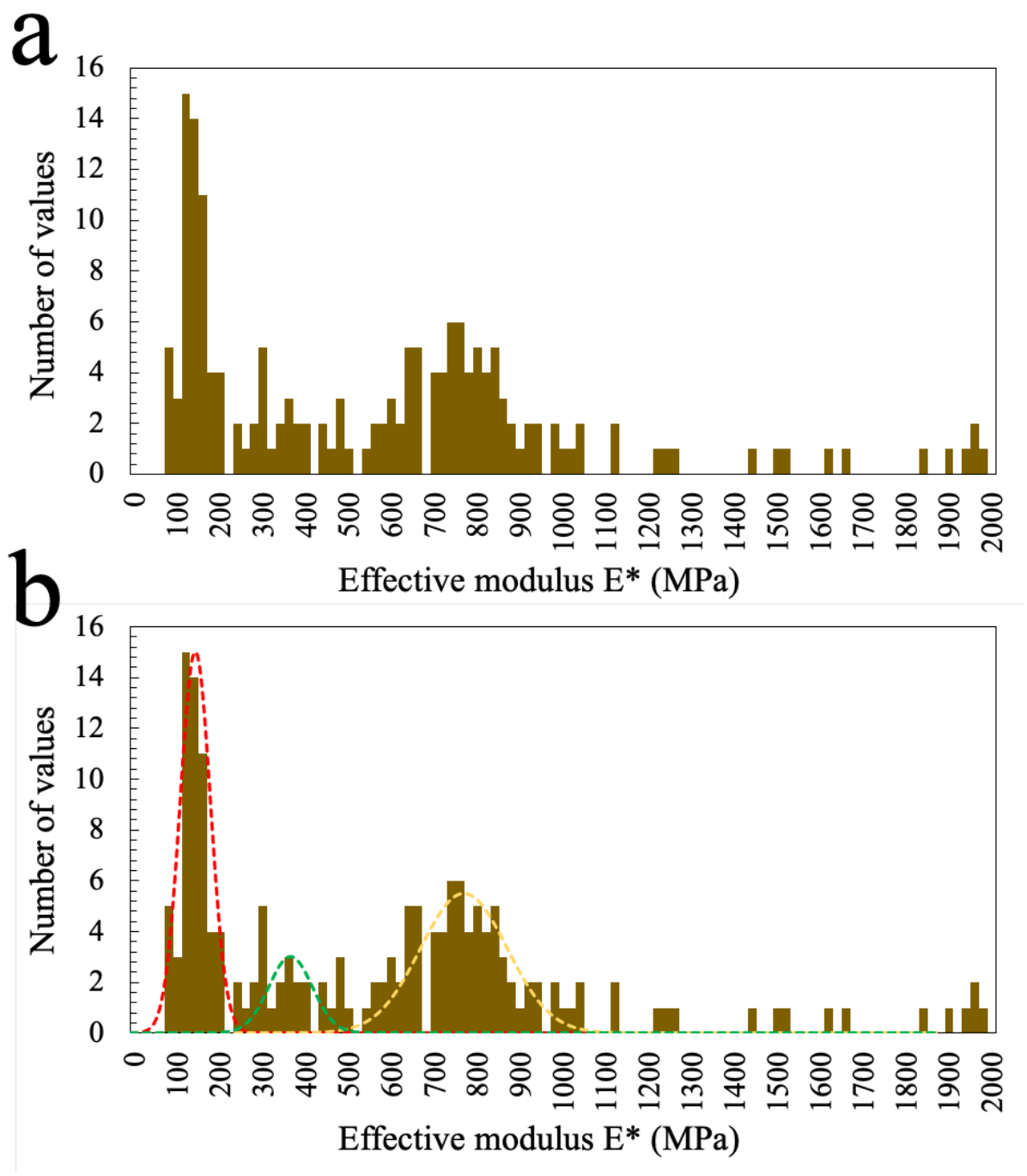

Figure 5. Histogrammes du module effectif extrait des fibres de lin à partir d'une phase de rouissage optimal. (a) Histogramme des valeurs triées correspondant au modèle hertzien, (b) Histogramme des valeurs triées correspondant au modèle hertzien avec un ajustement gaussien.

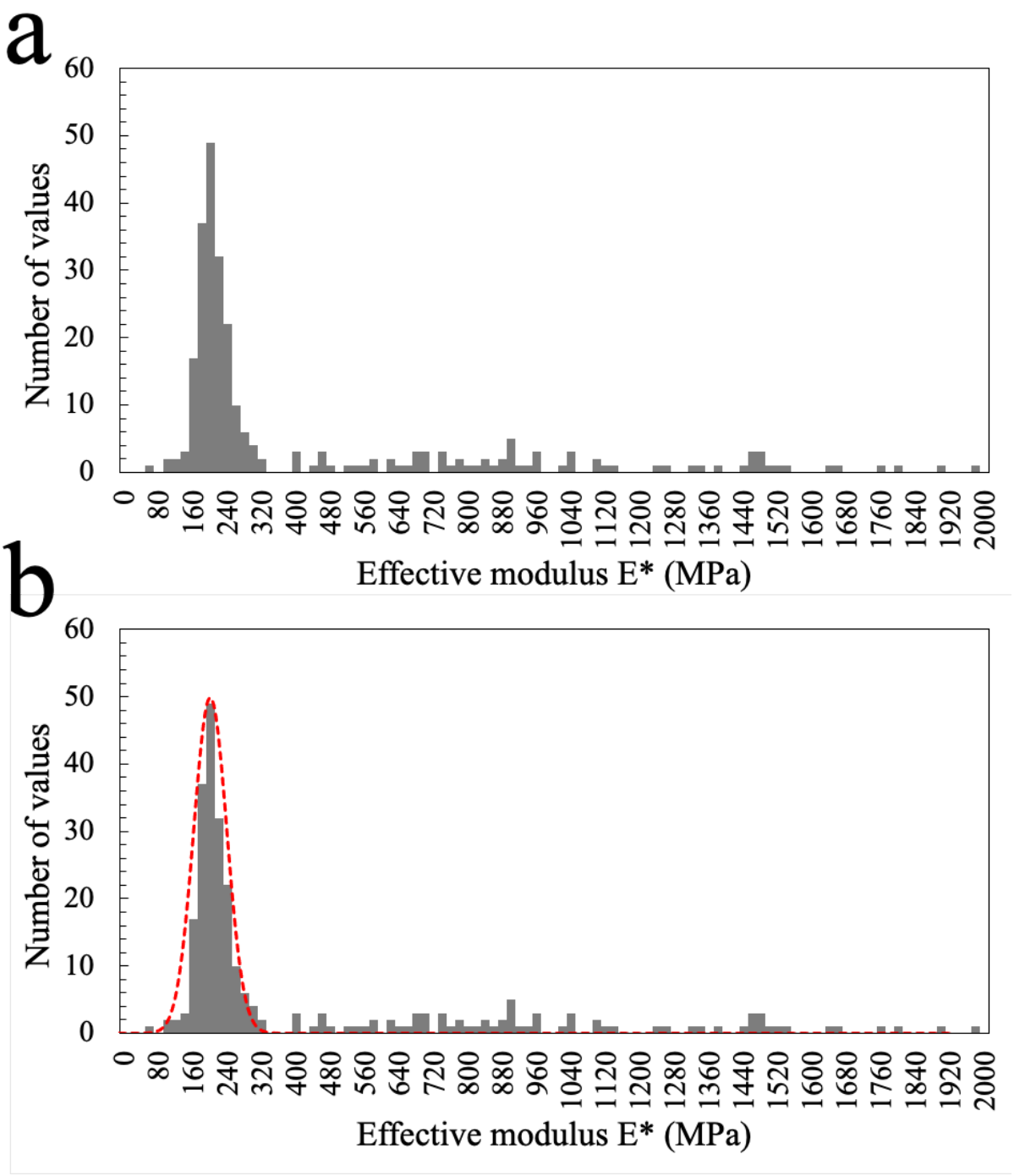

Figure 6. Histogrammes du module effectif extrait des fibres de lin à partir d'une phase de rouissage optimal. (a) Histogramme des valeurs triées correspondant au modèle hertzien, (b) Histogramme des valeurs triées correspondant au modèle hertzien avec un ajustement gaussien.

La figure 4 montre les histogrammes des données pour les phases de sous-retrait. La figure 4a représente les données brutes et montre deux pics distincts, l'un à 250 MPa et l'autre à 480 MPa. Pour mieux comprendre ces résultats, les histogrammes ont été ajustés avec des

fonctions gaussiennes, comme le montre la figure 4b. L'ajustement rouge correspond au pic à 250 MPa, tandis que l'ajustement vert correspond au pic à 480 MPa.

Au fur et à mesure que le processus de rouissage progresse et que le point de rouissage optimal est atteint, on observe un changement notable dans les modèles de données (voir figure 5a). Cette transformation est particulièrement évidente dans l'histogramme de gauche de la figure 5b. Le pic rouge subit un déplacement significatif vers une valeur plus basse et est maintenant enregistré à 150 MPa. Le pic vert reste relativement stable mais connaît une réduction du nombre de mesures à l'intérieur de ce pic par rapport à l'étape de sous-retrait. Dans le même temps, un nouveau pic caractérisé par la couleur jaune apparaît à environ 760 MPa, comme le montrent les histogrammes de droite de la figure 5b.

Cependant, lorsque le rouissage progresse au-delà de la phase optimale, tous les pics convergent vers une valeur de 220 MPa, comme le montrent les histogrammes des figures 6a et 6b. Ces résultats suggèrent fortement qu'il existe une variation significative à la surface de la fibre, indiquant l'influence du rouissage à différents stades sur la surface de la fibre. Pour mieux comprendre l'effet du temps de rouissage sur la surface de la fibre, l'analyse se concentrera sur les valeurs E* correspondant à ces pics. Par conséquent, les valeurs correspondant aux positions des pics sont tracées en fonction du temps de rouissage. La figure 7 montre le tracé obtenu.

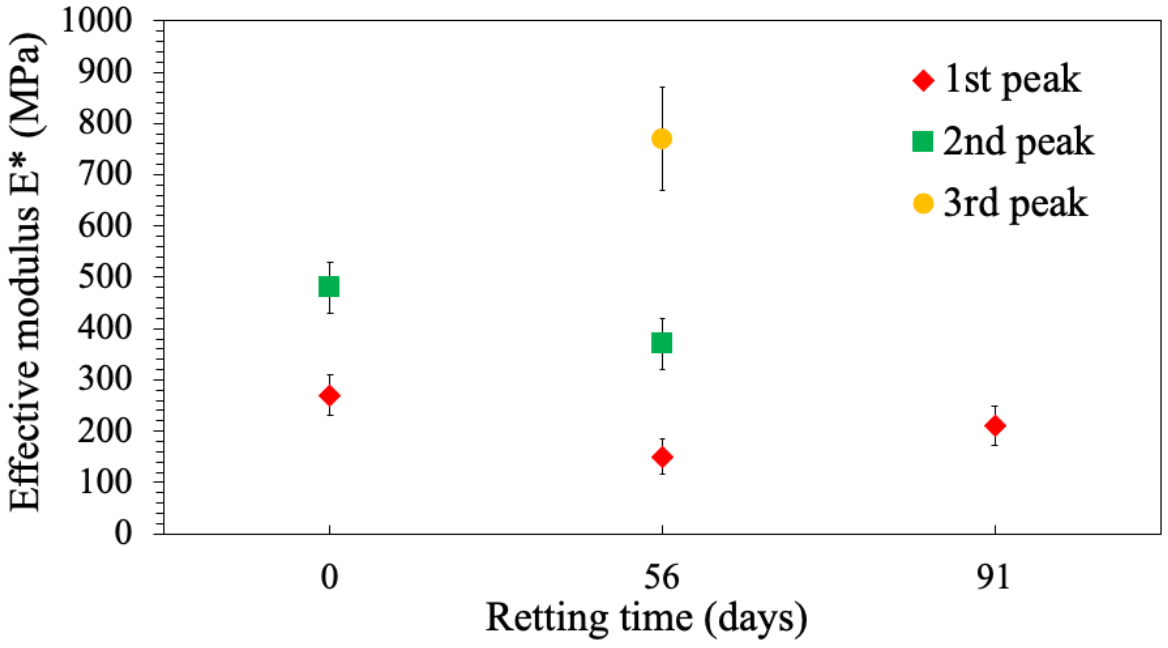

Figure 7. Graphique du module effectif moyen des faces de fibres de lin extraites par nanoindentation AFM en fonction de l'étape de rouissage.

La figure 7 montre un graphique du comportement du module effectif moyen maximal en fonction du temps de rouissage. Les résultats montrent un pic avec une valeur entre 150 et

250, qui est constant en fonction des 3 phases de rouissage, comme représenté par les diamants rouges. Le deuxième pic apparaît au début de la phase de rouissage à une valeur de 480 MPa, représentée par les carrés verts. Au fur et à mesure que le rouissage progresse, ce pic apparaît également au point de rouissage optimal à 360 MPa, représenté par le carré vert. Cependant, ce pic disparaît au-delà du point de rouissage optimal. Malgré les valeurs indentées, ce résultat indique que la nanoindentation a pu indenter la surface de la fibre de lin et produire une tendance qui montre de manière évidente et claire l'influence du rouissage sur la surface de la fibre de lin en fonction du temps de rouissage.

Considérons la figure 8. Dans le chapitre précédent, le module de l'ensemble de la fibre de lin hétérogène a été mesuré. La figure 8a montre la nature hétérogène d'une seule fibre de lin. Les mesures micromécaniques n'ont pas permis de distinguer les propriétés mécaniques des composants individuels des fibres. En revanche, l'AFM par nanoindentation de fibres de lin orientées planaire est capable de mesurer le module de la surface externe (paroi cellulaire primaire) des fibres de lin – voir Figure 8b. Comme c'est cette surface qui est « exposée » au rouissage, il semble raisonnable de mesurer l'évolution de cette surface en fonction du rouissage. Avant de poursuivre la discussion, rappelons que les mesures micromécaniques suggèrent que le module hétérogène des fibres de lin ne change pas significativement avec le rouissage, même au cours du rouissage. De plus, l'expérimentation AFM par nanoindentation de fibres de lin à orientation planaire à différentes étapes de rouissage et de surrouissage montre un changement dans leur surface externe.

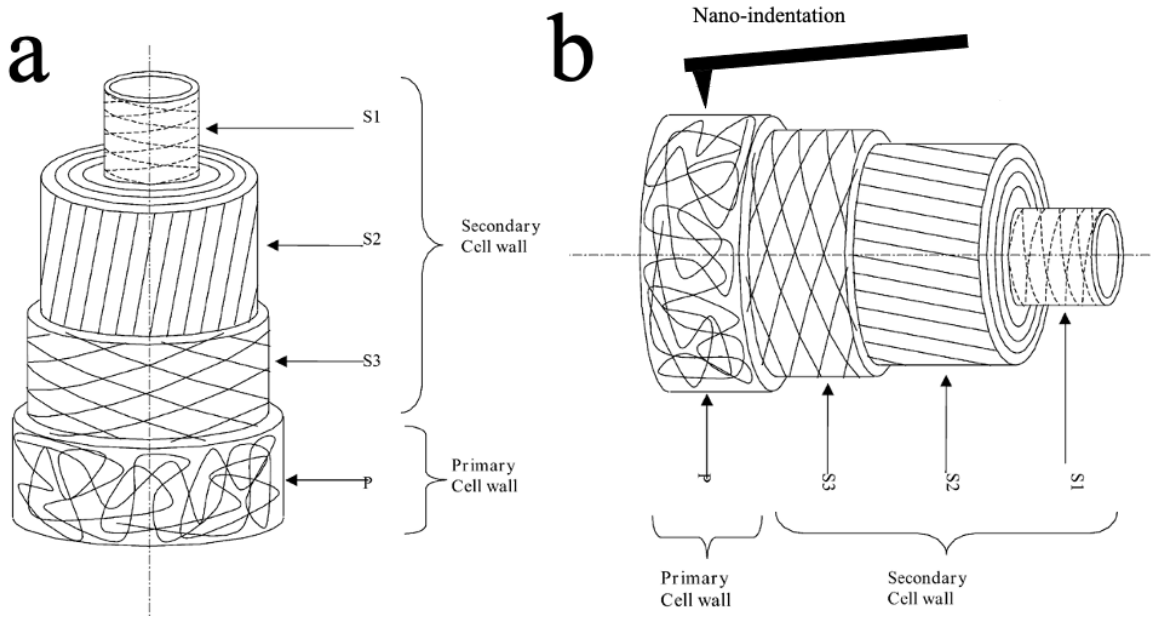

Figure 8. La structure complexe hétérogène du matériau composite en fibres de lin.

La résistance exacte à la flexion de la fibre a été déterminée en testant un ensemble de données de 11 échantillons. Ces tests aboutissent à une valeur moyenne de résistance à la flexion de 459,03 ± 28,06 MPa. Notre technique originale basée sur un cantilever fournit une faible dispersion des données. L'erreur sur ces mesures est bien inférieure à celle qui peut être obtenue à l'aide de moyens d'essai de traction macroscopiques.

La figure 8 fournit une représentation visuelle de la structure complexe et hétérogène de la fibre de lin, renforçant sa classification en tant que matériau composite complexe. En particulier, la figure 16a illustre la complexité interne de ce matériau. Le composite de fibres de lin est composé de parois cellulaires primaires et secondaires, un concept qui a été exploré précédemment. Dans la paroi cellulaire secondaire se trouvent trois couches distinctes appelées S1, S2 et S3. La présence de ces couches rend la paroi cellulaire secondaire plus rigide, et elles sont caractérisées de manière reconnaissable par l'orientation des fibres et ont une composition diversifiée de polysaccharides, notamment la pectine, la lignine et l'hémicellulose.

Compte tenu de la similarité de la composition chimique et des activités enzymatiques des micro-organismes lors du rouissage, il est alors possible que l'influence du rouissage sur la paroi cellulaire des fibres puisse être observée au niveau moléculaire, notamment en ce qui concerne les sucres présents dans cette région.

Afin de mieux comprendre ce phénomène, nous avons utilisé l'approche sans résine de nanoindentation AFM pour étudier les propriétés mécaniques de la surface des fibres de lin, avec un accent particulier sur la paroi cellulaire primaire. Ce choix repose sur la compréhension que la paroi cellulaire primaire est le premier élément structurel de la fibre à l'interphase avec la lamelle médiane à subir des modifications s'il y a influence du rouissage sur cette zone. La figure 16b fournit une représentation visuelle de la méthode utilisée dans notre étude. Cette méthode se concentre sur l’indentation de la surface latérale de la fibre de lin, fournissant avec précision un aperçu mécanique des composants primaires de la paroi cellulaire, comme le montre la figure 8b. Ce qui distingue notre approche est sa capacité à effectuer une indentation en temps réel, ce qui, contrairement aux méthodes précédentes utilisant de la résine et une orientation verticale, nous permet de démontrer efficacement l'influence du rouissage sur la surface des fibres.

Il convient de noter que le modèle de Hertz utilisé ici, bien que peu adapté à de tels échantillons, a été utilisé dans notre étude. Cette décision a été motivée par la possibilité de révéler des tendances dans les données. Ces tendances ne visent pas à quantifier précisément le module à l'échelle nanométrique, mais répondent à un objectif qualitatif : observer une tendance, illustrant l'influence du rouissage sur les propriétés mécaniques de la fibre en temps réel. Cependant, nous avons également pu obtenir des mesures quantitatives à l’échelle nanométrique. Les résultats montrent une tendance intéressante de trois pics différents, représentant trois valeurs différentes du module effectif, en fonction de la période de rouissage. Compte tenu du manque de recherches et d'investigations antérieures dans ce domaine spécifique, notamment en ce qui concerne l'indentation de la surface latérale de la fibre, nous sommes confrontés au défi d'identifier avec précision le

matériau exact soumis à l'indentation. Cependant, même si une identification définitive reste insaisissable, nous pouvons proposer des hypothèses possibles. Une de ces hypothèses concerne le module des polysaccharides présents dans la paroi cellulaire primaire de la fibre de lin. Il est concevable que les mesures de nanoindentation indentent les propriétés mécaniques de ces polysaccharides. Alternativement, les mesures peuvent inclure certains polysaccharides qui sont soit attachés de manière persistante à l'interface fibre-lamelle médiane, soit exposés après dégradation par l'activité enzymatique au cours du processus de rouissage. Des recherches et des analyses supplémentaires sont nécessaires pour clarifier cet aspect intrigant de l'étude.

Cependant, il convient de noter que la tendance obtenue par nanoindentation ne concorde pas avec le module obtenu par l'approche micromécanique. Cet écart est dû au fait que la valeur de nanoindentation représente uniquement le module de la surface de la fibre, comme décrit sur la figure 16b. Sachant que l'épaisseur de la paroi cellulaire primaire est de 0,2 um, dans ce test de nanoindentation, une profondeur de seulement 10 nanomètres est indentée. Il est donc clair que cette mesure est spécifique à la surface de la paroi cellulaire primaire et n'englobe pas l'intégralité de la paroi cellulaire fibreuse, ni même la fibre dans son ensemble composite hétérogène.

Les mesures ici peuvent être facilement comparées aux travaux de Capron et al. 2017. Caractérisation mécanique de la paroi cellulaire des fibres végétales par Microscopie à Force Atomique. Au CFM 2017-23ème Congrès Français de Mécanique. Capron et coll. utilisé les mesures Peak Force QNM AFM pour mesurer de manière semi-quantitative le module des sections transversales des fibres de lin incorporées dans la résine. Premièrement, ils montrent clairement que la résine est présente dans la partie lumière des fibres. Deuxièmement, ils rapportent un module d'environ 20 GPa pour l'ensemble de la fibre, ce qui concorde très bien avec nos mesures micromécaniques. Troisièmement, ils signalent un module beaucoup plus faible dans les tissus situés entre les fibres, là où il est peu probable que la résine atteigne. Cette valeur inférieure << 1 GPa semble ici en accord avec nos observations au niveau de la paroi latérale de la fibre.

Les conclusions du Chapitre 7

La microscopie à champ proche (nanoindentation AFM) peut être utilisée pour étudier la section transversale et les côtés des fibres de lin individuelles. En outre, cette étude peut être réalisée en fonction de l'avancement du rouissage. La nanoindentation AFM peut être utilisée pour mesurer le module mécanique localement sur une partie d'une fibre de lin. Dans un premier temps, une méthode standard de préparation des échantillons a été utilisée pour préparer des sections transversales de tiges de lin afin de permettre la microscopie en champ proche de leurs fibres de lin à différents stades de rouissage. Le module mécanique a été extrait de ces mesures par nanoindentation AFM en appliquant le modèle de Hertz. La méthode standard de préparation des échantillons consiste à imprégner la tige de lin d'une résine. Les mesures AFM par nanoindentation ont révélé quelques observations intéressantes. Le module a pu être extrait à partir du sondage des sections transversales des fibres, comme d'autres l'ont fait. Cependant, des tests ont également été effectués dans d'autres zones de la section transversale de la tige de lin, notamment les régions du xylème et leurs pores. Il est intéressant de noter que le module dans cette zone était similaire à celui mesuré dans les zones de fibres, ce qui suggère que la résine a imprégné de nombreuses parties de la tige.

Afin d'éviter l'utilisation de la résine et de ne sonder que la partie externe des fibres, nous avons mis au point une approche originale de montage planaire pour effectuer l'AFM sur des fibres uniques reposant à plat sur une puce hôte. Nous avons pu monter plusieurs fibres individuelles de cette manière à différents stades de rouissage. L'AFM a été réalisée sur plusieurs zones le long de la surface d'une seule fibre–c'est un autre avantage de ce montage d'échantillons avec l'absence de résine. Le nombre total de mesures était de 650. L'AFM a révélé des résultats intéressants pour le module à la surface des fibres en fonction du rouissage. Cependant, ces résultats ne concordent pas avec les résultats micromécaniques.

Tout d'abord, il est important de noter que le module obtenu par nanoindentation à l'aide de la microscopie à force atomique (AFM) est nettement inférieur à celui obtenu par l'approche micromécanique. La technique micromécanique a donné un module effectif moyen compris entre 150 et 770 MPa, tandis que la méthode de microindentation a donné un module de 22 GPa pour l'ensemble de la fibre. Cette différence de mesure est attribuée aux raisons suivantes. L'approche micromécanique fournit une évaluation du module pour l'ensemble de la fibre, y compris les parois cellulaires primaires et secondaires, leurs couches et les polysaccharides. En revanche, la nanoindentation AFM ne pénètre qu'à une profondeur de 10 nm. Notamment, la profondeur de la paroi cellulaire primaire dans le composite de fibres est d'environ 200 nm, comme l'indique la référence. Cela suggère que la technique de nanoindentation concerne principalement la surface de la paroi cellulaire primaire. Les résultats de cette technique montrent trois pics intéressants, chacun caractérisé par des valeurs de module différentes en fonction du temps de rouissage. L'évolution de ces pics au cours du rouissage montre une tendance convaincante : Le premier pic a une valeur constante et reste stable au fur et à mesure que le rouissage progresse. Le deuxième pic subit une diminution au point de rouissage optimal et disparaît ensuite au-delà de ce point, le troisième pic apparaît exclusivement au point de rouissage optimal.

Bien qu'il n'y ait pas d'études antérieures servant de point de référence pour identifier de manière concluante le matériau indenté, la tendance observée démontre clairement l'influence du rouissage sur la surface de la fibre. Cette observation est cohérente avec le fait que l'activité enzymatique prolongée pendant le rouissage excessif est connue pour avoir un effet néfaste sur la paroi cellulaire primaire des fibres et que le module effectif résultant pourrait être attribué aux propriétés mécaniques des structures biochimiques telles que la lignine, la pectine et les hémicelluloses présentes dans les parois cellulaires des fibres, en particulier la paroi cellulaire primaire.

Enfin, nous notons que l'approche du montage planaire n'exclut pas l'approche du montage en coupe transversale, mais qu'il s'agit plutôt d'une technique complémentaire qui peut être ajoutée à la boîte à outils des chercheurs, comme le sont d'ailleurs les autres techniques et approches originales développées dans le cadre de la thèse de doctorat.

Chapitre 8

Teneur en eau des tiges : Impact sur les performances des outils

Les principaux résultats du Chapitre 8

Le travail présenté dans ce chapitre diffère des chapitres précédents car il étudie la teneur en eau des tiges de lin, notamment sous l'effet de la pluie. Les tiges de lin, comme de nombreuses structures végétales, contiennent de l'eau par nature. Elles peuvent également contenir de l'eau en raison de l'exposition à la rosée et à la pluie. La quantité d'eau contenue dans les tiges de lin a une influence déterminante sur leurs propriétés mécaniques. Tout enfant qui a joué avec de la paille mouillée le sait. Dans le contexte de cette thèse, les variations de la teneur en eau peuvent affecter de manière significative la rigidité et la résistance des tiges de lin, ce qui complique la tâche des outils en temps réel (travaillant potentiellement sur le terrain) utilisés pour contrôler l'influence du rouissage sur l'extraction mécanique des fibres de lin. La nature variable de la teneur en eau des tiges de lin introduit un niveau de complexité dont il faut tenir compte lors de l'utilisation de capteurs sur le terrain, car elle pourrait conduire à une détermination incorrecte du point de rouissage optimal. La teneur en eau variable des tiges de lin provient principalement de deux sources : (i) l'exposition à la rosée et (ii) les précipitations. Afin de développer un outil fiable, une étude approfondie du comportement de la teneur en eau des tiges de lin est donc essentielle. Une telle étude pourrait permettre d'affiner le fonctionnement et la synchronisation des capteurs utilisés sur le terrain.

Dans la première expérience, nous avons utilisé une douchette à main spéciale salle blanche pour pulvériser doucement les échantillons préparés. L'idée était d'imiter la légère pluie d'été que l'on trouve dans la nature. Cela a été réalisé pendant 5 minutes à une température de salle blanche de 21°C. Une température de 21°C convient pour l'expérience car ce serait une température diurne typique en juillet/août dans les climats de culture du lin. Après la pulvérisation, nous avons retiré les échantillons et les avons pesés toutes les 5 minutes pendant qu'ils séchaient à température ambiante et la masse a été enregistrée. La figure 1 montre l'expérience décrite.

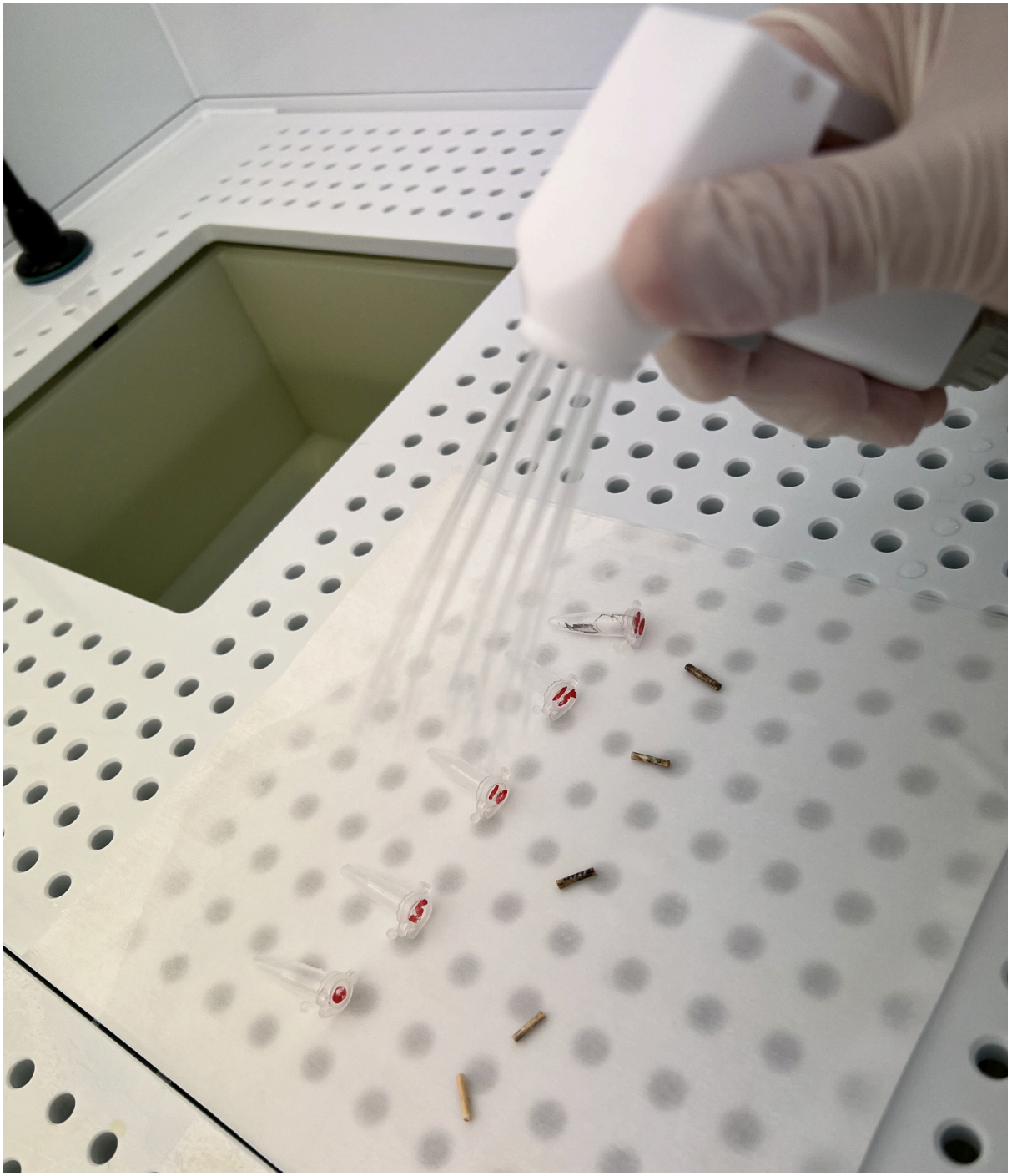

Figure 1. Expérience simulant une pluie légère (d'une durée de 5 minutes) sur les segments de tiges de lin. Il s'agit d'une légère pluie de soleil typique dans le champ.

Pour la deuxième expérience, nous avons attendu que les échantillons de la première expérience soient complètement secs (c'est-à-dire que la masse de l'échantillon est revenue à la masse initiale pondérée avant de réaliser l'expérience). Ces échantillons séchés ont ensuite été trempés dans des tubes Falcon d'un volume de 1 000 µl pendant une nuit. Cette expérience ressemble à une forte pluie qui dure environ 12 heures comme sur le terrain. Après trempage, les échantillons ont été retirés et laissés sécher à nouveau à température

ambiante. Comme auparavant, le poids des échantillons a été mesuré et enregistré manuellement toutes les 5 minutes pendant leur séchage. Voir la Figure 2.

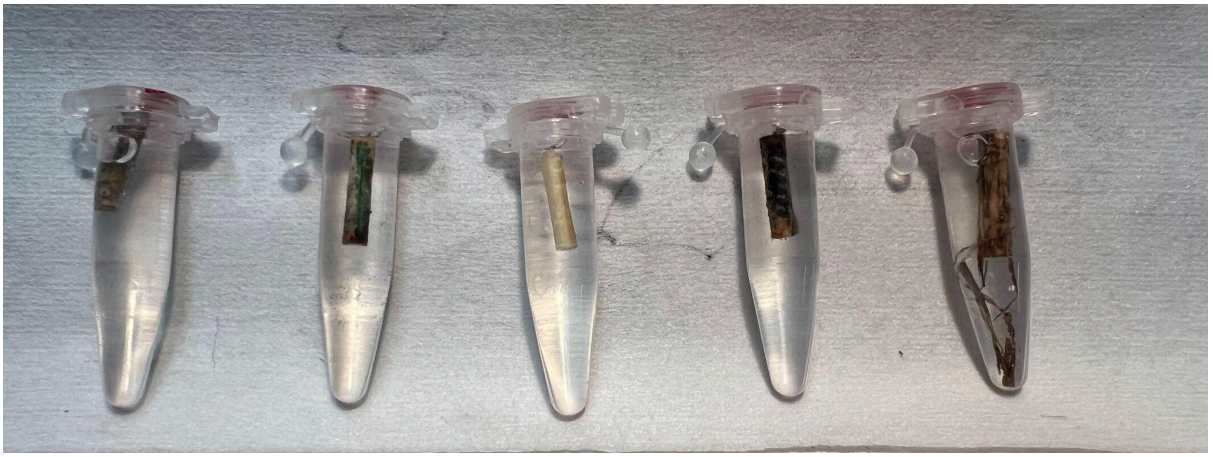

Figure 2. Expérience simulant de fortes pluies (d’une durée de 12 heures) sur les segments de tiges de lin. Il s'agirait d'une forte pluie atypique sur le terrain en été. Bien que rare, cela peut arriver.

Suite à l'enregistrement des variations de masse dans le temps à température ambiante, les données obtenues ont été tracées et analysées pour extraire les informations pertinentes. Voir la Figure 3

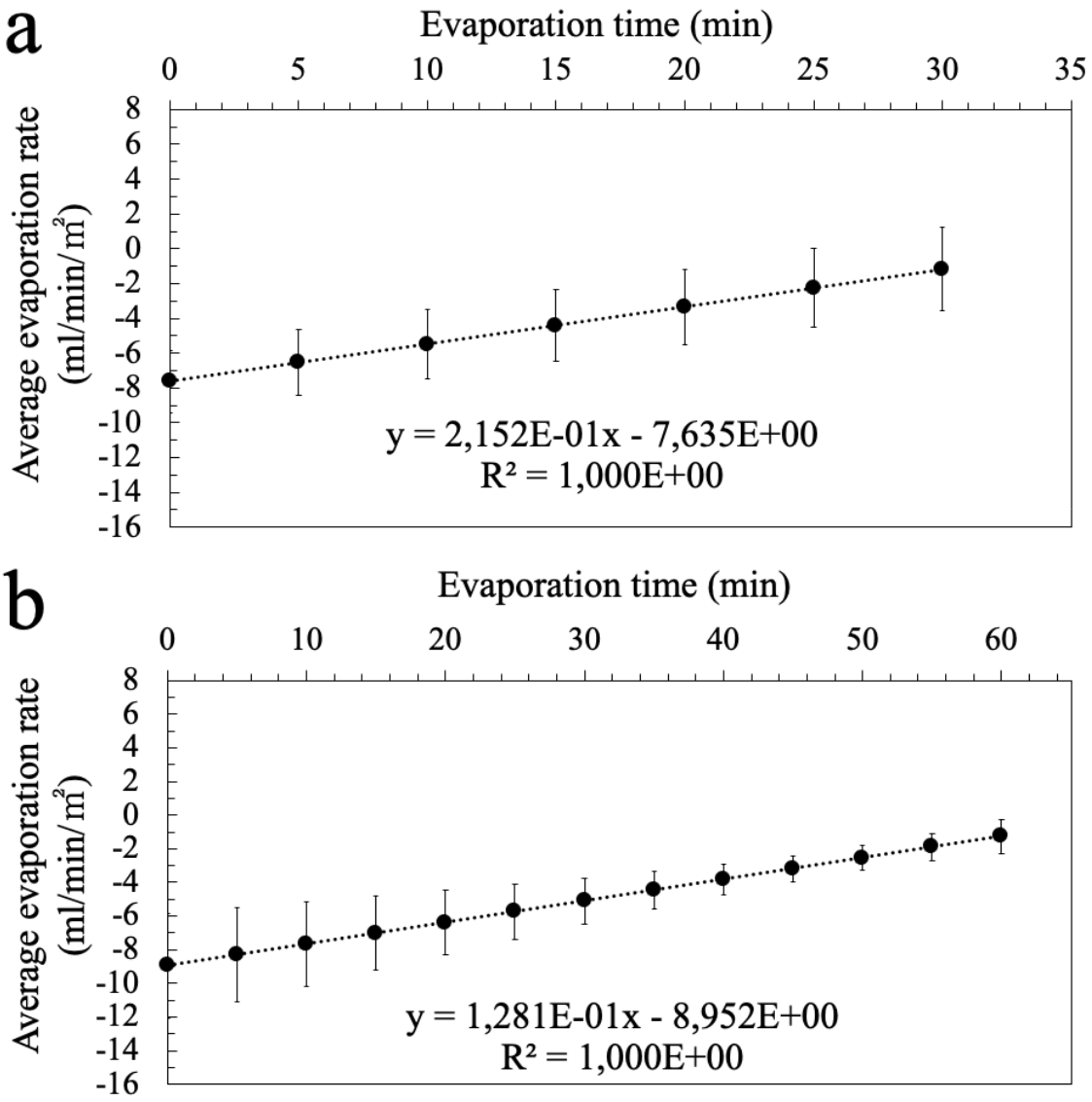

Figure 3. Tracé du taux d'évaporation volumique moyen (ml/min/m2) des tiges de lin mouillées en fonction du temps. (a) Données pour une pluie légère (5 min) sur les segments de tiges et (b) données pour une forte pluie (12 heures) sur les segments de tiges.

La figure 3 montre un graphique du taux d'évaporation moyen des tiges de lin rouies en fonction du temps après une simulation d'averse de 5 minutes - voir figure 3a - et de 12 heures de forte pluie - voir figure 3b. Ces graphiques sont très utiles et permettent de prévoir le temps de séchage du lin sur le terrain.

Discutons maintenant des résultats. Premièrement, les segments de tige absorbent l'eau. Cela est vrai pour une averse légère de 5 minutes et une forte pluie de 12 heures. Les

segments de tige absorbent plus d'eau après un trempage de 12 heures qu'une douche de 5 minutes. Au temps zéro, ces ratios sont respectivement de 1,88 ± 0,23 et 3,02 ± 0,15.

Deuxièmement, les segments de tige perdent du poids par évaporation de l'eau adsorbée. Cette perte de masse n'est pas linéaire dans le temps, contrairement par exemple à l'évaporation d'une surface d'eau. La perte de masse est également différente pour chaque tige, car chaque tige a un diamètre différent.

Troisièmement, la perte de masse en fonction du temps peut être ajustée à l'aide d'une fonction polynomiale pour toutes les tiges. Ces polynômes peuvent être différenciés par rapport au temps et tracés sous forme de fonctions linéaires. Ces fonctions linéaires peuvent être divisées par les surfaces des tiges individuelles pour « normaliser » les données et calculer le taux d'évaporation de l'eau des tiges. Lorsque cela est tracé, le taux d'évaporation des tiges semble être très comparable d'une tige à l'autre. De plus, les taux d'évaporation (et leurs pentes, c'est-à-dire le taux de variation des taux d'évaporation dans le temps) sont très comparables pour les pluies légères et pour les fortes pluies.

Le phénomène de perte de masse, de taux de perte de masse moyen et de taux d'évaporation moyen montre une plus grande accélération dans les échantillons R20. Ce phénomène peut être attribué à l'absence de tissus externes dans les échantillons R20, où un rouissage avancé conduit à une dégradation des tissus externes (illustré dans le chapitre macro-mécanique), exposant ainsi les tissus internes. En conséquence, le taux d'absorption de l'eau par les tissus externes ainsi que par les parties ligneuses est presque nul, ce qui entraîne une évaporation plus rapide de l'eau de la surface du bois.

Le taux d'évaporation variable observé des tiges de lin est intéressant. Le taux d'évaporation diminue linéairement avec le temps. Cela indique un problème lié au débit massique. Un séchage non linéaire de la paille de lin a déjà été observé et plusieurs groupes ont été modélisés. Nos ajustements polynomiaux sont en accord avec la modélisation de Midilli et Kucuk (2003).

Model name	*Equation*	*Reference*	*Equation no.*
Newton	$MR = e^{-kt}$	Ayensu (1997)	(2)
Page	$MR = e^{-kt^n}$	Karathanos and Belessiotis (1999)	(3)
Henderson and Pabis	$MR = a\, e^{-kt}$	Akpinar et al. (2003)	(4)
Modified Page	$MR = e^{(-kt)^n}$	Diamante and Munro(1993)	(5)
Logarithmic	$MR = a\, e^{-kt^n} + c$	Midilli and Kucuk (2003)	(6)
Wang and Singh	$MR = 1 + at + bt^2$	Midilli and Kucuk (2003)	(7)

Tableau 1. Différents modèles de séchage des tiges de lin trouvés dans la littérature. K est la constante de vitesse de séchage (min-1), les autres paramètres sont des constantes définies dans les références et MR est le taux d'humidité.

Enfin, nos données indiquent que dans le pire des cas, c'est-à-dire des tiges de grand diamètre (3 mm) soumises à 12 heures de fortes pluies, il faudrait attendre 4 heures pour être sûr que les tiges sont suffisamment sèches pour effectuer des tests mécaniques.

Les conclusions du Chapitre 8

Il a été possible de mesurer avec précision le taux d'évaporation de l'eau des tiges de lin ayant absorbé de l'eau par le biais d'une pluie simulée. Deux types de précipitations simulées ont été utilisés : une pluie légère de 5 minutes et une pluie forte de 12 heures. Les taux d'évaporation ont été mesurés pour des tiges de lin à différents stades de rouissage : du premier jour jusqu'à 3 mois plus tard. On a observé que les taux d'évaporation étaient comparables pour toutes les tiges (tous les stades de rouissage) qui contenaient encore leur tissu extérieur. Pour les tiges qui n'ont plus de tissu extérieur (R20/3 mois de rouissage au champ), les taux d'évaporation sont clairement différents : ils sont plus importants. On a observé que les taux d'évaporation de toutes les tiges diminuait avec le temps. Ceci est cohérent avec l'évaporation d'un matériau poreux. Les résultats sont également en accord avec les observations faites par d'autres. En outre, les taux d'évaporation ont diminué linéairement avec le temps. Cela implique une diminution quadratique de la masse en fonction du temps, et c'est ce que nous avons observé dans les expériences. Cela correspond à un modèle proposé pour l'évaporation de l'eau des tiges de lin humides. Enfin, en termes pratiques, cette expérience a produit un résultat significatif : la possibilité de déterminer le temps de séchage des tiges de lin sur le terrain. Le temps de séchage maximal observé pour des tiges de lin individuelles était de 75 minutes, c'est-à-dire des tiges qui seraient utilisées pour la fabrication d'un outil. Ce résultat important signifie que le capteur peut reprendre son fonctionnement après seulement 75 minutes de temps ensoleillé à une température de 21°C après une période de pluie. Indépendamment du stade de rouissage ou du diamètre de l'échantillon, les résultats montrent un taux d'évaporation constant tout au long du processus de rouissage. Cela suggère que tous les échantillons sur le terrain, quel que soit leur diamètre ou leur teneur en eau, ont le même taux d'évaporation. Ce résultat est prometteur car il suggère que le capteur peut être utilisé efficacement sur une large gamme d'échantillons sur le terrain, indépendamment de leur taille ou de leur teneur en eau.

Chapitre 9

Perspectives

Les travaux futurs

Trois axes principaux de travaux futurs peuvent être envisagés après le doctorat : (i) le développement d'un outil commercial pour le lin et l'extension de l'approche à d'autres cultures, (ii) la modélisation numérique des tiges et des fibres de lin, et (iii) l'approfondissement des techniques développées dans le cadre du doctorat.

Un outil commercial ?

Les résultats des essais mécaniques effectués dans le cadre de la thèse suggèrent qu'il est possible de mettre au point un outil capable de surveiller l'avancement du rouissage des tiges de lin. La base de cet outil est le dommage induit par la torsion sur le tissu extérieur des tiges de lin en cours de rouissage. Lorsque les tiges sont rouies de manière optimale, une certaine contrainte de cisaillement de surface quantifiable (induite par la torsion mécanique) induit des dommages observables qui peuvent être analysés par traitement d'image. Le traitement et l'analyse d'images constituent un point clé. Dans le présent travail, l'analyse des images a été effectuée manuellement. Si l'on devait utiliser plusieurs capteurs "sur le terrain", il faudrait étudier et utiliser une analyse d'image fiable pour identifier les dommages induits par la mécanique. On pourrait envisager qu'un ou plusieurs outils de ce type soient déployés de manière autonome sur le terrain et reliés sans fil dans le contexte de l'IOT. Les conditions météorologiques constituent un facteur important, car elles déterminent le taux de rouissage. Les conditions météorologiques peuvent être facilement obtenues à l'aide d'une station météorologique installée sur le terrain. Cependant, et c'est un grand cependant, les données présentées dans cette thèse, bien qu'originales et importantes, ne concernent qu'une seule période de rouissage (été 2022), une variété particulière de lin, un ensemble de conditions météorologiques (Killem 2022), un type de champ particulier. Pour valider les données mécaniques, nous concluons qu'il faudrait réaliser une étude sur dix ans. Ce travail nécessiterait un investissement important en termes d'argent, de temps, d'efforts et de volonté. Cela nécessiterait également un long partenariat entre un laboratoire de recherche public et une entreprise privée. A l'heure où nous écrivons ces lignes, il n'est pas évident de trouver un tel financement. Au-delà du lin, l'utilisation des propriétés mécaniques pour la détection dans l'agriculture 4.0 pourrait être utile pour d'autres cultures. Il est bien connu que les propriétés mécaniques des plantes évoluent avec leur croissance et leur maturité. Il est possible que des approches inspirées du travail présenté ici aient un impact sur l'optimisation d'autres cultures à base de tiges.

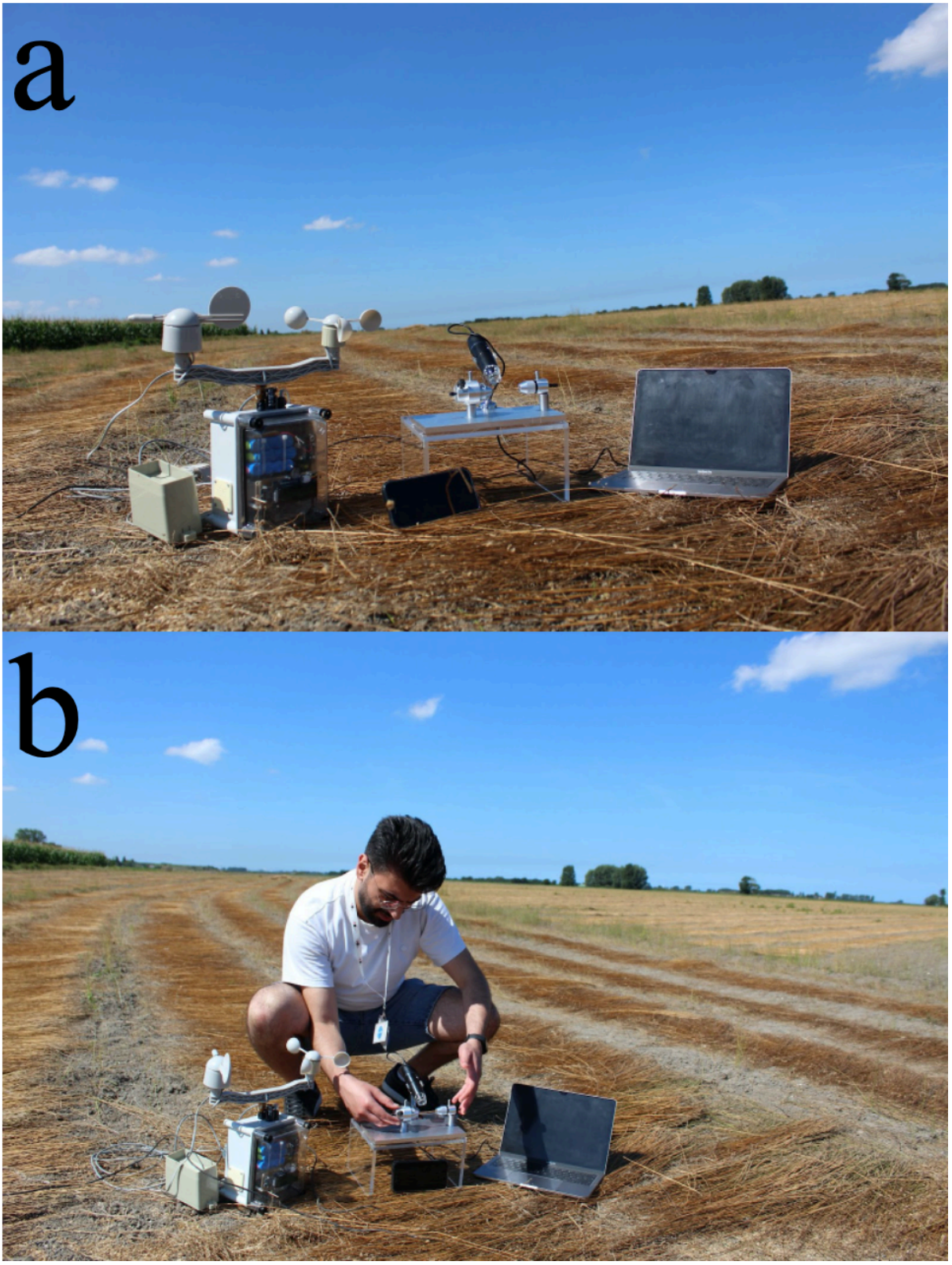

Figure 1. Évaluation d'un prototype d'outil sur le terrain lors du rouissage du lin à la rosée de l'été 2023. (a) station météorologique portable (à gauche), outil de rouissage optimisé, microscope, téléphone portable (au milieu) et PC (à droite). A noter que la station météo portable a été conçue et réalisée par Sébastien Grec (UGSF, Univ. Lille), David Delacrois et Redha Kassi (IEMN, Univ. Lille). (b) Test manuel de l'outil.

La figure 1 montre un prototype sur le terrain en évaluation lors du rouissage du lin à la rosée de l'été 2023. L'installation comprend une station météorologique portable, un outil de rouissage optimisé, un microscope, un téléphone portable et un PC connectés sans fil. La station météo portable (sondes de pluie, de vent, de température et de terrain) a été conçue et réalisée par Sébastien Grec (UGSF, Univ. Lille), David Delacrois et Redha Kassi (IEMN, Univ. Lille). Le microscope portable permet de visualiser la surface de la tige sous torsion contrôlée. La station météo est laissée sur le terrain et l'outil portable pourrait être utilisé quotidiennement.

La simulation numérique

Dans cette thèse, toutes les caractérisations mécaniques expérimentales (macro, micro et nano) des tiges et des fibres de lin ont été modélisées à l'aide d'approches analytiques. En effet, en première approximation, cela a été relativement efficace pour extraire le module mécanique et la résistance des tiges et des fibres. Les modèles analytiques utilisés à cet effet supposent une structure parfaite, élastique et homogène. Il est évident que les tiges et les fibres de lin ne sont pas parfaites et qu'il ne s'agit certainement pas de structures homogènes. C'est pourquoi la modélisation analytique ne peut extraire que le module composite et la résistance d'une structure hétérogène - en d'autres termes, les tiges et les fibres sont comme des boîtes noires. Les tiges et les fibres sont des structures très hétérogènes dont les structures internes sont complexes et composées de nombreux éléments différents. Pour aller au-delà de la modélisation très rudimentaire (bien que relativement réussie) utilisée dans cette thèse, il faudrait se tourner vers la modélisation numérique. Une telle approche pourrait être réalisée à l'aide d'un logiciel commercial tel que Comsol Multiphysics. On s'attend à ce qu'une telle étude soit très complexe car de nombreuses propriétés mécaniques des composants hétérogènes des tiges et des fibres de lin ne sont pas encore bien connues. Malgré cela, une étude pourrait être réalisée et comparée aux résultats expérimentaux.

L’extension des techniques développées dans la thèse

Comme nous l'avons vu, le travail de nanoindentation AFM dans la thèse a révélé quelques résultats et tendances intéressants en termes de valeurs de module mécanique de la surface des fibres de lin simples et de leur évolution au fur et à mesure que le rouissage progresse. Premièrement, ce travail pourrait être répété une autre année pour validation. Deuxièmement, les méthodes d'extraction des fibres simples pourraient être modifiées et affinées pour contrôler la surface mesurée. Cela pourrait impliquer des moyens chimiques qui n'ont pas été utilisés dans le travail actuel. Troisièmement, d'autres techniques de microscopie en champ proche pourraient être employées, au-delà de la nanoindentation utilisée dans l'étude actuelle. Par exemple, des techniques commerciales telles que les modes AFM <<Peak-Force>> et <<Peakforce Tapping>> de Bruker permettent d'obtenir des propriétés nano-mécaniques, telles que le module et l'adhérence, tout en obtenant simultanément une image de la topographie de l'échantillon à haute résolution. Les résultats obtenus à l'aide de ces modes peuvent être comparés à ceux obtenus par nanoindentation AFM. En plus de cette abondance d'informations physiques, des tests biologiques parallèles

sur les mêmes fibres de lin peuvent fournir des informations permettant d'interpréter et de comprendre les résultats physiques.

Les techniques mises au point pour les mesures micromécaniques pourraient être appliquées à toute une série d'autres fibres de diamètre micrométrique, comme les cheveux, afin de révéler leurs propriétés physiques.